Fakultät Wissenschaftszentrum Weihenstephan für Ernährung, Landnutzung und Umwelt

Lehrstuhl für Waldwachstumskunde

Pol-InSAR Forest Height estimation at different Frequencies: Opportunities and Limitations

Florian Albert Kugler

Vollständiger Abdruck der von der Fakultät Wissenschaftszentrum Weihenstephan für Ernährung, Landnutzung und Umwelt der Technischen Universität München zur Erlangung des akademischen Grades eines

Doktors der Forstwissenschaften

genehmigten Dissertation.

Vorsitzender: Univ.-Prof. Dr. Th. Knoke

Prüfer der Dissertation:

1. Univ.-Prof. Dr. Dr. h.c. H. Pretzsch
2. Univ.-Prof. Dr. R. Bamler
3. Univ.-Prof. Dr. I. Hajnsek (Eidgenössische Technische Hochschule Zürich/Schweiz)

Die Dissertation wurde am 03.07.2015 bei der Technischen Universität München eingereicht und durch die Fakultät Wissenschaftszentrum Weihenstephan für Ernährung Landnutzung und Umwelt am 27.11.2015 angenommen.

Doctoral Thesis

Pol-InSAR Forest Height estimation at different Frequencies: Opportunities and Limitations

presented by

DIPL.-ING. SILV. UNIV. Florian Kugler

For the degree

Dr. rer. silv.

Submitted to: **Technische Universität München (TUM)**

Doctoral Thesis

Pol-InSAR Forest Height estimation at different Frequencies: Opportunities and Limitations

presented by

DIPL.-ING. SILV. UNIV. Florian Kugler

For the degree

Dr. rer. silv.

Submitted to: **Technische Universität München (TUM)**

Abstract

Forest professionals, policy makers as well as scientists from different science fields demand a global quantitative forest inventory and a regular global forest monitoring to protect forests and to maintain the multifaceted functions of the forests for mankind. However, these demands could be fulfilled by the use of proper remote sensing tools.

This work contributes to the rapidly developing field of radar Synthetic Aperture Radar (SAR) remote sensing in particular the field of Polarimetric Interferometric SAR (Pol-InSAR). Pol-InSAR is a remote sensing technology perfectly suited for forest monitoring as it makes physical structural forest attributes accessible and may therefore also be used to get estimates of forest height. A forest height estimate may be already obtained from a single Pol-InSAR observation.

SAR offers a wide range of frequencies starting from VHF with ~100 MHz up to Ka-band with ~30 GHz. In the frame of this thesis the potential of Pol-InSAR forest height estimation and forest monitoring was investigated at X- , L- and P-band.

Forest height maps are an essential contribution to the quantitative monitoring of forests. So far, quantitative forest parameters are mainly obtained from ground measurements. Therefore, first state of the art in forest monitoring was reviewed and observation requirements for a remote sensing based forest monitoring were summarized. Subsequently, significance and role of the parameter forest height for forest inventories, forest mensuration and forest monitoring was lined out.

A survey of different remote sensing aproaches capable of providing quantitative forest information was compiled and critically reviewed, including optical remote sensing as well as LIDAR and radar remote sensing. This is followed by a chapter providing some background on SAR, polarimetry, interferometry and Pol-InSAR techniques relevant for this thesis.

Main observable of Pol-InSAR is the interferometric coherence at different polarizations. Structure models capable to explain the measured interferometric coherences were introduced, reviewed and adapted. An approach for a step by step estimation of forest height was introduced and the effect of the vertical wavenumber on the forest height inversion performance was evaluated. In addition, modified inversion approaches for single-pol data were introduced.

The behaviour of temporal decorrelation for different frequencies (X-, L- and P-band) and different temporal baselines was described.

Pol-InSAR forest height was successfully estimated and validated at L-band over boreal, temperate and tropical forests and at P-band over boreal and tropical forests. At X-band Pol-InSAR forest height estimation was demonstrated with dual-pol data and with single-pol data in combination with an external DTM by means of airborne and spaceborne (TanDEM-X) SAR.

Seasonal forest variations have been monitored by means of interferometric and polarimetric interferometric data at X-band through measurements of the polarimetric diversity and the penetration depth.

An adapted dual baseline forest height inversion approach for P-band was introduced able to compensate for the underestimation of forest height at boreal forests. Similarly, a dual baseline forest height inversion approach compensating for a scalar temporal decorrelation contribution was presented.

Looking at the results obtained in this thesis it can be concluded that Pol-InSAR forest height estimation is today a mature application, which can be operationally used and may

essentially contribute to a quantitative forest monitoring. L-band seems to be a universally applicable frequency and therefore perfectly suited for a Pol-InSAR based global forest monitoring system.

The polarimetric diversity at X-band is sometimes too small to allow Pol-InSAR forest height inversion. On the other hand penetration depth at P-band is often especially for boreal forest, too strong for a meaningful single baseline Pol-InSAR forest height inversion.

Temporal decorrelation was identified as the most disturbing factor, which can prevent Pol-InSAR forest height inversion.

Finally, suitable satellite SAR systems, i.e. SAR systems providing Pol-InSAR configurations were reviewed for their use for Pol-InSAR forest height estimation.

This doctoral thesis is a cumulative thesis and is based on six articles of which the author is in two articles first author, in three articles second author and in one article the 13th author.

Preface

The work on this thesis opened a new chapter in my life - it sent me on the longest journey I have ever taken. Geographically, it took me from the Equator to the North Pole, in the course of several measurement campaigns. However, most of the time, I spent at the Microwaves and Radar Institute of the German Aerospace Center in the beautiful surroundings of Oberpfaffenhofen. Emotionally, there were periods of great satisfaction and joy, but at the same time I had to face several disappointments. Scientifically, it gave me the unique opportunity to work with high-end technologies in the field of radar remote sensing in particular Synthetic Aperture Radar (SAR), allowing me to contribute to the design of future SAR satellite missions. However, in some situations, scientific work had to give priority to the fulfillment of basic needs (like the availability of clean drinking water during measurement campaigns). Moreover, often daily business inevitably had a higher priority than the progress of this thesis. After 11 years, 2 months and 19 days I eventually arrived at the destination “Ph.D. degree”. I hope that I never lost track to see things through the eyes of a forester and that there is practical benefit for the results produced.

Naturally, a Ph.D. thesis is influenced by different aspects in its environment and it goes without saying that after such a long time period many people passed my way, each of them leaving important marks. I am grateful to everybody who made a difference during this time with his/her help, scientific discussions or real support when there was a rough patch.

First and foremost, I would like to thank my supervisor Dr. Kostas Papathanassiou for his support and his scientific feedback and contribution. He accompanied nearly every step of my work and he was always a critical discussion partner, helping me to improve my way of scientific thinking.

A very special thanks goes to my Ph.D. advisor Prof. Dr. Dr. h.c. Hans Pretzsch for his patience and support throughout the years and for the opportunity to graduate at the chair of forest yield science of the Technische Universität München. I would also like to thank my group leader of the Pol-InSAR group, Prof. Dr. Irena Hajnsek, for her support and the organization of all measurement campaigns. I am also grateful to Prof. Dr. Alberto Moreira and Dr. Gerhard Krieger for the opportunity to do research at the Microwave and Radar Institute of the German Aerospace Center. Furthermore, I would like to thank Prof. Dr. Richard Bamler for being examiner of this thesis.

Special mention should be made of Dipl.-Ing. Ralf Horn, Dr. Rolf Scheiber, Jens Fischer and Martin Keller for their effort in E-SAR (Experimental Synthetic Aperture Radar system) data acquisition and processing. Moreover, I would like to mention the TanDEM-X team around Dr. Manfred Zink, in particular Dr. Markus Bachmann, Daniel Schulz and Dr. Michele Martone, for their straightforward support regarding TanDEM-X data.

Sincere thanks also goes to my former office mates and colleagues, Rafael Zandona-Schneider for introducing me to the basics of SAR and for his Brazilian spirit which always brought lightness to work, Dr. Seung-Kuk Lee for our joint works, valuable scientific discussions and his introduction into South Korean cuisine and Dr. Tobias Mette for the supervision during the first steps into my thesis.

A special thanks goes to Dr. Marcela Quinones and Dr. Dirk Hoekman for the great experience doing ground truth measurements in the forests of Borneo.

I would like to recognize Dr. Jaan Praks for our joint works and his company during numerous conferences.

I would also like to recognize Franziska Wanninger for her corrections of the English language.

A very special mention is reserved for Thomas Busche for his help, support and for his very special humor, Dr. Stefan Baumgartner for his help, our trip to polar bear country and to give me the viewpoint of engineering, Dr. Stefan Sauer for his help, for proof reading the SAR chapter of my thesis and for our excursions to higher mathematics and Christian Andres for his help, understanding and our discussions in Austrian dialect.

There are still many more who deserve credit and thanks: my Diploma, Master and Ph. D. students Dr. Astor Torano Caicoya, Angelo Coscia, Ernesto Imbembo and Dr. Giuseppe Parrella; Robert Metzig for our trip to the North Pole; my office mates Thomas Aulinger, Dr. Armando Marino, Dr. Esra Erten and “Frau” Friese; Dr. Matteo Nannini for his technical explanations; Dr. Koichi Iribe for my experiences in Japanese lifestyle; Ralf Moshammer for keeping in touch with forestry practice; Sybille Radzuweit for her friendly exceptional support; Dr. Viktor Böhm for the supply with LIDAR data; Dr. Robert Treuhaft for his discourse on the advantages of Cowboy boots; and Dr. Luigi Castaldo for introducing me to Naples coffee culture.

I would very much like to thank my parents Eva und Albert for their support and encouragement during the whole time.

The deepest gratitude goes to my beloved girlfriend Anja for her patience during the final phase of my thesis, for her tireless support and for taking care of most things allowing me to complete this thesis, and to my son Valentin for bringing fun and happiness to my life.

Contents

List of Symbols and Acronyms

Acronyms:

ALOS/ALOS-2	Advanced Land Observing Satellite; both are Japanese earth observation satellite with an L-band SAR antenna
ALOS PALSAR	L-band SAR of ALOS
ALOS PRISM	Optical sensor of ALOS
ASAR	Advanced Synthetic Aperture Radar; operated at C-band on ESAs' earth observation satellite Envisat
AVHRR	Advanced Very High Resolution Radiometer; multispectral remote sensing sensor operated by the National Oceanic and Atmospheric Administration of the US government
BIOMASS	Future radar earth observation satellite operating at P-band (from ESA)
CARABAS	Airborne SAR sensor operated at VHF by the Swedish Defence Research Agency
CORINE	Coordination of Information on the Environment; European land cover classification
dbh	Diameter at breast height
DEM	Digital Elevation Model
DSM	Digital Surface Model
DTM	Digital Terrain Model
ERS	European Remote Sensing Satellite; it was operated by ESA and carries beside other sensors also a C-band SAR
ESA	European Space Agency
FAO	Food and Agriculture Organization of the United Nations
FRA	Forest Resource Assessment of the FAO
FSC	Forest Stewardship Council (Forest Certification System)
GFOI	Global Forest Observation Initiative
GLAS	Geoscience Laser Altimeter System; on board of ICESat; it is a large footprint LIDAR sensor
ICESat	Ice, Cloud and Land Elevation Satellite; with GLAS sensor; large footprint LIDAR sensor
IKONOS	multispectral and panchromatic earth high resolution observation satellite (commercial)
InSAR	Interferometric SAR
IWCM	Interferometric Water Cloud Model
JERS	Japanese Earth Resources Satellite; it carried a L-band SAR (operated until 1998)
kNN	k nearest neighbor method
LAI	Leaf Area Index
Landsat	Series of optical earth observation satellite (from NASA/USGS)

LIDAR	LIght Detection And Ranging
MODIS	Moderate-resolution Imaging Spectroradiometer; it is a sensor on board of the NASA earth observation satellites Terra and Aqua
NASA	National Aeronautic and Space Administration (from USA)
NDVI	Normalized Differenced Vegetation Index (calculated from optical data)
NESZ	Noise Equivalent Sigma Zero
NFI	National Forest Inventory
NOAA	National Oceanic and Atmospheric Administration
OV	Oriented Volume
PCT	Polarimetric Coherence Tomography
PEFC	Programme for the Endorsement of Forest Certification (Forest Certification System)
PolSAR	Polarimetric SAR
Pol-InSAR	Polarimetric-Interferometric SAR
PRF	Pulse Repetition Frequency
Radar	Radio Detection and Ranging; microwave region of the electromagnetic spectrum
REDD	Reducing Emissions from Deforestation and Forest Degradation
RMSE	Root Mean Square Error
RSS	Remote Sensing Systems
RV	Random Volume
RVoG	Random Volume over Ground Model
SAR	Synthetic Aperture Radar
ScanSAR	SAR acquisition mode offering the opportunity to cover broad stripes (swaths)
SIR-C/X-SAR	Shuttle Imaging Radar C- and X-Band Synthetic Aperture Radar, space shuttle mission in 1994
SLC	Single Look Complex image
SNR	Signal to Noise Ratio
Spot	high-resolution optical imaging Earth observation satellite operated by the French space agency
SRTM	Shuttle Radar Topographic Mission
TanDEM-X	TerraSAR-X add-on for Digital Elevation Measurement; Radar earth observation satellite operating at X-band (from Germany)
Tandem-L	Future radar earth observation satellite operating at L-band (from Germany)
TerraSAR-X	Radar earth observation satellite operating at X-band (from Germany)
UN	United Nations
UNFCC	United Nations Framework Convention on Climate Change
USGS	United States Geological Survey
WRI	World Research Institute
VHF	Very High Frequency

VHR	Very High Resolution
VTD	Volume Temporal Decorrelation

Roman Symbols

A	amplitude of a complex number or received power
A_{ML}	radar amplitude multilooked
a	allometric factor
B	biomass or spatial baseline
$B_{\perp}$	effective baseline
c	allometric exponent
c_0	speed of light
ct	constant
dbh	diameter at breast height of a single tree
dbh_{mean}	mean diameter at breast of all measured trees
D	length of the antenna
e	base of natural logarithm
$E\{\}$	expectation value
$\vec{E}$	field of an electromagnetic wave
E_H	horizontal component of the field of an electromagnetic wave
E_V	vertical component of the field of an electromagnetic wave
$\vec{E}_0$	amplitude of the electromagnetic wave
E_{0H}	the amplitude of the electromagnetic field in the horizontal dimension
E_{0V}	the amplitude of the electromagnetic field in the vertical dimension
${}_2F_1(...), {}_3F_2(...)$	hypergeometric functions
f	frequency
f_0	center frequency
f_V	volume scattering contribution
F_{spec}	species specific form factor
$F(z')$	function of the vertical distribution of scatterer
g	basal area of a tree
G	total basal area of a forest stand
h	tree height
h_{50}	forest top height referring to the 50 thickest trees pre hectar
h_{100}	forest top height referring to the 100 thickest trees pre hectar
h_{200}	forest top height referring to the 200 thickest trees pre hectar
h_{DTM}	topographic height of a DTM

h_{Lorey}	Lorey's height
h_{mean}	mean height of all measured trees
h_{Topo}	terrain Height
h_V	height of the volume
H	height of antenna over ground
H_F	forest height obtained from Pol-InSAR
H_{acc}	interferometric height accuracy
i	imaginary unit
I	intensity or power
$\bar{I}$	expectation of intensity
I_S	received or backscattered Intensity
I_I	transmitted intensity
k	wavenumber
$\vec{k}$	propagation vector of an electromagnetic wave
$\vec{k}_{1\ 2d}$	two dimensional scattering vector
$\vec{k}_L$	scatterer vector with the lexicographic basis of a monostatic system
$\vec{k}_P$	scatterer vector with the pauli basis of a monostatic system
$\vec{k}_{P6}$	six-element scatterer vector associated to the Pauli basis
$[C_3]$	polarimetric covariance Matrix
$[T_3]$	polarimetric coherency Matrix
l_a	allometric level
L	number of looks
m	factor for bistatic $m=1$ or monostatic $m=2$ acquisitions or ground to volume ratio
m_G	ground scattering amplitude
m_S	direct ground scattering contribution
m_D	dihedral scattering contribution
$m_{\min}$	smallest ground to volume ratio
N	number of measurements or number of trees or noise power
P	received power
P_S	the mean signal power of the received unprocessed Signal
P_T	noise power
PS_{rg}	slant range distance between two consecutive range pixels
$\vec{r}$	position vector of electromagnetic wave
r^2	correlation coefficient
R , R_1 , R_2	distance between scatterer and antenna
R_0	minimum range distance between scatterer and antenna
S , S_1 , S_2	backscattered Signal or scattering matrix

S_{pq}	element of the scattering matrix with the polarization pq
$SPAN$	total scattered power
t	time
T_6	6 x 6 Pauli coherency matrix
v	platform velocity
V	tree Volume
V_{stock}	stock volume of a defined area
$\vec{w}$	polarization vector
$\vec{w}_{\min}$, $\vec{w}_{\max}$	minimum and maximum eigenvectors
W	bandwidth
W_{Az}	azimuth bandwidth
W_{Rg}	range bandwidth
z_0	height of the ground

Greek Symbols

α	terrain slope
β_1 , β_2	scattering phase of the observed scatterer
γ	interferometric coherence amplitude
$\tilde{\gamma}$	complex interferometric coherence
γ_{Az}	azimuth spectral decorrelation
γ_{COR}	coregistration decorrelation
$\tilde{\gamma}_{Obs}$	observed complex interferometric coherence
γ_{Rg}	range spectral decorrelation
$\tilde{\gamma}_{Scat}$	scatterer induced decorrelation processes
γ_{SNR}	SNR decorrelation
γ_{Sys}	system induced decorrelation processes
γ_{TG}	temporal decorrelation of the underlying ground
$\tilde{\gamma}_{TV}$	temporal decorrelation of the volume
$\tilde{\gamma}_{Tmp}$	temporal decorrelation
$\tilde{\gamma}_{V0}$	decorrelation of the volume part
$\tilde{\gamma}_{Vol}$	volume decorrelation
$\Gamma(...)$	gamma function
δ_H	absolute phase term in horizontal direction
δ_V	absolute phase term in vertical direction
δ_{rad}	radiometric resolution
Δf_{Az}	spectal shift in azimuth
Δf_{DC}	Doppler centroid difference
Δf_{Rg}	spectral shift in range

Δh	maximum height difference of the coherence region or polarimetric diversity
ΔH	height difference between two consecutive range samples
ΔR , ΔR_1 , ΔR_2	slant range difference between the two antennas of an interferometer
Δt	time between transmission and reception of a radar pulse
$\Delta \theta$	angular separation of the two acquisitions of an interferometer
$\Delta \varphi$	maximum phase difference of the coherence region
ς	slope of the triangular backscattering function
θ	local incidence angle (topography corrected)
θ_0	incidence angle
θ_1	look angle of first antenna of an interferometric constellation
κ_Z	vertical wavenumber
λ	wavelength or eigenvalue
$\lambda_{\min}$, $\lambda_{\max}$	minimum and maximum eigenvalues
ξ	tilt angle of the baseline
π	3.14159265359 – mathematical constant (circles)
ρ_{rg}	range resolution
ρ_{az}	azimuth resolution
ρ_{ground}	ground range resolution
σ	radar backscattering coefficient or mean extinction value
σ^0	radar cross section
σ_{mean}	standard error of the mean
σ_{Pixel}	standard error
σ_γ	standard deviation coherence
σ_ϕ	standard deviation of the interferometric phase
τ	pulse length
ν	standard deviation
φ	phase term of the received signal
φ_0	phase associated to the ground
φ_1 , φ_2	ground phase candidates
φ_{DTM}	interferometric phase obtained from a DTM
ϕ	interferometric phase
ϕ_1 , ϕ_2	phase term of the received signals S_1 and S_2
ϕ_{Flat}	flat earth phase
ϕ_{Scat}	scatterer phase
ϕ_{Topo}	topographic phase
χ	eccentricity of coherence boundary
ω	angular frequency

Ω_{12}	3 x 3 polarimetric interferometric coherency matrix

Notation and Operation Symbols

x, y	real number
$\tilde{x}$	complex number
$\vec{x}$	vector
$\bar{x}$	expectation value
X^T	transpose
X^*	complex conjugate
X^+	complex conjugate transpose
$[X]$	matrix X
Re()	real part of a complex number
Im()	imaginary part of a complex number

1 Introduction

Main objective of this thesis is Polarimetric SAR Interferomtry (Pol-InSAR) forest height inversion at different frequencies. Pol-InSAR is a radar remote sensing technique that enables to estimate forest height and may provide – if operated from a spaceborne system – globally wall-to-wall forest height mapping. The Pol-InSAR concept is introduced in section 4.4, the concepts of SAR, polarimetry and interferometry are explained in section 4.2 and 4.3. This work demonstrates Pol-InSAR forest height inversion at X-, L- and P-band, shows up limitations in the inversion process and introduces concepts how to overcome some of these limitations.

Forest height is an essential parameter for forest inventories and forest monitoring [291], [202], [287] [289]. New planned innovative satellite missions like BIOMASS (see section 7.2.1) or Tandem-L (see section 7.2.2) may provide forest height maps globally at least once per year [346], [251], [250] [183]. Both satellite missions will rely on Pol-InSAR techniques.

The importance of forest monitoring und the relevance of different quantitative forest parameters for forest monitoring should be pointed out in the following chapter. For this purpose, the state of the art in forest mensuration, forest inventories and forest monitoring is reviewed in section 1.1 and important forest parameters are identified. Section 1.2 summarizes user requirements for a regular forest monitoring with focus on important forest parameters and forest monitoring by means of remote sensing systems.

1.1 State of the art forest inventories

An evaluation of the state of a forest ecosystem requires, dependent on purpose, data about extent, stock volume, composition and condition of a forest area. In order to acquire relevant data to access these parameters, forest inventories are designed and regularly conducted [173].

Decisions concerning the acquisition of information have been mainly based on the accuracy of the acquired data and the costs of the data. Usually, the accuracy of standing mean stock volume is considered the most important benchmark to evaluate data quality [163]. Today other forest variables than stock volume gain more weight in forest inventories for instance structure and biodiversity parameters.

1.1.1 On national level

Forest inventories are traditionally based on ground measurements, partly supported by optical remote sensing data (mostly aerial photographs) used for stand delineation and forest area estimation [338], [135]. Inventory data from ground measurements rely usually on a grid of sample plots, the required parameters are recorded for each plot. The accuracy of a plot based forest inventory depends on the sample plot size, the homogeneity of the forest and the used grid density [173].

The Food and Agriculture Organization of the United Nations (FAO) seeks to evaluate the state of the global forests' resources since 1946 on a five to ten year basis (five-year intervals since 1990) in their "Global forest resource assessment" [65]. However, the available data base makes this request a challenge. Nevertheless, FAO provides the most complete summary of the state of the forests on country level and relies exclusively on the

individual countries' reporting's. These are largely founded on national statistics based on an inventory plot system and inventory reports. Each country has its own definition of forest and has developed its own forest inventory system with different sampling densities, sampling systems (ground measurements and remote sensing), plot designs and temporal repetitions [52]. Therefore, the database as well as the data quality of the forest inventory systems is rather heterogeneous [65]. International comparability is rarely considered. Consequently, the cross-countries' estimates are not direct comparable [367]. FRA 2000 [65] was the first forest resource assessment to use a homogeneous set of global definitions and it is to date the most comprehensive assessment of global forest resources [367].

Quantitative forest parameters such as stock volume or forest height are in all countries nearly exclusively obtained from ground measurements [67], [68], [69], [70], [71], [72], [80], [73] [74].

In the following the state of the art of forest inventories on country level is reviewed (mainly temporal and spatial sampling density) for selected countries with relevant forest cover including the five most densely wooded countries of the world i.e. the Russian Federation, Brazil, Canada, the United States of America and China [65], [67].

Some countries with a well-established forest management built up a rather dense sampling grid covering the entire forest area of the country. Germany's national forest inventory, for instance, relies on ground measurement plots on a 4 km x 4 km grid measured in a ten-year cycle [23], [73]. Therefore, the standard error of the estimated parameters (mainly stock volume) translates on national level into one percent [171]. Some federal states of Germany condense the sampling grid to 2.83 km x 2.83 km or 2 km x 2 km to improve precision of the estimated parameter on subnational level.

The US National Forest Inventory (NFI) is based on a 5 km x 5 km grid, which is remeasured every ten years [74].

France, forest is pre-stratified with optical remote sensing data, whereas ground point density depends on the stratum [75], [389] with a mean of 4 km x 4 km. Ground measurements are repeated every five years [389], [390].

In Romania the last quantitative forest inventory was done at the context of the national forest inventory in 1985 and showed a mean standing stock volume over bark of 211.5 m^3/ha which is used as a reference for forested land. Later, changes of the forest area are only reported (which corresponds to change of stock volume) every five to ten years [76].

China, however, has a regular forest inventory repeated every five years. They use either a 4 km x 4 km grid or 2 km x 2 km grid dependent on the forest region [77], [325].

Boreal countries adapt the sampling grid to the productivity, remoteness and heterogeneity of the forest: in highly productive and easy to access forest areas a 4 km x 4 km grid is used in Canada [70], [36] and a 6 km x 6 km in Finland [80]. In remote and low productive areas the grid density is reduced to at least 10 km x 10 km in Finland and 80 km x 80 km in Canada. Measurements are repeated in a ten-year cycle in both countries. In the Swedish National Forest Inventory each year 17,000 inventory plots are measured corresponding to a mean grid density of ~4.5 km x ~4.5 km, however, the sampling grid density decreases from South to North.

The last official forest inventory in Russia was done in 1988. Starting in 1998, inventory data relies on reportings from forest enterprises and are summarized every five years (only company relevant forest areas are measured). Due to the forest companies' various inventory systems, difficulties appear in combining the data. It is also claimed that the data is partly not reliable [69].

Quantitative information of the state of the forest in Gabon and the Democratic Republic of Congo relies on the estimation of the forest area from optical remote sensing data mainly

achieved from Landsat (in combination with MODIS) for forest area estimation [391], [78], [79]. Forest area is classified and each class is assigned with a mean stock volume obtained from previous forest inventories i.e. data from 1990 or older.

Indonesia estimates its forest area by means of optical remote sensing data (Landsat). Quantitative forest estimates were done in 2003 on 91 plots all over the country. Mean stock volume of these plots is used as a reference for the entire Indonesian forest area including forest plantations [72].

The extent of natural forest in Brazil is mapped using optical remote sensing data from Landsat. Natural forest area is a classified biome consisting of primary and secondary forests - generated by Landsat data. Plantation forest area is derived from the national land survey. Each forest class is assigned with a certain stock volume. In the Amazon for example, a mean stock volume of 300 m^3/ha is used. This is a mean value from several scientific studies [71].

Some countries such as Germany or Sweden update forest inventory information between the measurement periods by means of forest growth simulators [23], [68] and [73].

Certain European countries still gather national data by aggregating stand inventories originally designed for management planning purposes [365].

Inventory information, as described above, is in many countries the national data base for political decisions concerning forest management.

Nevertheless, the quality of quantitative forest information on country level is extremely heterogeneous. Countries such as Canada, China or France acquire national forest inventory data regularly on a nationwide basis, therefore allowing a rather precise tracking of forest development. Brazil, Romania or Indonesia, however, mainly map changes in the forest area. A quantitative description of the forests is either missing or not reliable. Forest degradation due to uncontrolled logging activities, thunderstorms, forest fires or other calamities may thus stay undetected [266].

Remote sensing is mainly used for forest area estimation and sometimes for forest classification. Some countries like Sweden, Finland or the USA use remote sensing data (mainly optical systems like Landsat) in combination with inventory samples to provide wall-to-wall maps of forest parameters by means of statistical correlations (kNN “k-nearest neighbour” method”) [89], [348]. This method provides high accuracy (10 percent RMSE) for spatial units on the order of 100 ha to 200 ha [296].

1.1.2 On enterprise level

Forest inventory information as provided by a national forest inventory is not sufficient for management decisions in forestry companies [173] p. 16. Each major forest enterprise is therefore keeping its own forest inventory and often even its own measurement (forest inventory) system. Typically, a grid based sampling method is used. Grid density ranges from a minimum of 100 m x 100 m to rather wide meshed grids of 1 km x 1 km and more. The mesh width depends on the required accuracy of the measured parameter (in particular stock volume) and the heterogeneity of the inventoried forest.

Forest inventories on company level are performed for economic planning and in order to guarantee a sustainable forest management (protection of the resources for the future, ecological stability and social aspects) [173] p. 16, [172], [360]. The most important parameter, however, is the harvestable stock volume. The stock volume on company level (~100ha to 3000ha) should be estimated with a standard error of at least five percent [173] p. 200. The five-percent accuracy requirement for wood volume is also valid for plantation forests as lined out in [221] for South Australian plantations.

Stock volume in forest stands (i.e. smallest forest management unit with an average size of three to four ha or smaller) contributing significantly to the harvested stock within the planning period should be rated with a standard error of five percent [173] p. 147. Here, additional measurements are inevitable to meet the required accuracy as only few inventory grid points fall within the limits of a single stand (dependent on the used inventory grid). Accuracy requirements on stand level are defined by the forest enterprises and depend on the respective forest conditions in a stand. In Finland, for instance, it is the rule that stand mean height and stand wood volume should be estimated with a maximum error between 10 and 15 percent [153].

A planning period for forest companies lasts usually 10 years and is also required for tax in Germany [173] p. 49. A forest inventory is therefore repeated every ten years. In case of a regular forest operating schedule (without large area storm damage), well documented and regularly updated harvesting activities as well as established forest growth models [288], forest inventory intervals can be extended up to 20 years [173] p. 351.

In general, a steady update of forest inventory information is desirable, for instance by means of remote sensing [173] p. 355.

Inventory data acquired in a ten-year cycle are relatively fast outdated. A stand-wise inventory performed only after harvesting measures, forest disturbances like storm throw or forest fires (dynamic forest inventory) could provide continuously up-to-date forest inventory data [96], [384], [336]. The forest development of a forest stand can then be extrapolated after an inventory by means of forest growth simulators [264] and monitored with remote sensing techniques [295].

Sagl [304] p. 46 claims, that for the trade of forest property in Central Europe the required forest parameters (e.g. harvestable wood volume) are at best available with a standard error of 10 percent. Effort and costs for additional measurements to improve accuracy are usually too high.

Generally, a remote sensing component is recommended for forest inventories [173]. Up to now, optical images (Landsat, aerial photographs) are the most important remote sensing information source for forest inventories in forest management and are mainly used for stand delineation [173], [291], [135] and [201]. Apart from aerial photographs and Landsat data, airborne LIDAR measurements start to become an important information source for operational planning in forest management [392]. This refers primarily to plantation forests but also to natural forests [278], [393] [300]. LIDAR is used for stand delineation, but it is also a means of quantifying wood volume for harvest planning and characterizing forest stands [300]. Forest management decisions of large forest enterprises like StoraEnso, Tembtec or Mondi already rely on LIDAR measurements [393], [300] [394]. LIDAR measures primarily tree and forest heights, which seems to be apparently sufficient for forest management issues.

1.1.3 State of the art ground measurements

The main objective of ground measurements is mostly to gather information about the stock volume V occurring in a given area. For this purpose, it is fundamental to measure at least the diameter at breast height dbh (diameter at 1.3m above the ground) for each single tree within a predefined reference area. In addition, the tree species has to be identified. In temperate and boreal forests, tree height is measured at only a few representative individuals [201] and [22]. The height of the unmeasured trees is derived from species-specific height to dbh relationships [201], [291], [287] [289]. Tree volume is then calculated as the volume of a cylinder corrected by a species-specific form factor F_{spec}

accounting for the tapered form of the stem and the relevant branches (> 7 cm diameter [291] p.7)

$$V = h \ \frac{dbh^2 \ \pi}{4} \ F_{spec} . \tag{1.1}$$

Typically, the standard error for the volume of a single tree in a temperate forest is between 10 and 15 percent [291] p. 115. The main uncertainty emerges usually from the tree height measurements and the form factor. Under perfect conditions tree height can be measured with a standard error of one percent [291] p. 111 (by the use of trigonometric methods). Measurement errors are introduced by wrong distance measurements, wind, bad visible crown (arched crowns as found for deciduous tree, firs and pines) or leaning trees [287]. In the case of leaning trees the standard error of tree height may reach values between 12.5 and 14.4 percent [228]. The measurement error increases with stand density and tree height. Tree height measurements should be verified on harvested trees.

As tree height is measured only in a small part of the collective, the height of the remaining trees is deduced from height - *dbh* relationships. The accuracy depends on the number of height measurements and the variance of these heights. With a sufficient number of height measurements the height - *dbh* relationship may be estimated with a bias on the order of one to two percent [291] p. 178. The standard deviation (or residuals) of the height - *dbh* relationship is species dependent [8] and increases with tree height. Prodan [291] p.177 specifies the standard deviation of a height - *dbh* relationship between approximately 4.5 and 12 percent. Assmann [8] mentions for Norway spruce (*picea abies*) a standard error of 5 percent and for beech (*fagus sylvatica*) and Douglas fir (*pseudotsuga menziesi*) a standard error of 8 percent. Bauer [16] reported 1.4 m standard deviation across all tree heights for tree height measurements acquired during a forest inventory, which corresponds to a height error of 13 percent for trees with a height of 10 m and a height error of 3.5 percent for 40 m high trees.

In contemplation of the above facts, tree heights or forest height is estimated on a small scale or on plot level with a standard error between 5 and 10 percent, dependent on the sampling area, the tree species and the number of measured tree heights.

In tropical rain forests tree height measurements are extremely difficult to perform, as the crown top is very difficult to see due to its arched crown form. In case a direct tree height measurement is not feasible, crown base height is measured. Total tree height is then derived from the assumption that the crown length equals 30 to 40 percent of the total height. Obtained tree heights are afterwards corrected by height to diameter relationships [150] p. 25.

In some tropical inventories tree height measurements are omitted [56] pp. 31 and tree heights are deduced from general height to diameter relationships [380].

Tropical forests are richer in species than boreal and temperate forests and each tree species is associated with a different form factor and a different wood density making an exact estimation of stock volume or biomass more difficult.

The *dbh* is usually measured in whole centimeters (values are rounded down) and can be considered as highly accurate. Errors are systematic (usually enlarged diameter due to jammed measurement device) and bias the *dbh* measurements in positive direction [291], [8].

On a large scale, the accuracy of the estimated forest parameters depends on the size of the single inventory plots and on the number of plots per area [201]. As long as there are no systematic or directed errors in the measurements, large scale estimates of forest stock

volume or mean forest height can be considered to be very accurate [291], [201]. But often the spatial information (e.g. 2-D distribution of stock volume) is more important than high statistical accuracy on large scales. The spatial information of a plot based forest inventory can only be used where the sampling grid is smaller than the spatial heterogeneity of the forest [242].

Often permanent inventory plots are used. Then, the same plot and if possible even the same trees are periodically remeasured. Permanent inventory plots produce unbiased estimates of forest growth and document harvesting activities [173] p. 201.

Forest inventory data from forest enterprises are usually not publicly available.

1.2 Observation requirements: parameters, temporal and spatial resolution

In awareness of its role in the global carbon cycle, the general interest in the world's forest has grown immensely. Forests release carbon in the atmosphere by deforestation and forest degradation and take up carbon from the atmosphere through afforestation and sustainable forest management [65].

Nevertheless, forests are naturally more than just carbon. 31 percent of the total land area is covered with forests and forests represent one of the ecosystems with the highest biodiversity on earth. Forests also provide employment and livelihood, including food, for a large proportion of the population particularly in developing countries. Furthermore, forests supply the natural resource timber. Forests are large drinking water reservoirs, alleviate flooding events and protect soils from erosion, especially in sloping terrain. They protect the valleys from avalanches, filter the air, provide a balanced climate to adjoining open land and urban areas and contribute to the global climate processes. Forests are also large recreational areas for human beings and provide habitat for numerous animal and plant species. At the same time some forest types are highly endangered ecosystems and must be protected [172], [377], [24] and [361].

On-going uncontrolled deforestation, large area forest degradation, unsustainable forest management and the changing climate compromise the forest functions and the forests themselves. To preserve the forests and to maintain the forest functions for the future, a regular survey of the conditions of the world's forests is unavoidable [24].

Therefore each nation developed its own National Forest Inventory system (NFI) tailored to their needs but also to their funding constraints [37].

Remote sensing measurements from spaceborne sensors are an essential supplement or even an alternative to NFI for a global forest monitoring (dependent on the requirements of an NFI). Of course forest parameters deduced from remote sensing never achieve the accuracy of ground-based inventories. However, the big advantage of remote sensing is that the spatial information can be used i.e. the information provided is continuously available all over the acquired area. The measured parameters and changes in the measured parameters can be spatially associated. As forest parameters were acquired globally by means of the same method, the findings would be easily bilaterally comparable. Hence, global statements on the forest status and forest development are more representative. Naturally, the used remote sensing method must be reliable and needs to be validated regularly by means of ground measurements of as many forest types as possible.

1.2.1 General requirements for a remote sensing based forest monitoring

Requirements for forest monitoring depend on purpose and user. Different applications demand different requirements and different user groups have different demands on the accuracy for the same application (see previous section) [174]. The requirements for various applications and different user groups are given below.

For most applications and user groups stock volume, biomass or carbon stock, occurring on a defined area as well as changes in stock volume are the key parameter in forest monitoring.

Framework conditions demanded for a remote sensing system for forest monitoring are [81], [109]:

- low cost or free of charge data availability,
- long term continuity in the acquisition of new data,
- long future life span and
- if possible past data recordings for change detection.

If global coverage is desired (comparison on national level), short repeating cycles are helpful [109]. Time series of remote sensing acquisitions should take into account the seasonal dynamics of the land cover [230], [383].

1.2.2 Forest management

Regular forest management has probably the most detailed demand for information about the state of a forest. Here, remote sensing may be only a complementary information source, in addition to the ground measurements, in the operational planning. Basic information is the amount (i.e. volume) of harvestable wood for each tree species [173]. Information about wood quality, forest health or regrowth is either difficult or not at all obtainable from remote sensing, so far.

In [173] p. 200 and [221] the standard error of the mean σ_{mean} for stock volume on stand level is set at five percent. Consequently, the requirements on spatial resolution depend on stand area and the accuracy (i.e. standard error σ_{Pixel}) of a stock volume estimate per resolution unit. For instance, assuming a homogeneous composed stand with an area of 3 ha (mean stand size for temperate forests [173]) and an unbiased estimate of stock volume with a standard error of 20 percent (taken from [125]) then according to

$$\sigma_{mean} = \frac{\sigma_{Pixel}}{\sqrt{N}} \tag{1.2}$$

a spatial resolution of 43 m x 43 m or 0.18 ha is required. In boreal forests, accuracy requirements on stand level with a σ_{mean} of 10 to 15 percent seem to be more relaxed [153], at least in the case of Finland. Stock volume estimates should be updated in a five to ten year cycle or contemporarily after harvesting events or wind throws [289], [173], [384].

Another important parameter in forest management is the site quality class of a forested area. The site quality is an estimate of the potential productivity of a forest site [291], [289], it is species dependent and can be deduced from the forest height, stock volume or biomass in a given age [289] p. 307. But the real productivity of a forest, depends beside site quality also on the logging scenario and small scale differences in the water and nutrient supply.

Differences in site quality arise from different heights at the same age for the same tree species. In primary forests when the age is unknown, site productivity for the prevailing tree species can also be deduced from the occurring biomass per unit area [227].

Yield tables reflect stand productivity for different site quality classes [18]. While some yield tables refer to the forest mean height, others refer to the forest top height [9]. The height difference between two site quality classes depends on age and tree species. In "Hilfstafeln für die Forsteinrichtung" [18] are yield tables for several temperate tree species listed. Across all tree species and age classes listed in [18] the smallest height difference between two site quality classes is 10 percent of the reference height. Half steps between two site quality classes have a height difference between six and ten percent of the reference height. A proper assignment of a stand to a certain site quality class, or half step, requires that the reference forest height should be estimated with an accuracy (σ_{mean}) half the difference between two site quality classes [335].

Assuming a height difference of seven percent of the reference forest height between two site quality classes (σ_{mean} = 3.5 percent), a homogeneous composed stand with an area of 3 ha and an unbiased estimate of forest height with σ_{Pixel} = 10 percent (taken from [125]), then a spatial resolution of 60 m x 60 m or 0.36 ha is required. If the forest height estimates are affected with a standard error of 20 percent, then a spatial resolution of 25 m x 25 m or 0.07 ha is required to meet the demanded accuracy.

Site quality estimates acquired through forest height estimates based on remote sensing become problematic in mixed forest stands. Therefore, the increase of forest height during a given time period (five to ten years) may be used as a measure to estimate site quality, but only if no harvesting activities have occurred. The measurement error should be clearly below the estimated forest height change [174].

The examples above do not take into account mixed pixels between two neighboring forest stands. In order to largely avoid mixed pixels the calculated spatial resolutions is too coarse and should be increased by 10 to 30 percent, dependent on the form of the stand [335].

Monitoring of forest operations in production forests including unexpected events like salvage logging after insect calamities and storm damage requires a yearly update.

1.2.3 Forest monitoring on national and global level

Forest monitoring on national level (national forest inventory) should give an overview of the forests' status of a country and is only inspected at random. It should provide information whether forest functions are preserved for the future and a sustainable forest management is granted. It should further be used to estimate national wood supply and to control harvesting concessions [24], [29], [348], [361], [362], [363]. A national forest inventory is usually repeated in a five to ten year cycle. However, this is country-dependent.

Monitoring in the context of NFI's or a global forest monitoring can be defined as systematic observation and documentation of the status of the forests in regular time intervals. Changes should be documented as well.

Stock volume per tree species is again one of the most important outcomes. Stock volume should be estimated with a standard error within the range of one percent on national level [23], [109].

Forest area is also a major result of a national forest inventory [174] and should be estimated with an accuracy of 10 percent, considering a spatial resolution of 0.5 ha [109].

The most complete overview of the status of the world's forest is given by the UN-FAO "Global Forest Resources Assessment" [37], [67]. The report was requested by the member countries of the FAO and summarizes data from national forest inventories all over the world. This "global forest inventory" was performed to gather information about the dimension of global forest resources and the rate of deforestation in order to evaluate forest benefits, forest functions as well as the economic and environmental dimensions of forest resources and biodiversity [37][65], [67].

Merging inventory data from different countries may bring up several handicaps as national forest inventory systems, stock volume definitions or biomass estimates and forest definition differ from country to country [367], [109], [174] and [81]. A global remote sensing approach for forest parameter estimation would overcome these constraints and would deliver harmonized information on forest change and land use dynamics on a global scale [81].

FAO's main expectation from a forest monitoring system is the documentation and statistical evaluation of changes including information on land use dynamics and forest maps [81]. Most important for the future are reliable and yearly updated forest non-forest maps.

FAO recommends a spatial resolution of 20 m to 30 m and acquisitions with optical systems complemented by SAR if no cloud-free optical images can be acquired. A remote sensing based sampling design could as well be sufficient, as demonstrated by the FAO remote sensing survey [82]. In this process a sampling grid of one degree by one degree (geographic coordinates) was used. At each sampling point a 10 km by 10 km Landsat scene was evaluated.

FAO seeks for an annual or biannual update of the "Forest resource assessment" mainly supported by remote sensing data [81].

For the detection of illegal logging a monthly or even more frequent monitoring with high spatial resolution is required [81]. Forest degradation or illegal logging may be identified directly by detecting canopy gaps, clearings or indirectly by mapping roads, logging tracks and log decks. According to the GFOI report [109] requires the mapping or Forest degradation very high resolution data with spatial resolutions on the order of 5 m which is, at least for tropical forests, equated to single tree detection [103]. Another method to discover forest degradation is to detect changes in vertical forest structure [109].

1.2.4 Disaster monitoring

A fast detection of the extent of forest disturbances is the key issue to prevent from further disturbances and to clear up the damages caused. In [109] a spatial resolution of 0.5 ha is demanded for near real-time forest change detection with bimonthly coverage of the endangered areas. Similarly, Hall states in [126] that for carbon flux monitoring high-resolution imagery is required soon after a disturbance event before the area recovers significantly (after one or two years significant regrowth could have already appeared in some regions).

Knocke et al. [173] pp. 149 underlines the usefulness of aerial photographs for the evaluation of forest disturbances (high resolution, rapidly available).

Spatial resolution for disaster monitoring should be on the order of 20 m to 30 m [81] but better than 70 m (0.5 ha) [109].

1.2.5 Forest fires:

The monitoring of forest fires requires for an initial fire-fighting full cover monitoring of endangered areas in rather short time intervals, preferably several times per day with heat sensitive sensors [81], [387]. In order to assess the damages induced by a forest fire burned areas, burned vegetation and slightly burned vegetation must be clearly detected [174].

1.2.6 Storm damages

After damages caused by storm or wind throw a fast detection of the extent of the affected areas is necessary for the operational planning in a forest enterprise [260]: At first, it is important to build up the logistics for a fast clean-up of the affected areas, the following step is to avoid additional biotic disturbances in the neighbouring areas ([321] p. 60, [3] p. 229) and preventing a biotic-induced wood devaluation [290].

Within 24 hours an estimate of the damaged area with an accuracy of 20 percent should be available including a rough estimate of the damaged stock volume [260]. Two weeks after a storm event an estimate of the damaged stock volume is demanded with an accuracy of 20 percent [388].

In unmanaged forests and remote forest areas the fast quantification of damage is of only minor importance.

1.2.7 Forest certification

A Forest Certification should ensure a sustainable and professional forest management. Therefore, requirements for two representative certification systems are reviewed: FSC (Forest Stewardship Council) [94] and PEFC (Programme for the Endorsement of Forest Certification) [275].

The proof that the criteria for a certification are met is in the responsibility of the forest enterprise. The forest enterprise needs to gather the required information and provide it to the certification organization. The control of certification criteria is done by means of a random sampling.

Important and remote-sensing relevant criteria for a successful certification are that:

- valuable ecosystems are preserved,
- sustainable logging is performed,
- depending on the forest ecosystem, clear-cuts should be avoided
- a certain proportion of primary forest is being conserved and
- appropriate and naturally occurring tree species are replanted.

A remote sensing supported control of the certification criteria requires a monitoring of upcoming changes once per year, particularly for sensitive areas. This includes the detection of clear-cut areas. A qualitative measure could already be sufficient. Moreover, wall-to-wall maps of forest height and changes in forest height could be a proper solution for an adequate control. Detection of structural changes, changes in stock volume and the identification of tree species or tree species groups would as well be helpful. Requirements for spatial resolution are similar to the requirements for forest management but should at least amount to 70 m x 70 m (0.5 ha) [109].

The detection of clear-cuts in Central Europe (according to FSC a minimum deforested area of 0.3 ha [322]) would require a spatial resolution of 20 to 30 m for forest/non-forest monitoring.

1.2.8 REDD

REDD (Reducing Emissions from Deforestation and Forest Degradation) is a mechanism established within the United Nations Framework Convention on Climate Change (UNFCCC) [138]. Its two main objectives are to mitigating climate change by reducing carbon emissions induced by forest degradation and deforestation through enhanced sustainable forest management in developing countries. REDD provides a financial incentive for climate protection activities in developing countries.

The implementation of the REDD mechanism requires a regular quantitative monitoring of the status of the forests of a country [83] p.62. Basic requirements for a forest monitoring in the context of REDD are [109]:

- classification of the forest into 3 classes: primary forest, modified natural forest and plantation forest (each class can be assigned to a biomass value),
- forest/non-forest monitoring to detect deforestation [110],
- detection of forest degradation and
- documentation of enhancement in C-stocks.

Remote sensing products used for a forest monitoring in the frame of the REDD mechanism need to be comparable over time (i.e. consistent time series over many years) and should be continuously available in the future [110], [133], [134]. Changes in forest area should be mapped with a spatial resolution of 30 m on an annual basis [110].

Quantitative monitoring for carbon storage change detection and forest degradation relies so far on national forest monitoring systems [108] and is therefore highly variable from country to country [83], [174]. Monitoring of forest degradation driven by remote sensing would then require forest structure change maps with a spatial resolution of 0.5 ha on an annual basis [109]. Quantitative monitoring of carbon storage (i.e. biomass) and carbon storage change requires a spatial resolution of 0.5 ha and should be repeated every five years [109].

1.2.9 Carbon storage estimation

Global mean surface temperatures have risen between 1906 and 2005 by 0.74° C [351]. A central concern in the climate- change discussion is the increasing atmospheric carbon dioxide content. Therefore, estimates of carbon fluxes between atmosphere, land surface and ocean are of major interest for global climate change predictions' and climate modelling. Only 15 percent of the terrestrial carbon pool is stored in above ground vegetation, the rest is mainly bound below ground in plants and in the soil [58]. Approximately 25 to 30 percent (2.6 PgC/year) of the global human induced carbon emissions are taken up by terrestrial ecosystems (mainly by forests) [102], [265]. The vegetation carbon pool is with 2000 PgC, 75 percent thereof are stored in forests and is therefore of special concern because deforestation may induce a direct release of the stored carbon into the atmosphere [64].

Approximately 10 to 15 percent (0.8 – 1.6 PgC/year) of the global carbon emissions are released by changes in land use (mainly by deforestation and forest degradation) [145].

Estimates of fossil fuels, land use change, terrestrial sinks, ocean uptake and atmospheric storage come from various data sources and are uncertain to various degrees [126]. Up to now estimates of terrestrial carbon fluxes are not based on direct measurements [381] so that carbon sinks cannot be locally assigned especially in less documented (monitored)

forest regions. A major source of uncertainty is the lack of spatially specific estimates of biomass [141], [143]. Therefore, questions that are still need to be answered are:

- Will the terrestrial carbon uptake be stable, increase or decrease in the future [381], [157]?
- How long the terrestrial carbon sinks will act as sinks [381]?
- How much carbon will be released when forests are changed to other land use types [142]?

Very useful in order to answer these questions are regularly acquired, spatially resolved global biomass maps. But remote sensing is only sensitive to aboveground biomass and changes in above ground biomass. Therefore, estimates of carbon stored in the soil needs to be deduced from laws of allometry or empirical relationships. The Global Forest Observation Initiative (GFOI) [109] claims that the estimation of biomass and change in aboveground biomass is considered to be from a remote sensing point of view in a very early phase. However, even annual maps of disturbances or deforestation could help to identify unknown terrestrial sinks due to recovery from such disturbances [126]. Imagery of disturbed area is needed before significant recovery for carbon flux monitoring [126].

A big step forward in improving the estimates of the global carbon fluxes would be to reduce the uncertainty of terrestrial net flux (+-0.9 PgC/year [102]) to the uncertainty of the net carbon uptake of oceans (+- 0.5 PgC/year).

In [126] is postulated that biomass measurements for carbon flux characterization must focus on estimates of biomass losses and biomass gains rather than on exact estimates of the biomass level. Biomass change should be estimated with a standard error lower than 19 percent.

Estimation errors of biomass fluxes are minimized when important scales of vegetation dynamics match the spatial resolution [149], [144]. Similarly, the required resolution for the mapping of deforestation processes depends on the size of patches of change in land use and may range from 30 m to 1 km [144]. For instance deforestation in the amazon basin appears at a scale of 1 ha and below [126]. In [175] was argued that a scale of roughly 1 ha is best suited for height-biomass allometry in tropical forests.

Requirements for a global carbon and carbon change monitoring of the terrestrial vegetation vary depending on author and user community.

Hall et al. [126] requests ideally a spatial resolution of 1 ha and a global monitoring once per year in order to track carbon fluxes. He thus adds that a spatial resolution of 1 km by 1 km with a 20 percent accuracy of the biomass estimates can already provide superior information about global carbon fluxes.

GFOI [109] demands a spatial resolution of 0.5 ha for biomass monitoring repeated in a five-year cycle, as observation intervals on the order of one year are according to Houghton in [144] too short for forest growth estimation.

ESA's earth observation programme board [63] lists observation requirements for a global biomass mapping from two user communities. The carbon research community requires a global biomass with 10 percent accuracy once per year and 1 ha spatial resolution. The Global Climate Observing System requires 5 percent accuracy at 10 to 30 m spatial resolution yearly.

1.2.10 Other applications

In addition to the above listed applications, several rather scientific applications such as process studies in ecology, forest growth studies [287], [289] or habitat [106] and

biodiversity mapping [53] would require wall-to-wall maps of forest parameters with different spatial resolutions. Studies on stand level require spatial resolutions on the order of 3 to 5 m and on landscape level a spatial resolution better than 30 m would be required [126], [19]. High repetition rates as well as global coverage are usually not required.

1.2.11 Summary user requirements

Forest monitoring requirements are strongly user or application dependent and therefore highly heterogeneous.

A remote sensing system for forest height or biomass estimation and being able to contribute to most of the before mentioned topics should provide products at a spatial resolution of 30 m x 30 m, a spatial resolution of 70 m x 70 m may also be useful for most of the relevant forest monitoring applications. A yearly update of forest height or biomass (i.e. stock volume) is for most applications sufficient including forest change detection. Detection of disturbances like wind throw or illegal logging requires much faster repetition cycles on the order of months or even weeks or acquisitions should be carried out on demand.

Estimation accuracy of forest height and forest biomass (stock volume) depends on the spatial unit (forest stand, forest enterprise or country) at which the information is required. Usually, estimates should be unbiased. Accuracy of height and biomass estimates should be better than 20 percent. In case height is used for biomass estimation, accuracy of height estimates should be significantly better than 15 percent.

2 Forest height: relevance as single parameter

This thesis is focused on the estimation of forest height by means of polarimetric SAR interferometry (Pol-InSAR). For this purpose, the significance of forest height as a single parameter in forest monitoring is subsequently pointed out.

In traditional forestry, measures of forest height are used to calculate the stand volume (in combination with species information and dbh measurements), to determine the site index of tree species (in combination with stand age), to predict forest growth (in combination with site index and age) as well as to represent a target variable in species trial (progeny and provenance) and silvicultural experiments [201]. In summary, it can be stated that forest height can be used to characterize a forest in a quantitative and in a qualitative way.

2.1 Definition of forest height

There are several definitions in forest mensuration to address the parameter forest height (or stand height) [201].

- The mean height (h_{mean}) is the arithmetic mean of all tree heights in a stand [291]:

$$h_{mean} = \frac{\sum_{i=1}^{i=N} h_i}{N} \tag{2.1}$$

- Lorey's height (h_{Lorey}) is a weighted mean height, the individual tree heights are weighed proportional to their basal area g_i with the total basal area G [291]:

$$h_{Lorey} = \frac{\sum_{i=1}^{i=N} g_i h_i}{G} \tag{2.2}$$

- Forest top height is the height of the dominant tree stratum i.e. the height of the most vital trees. There are several definitions for a forest top height [201], [291]. Depending on the definition the forest top height refers to:
  - the 100 tallest trees per hectare [119]
  - the 50 (h_{50}), 100 (h_{100}) or 200 (h_{200}) thickest trees per hectare [244]
  - dominating trees, defined as those belonging to Kraft's classes ([30], [177]) 1 and 2 [54]
  - the 20 percent thickest trees [375].

These definitions for forest top height are certainly only a selection, but contain the most important definitions including h_{100} which is used as reference for Pol-InSAR forest height estimates.

The mean height h_{mean} is used to estimate stand volume, it is sensitive to thinning processes, thinning from below as well as thinning from above and to forest degradation. Thinning and forest degradation induce an increase or a decrease of h_{mean}. Forest top height is less

sensitive to thinning, apart from the case that a large part of the trees forming the upper canopy layer is removed. Top height is therefore more suitable for predicting the site indices than h_{mean}.

Stand height is usually estimated by sampling with ground measurements [201].

2.2 Forest height for stock volume estimation

The volume calculation of a single tree requires a height measure, a dbh measure and a species-specific form factor (see Eq. (1.1)). Stand volume V_{stock} can be calculated by adding the tree single volumes in a stand or with an estimate of the mean forest height (h_{mean}) of a stand, the mean dbh (dbh_{mean}) of a stand, a species-specific form factor (F_{spec}) and in addition to the single tree volume calculation a density measure like basal area (G) or tree number (N) [201]:

$$\sum_{i=1}^{N} V_i(h_i, dbh_i, F_{spec}) \cong V_{stock} = \left(h_{mean} \frac{dbh_{mean}^2 \, \pi}{4} \; F_{spec} \right) N = h_{mean} \cdot G \cdot F_{spec} \tag{2.3}$$

which applies best for homogeneous forest conditions. Traditional height measures from the ground are costly and sometimes difficult to perform [201], [291]. Height estimates from another source (such as remote sensing) are therefore highly welcome for stand volume measurements.

2.3 Forest height for site index evaluation

Site indices are species-specific and can be used for indicating the productivity of a forest [291], [289]. Site quality is best characterized by forest mean height or forest top height [291] p. 596. In temperate forests strong thinning became standard in forest management, making forest top height a better indicator for site quality than forest mean height [289] p. 308. Measures of forest top height may also prove useful for site quality estimates in tropical forests [364].

However, in uneven aged highly structured mixed stands forest height loses its value for site quality estimation. Here tree development is beside site quality also dependent on internal competition [289] p. 308. In uneven aged mixed forests stand quality may be obtained from increase of forest height over a defined time span [289].

2.4 Forest height for biomass estimation

A measure of forest height is highly demanded for reliable remote sensing based aboveground biomass (AGB) estimates, especially for high biomass regions [19], [247], [109].

In the tropics it is often difficult or even impossible to accurately measure tree height from the ground [203] p.42. Therefore, remote sensing based forest height estimates would be an

essential contribution for reliable biomass estimates by themselves or in combination with other supplementary ground measurements [57], [148].

Conventionally, biomass is estimated by multiplying stock volume V_{stock} with a (mean) wood density. In contrast, biomass estimates derived from forest height measures only rely on allometric relationships [242] either by an allometric function or by a multiplicative expansion factor. Allometric functions describe deterministic size relations (x versus y) in organisms by a power function, the so-called "allometric equation":

$$y = a\ x^{c} \tag{2.4}$$

where, a is known as the allometric factor and c the allometric exponent [242], [20], [151]. For temperate forests Mette proposed in [242] the following height-biomass allometry:

$$B = l_a\ 1.66\ h_{100}^{1.58} \tag{2.5}$$

where B is the biomass, $a = 1.66$, $c = 1.58$ and l_a the allometric level. The allometric level scales a set of allometric relations with the same exponent. In the height-biomass allometry it accounts for different densities (for instance induced by thinning), tree species and site conditions. The allometric level needs to be a priori known or has to be estimated from ground measurements. On regional (i.e. landscape) scale an average allometric level may be assumed (similar tree species composition, logging practices, management concepts and growth conditions). The allometric level decreases from climax tree species to pioneer tree species. A poor performance of height-biomass allometry is expected for loose canopy closure and highly heterogeneous forests [242], [240]. Of course, height-biomass relationships may be affected by several uncertainties like differences in tree density induced by different logging scenarios or different provision with nutrients and water or by a small scale mosaic of different site quality conditions.

Similarly, Köhler [175] developed a height-biomass allometric relationship for tropical rainforest in Southeast Asia, which is based on simulated data but includes several disturbance regimes.

In [32] and [33] forest top height H100 estimated from TanDEM-X interferometric data is used to estimate biomass at boreal forests by means of allometric relations.

Several studies relate a remote sensing based forest height like height of the backscattering center, height of metrics or forest height obtained from a digital surface model (DSM) from LIDAR) empirically to biomass [246], [333], [334], [2]. Of course, the obtained height-to-biomass algorithms are site-dependent and may seasonally vary (backscattering properties change over the year) **Publication V [198]**.

2.5 Forest height for forest-non-forest mapping

The area under forest cover is of major concern for forest policy, forest management and nature conservation [174]. However, forest definition differs from country to country, with different thresholds for minimum forest area, tree crown cover and minimum tree height [109] [174]. Wall-to-wall forest height maps enable to consider different thresholds for tree height or crown cover in forest-non-forest mapping.

2.6 Forest height for forest management

Forest height maps allow a first evaluation of the forest conditions in a region, in order to assess the status of a forest in terms of erosion protection, avalanche protection, flood protection and as a drinking water reservoir [173], [30], [376]. They also provide a first assessment of the spatial distribution of the stock volume (or stage of forest development) in a region and give already a first idea of the overall stock volume [291], [162].

Knowing the spatial arrangement of stands with different height and the forest height gradient at the forest corners, allows in combination with the tree species to assess the risk of storm damages of forested areas [321], [3].

2.7 Forest height for change detection

Regularly conducted forest height surveys (with remote sensing) may be used to provide forest height change maps [25].

Decrease of forest height may be an indicator for logging activities or forest degradation. Nevertheless, a detection of logging events or forest degradation based merely on forest height is probably not sufficient, as some logging scenarios do not affect forest height [291], [287], [289], [201]. This could be overcome if, as an indicator for forest degradation, a change in canopy roughness is detected. Forest growth (i.e. increase of forest height) is more difficult to map and requires long observation intervals (five years and more) [144].

After storm events or snow clearances, forest change maps are useful tools for a reliable assessment of the extent of damage (particularly in order to record the affected area and to get an idea of the quantity of the resulting timber) [256], [290].

2.8 Forest height for spatial landscape modelling

For many years landscapes have been shaped by men. Human impact split former forested areas into patches of fields, settlements and forest. Shape, spatial dimension (i.e. area, height) and spatial distribution of forestry land (i.e. patterns) are an integral part of ecosystem, microclimate and landscape modeling [245].

Forested landscapes are also used as large recreational areas. The recreational value of a forest depends on the composition and dimension of the trees. For instance, high light forests are perceived as more beautiful, more aesthetic than low dense forests [305].

Forest height maps would contribute to evaluate the ecological and recreational value of a region.

2.9 Forest height for horizontal structure estimation

Wall-to-wall forest height maps resolve the horizontal height distribution or the canopy roughness and may allow detecting gaps in the canopy.

Forest gaps are primary sites of seedling germination and seedling growth [30]. Different light and shade patterns and a better water availability change the balance of species. In gaps caused by fallen trees, additional to the slow growing shade-tolerant plants, fast growing high-light species appear. Therefore, the species' composition in gaps depends on the gap type and gap dynamic. Forests rich in gaps are therefore rich in species, as well [147], [38], [53], [86]. Gap fraction deduced from forest height maps may be a good indicator for biodiversity.

Horizontal height distribution or canopy roughness may provide information about tree competition of the canopy forming trees and could therefore contribute to forest growth models [287] p. 220 264, [104].

Tropical lowland rainforests typically come with a two-layered canopy (bimodal forest height distribution). Above a 30 m to 35 m high closed canopy is a sparse layer of emergent trees [203] p.50. In addition, emergent trees occur usually in small groups or alone and are 40 m to 45 m tall (tropical Africa and Amazon Basin) but can also reach heights up to 60 m (only in South East Asia). The large crowns with crown radii on the order of 30 m can be easily detected in remote sensing based forest height maps, (e.g. **Publication III [124]**) which enable the detection of single emergent trees of the tropical lowland rainforest. Occurrence, number and height of emergent trees is a valuable information for biomass estimation (emergent trees contain up to 50 percent of the forest biomass [37]), but may be also used for forest characterization, for forest degradation detection and for forest disturbance detection [175], [150].

3 Remote sensing systems and applications

The term Remote Sensing appeared first in the 1960ies from geographers of the United States Office of Naval Research [329] and stands for a technique, which allows obtaining information about an object without getting in touch with it [170], [169], [135].

Two main categories of remote sensing systems (RSS) can be distinguished: passive RSS and active RSS. Passive systems make use of the radiation of the sun, either reflected or scattered from the earth surface or emitted from the earth surface. Active systems transmit a signal and receive a backscattered or reflected signal and operate basically at frequencies where the natural radiation of the sun and of the earth is low [226].

The following sections shortly introduce remote sensing systems (RSS) and methods contributing to the topic forest monitoring. In section 3.1 optical remote sensing is presented, in section 3.2 LIDAR remote sensing and in section 3.3 radar remote sensing. This should help to assess, compare and rate global forest height maps.

3.1 Optical remote sensing

Optical remote sensing methods are used worldwide for forest monitoring, the detection of deforestation and reforestation and for forest disturbance detection [320].

Aerial photographs are probably the most commonly used remote sensing product in forestry, as they have been available for a long time, they have a high spatial resolution and are easy to interpret. Traditionally, aerial photographs are used for stand delineation, forest area estimation and often for tree species estimation [173] p. 144, [135]. Stereoscopic acquired aerial photographs enable the use of photogrammetry.

Coarser resolution optical images as provided by satellites like Landsat, RapidEye, NOAA-AVHRR, Spot, MODIS, ALOS-PRISM or IKONOS lose the single-tree resolution. Optical satellite imagery suffers from cloud coverage, particularly in the tropics. Therefore, acquisitions sometimes need to be repeated until a cloud free image can be recorded.

3.1.1 Photogrammetry

Photogrammetry exploits stereoscopic acquired optical images to calculate digital surface models (DSM) [201], [135]. Photogrammetric DSM's with sufficient high resolution can be used to map tree crowns and detect changes induced by growth logging or disturbances [201], [243]. The detected height of a tree crown is resolution-dependent, coarser resolutions tend to underestimate tree crowns [201].

If tree top and trunk base are visible, the tree height can be measured quite accurately with photogrammetry [201]. In combination with digital terrain model (DTM) from LIDAR, forest height can be estimated from photogrammetric DSMs.[339]

3.1.2 Forest-non-forest

Forest-non-forest mapping is an established technique with optical data [1], [5], [95], [129], [225], [266], [279], [331]. Landsat and NOAA's AVHRR provide continuously data since the 1970's [158], [235], and were used by the WRI (World Resource Institute) and

the FAO for forest-non-forest monitoring and land use change monitoring (i.e. afforestation and deforestation) [82], [66], [377]. Hansen et al [115] provides a global tree cover map based on MODIS with a spatial resolution of 500 m x 500 m. A global forest-non-forest map as provided by FAO is shown in Figure 1 [65], [65] as deduced from Landsat and MODIS data [115].

The first global forest cover change map was produced by Hansen [116] documenting forest cover change between 2000 and 2012 with time series of cloud free Landsat data.

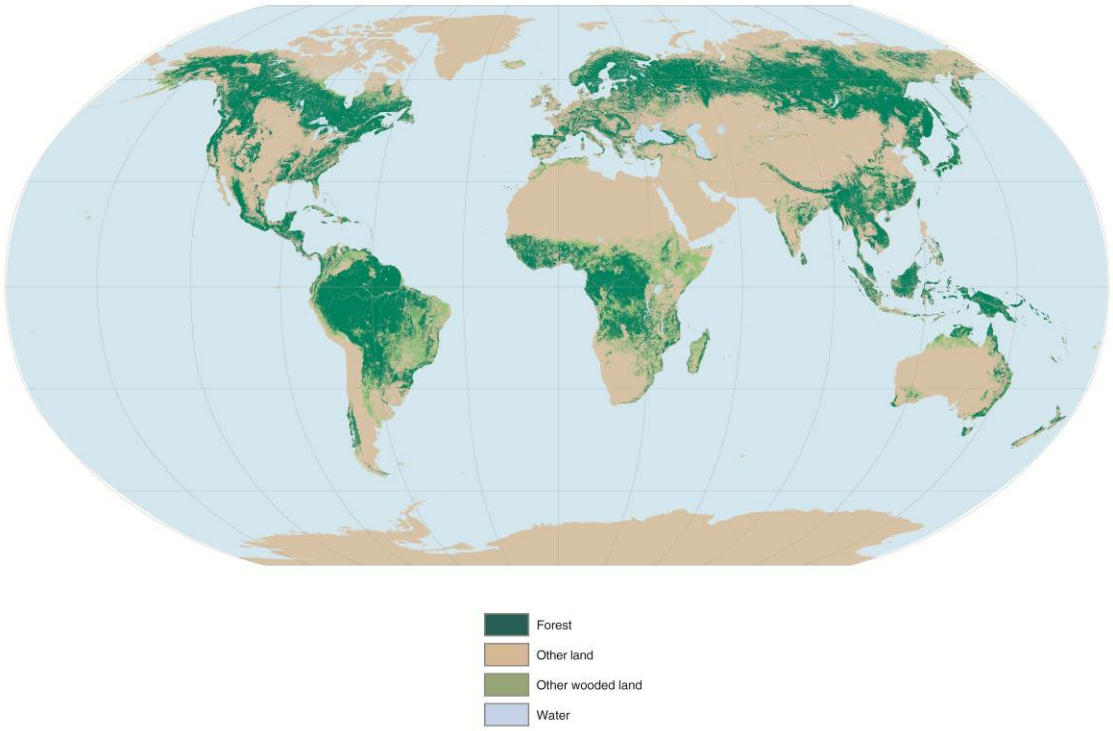

Figure 1: Global forest non forest map from FAO [65], [37] from Landsat and MODIS data © [2000] FAO

3.1.3 Forest stratification with optical data

Land cover classification has always been one major issue of optical satellite imagery as, for instance, the European land cover classification CORINE (Coordination of Information on the Environment) [49]. These classifications are generally able to map different stages of forest development and are therefore used for forest stratification [276], [337], [366] and forest disturbance monitoring [383], but have limited success in determining biomass in dense forests and in high biomass forests [107].

Hyper spectral data with a sufficiently high resolution (i.e. on tree level) may be used for tree species identification or at least to identify different species groups [17], [372] pp. 239. This works quite well for single-species forests but becomes problematic for mixed-species forests. Coniferous and deciduous trees can be well distinguished in the near infrared [135]. Near infrared is also most suitable for fire scar detection [174]

Forest stratification may be used to plan ground surveys. Knowing the prevailing forest classes enables an intelligent (i.e. adjusted to the forest classes) distribution of the ground measurement plots and may reduce the number of sampling plots [263].

3.1.4 LAI from optical data

Another parameter, typically derived from optical data, is the leaf area index (LAI) [335]. LAI is the ratio between the crown projection area and the corresponding leaf area. LAI is an important parameter in ecological modelling [287][280], [150]. Most optical sensors overestimate LAI [335]. LAI estimates from optical remote sensing usually saturate at values around 3 [335]. LAI values in forests start from 2 up to a maximum value of 16 (in the Pacific temperate rain forests). Most forest types have LAI values between 3 and 8 [330]. Consequently, optical LAI estimates are not suitable for biomass estimation in forests.

LAI is derived from vegetation indices like NDVI [372]. Vegetation indices may be also used to detect defoliation [332] and to monitor the phenological annual cycle [237]. Forest change detection with optical data has to take into account the phenological status.

3.1.5 Biomass from optical data

Optical data are not directly related to biomass [346], but biomass can be estimated assigning different forest classes to certain biomass values (primary forest, secondary forest, etc.) [335]. Biomass estimates from optical data are highly empirical and require a large effort and in situ reference measurements for calibration [335].

3.2 LIDAR remote sensing

Forest characterization with LIDAR has recently gained much scientific and operational interest [222], [224]. Light Detection and Ranging (LIDAR) is an optical remote sensing system but is listed separately as it is an active optical ranging system. LIDAR is a tool to characterize vertical forest attributes such as tree height and vertical forest structure [379]. Two categories of LIDAR systems are shortly discussed in the following: small footprint LIDAR (up to 20 cm footprint diameter), which is only operational from airborne systems and large footprint LIDAR (25 m to 70 m footprint diameter), which can be operated from airborne systems as well as from spaceborne systems. Technical characteristics of LIDAR system are well summarized in [379], [234] and [14].

3.2.1 Small footprint LIDAR

Airborne small footprint LIDAR is an established technology for the generation of Digital Elevation Models (DEM) [14]: Digital Surface Models (DSM) include vegetation height and Digital Terrain Models (DTM) are elevation models without vegetation [234]. LIDAR DTMs' over forested areas are with a standard error between 15 cm for flat terrain and 40 cm for strongly sloped terrain fairly accurate [154].

Swath width for airborne LIDAR forest monitoring is limited. LIDAR requires a close to nadir look angle, wider scan angles are problematic [155]. This limits the LIDAR swath width to some hundreds of meters (200 m – 500 m, dependent on flight height).

Therefore, forest monitoring with airborne LIDAR is expensive and there is not sufficient capacity for a national forest inventory [109]. LIDAR forest height measurements (subtracting DTM from DSM) have been shown to be more consistent than field-based measurements [254] and can be used for forest growth or forest change detection [25].

Forest height estimates from LIDAR measurements with low point densities (less than 1 hit per square meter) tend to underestimate forest height, as the probability of a laser pulse intercepting the apex of a tree crown is relatively low [258]. LIDAR forest height estimates refer usually to the mean height or the Lorey's height, sometimes data are maximum filtered to obtain a canopy top height [379].

LIDAR acquisitions with a sufficiently high point density (five to ten hits per square meter) are used for single-tree detection including tree height, crown height and crown diameter [379]. Single-tree mapping is mostly limited to the trees forming the upper canopy, inferior trees are rather difficult to detect. Dense forest conditions (more than 900 trees/ha) impede single-tree detection and the false alarm rate is growing [374], [201].

Multi-echo or multi-pulse laser scanning systems (full waveform LIDAR) are able to detect vertical forest structure attributes [234]. Figure 2 shows examples for laser hit profiles as obtained from a full waveform LIDAR on the left for a less dense two-layered forest stand and on the right for a dense single-layered forest stand from the temperate forest site Traunstein (for test site description see **Publication V [198]**).

In boreal forests LIDAR measurements are used for biomass estimation [105], [255], [4] [164]. Biomass estimation approaches rely usually on full waveform LIDAR data with high point densities or are based on height-biomass allometry when point density is low. Gobakken et al. [105] uses the percentiles of the height distribution of all laser hits within a predefined area (for instance the 90 percent percentile is the height containing 90 percent of the laser hits) to get biomass, the method from Kankare [164] applies a single tree detection approach for biomass estimation. Both approaches require a calibration or training with ground measurements. Height percentiles can also be used to estimate canopy LAI [233].

Relationships generated between LIDAR data and forest parameters such as stock volume are often test site specific and therefore not generally applicable [379].

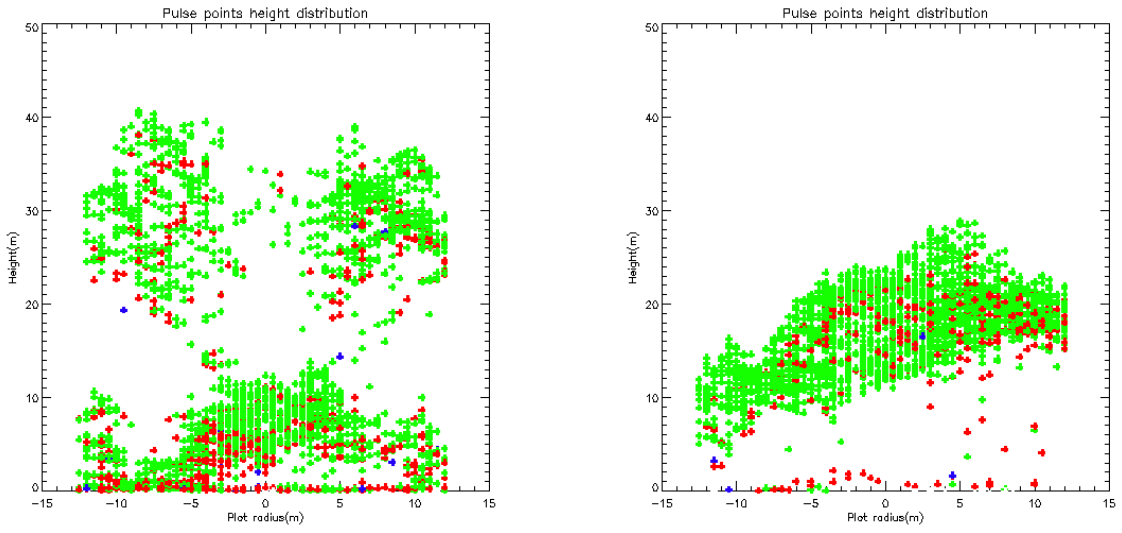

Figure 2: Full waveform LIDAR vegetation hits (Traunstein site – for test site description see Publication V [198]); green dots: first return; red dots: second return, blue dots: third return; left: less dense forest stand with second regrowth layer; right: dense single layered forest stand.

3.2.2 Large footprint LIDAR

Large footprint LIDAR systems are profiling systems and work on a sampling base. Fundamentals of large footprint LIDAR systems are for instance given in [108].

Figure 3 shows GLAS-ICESat (ICESat is part of NASA's earth observing system) profiles acquired over tropical rain forest in the Amazon Basin. On the left is a profile with a dedicated ground peak, in the right profile, however, a ground return cannot be clearly identified, thus, the LIDAR does not penetrate down to the ground. Large footprint LIDAR provide point measurements of the vertical forest structure and forest canopy height – reference height is mostly Lorey's height (see section 2.1) [117], [340].

LIDAR measurements from spaceborne systems are sometimes affected by clouds or fog, making the measurement unusable. Additionally, sloped terrain makes the interpretation of the backscattered profile a challenge [118]

Canopy height from large footprint LIDAR is estimated by subtracting the height of the ground peak from the top of the canopy return in the waveform [108], [59]. However, a ground peak is not always visible in the profile as demonstrated in Figure 3 on the left.

A global forest height map based on the combination of ICESat LIDAR measurements with optical (i.e. passive) remote sensing systems have been calculated and published by Lefsky et al. [224] and Simard et al. [328] with a spatial resolution of 1 km^2. They use optical data to interpolate between the single LIDAR samples and reach an overall accuracy between 4.4 m and 6.1 m.

Several authors use large footprint LIDAR height metrics (for instance the 90 percent metric is the height of the 90 percent cumulative energy) to estimate biomass [59], [223], [61] and achieve a mean standard error on the order of 20 percent on plot basis [108]. Biomass estimates rely on empirical relationships between LIDAR metrics and biomass and are mostly adapted to the test site, calibrated with ground measurements and therefore not generally applicable.

Spaceborne LIDAR sensors have usually difficulties to remeasure exactly the same spot, making interpretation of changes between two acquisitions difficult.

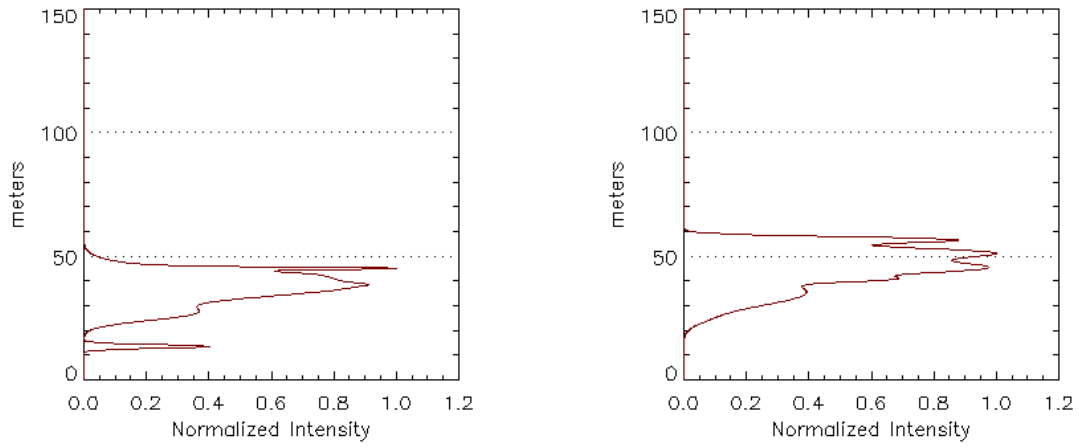

Figure 3: Profiles from large footprint LIDAR (ICESat – 65 m footprint) over tropical rain forest in the amazon basin; left: vegetation profile over a clearly visible ground peak; right: vegetation only profile, LIDAR does not penetrate down to the ground.

3.2.3 LIDAR H100

In this work forest height estimates from airborne LIDAR measurements are used to cross validate radar derived forest heights. Reference height for the radar height estimates is the upper canopy height H100 [238], [239], [242]. H100 is considered to represent the upper height of the tree crowns in a forest (see section 2.1) [201], [289].

Airborne LIDAR penetrates somewhat into the forest canopy and therefore underestimates the top vegetation height [277], [259]. An estimate of the forest top height H100 was obtained by taking the maximum LIDAR vegetation height within a 10 m by 10 m window **Publication III [124]**, [11]. This allows compensating for the underestimation of the LIDAR forest height estimates. This method has been successfully used for small footprint (~15 cm diameter) airborne LIDAR systems with ~1 to ~4 hits per square meter.

In Figure 4 LIDAR H100 was plotted against H100 calculated from ground measurements for the test site Traunstein - a temperate pre-alpine forest (a detailed test site description is given in **Publication V [198]**). Each point in Figure 4 represents LIDAR and ground measurements over a circular area with 25.23m diameter (corresponding to an area of 500 m²) [338]. A correlation coefficient r² of 0.91 underlines the good agreement between LIDAR H100 and ground measured H100. Some LIDAR height estimates tend to overestimate the ground measurements, here adjacent trees extend their crown into the plot area and are therefore measured by the LIDAR. However, they are not measured on the ground, as the stem is outside the plot area. Furthermore, the geolocation of the ground measurement plots is affected by an error which can account for a displacement of up to 50 m. Small errors may be introduced due to measurement errors in both, the ground measurements (human measurement error) and the LIDAR measurements (LIDAR missed the tallest trees) or by harvesting activities in the time span between the LIDAR acquisition (performed in September 2008) and the ground survey (performed in June, July and August 2008).

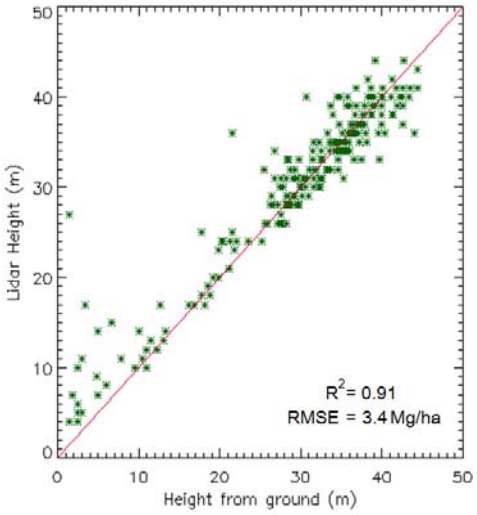

Figure 4: Validation plot Traunstein test site (Lat: 47.86°, Long: 12.65° see Publication V [198]): ground measured H100 from July 2008 versus LIDAR H100 from September 2008.

3.3 Radar remote sensing

In contrast to optical waves, radar is sensible to the geometrical and dielectric properties of a sensed object.

Radar (an acronym for Radio Detection and Ranging) systems operate in the microwave region of the electromagnetic spectrum [264] and generate a 2- dimensional reflectivity image.

Similar to the optical spectrum also the microwave spectrum is divided, dependent on frequency into several bands as summarized in Table 1. While Ku-band may still be affected by clouds and other atmospheric effects (i.e. snow and rain), all other frequencies starting from X-band pass the atmosphere widely unaffected and at the same time have the capability to penetrate into vegetation. The potential of penetrating into vegetation increases with decreasing frequency. Especially lower frequencies (e.g. L- and P-band) can provide 3-D structural information of vegetation or forest covers; they can penetrate into vegetation down to the ground, so that the signal contains information about the vegetation, as well as about the underlying topography [62], [170], [186].

Figure 5 shows radar amplitude images acquired on the island of Borneo (Lat: -1.32°, Long: 116.72°) in four different frequencies (X-, C-, L- and P-band) of the same scene. Images were acquired with DLR's airborne SAR system E-SAR [140]. The scene is dominated by grassland and different types of forest plantations (e.g. oil palm plantation, rubber tree plantations). In the lower right of the image a channel system for irrigation is located. A major forest area disperses from the middle of the image to the left. The dark areas in the upper part of the scene, mainly visible in the lower frequencies (L- and P-band), are grassland. Radar brightness (i.e. scattering intensity) varies wirth frequency over forested areas as well as over fields. The backscattering of the fields or open areas decreases with increasing wavelength.

Table 1: Radar Frequencies and Wavelength according to [368]

	Ku-band	X-band	C-band	S-band	L-band	P-band	VHF
Wavelength	2.40 – 1.67 cm	3.75 – 2.40 cm	7.50 – 3.75 cm	15.0 – 7.5 cm	30 – 15 cm	136 –63 cm	100 – 1 cm
Frequency	12500 – 18000 MHz	8000 – 12500 MHz	4000 – 8000 MHz	2000 – 4000 MHz	1000 – 2000 MHz	220 – 470 MHz	30 – 300 MHz

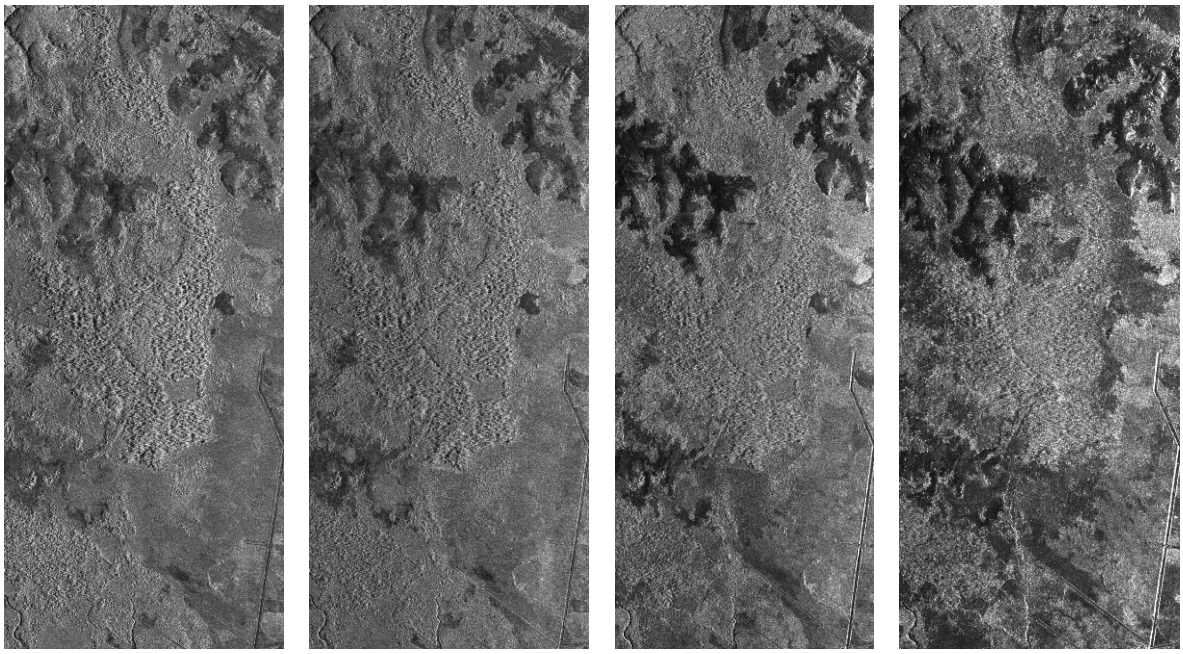

X-band C-band L-band P-band

Figure 5: Radar amplitude images VV polarization in different frequencies acquired with DLR's airborne SAR system E-SAR [140] over a scene composed of grassland areas and forest plantations in Indonesia east Kalimantan on the island of Borneo (Lat: -1.32°, Long: 116.72°).

Radar remote sensing contributes to several forest-related topics discussed below.

3.3.1 Forest-non-forest:

Forest-non-forest monitoring with SAR sensors is considered operational and can be used alone or to supplement optical forest-non-forest mapping [109]. A first global forest-non-forest map from ALOS PALSAR data with 25 m x 25 m was presented in [326]. In [308] ALOS PALSAR multi-temporal data stacks were used for clear-cut detection in boreal forests of Scandinavia.

Forest-non-forest mapping relies in most cases on the analysis of radar amplitude. As radar backscattering is highly dependent on terrain slope [358], a DEM (with sufficient high resolution) is required for a proper calibration and interpretation of the radar amplitude [326].

3.3.2 Forest classification

Classification with single channel SAR relies mainly on the radar amplitude while full polarimetric SAR (PolSAR) provides a total of nine parameters, embedded in three real and three complex parameters per pixel. Terrain and land use classification is arguably the most important application of PolSAR [208].

Classification of single-pol radar data is similar to that of optical images; however the class separability is in general lower in SAR images than for optical images [109], [310].

For the classification of polarimetric data several approaches exist. Wishart statistics are used in [206] to describe the statistical variation in PolSAR data, Cloude et al. [39] describes the statistics of a class by the three parameters entropy, alfa and anisotropy. These parameters respectively describe purity and type of a scattering mechanism as well as the number of scattering components. A model-based polarimetric decomposition identifies different scattering mechanisms like surface scattering, dihedral scattering and volume scattering, for instance the Freeman decomposition [92], [386].

In contrast to the above-mentioned unsupervised classification techniques, supervised classifications train a classification algorithm with statistical characteristics of predefined land cover types [208], [84].

Time series (i.e. temporal stacks) at the same or at different frequencies are commonly used for classification, as well [109].

Large-scale classification of forests has been successfully demonstrated several times. For instance, Walker [371] used ALOS PALSAR data for forest classification of the Brazilian Amazon. In [137] a land classification map of Borneo including several forest classes was provided using dual pol (HH HV) ALOS PALSAR data.

Detection of selective logging with high resolution TerraSAR-X is presented in [200], the detection of windthrow areas with TerraSAR-X is depicted in [236].

Forest classification (i.e. open forest and closed forest) with interferometric data (interferometric coherence) was demonstrated in [319] and [307], Pol-InSAR forest type classification in [85] and [209].

3.3.3 Forest height

Several radar-remote sensing techniques provide estimates of forest height, wherein each forest height refers to another reference height.

3.3.3.1 Forest height estimates from DSMs

Radargrammetry exploits, similar to photogrammetry, stereoscopic (i.e. with different incidence angle) acquired radar images for DSM generation [132]. In combination with a DTM (as for instance obtained from LIDAR measurements), DSMs obtained from radargrammetry may be used to get forest height estimates (DSM minus DTM), as demonstrated by Vastaranta et al. [365] and Raggam et al. [293] with TerraSAR-X data.

In a similar manner forest height estimates are obtained from interferometric SAR (InSAR) data **Publication V [198]**, [323]. With InSAR DSMs can be calculated [15] and may be used together with a DTM from another source to get an estimate of forest height, which is also called the height of the scattering center **Publication V [198]**. X-band is, due to its short wavelength, assumed to penetrate only marginally into forest canopy and is therefore most suitable for forest height estimates. Forest height estimates of temperate forests and mangrove forest with SRTM X-band are demonstrated in [370], [327] and [167].

If a DTM is missing, some authors suggest calculating forest height by subtracting a P-band DSM from an X-band DSM. P-band is due to its long wavelength assumed to have its phase center down on the ground [60], [11].

Height information from radargrammetry and interferometry depends on the penetration depth. Mette [242] claims that X-band penetrates into the forest canopy and a P-band DSM does not match the absolute ground (shifted upward due to vegetation), therefore forest heights obtained from DSM's are usually underestimated.

3.3.3.2 Model derived forest height

Another parameter obtained from SAR interferometry is the interferometric coherence i.e. the correlation between two image pairs [15] (see also section 4.3.4) it scales between zero and one. The interferometric coherence decreases due to temporal changes between the two acquisitions, system noise or when the vertical and horizontal components of the scatterers are differently projected into the two SAR images (due to the slightly different viewing angle of the two images). Decorrelation induced by vertical displacement of the scatterer between the two images is termed *volume decorrelation* and is nearly always observed over forested areas [382], [6], [113] and [15]. Generally, it can be assumed that volume decorrelation increases with forest height, however, volume decorrelation also depends on other physical attributes of the scatterer, as lined out below.

Volume decorrelation is a function of the baseline configuration, forest height and the vertical distribution of the scatterers (i.e. vertical structure) at the given frequency, geometry and polarisation [113], [6], [46], [43], [352] and [354]. An estimate of volume decorrelation basically allows to invert vertical structure parameters as forest height assuming that all other non-volumetric decorrelation sources are corrected.

In order to estimate forest height from a coherence measure, a realistic model of the vertical distribution of the scatterer along height is required. Such a model is provided by the Random Volume over Ground Model (RVoG) [10], [354], [40], [269], [267] and [268]. The RVoG assumes an exponential vertical backscatter function over a Dirac-like ground contribution (see Figure 1). The exponential backscatter function can also be interpreted as a mean extinction. The RVoG model introduces apart from forest height three more unknowns: the "extinction", the position as well as the amplitude of the ground scattering. Therefore, a solution can only be obtained by increasing the number of observations. The concept of Pol-InSAR provides coherent estimates in different polarizations and allows forest height estimation [40], [269], [41]. First forest height results from L-band Pol-InSAR in combination with the RVoG model over a boreal forest are shown in [269], [41]. Note that Pol-InSAR forest height estimates refer to the forest top height H100 [238], [242] and [239].

Forest height and structure parameter estimation from polarimetric single- and multi-baseline have been successfully demonstrated in a series of airborne experiments in natural as well as commercial, boreal, temperate and tropical test sites for different stand and terrain conditions: over tropical forest in L-, P- and X-band **Publication III [124]**, [190], **Publication V [198]**, **Publication I [196]**, [271], over temperate forest in L-band , P-band and X-band [97], [219], [242], [188], **Publication IV [218]**, [98], [257], [192], **Publication V [198]**, [189], [220] and over boreal forest in L-, P- and X-band [212], [213], [214], [280], **Publication II [281]**, [282], [283], [286], **Publication IV [218]**, [205], **Publication I [196]**, [220].

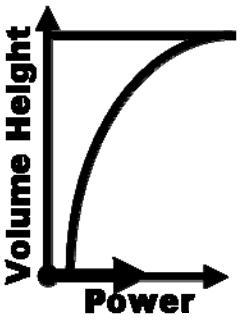

Figure 6: Schematic representation of the RVoG with exponential vertical backscatter function for the volume and a Dirac ground contribution.

3.3.4 Biomass

3.3.4.1 Backscatter biomass relations

Already during the early days of SAR remote sensing it was noted that the backscattered signal from a young forest with low biomass is weaker than the signal from an old taller forest with high biomass [378]

Biomass estimation from SAR measurements relies mostly on empirical relationships between radar amplitude and biomass. Sensitivity increases with increasing wavelength. Authors generally agree upon that L-Band saturates somewhere between 40 t/ha and 100/t/ha, and P-band between 120 t/ha and 200 t/ha [306], [345], [303], [166], [167], [166], [156]. Lower frequencies like VHF (see Table 1) as provided by the Swedish VHF sensor CARABAS are sensitive to biomass levels beyond 200 t/ha [91].

Backscatter - biomass relationships usually vary with forest type frequency, test site and polarization [314]. Therefore, GFOI [109] claims a lack of consistency in backscatter-based biomass estimates.

In [309] hyper-temporal data stacks (> 100 acquisitions per year) are used to derive biomass estimates from C-band radar backscatter. Averaging over large data sets, acquired under different weather conditions and under slightly different incidence angles (speckle is reduced see section 4.1.3.3), seem to overcome the saturation limitations found in other biomass backscatter relationships. Santoro et al. [309] generated a stock volume map of the boreal zone from Envisat ASAR data with a resolution of 1 km x 1 km. Up to 300 m^3/ha no saturation effect could be detected.

3.3.4.2 Coherence biomass estimation

Some authors relate the interferometric coherence empirically to biomass or stock volume [369], [176]. In [369] ERS interferometric coherence in combinations with JERS backscattering was used for biomass classification in the boreal forest of Siberia.

The decrease of coherence with increasing height was interpreted in [6], [7], [46], [307] with the Interferometric Water Cloud Model (IWCM) and was used for stock volume estimation.

3.3.4.3 Height of the scattering center for biomass estimation

The height of the scattering center derives from the subtraction of a LIDAR DTM from a SRTM or a TanDEM-X DSM. Scattering center heights are in [333], [334] related to stock volume and biomass of a boreal forest. In addition, the scattering center height depends on the penetration depth of the electromagnetic wave. Assuming that penetration is density-dependent, forest stands with the same height but different density have different scattering center heights. Density is accounted for in the scattering center heights, making the scattering center height particularly suitable for biomass estimation. Nevertheless, the height of the scattering center may also change with different weather conditions, i.e. dry or frozen forests allow a deeper penetration of the radar or vice versa, wet forest conditions may result in a taller scattering center height **Publication V [198]**. Therefore, an algorithm for biomass estimations not only depends on the characteristics of the test site but also on the weather and environmental conditions.

Treuhaft uses in [357] interferometric phase (phase center height) and interferometric coherence from TanDEM-X data to estimate biomass at a tropical forest test site in the Amazon Basin.

3.3.4.4 Height to biomass

Pol-InSAR height estimates refer always to the same reference height and can therefore be used for a general allometric height-to-biomass relationship [242], [32], [33]. The allometric level (see section 2.4) as required in [242] for successful biomass estimation may be either deduced from a few representative ground samples or from remote sensing derived structural parameters [31]. An approach that uses top height H100 for biomass estimation in boreal forests is introduced by Caicoya in [32], [33].

3.3.5 Forest structure

An extension of conventional two-dimensional SAR imaging is SAR tomography. SAR tomography allows the reconstruction of the three dimensional scatterer distribution and was first demonstrated in [297]. The tomograms resolve clearly forest height, the tree crowns and the ground topography, as seen in the tomographic transect in Figure 7 [273]. The concept of SAR tomography is explicitly described in [256], [298], [297] and [311].

Several methods for resolving the three dimensional scatterer distribution have been suggested: Reigber et al. [297] suggests Fourier tomography, in [344] and [316] Kronegger product decomposition combined with Capon tomography is applied and in [355] Fourier decomposition/analysis is used. Most tomographic techniques need a large number of acquisitions (~5 depending on the required vertical resolution and unambiguous range targeted).

Another method to access vertical structure is Polarimetric Coherence Tomography (PCT). PCT was introduced by Cloude in [43], [44] and [45] in [139] a new set of vertical structure function is proposed. PCT approximates the vertical distribution of scatterers by a set of predefined vertical structure functions. The used functions need to reflect somehow the true vertical backscatter structure. In [43], [44], [45], [284] and [285] the LeGendre polynomials are used. The number of LeGendre polynomials used for the reconstruction of the vertical distribution of scatterers depends on the required vertical resolution.

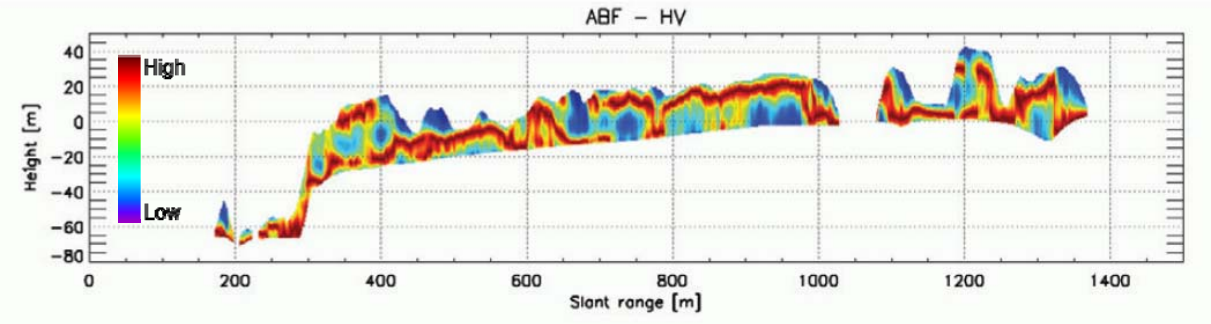

Figure 7: Tomographic transect (vertical power distribution) in a hilly area of the temperate forest Traunstein test site (Lat: 47.86°, Long: 12.65° – see Publication V [198]) [273]. © [2013] IEEE

The more polynomials are required to describe the vertical backscatter function, the more interferometric acquisitions are needed. However, PCT requires usually less acquisitions than conventional tomography.

3.3.5.1 Structure to biomass

In [136] and [356] tomographic profiles (i.e. the vertical backscatter distribution) are directly linked with empirical relations to biomass by means of the backscattering coefficient at a defined forest height.

Caicoya uses in [31] [34] and [35] vertical structure attributes in combination with forest height to estimate biomass and demonstrated his approach with ground measurements taken at temperate forest sites.

4 SAR principles

A detailed description of SAR systems, data acquisition and processing can be found in [50], [62], [90], [262], [264], [146], [329], [130] and [347]. In the following, only a basic description of an imaging SAR will be given focused on concepts relevant for the understanding of this thesis. In section 4.1 the SAR principle is explained. Section 4.2 introduces polarimetry and section 4.3 interferometry. A focus of section 4.3 is the interferometric coherence and non - volumetric decorrelation sources reducing the measured interferometric coherence. Finally, section 4.4 introduces Polarimetric SAR Interferometry (Pol-InSAR) – the combination of polarimetry and interferometry – as used in this thesis.

4.1 SAR system characteristics

4.1.1 Acquisition geometry

Typical for Radar Systems is the side looking geometry as shown in Figure 8. Radar imaging systems are active systems: an electromagnetic pulse is transmitted by the antenna perpendicular to the flight direction (range direction); the pulse is backscattered from the ground towards the sensor and received by the antenna.

Due to the side looking geometry pulses backscattered from scatterer closer to the antenna (near range) arrive earlier than the pulses backscattered from scatterer located more far away (far range). The time between transmission and reception Δt corresponds to the distance R between the scatterer and the antenna

$$R = \frac{c_0 \Delta t}{2} \tag{4.1}$$

where c_0 denotes the speed of light. The area illuminated with a single pulse is called antenna footprint.

The antenna moves forward (i.e. in azimuth direction) and transmits pulses with a given pulse repetition frequency (PRF). In between the antenna receives the pulses backscattered from the scene.

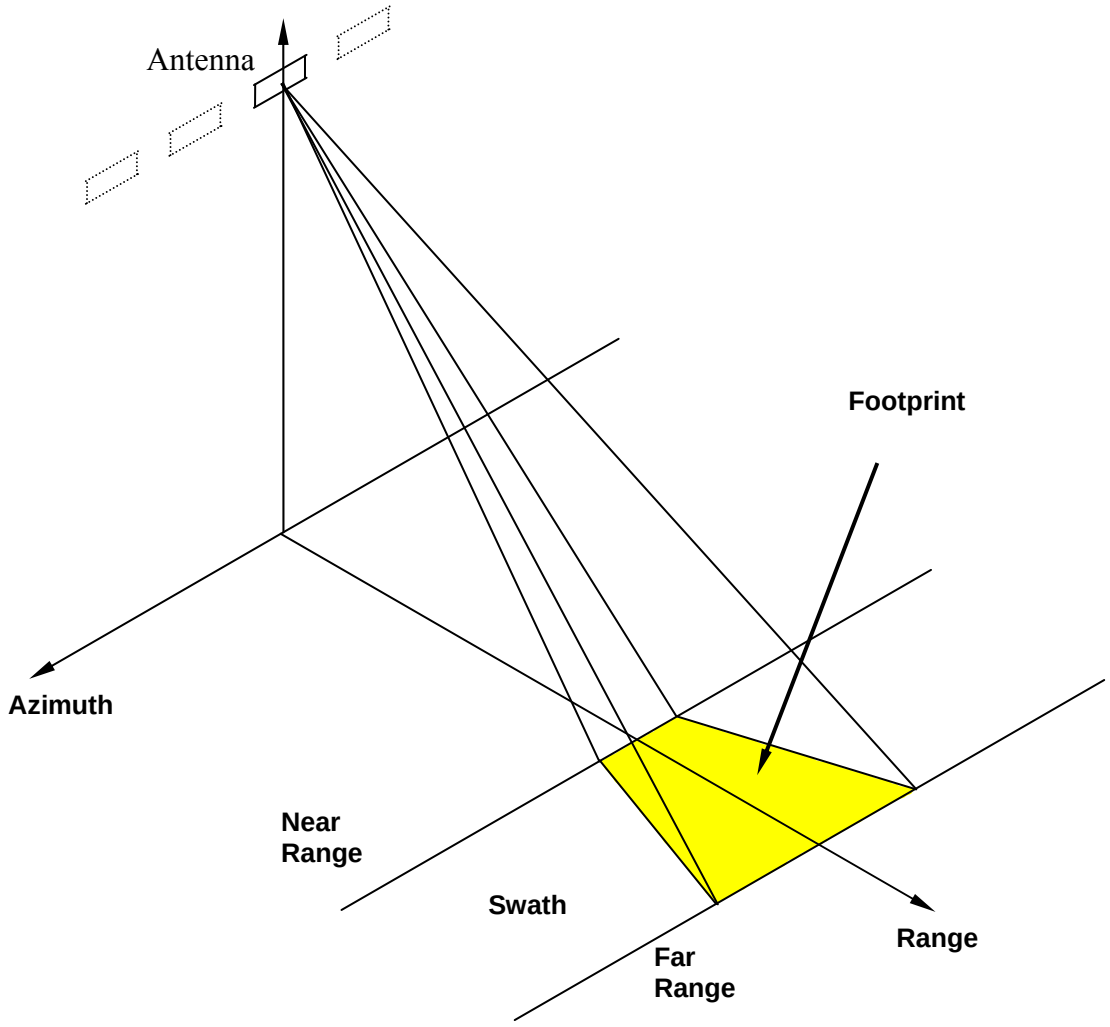

Figure 8: SAR imaging Geometry

4.1.2 Spatial resolution

One of the most important quality criteria of imaging systems is the spatial resolution. It describes the capability of an imaging system to separate spatially two scatterers from each other. In the case of a SAR the resolution in range direction differs from the resolution in azimuth direction.

4.1.2.1 Range resolution

The range resolution ρ_{rg} is given by the pulse length τ: Two objects can be resolved if their backscattered pulses do not overlap (see Figure 9 left):

$$\rho_{rg} = \frac{c * \tau}{2}. \tag{4.2}$$

The resolution can be only improved by a shorter pulse length τ.

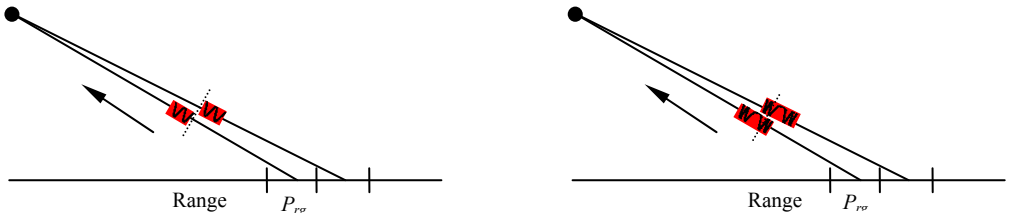

Figure 9: Range Resolution: comparison unmodulated signal (left) versus modulated signal (right).

In order to improve range resolution a frequency modulated pulse is often used: the frequency of the transmitted pulse changes linearly in time (see Figure 9 right). The extent of the frequency modulation is called bandwidth W. Frequency modulation requires further processing of the signal after recording by a matched filtering operation [169]. Then resolution in range becomes a function of the bandwidth:

$$\rho_{rg} = \frac{c}{2W}. \tag{4.3}$$

The higher the bandwidth, the better becomes the resolution. For example, a bandwidth of 100 MHz corresponds to a range resolution of 1.5 m.

The ground range resolution ρ_{ground} is the projection of the slant range geometry to the ground and depends therefore on the local incidence angle θ and is given by $\rho_{ground} = \rho_{rg} / \sin(\theta)$.

4.1.2.2 Azimuth resolution

The azimuth resolution of conventional radar imaging system depends on their swath width. Two scatterers can only be resolved as long as they are not within the same footprint. Therefore, azimuth resolution becomes a function of the distance between the antenna R, the wavelength λ and the length of the antenna D

$$\rho_{az} = \frac{R\lambda}{D}. \tag{4.4}$$

A long antenna reduces the beam width allowing a higher resolution, while a larger distance between antenna and scatterer results in poorer resolution.

SAR systems operate in a coherent mode: beside amplitude information (related to signal strength) also phase information (related to distance measurement) is recorded.

This allows to improve the azimuth resolution. The pulses backscatterd from a scatterer are received during the whole time the scatterer is illuminated by the radar footprint (see Figure 10). During azimuth processing all the energy received from the scatterer, distributed over the illumination time, is focussed: all pulses containing a contribution of the scatterer are coherently summed up [359]. For this the azimuth compressed signal $S(t)$ is obtained by a convolution of the received signal $a(t)$ with a reference function $H(t)$:

$$S(t) = a(t) * H(t) \quad \text{with} \quad H(t) = e^{i\frac{4\pi}{\lambda}\sqrt{R_0^2 + v^2 t^2}} \tag{4.5}$$

where $*$ is the convolution operator, R_0 the minimum range distance when the scatterer is at broadside, v the velocity of the platform, λ the wavelength and t the azimuth time. Eq. (4.5) is also called "Matched Filter".

Finally, the obtained azimuth resolution is independent of the distance between antenna and scatterer (R) and is only a function of the antenna length D :

$$\rho_{az} = \frac{D}{2}. \tag{4.6}$$

The price to be paid is that with a smaller antenna the same amount of energy is distributed over a large footprint reducing the signal-to-noise level in the received data.

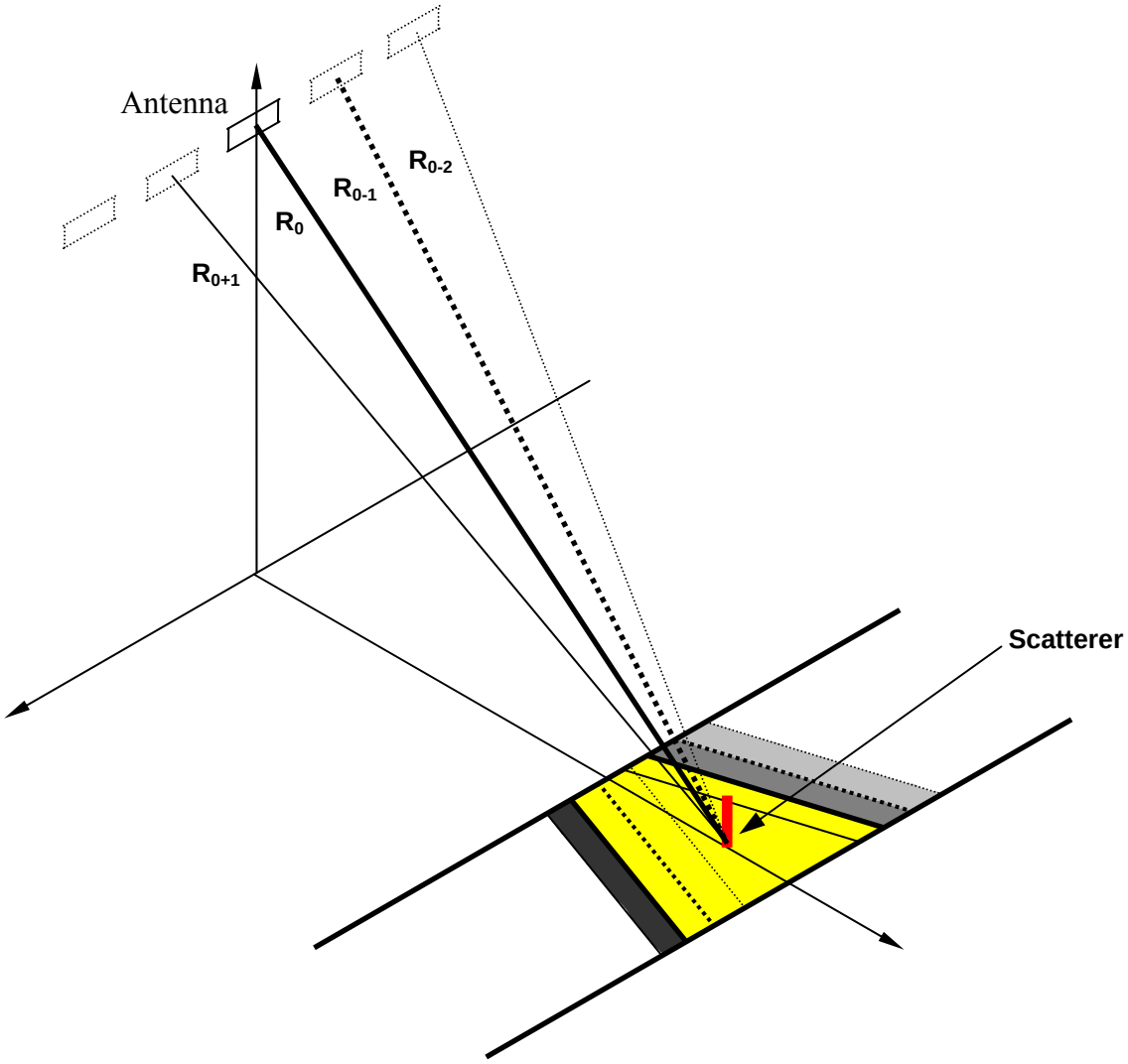

Figure 10: Acquisition of a point scatterer along azimuth

4.1.3 Effects in SAR images

4.1.3.1 Incidence angle

Typically the backscattered power depends on system parameters like frequency and polarizaiton and acquisition geometry parameters as the incidence angle but also on the

scatterer itself. The incidence angle θ_0 is defined as the angle between the incident radar beam and the surface normal (see Figure 11). Especially airborne systems deal with a huge variance of the incidence angle along the footprint, in the case of DLR's E-SAR [140] incidence angle changes from 25° (near range) to 55° (far range). Along with the incidence angle also the scattering behavior changes [42], [317].

4.1.3.2 Elevation changes

Since the radar is side-looking, changes in terrain elevation caused either by topographic variations (mountains) or abrupt changes in vegetation height introduce geometric distortions. Considering forests two main effects can be observed (see Figure 11):

Shadow results from illuminating a forest on a front side, while casting a shadow behind. This effect appears quite strong at higher frequencies like at X-band where the capability to penetrate in vegetation is low. Shadow regions appear as dark areas in the SAR image, corresponding to absence of backscattered power, but solely due to the system noise level of the radar sensor the intensity level may not be zero.

Layover effects appear when the top of a forest corner is closer to the sensor than the bottom. In this case one resolution cell encloses scattering from the forest canopy as well as from the field (area) in front of the forest. Layover regions appear bright in the radar image.

As already mentioned the signal S received consists of two parameters: phase and amplitude. Alternatively it can be represented by its real x and imaginary y part:

$$S = x + iy \,. \tag{4.7}$$

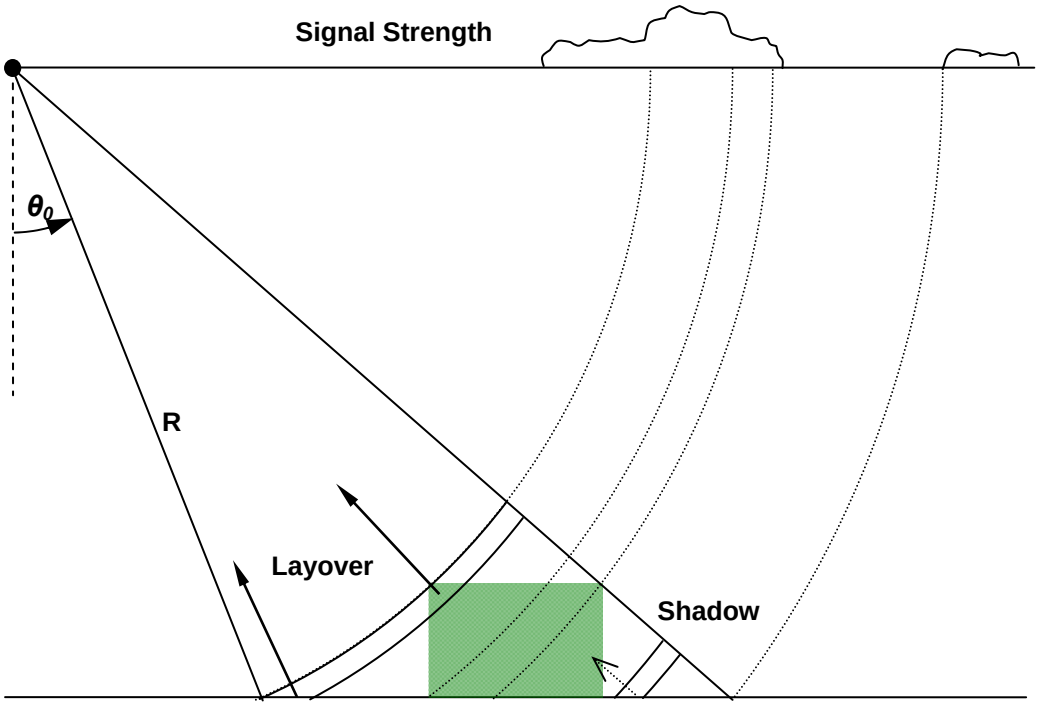

Figure 11: Acquisition Geometry: Shadow and Overlay effects in the case of a forest corner; R is the distance between scatterer and Antenna and θ_0 the incidence angle

The phase φ is given by the angle of the complex vector on the complex plane with the positive real axis $\tan(\varphi) = \frac{y}{x}$. The amplitude of the complex number (A) the signal strength (see Figure 12 left) is given by the length of the complex vector ($A = \sqrt{x^2 + y^2}$).

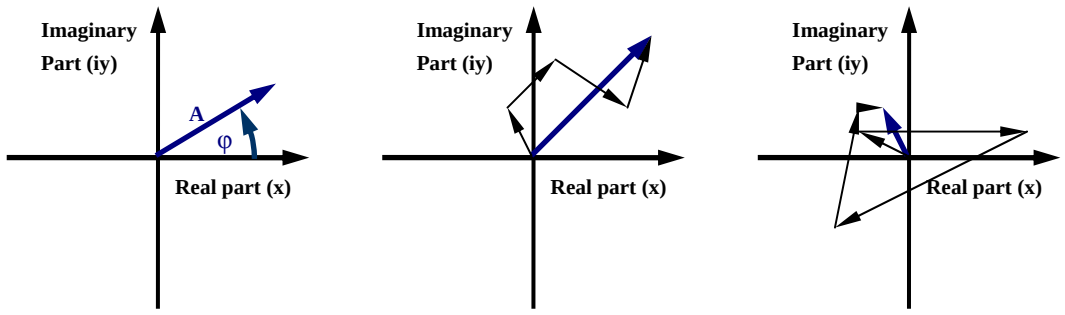

Figure 12: left: Representation of a SAR signal as a complex number; Middle: Coherent sum of signals resulting in a strong signal; Right: Coherent sum of signals resulting in a weak signal.

4.1.3.3 Speckle

When, the size of a resolution cell is many times larger than the radar wavelength and many elementary scatterers are loacated within it [51], [186], the relative distances between the elementary scatterers depending on their random positions affect the phase of the received SAR signal. The total backscattered signal (S) received is given by the coherent sum of the signals scattered by each single scatterer (S_i) within a resolution cell (see Figure 13 left)

$$S = \sum_{i=1}^{N} S_i(\varphi, A) \,. \tag{4.8}$$

Eq. (4.8) can be represented in the complex plane as a vector sum (see Figure 12 middle and right). A strong signal is received if the signals of all scatterers within a resolution cell are added in a constructive way (see Figure 12 middle), while a weak signal appears if the single waves are added in a destructive way (Figure 12 right) or when backscattering is weak. As the locations of the scatterers within a resolution cell vary from pixel to pixel a granular noise pattern appears in SAR images, due to the induced amplitude and phase variation. Such scatterers are called distributed scatterer. Typically this scattering behavior appears at distributed scatterers including several natural scatterers such as forests and fields. If a resolution unit is dominated by a single scatterer then the returned signal is mainly dependent on the scattering behavior of this scatterer.

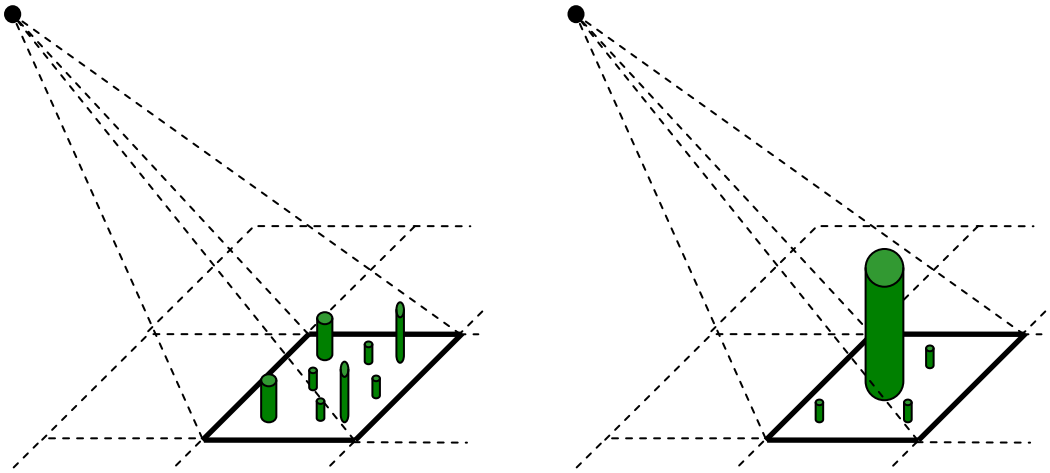

Figure 13: Scattering within one resolution cell, left: Distributed scatterer, right: Point scatterer

The change in amplitude and phase from pixel to pixel (speckle) makes the measure of intensity in the case of distributed scatterer erroneous. A common approach to reduce speckle effects is to average several independent measurements. One possibility of speckle reduction is to divide the length of the synthetic aperture (i.e. the swath width along azimuth) into L (number of looks) segments whereas every segment is processed independently and added to each other. The signal amplitude of the scene (A_{ML}) becomes the mean value of the amplitudes (S_{im}) corresponding to the (total) illumination time of the scatterer by the SAR of all scenes added [252], [208]:

$$A_{ML} = \frac{1}{L}\sum_{i=0}^{L}\left|S_{im}\left(A_{im},\varphi_{im}\right)\right|. \tag{4.9}$$

This process is called Multilooking and goes along with a reduction in azimuth resolution. In a similar way Multilooking can also be implemented in range where samples corresponding to different Parts of the bandwidth are averaged. Note that in this case a coherent summation of L images does not reduce speckle because this process is equal to a vector sum of the total number of scatterer within a resolution unit. With increasing number of looks the standard deviation ν of signal amplitude is reduced by a factor of $\sqrt{L}$ [208], [252] and [248].

$$\nu_{ML} = \frac{\nu_{SL}}{\sqrt{L}} \tag{4.10}$$

where the ν_{ML} stands for the standard deviation of the multilooked image and ν_{SL} for standard deviation of the single look (SLC) image. Figure 14 presents details of an acquisition over Traunstein site (see for test site description **Publication V [198]**) before (left) and after (right) multi looking using a time series of 30 acquisitions.

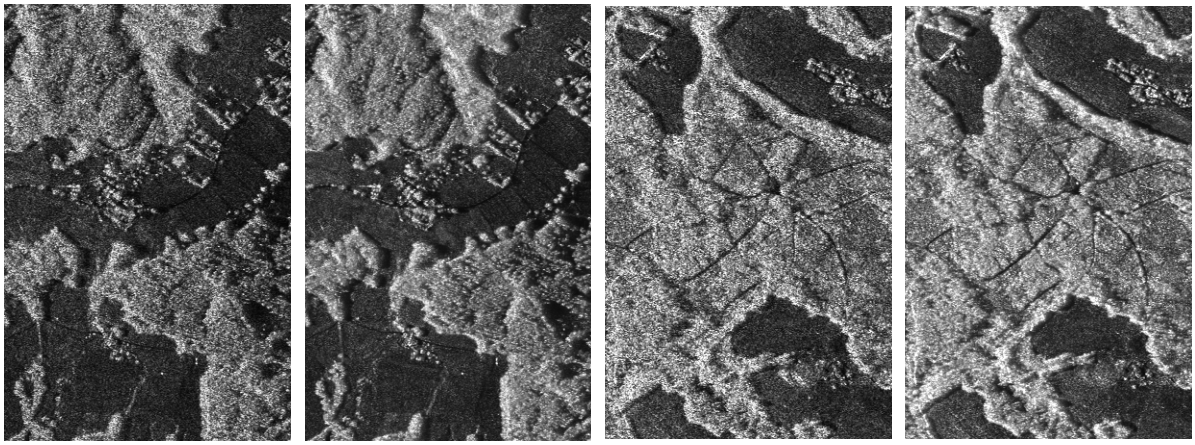

A **B** **C** **D**

Figure 14: Details HH Amplitude Image Traunstein site (for test site description see Publication V [198]); A and C: single look images, B and D: the corresponding multi look images (combination of 30 independent images/looks)

4.1.4 Radiometric resolution

The radiometric resolution refers to the capability of an imaging system, in this case of an SAR system, to separate two scatterers from each other based on the received intensity. The intensity is defined as the square of the amplitude $I = A^2$ [170]. The radiometric resolution δ_{rad} [252] is defined as follows:

$$\delta_{rad} = 10 \log_{10}\left(\frac{\bar{I} + \nu_{ML}}{\bar{I}}\right) \tag{4.11}$$

where $\bar{I}$ is the expectation of intensity [170]. In SAR images intensity is exponential distributed [208], [252] so that expectation $\bar{I}$ becomes equal to the standard deviation ν. Then Eq. (4.11) can be rewritten using Eq. (4.10) as follows

$$\delta_{rad} = 10 \log_{10}\left(1 + \frac{1}{\sqrt{L}}\right) \tag{4.12}$$

and the radiometric resolution becomes just a function of the number of looks L.

4.1.5 Radar backscattering coefficient

The radar backscattering coefficient σ is defined as the ratio of the received intensity I_S to the transmitted intensity I_I [170]

$$\sigma = \frac{I_S^2}{I_I^2} \quad . \tag{4.13}$$

Relating the measurement to an area and normalizing it to the ground yields the radar cross section sigma naught σ^0

$$\sigma^0 = 10\log_{10}\left(\frac{\sigma}{\delta_{rg}\delta_{az}}\sin(\theta)\right) \tag{4.14}$$

where θ is the local incidence angle which is a function of terrain slope and $\sin(\theta)$ projects the reference area from radar geometry to ground geometry. The unit of sigma naught is decibel [dB].

4.1.6 Signal to Noise Ratio

The potential of a radar system in detecting weak signals is limited by the noise level of the receiver [170]. The noise power (P_T) basically originates from the thermal noise on the receiver and depends on the system bandwidth [51]. The Signal to Noise Ratio (SNR) is the ratio between signal power and noise level

$$SNR = \frac{P_S}{P_T} \tag{4.15}$$

where (P_S) is the mean signal Power of the received unprocessed Signal and can be determined by the radar equation [358]. It shows that SNR is influenced by two classes of parameters, those which are determined by the design of the system and those determined by the acquired scene which is only expressed by σ^0.

4.2 SAR-polarimetry

4.2.1 Polarimetry basics

An important extension to single channel SAR remote sensing is by the utilization the vectorial nature of waves in terms of SAR polarimetry [274], [208], [46]. Polarimetry allows to discriminate different scattering mechanisms occuring within one resolution cell.

SAR polarimetry investigates the way a polarized electromagnetic wave is modified by its interaction with a scatterer. Basic concepts of SAR polarimetry can be found in [208], [26], [27] and [28]. In the following a short introduction into SAR polarimetry is given.

Electromagnetic waves, as the transmitted /received SAR pulses, are described by Maxwell's equations. For the special case of constant amplitude monochromatic plane waves, propagation of an electromagnetic wave can be expressed as

$$\vec{E}(\vec{r},t) = \vec{E}_0 e^{-i\left(\omega t \pm \vec{k}\vec{r}\right)} \tag{4.16}$$

where $\vec{k}$ is the propagation vector, $\vec{r}$ the position vector, $\vec{E}_0$ the amplitude and ω the angular frequency $\omega = 2\pi f$. This can be simplified by representing the electric field in an orthogonal basis (x, z, y) so that the direction of propagation $\vec{k} = z$.

Polarization is related to the vectorial nature of electromagnetic waves and describes the orientation of the electric field vector in the plane perpendicular to the direction of

propagation as a function of time, spanned by any orthogonal polarization basis. Here the horizontal (H) - vertical (V) basis is chosen.

The horizontal component (H) of $\vec{E}$ is projected on the x-axis while the vertical component (V) of $\vec{E}$ is projected on the y-axis. Then the expression takes the form

$$\vec{E}(z,t) = \begin{bmatrix} E_{0H}\cos(\omega t \pm kz + \delta_H) \\ E_{0V}\cos(\omega t \pm kz + \delta_V) \\ 0 \end{bmatrix} \tag{4.17}$$

where

$$k = \frac{2\pi}{\lambda} \tag{4.18}$$

is the wavenumber that depends on the wavelength λ. δ_H and δ_V are the absolute phase terms in the horizontal (H) and vertical (V) direction. Eq. (4.17) implies that the electric field is composed by two orthogonal sinusoidal waves with, in general, different amplitudes and phases at the origin

$$E_H = E_{0H}\cos(\omega t + \delta_H) \tag{4.19}$$

and

$$E_V = E_{0V}\cos(\omega t + \delta_V). \tag{4.20}$$

Accordingly, the electric field describes a parametric curve with three degrees of freedom (see Figure 15) the amplitude in the horizontal dimension E_{0H}, the amplitude in the vertical dimension E_{0V} and the phase difference $\delta_H - \delta_V$. Three types of polarizations can be specified:

- Linear polarizations (see Figure 15 I + II): For Linear polarizations the phase difference $\delta_H - \delta_V = 0$ while the Amplitudes E_{0H} and E_{0V} can have any values. For the special cases of horizontally polarized (see Figure 15 II) waves $E_{0V} = 0$ while for vertically polarized waves $E_{0H} = 0$.
- Circular polarizations (see Figure 15 III): For circular polarizations $\delta_H - \delta_V = \pm\frac{\pi}{2} + n\pi,\ n \in Z$ and $E_{0H} = E_{0V}$. Here the electric field rotates circularly around the z-axis (propagation direction).
- Elliptic polarizations (see Figure 15 IV): Represents all other cases.

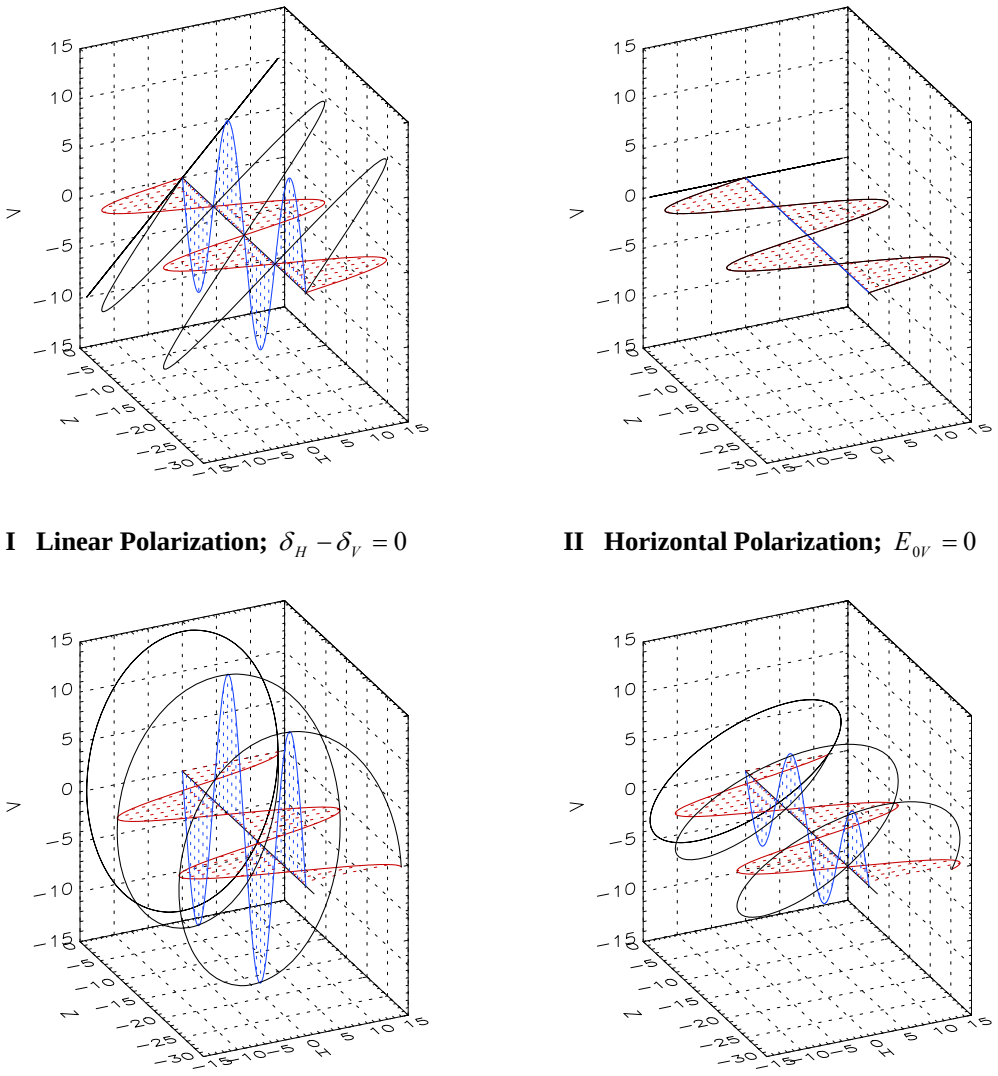

I Linear Polarization; $\delta_H - \delta_V = 0$

II Horizontal Polarization; $E_{0V} = 0$

III Circular Polarization; $E_{0H} = E_{0V}$ **and** $\delta_H - \delta_V = \pm\frac{\pi}{2} + n\pi,\ n \in \mathrm{N}$

IV Elliptic Polarization

Figure 15: Polarization stages; red: horizontal component of electric field; blue: vertical component of electric field; black: total electric field

4.2.2 Jones vector and scattering matrices

For describing the electromagnetic field in a complex vector form, the Jones vector is used [159], [160]

$$\vec{E} = \begin{bmatrix} E_H \\ E_V \end{bmatrix} = \begin{bmatrix} E_{0H} e^{i\delta_H} \\ E_{0V} e^{i\delta_V} \end{bmatrix}. \tag{4.21}$$

The Jones vector expresses the electromagnetic field ($\vec{E}$) in any orthogonal basis, in Eq. (4.21) the lexicographic polarization basis (horizontal and vertical) was chosen. A scatterer acquired in an orthogonal polarization basis can be expressed in any polarization basis by a

mathematical transformation and does not require any additional measurements [231], [232].

As shown in Eq. (4.13) the backscattered signal can be characterized by the backscattering coefficient σ and its polarization state (Eq. (4.21)). The interaction of an electromagnetic wave with a scatterer generally modifies its polarization state. If a is the polarization of the incident field and b the polarization of the scattered field then the radar cross section becomes polarization dependent

$$\sigma_{ab} = \frac{|\vec{E}_{Ia}|^2}{|\vec{E}_{Sb}|^2}. \tag{4.22}$$

Eq. (4.22) does not exploit the complete polarimetric information of the vector nature of polarized electromagnetic waves. In order to take advantage of the full polarimetric information the concept of the scattering matrix that realtes the incident to the scattered Jones vector is used:

$$\vec{E}_S = \frac{e^{ikr}}{r} S \ \vec{E}_I = \frac{e^{ikr}}{r} \begin{bmatrix} S_{11} & S_{12} \\ S_{21} & S_{22} \end{bmatrix} \vec{E}_I. \tag{4.23}$$

The term $\frac{e^{ikr}}{r}$ accounts for the propagation effects in amplitude and phase of the electromagnetic wave (r is the distance), S is the 2 x 2 complex scattering matrix and S_{ij} are the complex scattering coefficients where i is the receive polarization and j the transmit polarization [28]. In the horizontal- vertical basis the scattering matrix is given by

$$S = \begin{bmatrix} S_{HH} & S_{HV} \\ S_{VH} & S_{VV} \end{bmatrix} = e^{j\phi HH} \begin{bmatrix} |S_{HH}| & |S_{HV}| e^{i\phi HV - \phi HH} \\ |S_{VH}| e^{i\phi VH - \phi HH} & |S_{VV}| e^{i\phi VV - \phi HH} \end{bmatrix}. \tag{4.24}$$

The diagonal elements of S are called co-polarized (incident and scattered polarization are the same), the off- diagonal cross-polarized (incident and scattered polarization are orthogonal to each other). The scattering matrix describes completely how the polarization of an incident wave is modified by the interaction with a scatterer and contains seven parameters (4 amplitudes and three relative phases. For monostatic scattering i.e. when transmitter and receiver are colocated the reciprocity theorem [42] forces the cross-polarized channels to be equal $S_{HV} = S_{VH}$. In this case the scattering matrix is characterized by only five parameters (3 amplitudes and 2 relative phases).

The total scattered power $SPAN$ is the sum of the absolute squares of S.

$$SPAN = |S_{HH}|^2 + |S_{VV}|^2 + 2|S_{HV}|^2. \tag{4.25}$$

The scattering matrix is suitable to describe completely polarimetric deterministic scatterers. In contrast polarimetric stochastic scatterers consist of multiple scatterers (see Figure 13 left side) each with a different scattering matrix causing a depolarization of the backscattered field. Such scatterers require for a complete description a second order

formulation. For this the scattering matrix is vectorized to get a scatterer vector that contains the whole coherent polarimetric information [358].

There are several basis sets that can be used for the vectorization of the scattering matrix. Most important are the lexicographic basis set which corresponds to a straightforward ordering of the system measurements and the Pauli basis set which allows a more straightforward physical interpretation by means of elementary scattering mechanisms (single bounce scattering, double bounce scattering and volume scattering).

The scatterer vector associated with the lexicographic basis of a monostatic system is given by:

$$\vec{k}_L = [S_{HH}, \sqrt{2}S_{HV}, S_{VV}]^T \tag{4.26}$$

and the scatterer vector for the Pauli basis by:

$$\vec{k}_P = \frac{1}{\sqrt{2}}[S_{HH} + S_{VV}, S_{HH} - S_{VV}, S_{HV} + S_{VH}]^T \tag{4.27}$$

The Pauli basis can also be used as a first order representation of different scattering mechanisms. Then $S_{HH} + S_{VV}$ represents surface scattering, $S_{HH} - S_{VV}$ ground scattering and $S_{HV} + S_{VH}$ volume scattering. An RGB color composite of the Pauli scattering mechanisms is shown in Figure 16 C for the Traunstein site (for test description see **Publication V [198]**) where red indicates dihedral scattering ($S_{HH} - S_{VV}$), green volume scattering ($S_{HV} + S_{VH}$) and blue surface scattering ($S_{HH} + S_{VV}$). Volume scattering and a mixture of all three scattering mechanisms (white) seem to be the dominant scattering mechanisms over the forested areas. For comparison also an optical image (Figure 16 A) and the HH polarized intensity is added (see Figure 16 B)

Eq. (4.26) and Eq. (4.27) are coherent representations of the scattering matrix and their norm equals the $SPAN$ of the scatterer (which explains the factors $\frac{1}{\sqrt{2}}$ and $\sqrt{2}$).

In order to compensate for the absolute phase term induced by the sensor-reflector path and to study the second order polarimetric statistics, i.e. the correlation between different polarizations the polarimetric covariance matrix and / or coherency matrix are introduced. The polarimetric covariance matrix is defined as

$$[C_3] = \left\langle \vec{k}_P \vec{k}_P^{+} \right\rangle = \begin{bmatrix} \left\langle |S_{HH}|^2 \right\rangle & \sqrt{2}\left\langle S_{HH} S_{HV}^{*} \right\rangle & \left\langle S_{HH} S_{VV}^{*} \right\rangle \\ \sqrt{2}\left\langle S_{HV} S_{HH}^{*} \right\rangle & 2\left\langle |S_{HV}|^2 \right\rangle & \sqrt{2}\left\langle S_{HV} S_{VV}^{*} \right\rangle \\ \left\langle S_{VV} S_{HH}^{*} \right\rangle & \sqrt{2}\left\langle S_{VV} S_{HV}^{*} \right\rangle & \left\langle |S_{VV}| \right\rangle \end{bmatrix} \tag{4.28}$$

while the polarimetric coherency matrix as

$$[T_3] = \left\langle \vec{k}_P \vec{k}_P^{+} \right\rangle = \frac{1}{2}\begin{bmatrix} \left\langle |S_{HH} + S_{VV}|^2 \right\rangle & \left\langle (S_{HH} + S_{VV})(S_{HH} - S_{VV})^{*} \right\rangle & 2\left\langle (S_{HH} + S_{VV})\ S_{HV}^{*} \right\rangle \\ \left\langle (S_{HH} - S_{VV})(S_{HH} + S_{VV})^{*} \right\rangle & \left\langle |S_{HH} - S_{VV}|^2 \right\rangle & 2\left\langle (S_{HH} - S_{VV})\ S_{HV}^{*} \right\rangle \\ 2\left\langle S_{HV}^{*} (S_{HH} + S_{VV}) \right\rangle & 2\left\langle S_{HV}^{*} (S_{HH} - S_{VV}) \right\rangle & 4\left\langle |S_{HV}| \right\rangle \end{bmatrix} \tag{4.29}$$

where $\langle\ \rangle$ denotes the expected value, implemented as spatial averaging, the superscript $^+$ the complex conjugate transpose and the superscript * the complex conjugate only. Both, $[C_3]$ and $[T_3]$ are equivalent and can be transformed to each other by a change of base unitary transformation [42]. $[C_3]$ and $[T_3]$ contain nine independent parameters, three real power values, on the main diagonal, and three off diagonal complex correlations between the single elements of the scattering matrix S.

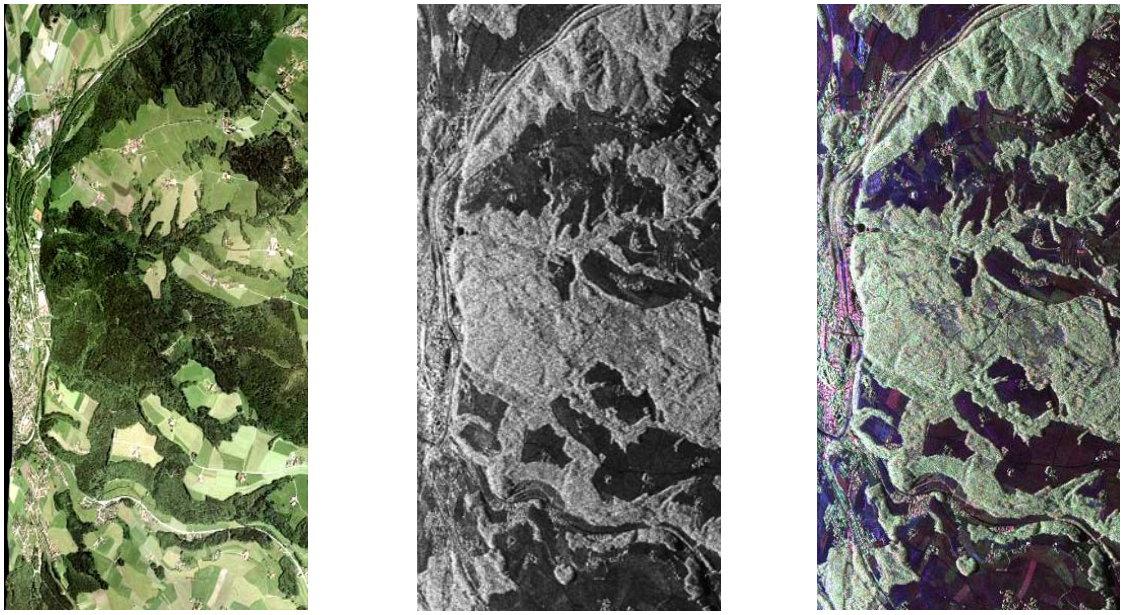

A **B** **C**

Figure 16: Traunstein site (for test description see Publication V [198]); A: optical image obtained from aerial photography; B: greyscale single channel SAR image in HH polarization; C: Color composite of the pauli basis (see Eq. 4.27) where red = dihedral scattering, green = volume scattering and blue = surface scattering

4.3 SAR-interferometry

Across-track interferometric SAR (InSAR) is a technique that provides topographic information by combining two SAR images acquired with slightly different incidence angles. SAR interferometry was probably first demonstrated by Graham [111]. The idea of SAR interferometry is explained in detail in [301], [15] and [114]. Here only basic concepts are introduced.

4.3.1 Interferometric measurement principle

A characteristic of SAR received pulses is a phase term that linearly depends on the slant range distance between the antenna and the scatterer. Through the combination of two SAR images of a scene separated by a spatial (across-track) baseline (see acquisition geometry in Figure 17) a phase difference can be measured and linked to topography [15], [114]. Before generating an interferogram, the two SAR images must be coregistered [249], [93].

An interferogram S_{Int} is formed by multiplying one image S_1 by the complex conjugate of a second (coregistered) image S_2

$$S_{Int} = S_1 \, S_2^* \, . \tag{4.30}$$

Then the interferometric phase ϕ is given by

$$\phi = \text{atan}\left(\frac{\text{Im}(S_{I\,\text{int}})}{\text{Re}(S_{I\,\text{int}})} \right) \tag{4.31}$$

where Im denotes the imaginary part and Re the real part of a complex number. In an ideal case the interferogram formation cancels out the speckle phase pattern, but preserves the phase term dependent on the path length difference between the two images [301].

InSAR measurements can be either made in a single pass mode or in a repeat pass mode. In the single pass mode, both images are simultaneously acquired, in the repeat pass mode, however, the two images are successively acquired with a given temporal baseline that can range from seconds to months.

Moreover, the single pass mode can be further divided into monostatic and bistatic mode. In the monostatic mode the two antennas are operated independently from each other: each antenna transmits and receives. In the bistatic mode only one antenna acts as transmitter and both antennas receive simultaneously.

A sketch of the across-track interferometric acquisition geometry is given in Figure 17. Two antennas A_1 and A_2 are separated by a spatial baseline B, which has a component perpendicular to the look direction, called perpendicular or effective baseline $B_\perp$ and ξ is the tilt angle of the baseline. R_1 and R_2 are the distances of the two antennas A_1 and A_2 (i.e. slant range distance) to the scatterer P. R_1 can be calculated by the propagation time of the signal. The slant range difference ΔR can be calculated by

$$\Delta R = R_2 - R_1 \tag{4.32}$$

with

$$R_2 = \sqrt{R_1^2 + B^2 - 2R_1 B \sin(\theta_1 - \xi)} \, . \tag{4.33}$$

This can be reformulated as

$$\sin(\theta_1 - \xi) = \frac{R_2^2 - R_1^2 - B^2}{2R_1 B} \, . \tag{4.34}$$

If the baseline parameters B and ξ are known, the look angle θ_1 can be calculated from Eq. (4.34) and terrain height h_{Topo} can be estimated as

$$h_{Topo} = H - R_1 \cos(\theta_0) \tag{4.35}$$

where H is the height of antenna A_1 over the reference ground. In a conventional SAR the estimation of R_1 is rather imprecise and the estimation precision of h_{Topo} depends on the sampling frequency, i.e. the accuracy of h_{Topo} is on an order proportional to the image resolution. In general the method delivers only coarse terrain height estimates. InSAR allows a considerably finer resolution in vertical direction because ΔR is estimated by means of a phase difference and is therefore much more precise than each range distance.
The two phases ϕ_1 and ϕ_2 of the signals S_1 and S_2 measured at each end of the baseline can be written as

$$\phi_1 = -m\frac{2\pi}{\lambda}R_1 + \beta_1 \tag{4.36a}$$

and

$$\phi_2 = -m\frac{2\pi}{\lambda}R_2 + \beta_2 . \tag{4.36b}$$

β_1 and β_2 correspond to the scattering phase of the observed scatterer, m accounts for the acquisition mode. For monostatic acquisitions $m = 2$ while for bistatic acquisitions $m = 1$. Assuming $\beta_1 = \beta_2$, i.e. the same speckle pattern in both acquisitions, the interferometric phase ϕ is given by:

$$\phi = \phi_1 - \phi_2 = m\frac{2\pi}{\lambda}(R_1 - R_2) = m\frac{2\pi}{\lambda}\Delta R . \tag{4.37}$$

But note that ϕ is known only in modulo 2π. Phase unwrapping allows to overcome this problem. Phase unwrapping methods are described in [15] and [114].

4.3.2 Flat earth

Two points with different slant range coordinates but with the same terrain height are characterized by a phase difference in their interferometric phase known as flat earth phase ϕ_{Flat}. This phase often needs to be removed before associating a change of phase to a change in terrain height. ϕ_{Flat} is induced by the difference in ΔR (see Eq. 4.32) between two consecutive range pixels (ΔR_1 and ΔR_2) under the assumption of a flat earth.

$$\phi_{Flat} = m\frac{2\pi}{\lambda}(\Delta R_1 - \Delta R_2) \tag{4.38}$$

After removal of the flat earth changes in the interferometric phase are in first order only induced by changes in the topography. The topographic phase ϕ_{Topo} is then given by:

$$\phi_{Topo} = \phi - \phi_{Flat} . \tag{4.39}$$

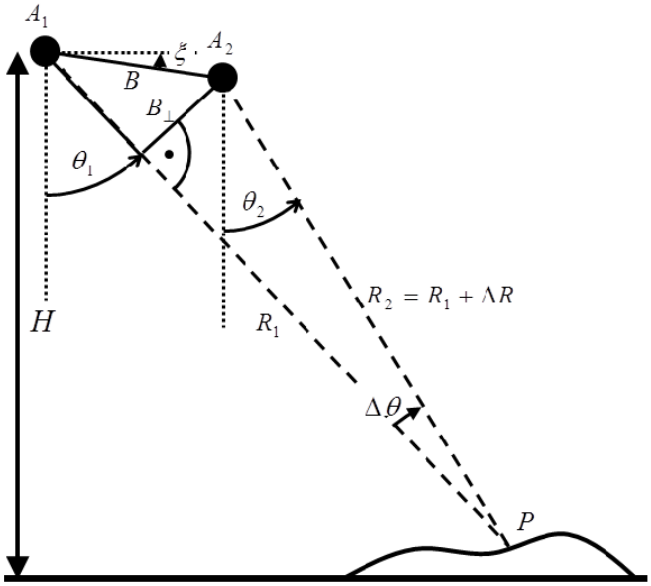

Figure 17: Interferometric SAR acquisition geometry; H is the height of the antenna A_1 over ground, R_1 the distance between A_1 and the ground point P, R_2 the distance between A_2 and P, θ_1 the incidence angle of A_1 at P, θ_2 the incidence angle of A_2 at P, $\Delta\theta$ is the difference between the two incidence angles θ_1 and θ_2 at P, B the baseline between A_1 and A_2, ξ the tilt angle of the baseline, $B_\perp$ the perpendicular baseline and ΔR is the difference in range from each antenna to P.

4.3.3 Phase to height conversion

The performance of quantitative interferometric techniques critically depends on the effective spatial baseline used for the interferometric acquisition(s). The parameter commonly used to express the effective spatial baseline is the vertical wavenumber κ_Z approximated by

$$\kappa_z = \mathrm{m}\frac{2\pi}{\lambda}\frac{\Delta\theta}{\sin\theta_1}. \tag{4.40}$$

If the baseline B is small compared to the slant range distance R_1, as it is the case for spaceborne interferometric systems where B is on the order of some hundreds of meters and R_1 on the order of hundred kilometers, κ_Z can also be approximated by

$$\kappa_z = \mathrm{m}\frac{2\pi}{\lambda}\frac{B_\perp}{\sin\theta_1 R_1}. \tag{4.41}$$

$\Delta\theta$ is the angular separation of the two acquisitions in the direction of the resolution cell and $B_\perp$ is the effective (perpendicular) baseline. The interferometric phase is then related to terrain height h_{Topo} by:

$$h_{Topo} = \frac{\phi_{Topo}}{\kappa_Z} \tag{4.42}$$

where the vertical wavenumber κ_Z scales the interferometric phase ϕ_{Topo} to height h_{Topo}. The height that corresponds to an interferometric phase change of 2π is called height of ambiguity (HoA) and is defined as:

$$HoA = \frac{2\pi}{\kappa_Z} \tag{4.43}$$

4.3.4 Coherence

Coherence is a statistical comparison between neighbouring pixels in two SAR images and measures the interferogram quality. The assumption $\beta_1 = \beta_2$ is not necessarily true when the vertical and horizontal components of the scatterers are differently projected into the two SAR images. Then the interferometric phase contains another phase term, the scatterer phase ϕ_{Scat}

$$\phi_1 - \phi_2 = \phi_{Topo} + \phi_{Flat} + \phi_{Scat}\,. \tag{4.44}$$

ϕ_{Scat} decorrelates the interferometric coherence but contains information about the properties of a scatterer.

Let $S_1(\vec{w})$ and $S_2(\vec{w})$ be two interferometric images acquired with a given spatial and temporal baseline (see acquisition geometry in Figure 17). The unit vector $\vec{w}$ indicates the polarimetric dependency, i.e. the polarization of the two images [352], [40]. The complex interferometric coherence $\tilde{\gamma}_{Obs}(\vec{w})$ is given by

$$\tilde{\gamma}_{Obs}(\vec{w}) := \frac{\left\langle S_1(\vec{w}) \cdot S_2^*(\vec{w}) \right\rangle}{\sqrt{\left\langle S_1(\vec{w}) \cdot S_1^*(\vec{w}) \right\rangle \left\langle S_2(\vec{w}) \cdot S_2^*(\vec{w}) \right\rangle}} \tag{4.45}$$

which includes both, the interferometric coherence (or correlation) coefficient $|\tilde{\gamma}_{Obs}(\vec{w})| = \gamma_{Obs}(\vec{w})$ and the (multi-looked) interferometric phase $\arg(\tilde{\gamma}_{Obs}(\vec{w}))$. Coherence scales between 0 (no correlation) and 1 (total correlation).

In practice, coherence is approximated by a spatial averaging of neighboring pixels [15]. Figure 17 shows the radar amplitude image (A), the interferometric coherence (B) and the interferometric phase of a TanDEM-X acquisition over Traunstein site (for test description see **Publication V [198]**). Coherence over forested areas is due to volume decorrelation (extensively discussed in section 5.1) significantly lower than over agricultural land. Changes in the interferometric phase in Figure 17 C reflect changes in the topography.

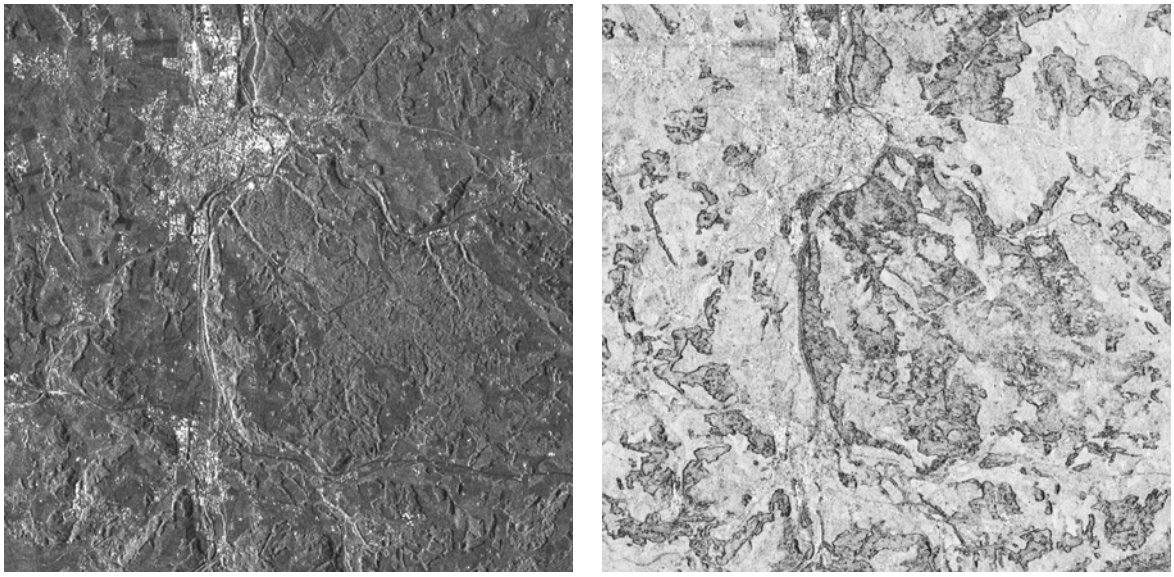

A B

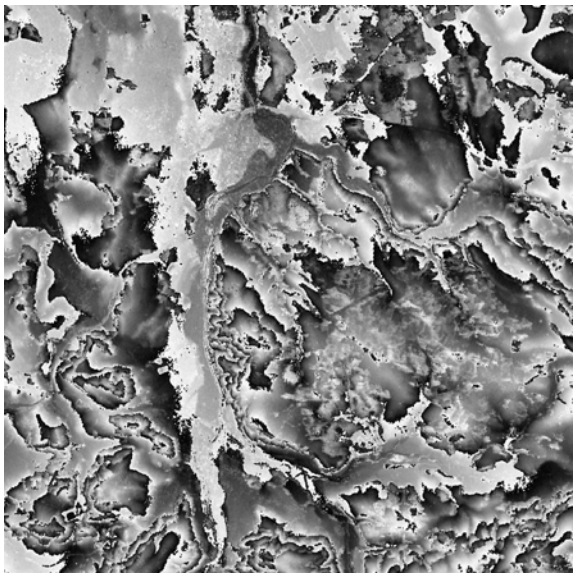

C

Figure 18: TanDEM-X acquisition over Traunstein site (for test description see Publication V [198]) from 2013-05-18 in HH polarization; A: greyscale radar amplitude image; B: interferometric coherence scaled from 0 (black) to 1 (white); C: interferometric phase scaled from $-\pi$ (black) to $-\pi$ (white).

4.3.5 Coherence and phase statistics

The estimation accuracy of the measured coherence $\tilde{\gamma}_{Obs}(\vec{w})$ depends on the underlying coherence level and is given by the standard deviation of its magnitude $\sigma_{\gamma}(|\tilde{\gamma}_{Obs}|, L)$ and phase $\sigma_{\phi}(|\tilde{\gamma}_{Obs}|, L)$. Both are defined by the coherence level $|\tilde{\gamma}_{Obs}|$ and the number of looks L used for the estimation of $\tilde{\gamma}_{Obs}$ [15], [349], [350], [161], [207]

$$\sigma_{\phi}^2 = \int_{-\pi}^{\pi} [\varphi - E\{\phi\}]^2 \; pdf(\phi, |\tilde{\gamma}_{Obs}|, \phi_0) \; d\phi \tag{4.46}$$

with

$$pdf(\phi,\gamma_{Obs},\phi_0)=\frac{\Gamma(L+0.5)(1-\gamma_{Obs}^2)^2|\gamma_{Obs}|\cos(\phi-\phi_0)}{2\sqrt{\pi}\ \Gamma(L)\ \left(1-\gamma_{Obs}^2\cos^2(\phi-\phi_0)\right)^{N+0.5}}+\frac{(1-\gamma_{Obs}^2)}{2\pi}\ {}_2F_1\left(L,1,0.5,\gamma_{Obs}^2\cos^2(\phi-\phi_0)\right)$$

with $\phi=\arg(\tilde{\gamma}_{Obs})$ and $E\{\phi\}$ is the expectation value of ϕ, ${}_2F_1(...)$ a hypergeometric function and $\Gamma(...)$ the Gamma function. The expectation value of $\tilde{\gamma}_{Obs}$ is given through

$$\sigma^2_{|\hat{\gamma}_{Obs}|}=\left[\frac{\Gamma(L)\ \Gamma(2)}{\Gamma(L)}\ {}_3F_2(2,L,L;L+1,1;|\hat{\gamma}_{Obs}|^2)(1-|\hat{\gamma}_{Obs}|^2)^N\right]-E\{|\hat{\gamma}_{Obs}|\}^2 \tag{4.47}$$

where $E\{|\tilde{\gamma}_{Obs}|\}$ is and ${}_3F_2(...)$ a hypergeometric function. The expectation value of $E\{|\tilde{\gamma}_{Obs}|\}$ is described by [349]:

$$E\{|\tilde{\gamma}_{Obs}|\}=\frac{\Gamma(L)\Gamma(3/2)}{\Gamma(L+1/2)}\ {}_3F_2(3/2,L,L,L+1/2,1;|\gamma|^2)(1-|\gamma|^2)^N \tag{4.48}$$

where γ is the 'true' coherence value. Unfortunately, the coherence estimate is biased it tends to overestimate low coherences (see Figure 19 C).

Plots of the phase standard deviation, the coherence standard deviation and the coherence bias as a function of coherence level are shown in Figure 19 A, B and C for 16 and 64 looks respectively. The higher the number of looks L the more accurate is the coherence estimation of $\tilde{\gamma}_{Obs}(\vec{w})$. But at the same time a large number of looks reduces the spatial resolution and may compromise the requirement of spatial homogeneity. High coherences indicate a precise estimate of ϕ_{Topo} in terms of standard deviation. Too low coherence levels (< 0.3) are due to the increased phase variance not suitable for a deeper analysis or any physical interpretation at least for a reasonable number of looks.

In this study coherence is estimated with at least 64 looks, so that the coherence bias can be widely neglected.

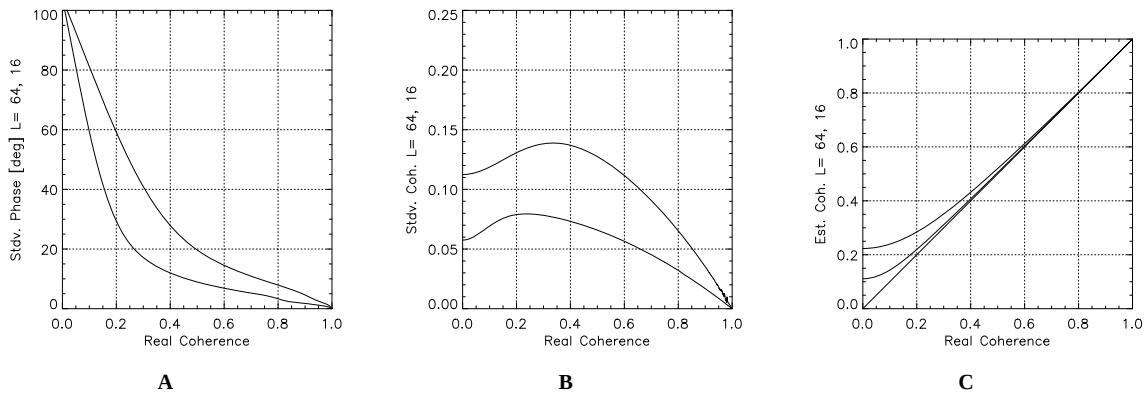

Figure 19: Coherence and phase statistics for L = 16 and for L = 64; A: standard deviation of phase; B: standard deviation of coherence; C: coherence bias

4.3.6 Coherence interpretation

$\tilde{\gamma}_{Obs}(\vec{w})$ comprises several decorrelation contributions [382], [178], [179], [15]

$$\tilde{\gamma}_{Obs}(\vec{w}) = \gamma_{Sys}(\vec{w})\ \tilde{\gamma}_{Tmp}(\vec{w})\ \tilde{\gamma}_{Scat}(\vec{w}). \tag{4.49}$$

$\gamma_{Sys}(\vec{w})$ are system induced decorrelation processes, $\tilde{\gamma}_{Tmp}(\vec{w})$ is temporal decorrelation and $\tilde{\gamma}_{Scat}$ are scatterer induced decorrelation processes.

Starting from the right side of Eq. (4.49), $\tilde{\gamma}_{Scat}$ reflects the phase stability of the scatterer under the different incidence angles induced by the interferometric baseline: The fact that the two interferometric acquisitions are acquired with (slightly) different look angles make the projection of the 3-dim (complex) reflectivity of the scene (described in the x, y, z coordinate system) into the 2-dim SAR image (described in the range, azimuth coordinate system) to be different for the two images $S_1(\vec{w})$ and $S_2(\vec{w})$. This causes a decorrelation when forming the interferogram [382], [101]. $\tilde{\gamma}_{Scat}$ can be further decomposed into

$$\tilde{\gamma}_{Scat}(\vec{w}) = \gamma_{Az}\ \ \gamma_{Rg}\ \ \tilde{\gamma}_{Vol}(\vec{w}). \tag{4.50}$$

The volume decorrelation contribution $\tilde{\gamma}_{Vol}(\vec{w})$ appears when different scattering processes occur at different heights within the resolution cell. In this case the vertical component of the scatterer reflectivity project differently into the two images and causes, when forming the interferogram, a loss of coherence [113], [352] and [354]. Accordingly, $\tilde{\gamma}_{Vol}(\vec{w})$ is related to the vertical structure of the individual scatterers. Modeling of the vertical distribution of scatterer is discussed in section 5.1.

The range γ_{Rg} and azimuth γ_{Az} spectral decorrelation contributions are introduced by the slightly different projection of the horizontal component of the scatterer reflectivity into the slant-range and Doppler-zero direction respectively.

4.3.6.1 Spectral decorrelation calibration

In the spectral domain the baseline-induced difference in the projection of the horizontal component of the scatterer reflectivity in the two acquisitions make the scatterer reflectivity spectrum contained in the two images to be shifted with respect to each other. The spectral shifts in the range Δf_{Rg} and azimuth Δf_{Az} spectrum are given by [382], [101]

$$\Delta f_{Rg} = f_0 \Delta\theta / \tan(\theta_0) \qquad \text{and} \qquad \Delta f_{Az} = \Delta f_{DC} \tag{4.51}$$

where f_0 is the central system frequency, Δf_{DC} the Doppler-centroid difference between the two acquisitions. For distributed scatterers, assuming a white reflectivity spectrum the decorrelations induced by this spectral shift are [101]

$$\gamma_{Rg} = 1 - \frac{|\Delta f_{Rg}|}{W_{Rg}} \qquad \text{and} \qquad \gamma_{Az} = 1 - \frac{|\Delta f_{DC}|}{W_{Az}} \tag{4.52}$$

where W_{Rg} and W_{Az} are the (processed) range and azimuth bandwidths respectively. The coherence decreases linearly with increasing (angular) baseline $\Delta\theta$ and with increasing Doppler-centroid difference. Note that Eq. (4.52) holds as long as the spectral shifts are small compared to the available bandwidth i.e., for $|\Delta f_{Rg}| << W_{Rg}$ and $|\Delta f_{DC}| << W_{Az}$.

Both contributions can be compensated by band-pass filtering of the two images before forming the interferogram [101]. In this case both, the coherence bias and the increased phase variance introduced by γ_{Rg} and γ_{Az} are compensated.

Band pass filtering is always connected to a loss of spatial resolution. Alternatively, the coherence bias induced by γ_{Rg} and γ_{Az} can be compensated directly by means of Eq. (4.52) without any loss in spatial resolution. However, in this case the increased phase variance induced by γ_{Rg} and γ_{Az} remains unaffected.

4.3.6.2 System induced decorrelation contributions

$\gamma_{Sys}(\vec{w})$ are decorrelation contributions introduced by the acquisition system and the processing chain. The most relevant system decorrelation process for airborne as well as for spaceborne systems is the Signal-to-Noise-Ratio (SNR) decorrelation $\gamma_{SNR}(\vec{w})$ due to the system noise. Two independent noise contributions in the two signals of an interferometric acquisition will not correlate.

By modeling the received signal to be composed of the scattering amplitude $a(\vec{w})$ and the noise amplitude $n(\vec{w})$, i.e. $s(\vec{w}) := a(\vec{w}) + n(\vec{w})$, $\gamma_{SNR}(\vec{w})$ can be written as [382], [161]

$$\gamma_{SNR}(\vec{w}) = \frac{1}{1 + SNR(\vec{w})^{-1}} = \frac{A(\vec{w})}{A(\vec{w}) + N(\vec{w})} = \frac{A(\vec{w})}{P(\vec{w})} \tag{4.53}$$

where $SNR(\vec{w}) = P(\vec{w}) / N(\vec{w})$ is the polarization dependent signal-to-noise ratio, with $P(\vec{w}) = < s(\vec{w}) \cdot s^*(\vec{w}) >$ the received power $A(\vec{w}) = < a(\vec{w}) \cdot a^*(\vec{w}) >$ the scattering power and $N(\vec{w}) = < n(\vec{w}) \cdot n^*(\vec{w}) >$ the noise power.

The availability of fully polarimetric data allows an accurate data based estimation of $\gamma_{SNR}(\vec{w})$. Starting point is the polarimetric coherence between the two cross-polarized channels: Due to reciprocity the two cross-polarized channels are identical up to the additive noise contributions. In this sense, the (polarimetric) coherence between the two cross-polarized channels corresponds to the cross-polarized SNR decorrelation [120]

$$\gamma_{SNR}^{HV} = \frac{|< S_{HV} S_{VH}^* >|}{\sqrt{< S_{HV} S_{HV}^* >< S_{VH} S_{HV}^* >}} = \frac{A_{HV}}{P_{HV}} . \tag{4.54}$$

The associated scattering and noise power are given by

$$A_{HV} = \gamma_{SNR}^{HV} P_{HV} \quad \text{and} \quad N_{HV} = (1 - \gamma_{SNR}^{HV}) P_{HV} . \tag{4.55}$$

Assuming the noise power to be the same in all polarimetric channels, i.e. $N(\vec{w}) = N_{HV}$, the SNR decorrelation in each channel can be estimated as:

$$\gamma_{SNR}(\vec{w}) = \frac{P(\vec{w}) - N(\vec{w})}{P(\vec{w})} = \frac{P(\vec{w}) - N_{HV}}{P(\vec{w})}. \tag{4.56}$$

In case the $NESZ$ (Noise Equivalent Sigma Zero) patterns of a sensor Sen are known $SNR(\vec{w})$ is calculated by

$$SNR_{Sen}(\vec{w}) = \frac{\sigma_{0\,Sen}(\vec{w}) - NESZ_{Sen}(\vec{w})}{NESZ_{Sen}(\vec{w})}. \tag{4.57}$$

The SNR induced decorrelation $\gamma_{SNR}(\vec{w})$ in the corresponding interferogram acquired by two different sensors ($Sen1$ and $Sen2$) is then obtained as [15]

$$\gamma_{SNR}(\vec{w}) = \frac{1}{\sqrt{\left(1 + \frac{1}{SNR_{Sen1}(\vec{w})}\right)\left(1 + \frac{1}{SNR_{Sen2}(\vec{w})}\right)}} \tag{4.58}$$

A typical processing induced decorrelation source is inaccuracies in the coregistration. Coregistration decorrelation γ_{COR} is given by [318].

$$\gamma_{COR} = \frac{\sin(\pi\delta_{RG})}{\pi\delta_{RG}} \frac{\sin(\pi\delta_{AZ})}{\pi\delta_{AZ}} \tag{4.59}$$

where δ_{AZ} and δ_{RG} are the relative shifts between the images in azimuth and range respectively. A shift of a full resolution cell leads to complete decorrelation. Assuming a coregistration accuracy of about 1/50 (1/10) of an image pixel leads to γ_{COR}=0.98 (0.97). Note that locally the coregistration accuracy depends on the actual coherence level. Accordingly, in low coherence areas the coregistration performance decreases, thus increasing the decorrelation level. The coregistration accuracy as a function of a given coherence level and the associated decorrelation γ_{COR} can be estimated empirically and used to calibrate the interferometric coherence.

In the section above the most system-relevant system decorrelation processes are discussed. Other potential system or processing induced decorrelation sources are induced by range and azimuth ambiguities, quantization noise interpolation decorrelation or due to non-optimal resampling [178], [179] and [51].

4.3.6.3 Temporal decorrelation

The temporal decorrelation contribution $\tilde{\gamma}_{Tmp}$ is introduced by geometric and/or dielectric changes of the scatterers within the scene in the time interval between two interferometric acquisitions. This is the most critical decorrelation contribution when it comes to interferometric acquisitions with non-zero temporal baseline. Temporal decorrelation is difficult if not impossible to predict, to address or even to compensate.

In several studies temporal decorrelation was modeled assuming only changes in the position of the scatterers. If the motion of the scatterers is characterized by a Gaussian-statistic an exponential temporal decorrelation model is derived [382]. This model was first validated using L-band SEASAT data. The exponential model was extended by a

Brownian motion model [299] that implies an exponential decay of the temporal decorrelation with time. However, the temporal decorrelation in forest at small temporal baselines (i.e., shorter than an hour) is mainly caused by wind-induced motion making the Brownian motion inadequate to model temporal decorrelation for such temporal scales [257]. More recently, a physical model of temporal decorrelation was proposed assuming a variable Gaussian motion along the vertical direction of forests [204]. This model was also validated at L-band data acquired by the JPL's UAVSAR system.

A detailed discussion on effects, modeling and compensation of temporal decorrelation can be found in **Publication III [124]**, **Publication IV [218]**, [270] and [211].

4.4 Pol-InSAR

4.4.1 Pol-InSAR fundamentals

Polarimetric SAR Interferometry (Pol-InSAR) measures the full polarimetric scattering matrix at both ends of the baseline of an interferometer [46], [40]. PolSAR and InSAR techniques are coherently combined. The technique was first demonstrated in [40] and [269] using SIR-C/X data. In the reciprocal monostatic case are three independent polarizations measured by two apertures. The six-element scatterer vector associated to the Pauli basis k_{P6} is formed by cumulating the scatterer vectors of each end of the interferometric baseline k_{P1} and k_{P2}

$$\vec{k}_{P6} = \begin{bmatrix} \vec{k}_{P1} \\ \vec{k}_{P2} \end{bmatrix}. \tag{4.60}$$

The 6 x 6 Pauli coherency matrix T_6 is defined as the outer product of the scatterer vector k_{P6} with its conjugate transpose [40]

$$T_6 = \left\langle \vec{k}_{P6} \cdot \vec{k}_{P6}^{*+} \right\rangle = \begin{bmatrix} \left\langle \vec{k}_{P1} \cdot \vec{k}_{P1}^{*+} \right\rangle & \left\langle \vec{k}_{P1} \cdot \vec{k}_{P2}^{*+} \right\rangle \\ \left\langle \vec{k}_{P2} \cdot \vec{k}_{P1}^{*+} \right\rangle & \left\langle \vec{k}_{P2} \cdot \vec{k}_{P2}^{*+} \right\rangle \end{bmatrix} = \begin{bmatrix} T_{11} & \Omega_{12} \\ \Omega_{12}^{*+} & T_{22} \end{bmatrix} \tag{4.61}$$

where T_{11} and T_{22} are the conventional polarimetric coherency matrices (see Eq. (4.60) and Eq. (4.29) in section 4.2.2 – $[T_3]$). Ω_{12} is a new 3 x 3 polarimetric interferometric coherency matrix that contains polarimetric information as well as interferometric phase information of the different polarimetric channels and is defined as

$$\Omega_{12} = \frac{1}{2} \begin{bmatrix} \left\langle (S_{1HH} + S_{1VV})(S_{2HH} + S_{2VV})^* \right\rangle & \left\langle (S_{1HH} + S_{1VV})(S_{2HH} - S_{2VV})^* \right\rangle & \left\langle (S_{1HH} + S_{1VV})(S_{2HV} + S_{2VH})^* \right\rangle \\ \left\langle (S_{2HH} - S_{2VV})(S_{1HH} + S_{1VV})^* \right\rangle & \left\langle (S_{1HH} - S_{1VV})(S_{2HH} - S_{2VV})^* \right\rangle & \left\langle (S_{1HH} - S_{1VV})(S_{2HV} + S_{2VH})^* \right\rangle \\ \left\langle (S_{2HV} + S_{2VH})(S_{1HH} + S_{1VV})^* \right\rangle & \left\langle (S_{2HV} + S_{2VH})(S_{1HH} - S_{1VV})^* \right\rangle & \left\langle (S_{1HV} + S_{1VH})(S_{2HV} + S_{2VH})^* \right\rangle \end{bmatrix} \tag{4.62}$$

where 1 and 2 denote the corresponding ends of the baseline. Pol-InSAR aims to interpret the positions of the polarization dependent scattering mechanisms.

In order to extend the interferometric coherence to diverse polarizations the normalized vectors $\vec{w}_1$ and $\vec{w}_2$ are introduced and can be interpreted as two different scattering mechanisms or two different polarizations stages.
The scattering amplitude $S_i(\vec{w})$ of any polarization state $\vec{w}$ can be defined by the projection of the scattering vector $\vec{k}_i$ (where $i \in [1,2]$ defines the two ends of the baseline) on the unitary complex vector $\vec{w}$ as [46]

$$S_1(\vec{w}) := \vec{w}^{+} \cdot \vec{k}_1 . \tag{4.63}$$

A general formulation of the complex interferometric coherence for an arbitrary choice of the scattering mechanisms is formulated through [40]

$$\tilde{\gamma}_{Obs}(\vec{w}_1, \vec{w}_2) := \frac{\left\langle \vec{w}_1^{*+} \Omega_{12} \vec{w}_2 \right\rangle}{\sqrt{\left\langle \vec{w}_1^{*+} T_{11}(\vec{w}) \right\rangle \left\langle \vec{w}_1^{*+} T_{22} \vec{w}_2 \right\rangle}} . \tag{4.64}$$

where $\vec{w}_1$ is the polarization used at the first end of the baseline and $\vec{w}_2$ the polarization from the second end of the baseline. If $\vec{w}_1 \neq \vec{w}_2$ then additionally to the decorrelation sources listed in Eq. (4.49) polarimetric decorrelation degrades the interferometric coherence. In case $\vec{w}_1 = \vec{w}_2 = \vec{w}$ the polarimetric term is omitted resulting in the following representation of the interferometric coherence:

$$\tilde{\gamma}_{Obs}(\vec{w}) := \frac{\left\langle \vec{w}^{*+} \Omega_{12} \vec{w} \right\rangle}{\sqrt{\left\langle \vec{w}^{*+} T_{11}(\vec{w}) \right\rangle \left\langle \vec{w}^{*+} T_{22} \vec{w} \right\rangle}} \tag{4.65}$$

The interferometric coherence change noticeably with polarization, an approach to calculate the polarization combination giving the highest coherence was developed in [40] and is called coherence optimization. Multi-baseline Pol-InSAR scenarios over forested area have been investigated by [257]. Besides forest parameter inversion, Pol-InSAR has been applied for the estimation of biophysical parameters from crops [13], [229], urban areas [312], [313], [315] and glaciers [324].

4.4.2 Coherence region

$\tilde{\gamma}_{Obs}(\vec{w})$ (see Eq. (4.65)) includes both the interferometric coherence (or correlation coefficient) $|\tilde{\gamma}_{Obs}(\vec{w})|$ and the interferometric phase $\arg(\tilde{\gamma}_{Obs}(\vec{w}))$. When using polar coordinates, $\tilde{\gamma}_{Obs}(\vec{w})$ is represented by a point on the complex plane within the unit circle. Eq. (4.65) indicates that the interferometric coherence is polarization dependent. The set of interferometric coherences $\tilde{\gamma}_{Obs}(\vec{w})$ obtained for all possible polarizations $\vec{w}$ plotted on the complex plane, also named polarimetric diversity, defines the so-called coherence region which lies within the unit circle [46], [87], [342], [88] (see also red ellipse in Figure 20). Shape, size and orientation of the coherence region are determined by the nature of the scattering processes, the interferometric geometry and the number of looks [46]. Different system induced decorrelation processes in each polarization channel (for instance different SNR due to different signal strength) may also affect the shape of the coherence region.

The polarimetric diversity of the interferometric coherence is established by the coherence region concept and is used to interpret the polarimetric interferometric signature of the underlying scatterer. The radial extent of the coherence region indicates the variation of the absolute value of the interferometric coherence as a function of polarization. The angular extent of the coherence region indicates the variance of the interferometric phase (center) as a function of polarization. The maximum phase difference $\Delta\varphi$ (see orange arrow in Figure 20) established by the coherence region indicates the maximum variation of the interferometric phase (center) obtained by changing the polarization of the images used to form the interferogram and it can be converted to a (baseline independent) maximum height difference Δh by scaling with the vertical wavenumber, $\Delta h = \Delta\varphi / \kappa_z$. Δh in the following referred to as polarimetric diversity. Large Δh values indicate the presence of (polarized) scattering contributions at different heights within the scattering volume. However, a note of caution is required when interpreting the interferometric coherence on the unit circle: the estimation of both, the absolute value and the argument of the interferometric coherence is affected by an inherent variance defined by the (absolute) coherence value and the number of looks used for its estimation [161] (see also section 4.3.5).

The boundary of the coherence region of a full polarimetric acquisition can be computed numerically for the constrained case $\vec{w}_1 = \vec{w}_2$ by solving the following eigenvalue problem [48], [342], [87].

$$\gamma(\vec{w},\varphi) = \frac{\langle \vec{w}^{*+} \Omega \ \vec{w} \rangle}{\langle \vec{w}^{*+} T \ \vec{w} \rangle} \Rightarrow T^{-1}\Omega \ \vec{w} = \lambda \vec{w} \tag{4.66}$$

where $\Omega = (\Omega_{12} e^{j\varphi} + \Omega_{12}^{*+} e^{-j\varphi})/2$ and $T = (T_{11} + T_{22})/2$.

For each rotation angle φ the minimum and maximum eigenvalues $\lambda_{\min}$ and $\lambda_{\max}$ and eigenvectors $\vec{w}_{\min}$ and $\vec{w}_{\max}$ are obtained. The corresponding coherences represent two points of the coherence boundary and can be calculated by using $\vec{w}_{\min}$ and $\vec{w}_{\max}$ in Eq. (4.65). By varying $\varphi \in [0, \pi]$ the whole boundary of the coherence region can be estimated where all possible polarizations lie inside.

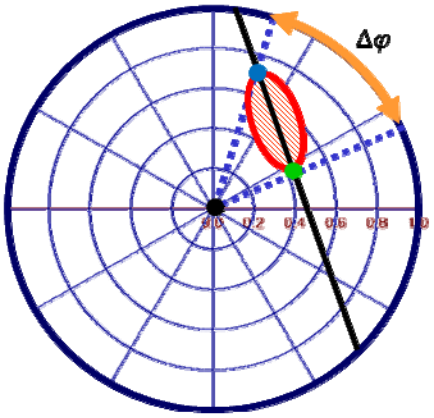

Figure 20: Unit circle with coherence region (red ellipse), green dot and blue dot: the most diverse (different) polarizations, $\Delta\varphi$: maximum phase difference.

If only a dual pol subspace of a Pol-InSAR acquisition is analyzed or for dual pol acquisition (2 x 2 scattering matrix), the coherence region has the form of an ellipse [253], [46] simplifying considerably the estimation of the coherence boundary.

Polarimetric diversity Δh may be used as a first order interpretation of the scattering processes in a scene**. Hajnsek, Kugler et al.** demonstrate in **Publication III [124]** for the first time the use of polarimetric diversity for the interpretation of scattering mechanisms in response to terrain slope with L-band.

In the case of a dual-pol InSAR configuration operating in HH and VV, as provided for example by the TanDEM-X mission, a 2-dimensional scattering vector $\vec{k}_{1\,2d} = [S_{1HH} S_{1VV}]^T$ and $\vec{k}_{2\,2d} = [S_{2HH} S_{2VV}]^T$ is acquired at each end of the (spatial) baseline with

$$\vec{k}_{1\,2d} \cdot \vec{k}_{2\,2d}^{*+} = \Omega_{12\,2d} = \begin{bmatrix} \langle (S_{1HH})(S_{2HH})^* \rangle & \langle (S_{1HH})(S_{2VV})^* \rangle \\ \langle (S_{1VV})(S_{2HH})^* \rangle & \langle (S_{1VV})(S_{2VV})^* \rangle \end{bmatrix} \tag{4.67}$$

and

$$\vec{k}_{i\,2d} \cdot \vec{k}_{i\,2d}^{*+} = T_{ii\,2d} = \begin{bmatrix} \langle |S_{iHH}|^2 \rangle & \langle S_{iHH} S_{iVV}^* \rangle \\ \langle S_{iHH} S_{iVV}^* \rangle & \langle |S_{iVV}| \rangle \end{bmatrix} \text{ where } i \in [1,2]\,. \tag{4.68}$$

Krieger et al. Publication VI [185] showed the use of polarimetric diversity Δh for differentiating several crop types over agricultural areas north of the Caucasus by means of TanDEM-X dual-pol (X-band HH/VV polarization) data.

Figure 21 shows the polarimetric diversity for three TDX dual-pol acquisitions (X-band HH/VV polarization) over the floodplain forest of river Isar close to Plattling (Lat: 48°44', and Long: 12°51'). It is covered by a typical floodplain forest of the temperate forest zone, mainly composed of deciduous trees like ash, alder, oak and maple.

The three acquisitions cover the foliation period of the floodplain forest. Images of the polarimetric diversity of the three acquisitions are shown in Figure 21. The first acquisition (2011-04-12, Figure 21 (A)) covers the forest in the leafless stage. The polarimetric diversity has in the most of the forested area values larger than 4 m. In the second acquisition, (2011-05-04, Figure 21 (B)) foliation has already started and polarimetric diversity decreases. In the third acquisition, (2011-05-15, Figure 21 C) foliation is nearly completed and polarimetric diversity reaches barely values greater than 4 m (see also [197]).

Dense forest conditions seem to decrease polarimetric diversity Δh. Increasing forest density (or more foliage in the canopy) decreases the capability of X-band to penetrate into a forest. As a consequence, the strongly polarized backscattering of the ground is reduced which implies that the difference in the backscattering in the polarization channels shrinks.

Polarimetric diversity may be used to document biophysical changes in the scatterer as induced for instance by foliation, but may be also used to detect selective logging activities or defoliation induced by insect calamities.

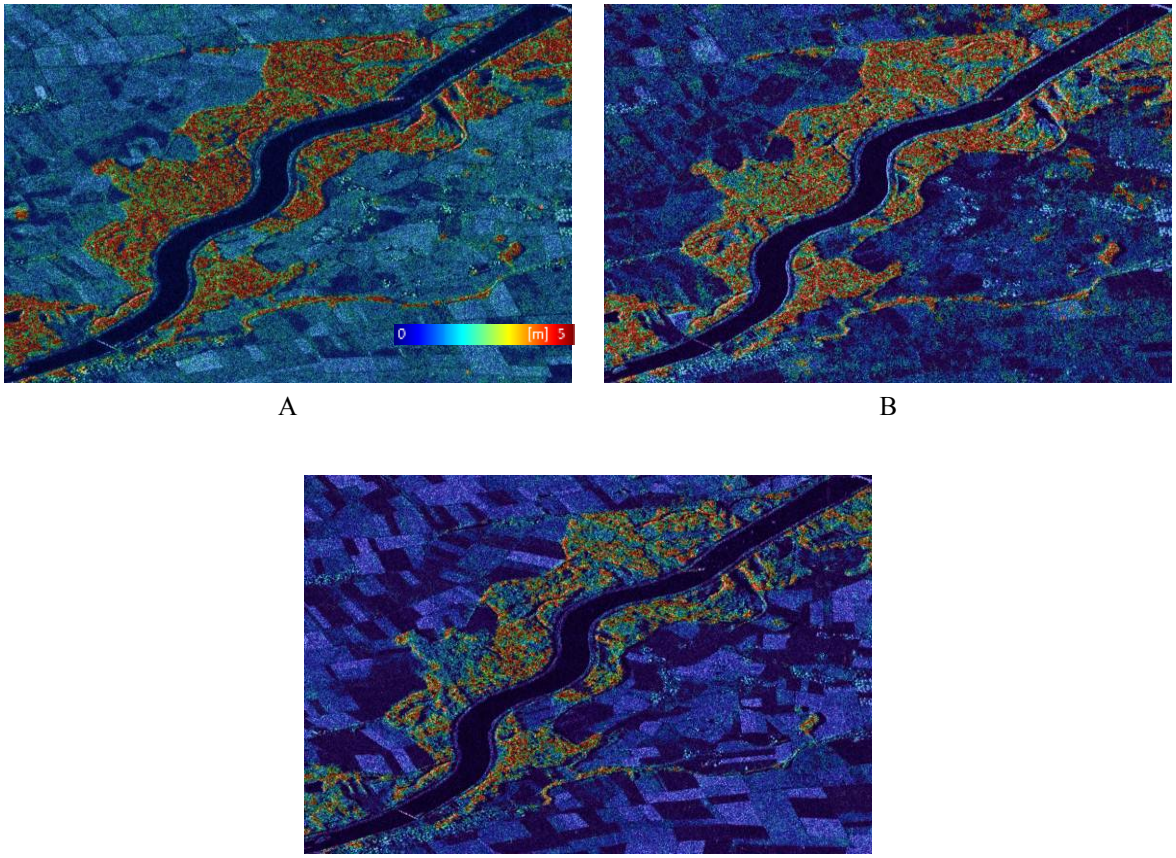

A B

C

Figure 21: TanDEM-X time series of polarimetric diversity Δh test site Plattling scaled from 0 to 5 m; A: 2011-04-12; B: 2011-05-04; C: 2011-05-15. © [2014] IEEE

5 Model based Pol-InSAR parameter estimation

This chapter concentrates on forest parameter retrieval by means of Polarimetric SAR Interferometry with P-, L- and X-band.

In the previous chapter, factors degrading the interferometric coherence have been discussed. Volume decorrelation was identified as the most important parameter decorrelating the interferometric coherence. The concept of the coherence region to describe polarimetric diversity of Pol-InSAR data was introduced and its dependence on biophysical parameters was discussed. The idea is now extended by relating the obtained coherence loci to physical forest parameters using a scattering model [40], [269]. A widely as well as successfully used model to interpret the loci of the interferometric coherence is the Random Volume over Ground model (RVoG) [352], [354], [40], [269]. It is a two-layer model consisting of a volume layer with randomly distributed scatterer and a Dirac-like ground layer. In the following the RVoG model is introduced (see section 5.1), the role of the baseline in the inversion process (i.e. vertical wavenumber κ_Z; see section 5.2 and section 5.3.2) and different distributions of scatterer (i.e. vertical backscatter functions) are discussed (see section 5.1.2). Before interpreting volume decorrelation, it must be ensured that other non-volumetric decorrelation processes are compensated or are negligibly low.

Section 5.3 includes a step-by-step description of the forest height inversion process. In section 5.4 impacts and modelling of temporal decorrelation are discussed. Obtained inversion results are presented in section 5.5. Finally a dual baseline inversion approach is introduced in section 5.6 to account a residual ground component in the received signal or to compensate a residual scalar temporal decorrelation contribution in forest height inversion.

5.1 Modelling of volume decorrelation

The key observable used in Pol-InSAR applications is the complex interferometric coherence $\tilde{\gamma}(\vec{w})$ estimated at different polarizations $\vec{w}$ [40], [269].

Volume decorrelation $\tilde{\gamma}_{Vol}$ is the decorrelation caused by the different projection of the vertical component of the scatterer into the two images $S_1(\vec{w})$ and $S_2(\vec{w})$. $\tilde{\gamma}_{Vol}$ is directly linked to the vertical distribution of scatterers $F(z')$ through a (normalized) Fourier transformation relationship [352], [354]

$$\tilde{\gamma}_{Vol} = \exp(i\kappa_z z_0)\frac{\int_0^{h_V} F(z')\exp(i\kappa_z z')dz'}{\int_0^{h_V} F(z')dz'} \tag{5.1}$$

where z denotes the vertical position, and the phase $\varphi_0 = \kappa_z z_0$ is related to the height of the ground topography z_0. In the context of Eq. (5.1), κ_z maps $F(z)$ to $\tilde{\gamma}_{Vol}(\vec{w})$ determining the sensitivity of the interferometer to a given $F(z)$ and especially to a given h_V. In the case of forest scatterers F(z) is a rather complex function that depends on the vertical forest or tree structure and the distribution of the dielectric constant along it.

Eq. (5.1) allows the estimation of $F(z)$ (and associated structure parameters) from measurements of $\gamma_{Vol}(\vec{w},\kappa_z)$. One way to do so is to parameterize $F(z)$ into a set of geometrical and scattering parameters and to use then $\gamma_{Vol}(\vec{w},\kappa_z)$ measurements to estimate these parameters by inverting Eq. (5.1) [43], [269], [44], [45]. In general, for a robust inversion, the number of parameters used to parameterize $F(z)$ has to be balanced by the number of available $\gamma_{Vol}(\vec{w},\kappa_z)$ measurements.

5.1.1 Exponential vertical backscatter function

In the simplest case, F(z) is approximated by a homogeneous vertical distribution of scatterers.

$$F(z) = ct \quad \text{with} \quad z_0 \le z \le z_0 + h_V \tag{5.2}$$

represents a uniform distribution of the scatterer along height (see Figure 22 A). From Eq. (5.1) results then the characteristic sinc-decorrelation function

$$\tilde{\gamma}_{Vol}(\kappa_z, h_V) = \exp(\, i\kappa_z z_0 \,)\exp(\, i\frac{\kappa_z h_V}{2})\,\mathrm{sinc}\,(\frac{\kappa_z h_V}{2}) \tag{5.3}$$

where $\mathrm{sinc}(x) := \sin(x)/x$. According to Eq. (5.3), the coherence, at a given baseline, depends only on the volume height h_V - interpreted as H100 [238], [236], [239] while the phase center is located at the middle of the volume height.

For vegetation applications two-layer statistical models have been proven to be sufficient (in terms of robustness and performance) especially at lower frequencies [40], [269], [352], [46]. In these models $F(z)$ includes a vegetation scattering contribution and a Dirac-like component $m_G(\vec{w})\ \delta(z - z_0)$ that accounts for the scattering contribution(s) occurring on (or with) the underlying ground (i.e. direct surface and dihedral vegetation-surface contributions):

$$F(z,\vec{w}) = f_V(z,\vec{w}) + m_G(\vec{w})\ \ \delta(z - z_0) \tag{5.4}$$

where m_G is the ground scattering amplitude. Substituting (5.4) into (5.1) leads to

$$\tilde{\gamma}_{Vol}(\vec{w},\kappa_z) = e^{i\varphi_0}\ \frac{\tilde{\gamma}_{V0}(\kappa_z) + m(\vec{w})}{1 + m(\vec{w})} \tag{5.5}$$

where

$$\tilde{\gamma}_{V0}(\kappa_z,\vec{w}) = \frac{\int_0^{h_V} f_V(z,\vec{w})\exp(i\kappa_z z)dz}{\int_0^{h_V} f_V(z,\vec{w})dz} \tag{5.6}$$

is the volume only coherence and $m(\vec{w}) = m_G(\vec{w}) / \int_o^{h_V} f_V(z,\vec{w})\ dz$ is the effective ground-to-volume amplitude ratio.

In the case of bistatic configurations, the direct and the dihedral contributions of the underlying ground are no longer equivalent [46], [354]. While the direct ground contribution remains deterministic (i.e. associated to a coherence that after range spectral filtering equals 1) the dihedral contribution becomes distributed in height and thus affected by volume decorrelation:

$$\tilde{\gamma}_{Vol}(\vec{w},\kappa_z) = e^{i\varphi_0}\ \frac{\tilde{\gamma}_{V0}(\kappa_z) + m_S(\vec{w}) + m_D(\vec{w})\dfrac{\sin(\kappa_z h_V)}{\kappa_z h_V}}{1 + m_S(\vec{w}) + m_D(\vec{w})} \tag{5.7}$$

where m_S is the direct ground (surface) m_D the dihedral scattering contributions and $m_D + m_S = m$. However, small bistatic angles and low dihedral scattering contributions (as it is the case for TanDEM-X) legitimatize the use of Eq. (5.5) instead of Eq. (5.7).

For the (vertical) distribution of scatterers in the vegetation layer $f_V(z,\vec{w})$ different models have been proposed. A very successful and widely used model is an exponential distribution of scatterers [46], [269], [352], [113] (see Figure 22 B)

$$f_V(z) = \exp[2\sigma(\vec{w})z / \cos(\theta_0)] \tag{5.8}$$

where $\sigma(\vec{w})$ is a mean extinction value for the vegetation layer that defines the "attenuation rate" of the profile and is usually expressed in [dB/m]. The special case of $\sigma = 0$ dB/m represents a uniform distribution i.e. the sinc-decorrelation function as described by Eq. (5.3).

The solution of Eq. (5.6) for the exponential structure function described by Eq. (5.8) is given through

$$\tilde{\gamma}_{V0} = \frac{2\sigma\left(e^{\left(-i\kappa_Z + \frac{2\sigma}{\cos(\theta)}\right)h_V} - 1\right)}{\cos(\theta)e^{-i\kappa_Z h_V} + \left(-i\kappa_Z + \dfrac{2\sigma}{\cos(\theta)}\right)\left(e^{\frac{2\sigma}{\cos(\theta)}h_V} - 1\right)}. \tag{5.9}$$

Inverse scattering distributions, i.e. cases where more effective scatterers are located in the lower forest layers than on the higher ones may violate the assumption of an exponential vertical distribution of scatterers. This can be the case in sparse forest environments with more or less distinct understory, or at lower frequencies when the effective scatterers become larger and therefore located lower within the forest architecture. In this case, the exponential decay of $f_V(z)$ as assumed in Eq. 38 is no longer valid resulting in an underestimation of forest height and/or an overestimation of extinction.

5.1.2 Modifications of the vertical backscatter function

A way to account for inverse scattering distributions is to allow the extinction coefficient of the volume σ to be negative. Then the term extinction is no longer appropriate, σ is

then interpreted as a form factor of the vertical backscatter function $f_V(z)$ and no more as signal attenuation. In order to refer negative values of σ to an exponential distribution of scatterer the term negative extinction is used for negative σ in the following. Negative extinction values in Eq. (5.8) allow to approximate inverse scattering distributions as indicated in Figure 22 C. The extended solution space for $\tilde{\gamma}_{V0}$ values – including positive and negative extinction solutions – is shown in form of red (= positive extinction values) and blue dots (= negative extinction values) in Figure 23 A for κ_Z = 0.1 rad/m. The green dots represent solutions for a volume height of 20 m across all σ.

Besides the exponential profile that appears to fit better higher frequencies, Gaussian [99], [100], or even linear scattering distributions have been proposed and used especially at lower frequencies [191].

The linear or triangular structure function will be considered in more detail and is given through (see Figure 22 D and E):

$$f_V(z) = \varsigma\ z - 1 \tag{5.10}$$

where ς is the slope of the line which can be positive as well as negative. Figure 23 B shows the solution space for $\tilde{\gamma}_{V0}$ on the unit circle for the linear profile for κ_Z = 0.1 rad/min in form of red (= positive values) and blue dots (= negative values). The green dots represent solutions for a volume height of 20 m across all ς.

The solution of Eq. (5.6) for the triangular structure function Eq. (5.10) is given through

$$\gamma_{V0} = \frac{\left(h_V - \frac{\varsigma}{2}h_V^2\right)j\kappa_Z}{e^{-j\kappa_Z h_V} + \varsigma\ h_V - \frac{\varsigma}{j\kappa_Z}e^{-j\kappa_Z h_V} + \frac{\varsigma}{j\kappa_Z}}. \tag{5.11}$$

The exponential profile is the original proposed one able to describe also high attenuation, while the linear profile has his advantages in the low attenuation case. The positive versions of the two profiles describe vertical distributions affected by attenuation so that the number of effective scatterers in the volume decreases with depth and are characteristic for rather dense (in an EM sense) forest conditions. The negative versions represent inverse scattering distributions, i.e. cases where more effective scatterers are located in the lower forest layers than in the higher ones. This is the case in rather sparse forest environments with more or less distinct understory. Inverse scattering distributions are more common at longer frequencies like P-band where the effective scatterers are larger and therefore located deeper within the forest layer.

Equally important as the shape of the vertical distribution of scatterers $F(z,\vec{w})$ is its polarimetric characterization.

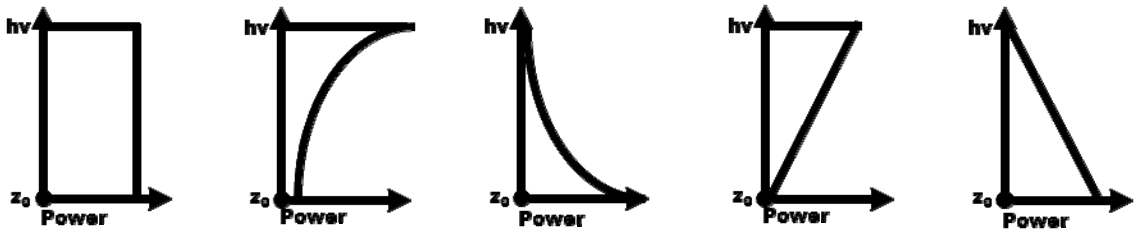

Figure 22: Vertical backscatter functions $f(z)$; A: sinc Eq. (5.2); B: positive exponential Eq. (5.8); C: negative exponential Eq. (5.8); D: positive triangular Eq. (5.10); negative triangular Eq. (5.10).

While the ground scattering component is strongly polarized $m_G = m_G(\vec{w})$, the volume scattering component can be both: polarization dependent, i.e. $f_V(z) = f_V(z,\vec{w})$, or independent of polarization, $f_V(z)$. In the first case the volume is called Oriented Volume (OV) [353], [121]; in the second the volume is referred to as Random Volume (RV) [10], [354]. The analysis of a large number of experimental data indicates that across a wide range of frequencies (from X- down to P-band) the random volume assumption is valid for several different forest conditions **Publication III [124]**, **Publication I [196]**.

Assuming a Random Volume, (Eq. 5.5) is known as the Random Volume over Ground (RVoG) model. In this case (Eq. 5.5) can be rewritten as [41]

$$\tilde{\gamma}_{Vol}(\vec{w}) = e^{i\varphi_0}\left(\tilde{\gamma}_{V0} + \frac{\tilde{\gamma}_{V0} + m(\vec{w})}{1 + m(\vec{w})}\left(1 - \tilde{\gamma}_{V0}\right)\right). \tag{5.12}$$

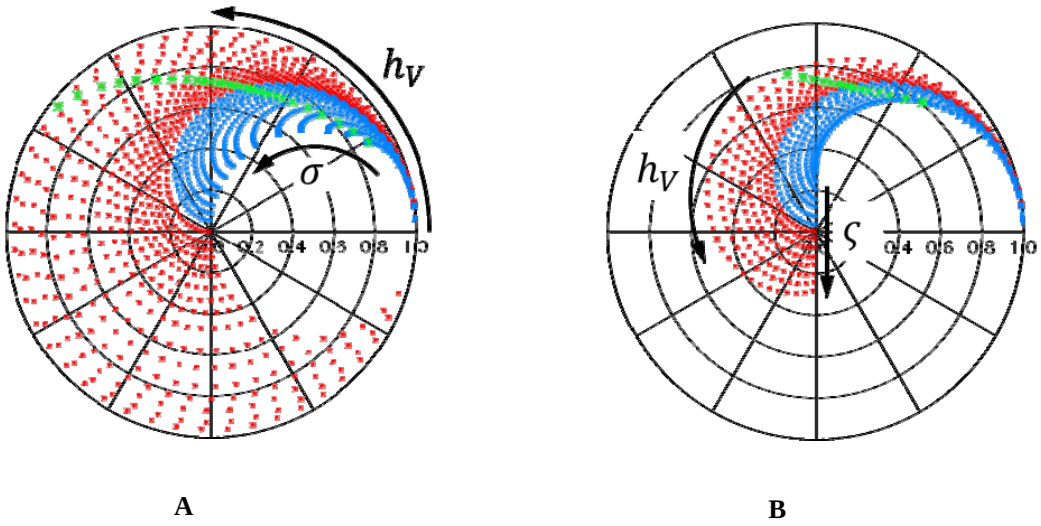

Figure 23: Solution space for the vertical backscatter functions $f(z)$; A: exponential vertical backscatter function Eq. (5.8); B: triangular vertical backscatter function Eq. (5.10); red dots represent solutions obtained for positive values of ς and σ; blue dots represent solutions for the negative values of ς and σ; green dots represent solutions for a volume height of 20 m across all ς and σ; $\varsigma \in [100,-100]$; $\sigma \in [-2,2]$; κ_Z = 0.1 rad/m. © [2015] IEEE

Eq. (5.12) indicates that as long as $\tilde{\gamma}_{V0}$ is independent of polarization, the RVoG coherence region is a segment of a straight line [269]. This simple geometrical representation has been exploited for the validation and inversion of the RVoG model and will be further discussed in section 5.3.

5.2 The vertical wavenumber

As already mentioned above, the vertical wavenumber κ_z scales the interferometric phase and coherence to forest height h_V (see Eq. (5.3), Eq. (5.5) and Eq. (5.6). Figure 24 shows in the top row the absolute value of the volume coherence $|\tilde{\gamma}_{V0}|$ as a function of the vertical wavenumber κ_z for five different forest heights (10 m, 20 m, 30 m, 40 m and 50 m) and for three extinction values, 0 dB/m (top), 0.1 dB/m (middle) and 0.5 dB/m (bottom). For a constant forest height, the volume coherence decreases with increasing κ_z. Decreasing extinctions also lead for a constant height and a fixed κ_z to lower coherence levels.

In the bottom row of Figure 24 the corresponding plots for the interferometric phase $\arg(\tilde{\gamma}_{V0})$ are shown. The coherence-to-height sensitivity is larger at low σ levels and decreases with increasing σ, while the phase-to-height sensitivity is higher for higher extinction levels. Accordingly, forest height inversion performance relies on the choice of an appropriate vertical wavenumber κ_z.

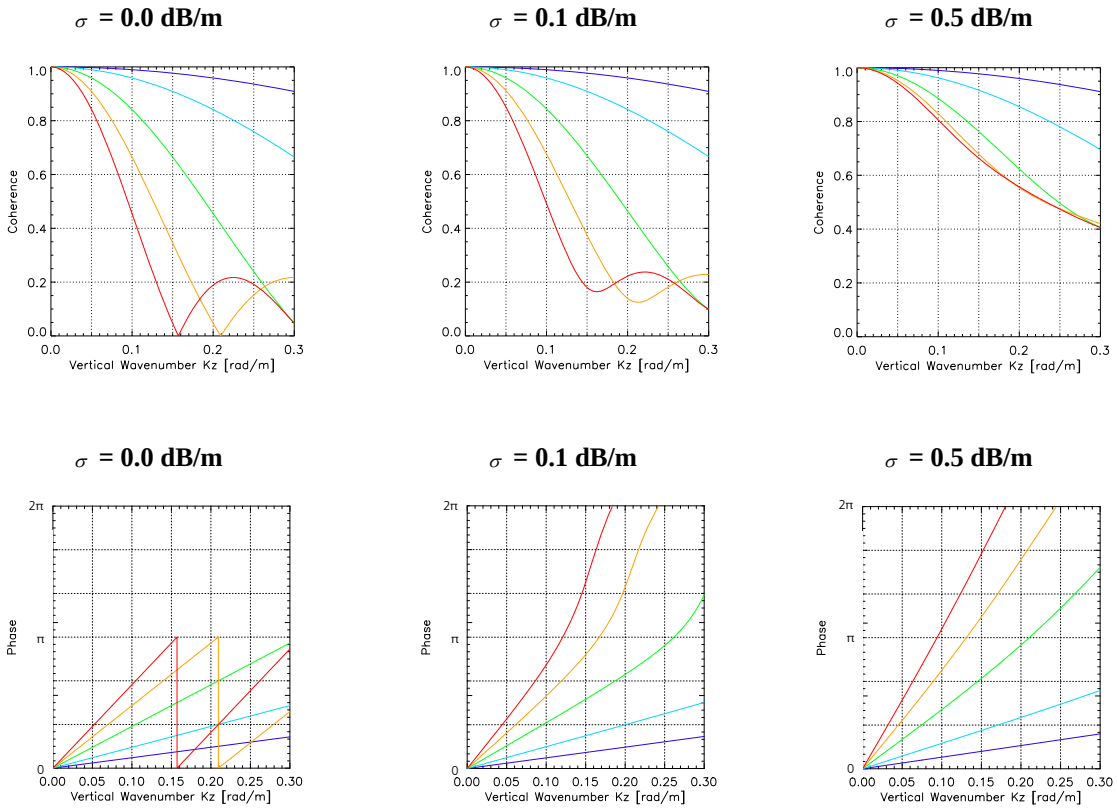

Figure 24: Volume coherence $\tilde{\gamma}_{V0}$ - amplitude $|\tilde{\gamma}_{V0}|$ in the top row and phase $\arg(\tilde{\gamma}_{V0})$ in the bottom row as function of κ_z for five different forest heights: 10 m (dark blue), 20 m (light blue), 30 m (green), 40 m (orange) and 50 m (red) and for 3 different σ values: left 0.0 dB/m, middle: 0.1 dB/m and right: 0.5 dB/m. © [2015] IEEE

For (too) large κ_z values the sensitivity of the coherence to forest height saturates at a given height so that larger heights become underestimated.
On the other hand, for (too) small κ_z values, even small (residual) decorrelations introduce large height errors due to the unfavorable coherence to height scaling.
A detailed discussion about the role of κ_z in the height inversion process is given in **Publication I [196]** and section 5.3.2.

5.3 Pol-InSAR forest height inversion

The challenge now is the estimation of forest height h_V and other associated structure parameters used to parameterize $f_V(z)$ from $\tilde{\gamma}_{Vol}(\vec{w},\kappa_z)$ measurements at different polarizations and (spatial) baselines by means of Eq. (5.5). For a given baseline the achieved performance depends critically on two steps. The first step is the estimation of the volume decorrelation contribution $\tilde{\gamma}_{Vol}(\vec{w},\kappa_z)$ from the overall measured interferometric coherence by compensating for all other (non-volumetric) decorrelation contributions. Note, that in most cases the calibration of non-volumetric decorrelation contributions compensates the coherence bias but not the increased variance - in phase and coherence amplitude - caused by the lower coherence level. The second step is to establish a balanced and well-conditioned inversion problem based on the available observation space introducing - if required - additional assumptions and / or external information. Both steps will be discussed in the next sections.

5.3.1 Three stage inversion steps

Forest height inversion by means of the RVoG model as given in Eq. (5.5) using a single-baseline quad-polarimetric acquisition can be addressed either in terms of a multi-dimensional optimization problem [205], [204] or by using its geometrical representation on the unit circle [269], [41], [241] (see also Eq. (5.12)). While the first approach allows the inversion of all parameters in a single step, the second approach provides a more controlled way to invert step-by-step Eq. (5.5). The original idea for the geometrical inversion of Eq. (5.5) has been proposed in [41] and is reviewed in the following, some modifications are introduced.

5.3.1.1 Line fit

The most critical step in the inversion is the estimation of the straight line segment represented by the coherence region. In general this is performed by a line fit through a set of coherence loci on the complex plane. The quality of the line fit is affected by three parameters:

1.) the validity of the Random Volume assumption,

2.) the statistical variance of the coherence loci defined by the individual coherence levels (see [349], [350], and section 4.3.5) and

3.) the length of the visible line segment that depends on the "visibility" and the physical properties of the underlying ground **Publication III [124]**, [40].

In order to reduce the bias introduced by the coherence estimation and to maximize the length of the "visible" line segment the coherence region (indicated by the black dots in Figure 25) is estimated [87], [88] and [342]. A straight line is then fitted through the two coherence loci that are furthest apart from each other i.e. the two points that yield the

maximum phase difference $\Delta\varphi$, $\tilde{\gamma}_{Obs}(m_{\min})$ and $\tilde{\gamma}_{Obs}(m_{\max})$ displayed as red and green dots and blue line in Figure 25.

5.3.1.2 Estimation of the underlying ground

The two intersection points of the fitted line with the unit circle (blue and orange dot in Figure 25) are the two possible solutions for the "ground only" point, i.e. the coherence that corresponds to the underlying ground

$$\tilde{\gamma}_{Vol}(m \to \infty) = e^{i\varphi_0} = e^{i\kappa_z z_0}. \tag{5.13}$$

In [41] the selection of the right "ground only" was proposed based on the fact that - according to Eq. (5.12) - the movement along the "visible" line segment corresponds to a monotonic change of m. Assuming the smallest ground-to-volume ratio in the cross-polarized channel $m(HV)$, the right "ground only" is the one with the bigger distance from $\tilde{\gamma}_{Obs}(HV)$ than from other, (for example co-polar), coherence loci. Polarimetric tomographic analysis showed that significant single bounce scattering (= surface scattering) may also occur in the canopy of a forest [316] or a dense understory shifts the backscattering in the HV channel towards the ground [99] then the assumption that $\tilde{\gamma}_{Obs}(HV)$ is the polarization with the smallest ground to volume ration is not necessarily true. A more robust criterion can be derived from the monotonic lowering of the phase center with increasing ground to volume ratio $m(\vec{w})$. Assuming a tree height less than π/κ_Z, φ_1 and φ_2 to be the phase of the two intersection points, the following decision rules can be derived:

For $\kappa_Z > 0$:

if	$\arg\left(\exp(i\varphi_1)\exp(i\varphi_2)^*\right) > 0$	then	$\varphi_0 = \varphi_1$	(5.14a)
if	$\arg\left(\exp(i\varphi_1)\exp(i\varphi_2)^*\right) < 0$	then	$\varphi_0 = \varphi_2$	(5.14b)

For $\kappa_Z < 0$

if	$\arg\left(\exp(i\varphi_1)\exp(i\varphi_2)^*\right) < 0$	then	$\varphi_0 = \varphi_1$	(5.15a)
if	$\arg\left(\exp(i\varphi_1)\exp(i\varphi_2)^*\right) > 0$	then	$\varphi_0 = \varphi_2$	(5.15b)

This approach holds even for tree heights up to $1.3*\pi/\kappa_Z$ as long as the extinction remains smaller than 0.3dB/m. For tree heights higher than $1.3*\pi/\kappa_Z$ the estimated coherence $\tilde{\gamma}_{Vol}(\vec{w})$ becomes very low, , making the selection of the right "ground only" point problematic as the statistical variance of the coherence loci is dramatically increased [349] (see also coherence and phase statistic in section 4.3.5).

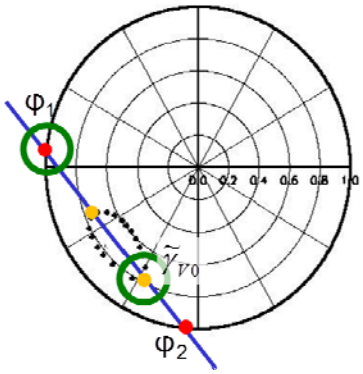

Figure 25: Inversion scenario in the unit circle; black dots: coherence region; blue line: line fitted through coherence region; red dots: ground phase candidates φ_1 and φ_2; orange dots: volume only coherence $\tilde{\gamma}_{V0}$ candidates green circle: mark selected ground phase φ_1 and the selected volume only coherence $\tilde{\gamma}_{V0}$. © [2015] IEEE

5.3.1.3 Height inversion

Having estimated φ_0 and assuming $m_{\min}=0$, i.e. no response from the ground in at least one polarization channel, $\tilde{\gamma}_{Obs}(m_{\min})\exp(-i\phi_0)=\tilde{\gamma}_{V0}$ whereas $\tilde{\gamma}_{Obs}(m_{\min})$ is corrected for non-volumetric decorrelation processes. The height h_V and the extinction σ can be estimated unambiguously by means of a two dimensional non-linear optimization problem

$$\min_{h_V,\sigma}\left\| \left[\tilde{\gamma}_{Obs}(m_{\min})\exp(-i\varphi_0)\right]-\left[\tilde{\gamma}_{V0}(h_V,\sigma,\kappa_Z)\right] \right\|. \tag{5.16}$$

that can be implemented in terms of a two dimensional look-up table (see red dots in Figure 26).

The inversion complicates when $m_{\min}>0$, i.e. when a (significant) ground scattering contribution is present in all polarizations.

In this case, when the ground scattering contribution is neglected and $\tilde{\gamma}_{V0}(h_V,\sigma,\kappa_Z)$ is associated to $\tilde{\gamma}_{Vol}(h_V,\sigma,m_{\min})=\tilde{\gamma}_{Obs}(m_{\min})\exp(-i\varphi_0)$, may lead to coherences outside the solution space provided by Eq. (5.6). At the same time, accepting $\tilde{\gamma}_{Vol}(h_V,\sigma,m_{\min})=\tilde{\gamma}_{Obs}(m_{\min})\exp(-i\varphi_0)$ the 3 unknown parameters in Eq. (5.5) (i.e. $h_V,\sigma,m_{\min}$) cannot anymore be estimated from a single $\tilde{\gamma}_{Obs}(m_{\min})$ measurement only. One way to overcome this problem for $\sigma\geq 0$ without introducing more measurements is to fix the extinction value as suggested in [98] or [43]. In many cases, a high ground scattering contribution is the result of a low extinction level, justifying to fix $\sigma := 0$ dB/m. In this case the inversion of Eq. (5.16) becomes

$$\min_{h_V,m}\left\|\left[\tilde{\gamma}_{Obs}(m_{\min})\exp(-i\varphi_0)\right]-\left[\tilde{\gamma}_{Vol}(h_V,m,\kappa_Z,\sigma=0\ dB/m)\right]\right\|. \tag{5.17}$$

The solution space of Eq. (5.17) is indicated by the blue dots in Figure 26.

The inversion of the RVoG model using Pol-InSAR data has been primarily addressed at L-band. The assumption of $m_{\min}=0$ - that is not necessarily associated to the HV channel -

has been derived based on the general L-Band scattering scenario, with moderate extinction and relative small m values.

In the case of a single-polarimetric acquisition, where $m(\vec{w}) = 0$ holds as it may be the case for short wavelength like X-band **Publication V [198]**, the parameterization of the measured interferometric coherence in terms of Eq. (5.5) requires four parameters: the forest height h_V, the extinction σ, the ground topography phase φ_0, and the ground-to-volume amplitude ratio $m(\vec{w})$.

The assumption of no ground contribution, i.e. of zero ground-to-volume amplitude ratio, is not sufficient for getting a balanced inversion problem. In this case inversion relies on additional assumptions or the availability of external information.

An alternative way to enforce a balanced inversion problem is to fix the extinction value **Publication II [280]**. Ignoring the ground phase, by considering the absolute values only, a single parameter inversion problem is obtained

$$\min_{h_V} \left\| \gamma_{Obs}(\kappa_Z, \vec{w}) \right| - \left| \tilde{\gamma}_{Vol}(h_V, \kappa_Z, \varphi_0, \sigma = ct) \right\| \tag{5.18}$$

Dependent on the forest conditions σ needs to be adapted. In tropical peat swamp forests $\sigma = 0.3$ dB/m worked fine for X-band **Publication V [198]**, while for boreal forests $\sigma = 0.01$ dB/m gave best results **Publication II [280]**.

Fixing the extinction σ has been proved to compromise the inversion performance as it restricts the ability of the RVoG model to interpret the spatial variability of forest structure **Publication III [124]**.

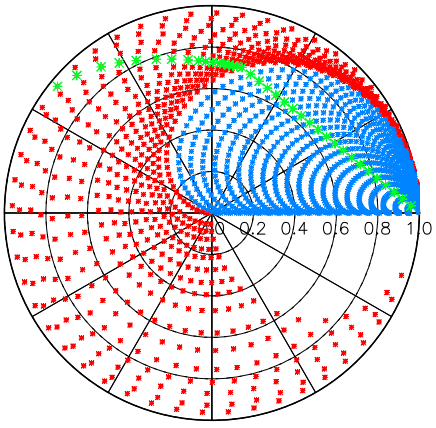

Figure 26: RVoG solution space for different h_V (up to 50 m), σ (0 dB/m to 2 dB/m) and m (0 to 10) values for a κ_Z of 0.13 rad/mand $\varphi = 0°$ as given by (7); red dots: $\tilde{\gamma}_{V0}(h_V, \sigma \mid \kappa_Z, m = 0)$; blue dots: $\tilde{\gamma}_{V0}(h_V, m \mid \kappa_Z, \sigma = 0dB/m)$; green dots: constant height $\tilde{\gamma}_{V0}(\sigma \mid h_V = 20\text{m}, \kappa_Z, m = 0)$ and $\tilde{\gamma}_{V0}(m \mid h_V = 20\text{m}, \kappa_Z, \sigma = 0)$; black arrows indicate increment of h_V and σ. © [2015] IEEE

The best – with respect to inversion performance – scenario is to use an external DTM to estimate the ground topographic phase $\exp(i\varphi_0)$. For this, the DTM is converted to phase: $\exp(i\varphi_{DTM}) = \exp(ih_{DTM}\kappa_Z)$. Then the phase offset between $\exp(i\varphi_{DTM})$ and $\tilde{\gamma}_{Obs}(\kappa_Z, \vec{w})$ is

calibrated by means of a corner reflector or a bare area with sufficient high coherence $|\tilde{\gamma}_{Obs}(\kappa_Z,\vec{w})|>0.98$. $\tilde{\gamma}_{Obs}(\kappa_Z,\vec{w})$ can then be inverted for forest height h_V and extinction σ by **Publication V [198]**

$$\min_{h_V,\sigma}\left\|\gamma_{Obs}(\kappa_Z,\vec{w})\exp(-i\varphi_{DTM})-\tilde{\gamma}_{Vol}(h_V,\kappa_Z,\sigma)\right\|. \tag{5.19}$$

5.3.2 The role of the vertical wavenumber in forest height inversion

In section 5.2 the vertical wavenumber κ_z and in section 4.3.6 the compensation of non-volumetric decorrelation processes were identified as critical parameters in forest height inversion. The multifaceted effect of the effective spatial baseline, as expressed through κ_z, on the inversion of forest height from Polarimetric Interferometric SAR (Pol-InSAR) data is examined and published in **Publication I [196]**. Therefore, only a brief summary of **Publication I [196]** is given in the following.

The inversion performance depends strongly on the accurate compensation of non-volumetric decorrelation contributions, the choice of the appropriate vertical wavenumber κ_z and the knowledge about its variation within the scene.

In a quantitative analysis (Monte Carlo simulation) it was demonstrated that a single κ_z allows accurate inversion only for a limited range of forest heights. For taller stands, the performance is limited by the variance induced by the low coherence levels. This can partially be compensated by increasing the number of looks at the expense of spatial resolution. With further increasing stand height the sensitivity of the interferometric coherence to forest height saturates leading to underestimated forest height estimates. For lower forest heights, the performance is limited primarily by the bias induced by the residual non-volumetric decorrelation contributions. In consequence, in order to obtain the optimum inversion performance over a wide range of forest heights multiple Pol-InSAR acquisitions with variable κ_z values are required. A concept for defining the optimum κ_z values for a given height range has been introduced in **Publication I [196]**. Across all extinctions three baselines are sufficient to map heights from 5 m to 60 m with a height error better than 10 percent (see Figure 27 A-C). For higher extinctions (> 0.5 dB/m) two baselines would be sufficient (see Figure 27 C), as here the higher coherence values reduce the statistical variance. In Figure 27 the baselines (green arrows) are selected to cover a height range between 5 m and 60 m with a minimum number of baselines.

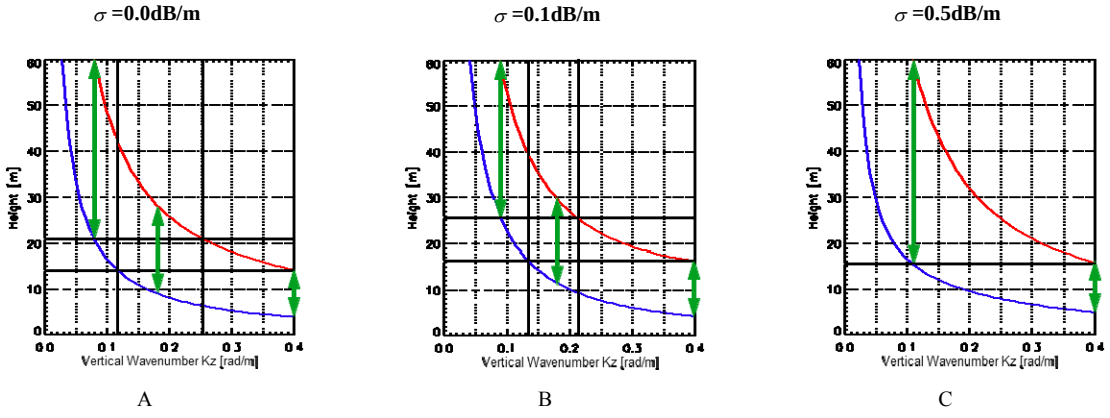

Figure 27: Inversion performance as a function of forest height h_V and vertical wavenumber κ_z for three extinctions assuming a height error better than 10 percent; blue : lower boundary; red: upper boundary; green arrows: baselines to cover a height range from 5 m to 60 m. © [2015] IEEE

If only one baseline is available then the estimation performance depends strongly on the prevailing forest heights.

A good compromise in order to obtain reliable forest height estimates with sufficient accuracy for single baseline acquisitions is to mask $\kappa_z < 0.05$ rad/m and $\kappa_z > 0.15$ rad/m.

The vertical interferometric wavenumber κ_z is defined by the acquisition geometry and depends on the incidence angle and on the range component of the local terrain slope. Consequently, for a precise estimation of κ_z a DEM is required.

While terrain slopes in azimuth have no effect on κ_z, terrain slopes in range direction modify the local incidence angle $\theta = \theta_0 + \alpha$ and as a consequence (see Eq. (4.40)) the vertical wavenumber κ_z results in (see **Publication I [196]**)

$$\kappa_z = m \frac{2\pi}{\lambda} \frac{\Delta\theta}{\sin(\theta_0 + \alpha)}. \tag{5.20}$$

Compensation of terrain slope can be regarded as a two-step process in the height inversion.

Firstly the range component of the terrain slope α is used to correct the (nominal) incidence angle θ_0. For this, the used DEM is projected in slant range geometry. The local terrain slope α is then calculated by:

$$\alpha = \tan^{-1}\left(\frac{\Delta H}{\frac{PS_{rg}}{\sin(\theta)} + \tan(\theta)\ \Delta H} \right) \tag{5.21}$$

where ΔH is the height difference between two consecutive range samples and PS_{rg} the corresponding slant range distance.

Secondly the resulting volume heights h_V are transferred into a forest height H_F. Then, for flat terrain it results in

$$H_F = h_V \tag{5.22}$$

while for sloped terrain

$$H_F = \frac{h_V}{\cos|\alpha|} \tag{5.23}$$

is valid.

In order to assess the required DEM quality, several available DEM products have been tested in **Publication I [196]** on their suitability for topographic correction in the Pol-InSAR inversion process. While the low resolution SRTM DEM was not able to fully compensate terrain slope effects, the TanDEM-X DEM as well as the LIDAR DEM and the (L-Band) DEM obtained from the Pol-InSAR measurements itself performed similar and were able to correct the topographic effects.

5.3.3 Incoherent multibaseline combination/selection

According to Eq. (4.40) or Eq. (4.41), a change of incidence angle θ goes along with a change of κ_z, even if the spatial baseline remains the same. This is why in airborne (repeat-pass) interferometric systems κ_z is two dimensional: it varies along azimuth with the variation of the spatial baseline components induced by the non-ideal platform motion and across range with the incidence angle. The changes of κ_z induced by different flight constellations are shown and discussed in **Publication I [196]**. It is apparent that the for airborne SAR systems typical wide variation of the incidence angle in range causes a (significant) variation of κ_z. In order to cover a complete scene with similar performance several interferometric acquisitions with different baselines are required. In addition temporal decorrelation – that can never be excluded in repeat pass acquisitions – may degrade inversion accuracy. To counter these constraints and to improve the quality of forest parameter inversion an incoherent multibaseline Pol-InSAR inversion approach has been proposed **Publication III [124],** [216].

The shape and size of the coherence boundary are besides differences in the ground contribution determined by statistical deviations of the coherence measurements [349], [350], [161] uncompensated decorrelation effects and the vertical wavenumber κ_z.

Two different incoherent methods are investigated: The first one is the selection of individual inversion heights by using the eccentricity χ of the coherence boundary **Publication III [124],** [87] (see also Figure 20, Figure 25 and section 4.4.2)

$$\chi = \sqrt{1-(b/a)^2} \tag{5.24}$$

where a is the major axis and b is the minor axis of the ellipse. When more than two Pol-InSAR measurements are available, the inversion height for the baseline corresponding to the largest eccentricity will be selected.

$$\max_{\kappa_z,\vec{k}_1,\vec{k}_2} = \left\| \begin{matrix} \chi(\kappa_{z\,1},\vec{k}_{1\,1},\vec{k}_{2\,1}) \\ \chi(\kappa_{z\,2},\vec{k}_{1\,2},\vec{k}_{2\,2}) \\ \vdots \\ \chi(\kappa_{z\,J},\vec{k}_{1\,J},\vec{k}_{2\,J}) \end{matrix} \right\| \tag{5.25}$$

where J is the number of available baselines for each pixel.

The second criterion used to combine multiple baselines is the conventional interferometric height accuracy H_{acc} defined by the standard deviation of the interferometric phase [301] and the vertical wavenumber κ_z.

$$H_{acc} = -\frac{1}{\kappa_z}\sigma_\phi \tag{5.26}$$

The standard deviation of the interferometric phase σ_φ (see Eq. (4.46)) may also be approximated with the aid of the Cramer Rao bounds [15]

$$\sigma_\phi = \sqrt{\frac{1-|\gamma_{Obs}(m_{\min})|^2}{2N|\gamma_{Obs}(m_{\min})|^2}}. \tag{5.27}$$

The increase of the standard deviation of the interferometric phase with decreasing coherence caused by decorrelation contributions reduces the quality of the height accuracy. This means the lower height accuracy the more reliable is the inversion result. In case several interferometric acquisitions are available, the baseline that corresponds to the minimum height accuracy is selected

$$\max_{\kappa_z,\gamma_{Obs}(m_{\min})} = \left\| \begin{matrix} H_{acc}(\kappa_{z\,1},\gamma_{Obs1}(m_{\min}),N) \\ H_{acc}(\kappa_{z\,2},\gamma_{Obs2}(m_{\min}),N) \\ \vdots \\ H_{acc}(\kappa_{z\,J},\gamma_{Obs\,J}(m_{\min}),N) \end{matrix} \right\|. \tag{5.28}$$

5.4 Temporal decorrelation

In repeat-pass airborne and spaceborne implementations the inherent presence of temporal decorrelation is biasing the interferometric coherence estimates degrading the sensitivity to vertical scattering structure and limiting the performance of Pol-InSAR inversion techniques [215], [270], **Publication IV [218]**. Temporal decorrelation $\tilde{\gamma}_{Temp}$ can be real (i.e. affecting the absolute value of $\tilde{\gamma}_{Obs}(\vec{w})$ only) – mainly induced by a movement of the scatterer – or complex (i.e. biasing the phase of $\tilde{\gamma}_{Obs}(\vec{w})$) – mainly induced by changes in the dielectricity or the scatterer. However, many temporal decorrelation models proposed (see section 4.3.6.3) the assumption that the dielectric properties of the scatterers remain unchanged between the two acquisitions. At long temporal baselines (i.e. longer than a day), temporal decorrelation may be also caused by the change of dielectric properties due to environmental and weather effects.

There are different approaches to assess the impact of temporal decorrelation on the Pol-InSAR forest height inversion. The Random Volume over Ground with Volume Temporal Decorrelation (RVoG + VTD) model was introduced in [41] and [267] incorporating a temporal decorrelation component into the two-layer (volume/ground) scattering model. The inversion results in the presence of temporal decorrelation (2 days temporal baseline) demonstrated that forest height inversion without accounting or compensating for temporal decorrelation leads to significantly overestimated heights [267]. In **Publication III [124]**, the quantification of temporal decorrelation in L- and P-band repeat-pass interferograms was discussed, with about 40 minutes temporal baseline, assuming that the scattering properties of the ground do not change in that time. In **Publication IV [218]** temporal decorrelation coefficients are estimated for temporal baselines ranging from 10 minutes to 54 days and temporal decorrelation was split into a ground decorrelation component and a volume decorrelation component.

Temporal decorrelation affects the volume component that represents the vegetation layer and the underlying ground layer in a different way. Both temporal decorrelation effects can be incorporated in the two-layer scattering model [41], [267], [204]

$$\tilde{\gamma}_{Vol}(\vec{w}) = e^{i\phi_0}\frac{\tilde{\gamma}_{TV}\tilde{\gamma}_{V0}+\gamma_{TG}m(\vec{w})}{1+m(\vec{w})} \tag{5.29}$$

where γ_{TG} represents the scalar decorrelation coefficient describing temporal decorrelation of the underlying surface scatterers and $\tilde{\gamma}_{TV}$ denotes the *complex* correlation coefficient describing the temporal decorrelation of the volume layer. In case of a constant temporal decorrelation function, temporal decorrelation in volume becomes a *scalar* value γ_{TV} (i.e. no bias of phase). Both $\tilde{\gamma}_{TV}$ and γ_{TG} are functions of the temporal baseline. However the decorrelation processes in the volume layer occur at different – in general much smaller – time scales than the decorrelation of the surface layer. Moreover, both temporal decorrelation coefficients may be polarization dependent.

When the temporal baseline is considerably short (i.e. smaller than one hour), it is realistic to assume that the ground remains stable (i.e. $\gamma_{TG} = 1$), and that the dielectric and statistical properties of the volume do not change. In this case Eq. (5.29) can be simplified as

$$\tilde{\gamma}_{Vol}(\vec{w}) = e^{i\phi_0} \frac{\gamma_{TV}\tilde{\gamma}_{V0} + m(\vec{w})}{1 + m(\vec{w})}. \tag{5.30}$$

The Pol-InSAR coherence loci contaminated by γ_{TV} still lie on a straight line segment in the complex plain. The ground point remains unchanged, while the volume coherence $\tilde{\gamma}_{Vol}$ is shifted towards the origin by γ_{TV}. The inversion of Pol-InSAR data contaminated by temporal decorrelation γ_{TV} leads to overestimated forest height estimates [41], [267], **Publication IV [218]**.

Effects of temporal decorrelation and quantification of temporal decorrelation – including methods of quantification is detailed discussed and published in **Publication III [124]** and **Publication IV [218]** and is therefore only briefly summarized below.

Hajnsek, Kugler et al. Publication III [124] describe and quantitatively assess temporal decorrelation effects in short time repeat-pass interferometric acquisitions. A key element in the quantitative assessment of temporal decorrelation was the single-pass single-channel (VV) X-band data set – not affected by temporal decorrelation. In a first step a modification of the conventional Pol-InSAR forest height inversion scheme has been proposed adapted to the single channel X-band interferometric observation space (see Eq. (5.19)). The neglect of the ground scattering component and fixing the extinction value allowed to obtain sensitive height estimates at X-band. In a second step, the X-band height estimates have been used to assess the amount of temporal decorrelation at L- and P-band. Looking on temporal baselines of about 40 minutes the obtained results indicate, as expected, a higher temporal stability at P-band (with temporal decorrelation on the order of 0.93) than at L-band (with temporal decorrelation on the order of 0.85 - 0.89). However, the decorrelation levels are at both frequencies sufficient to cause - if not compensated - an overestimation on the order of 30-40 percent depending on the actual forest height level.

Lee, Kugler et al Publication IV [218] address the impact of temporal decorrelation on Pol-InSAR forest height inversion performance. Temporal decorrelation as a function of the temporal baseline has been investigated for a wide range of temporal baselines. Different temporal decorrelations for the volume and the ground layer have been incorporated into the two-layer (volume/ground) RVoG scattering model. Both decorrelations bias the Pol-InSAR inversion results, but in a different way:

- while volume temporal decorrelation γ_{TV} biases the volume decorrelation contribution,
- temporal decorrelation on the ground layer γ_{TG} introduces a ground phase error.

Both effects lead to an overestimation of forest heights. The impact of temporal decorrelation has been separately assessed at L-band on three different levels of temporal baseline: long-term (months—weeks), mid-term (weeks–day) and short-term (hour–minutes) temporal baselines.

Long-term temporal baselines:

The level of temporal decorrelation after 54-day repeat pass time (with cohrerences around 0.3) makes Pol-InSAR applications no longer possible. In the case of 32-day temporal baseline, the level of coherences in forest was higher than 0.3 so that Pol-InSAR inversion was still able to be applied but forest height was quite overestimated due to the uncompensated temporal decorrelation. The decorrelation level is sufficient to cause height errors on the order of 20–200 percent in dependence on forest height and spatial baseline setup.

Mid-term temporal baselines:

Using multibaseline Pol-InSAR data sets with temporal baselines on the order of 1 day, up to 2 weeks, it is possible to estimate the different temporal decorrelation contribution γ_{TV} and γ_{TG}. The decorrelation processes within the volume layer occur much faster than on the ground. The reason for this is that the scatterers in the canopy are less stable than those on the ground and γ_{TV} and γ_{TG} are not only dependent on the wind-induced movements, but rely also strongly on the rain-induced dielectric changes in the volume and on the ground. The estimated temporal decorrelations γ_{TV} and γ_{TG} were converted to height errors and then validated against the direct estimated height error from Pol-InSAR inversion. The obtained results are highly correlated with a correlation coefficient of 0.94 and a RMSE of 3.34 percent. This is a strong indication for the validity of the model used, as well as for a successful estimation of γ_{TV} and γ_{TG} at temporal baselines on the order of days.

Short-term temporal baselines:

The behavior of temporal decorrelation on the order of minutes was strongly related to wind-induced movement and showed a rather random nature in forests due to the variability of wind patterns in space and time (see also **Publication III [124])**. For this time scale changes in the dielectric properties of the canopy and the ground layer can be ignored. The wind speed of 2 m/s already reduces the performance of Pol-InSAR inversion dramatically as volume decorrelation is biased. Therefore, the wind speed during the acquisition is the most critical parameter concerning the amount of temporal decorrelation for short-term repeat-pass times.

5.5 Obtained results

In the following, Pol-InSAR forest height inversion results are presented as obtained for X-, L- and P-band for different forest types – boreal forests as well as temperate and tropical forests.

It turned out that Pol-InSAR forest height corresponds best to forest top height H100 from ground measurements [238], [242] and [239]. For validation purposes H100 calculated from LIDAR measurements is used (see section 3.2.3).

Cross validation was done on stand level i.e. with homogeneous forest areas with a mean size of ~ 3 ha – 5 ha. Every stand is represented by its mean value. This is necessary to compensate for the residual spatial misregistration between SAR and LIDAR reference data, occurring when georeferencing both data sets. Of course averaging also reduces the variation of the obtained estimates.

5.5.1 Pol-InSAR inversion results for different frequencies and forest types

Most of the obtained results are published in **Publication I [196]**, **Publication II [280]**, **Publication III [124]** and **Publication V [198].**

Publication II [280] compares forest heights obtained from the inversion of quad-pol POL-InSAR data sets at L-band (Eq. (5.16) in combination with Eq. 5.17) and forest heights obtained from the inversion of single-pol X-band InSAR data (Eq. (5.18) with σ = 0.01 dB/m) – both acquired with DLR's E-SAR system [139] – over a boreal test site in southern Finland near Helsinki (Lat: 60° 11′, Long: 24° 29′) with forest height estimates from HUTSCAT scatterometer data [127], [152]. The results are displayed in Figure 28 (top row for X-band and bottom row for L-band) and show that the forest height values estimated by means of two different radar instruments are in good agreement. A single measurement is somewhat noisy, but the general trend follows tree top level rather closely. For the higher forest stands, the variability in height estimates is higher while for smaller forest stands the variability is smaller, due to the variance of the volumetric coherence.

The X-band follows better the actual tree crown structure and penetrates deeper in gaps between the trees than the L-band. In very sparse areas it performs better than L-band which has the tendency to underestimate forest heights therein.

A profiling scatterometer instrument, like HUTSCAT, can give valuable information to support validation of POL-InSAR methods and helps to better understand backscattering processes in vertically distributed media like forests.

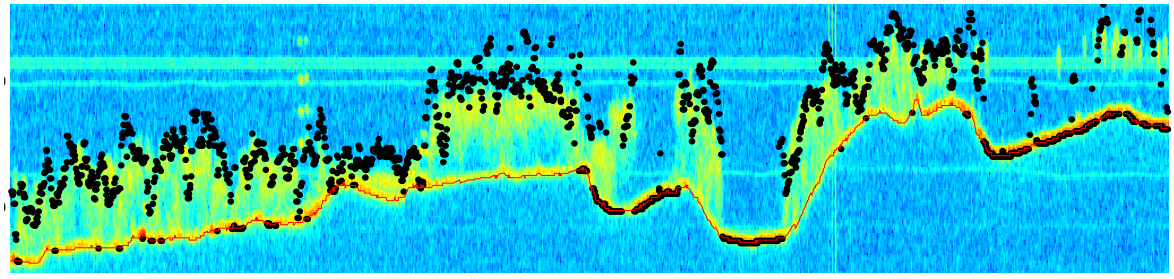

A

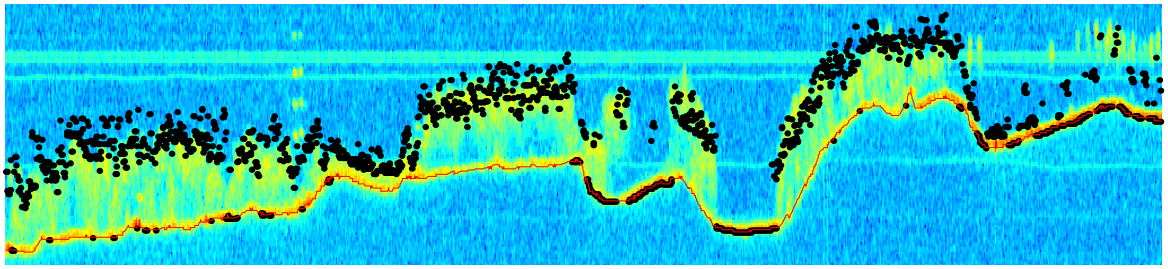

B

Figure 28: Transect of Pol-InSAR forest height estimates on top of HUTSCAT X-band vertical forest backscattering profile. Black dots represent the POL-InSAR forest height estimates for A: L-band and B: X-band. The x-axis is HUTSCAT flight direction, and the y-axis is HUTSCAT vertical range. Yellow areas correspond to backscattering from trees and ground. The red line corresponds to the automatically detected ground level. The transect length is approx. 2.5 km. © [2007] IEEE

In **Publication III [124]** Pol-InSAR forest height estimates are presented over a tropical peat swamp forest and a tropical Dipterocarp forest in Southeast Asia (Indonesia) [122], [123], [187]. Pol-InSAR forest height inversion is primarily assessed at L- and P-band but also at higher frequencies, namely X-band. Critical performance parameters such as the

"visibility of the ground" at L- and P-band are addressed. Data were acquired with DLR's E-SAR system [139].

First the question about the "visibility" of the ground was faced. The polarimetric and interferometric analysis demonstrated clearly the capability of both frequencies, L- and P-band, to penetrate until the ground through dense Dipterocarp forest, with individual tree heights up to 60 m and local biomass levels even beyond 600 t/ha (for visualization of ground measurements see Figure 29).

In the case of the Dipterocarp forest the Pol-InSAR forest height estimates have been validated against H100 values estimated from the ground measurements. For forest heights ranging from 15 up to 45 m the L- and P-band estimates where within 10 percent accuracy, even in hilly terrain. For the peat swamp forest the validation was done against LIDAR derived H100. For forest heights ranging from 5 to 27 m L-band estimates where characterized by an r^2 of 0.91 with an RMSE of 1.97 m, while the best P-band estimates show an r^2 of 0.94 with an RMSE of 1.74 m. The overall estimation accuracy for both test sites was better than 10 percent for both frequencies. The key limiting factor in estimation accuracy appears to be uncompensated non-volumetric decorrelation effects, especially temporal decorrelation.

In the less dense peat swamp forest X-band is able to penetrate until the ground providing forest height estimates characterized by surprisingly high r^2 values on the order of 0.94 with an RMSE of 1.77 m. This is a strong indication for the potential Pol-InSAR performance expected in the absence of temporal decorrelation. Generalisation of the X-band performance is however critical as the "visibility" of the ground required for an unbiased inversion gets lost when going to denser forest conditions.

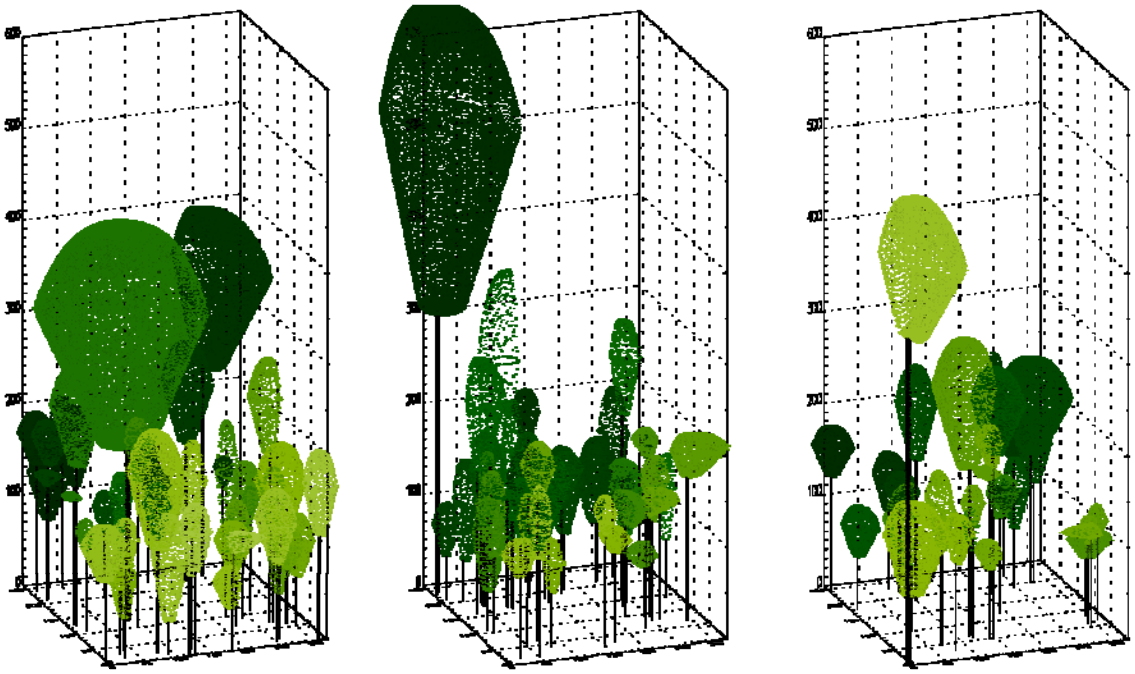

Figure 29: **Visualization of three 25 m x 32 m ground measurements plots of a Dipterocarp forest in Indonesia on the island of Borneo (Lat: -1°6', Long: 116°49') Publication III [124].**

In **Publication I [196]** Pol-InSAR forest height estimation was successfully demonstrated in L- and P-band for forest heights up to 40 m in three different test sites representing three ecologically different forest types: boreal forest, temperate forest and tropical forest. A P-band acquisition over dense tropical lowland forest in Indonesia with tree heights up to 60

m **Publication V [198]** could be successfully inverted and cross validated with LIDAR measurements.

Publication V [198] addresses Pol-InSAR forest height estimation in X-band by means of TanDEM-X satellite data. For this, a large number of single- and dual-pol TDX data sets acquired over three different forest sites - a boreal, a temperate and a tropical site - at different acquisition modes have been analyzed.

The suitability of TDX for Pol-InSAR forest applications depends on a) the penetration capability of X-band into forest vegetation and b) the polarimetric diversity of the interferometric coherence. Both effects were evaluated over all three sites for different acquisition geometries (i.e. on the incidence angle and spatial baseline) and for different environmental and seasonal conditions.

For all sites, a strong correlation between the (height of the) phase center location and forest (top) height could be established. The corresponding correlation coefficients reached values of 0.9 and higher. The correlation varies with seasonal and environmental changes. A clear seasonal dependence could be observed between summer and winter acquisitions at the European test sites. For the tropical site the difference between wet and dry season was weaker.

For the boreal site acquisitions at different look angles (19° and 32°) were analyzed indicating only a weak effect of the incidence angle on the penetration. For the Temperate site, impact of incidence (look) angle appeared stronger than at the boreal site. But here differences in phase center height due to different incidence (look) angles are mixed up with seasonal effects.

The synthesis of the results suggest an unexpected high penetration at X-band but leave open the question of whether the penetration is induced by the propagation through the vegetation volume or partially through gaps in the vegetation layer that become relevant at the spatial resolution of the TDX data [385].

The polarimetric dependency of the interferometric coherence (expressed by means of the length of the dual-pol coherence region or polarimetric diversity) was strongly correlated to forest height in all sites. At the same time the effect of seasonal and environmental variability was clearly visible: For the boreal site, the penetration during the winter can be interpreted only with a sufficient large ground scattering contribution that makes an inversion based on the assumption of a “zero ground component” sub-optimal.

The summer acquisitions were characterized by a smaller ground contribution supporting “zero ground component” inversion schemes. For the temperate site the winter acquisitions seemed to be better suited for inversion than the summer acquisitions as penetration was higher and the whole volume is “seen” by the radar (due to the lower attenuation in winter). In the tropical case the impact of seasonal effects on the polarimetric diversity was rather small. This allows to conclude that seasonal adapted acquisitions could improve the inversion performance and increase probably the number of forest types that can be investigated by means of Pol-InSAR techniques at X-band.

Based on these observations, two forest height estimation approaches - one for the single-pol case based on the availability of an external DTM and one for the dual-pol case that does not require any a priori knowledge have been proposed, implemented and applied on the available data sets. The obtained height estimates have been cross validated against LIDAR reference measurements.

In forest conditions that allow a sufficient penetration at X-band, the performance of the two approaches was comparable and surprisingly high with a correlation of $r^2 = 0.86$ in the boreal and $r^2 = 0.77$ in the temperate site for the dual-pol case. At denser forest conditions, the variance of the dual-pol estimates increased ($r^2 = \sim 0.50$ in the tropical site) and finally

saturated with increasing height due to the insufficient penetration. Note that the single-pol inversion was not affected by saturation as it does not require a penetration until the ground.

The achieved performance clearly indicates the advantage of a spaceborne single-pass interferometric implementation for forest applications. The absence of temporal decorrelation allows the achievement of a new quality in measurement accuracy that may allow the development of new applications and make a systematic monitoring of forest structure parameters - preferably at a lower frequency band – possible.

5.5.2 Extinction

Beside the forest height, Pol-InSAR inversion provides the value σ, scaling the used backscatter function $f_V(z)$ which can be interpreted as signal extinction or form factor (σ in Eq. (5.8) or ς in Eq. (5.10)) [269], [352]. The extinction coefficient (or form factor) increases with increasing frequency [21] modifying $f_V(z)$ and makes the interferometric coherence according to Eq. (5.8) frequency-dependent.

An evaluation of σ (in this case interpreted as signal extinction) of an airborne X-band acquisition (with DLR's ESAR [139]) is shown in [192] over Kobernausser Wald. Kobernausser Wald is a temperate forest with single species even aged forest stands located in upper Austria (Lat: 48°04', Long: 13°14'). H100 is between 5 m and 40 m. A detailed description of Kobernausser Wald test site is given in [188]. In case, extinction is considered as an indicator for canopy closure or canopy density, then extinction values reflect forest management strategy. In Figure 30 C, extinction is plotted as a function of forest height. Extinction increases until the forest reaches a height where harvesting activities i.e. thinning starts (σ = 1 dB/m). Then, thinning is repeated in regular time intervals, decreasing canopy density and decreasing extinction as well, until the maximum heights are reached (σ = 0.4 dB/m). A validation plot for the obtained forest heights applying Eq. (5.19) (Figure 30 A) and phase center height vs. reference height H100 (Figure 30 B) are displayed as well. Reference H100 was obtained from LIDAR data.

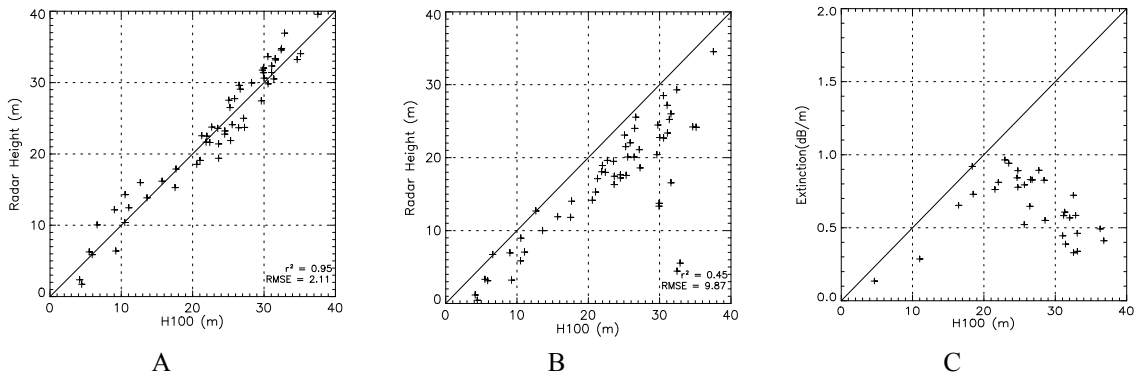

A B C

Figure 30: Kobernausser Wald test site; left: InSAR height estimates Eq. (5.19) vs. LIDAR H100 validation plot; middle: InSAR phase center height vs. LIDAR H100 validation plot; Extinction from Eq. (5.19) vs. LIDAR H100 plot, © [2010] IEEE

5.5.3 Change detection

Repetitions of Pol-InSAR acquisitions enable to detect changes of forest height. In order to demonstrate forest change detection by means of Pol-InSAR estimated forest heights, two Pol-InSAR acquisitions made over Traunstein test site (for test site description see [198]) have been evaluated. The first acquisition took place in 2003 and the second in 2008, with both acquisitions a five year time period is covered. Forest height inversion was done by means of Eq. (5.16) in combination with Eq. (5.17).

For validation homogeneous stands were delineated by means of ground measurements and aerial photographs. A validation plot for the 2008 Pol-InSAR acquisition with LIDAR H100 reference measurements is shown in Figure 31 C. A correlation coefficient r^2 of 0.93 in combination with a RMSE (Root Mean Square Error) of 1.97 indicates fairly accurate Pol-InSAR height estimates. Figure 31 A shows the forest height map obtained from the Pol-InSAR data acquired in 2003 and Figure 31 B shows the forest height map from the 2008 acquisition. A first visual comparison between the two acquisitions reveals already severe changes over large areas. Only small sections of the considered forest area remain unchanged. Changes may be caused by:

- height growth,
- logging or
- disturbances (bark beetle, wind throw induced by thunder storms)

Forest height growth is strongly dependent on the growth stage i.e. age of the trees and site conditions of a forest. Most tree species are highly productive at an age between 20 and 60 years which corresponds to tree heights ranging from 10 m to 25 m. For this age classes height growth could reach 2 m to 5 m over a five-year period [289], [18]. For older trees height growth is slowing down to a maximum height growth of 1 m to 2 m during a five year period but is mostly even less.

Three logging scenarios can be distinguished: Two selective logging scenarios and clear cuts or when all trees of one generation are removed. In the first selective logging scenario competitors of the dominant trees are removed (crown thinning) which has only a minor impact on H100. The second selective logging scenario starts when several trees in a stand have reached the predefined harvestable dimension, then the dominant trees i.e. the trees that reached the harvestable dimension, are removed, which lowers H100. In Traunstein selective logging of harvestable trees is actually the most abundant method for harvesting timber, which means that in old (=high) stands large trees are preferentially logged lowering H100.

Disturbance events can be distinguished into large area and small area disturbances. Large area disturbances are often induced by strong winds i.e. hurricanes as they have the potential to tilt in one turn large forest areas, in some cases only single trees exposed to the wind are thrown down. Typical small area disturbances are small-scale deforestation to combat insect pests, for instance bark beetle in Norway spruce (*picea abies*). Forest disturbances are the most complex forest change scenarios and appear in many different forms.

At Traunstein site large forest areas were affected by windthrow caused by the thunder storm “Kyrill” in 2007. These areas are indicated by a severe decrease of forest height (from 35 m to 5 m) between the acquisition in 2003 (Figure 31 A) and the acquisition in 2008 (Figure 31 B) and are mainly found in the middle and on the left side of the scene.

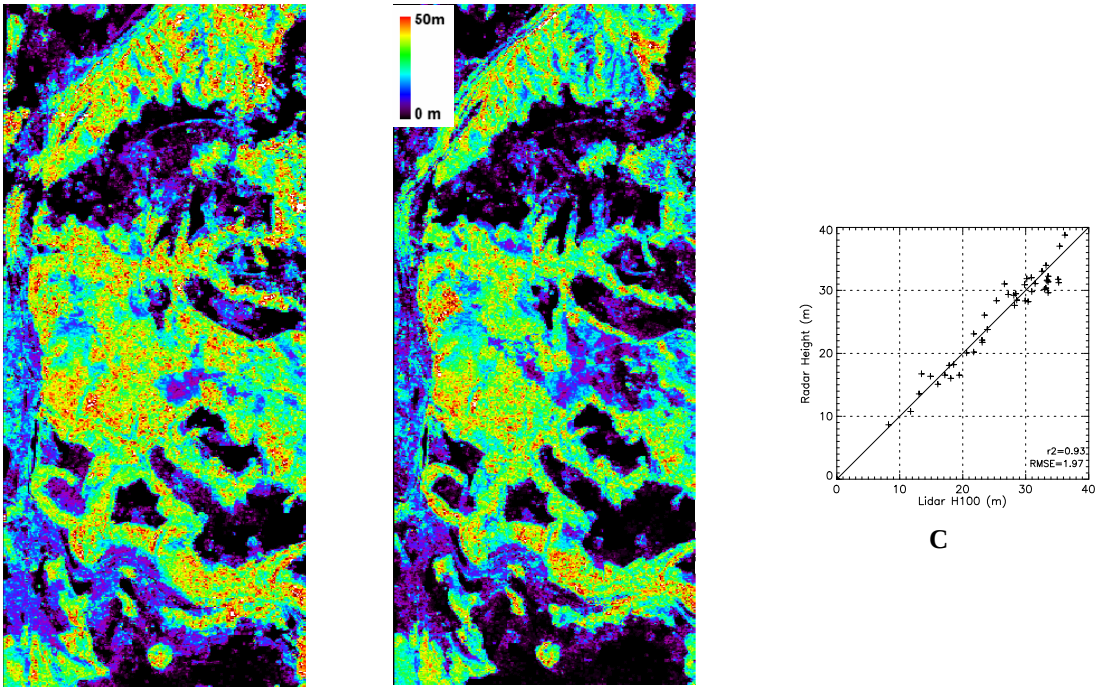

Figure 31: Pol-InSAR forest height estimates over Traunstein site (for test site description see [198]) scaled from 0 m to 50 m; A: Forest height map from the acquisition of September 2003; B: Forest height map from the acquisition of July 2008; C: Validation plot LIDAR H100 vs. Pol-InSAR forest height estimates from July 2008. © [2013] IEEE

Here are just a few selected examples for detected forest changes between the two acquisitions listed. Figure 32 shows selected details of the forest height maps presented in Figure 31 A and B. The forest height maps in the top row are from the 2003 acquisition (Figure 32 A, B and C) and the height maps in the bottom row from the 2008 acquisition (Figure 32 D, E and F). Figure 33 top row shows the associated histograms for the 2003 acquisition in red, for the 2008 acquisition in blue and for the LIDAR H100 from 2008 in green, in the bottom row the pixel by pixel comparison between the forest height map of the 2003 acquisition and the forest height map of the 2008 acquisition is illustrated in form of a two-dimensional histogram where the color indicates the frequency in which a pixel combination appears (blue: rarely, yellow: moderate, dark red: often).

Growth in large parts of the scene cannot be detected as here the forest is older than 60 years and height growth for five years is small and is additionally mixed up with logging operations - the measurement accuracy is too insufficient as to detect such small changes.

Figure 32 A shows a forest stand acquired in 2003 with a mean height of 18 m in which forest height growth of 2 m to 3 m can be expected for a five-year period. The 2008 acquisition of this detail is displayed in Figure 32 B and reveals an increase of forest height in the order of 2 m (mean Pol-InSAR height in 2008 is 20 m) which is confirmed by the histograms in Figure 33 A and D and also by the LIDAR measurements (see green histogram in Figure 33 A).

A disturbance scenario is given in the forest height map details shown in Figure 32 B for 2003 and in Figure 32 D for 2008. The thunderstorm Kyrill caused severe windthrow in the lower part of the displayed map detail, in the upper part only a few large (emergent) trees were affected. The lower part, however, is of particular interest as the thunderstorm uncovered a second forest layer of advanced regeneration. In the lower part forest height dropped down from 35 m to 10 m. This is also clearly visible in the corresponding

histograms Figure 33 B and D. While in 2003 forest height was uniformly distributed (red histogram in Figure 33 B), in 2008 the histogram changed to a bimodal distribution (blue histogram in Figure 33 B).

Forest height map details with a logging scenario revealing where the dominant trees are removed are shown in Figure 32 C for 2003 and in Figure 32 D for 2008. Typical for this scenario is that two processes are mixed up: first, forest growth for the considered period of time and second, decrease of forest height induced by removing a fraction of the largest trees. For this example height decrease was the dominant process. Mean Pol-InSAR forest height decreased from 30 m in 2003 to 27 m in 2008. The change of forest height can also be traced in the histograms in Figure 33 C and Figure 33 F. The broad distribution in the 2-D histogram in Figure 33 F reflects the modified horizontal crown structure induced by logging of dominant trees and its impact on forest growth.

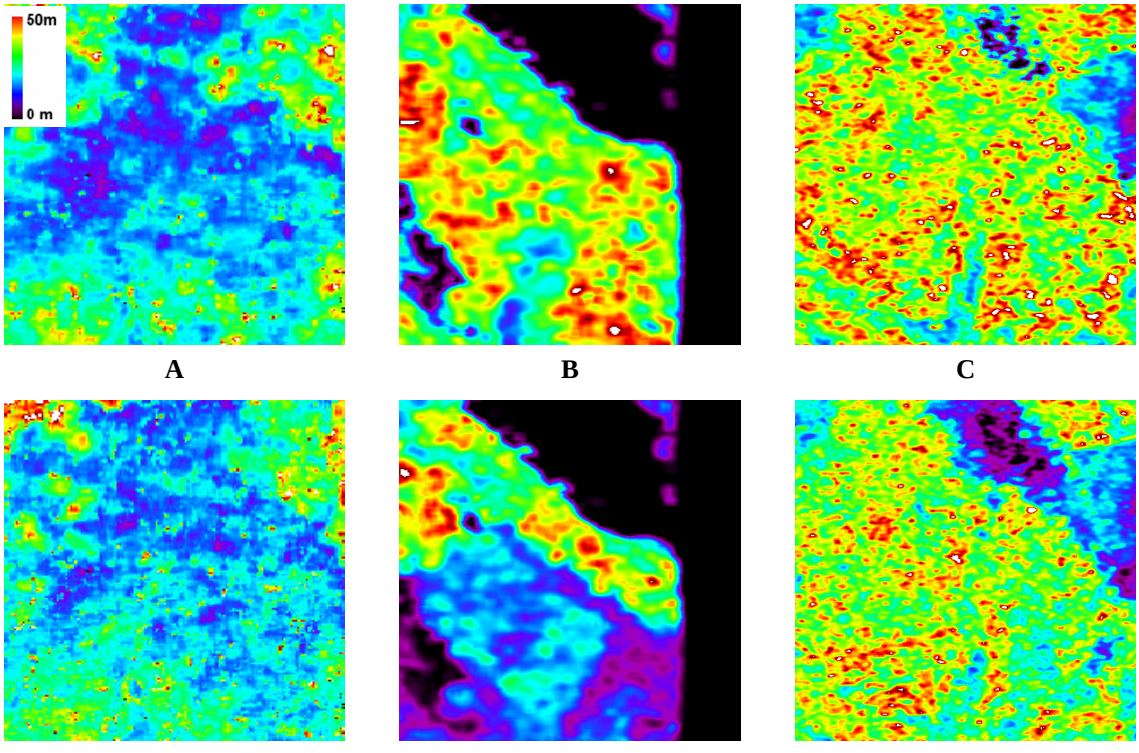

Figure 32: Details of forest height maps over Traunstein site (for test site description see Publication V [198]) displayed in Figure 31 A and B; Top row from 2003 acquisition; Bottom row from 2008 acquisition; A and D: Forest growth between 2003 and 2008; B and E: Forest disturbance; C and F: Logging scenario

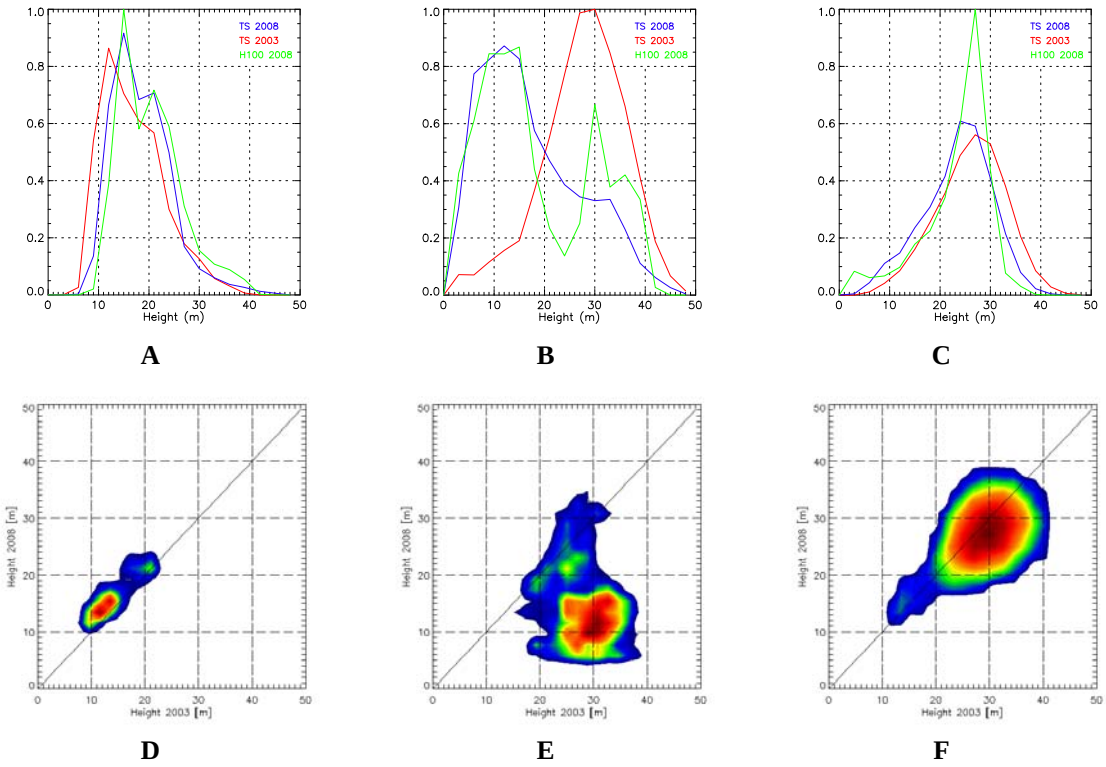

Figure 33: Comparison forest heights 2003 vs. 2008 from the forest height maps details displayed in Figure 32; Top row: Histograms of the height distribution of the selected area for the 2003 acquisition in red, the 2008 acquisition in blue and the corresponding LIDAR measurements from 2008 in green; Bottom row: a pixel by pixel comparison between the 2003 and the 2008 acquisition in form of a 2-D histogram where the color indicates the frequency a pixel combination appears (blue: rarely, yellow: moderate, dark red: often)

5.6 Dual baseline forest height inversion

Forest height inversion based on Eq. (5.16) in combination with Eq. (5.17) has been used successfully over a variety of forest and terrain conditions at L-band [269], [186], **Publication II [280] Publication IV [218], Publication III [124],** [211], at X-band **Publication V [198], Publication II [280],** [186], as well as in dense (tropical) forests at P-band **Publication III** [124]**, Publication I [196]**. However, the validity of this assumption is not expected to be universal. The impactions arising when this assumption is no longer valid are discussed in the following. Particularly at P-band in combination with less dense forest conditions $m_{\min} > 0$ has to be considered in the inversion. Additionally, the vertical backscatter function sometimes needs to be revised. A triangular vertical backscatter function as introduced in Eq. (5.10) is at times preferable to the exponential vertical backscatter function especially for long wave length over sparse and open forests.

In repeat pass acquisitions it is always possible that data are affected by temporal decorrelation. A scalar temporal decorrelation contribution affecting only the volume part (see γ_{TV} in Eq. (5.30)) may be compensated by means of a multi-baseline Pol-InSAR approach.

5.6.1 Dual baseline forest height inversion accounting for $m_{\min} > 0$

The general RVoG case with $m_{\min} \geq 0$ contains six real unknowns $h_V, \sigma, m_1, m_2, m_3$ and φ_0. In contrast to Eq. (5.16) unique inversion results for all unknowns can be obtained only by means of a second Pol-InSAR observation [191].

Each of the two available spatial baselines with corresponding vertical wave numbers κ_{zi} where $i \in \{1,2\}$ provides a set of three different complex coherences $[\tilde{\gamma}(\vec{w}_1) \quad \tilde{\gamma}(\vec{w}_2) \quad \tilde{\gamma}(\vec{w}_3)]_i$. A direct combination requires relative and absolute baseline to baseline phase calibration. An alternative way that relaxes the phase calibration requirements is to estimate first for each single baseline the complex coherence $\tilde{\gamma}(\vec{w}_3 \,|\, \kappa_{zi})$ with the minimum ground component, i.e. the one associated with $\tilde{\gamma}_V(\{h_V, \sigma, m_{\min}\} \,|\, \kappa_{zi})$. Then in a second step h_V, σ and $m_{\min}$ (that are baseline invariant) are estimated according to

$$\min_{h_V, \sigma, m_{\min}, \varphi_0} \left\| \begin{bmatrix} \tilde{\gamma}(\vec{w}_{m_{\min}} \,|\, \kappa_{z1}) \\ \\ \tilde{\gamma}(\vec{w}_{m_{\min}} \,|\, \kappa_{z2}) \end{bmatrix} - \begin{bmatrix} \tilde{\gamma}_{Vol}(\kappa_{z1}, \{h_V, \sigma, m_{\min}\}) \\ \\ \tilde{\gamma}_{Vol}(\kappa_{z2}, \{h_V, \sigma, m_{\min}\}) \end{bmatrix} \right\|. \tag{5.31}$$

Dual baseline forest height inversion follows in principle the three stage inversion process as described in section 5.3.1. But instead of a unique solution in terms of h_V and σ combinations of different solutions for all possible $m_{\min}$ values – so called triplets of h_V, σ and $m_{\min}$ – are obtained for each baseline. Then the solution space for the first baseline is $S_1 = (h_{Vk},\ \sigma_k,\ m_{\min k})$ and for the second baseline $S_2 = (h_{Vl},\ \sigma_l,\ m_{\min l})$ where k is the number of triplets for the first baseline and l for the second baseline. A unique result is obtained through the norm

$$\min_{h_V, \sigma, m_{\min}} \left\| S_1 \begin{bmatrix} (h_{V1}, \sigma_1, m_{\min 1}) \\ \vdots \\ (h_{Vk}, \sigma_k, m_{\min k}) \end{bmatrix} - S_2 \begin{bmatrix} (h_{V1}, \sigma_1, m_{\min 1}) \\ \vdots \\ (h_{Vl}, \sigma_l, m_{\min l}) \end{bmatrix} \right\|. \tag{5.32}$$

In order to avoid baseline scaling effects it is recommended to rank (classifying in integer) h_V, σ and $m_{\min}$ according to the used values in the look up table before applying Eq. (5.32).

5.6.2 Dual baseline forest height inversion accounting for temporal decorrelation in the volume part γ_{TV}

The most usual non-volumetric decorrelation contributions in terms of repeat pass acquisitions is wind induced temporal decorrelation which is well described by the scalar term γ_{TV} in Eq. (5.30). It assumes that the scattering properties of the ground and the volume as well as the propagation properties through the volume do not change in the time between the two acquisitions. Note, that even if γ_{TV} is real it biases the amplitude of $\tilde{\gamma}_{Vol}(\vec{w})$. But the ground only point ($m \to \infty$) remains unaffected by the presence of γ_{TV}. γ_{TV} usually differs from acquisition to acquisition $\gamma_{TV1} \neq \gamma_{TV2}$ [217] introducing two additional scalar unknowns in Eq. (5.31). Assuming again $m_{\min} = 0$ h_V, σ, γ_{TV1} and γ_{TV2} can be estimated according to [217] through

$$\min_{h_V,\sigma,m_{\min},\varphi_0} \left\| \begin{bmatrix} \tilde{\gamma}(\vec{w}_{m_{\min}} \mid \kappa_{z1}) \\ \tilde{\gamma}(\vec{w}_{m_{\min}} \mid \kappa_{z2}) \end{bmatrix} - \begin{bmatrix} \tilde{\gamma}_{Vol}(\kappa_{z1}, \{h_V, \sigma, \gamma_{TV1}, m_{\min} = 0\}) \\ \tilde{\gamma}_{Vol}(\kappa_{z2}, \{h_V, \sigma, \gamma_{TV2}, m_{\min} = 0\}) \end{bmatrix} \right\|. \tag{5.33}$$

Similar to the dual baseline inversion approach presented in the previous section here combinations of different solutions for all possible γ_{TV} – in this case triplets of h_V ,σ and γ_{TV} – are obtained for each baseline. Then the solution space for the first baseline is $S_1 = (h_{Vk},\ \sigma_k,\ \gamma_{TV1\ k})$ and for the second baseline $S_2 = (h_{Vl},\ \sigma_l,\ \gamma_{TV2\ l})$ where k is the number of triplets for the first baseline and l for the second baseline. A unique result is then obtained through the norm

$$\min_{h_V,\sigma,\gamma_{TV1},\gamma_{TV2}} \left\| S_1 \begin{bmatrix} (h_{V1},\sigma_1,\gamma_{TV1\,1}) \\ \vdots \\ (h_{Vk},\sigma_k,\gamma_{TV1\,l}) \end{bmatrix} - S_2 \begin{bmatrix} (h_{V1},\sigma_1,\gamma_{TV2\,1}) \\ \vdots \\ (h_{Vl},\sigma_l,\gamma_{TV2\,l}) \end{bmatrix} \right\|. \tag{5.34}$$

Also here a ranking (classifying in integer) of h_V ,σ according to the used values in the look up table is strongly recommended before applying Eq. (5.34).

5.6.3 Results dual baseline forest height inversion

The aforementioned algorithms (Eq. (5.31) in combination with Eq. (5.32) and Eq. (5.33) in combination with Eq. (5.34)) are now demonstrated by means of P-band data acquired over a (hemi-) boreal forest in southern Sweden – stated Remningstorp test site (Lat: 58,46°, Long: 13,63°).

The Remningstorp forest is part of the southern ridge of the boreal forest zone in transition to the temperate forest zone. Forest in Remningstorp site is clearly less dense / more sparse then in the before introduced temperate and tropical test sites. Topography is fairly flat with some small hills and ranges between 120 m and 145 m AMSL. It is a managed forest, divided into several stands with similar forest structure. Prevailing tree species are Norway spruce (*Picea abies*), Scots pine (*Pinus sylvestris*) and birch (*Betula spp.*). Forest height ranges from 5 m to 35 m, with biomass levels from 50 t/ha to 300 t/ha. For the test site a LIDAR data set is available for validation. 78 homogeneous stands have been delineated on the basis of LIDAR measured height H100 (see section 3.2.3). The mean area of a stand is on the order of 5.9 ha.

All in all three Pol-InSAR data sets at P-band were acquired with DLR's E-SAR system [139]. Data acquisitions were done on three different dates: 9th March, 2nd April and 2nd May 2007 [210]. From these three data acquisitions, two temporal baselines on the order of one month could be generated: 9th March – 2nd April (24 days) and 2nd April – 2nd May 2007 (30 days). Data enable forest height inversion for single acquisition day as well as the combination of two acquisition dates with the corresponding temporal baseline.

The images in Figure 34 provide a first impression of Remningstorp site. Figure 34 A shows the aerial photograph of the scene, Figure 34 B the corresponding Pauli amplitude image where the colors indicate different scattering mechanisms (red = double bounce scattering, green = volume scattering and blue = single bounce scattering; see section 4.2.2). It is striking that in the Pauli image the forested area is much more dominated by double bounce scattering than in the denser forest of the Traunstein site acquired at L-band(see Figure 16 C). Figure 34 C and D show the interferometric coherence over the

scene for the acquisitions taken on the 2nd May for a 15 m (κ_z ranges between 0.03 rad/m and 0.12 rad/m) and a 30 m (κ_z ranges between 0.08 rad/m and 0.21 rad/m) baseline where white indicates a coherence of 1 and black a coherence of 0. Coherence decreases over the forested parts with increasing baseline which is an indication that volume decorrelation is the dominant decorrelation process over the forested areas.

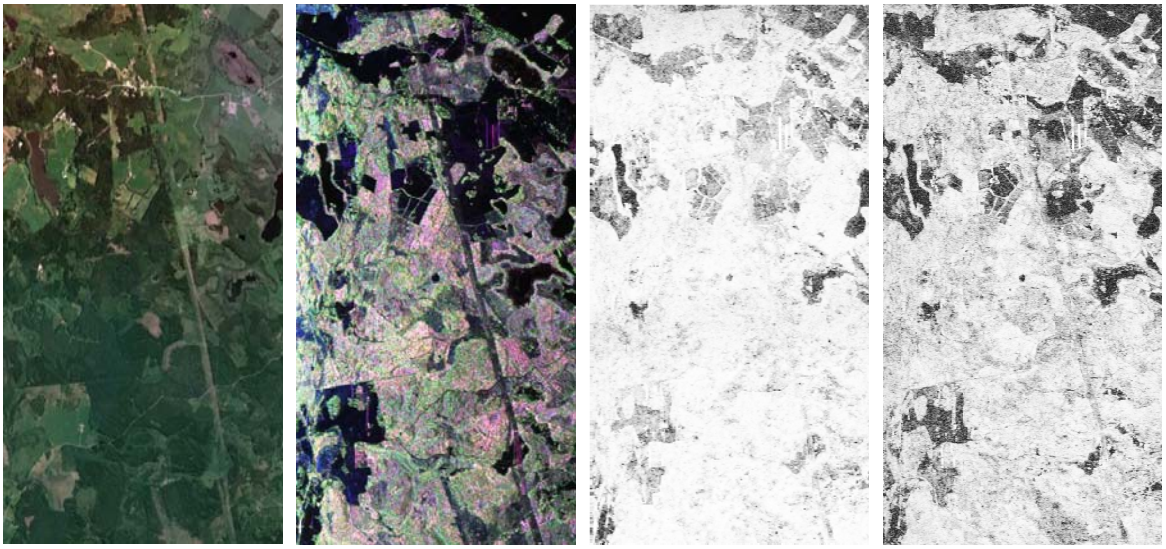

A **B** **C** **D**

Figure 34: Remningstorp site (Lat: 58,46°, Long: 13,63°) P-band airborne data 2nd May 2007; A: Aerial photograph; B:Pauli amplitude image, red: double bounce scattering; green: volume scattering (multi bounce) blue = single bounce scattering (surface); C: Interferometric coherence for a 15 m baseline scaled from 0 (black) to 1 (white); D: Interferometric coherence for a 30 m baseline scaled from 0 (black) to 1 (white)

Impact of the reflectivity funtion

A Forest height map as obtained applying Eq. (5.16) in combination with Eq. (5.17) is displayed in Figure 35 B and the corresponding validation plot in Figure 35 E. The LIDAR reference height H100 used for validation is displayed in Figure 35 A.

Forest height estimates in Remningstorp site are clearly underestimated and at the same time characterized by a significant larger variance. While the reason for the higher variance may be the reduced sensitivity of P-band to forest vegetation in this forest environment, the reason for the underestimation is expected to be in the mismatch between the inversion model (i.e. assumption on the vertical backscatter function) and the data. To evaluate better the second point, the inversion of the Remningstorp data set has been repeated under the assumption of an exponential volume profile allowing this time also height solutions corresponding to negative exponential profile functions i.e. inverse scattering distributions - as shown in the vertical reflectivity function $f_V(z)$ in Figure 22 C, the corresponding solution space is indicated by the blue dots in Figure 23 A - then the inversion is solved by Eq. (5.16) only. The obtained results improve. The corresponding forest height map is displayed Figure 35 C and the validation plot in Figure 35 F.

The impact of the vertical reflectivity function $f_V(z)$ on the underestimated forest heights is further investigated by introducing $m_{\min} > 0$. In this case, the inversion problem obtained for a single baseline is balanced but not unique solvable. A second baseline is required in order to establish uniqueness (see Eq. (5.31)). The forest height map obtained is shown in Figure 35 D, the corresponding validation plot in Figure 35 F. The obtained results

improve again – the RMSE reduces from 5.3m in Figure 35 F to 3.9 m in Figure 35 G but are still significantly higher than obtained for an L-band acquisition over the same test site with a RMSE of 1.6 m as shown in **Publication IV [218]**.

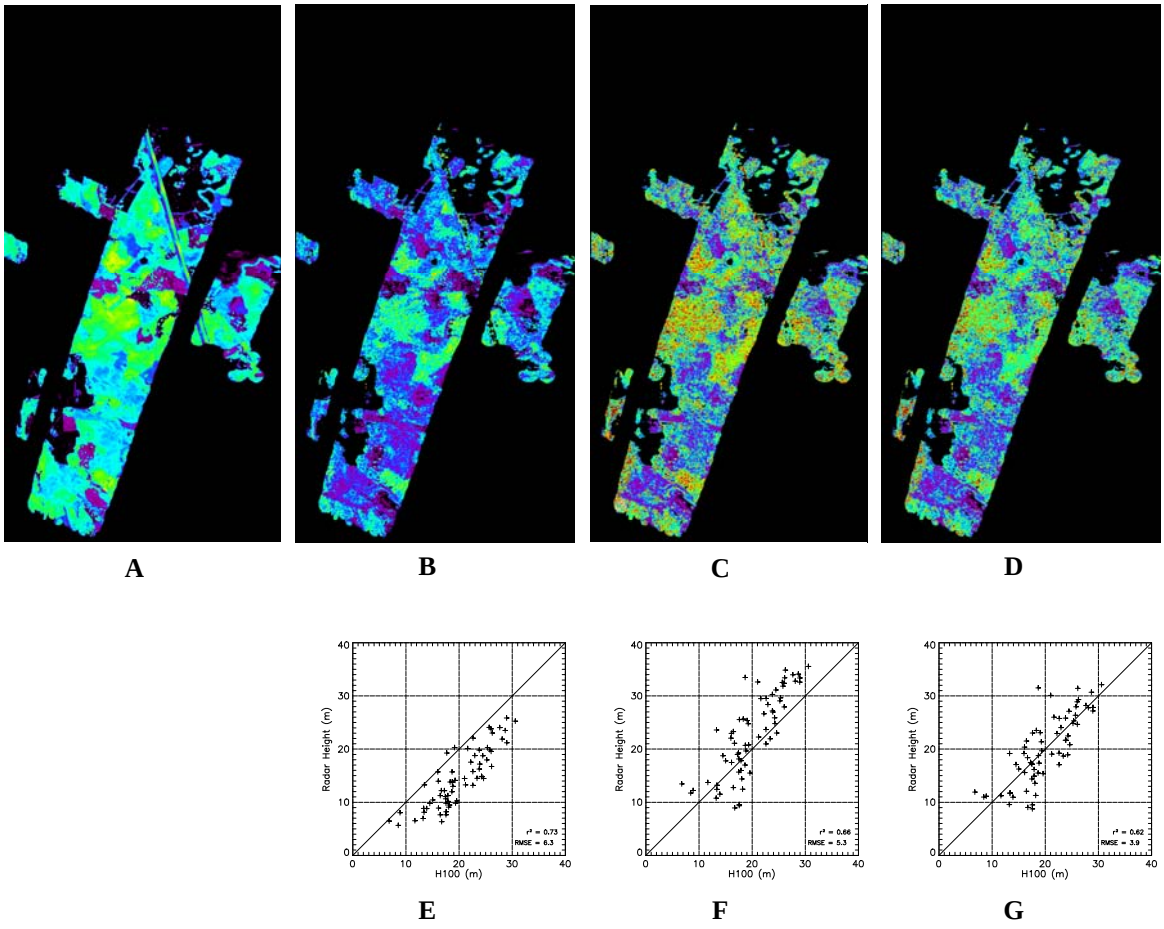

Figure 35: Remningstorp site forest height maps (A-D) with corresponding validation plots (E–G);
A: LIDAR H100 forest height map;

B: Pol-InSAR forest height map applying a positive exponential profile $m_{\min} = 0$ obtained from the 9th March acquisition – single baseline Eq. (5.16) in combination with Eq. (5.17);

C: Pol-InSAR forest height map applying a positive as well as a negative exponential profile and $m_{\min} = 0$ obtained from the 9th March acquisition – single baseline Eq. (5.16);

D: Pol-InSAR forest height map applying a positive as well as a negative exponential profile and $m_{\min} > 0$ obtained from the 9th March acquisition – dual baseline Eq. (5.31);

E: Validation plot LIDAR H100 vs. Pol-InSAR forest heights applying a positive exponential profile $m_{\min} = 0$ obtained from the 9th March acquisition – single baseline Eq. (5.16) in combination with Eq. (5.17) (forest height map B);

F: Validation plot LIDAR H100 vs. Pol-InSAR forest heights applying a positive as well as a negative exponential profile and $m_{\min} = 0$ obtained from the 9th March acquisition – single baseline Eq. (5.16) (forest height map C);

G: Validation plot LIDAR H100 vs. Pol-InSAR forest heights applying a positive as well as a negative exponential profile and $m_{\min} > 0$ obtained from the 9th March acquisition – dual baseline Eq. (5.31) (forest height map D);

Single-baseline inversion has been repeated for the Remningstorp data set assuming again $m_{\min} = 0$ and using instead of the exponential the linear volume profile allowing also negative profiles as displayed in the vertical reflectivity profiles in Figure 22 D (positive) and E (negative) using Eq. (5.16). The corresponding solution space is shown by the red (positive reflectivity profile) and blue (negative reflectivity profile) dots in Figure 23 B. The achieved forest height map is shown in Figure 36 A, the corresponding validation plot in Figure 36 E. The results indicate a better performance when compared to the corresponding results achieved by the exponential volume profile shown in Figure 35 C and F.

Finally, dual-baseline inversion has been performed for the Remningstorp data set using the linear volume profile, allowing inverse scattering distributions and assuming $m_{\min} > 0$ by means of the dual baseline inversion introduced in Eq. (5.31). The obtained forest height map is shown in Figure 36 B, the corresponding validation plot in Figure 36 F. The Results indicate a superior performance compared to all other previously investigated inversion scenarios.

Impact of temporal decorrelation

The impact of temporal decorrelation as the most prominent and at the same time most critical representative of non-volumetric decorrelation contributions has been investigated subsequently for the previously used test site Remningstorp at P-band. For the investigations a realistic temporal decorrelation scenario for a spaceborne sensor has been selected. The semi-boreal forest site of Remningstorp has been acquired three times within three months (March, April and May) in 2007 with a temporal baseline of about one month.

Figure 36 C shows the forest height map and Figure 36 G the corresponding validation plot for a forest height inversion based on the 9th March in combination with the 2nd April data with one month temporal baseline applying a positive as well as a negative linear profile and assuming $m_{\min} = 0$ using Eq. (5.16). Temporal decorrelation was not accounted for. Forest height is significantly overestimated (biased), $r^2 = 0.42$ and RMSE = 5.4 m.

In order to compensate for temporal decorrelation the dual baseline height inversion scenario of Eq. (5.33) was applied to the Remningstorp data. The two one month temporal baselines 9th March in combination with 2nd April and 2nd April in combination with 2nd May were used. Figure 36 D shows the obtained forest height map and Figure 36 H the corresponding validation plot for the dual baseline inversion scenario accounting for two different scalar temporal decorrelation coefficients for the volume part (γ_{TV1} and γ_{TV2}). The inversion performance is significantly improved ($r^2 = 0.46$ RMSE = 4.2 m) and the height bias is removed. Results showed that a compensation of two scalar temporal decorrelation factors (one for each baseline) is feasible.

Of course the suggested algorithm provides only a rough compensation of temporal decorrelation effects in the inversion. The assumption of a scalar temporal decorrelation coefficient does not account for changes of the phase (i.e. height of the scattering center or the form factor) between two acquisitions. Phase changes are usually induced by changes in the dielectric properties of the scatterer induced by rain, snow or significant changes of the temperature (for instance frozen vs. non frozen conditions **Publication V [198]**). Additionally, Remningstorp data were acquired during foliation period (March to May). Even though change effects of foliation in coniferous forests play only a minor role nonetheless during this period trees start to produce new twigs and needles. However, P-band seems to be anyway less sensitive to small forest compartments like twigs and needles.

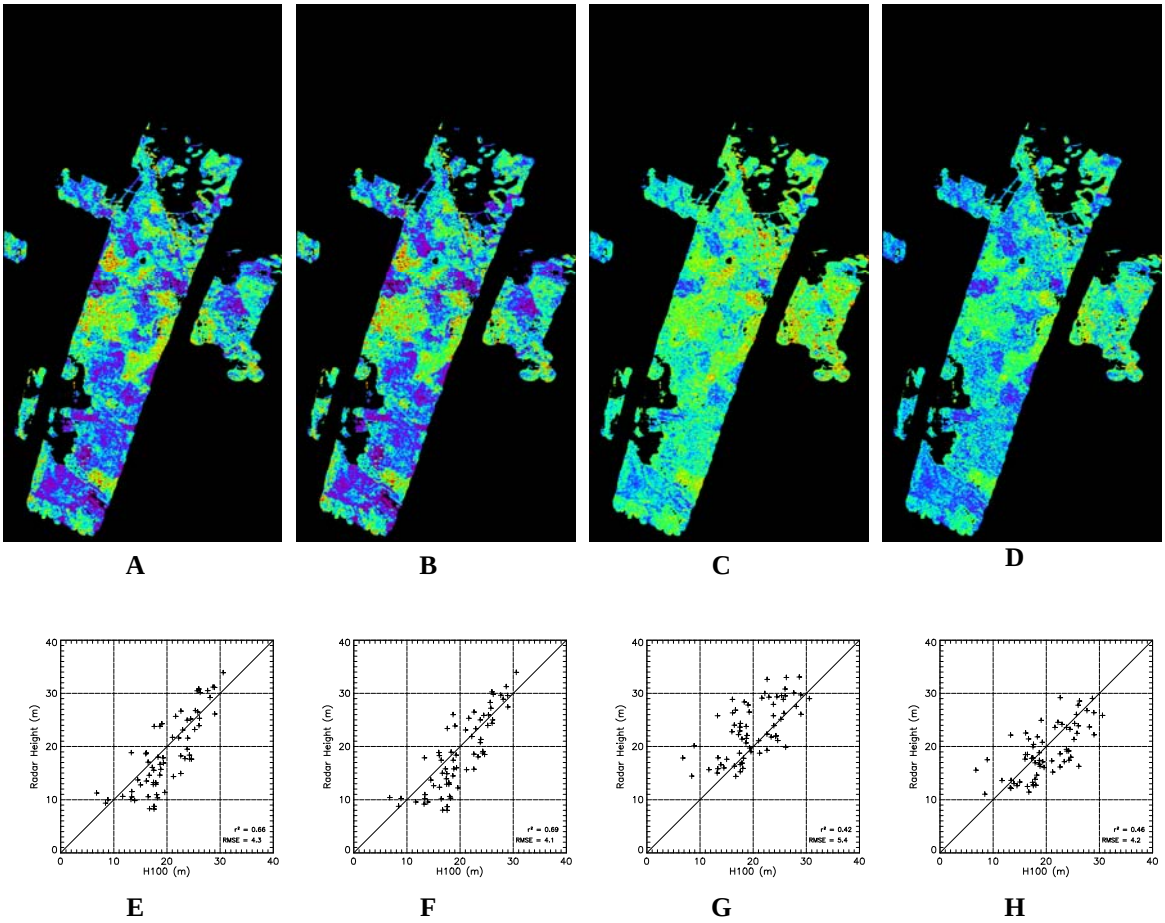

Figure 36: Remningstorp site forest height maps (A-D) with corresponding validation plots (E–H);

A: Pol-InSAR forest height map applying a positive as well as a negative linear profile and $m_{\min}=0$ obtained from the 9th March acquisition – single baseline Eq. (5.16);

B: Pol-InSAR forest height map applying an positive as well as a negative linear profile and $m_{\min}>0$ obtained from the 9th March acquisition – dual baseline Eq. (5.31);

C: Pol-InSAR forest height map applying a positive as well as a negative linear profile and $m_{\min}=0$ with one month temporal baseline obtained from the 9th March and the 2nd April acquisition – single baseline Eq. (5.16);

D: Pol-InSAR forest height map applying a positive as well as a negative linear profile $m_{\min}=0$ and accounting for γ_{TV1} and γ_{TV2} with one month temporal baseline obtained from the 9th March, the 2nd April and the 2nd May acquisition – dual baseline Eq. (5.33);

E: Validation plot LIDAR H100 vs. Pol-InSAR forest height map applying a positive as well as a negative linear profile and $m_{\min}=0$ obtained from the 9th March acquisition – single baseline Eq. (5.16) (forest height map A);

F: Validation plot LIDAR H100 vs. Pol-InSAR forest height map applying an positive as well as a negative linear profile and $m_{\min}>0$ obtained from the 9th March acquisition – dual baseline Eq. (5.31) (forest height map B);

G: Validation plot LIDAR H100 vs. Pol-InSAR forest height map applying a positive as well as a negative linear profile and $m_{\min}=0$ with one month temporal baseline obtained from the 9th March and the 2nd April acquisition – single baseline Eq. (5.16) (forest height map C);

H: Validation plot LIDAR H100 vs. Pol-InSAR forest height map applying a positive as well as a negative linear profile $m_{\min}=0$ and accounting for γ_{TV1} and γ_{TV2} with one month temporal baseline obtained from the 9th March, the 2nd April and the 2nd May acquisition – dual baseline Eq. (5.33) (forest height map D).

6 Relevant SAR satellite missions for Pol-InSAR forest monitoring

SAR is a remote sensing technology which is most advantageously operated from spaceborne platforms. The particular characteristics of SAR technology such as spatial resolution, spatial coverage or acquisition capacity can only prove effective (most economical) from space.

In order to apply Pol-InSAR techniques to spaceborne SAR sensor at least a dual pol mode is required [46] and then Pol-InSAR data are acquired in a repeat pass mode. It should be noted that in order to keep temporal decorrelation effects as small as possible, the repeat pass time should be kept shortest possible. Of course, in order to obtain best results, acquisitions in a quad pol mode are highly demanded.

However, when it comes to spaceborne repeat-pass implementations, the inherent presence of temporal decorrelation biases the interferometric coherence estimates, thus degrading the sensitivity to vertical scattering structure and limiting the performance of Pol-InSAR inversion techniques **Publication III [124], Publication IV [218]**, [267], [211], [204]. Short term decorrelation effects (for example, wind induced temporal decorrelation) may affect Pol-InSAR acquisitions even at short temporal baselines in the order of a few hours up to a few days **Publication III [124]**, **Publication IV [218]**. However, most spaceborne SAR systems are operated with a repeat pass time in the order of weeks to months. This is the main reason why polarimetric spaceborne missions such as the CSA's (Canadian Space Agency) RadarSAT-2 (Radarsatellite-2 operated at C-band) or JAXA's (Japan Aerospace Exploration Agency) ALOS-PALSAR (Advanced Land Observing Satellite – Phased Array type L-band Synthetic Aperture Radar) could not essentially contribute to a large scale demonstration of Pol-InSAR techniques nor to the development of new Pol-InSAR applications [204], **Publication IV [218]**.

Subsequently ALOS/ALOS-2 (see section 6.1) and TanDEM-X (see section 6.2) have been investigated in more detail for their suitability to apply Pol-InSAR techniques.

6.1 ALOS, ALOS-2

After the SIR-C/X-SAR (Shuttle Imaging Radar C- and X-Band Synthetic Aperture Radar) mission in 1994 [373] ALOS-PALSAR was the first mission providing again quad-pol SAR data at L-band and offering the opportunity to apply Pol-InSAR techniques. Unfortunately, ALOS quad-pol repeat pass data were only offered for experimental acquisitions and not as operational standard product.

6.1.1 System characteristics

The main technical characteristics of the ALOS-PALSAR instrument are summarized in Table 2 [302]. ALOS PALSAR has a repeat pass time of 46 days. Full chirp bandwidth (28 MHz) is only available for single-pol acquisitions. In case of dual- or quad-pol acquisitions bandwidth is reduced to 14 MHz. Single- and dual-pol acquisitions were acquired by default with 41.5° off-nadir angle while quad-pol acquisitions were acquired by default with 21.5° off-nadir angle. In the standard single-pol data acquisition mode (stripmap) the swath width is 70 km with a spatial resolution of 9 m x 10 m (range x azimuth) with one look in range and two looks azimuth. At quad-pol acquisitions swath width is reduced to

30 km with a spatial resolution of 30 m x 10 m (range x azimuth) with one look in range and two looks azimuth. In the ScanSAR mode swath width can be extended to 350 km in which an incidence angle range from 20.1° to 36.5° is covered, but then spatial resolution is reduced to 100 m in azimuth (two looks). ScanSAR acquisitions can only be performed in a single polarization (HH or VV). A detailed description of the ScanSAR mode can be found in [112].

Unfortunately, ALOS stopped working in April 2011. The follow-on mission ALOS-2 with the PALSAR-2 sensor was launched in May 2014.

Table 2: ALOS PALSAR System Characteristics according to [302]

Center frequency/ wavelength	**Repeat pass time**	**Acquisition modes**	**Spatial resolution (range - 1 look x azimuth - 2 looks)**	**Chirp band width**	**Coverage (Swath width)**	**Off nadir angle θ_0**
1270 MHz/ 23.6 cm (L-band)	46 days	Single Pol (HH or VV)	9 m x 10 m	28 MHz	70 km at 41.5° off-nadir angle	9.9° - 50.8°
		Dual Pol (HH + HV, VV + VH)	19 m x 10 m	14 MHz		
		Quad Pol (HH + HV + VV + VH)	30 m x 10 m		30 km at 21.5° off-nadir angle	
		ScanSAR (HH or VV)	17 m – 40 m x 100 m		350 km	20.1° - 36.5°

Table 3: ALOS-2 PALSAR-2 System Characteristics according to [341] and [261]

Center frequency/ wavelength	**Repeat pass time**	**Acquisition modes**	**Spatial resolution (range - 1 look x azimuth - 2 looks)**	**Chirp band width**	**Coverage (Swath width)**	**Off nadir angle θ_0**
1270 MHz/ 23.6 cm (L-band)	14 days	Single Pol (HH or VV)	3 m x 3 m	84 MHz	50 km at 41.5° off-nadir angle	30° - 40°
		Dual Pol (HH + HV, VV + VH)				
		Quad Pol (HH + HV + VV + VH)	6 m x 6 m	42 MHz	50 km at 21.5° off-nadir angle	
		ScanSAR (Single- Pol and Dual-Pol)	100/60 m x 100/60 m	14/28 MHz	350/490 km	30° - 40°

System characteristics of ALOS-2 are summarized in Table 3 [341], [261]. So far (August 2014), there is no data from PALSAR-2 available. Compared to the previous mission the repeat pass time with 14 days now is strongly reduced. Spatial resolution is improved. In the single- and dual-pol mode ALOS-2 takes advantage of the 84 MHz Chirp band width which results in a maximum spatial resolution of 3m x 3m in the quad-pol mode Chirp band width is reduced to 42 MHz which translates to a maximum spatial resolution of 6 m x 6 m. ScanSAR mode is similar to ALOS PALSAR.

6.1.2 Pros

Results in section 5.5 and 5.6 as well as results in literature (see section 3.3.3.2) indicate that L-band is a well-suited frequency for Pol-InSAR vegetation applications. Obtained results from L-band data convinced for boreal forests, for temperate forests as well as for various types of tropical forests [269], **Publication III [124], Publication IV [218] and Publication I [196]**.

ALOS as well as ALOS-2 quad-pol repeat pass acquisitions would enable an exemplary Pol-InSAR in orbit demonstration. Unfortunately, ALOS did not provide a systematic acquisition strategy neither in quad-pol mode nor for quad-pol repeat pass (Pol-InSAR) acquisitions [302]. ALOS-2 provides at least a systematic quad-pol acquisition strategy with nearly global coverage (all forested areas are covered) [341].

The availability of quad-pol data is a favourable condition for Pol-InSAR demonstration and Pol-InSAR vegetation applications.

6.1.3 Cons

The most restrictive condition of the ALOS system for Pol-InSAR vegetation applications is the long repeat pass time. Vegetation cover decorrelates during the 46 days repeat pass time almost completely.

A typical temporal decorrelation scenario of ALOS-PALSAR is now demonstrated by means of an ALOS Pol-InSAR acquisition over Oberpfaffenhofen test site (see Figure 37)

Oberpfaffenhofen site is located in the South-East of Germany around the center coordinates Lat: 48°04’ and Long: 11°19’. The climatic conditions favour temperate mixed mountainous forest stands, dominated by Norway spruce, beech and fir. It is a managed forest composed of even-aged stands (mainly older forest parts) and mixed uneven-aged stands (mainly younger forest parts), with forest heights from 10 m up to 40 m and higher. The mean biomass level is in the order of 210 t/ha.

Figure 37 A shows the amplitude image in HH polarization over Oberpfaffenhofen site and Figure 37 C the corresponding interferometric coherence after 46 days repeat pass time with a mean height of ambiguity of 57 m (κ_z ~0.11 rad/m) which is optimum for a wide range of forest heights (see Figure 27)

In order to characterize the scattering processes Freeman decomposition was applied according to [92], [386] (see Figure 37 B). Three different scattering types are identified: surface scattering (mainly agricultural areas), dihedral scattering (mainly urban areas) and volume scattering (mainly forest areas).

The measured interferometric coherences assigned to a certain scattering process are displayed in Figure 38 in form of histograms (blue: surface scattering, red: dihedral scattering and green: volume scattering). As a rule of thumb and in order to allocate a pixel

to a certain scattering mechanism, at least two third of the total backscattered power in all polarizations (*SPAN*) must correspond to that scattering mechanism.

Lowest coherences are measured for volume scatterers – $\gamma_{Obs} \cong 0.2$ which corresponds approximately to the coherence bias induced by the coherence estimation method for $\gamma \cong 0$ i.e. complete decorrelation (see Figure 19 C) – followed by surface scatterers and dihedral scatterers. In case of volume scatterer temporal decorrelation seems to be the dominant decorrelation source. Volume decorrelation plays only a minor role [352], [269], [41]. Indeed, for the given baseline a forest height of 50 m (which is by far too high for this test site) would explain a maximum volume decorrelation of only 0.4.

In the upcoming ALOS-2 mission repeat pass time is reduced to 14 days. Investigations of airborne L-band data with 15 days temporal baseline revealed that even for this scenario temporal decorrelation may be too high to be compensated or to obtain reliable Pol-InSAR inversion results (see **Publication IV [218],** [197]).

In section 5.2 (see also **Publication I [196])** the vertical wavenumber κ_z was identified as one of the most critical parameters for an accurate Pol-InSAR forest height estimation. In **Publication I [196]** it is stated that the baseline needs to be adapted to the prevailing forest conditions on the ground. But the baseline at spaceborne repeat pass scenarios (for instance for ALOS-PALSAR) is mainly set through arbitrary deviations of the platform within the orbital tube. Usually several acquisitions are required in order to get a usable interferometric pair of a scene. In the case of ALOS both too small ($\kappa_z > 0.15$) and too large baseline ($\kappa_z < 0.05$) are often obtained.

Two main conditions need to be fulfilled for a usable Pol-InSAR repeat pass data set: low temporal decorrelation and a flight constellation forming an appropriate baseline. The achievement of both conditions turns the acquisition of Pol-InSAR data with ALOS-PALSAR as well as with ALOS-2-PALSAR-2 into a challenge difficult to meet.

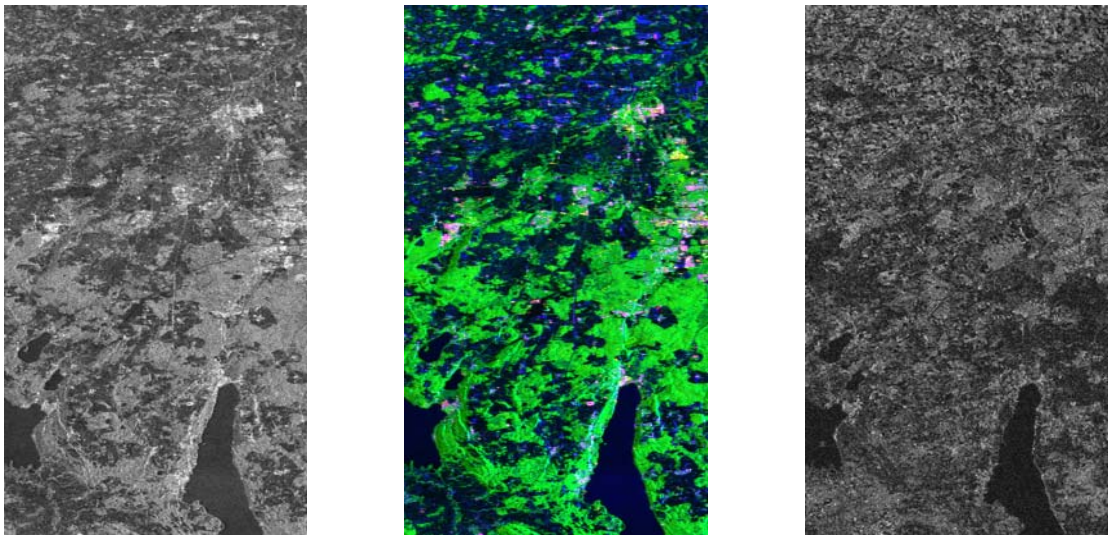

A **B** **C**

Figure 37: ALOS-PALSAR quad-pol acquisition Oberpfaffenhofen test site (Lat: 48°04', Long: 11°19'); A: amplitude image 2007-04-02 HH Polarization; B: RGB-coded Freeman decomposition image from 2007-04-02, blue: surface scattering; red: dihedral scattering; green: volume scattering; C: interferometric coherence HH Polarization between images 2007-02-15 and 2007-04-02 scaled from 0 (black) to 1 (white) for a height of ambiguity of 57 m (κ_z ~ 0.11 rad/m) and 49 looks.

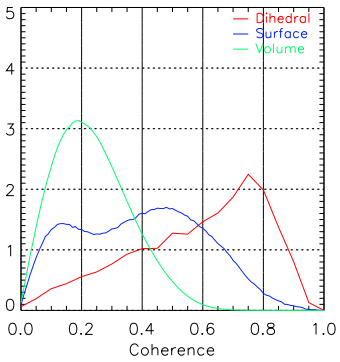

Figure 38: Histogram interferometric coherence between 2007-02-15 and 2007-04-02 for different scattering mechanisms: dihedral (red), surface (blue) and volume (green).

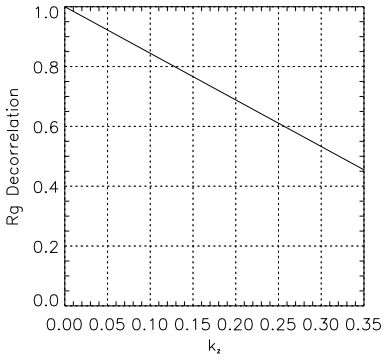

Figure 39: Range decorrelation γ_{Rg} (Eq. (4.52)) as a function of baseline (κ_z) for the ALOS-PALSAR sensor in quad-pol mode (f_0 =1.270GHz; W = 14 MHz)

Another cause reducing inversion performance is the limited bandwidth of ALOS-PALSAR in the quad-pol mode with only 14 MHz. Figure 39 shows γ_{Rg} (Eq. (4.52)) as a function of baseline (κ_z) for the ALOS-PALSAR sensor. γ_{Rg} is, with values between 0.92 for κ_z = 0.05 rad/m and 0.78 rad/m for κ_z = 0.15 rad/m i.e. the κ_z range of high performance, rather high. A compensation of γ_{Rg} through range spectral filtering would dramatically decrease the already sparse resolution. Of course a scalar compensation of γ_{Rg} would be possible too. But the high γ_{Rg} values introduce additional statistical deviations to the interferometric phase and coherence estimates decreasing Pol-InSAR inversion performance. The 46 MHz bandwidth of ALOS-2 is therefore more favourable for Pol-InSAR forest height inversion.

In the field of forest monitoring ALOS–PALSAR was mainly used for forest classification applications (see for instance [137]) or to obtain empirical backscatter to biomass relations (see for instance [247]).

6.2 TanDEM-X

The TanDEM-X (TDX, launched in June 2010) and TerraSAR-X (TSX, launched in June 2007) platforms, together form the first single-pass polarimetric interferometer in space

and allow, for the first time, the acquisition of single-, dual-, and quad-polarimetric Pol-InSAR data without the disturbing effect of temporal decorrelation.

The primary objective of the TanDEM-X mission is the generation of a world-wide, consistent, timely, and high-precision digital elevation model (DEM) [179], **Publication VI [185]** second objective is to carry out different scientific radar experiments that show the great potential of future formation-flying interferometric SAR missions to serve novel remote sensing applications **Publication VI [185]**. An overview of the TanDEM-X mission and its actual status and performance including results from scientific SAR experiments is given in **Publication VI [185]**. The TanDEM-X mission enables not only the acquisition of a global DEM with unprecedented accuracy, but also the demonstration of highly innovative bistatic and multistatic SAR techniques and applications including Pol-InSAR vegetation applications.

6.2.1 System Characteristics

The TanDEM-X mission scenario (see sketch in Figure 40) and orbit parameters are designed to fulfill the specifications of the DEM product. To accomplish this, Earth's total landmass is mapped at least twice, in two acquisition periods, with heights of ambiguity ranging from 35 m to 60 m [12]. Important system parameters of TanDEM-X are summarized in Table 4 (see also [343] and [179]). The rather high bandwidth with 150 MHz in the standard operation mode and even 300 MHz on request results a high spatial resolution.

Table 4: TanDEM-X System Characteristics according to [343] and [179]

Center frequency/ wavelength	**Repeat pass time**	**Acquisition modes**	**Spatial resolution (range - 1 look x azimuth - 2 looks)**	**Chirp band width**	**Coverage (Swath width)**	**Off nadir angle θ_0**
9.65 GHz/ 3.2 cm (X-band)	single pass system	Single Pol (HH, HV, VV, VH)	3.5 – 1.7 m x 3.3 m dependent on incidence angle	150 MHz (max. 300 MHz)	~30 km depends on off-nadir angle	20° - 45°
		Dual Pol (HH + VV, HH + HV, VV + VH)	3.5 – 1.7 m x 6.6 m dependent on incidence	150 MHz	15 km depends on off-nadir angle	
		Quad Pol (HH + HV + VV + VH) only for experimental acquisitions				
		ScanSAR (HH, HV, VV, VH)	3.5 – 1.7 m x 18.5 m dependent on incidence angle		100 km	

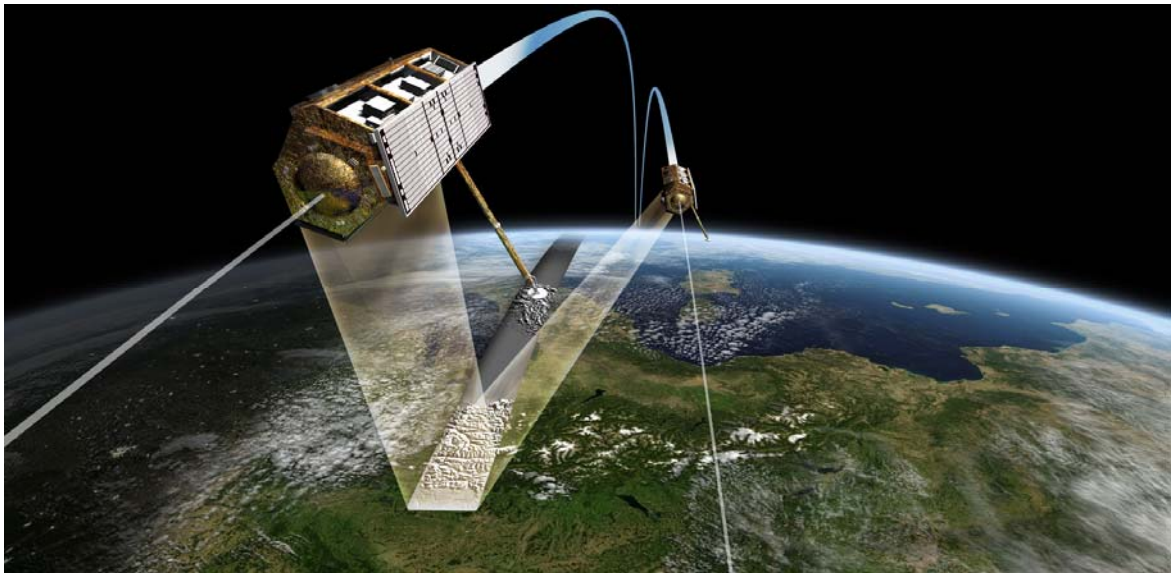

Figure 40: TanDEM-X satellite constellation provided by DLR. © [2007] DLR

But the mapping capacity of TanDEM-X is compared to ALOS/ALOS-2 (see Table 2 and Table 3) due to the smaller swath width (50 km for ALOS/ALOS-2 vs. 30 km for TanDEM-X single-pol acquisitions and 15 km for TanDEM-X dual-pol and quad-pol acquisitions) much lower.

6.2.2 Pros

Of course, greatest benefit of TanDEM-X for Pol-InSAR applications is the single pass bistatic mode. The absence of temporal decorrelation facilitates Pol-InSAR forest height inversion and is in the case of X-band a necessary precondition that enables Pol-InSAR applications.

Regarding the choice of polarization, the TDX and TSX instruments allow the acquisition of conventional co-/cross-polarized dual-pol data (i.e. HH and VH, or VV and HV) but also co-polarized dual-pol data (i.e. HH and VV) – a precondition for Pol-InSAR applications. The relatively small ground scattering contributions at X-band compared with the high additive noise level at the cross-polarized channels (with a noise equivalent sigma zero NESZ on the order of 20dB – 24dB – see [194]) make the co-polarized dual-pol mode better suited (in terms of performance) for Pol-InSAR applications [47], [194].

The availability of quad-pol acquisitions - acquired in a dedicated quad-pol operation phase - may improve Pol-InSAR inversion performance. However, constrains imposed by the penetration depth and the low NESZ will remain.

6.2.3 Cons

Unfortunately, the fact that vegetation extinction increases with frequency, reducing the penetration into (and through) vegetation layers, makes X-band a rather sub-optimal choice for forest structure mapping at least in a global sense **Publication V [198]**, [192].

However, a number of InSAR experiments have indicated that in several cases - primarily in boreal and less dense forest environments - a rather surprising penetration into forest and vegetation scatterers occurs [192], **Publication III [124]**, **Publication II [280]**, [97], [333].

This has been supported by interferometric and radargrammetric analyses of spaceborne repeat pass data from TSX and COSMO-SkyMed [277].

Feasibility and performance of forest Pol-InSAR applications at X-band critically depends on two effects:

1) The capability of X-band to penetrate into and through the forest: The penetration is required in order to “see” enough from the forest volume: The maximum vegetation height that can be resolved is given by the penetration depth. With further increasing height the interferometer does not "see" anymore the whole volume and the height estimation "saturates". The penetration capability depends in general on the density and dielectric properties of the forest or canopy layer. Both parameters vary spatially and in time for many forest types in a seasonal cycle.
2) The dependency of the interferometric coherence (in amplitude and phase) on the polarization(s) of the images used to form the interferogram. This again depends on the polarimetric properties of the individual scatterers and their distribution in height. A reduced polarization dependency indicates a limit in the information content of the Pol-InSAR observation space reducing the value of the polarimetric diversity in interferometric measurements and makes a successful Pol-InSAR inversion impossible.

The choice of the spatial baseline (expressed in terms of the vertical wavenumber) has a critical impact on the inversion performance **Publication I [196]**. Too small spatial baselines limit the sensitivity to forest height variation and / or increase the errors induced by uncompensated non-volumetric decorrelation contributions **Publication IV [218]**. Too large baselines lead to (too) low coherence levels and limit the range of heights that can be mapped. The fact that TDX follows pre-defined vertical wavenumber cycles that are optimized with respect to the DEM acquisition strategy, restricts the availability of optimum vertical wavenumber regimes for forest parameter estimation. However, the selection of a more appropriate beam (i.e. look angle) provides one degree of freedom to partially optimize the given spatial baseline configuration.

The main mission objective of the TanDEM-X mission is the acquisition of the global DEM [179], **Publication VI [185]**. Pol-InSAR acquisitions are only available as experimental requests and are competing with other experiments making a systematic Pol-InSAR acquisition of the earth with proper baselines impossible. Therefore, TanDEM-X can only be used for an exemplary demonstration of Pol-InSAR at X-band from a spaceborne sensor (see **Publication VI [185]**).

The rather high noise level especially at the HV channel causes a rather high noise decorrelation making HV polarization suboptimal for any Pol-InSAR applications. Therefore, Pol-InSAR applications are in the case of TanDEM-X limited to the HH and the VV channel [194].

6.2.4 Summary TanDEM-X

Nonetheless, TanDEM-X opened opportunities for several new innovative approaches of forest monitoring mainly using interferometric data [32], [333], [357], [7], for instance biomass classification as demonstrated in [32] for boreal forests. X-band has its strength mainly in less dense forest conditions as found in boreal forests.

Pol-InSAR forest height inversion could be successfully demonstrated with TanDEM-X data **Publication VI [185]**, [195], [196].

6.2.5 Temporal decorrelation at TanDEM-X monostatic acquisitions

From July until September 2010 both TanDEM-X and TerraSAR-X were operated in a monostatic mode separated by approximately 20 km in the along-track direction that translates in a temporal baseline of approximately three seconds. During the monostatic phase several acquisitions were taken over Mawas site.

The Mawas site is an Indonesian forest conservation area located on the island of Borneo in Central Kalimantan (Lat: -2°09', Long: 114°27'). It is covered with tropical peat swamp forest that is still marked by strong logging activities carried out in the early 1990's. Forest height reaches up to 30 m; the mean biomass is around 200 t/ha with maximum values up to 300 t/ha. The terrain topography is rather flat and varies slowly from 5 m to 50 m A.M.S.L.

Figure 41 C and Figure 41 D show the interferometric coherence of two TanDEM-X monostatic single-pass acquisitions (2010-09-06 and 2010-08-04) over the Mawas site in HH polarization. In Figure 41 A and C the corresponding amplitude images are displayed. The scene is nearly completely covered with forest. Both acquisitions had rather small interferometric baselines as indicated by their height of ambiguity.

The acquisition of 2010-09-06 has a height of ambiguity of 157 m (κ_z ~0.04 rad/m). Here, for the given baseline, a forest height of 50 m (which is by far too high for this test site) would explain a maximum volume decorrelation of only 0.9. The acquisition from 2010-08-04 has a height of ambiguity of 104 m (κ_z ~0.06 rad/m). Here, for the given baseline, a forest height of 50 m (which is by far too high for this test site) would explain a maximum volume decorrelation of only 0.8. But in both images appear over large areas lower coherences.

In the lower part of the coherence image of 2010-08-04 (Figure 41 D) patches of coherence around 0.2 are visible, while the coherence image from 2010-09-06 (Figure 41 B) is all over impaired by patches of low coherence. In fact, both images are affected by temporal decorrelation induced by a thunderstorm during the image acquisition.

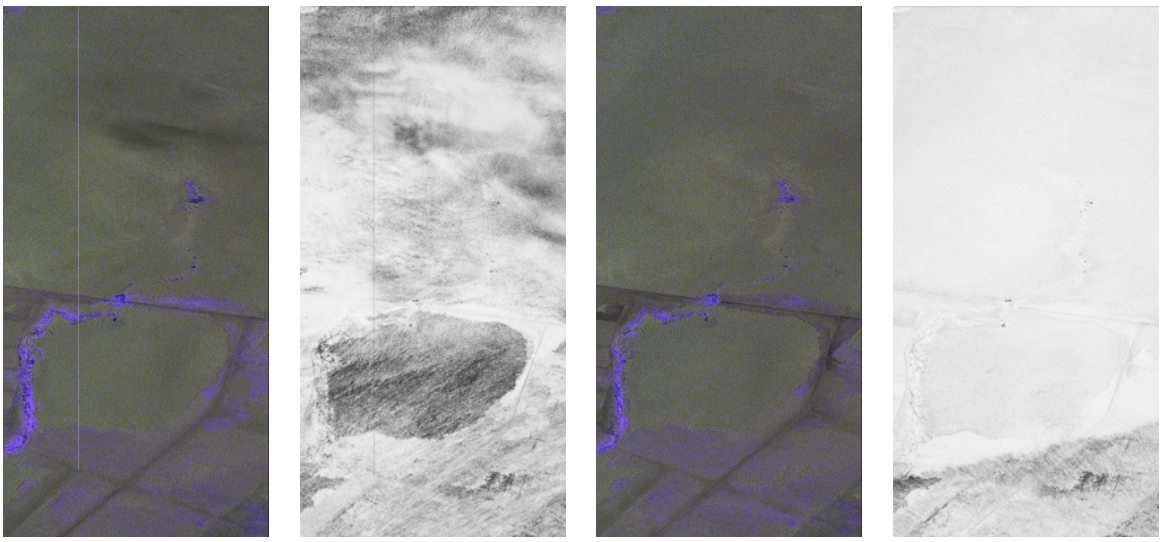

A **B** **C** **D**

Figure 41: Pursuit monostatic acquisitions Mawas test site (Lat: -2°09', Long: 114°27'); A: amplitude image in HH polarization, 2010-09-06 B: Interferometric coherence in HH polarization scaled from 0 (black) to 1 (white), 2010-09-06 (height of ambiguity = 104 m); C: amplitude image in HH polarization, 2010-08-04 D: interferometric coherence in HH polarization scaled from 0 (black) to 1 (white), 2010-08-04 (height of ambiguity = 157 m).

In the 2010-09-06 acquisition, the thunder- storm approaches from the lower part of the image, while the rest of the image is unaffected. Conversely, the 2010-08-04 acquisition is all over affected by a thunderstorm. In both acquisitions the loss of coherence due to temporal decorrelation is evident. The storm cell can be even detected in the amplitude image Figure 41 A as an area of low backscatter (nearly black) in the upper part of the image as in the cell of a thunderstorm backscattering is strongly attenuated.

In summary, even monostatic single-pass acquisitions with only a short term temporal baseline of ~ 3 sec. may be affected by severe temporal decorrelation under unfavorable acquisition conditions. This again underlines the benefits of bistatic acquisitions that usually are not affected by temporal decorrelation.

7 Conclusions, Outlook and Own Contributions

This chapter summarizes and discusses the main results of the thesis (see section 7.1) and provides an outlook to future directions of forest monitoring with Pol-InSAR. In this context two future SAR missions (BIOMASS and Tandem-L), which will rely on Pol-InSAR technology are reviewed (see section 7.2). Finally, a summary of the authors' original contributions in this thesis is given (see section 7.3).

7.1 Conclusions

Regular global forest monitoring is today highly demanded by several forest-related institutions (like FAO, forest authorities or governments) in order to protect endangered forests from illegal logging, to guarantee sustainable forest management and to monitor carbon fluxes (see chapter 1). In this context quantitative information on stock volume or biomass is usually considered the most important parameter. To evaluate the status of a global forest survey, the forest inventories systems of the countries with the largest proportion of forest were reviewed. In almost all countries quantitative information on forest status is nearly exclusively taken from ground measurements and is associated with a high measurement effort. Usually they are updated in a ten-year cycle, while most users require an update at least within five years or even faster. Some countries do not have at all quantitative information on their forest status.

Remote sensing (including SAR) is at present mostly used for land cover classification meaning, in terms of forests, mainly forest- non-forest-classification. Quantitative forest parameters from remote sensing sources on a global scale and on a regular or systematic way are currently not available.

Single channel SAR systems are not able to describe backscattering from such complex media such as forests in an unambiguous way. Multi parameter SAR systems capable of acquiring multi dimensional data, may essentially contribute to quantitative forest monitoring on a global scale. As demonstrated in this work, a single Pol-InSAR acquisition may allow to measure forest height.

Forest height is a useful parameter which contributes to derive other, more relevant forest parameters such as stock volume or biomass. But biomass is by far not the only parameter users may like to know. Nevertheless, forest height can be also used to detect changes induced by logging as well as to detect clearings and/or large area forest destruction by natural disasters (see section 1.2 and 5.5.3).

In this work Pol-InSAR forest height estimation has been demonstrated by means of different frequencies: X-band, L-band and P-band for the most important global forest types boreal, temperate and tropical.

A scheme for Pol-InSAR forest height inversion was published for the first time by Cloude & Papathanassiou in [41]. This approach was modified and extended to a more robust and efficient algorithm (see section 5.3.1), which is today the basis for Pol-InSAR forest height inversion.

A successful Pol-InSAR forest height inversion depends on several factors:

1.) The baseline expressed by the vertical wavenumber κ_z (see section 5.3.2 and **Publication I [196]**)

2.) The quantification and compensation of system induced decorrelation sources (see section 4.3.6 **Publication I [196]**)

3.) The presence of temporal decorrelation (see section 4.3.6.3, section 5.4 and **Publication III [124]** and **IV [218]**).

A critical factor for a successful Pol-InSAR inversion is the selection of a suitable baseline for the prevailing forest heights in a scene. The role of the baseline in Pol-InSAR forest height inversion is exhaustively investigated in **Publication I [196].** A single κ_z allows accurate inversion only for a limited range of forest heights. For taller forest stands the performance is limited by the higher variance induced by the low coherence level, or the sensitivity of the interferometric coherence to forest height tends to be saturated. For lower forest stands, the performance is limited primarily by the bias induced by the residual non-volumetric decorrelation contributions. In addition, slopes in range direction modulate the effective baseline and need to be included in the estimation of the vertical wavenumber κ_z (see **Publication I [196]** and section 5.3.2).

Before inversion non-volumetric decorrelation contributions need to be quantified and or compensated. In most cases the calibration of non-volumetric decorrelation contributions compensates the coherence bias but not the increased variance, in phase and coherence amplitude, caused by the lower coherence level. Therefore, a scalar compensation of non – volumetric decorrelation sources is limited to small amounts of decorrelation. High levels of non – volumetric decorrelation contributions are difficult to be estimated with sufficient accuracy and the associated compensation decrease in combination with the increased statistical variance Pol-InSAR height inversion performance (see section 4.3.6 **Publication I [196]**).

The most critical factor for a successful Pol-InSAR inversion is the presence of temporal decorrelation. Temporal decorrelation usually increases with time and results in a (severe) overestimation of forest height (**Publication IV [218]**). Of course, the best way to avoid temporal decorrelation is the employment of a single pass interferometer as demonstrated in **Publication V [198]** and **Publication VI [185]**. However, most of the data sets presented in the frame of this thesis were acquired with an airborne sensor with temporal baselines between 20 and 40 minutes leading to satisfactory results. Suitable short-term repeat pass acquisitions i.e. acquisitions with low or no temporal decorrelation are only feasible under good weather conditions such as no (or nearly no) wind and no precipitation on the ground between the acquisitions. In section 6.2.5 it was demonstrated that severe short-term temporal decorrelation may already appear, dependent on the weather conditions on the ground, after three seconds. In **Publication IV [218]** wind induced temporal decorrelation is extensively discussed. Short term temporal decorrelation induced by wind (or the weather conditions) has a rather stochastic character (see **Publication III [124]**), affects mainly the volume part of the scatterer and can be modeled by a a scalar temporal decorrelation contribution.

Long-term temporal decorrelation affects the volume part as well as the ground part of the backscattered signal (see section 4.3.6.3 and **Publication IV [218]**). This usually induces a change in the dielectric properties of the scatterers causing, a shift in the interferometric phase making interpretation and compensation (with a limited number of observations) a challenge.

Long wavelengths like at P-band seem to be less affected by temporal decorrelation compared to L-band or X-band. In section 5.6.2 a dual baseline approach for the compensation of temporal decorrelation effects in a P-band acquisition is suggested (results are shown in 5.6.3). The algorithm accounts only for a scalar decorrelation in the volume layer. Also, here the increased statistical variance of the coherence phase and amplitude is not compensated resulting in a poorer inversion performance. In case of a

repeat pass acquisition there is always the possibility (due to the random character of temporal decorrelation) that acquisitions become unusable making a systematic acquisition planning difficult.

A main task in this thesis was Pol-InSAR forest height inversion at different frequencies. The inversion process as developed for L-band [41] and modified according to **Publication I [196]** (see also section 5.3.1) could be easily transferred to P-band and X-band. At L- and P-band data were nearly exclusively acquired by DLR's E-SAR system [139]. At X-band, beside airborne data (DLR's E-SAR), mainly satellite data from the TanDEM-X sensor were used, (see **Publication V [198]** and **Publication VI [185]**).

In the available acquisitions L-band performed quite well for all forest types (from boreal to tropical see **Publication I [196]**, **Publication II [280]**, **Publication III [124]** and **Publication IV [218]** and section 5.5.3). L-band seems to be a universally applicable frequency.

P-band performed quite well over temperate and tropical forest systems (see **Publication I [196]**, **Publication III [124]** and section 5.6). In case of less dense forest conditions as found for boreal forests, P-band systematically underestimates forest height and results have a higher statistical variance (see results of Remningstorp site in [215] and section 5.6.3). For this scenario, the assumption of an exponential backscatter function and no ground contribution in at least one polarization is violated. In order to account for the different backscatter properties of boreal forests, the vertical backscatter function was modified to a triangular backscatter function (negative and positive, see section 5.1.2, and for the results 5.6.3). If a residual ground contribution is considered as well, a second baseline is required in order to invert forest height as suggested in section 5.6.1 (results are shown in section 5.6.3). The mentioned modifications correct the bias but do not completely correct the increased variance. Even after the corrections mentioned L-band gives significant better results than P-band (see **Publication IV [218]**). However, it should be taken into account when interpreting P-band results of Remningstorp site that data were acquired in the very beginning of the growing season and seasonal effects like freezing, non-freezing or incomplete foliation may have had an impact on the results.

Compared to L-band, P-band seems to be less affected by temporal decorrelation (see **Publication IV [218]**) and may allow a compensation of temporal decorrelation effects even after a larger temporal baselines by means of a dual baseline approach (see section 5.6.2 and for the obtained results 5.6.3). In this case, temporal decorrelation was modeled as a multiplicative scalar contribution on the estimated volume coherence, which is a very simple model that allows forest height inversion with only two baselines. Even so, the bias induced by temporal decorrelation in the inversion results could be removed but the increased statistical variance of the results not.

X-band is the shortest wavelength discussed in this work. Forest height inversion at X-band, in particular with TanDEM-X data is exhaustively discussed in **Publication V [198]**. Compared to P-band, X-band has rather the problem to penetrate deep enough into a forest.

In this work only single- and dual-pol data in HH and VV polarization at X-band have been used. Dual-pol data were sufficient to allow Pol-InSAR forest height inversion at X-band.

An important indicator at X-band, for the Pol-InSAR inversion feasibility is the polarimetric diversity associated with the penetration capability (see section 4.4.2). A high polarimetric diversity indicates the presence of polarizations with different ground contributions and promises good inversion performance. A low polarimetric diversity indicates no or only very small ground contributions making a forest height inversion problematic. Penetration at X-band was for all sites unexpectedly high. However, the

polarimetric diversity is for some tests sites, for instance for fully foliated temperate or tropical forests or after rain, too small.

The data allowed surprisingly good inversion results for boreal forests and for a winter acquisitions of temperate forests (see **Publication V [198]**). The forest height estimates obtained from dual-pol acquisitions over the tropical peat swamp forest site were less convincing.

The availability of quad-pol data may improve forest height inversion performance at X-band. An additional HV channel would probably increase the polarimetric diversity which improves the performance in terms of variance and reduces the number of samples with non-valid solutions.

The standard mode of TanDEM-X is a single-pol mode. Therefore a second forest height estimation approach was suggested for the single-pol case based on the availability of an external DTM (see section 5.3.1.3). This single-pol inversion revealed for all forest types a surprisingly high performance (see **Publication V [198]**).

Forests undergo a natural change over the course of the year. Deciduous forests, for instance, drop off and grow their leaves once per year. Additionally, precipitation events (snow, rain or flooding) and changes of temperature between freezing and non-freezing conditions change the dielectric properties of a forest and therefore also its backscattering behavior. Those natural changes could also be detected in the X-band Pol-InSAR data. Polarimetric diversity and penetration depth seem to be good indicators to detect seasonal variations at X-band (see **Publication V [198]** and section 4.4.2.). Dependent on forest type, an acquisition in another season may reveal better height inversion results. This allows to conclude that seasonal adapted acquisitions could improve the inversion performance and increase probably the number of forest types that can be investigated by means of Pol-InSAR techniques at X-band.

However, changes in the polarimetric diversity (i.e. in the penetration depth) may be used as well to monitor seasonal changes (see section 4.4.2.) or even disturbances. But, in order to detect forest disturbances, natural changes in backscattering need to be understood before.

Pol-InSAR applications at X-band are limited by dense forest conditions but the limits are not yet fully explored. Up to now there is no experience at forest height estimation with X-band quad-pol data and time series documenting seasonal changes over the course of the year are still missing for many forest types.

Forest changes may also occur due to human activities and environmental disturbances such as insect damages, storms or fires. An example for forest change detection by means of forest height estimates is given in section 5.5.3.

Due to the fact that Pol-InSAR forest height estimates at different frequencies always refer to the same reference height (i.e. forest top height H100), a long-lasting persistent forest monitoring may be established by the use of different sensors (X-, L- and P-band) depending on their individual availability and their suitability for Pol-InSAR applications.

In the light of the current practice in forest mensuration (see section 1.1.3), Pol-InSAR forest height estimates may easily compete with ground measurements. The compilation of large area wall-to-wall forest height maps is mostly preferable to highly accurate forest height estimates in a grid with usually more than 200 m grid spacing. To conclude, using an optimized configuration the accuracy of Pol-InSAR forest height estimates is hardly worse than the measurement accuracy of ground measurements.

7.2 Outlook

This thesis contributes in the interpretation and inversion of quantitative forest parameters from Pol-InSAR techniques. However, more important than forest height is for many users a measure of the stock volume (see section 1.2). In order to provide an estimate of stock volume or biomass, in addition to forest height a further parameter describing forest density is required [236] (see also section 2.4). Torano Caicoya et al. suggest in [31], [34] and [35] to use vertical forest structure attributes in combination with forest height for robust biomass estimation. Hence, the next step towards a quantitative forest stock volume or forest biomass estimation is the development of algorithms for the estimation of (relevant) vertical forest structure attributes.

So far, there is no satellite mission which allows a systematic observation of the forested areas of the earth with Pol-InSAR data. Although ALOS or ALOS-2 acquires quad-pol data at L-band, the temporal baseline is inadequate making temporal decorrelation too high for meaningful Pol-InSAR inversions (see section 6.1). TanDEM-X is capable of acquiring single-pass Pol-InSAR data at X-band and Pol-InSAR forest height inversion could be successfully demonstrated with TanDEM-X **Publication V [198]**. However, standard acquisition mode of TanDEM-X is a single-pol mode (see section 6.2) and at the same time X-band performance is limited in denser forest conditions.

At present, two spaceborne missions are under discussion, designed to acquire systematically Pol-InSAR data: BIOMASS and Tandem-L. Both missions are presented in the next two sections.

7.2.1 BIOMASS

The BIOMASS mission is part of ESA's Earth Explorer Program. Mission objectives are to quantify magnitude and spatial distribution of forest biomass globally in order to improve, carbon accounting and carbon modeling as well as to monitor and quantify changes in terrestrial biomass on an annual basis. BIOMASS is a P-band polarimetric SAR operated in an interferometric repeat pass mode [346].

7.2.1.1 System Characteristics

The exact mission design of BIOMASS is in many parts still under discussion. Important system parameters of BIOMASS are summarized in Table 5 (status June 2015). The objectives of the mission require to measure above ground forest biomass at a spatial scale of 4 ha [131] with an error not exceeding 20 percent and forest height with an error better than 30 percent [292]. Forest biomass maps should be provided on an annual basis. Biomass should be estimated either directly from intensity data [345] or from Pol-InSAR forest height estimates using allometric equations (see section 2.4, [236] [242] and [37]). Deforestation should be detected on a spatial scale of 50 m with a classification accuracy of 90 percent. Global coverage should be obtained after six months [131], [294].

The signal bandwidth is with 6 Mhz quite small but this is the maximum allowed at P-band.

Table 5: BIOMASS System Characteristics according to [131], [294] and [346] as actually planned

Center frequency/ wavelength	Repeat pass time	Acquisition modes	Spatial resolution (range x azimuth – 2 looks)	Chirp band width	Coverage (Swath width)	Off nadir angle θ_0
435 MHz/ 68.7 cm (P-band)	17 days/ 4 days	Quad Pol (HH + HV + VV + VH)	60 m x 50 m	6 MHz	80 km	23° - 35°

7.2.1.2 Pros

BIOMASS is the first remote sensing mission exclusively designed to measure forest biomass globally. Forest biomass or stock volume is the most relevant forest parameter for the majority of the user groups (see section 1.2). Therefore a remote sensing system providing biomass fills a gap in remote sensing and is highly appreciated.

Biomass estimates of the BIOMASS mission rely on two complementary measurement principles: biomass backscatter relationships and height to biomass allometry from Pol-InSAR height estimates. The combination of both, biomass estimates will probably compensate for uncertainties, estimation errors or weaknesses of both estimation approaches.

BIOMASS would be the first P-band sensor in space. The opportunity to view the whole planet at P-band may provide an essential scientific contribution in the understanding of P-band backscattering and may open the way to yet unidentified applications.

7.2.1.3 Cons

In terms of Pol-InSAR, the main disadvantage of the BIOMASS mission is probably the long repeat pass time. Although, in section 5.6.2 and section 5.6.3 an approach for the compensation of a scalar temporal decorrelation term has been introduced, compensation of temporal decorrelation remains due to its random behaviour a challenge **Publication III [124], Publication IV [218],** [55], [128]. At the same time the limited Bandwidth constrains the realisation of large spatial baselines required to compensate for temporal decorrelation.

The 6 MHz bandwidth limits also the spatial resolution and reduces Pol-InSAR height estimation accuracy, due to the limited number of possible looks and thereby associated increased variance of the coherence and phase estimates (see section 4.3.5). Coarse resolution may also compromise the requirement of spatial homogeneity for coherence estimation (see section 4.3.5)

Both biomass estimation algorithms suffer from several constrains. Backscatter to biomass relationships tend to saturate from biomass levels larger than 150 t/ha [345] and require extremely high radiometric accuracy. Pol-InSAR forest height estimates suffer from a reduced accuracy due to temporal decorrelation effects (see section 5.6.2 and section 5.6.3) and an allometric level as required for a precise height to biomass allometry (see section 2.4 and [236]) is for most forest types unknown.

Ionospheric effects (Faraday rotation and scintilation) cause distortions of the signal, need to be corrected before data inversion and may cause a further decrease in inversion performance [294], [168].

Finally, Terrestrial Space Objects Tracking Radars (SOTR) which are under US military authority, interfere with a P-band SAR (same frequency) and limit coverage of BIOMASS. North and Central America as well as Europe cannot be covered by the BIOMASS mission. Even if these regions are well covered by terrestrial forest inventories, a global biomass survey requires a consistent measurement method, i.e. biomass estimates should always be obtained by the same measurement method.

7.2.2 Tandem-L

Tandem-L is a DLR mission proposal for an L-band SAR that enables the systematic monitoring of the dynamic earth processes in the biosphere, hydrosphere cryosphere and geosphere. This includes measurements of forest biomass, forest height and vertical forest structure based on Pol-InSAR observations.

Tandem-L means two in a close formation flying satellites with a fully polarimetric SAR operated at L-band in a single pass mode. A sketch of the Tandem-L formation is given in Figure 42. The satellites are almost identical and are equipped with a reflector antenna.

7.2.2.1 System Characteristics

The satellite systems as planned up to now will operate in two acquisition modes. In the 3-D structure mode Pol-InSAR data are acquired to get structural parameters including forest height and vertical forest structure of volume scatterers like vegetation sand and ice [181], [193], [251] and [250]. In the deformation mode repeat pass interferometric data are acquired in a dual- or single-pol mode mainly for geophysical applications. From a Pol-InSAR perspective the 3-D structure mode is of primary interest.

Tandem-L should provide forest height maps and forest structure maps twice per year with a spatial resolution of 10 - 50 m. Height and vertical structure should then be used to derive biomass maps by means of allometric relationships, with a spatial resolution from 30 m to 50 m (see section 3.3.5, section 2.4, [31], [34] and [35]).

Tandem-L may provide global coverage over a period of 16 days in Pol-InSAR mode enabled by digital beamforming techniques. In a coarser resolution a global coverage may be provided within 4 days at a dual-pol mode. System characteristics of Tandem-L 3D-structure mode are summarized in Table 6.

Table 6: Tandem-L 3D-structure mode System Characteristics according to [183], [249] and [182] as actually planned (June 2015)

Center frequency/ wavelength	Repeat pass time	Acquisition mode	Spatial resolution (range x azimuth)	Chirp band width	Coverage (Swath width)	Off nadir angle θ_0
1300 MHz/ 23 cm (L-band)	Single pass	Quad Pol (HH + HV + VV + VH)	3 m x 1 m – 10 m	85 MHz	330 km – 680 km	23.3° - 40.5°

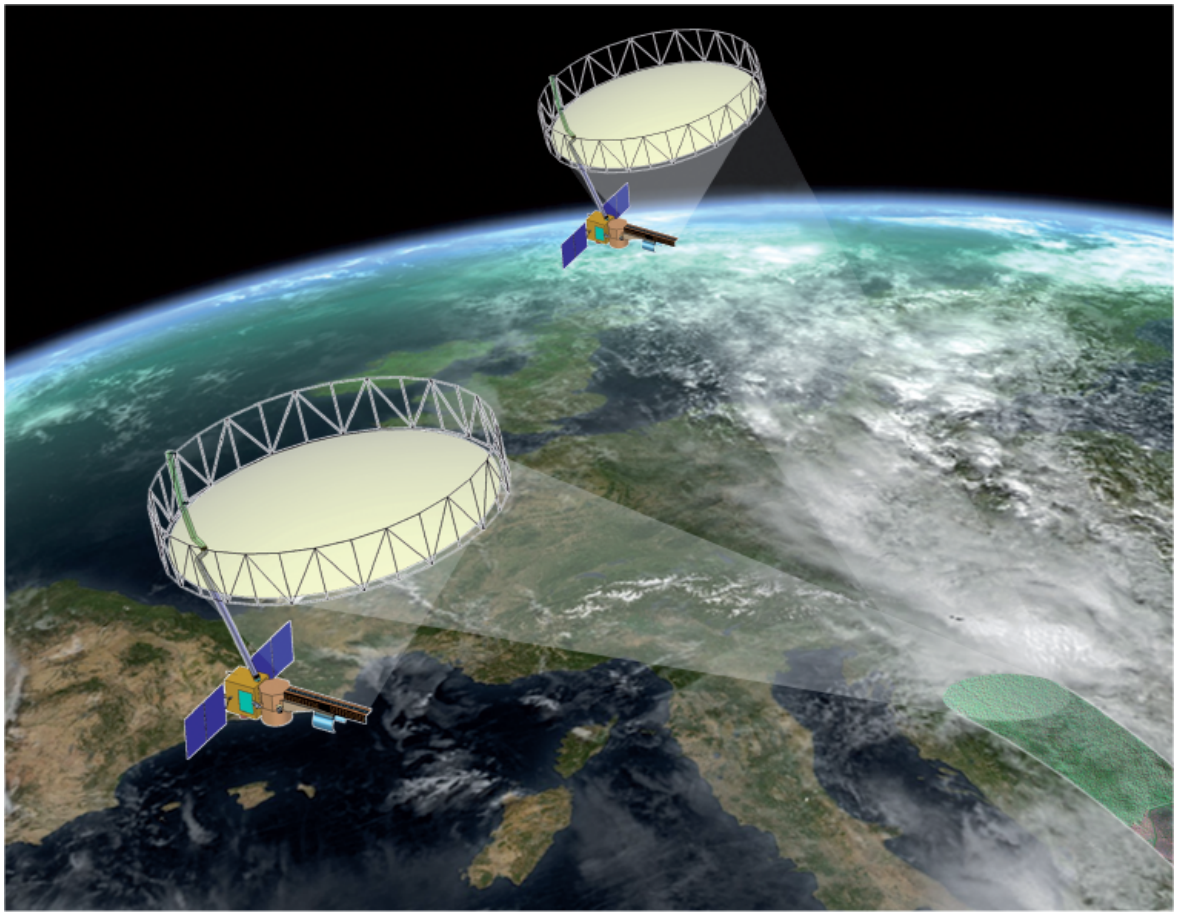

Figure 42: Tandem-L satellite constellation; image provided by DLR. © [2009] DLR

7.2.2.2 Pros

In terms of Pol-InSAR applications, the greatest benefit of Tandem-L is its design as a single pass system. The absence of temporal decorrelation is an important precondition for a systematic acquisition planning and facilitates the interpretation of the interferometric coherence.

A comparison of the results obtained for the different frequencies within the frame of this thesis revealed that L-band is most general (see **Publication V [198]**, **Publication III [124]**, **Publication II [280]**, **Publication I [196]** section 5.5 and section 5.6.3). A proper i.e. seasonal adapted acquisition planning would ensure no restrictions for L-band for all known forest types, from boreal forests to the tropical belt.

Tandem-L allows a large-scale demonstration of new SAR technologies like digital beamforming [180]. Digital beamforming is the key technology to provide wide swath coverage, a precondition for a global coverage with Pol-InSAR measurements within 16 days. A systematic acquisition of wide areas with single pass interferograms will open a new era in radar remote sensing and the way to new applications.

Goal of the mission is to provide level-2 products such as forest height maps, forest biomass maps and forest structure maps instead of SAR data products. By creating higher level data Tandem-L increases the number of users especially in the field of non-SAR specialists.

7.2.2.3 Cons

The large amount of data acquired in order to provide the data products mentioned above requires an on-board data compression before data downlink (as the data downlink capacity is limited). This data compression introduces an additional system decorrelation contribution to the measured interferometric coherence γ_{BAQ} [184], **Publication VI [185]**. γ_{BAQ} is difficult to estimate making a correction nearly impossible and may decrease Pol-InSAR forest height inversion performance.

In order to cover a wide range of forest heights with similar performance, several Pol-InSAR acquisitions with different baselines are necessary (see **Publication I [196]** and section 5.3.2). Similarly, the estimation of vertical structure attributes requires several different baselines [272], [273].

The flight constellation of the two satellites in form of a Helix (see [184] and **Publication VI [185]**) does not allow fast changes of the baseline making a fast coverage of the earth with Pol-InSAR forest height estimates, i.e. reliable forest height estimates over large areas, challenge. Additionally, the long time period required to change the baseline increases temporal decorrelation between the Pol-InSAR acquisitions required for the structure estimates.

The higher sensitivity of L-band to forest canopy elements – when compared to P-band- make L-band acquisitions more prone to seasonal and environmental effects (Leaves on – off, snow, rain).

7.3 Author's contributions

The primary objective of this thesis was Pol-InSAR forest height inversion at different frequencies i.e. at L-, P-, and X-band and it was intended to demonstrate potential and limitations of each frequency. Forest height inversion relies on the Random Volume over Ground model, its capability was demonstrated by several Pol-InSAR data sets at X-, L- and P-band and several interferometric data sets at X-band acquired from airborne (X-, L-, and P-band) and spaceborne (X-band) sensors. The novel contribution of this thesis in the context of SAR remote sensing and in particular of Pol-InSAR in the context of forest monitoring can be summarized into 10 points:

- The fundamentals of Pol-InSAR forest height inversion were described by Cloude and Papathanassiou in [41]. This approach has been revised and complemented in order to obtain a robust inversion algorithm (see section 5.3.1 and **Publication I [196]**) which includes the compensation of non-volumetric system induced decorrelation sources (see section 4.3.6 and **Publication I [196]**) and the integration of terrain slope in the inversion process (see section 5.3.2 and **Publication I [196]**).

- The vertical wavenumber κ_z has been identified as a critical parameter affecting Pol-InSAR forest height inversion performance. The role of κ_z in the forest height inversion process has been investigated by means of a Monte Carlo simulation. κ_z fields of high performance have been identified for all possible forest heights. At least two acquisitions with different baselines are required to cover the prevailing forest heights on the ground with similar performance (see section 5.3.2 and **Publication I [196]**).

- The behaviour of temporal decorrelation for different temporal baselines, under different weather conditions and at different frequencies has been investigated (see section 5.4, section 6.1.3 and section 6.2.5, **Publication III [124]**, **Publication IV [218]** and **Publication VI [185]**). The impact of temporal decorrelation on Pol-InSAR forest height inversion has been estimated quantitatively. Temporal decorrelation has been quantified and could be divided into a volume dependent part γ_{TV} and a ground dependent part γ_{TG} (see section 5.4 and **Publication IV [218]**).

- Pol-InSAR forest height inversion has been successfully demonstrated at L-band over boreal forests (see **Publication II [280]** and **Publication I [196]**), temperate forests (see section 5.5.3, **Publication III [124]** and **Publication IV [218]**) and tropical forests (see **Publication III [124]**) and at P-band over boreal (see section 5.6.3) and tropical forests (see **Publication I [196]** and **Publication III [124]**).

- At X-band a simplified inversion approach for single-pol data has been developed. For that either the extinction was assumed as constant i.e. fixed at a certain value (see Eq. 5.18 in section 5.3.1.3, **Publication II [280]** and **Publication V [198]**), or an external Digital Terrain Model (DTM) was used to get an estimate of the ground phase (see Eq. 5.19 in section 5.3.1.3 and **Publication V [198]**).

- Pol-InSAR forest height estimation has been demonstrated for the first time with X-band dual-pol data and with X-band single-pol data in combination with an external DTM from a spaceborne system (TanDEM-X) over a boreal, a temperate and a tropical forest test site (see **Publication V [198]**).

- Seasonal differences in the backscattering behaviour of the forest at Interferometric (InSAR) and Polarimetric Interferometric (Pol-InSAR) data at X-band has been described for the first time by means of TanDEM-X data. Differences are caused by the falling of the leafs and the foliation as well as by the frozen or non-frozen stage of tree compartments and were also found between wet and dry season in a tropical peat swamp forest. An indicator for seasonal differences could be the polarimetric difference and the penetration depth (see section 4.4.2 and **Publication V [198]**). The polarimetric difference at X-band was found a useful parameter for the characterization of volume scatterer with Pol-InSAR data (see section 4.4.2, **Publication V [198]** and **Publication VI [185]**).

- The use of Pol-InSAR forest heights for forest change detection could be demonstrated for the first time. Therefore, two L-band forest height maps over a temperate forest test site (Traunstein site) have been compared. Both acquisitions cover a five year period (see section 5.5.3).

- The analysis of P-band data over boreal forest revealed that here the model of an exponential vertical backscatter function reached its limits. In order to overcome these limits modifications of the vertical backscatter function have been proposed (see section 5.1.2) and a dual-baseline inversion approach has been introduced which resolves also a residual ground contribution in the backscattered signal (see

section 5.6.1). Dual baseline forest height estimation at P-band over a boreal test site has been demonstrated (see section 5.6.3).

- A dual-baseline approach for the compensation of a scalar temporal decorrelation contribution has been proposed (see section 5.6.2). Dual-baseline forest height estimation has been demonstrated by means of a P-band repeat pass data set with a one-month temporal baseline acquired over a boreal forest test site (Remningstorp site, see section 5.6.3).

Looking at the results obtained in this thesis, it can be concluded that Pol-InSAR forest height estimation seems to be a mature technology, which can be operationally used and may essentially contribute to a quantitative forest monitoring. The parameter forest height contributes in many ways to the information demands of different user groups. In order to evaluate the value of the parameter forest height, state of the art in forest inventories have been reviewed (see section 1.1) and user requirements from different user groups have been summarized (see section 1.2) including the relevance of the parameter forest height for forest monitoring (see section 2). An overview of other remote sensing systems and methodologies contributing to the topic forest monitoring, which may supplement or substitute forest height estimates have been summarized as well (see section 3).

Of course, an operational use of Pol-InSAR for forest height estimation requires a satellite-borne sensor providing Pol-InSAR data. Suitable satellite SAR systems, i.e. SAR systems providing Pol-InSAR data, which are currently in operation (ALOS/ALOS-2 and TanDEM-X), have been evaluated according to their suitability for Pol-InSAR forest height inversion (see section 6). Equally, two planned satellite missions which are developed to acquire Pol-InSAR data (BIOMASS and Tandem-L) are described and their benefits and drawbacks have been lined out (see section 7.2).

8 Reviewed papers and author's contribution

In this chapter all publications relevant for this thesis are listed in a logical order (not chronologically) and the contributions of the author to each publication are lined out.

8.1 Publication I

Title: **"Forest Height Estimation by means of Pol-InSAR Data Inversion: The Role of the Vertical Wavenumber"**

Authors: Florian Kugler (florian.kugler@dlr.de)[a]
Seung-Kuk Lee (seungkuk.lee@nasa.gov)[b]
Irena Hajnsek (hajnsek@ifu.baug.ethz.ch)[c]
Konstantinos P. Papathanassiou (kostas.papathanassiou@dlr.de)[a]

Affiliation: [a] Radar Concepts Department, Microwaves and Radar Institute, German Aerospace Center (DLR-HR), DLR-HR, Münchener Straße 20, 82234 Wessling, Germany

[b] Science and Exploration Directorate, Goddard Space Flight Center at NASA (NASA/GSFC), 8800 Greenbelt Road - Code 130 Greenbelt, MD 20771

[c] Institut für Umweltingenieurwissenschaften, ETH Zürich, Schafmattstr. 6, 8093 Zürich, Switzerland

Publication: IEEE Transactions on Geoscience and Remote Sensing, Volume 53, Issue: 10, Pages 5294 - 5311

DOI: 10.1109/TGRS.2015.2420996

Publication Year: 2015

Cited: 2 (5) times (August 2016)

Impact Factor: 3.47

Abstract:
This paper examines the multifaceted effect of the effective spatial baseline, as expressed through the vertical (interferometric) wavenumber, on the inversion of forest height from Polarimetric Interferometric SAR (Pol-InSAR) data. First the role of the vertical wavenumber in relating forest height to the interferometric (volume) coherence is introduced. Through the review of the forest height inversion from Pol-InSAR data the effect of the vertical wavenumber on the inversion performance is evaluated. The selection

of optimum - with respect to forest height inversion performance - vertical wavenumbers is discussed. The impact of the acquisition geometry and terrain slopes on the vertical wavenumber and their consideration in the inversion methodology is addressed. The individual effects discussed are demonstrated by means of airborne repeat pass Pol-InSAR acquisitions in L- and P-band acquired over different forest conditions including a boreal, a temperate and a tropical forest test site. The achieved forest height inversion performance is validated against reference height data derived from airborne LIDAR acquisitions.

Contribution:

This publication has been done mainly by the author. Most of the ideas presented in this article have been developed by the author. However, co-authors contributed with data processing issues and to the wording of some text parts. Most of the writing was done by the author. Seung-Kuk Lee processed and validated the L-band data of Krycklan site, did the comparison of the different DEM's for terrain correction, gave the idea for the validation of the DEM comparison and processed the P-band data of Sungai Wain site. The author prepared the LIDAR reference data for Sungai Wain scene and Kobernausser Wald scene, processed Kobernausser Wald scene and did the validation of both test sites. Kostas Papathanassiou gave the idea for the comparison of the different DEM's for terrain correction, did most of the writing for the theoretical background in section II, supervised data evaluation and writing of this paper and revised the paper. Irena Hajnsek organized and coordinated SAR data acquisitions and revised the paper. The ideas for the modifications in the inversion algorithm, for the analysis of the role of the vertical wavenumber in the inversion process and for the analysis of the impact of terrain slope on forest height inversion have been developed by the author. The original idea of the paper was proposed by the author.

8.2 Publication II

Title: **"Height Estimation of Boreal Forest: Interferometric Model-Based Inversion at L- and X-Band versus HUTSCAT Profiling Scatterometer"**

Authors: Jaan Praks (jaan.praks@aalto.fi)[c]
Florian Kugler (florian.kugler@dlr.de)[a]
Konstantinos P. Papathanassiou (kostas.papathanassiou@dlr.de)[a]
Irena Hajnsek (irena.hajnsek@dlr.de)[b]
Martti T. Hallikainen (martti.hallikainen@aalto.fi)[c]

Affiliation: [a]Radar Concepts Department, Microwaves and Radar Institute, German Aerospace Center (DLR-HR), DLR-HR, Münchener Straße 20, 82234 Wessling, Germany

[b]Institut für Umweltingenieurwissenschaften, ETH Zürich, Schafmattstr. 6, 8093 Zürich, Switzerland

[c]Department of Radio Science and Engineering, Aalto University, Finland, Otakaari 5A, Espoo, FI-00076 AALTO, Finland

Publication: IEEE Geoscience and Remote Sensing Letters, Volume: 4, Issue: 3, Pages: 466 - 470

DOI: 10.1109/LGRS.2007.898083

Publication Year: 2007

Cited: 21 (39) times (August 2016)

Impact Factor: 1.82

Abstract:
In this letter, we present results from the FinSAR project, where the E-SAR and Helsinki University of Technology Scatterometer (HUTSCAT) instruments were operated together in order to validate tree-height retrieval algorithms for boreal forest. The campaign was carried out in Finland in fall 2003. The main instruments of the campaign were the E-SAR airborne radar (operating at L- and X-band) and the HUTSCAT helicopter-borne profiling scatterometer (operating at X- and C-band).We compare and discuss forest height obtained from the inversion quad-pol polarimetric interferometric synthetic aperture radar (SAR) datasets at L-band and forest height obtained from the inversion of single-pol X-band in SAR data with forest height estimates from HUTSCAT scatterometer data. Our results show that the forest height values, which are estimated by means of two different radar instruments, are in good agreement. The correlation between HUTSCAT and E-SAR

height estimates (R^2 = 0.77 at L-band and R^2 = 0.75 at X-band) underlines the good agreement between the results obtained by the two approaches.

Contribution:

This work was done by the author in collaboration with Jaan Praks. The author provided Pol-InSAR forest height inversion at L- and X-band and developed the corresponding inversion algorithms. Jaan Praks analyzed ground measurements and HUTSCAT measurements, extracted tree height estimates from HUTSCAT measurements and made the comparison between HUTSCAT and Pol-InSAR forest height estimates. Kostas Papathanassiou gave the idea for the L- and X-band inversion algorithms and revised the paper. Irena Hajnsek organized and coordinated SAR data acquisitions and revised the paper. Martti Hallikainen developed the HUTSCAT sensor and revised the paper. The original idea of the paper was proposed by Jaan Praks.

8.3 Publication III

Title: **"Tropical-Forest-Parameter Estimation by Means of Pol-InSAR: The INDREX II Campaign"**

Authors: Irena Hajnsek (irena.hajnsek@dlr.de)[b]
Florian Kugler (florian.kugler@dlr.de)[a]
Seung-Kuk Lee (seungkuk.lee@nasa.gov)[c]
Konstantinos P. Papathanassiou (kostas.papathanassiou@dlr.de)[a]

Affiliation: [a]Radar Concepts Department, Microwaves and Radar Institute, German Aerospace Center (DLR-HR), DLR-HR, Münchener Straße 20, 82234 Wessling, Germany

[b]Science and Exploration Directorate, Goddard Space Flight Center at NASA (NASA/GSFC), 8800 Greenbelt Road - Code 130 Greenbelt, MD 20771

[c]Institut für Umweltingenieurwissenschaften, ETH Zürich, Schafmattstr. 6, 8093 Zürich, Switzerland

Publication: IEEE Transactions on Geoscience and Remote Sensing, Volume: 47, Issue: 2, Pages: 481 - 493

DOI: 10.1109/TGRS.2008.2009437

Publication Year: 2009

Cited: 64 (109) times (June 2015)

Impact Factor: 3.47

Abstract:
This paper addresses the potential and limitations of polarimetric synthetic aperture radar (SAR) interferometry (Pol-InSAR) inversion techniques for quantitative forest-parameter estimation in tropical forests by making use of the unique data set acquired in the frame of the second Indonesian Airborne Radar Experiment (INDREX-II) campaign – including Pol-InSAR, light detection and ranging (LIDAR), and ground measurements – over typical Southeast Asia forest formations. The performance of Pol-InSAR inversion is not only assessed primarily at L- and P-band but also at higher frequencies, namely, X-band. Critical performance parameters such as the "visibility of the ground" at L- and P-band as well as temporal decorrelation in short–time repeat-pass interferometry are discussed and quantitatively assessed. Inversion performance is validated against LIDAR and ground measurements over different test sites.

Contribution:

The work was done by the author in cooperation with Seung-Kuk Lee and Kostas Papathanassiou. This work was part of the INDREX II campaign with the aim to apply Pol-InSAR forest height inversion to tropical forest data at L- and P-band. Irena Hajnsek organized the INDREX II campaign, coordinated SAR data acquisitions and ground measurements and thus laid the foundation for this article as well as revised it. Pol-InSAR forest height inversion was first proposed by Papathanassiou and Cloude in [269] and [41]. The author organized and participated in the ground measurement campaign, analyzed the ground data, organized and analyzed the LIDAR reference data, developed the forest height inversion procedure, estimated forest heights at different frequencies (L-band, P-band and X-band), developed the validation concept, validated Pol-InSAR forest height estimates with LIDAR reference measurements, estimated temporal decorrelation and gave the idea to use the length of the coherence region as an indicator for the visibility of the ground. Seung-Kuk Lee estimated the polarimetric alfa angle and the length of the coherence region and made their comparison with terrain slope. Kostas Papathanassiou gave the idea for forest height estimation at L-, P- and X-band and for the estimation of temporal decorrelation, did large parts of the writing, supervised data evaluation and the writing of this paper and revised it.

8.4 Publication IV

Title: **"Quantification of Temporal Decorrelation Effects at L-Band for Polarimetric SAR Interferometry Applications"**

Authors: Seung-Kuk Lee (seungkuk.lee@nasa.gov)[c]
Florian Kugler (florian.kugler@dlr.de)[a]
Konstantinos P. Papathanassiou (kostas.papathanassiou@dlr.de)[a]
Irena Hajnsek (irena.hajnsek@dlr.de)[b]

Affiliation: [a]Radar Concepts Department, Microwaves and Radar Institute, German Aerospace Center (DLR-HR), DLR-HR, Münchener Straße 20, 82234 Wessling, Germany

[b]Science and Exploration Directorate, Goddard Space Flight Center at NASA (NASA/GSFC), 8800 Greenbelt Road - Code 130 Greenbelt, MD 20771

[c]Institut für Umweltingenieurwissenschaften, ETH Zürich, Schafmattstr. 6, 8093 Zürich, Switzerland

Publication: IEEE Journal of Selected Topics in Applied Earth Observation and Remote Sensing, Volume: 6, Issue: 3, Pages: 1351 - 1367

DOI: 10.1109/JSTARS.2013.2253448

Publication Year: 2013

Cited: 15 (21) times (August 2016)

Impact Factor: 2.87

Abstract:
Temporal decorrelation is the most critical issue for the successful inversion of polarimetric SAR interferometry (Pol-InSAR) data acquired in an interferometric repeat-pass mode, typical for satellite or lower frequency airborne SAR systems. This paper provides a quantitative estimation of temporal decorrelation effects at L-band for a wide range of temporal baselines based on a unique set of multibaseline Pol-InSAR data. A new methodology that allows to quantify individual temporal decorrelation components has been developed and applied. Temporal decorrelation coefficients are estimated for temporal baselines ranging from 10 min to 54 days and converted to height inversion errors caused by them. The temporal decorrelations of γ_{TV} (volume temporal decorrelation) and γ_{TG} (ground temporal decorrelation) depend not only on the wind-induced movement but also strongly on the rain-induced dielectric changes in volume and on the ground at temporal baseline on the order of day or longer. At temporal baselines on the order of

minutes, the wind speed is a critical parameter and the speed of 2 m/s already hampers the application of Pol-InSAR forest parameter inversion. The approach is supported and validated by using L-band E-SAR repeat-pass data acquired in the frame of three dedicated campaigns, BioSAR 2007, TempoSAR 2008, and TempoSAR 2009.

Contribution:

The main work for this article was done by the first author, Seung-Kuk Lee. He was also the one who has developed the main ideas. The author of this thesis contributed to the used Pol-InSAR forest height estimation algorithm, contributed ideas for the development of an algorithm for the estimation of different temporal decorrelation contributions, discussed obtained results with the first author, Seung-Kuk Lee and revised the paper. Kostas Papathanassiou had the idea for the estimation of different temporal decorrelation contribution, supervised data evaluation and writing of this paper and revised it. Irena Hajnsek organized and coordinated SAR data acquisitions and revised the paper. The original idea of the paper was proposed by Seung-Kuk Lee.

8.5 Publication V

Title: **"TanDEM-X Pol-InSAR Performance for Forest Height Estimation"**

Authors: Florian Kugler (florian.kugler@dlr.de)[a]
Daniel Schulze (daniel.schulze@dlr.de)[a]
Irena Hajnsek (irena.hajnsek@dlr.de)[b]
Hans Pretzsch (hans.pretzsch@lrz.tum.de)[c]
Konstantinos P. Papathanassiou (kostas.papathanassiou@dlr.de)[a]

Affiliation: [a]Radar Concepts Department, Microwaves and Radar Institute, German Aerospace Center (DLR-HR), DLR-HR, Münchener Straße 20, 82234 Wessling, Germany

[b]Institut für Umweltingenieurwissenschaften, ETH Zürich, Schafmattstr. 6, 8093 Zürich, Switzerland

[c]Chair for Forest Growth and Yield Science, Department for Ecosystem and Landscape Management, Center of Life and Food Sciences, Technische Universität München, 85354 Freising, Germany

Publication: IEEE Transactions on Geoscience and Remote Sensing, Volume: 52, Issue: 10, Pages: 6404 - 6422

Publication Year: 2014

DOI: 10.1109/TGRS.2013.2296533

Cited: 20 (32) times (August 2016)

Impact Factor: 3.47

Abstract:
TanDEM-X and TerraSAR-X platforms form together the first spaceborne single-pass polarimetric interferometer in space. This allows, for the first time, the acquisition of spaceborne polarimetric synthetic aperture radar interferometry (Pol-InSAR) data without the disturbing effect of temporal decorrelation. This paper aims to assess the potential of such data for forest applications. For this, single- and dual-pol data acquired over a boreal, a temperate, and a tropical site were investigated to characterize X-band penetration and polarization diversity of the interferometric coherence measurements. Pol-InSAR forest height inversion schemes have been proposed and implemented for the single- and dual-pol cases and cross validated against LIDAR reference measurements for all sites. The single-pol inversion relies on an external ground digital terrain model (DTM) and performed well

for all sites with correlation coefficients r^2 between 0.80 and 0.98. The dual-pol inversion does not require an external DTM but depends on the visibility of the whole forest layer. Accordingly, its performance varied with forest structure and season: The best performance was achieved for the summer acquisition of the boreal test site ($r^2 = 0.86$) and for the winter acquisition of the temperate test site ($r^2 = 0.77$). For the tropical test site, only a weak correlation ($r^2 = \sim 0.50$) could be established.

Contribution:

The ideas presented in this article were developed by the author. Calculations, data processing and writing were done nearly exclusively by the author. However, co-authors contributed to the paper with their calculations and with the wording of some text parts. Daniel Schulze provided the graphs for the development of the vertical wavenumber during the TanDEM-X mission as a function of time and as a function of argument of latitude. Kostas Papathanassiou did large parts of the writing for the theoretical background, supervised data evaluation and the writing of this paper and revised it. Irena Hajnsek organized the TanDEM-X SAR data acquisitions and revised the paper. Hans Pretzsch supervised the writing, provided ground truth data and revised the article. The original idea of the paper was proposed by the author.

8.6 Publication VI

Title: **"TanDEM-X: A radar interferometer with two formation-flying satellites"**

Authors: Gerhard Krieger (gerhard.krieger@dlr.de)[a]
Manfred Zink (manfred.zink@dlr.de)[a]
Markus Bachmann (markus.bachmann@dlr.de)[a]
Benjamin Bräutigam (benjamin.bräutigam@dlr.de)[a]
Daniel Schulze (daniel.schulze@dlr.de)[a]
Michele Martone (michele.matone@dlr.de)[a]
Paola Rizzoli (paola.rizzoli@dlr.de)[a]
Ulrich Steinbrecher (ulrich.steinbrecher@dlr.de)[a]
John Walter Antony (john.walterantony@dlr.de)[a]
Francesco De Zan, (Francesco.dezan@dlr.de)[a]
Irena Hajnsek (irena.hajnsek@dlr.de)[b]
Konstantinos P. Papathanassiou (kostas.papathanassiou@dlr.de)[a]
Florian Kugler (florian.kugler@dlr.de)[a]
Marc Rodriguez Cassola (marc.rodriguez@dlr.de)[a]
Marwan Younis (Marwan.younis@dlr.de)[a]
Stefan Baumgartner (stefan.baumgartner@dlr.de)[a]
Paco López-Dekker (Francisco.lopezdekker@dlr.de)[a]
Pau Prats (pau.prats@dlr.de)[a]
Alberto Moreira (alberto.moreira@dlr.de)[a]

Affiliation: [a]Radar Concepts Department, Microwaves and Radar Institute, German Aerospace Center (DLR-HR), DLR-HR, Münchener Straße 20, 82234 Wessling, Germany

[b]Institut für Umweltingenieurwissenschaften, ETH Zürich, Schafmattstr. 6, 8093 Zürich, Switzerland

Publication: Acta Astronautica Volume: 89, August- September, Pages: 83 - 98

Publication Year: 2013

DOI: 10.1016/j.actaastro.2013.03.008

Cited: 28 times (August 2016)

Impact Factor: 0.70

Abstract:
TanDEM-X (*T*erraSAR-X *a*dd-o*n* for *D*igital *E*levation *M*easurements) is an innovative formation-flying radar mission that opens a new era in spaceborne radar remote sensing. The primary objective is the acquisition of a global digital elevation model (DEM) with

unprecedented accuracy (12 m horizontal resolution and 2 m relative height accuracy). This goal is achieved by extending the TerraSAR-X synthetic aperture radar (SAR) mission by a second, TerraSAR-X like satellite (TDX) flying in close formation with TerraSAR-X (TSX). Both satellites form together a large single-pass SAR interferometer with the opportunity for flexible baseline selection. This enables the acquisition of highly accurate across-track interferograms without the inherent accuracy limitations imposed by repeat-pass interferometry due to temporal decorrelation and atmospheric disturbances. Besides the primary goal of the mission, several secondary mission objectives based on along-track interferometry as well as new bistatic and multistatic SAR techniques have been defined, representing an important and innovative asset of the TanDEM-X mission. TanDEM-X is implemented in the framework of a public–private partnership between the German Aerospace Center (DLR) and EADS Astrium GmbH. The TanDEM-X satellite was successfully launched in June 2010 and the mission started its operational data acquisition in December 2010. This paper provides an overview of the TanDEM-X mission and summarizes its actual status and performance. Furthermore, results from several scientific radar experiments are presented that show the great potential of future formation-flying interferometric SAR missions to serve novel remote sensing applications.

Contribution:

This article was mainly written by Gerhard Krieger. It gives an overview of the TanDEM-X mission and summarizes the work and experimental results of many people from the DLR-HR TanDEM-X team. The author of this thesis calculated the coherence images at page 86, the forest height maps at page 95 and the polarimetric diversity of the agricultural areas on page 96.

Bibliography

[1] Achard F., “Estimating tropical deforestation from earth observation data.” ,Carbon Management, Vol. 1, pp. 271-287, 2010

[2] Ahmed R., Siqueira P., Hensley S., “A study of forest biomass estimates from LIDAR in the northern temperate forests of New England“, Remote Sensing of Environment, Volume 130, 15 March 2013, Pages 121-135

[3] Altenkirch W., Majunke C., Ohnesorg B., “Waldschutz auf Ökologischer Grundlage“, Eugen Ulmer GmbH & Co, ISBN 3-8001-3684-8, 2002

[4] Anderson H.-E., “Estimating forest biomass on the western lowlands of the Kenai Peninsula of Alaska using airborne LIDAR and field plot data in a model-assisted sampling design.” Quebec, Canada : s.n., EUFRO Division 4 Conference "Extending forest inventory and monitoring over time and space", 2009

[5] Armston J. d., “Prediction and validation of foliage projective cover from Landsat-5 TM and Landsat-7 ETM+ imagery.”, Journal of Applied Remote Sensing, Vol. 3, 2009

[6] Askne J., Dammert P. B., Ulander L. M., and Smith G., “C-Band Repeat-Pass Interferometric SAR Observations of the Forest”, IEEE Transactions on Geoscience and Remote Sensing, vol. 35, no. 1, pp. 25-35, January 1997

[7] Askne J. I. H., Fransson J. E. S., Santoro M., Soja M. J., Ulander L. M. H., “Model-Based Biomass Estimation of a Hemi-Boreal Forest from Multitemporal TanDEM-X Acquisitions”, Remote Sensing, 11/2013; 5(11):5574-5597., 2013

[8] Assmann E., „Holzmesslehre“, translation: „Wood mensuration“, In: Neudammer Forstliches Lehrbuch (Ed. K. Rubner), Radebeul, pp 209–273, 1957

[9] Assmann E., und Franz F., „Vorläufige Fichten – Ertragstafel für Bayern“, Forstwissenschaftliches Centralblatt, 84(1): 13 – 43, 1965

[10] Attema E. .P. W., & Ulaby F. T., “Vegetation modeled as a water cloud”, Radio Science, vol. 13, pp. 357–364, 1978.

[11] Aulinger T., Mette T., Papathanssiou K. P., Hajnsek I., Heurich M., Krzystek P., “Validation of heights from Interferometric SAR and LIDAR over the temperate Forest Site Nationalpark Bayerischer Wald”, Proceedings of the 2nd International Workshop POLinSAR 2005 (CD), 17-21 January, Frascati, Italy 2005

[12] Bachmann M., Schulze D., Ortega-Miguez C., Polimeni D., Böer J., Hueso J. Gonzalez, Walter Antony J., Krieger G., Bräutigam B., Schwerdt M., Zink M., “Acquisition Status and Calibration of the interferometric system“, Proceedings of the Geoscience and Remote Sensing Symposium (IGARSS), Munich July, 2012

[13] Ballester-Berman, J.D.; Lopez-Sanchez, J.M. ; Fortuny-Guasch, J., “Retrieval of biophysical parameters of agricultural crops using polarimetric SAR interferometry”, IEEE Transactions on Geoscience and Remote Sensing, Volume: 43 , Issue: 4, 2005

[14] Baltasitas E. P., “Airborne laser scanning: Existing systems and firms and other resources”, ISPRS Journal of Photogrammetry & Remote Sensing: ISPRS, pp. 54 (2-3):164-198, 1999

[15] Bamler R., and Hartl P., “Synthetic Aperture Radar Interferometry”, Inverse Problems, vol. 14, no. 4, pp. R1-R54, 1998

[16] Bauer A., “Möglichkeiten zur Extensivierung der Forsteinrichtung im Hochgebirge durch Einsatz moderner Techniken der Luftbildauswertung”, Forstliche Forschungsberichte München, ISSN 0174-1810, 2001

[17] Baulis X., Pons X., “Approach for forest monitoring and mapping by means of multi-spectral airborne data”, International Journal of Remote Sensing, 16(1): 61-80, 1995

[18] Bayerisches Staatsministerium für Ernährung Landwirtschaft und Forsten, „Hilfstafeln für die Forsteinrichtung“, translation: “Collection of yield tables for forest managment“, 1990

[19] Bergen K., Knox R. G., Saatchi, S., “Final report on the NASA workshop: Multidimensional Forested Ecosystem Structure Requirements for Remote Sensing Observations“, NASA/CP-2005-212778, March 2006

[20] Bertalanffy L. v., “Theoretische Biologie. Zweiter Band: Stoffwechsel und Wachstum.“ Bornträger, Berlin, 1942

[21] Bessette L.A., Ayasli S., “Ultra Wide band P-3 and Carabas II Foliage Attenuation and backscatter Analysis”, Proceedings of IEEE Radar Conference, pp. 357-362, 2001

[22] Biermayer, Ziele und Konzept der Forsteinrichtung im Staatswald Bayern”, AFZ/Der Wald 20/1999.

[23] BMELV “BWI2 : Kurzbericht und Ergebnisband mit ausführlicher Darstellung von Methoden, Ergebnissen sowie fachlicher und politischer Wertung“, 2004

[24] BMELV, Bundesministerium für Ernährung Landwirtschaft und Verbraucherschutz, „Waldbericht der Bundesregierung 2009“, Juni 2009

[25] Böhm H.-D. V., Liesenberg V., Limin S. H., ”Multi-Temporal Airborne LIDAR-Survey and Field Measurements of Tropical Peat Swamp Forest TGRS-2013-00576.R1 19 to Monitor Changes“, IEEE journal of selected topics in applied earth observations and remote sensing (JSTARS), vol. 6, vo. 3, June 2013

[26] Boerner W.-M., ”Use of Polarization in Electromagnetic Inverse Scattering”, Radio Science, 16(6), Special Issue: 1980 Munich Symposium on EM Waves), 1037-1045, November/December, 1981

[27] Boerner W.-M. & El- Arini M. B., ”Polarization dependence in electromagnetic inverse problem, IEEE Transactions on Antennas and Propagation, 29(2), 262 – 272, 1981

[28] Boerner W.-M., Mott H., Lüneburg E., Livingstone C., Brisco B., Brown R.J. & Paterson J.S., “Polarimetry in Radar Remote Sensing: Basic Applied Concepts”, Manual of Remote Sensing Vol. 2, Chapter5, John Wiley & Sons, New York, 1998

[29] Bundesministerium der Justiz und für Verbraucherschutz, „Gesetz zur Erhaltung des Waldes und zur Förderung der Forstwirtschaft“

[30] Burschel P., Huss J., “Grundriß des Waldbaus”, translation: “forestry basics“, Parey Studientexte 49, 2. Neubearbeitete und erweiterte Auflage, Parey Buchverlag, ISBN 3-8263-3045-5, 1997

[31] Caicoya A. T., **Kugler F.**, Papathanassiou K., Biber P., Pretzsch H., ” Biomass estimation as a function of vertical forest structure and forest height - Potential and limitations for Radar Remote Sensing”, 8th European Conference on Synthetic Aperture Radar (EUSAR), 2010

[32] Caicoya A. T., **Kugler F.**, Hajnsek I., Papathanassiou K., “Boreal Forest Biomass Classification with TanDEM-X”, Proceedings of the Geoscience and Remote Sensing Symposium (IGARSS), Munich July, 2012

[33] Caicoya A. T., **Kugler F.**, Hajnsek I, Papathanassiou, K., "Boreal Forest Biomass Classification with TANDEM-X", Proceedings of POLinSAR, Workshop, 2013

[34] Caicoya A. T., **Kugler F.**, Hajnsek I., Papathanassiou K., "Vertical forest structure characterization for the estimation of Above Ground Biomass. Potential and limitations for Radar Remote Sensing", Proceedings of the 10th European Conference on Synthetic Aperture Radar (EUSAR), Berlin, 2014

[35] Caicoya A., T., **Kugler F.**, Pardini M., Hajnsek I., Papathanassiou K., "Vertical forest structure characterization for the estimation of Above Ground Biomass: first experimental results using SAR vertical reflectivity profiles." IEEE International Geoscience and Remote Sensing Symposium (IGARSS), 13-07-2014 - 18-07-2014, Quebec, Canada, 2014

[36] Canadian Forest Service, „The State of Canada's Forests: Annual Report 2012"

[37] Chave J., Andalo C., Brown S., et al. "Tree allometry and improved estimation of carbon stocks and balance in tropical forests", Oecologia 145(1), 87-99, 2005

[38] Chazdon, R. L., Colwell, R. K., and Denslow, J. S. "Tropical tree richness and resource-based niches: Technical comments", Science 285: 1459, 1999

[39] Cloude S. R. & Pottier E., "An entropy-based classification scheme for land applications of polarimetric SAR data," IEEE Transactions of Geoscience and Remote Sensing, vol. 35, no. 1, pp. 68–78, Jan. 1997.

[40] Cloude S. R. & Papathanassiou K. P. 1998, "Polarimetric SAR Interferometry", IEEE Transactions on Geoscience and Remote Sensing, vol. 36, no. 5, pp. 1551-1565, September 1998

[41] Cloude S. R. & Papathanassiou K.P., "Three-stage inversion process for polarimetric SAR interferometry", IEE Proceedings - Radar Sonar and Navigation, vol. 150, no. 3, pp. 125-134, 2003

[42] Cloude S. R. & Pottier E., "A review of target decomposition theorems in radar polarimetry", IEEE Transactions on Geoscience and Remote Sensing, Vol.41, Nr.2, pp. 727 – 744, April 2003

[43] Cloude S. R., "Polarization Coherence Tomography", Radio Science, vol. 41, RS-4017, 2006.

[44] Cloude S. R., "Multibaseline Polarization Coherence Tomography", Proceedings of POLinSAR, Workshop, 2007

[45] Cloude S. R., "Dual-Baseline Coherence Tomography." IEEE Geoscience and Remote Sensing Letters, 4(1):127-131, January 2007

[46] Cloude S. R., "Polarization applications in remote sensing", Oxford University Press, ISBN: 978–0–19–956973–1, 2010

[47] Cloude S. R., "An assessment of the Pol-InSAR Performance of TanDEM-X for Forestry applications", Proceedings of PolInSAR 2011, 24th -28th of January Frascati, Italy, 2011

[48] Colin, E. ; Titin-Schnaider, C. ; Tabbara, W., "An interferometric coherence optimization method in radar polarimetry for high-resolution imagery", IEEE Transactions on Geoscience and Remote Sensing, Volume: 44 , Issue: 1, 2006

[49] CORINE land cover report: **http://www.eea.europa.eu/publications/COR0-landcover**., observed: 22/11/2013

[50] Cumming I. G. "Digital Processing of Synthetic Aperture Radar Data: Algorithms and Implementation", ARTECH HOUSE INC., ISBN 1-58053-058-3, 2005

[51] Curlander J. C., McDonough R. N., "Synthetic Aperture Radar: Systems and Signal Processing Theory", John Wiley & Sons, New York, 1991

[52] Czaplewski, R., "Can a sample of Landsat sensor scenes reliably estimate the global extent of tropical deforestation? International Journal of Remote Sensing", 24, 1409-1412., 2003

[53] Denslow, J. S., "Tropical rainforest gaps and tree species diversity.", Annual Review of Ecology and Systematics 18: 431-451, 1987

[54] Dietrich V., "Beiträge zur Zuwachslehre.", Silva, 1923

[55] Dinh H. T. M., Tebaldini S., Rocca F., Le Toan T., Borderies P., Koleck T., Albinet C., Hamadi A., Villard L., "Vertical Structure of P-Band Temporal Decorrelation at the Paracou Forest: Results From TropiScat", IEEE Geoscience and Remote Sensing Letters, 2014

[56] Ditzer T., " Struktur und Dynamik natürlicher und bewirtschafteter Dipterocapaceenwälder: Eine Fallstudie der Modellbildung und Simulation für die Bewirtschaftung natürlicher Ressourcen unter Unsicherheit", Göttinger Beiträge zur Land- und Forstwirtschaft in den Tropen und Subtropen, ISBN 3-88452-392-9, Verlag Erich Goltze GmbH & Co. KG, Göttingen 1999

[57] Djomo A. N., Ibrahima A., Saborowski J., Gravenhorst G., "Allometric equations for biomass estimations in Cameroon and pan moist tropical equations including biomass data from Africa", Original Research Article Forest Ecology and Management, Volume 260, Issue 10, 15 October 2010, Pages 1873-1885, 2010

[58] Dixon R. K., Brown S., Houghton R. A., "Carbon pools and flux of global forest ecosystems", Science 299 , pp. 185-190, 1994

[59] Dubayah R. O., Sheldon S. l., Clark D. B., Hofton M. A., Blair J. B., Chazdon R. L., "Estimation of tropical forest height and biomass dynamics using LIDAR remote sensing at La Selva, Cosat Rica", Journal of Geophysical Research Biogeoscience 115, 2010

[60] Dutra, L.V., dos Santos, J.R., Freitas, C., Mura, J.C., Neeff, T., Elmiro, M.A.T., Moura, P., " Digital Height Modeling (DHM) of Tropical Forests using Multi-frequency InSAR Methodology", IEEE International Conference on , 2006

[61] Drake J. B., Knox R. G., Dubayah R. O., Clark D. B., Condits R., Blair B. J., Hofton M., "Aboveground biomass estimation in closed canopy Neotropical forests using LIDAR remote sensing: factors affecting the generality of relationships", Global Ecology & Biogeography, 12, 147-159, 2003

[62] Elachi C., "Spaceborne Radar Remote Sensing: Applications and Techniques", IEEE Press, New York, 1988

[63] ESA, "Earth Observation Programme Board Programme Proposal ESA Initiative on Climate Change", ESA/PB-EO(2008)37, rev.1, 2008

[64] Falkowski S., Scholes R. J:, Boyle E., Canadell J., Canfield D., Elser J., Hibbard K., Högberg P., Linder S., MacKenzie F. T., Moore III B., Pederson T., Rosenthal Y., Seitzinger S., Smetacek V., Steffen W., "The global carbon cycle: a test of our knowledge of the earth as a system", Science 290, pp. 291 – 295, 2000

[65] FAO Forestry Department, "Global forest resource assessment 2000", 2000

[66] FAO, "FRA 2000: Pan-tropical survey of forest cover changes 1980 – 2000", FRA working Paper No. 49, 2001

[67] FAO Forestry Department, "Global forest resource assessment 2010", 2010

[68] FAO Forestry Department, "Global forest resource assessment 2010 Country report Sweden", 2010

[69] FAO Forestry Department, “Global forest resource assessment 2010 Country report Russia”, 2010

[70] FAO Forestry Department, “Global forest resource assessment 2010 Country report Canada”, 2010

[71] FAO Forestry Department, “Global forest resource assessment 2010 Country report Brazil”, 2010

[72] FAO Forestry Department, “Global forest resource assessment 2010 Country report Indonesia”, 2010

[73] FAO Forestry Department, “Global forest resource assessment 2010 Country report Germany”, 2010

[74] FAO Forestry Department, “Global forest resource assessment 2010 Country report United States of America”, 2010

[75] FAO Forestry Department, “Global forest resource assessment 2010 Country report France”, 2010

[76] FAO Forestry Department, “Global forest resource assessment 2010 Country report Romania”, 2010

[77] FAO Forestry Department, “Global forest resource assessment 2010 Country report China”, 2010

[78] FAO Forestry Department, “Global forest resource assessment 2010 Country report Gabon”, 2010

[79] FAO Forestry Department, “Global forest resource assessment 2010 Country report République Démocratique du Congo”, 2010

[80] FAO Forestry Department, “Global forest resource assessment 2010 Country report Finland”, 2010

[81] FAO, Ridder R. M. “Global Forest Resources Assessment 2010 Options and Recommendations for a Global Remote Sensing Survey”, 2010

[82] FAO & JRC. 2012. Global forest land-use change 1990–2005, by E.J. Lindquist, R. D’Annunzio, A. Gerrand, K. MacDicken, F. Achard, R. Beuchle, A. Brink, H.D. Eva,P. Mayaux, J. San-Miguel-Ayanz & H-J. Stibig. FAO Forestry Paper No. 169. Food and Agriculture Organization of the United Nations and European Commission Joint Research Centre. Rome, FAO, 2012

[83] FAO. “Climate change guidelines for forest managers. FAO Forestry Paper No. 172.” Rome, Food and Agriculture Organization of the United Nations., 2013

[84] Ferrazzoli P., Guerriero L., & Schiavon G., “Experimental and model investigation on radar classification capability,” IEEE Transactions on Geoscience Remote Sensing, Vol. 37, no. 2, pp. 960–968, Feb. 1999

[85] Ferro-Famil L., **Kugler F.**, Pottier E., Lee J.-S., “Forest Mapping and Classification at L-band using Pol-InSAR Optimal Coherence Set statistics”, Proceedings on the 6th European Conference on Synthetic Aperture Radar (EUSAR), 2006

[86] Fischer A., “Forstliche Vegetationskunde”, Pareys Studientexte 82, Blackwell Wissenschafts-Verlag Berlin Wien 1995 ISBN 3-8263-3061-7, 1995

[87] Flynn T., Tabb M. & Carande R., “Coherence region shape extraction for vegetation parameter estimation in polarimetric SAR interferometry”, IEEE Geoscience and Remote Sensing Symposium, IGARSS 2002 , vol. 5, pp. 2596-2598, 2002.

[88] Fomena, R. T., Cloude S. R., “On the Role of Coherence Optimization in Polarimetric SAR Interferometry”, CEOS SAR Cal/ Workshop, Adelaide, Australia, 2005

[89] Franco-Lopez H., Ekb A. R., Bauer M. E., “Estimation and mapping of forest stand density, volume, and cover type using the k-nearest neighbors method”, Remote Sensing of Environment, Volume 77, Issue 3, pp.: 251 - 274 September, 2001

[90] Franceschetti & Lanari, “Synthetic Aperture Radar Processing”, CRC ss, p. 307, 1999

[91] Fransson J. E. S., Walter F., Ulander L. M. H-, “Estimation of forest parameter using CARABAS-II VHF SAR data”, IEEE Transactions on Geoscience and Remote Sensing , 38(2): 720 – 727, 2000

[92] Freeman A. & Durden S. L., “A three-component scattering model for polarimetric SAR Data,” IEEE Transactions on Geoscience and Remote Sensing, vol. 36, no. 3, pp. 963–973, May 1998

[93] Fronaro G., Franceschetti G., “Image registration in interferometric SAR processing”, IEEE Radar Sonar and Navigation, 142(6): 313 – 320, 1995

[94] FSC Arbeitsgruppe Deutschland, “Deutscher FSC Standard” Deutsche übersetzte Fassung Version 2.3 vom 01.07.2012“, **http://www.fsc-deutschland.de/prinzipien.10.htm**, FSC Waldstandard, information from 30.08.2013

[95] Furby S. L., “Continental scale land cover change monitoring in Australia using Landsat imagery.” Lesvos, Greece : s.n., 2008. International Conference on Studying, Modeling and Sense Making of Planet Earth, 2008

[96] Gadow K., Schmidt M., Periodische Inventuren und Eingriffsinventuren.” Forst und Holz Nr. 22, S. 667 – 671, 1998

[97] Garestier F., Dubois-Fernandez P. C., Papathanassiou K. P., “Pine Forest Height Inversion Using Single-Pass X-band Pol-InSAR Data”, IEEE Transactions on Geoscience and Remote Sensing, vol. 46, NO.1, January, 2008.

[98] Garestier, F. ; Dubois-Fernandez, P.C. ; Champion, I., „Forest Height Inversion Using High-Resolution P-band Pol-InSAR Data“, IEEE Transactions on Geoscience and Remote Sensing, Volume: 46 , Issue: 11 , Part: 1, 2008

[99] Garestier F., Le Toan T., “Forest Modeling For Height Inversion Using Single-Baseline InSAR/Pol-InSAR Data”, IEEE Transactions on Geoscience and Remote Sensing, vol. 48, no. 3, pp. 1528-1539, 2010.

[100] Garestier F., Le Toan T., “Estimation of the Backscatter Vertical Profile of a Pine Forest Using Single Baseline P-band (Pol-)InSAR Data”, IEEE Transactions on Geoscience and Remote Sensing, vol. 48, no.9, pp. 3340-3348, 2010.

[101] Gatelli F., Monti Guamieri A., Parizzi F., Pasquali P., Prati C., & Rocca F., ‘The wavenumber shift in SAR Interferometry’, IEEE Transactions on Geoscience and Remote Sensing, vol. 32, no. 4, pp. 855-865, 1994

[102] GCP Report No. 7 GCP. 2010. “Ten Years of Advancing Knowledge on the Global Carbon Cycle and its Management”, 2010

[103] GEO-FCT “Observations, Group on Earth. Product Development” Team Technical Status Report v2.0. s.l.: GEO, 2012.

[104] Getzin S., Wiegand K., Schumacher J., Gougeon F. A., “ Scale-dependent competition at the stand level assessed from crown areas”, Forest Ecology and Management, Volume 255, Issue 7, 20 April 2008, Pages 2478-2485, 2008

[105] Gobakken T., “Estimating biomass in Hemark County, Norway, using national forest inventory field plots and airborne laser scanning.”, Remote Sensing of Environment, Vol. 123, pp. 443-456, 2012

[106] Goetz S., Steinberg D., Dubayah R., Blair B., ”Laser remote sensing of canopy habitat heterogeneity as a predictor of bird species richness in an eastern temperate forest, USA “,Volume 108, Issue 3, 15 June 2007, Pages 254–263, 2007

[107] Goetz S. J., Baccini A., Laporte N., Johns T., Walker W. S., “Mapping and monitoring carbon stocks with satellite observations: a comparison of methods”, Carbon Balance Manage. 4, doi:10.1186/1750-0680-4-2 , 2009

[108] Goetz S., Dubayah R., “Advances in remote sensing technology and implications for measuring and monitoring forest carbon stocks”, Carbon Management (2011) 2(3),231-244, 2011

[109] GFOI, “Global Forest Observation Initiative (GFOI) – Review of Priority Research and Development Topics”, GEO Geneva, Switzerland, 2013

[110] GOFC-GOLD “A sourcebook of methods and procedures for monitoring and reporting anthropogenic greenhouse gas emissions and removals caused by deforestation, gains and losses of carbon stocks in forests remaining forests, and forestation.” GOFC-GOLD Report version COP16-1, (GOFC-GOLD Project Office, Natural Resources Canada, Alberta, Canada), 2010

[111] Graham L., “Synthetic interferometer radar for topographic mapping.“, Proceedings of the IEEE, vol. 62, No. 6 pp. 763-768, 1974.

[112] Guarnieri M., Prati C., “ScanSAR focusing and interferometry”, IEEE Transaction on Geoscience and Remote Sensing”, Volume 34, Issue 4, 1996

[113] Hagberg J. O., Ulander L. M., & Askne J., “Repeat-Pass Interferometry over Forested Terrain”, IEEE Transactions on Geoscience and Remote Sensing, vol. 33, no. 2, pp. 331-340, 1995

[114] Hanssen R. F., “Radar Interferometry Data Interpretation and Error Analysis”, Kluwer Academic Publishers, ISBN 0-7923-6945-9, 2001

[115] Hansen M., DeFries R. S., Townshend J. R. G., Carroll M., Dimiceli C., & Sohlberg R.A., "Global Percent Tree Cover at a Spatial Resolution of 500 Meters: First Results of the MODIS Vegetation Continuous Fields Algorithm", Earth Interactions, vol. 7, No 10, pp. 1-15, 2003

[116] Hansen M.C., Potapov P.V., Moore R., Hancher M., Turubanova S.A., Tyukavina A., Thau D., Stehman S. V., Goetz S. J., Loveland T. R., Kommareddy A., Egorov A., Chini L., Justice C. O., Townshend J. R. G., “High-resolution global maps of 21st-century forest cover change”, Science, 342 (6160), pp. 850–853, 2013

[117] Harding D. J., Lefsky A. M., Parker G., & Blair J., “Laser altimeter canopy height profiles. Methods and validation for closed canopy broadleaved forest”, Remote Sensing of Environment, 96(3-4), pp. 427 – 437, 2001

[118] Harding, D. J., Carabajal, C. C., “ICESat waveform measurements of within – footprint topographic relief and vegetation vertical structure”, Geophysical Research letters, 32, 2005

[119] Hart M. J. “Stamtal en dunning.” Dissertation, Wageningen, 1928

[120] Hajnsek I., Papathanassiou K. P., and Cloude S. R., “Removal of Additive Noise in Polarimetric Eigenvalue Processing”, Proceedings IGARSS’01, Sydney Australia, 2001

[121]Hajnsek I. and Cloude S.R., ”Differential Extinction Estimation over Agricultural Vegetation from POL-InSAR”, Proceedings of the 2nd International Workshop POLinSAR 2005 (CD), 17-21 January, Frascati, Italy 2005

[122]Hajnsek I., **Kugler F.**, Papathanassiou K., Horn R., Scheiber R., Moreira A., Hoekman D., Davidson M., “INDREX II – Indonesian airborne radar experiment campaign over tropical forest in L- and P-band: first results”, Proceedings of the IEEE international Geoscience and Remote Sensing Symposium IGARSS 05, Seoul, Korea, Volume 6, P. 4335 – 4338, 2005

[123]Hajnsek I., **Kugler F.**, Papathanassiou K., Scheiber R., Horn R., Moreira A., Hoekman D., Davidson M., Attema E., “INDREX II Indonesian Airborne Radar Experiment campaign over tropical forest in L- and P-band, Proceedings of the 2nd International Workshop POLinSAR 2005 (CD), 17-21 January, Frascati, Italy, 2005

[124]Hajnsek I., Kugler F., Lee S.-K., Papathanassiou K., “Tropical Forest Parameter Estimation by means of Pol-InSAR: The INDREX II Campaign”, IEEE Transactions on Geoscience and Remote Sensing, vol. 47, No. 2, 2009, © [2009] IEEE

[125]Hajnsek I., Shimada M., Eineder M., Papathanassiou K., Motohka T., Watanabe M., Ohki M., De Zan F., Lopez-Dekker P., Krieger G., Moreira A., “ Tandem-L: Science Requirements and Mission Concept”, Proceedings of the 10th European Conference on Synthetic Aperture Radar, EUSAR 2014

[126]Hall F. G., Bergen K., Blair J. B., Dubayah R., Houghton R., Hurtt G., Kellndorfer J., Lefsky M., Ranson J., Saatchi S., Shugart H. H., Wickland D., „ Characterizing 3D vegetation structure from space: Mission requirements”, Remote Sensing of Environment, 115, 2753 – 2775, 2011

[127]Hallikainen M., Hyyppä J., Haapanen J., Tares T., Ahola P., Pulliainen J., Toikka M., “A Helicopter-Borne Eight-Channel Ranging Scatterometer for Remote Sensing: Part I: System Description”, IEEE Transactions on Geoscience and Remote Sensing, vol. 31, no. 1, pp. 161-169, 1993

[128]Hamadi A., Borderies P., Albinet C., Koleck T., Villard L., Ho Tong Minh D., Le Toan T., Burban B., “Temporal Coherence of Tropical Forests at P-Band: Dry and Rainy Seasons”, IEEE Geoscience and Remote Sensing Letters, 2014

[129]Häme T., Kilpi J., Ahola H. A., Rauste Y., Antropov O., Rautiainen M., Sirro L., Bounpone S., “Improved mapping of tropical forests with optical and SAR imagery, Part I: Forest cover and accuracy assessment using multi-resolution data.”, IEEE Journal of Selected Topics in Applied Earth Observations and Remote Sensing, Vol. 6, No. 1, pp. 74-91, 2013

[130]Hein A., “Processing of SAR Data Fundamentals, Signal Processing, Interferometry”, Springer-Verlag Berlin Heidelberg New York, ISBN 3-540-05043-4, 2004

[131]Heliere F., Fois F., Arcioni M., Bensi P., Fehringer M., Scipal K., “Biomass P-band SAR interferometric mission selected as 7th Earth Explorer Mission”, Proceedings of EUSAR 2014; 10th European Conference on Synthetic Aperture Radar, Berlin, 2014

[132]Henderson F.M., Lews A. J., (ed.) “Principles & Applications of Imaging Radar Manual of Remote Sensing”, 3rd Edition, Volume 2, John Wiley & Son, Inc. New York, pp. 1-120, 1998

[133]Herold, M. & Johns, T. “Linking requirements with capabilities for deforestation monitoring in the context of the UNFCCC-REDD process. - Environmental

Research Letters", Vol. 2, No. 4, 045025, DOI: 10.1088/1748-9326/2/4/045025, http://stacks.iop.org/1748-9326/2/i=4/a=045025, 2007

[134] Herold, M. "An assessment of national forest monitoring capabilities in tropical non-Annex I countries: recommendations for capacity building", report prepared for the Prince's Rainforest Project http://unfccc.int/files/methods_science/redd/country_specific_information/application/pdf/redd_nat_capacity_report_herold_july09_publ.pdf, 2009

[135] Hildebrandt G., "Fernerkundung und Luftbildmessung für Forstwirtschaft, Vegetationskartierung und Landschaftsökologie", Herbert Wichmann Verlag, ISBN 978-3879072385, 1996

[136] Ho Tong Minh D., Le Toan T., Rocca F., Tebaldini S., Villard L., "Relating P-Band Synthetic Aperture Radar Tomography to Tropical Forest Biomass", IEEE Transactions on Geoscience and Remote Sensing 01/2013

[137] Hoekman D., Vissers M. A. M. & Wielaard N. "PALSAR wide-area mapping of Borneo: Methodology and map validation.", 2010, IEEE Journal of Selected Topics in Applied Earth Observations and Remote Sensing, Vol. 3, pp. 605-617, 2010

[138] Holloway V. & Giandomenico E. "Carbon Planet White Paper: The History of REDD Policy", http://unfccc.int/files/methods_science/redd/application/pdf/the_history_of_redd_carbon_planet.pdf, 2009

[139] Hong Z., Peifang M., Chao W., "A new function expansion for polarization coherence tomography", IEEE Geoscience and Remote Sensing Letters, Volume: 9, Issue: 5, 2012

[140] Horn R., " The DLR airborne SAR project E-SAR", Proceedings of IEEE Transactions of Geoscience and Remote Sensing, Symposium, Lincoln, Nebraska, vol. 3, May, 1996

[141] Houghton R. A., "Revised estimates of the annual flux net flux of carbon to the atmosphere from changes in land use and land management 1850 – 2000", Tellus, Ser. B, 55, 378-390, 2003

[142] Houghton R. A., "Aboveground forest biomass and the global carbon balance", Global Change Biology, 11, 945 – 958, 2005

[143] Houghton R. A., "Biomass", in S.E. Jorgensen & B. D. Fath, Encyclopedia of Ecology (pp. 448 – 453), (1st Edition), Oxford Elsevier, 2008

[144] Houghton R. A., Hall F., Goetz S. J., "Importance of biomass in the global carbon cycle", Journal of Geophysical Research, vol. 114, G00E03, 2009

[145] Houghton R. A., "How well do we know the flux of CO2 from land- use change?", Tellus, Series B Chemical and Physical Meteorology, International Meteorological Institute of Stockholm, 2010

[146] Hovanessian F. T., "Introduction to Synthetic Array and Imaging Radars", Artech House, Inc., Norwood, MA, 1980

[147] Hubbell, S. P., Foster, R. B., O'Brien, S. T., Harms, K. E., Condit, R., Wechsler, B., Wright, S. J., and Loo de Lao, S., " Light-gap disturbances, recruitment limitation, and tree diversity in a Neotropical forest". Science 283: 554-557, 1999

[148] Hunter M. O., Keller M., Victoria D., Morton D. C., "Tree height and tropical forest biomass estimation", Biogeoscience, 10, 8385–8399, 2013

[149] Hurtt G. C., Fisk J., Thomas R. Q., Dubayah R., Moorcraft P. R., & Shugart H. H., "Linking models and data on vegetation structure." ,Journal of Geophysical Research 115(G00E10), 2010

[150]Huth A., Ditzer T., Bossel H., „The Rain Forest Model FORMIX3 Model Description and Analysis of Forest Growth and Logging Scenarios for the Deramakot Forest Reserve (Malaysia)“, Göttinger Beiträge zur Land- und Forstwirtschaft in den Tropen und Subtropen, Heft 24, ISBN 3-88452-385-6, 1998

[151]Huxley J. S., “Problems of relative growth”, New York: Mac Veagh, 1932

[152]Hyyppä J., Hallikainen M., “A Helicopter-Borne Eight-Channel Ranging Scatterometer for Remote Sensing: Part II: Forest Inventory”, IEEE Transactions on Geoscience and Remote Sensing, vol. 31, no. 1, pp. 170-179, 1993

[153]Hyyppä, J., Pulliainen J., Hallikainen M., Satsi Asko, „Radar-derived standwise forest inventory“, IEEE Transactions on Geoscience and Remote Sensing 35(2):392-404, 1997

[154]Hyyppä J., Pyysalo U., Hyyppö H., Samberg A., “Elevation Accuracy of Laser Scanning –Derived Digital Terrain and Target Models in Forest Environments“, Proceedings of EARSeL-SIG-Workshop LIDAR, Dresden/FRG, June 16 – 17, 2000

[155]Hyyppä J, Hyyppä H,, Leckie D,, Gougeon F,, Yu X,, Maltamo M., “Review of methods of small-footprint airborne laser scanning for extracting forest inventory data in boreal forests.”, International Journal of Remote Sensing, 29, 5, pp. 1339-1366, 2008

[156]Imhoff M. L., “Radar backscattering and biomass saturation ramifications for global biomass inventory”, IEEE Transactions on Geoscience and Remote Sensing , 33/3: 511-518, 1995

[157]IPCC (Intergovernmental Panel on Climate Change), ”Climate Change 2001: The scientific basis. Contribution of Working Group I to the third Assessment Report of the IPCC”, Cambridge University Press, Cambridge 2001

[158]Irons J.R. and Dwyer J.L., “An Overview of the Landsat Data Continuity Mission,” Proceedings of the SPIE, Vol. 7695, 12 May 2010.

[159]Jones R. C., “A new Calculus for the Treatment of optical Systems I. Description and Discussion”, Journal of the Optical Society of America, vol.31, pp. 488 – 493, 1941

[160]Jones R. C., “A new Calculus for the Treatment of optical Systems II. Description and Discussion”, Journal of the Optical Society of America, vol.31, pp. 493 – 499, 1941

[161]Just D. & Bamler R., “Phase statistics of interferograms with applications to synthetic aperture radar”, Appl. Opt., vol.33, no.20, pp. 4361 – 4368, July 1994

[162]Kangas A., Maltamo M., “Forest Inventory: Methodology and Application”, Published by Springer, ISBN: 1-420-4379-1, 2006

[163]Kangas A., “Value of forest information”, European Journal of forest research, 129: 863-874, 2010

[164]Kankare V., Vastaranta M., Holopainen M., Räty M., Yu X., Hyyppä J., Hyyppä H., Alho P., Viitala R., “Retrieval of Forest Aboveground Biomass and stem Volume with airborne Scanning LIDAR”, Remote Sensing, ISSN 2072-4292, 5,2257-2274, 2013

[165]Kasischke, E.S. ; Christensen, N.L., Jr. ; Bourgeau-Chavez, L.L., „Signature extraction from mesoscale surface patterns observed on synthetic aperture radar imagery”, IEEE Transactions on Geoscience and Remote Sensing, Volume: 15 , Issue: 2 , 1995

[166] Kellndorfer J. M., Dobson M. C., Vona, J. D., Clutter M., "Toward precision forestry: plot-level parameter retrieval for slash pine plantations with JPL AIRSAR", IEEE Transactions on Geoscience and Remote Sensing ,Volume: 41 , Issue: 7 , Part: 1, 2003

[167] Kellndorfer J., Walker W., Pierce L., Dobsona C., Fites J. A., Hunsaker C., Vonad J., Clutter M., "Vegetation height estimation from Shuttle Radar Topography Mission and National Elevation Datasets", Remote Sensing of Environment 93 339–358, 2004

[168] Kim J. S., Papathanassiou K.P., Quegan S., Rogers N., "Estimation and correction of scintillation effects on spaceborne P-band SAR images", IEEE International Geoscience and Remote Sensing Symposium (IGARSS), München, 2012

[169] Klauder J.R., Price A.C., Darlington S. & Albersheim W.J., "The Theory and Design of Chirp Radars", The Bell System Technical Journal, Vol.39, Nr.4, July 1960

[170] Klausing H. & Holpp W., "Radar mit realer und synthetischer Apertur: Konzeption und Realisierung", Oldenburg Verlag München, p. 399, 2000

[171] Klemmt H.-J. & Neubert M., "Möglichkeiten und Grenzen der Auswertung der BWI in Bayern, Wald Wissenschaft Praxis, LWF aktuell 85/2011.

[172] Knocke T., Weber M., "Expanding Carbon Stocks in Existing Forests – A Methodological Approach for Cost Appraisal on the Enterprise Level", Mitigation and Adaption Strategies for Global Change, 11:579 – 605, 2006

[173] Knocke T., „Forstbetriebsplanung", Eugen Ulmer KG, ISBN:978-3-8001-7611-3, 2012

[174] Köhl M., Magnussen S., Marchetti M., "Sampling Methods, Remote Sensing and GIS Multisource Forest Inventory", ISBN 3-540-32571-9, 2006

[175] Köhler, P. and Huth, A., "Towards ground-truthing of spaceborne estimates of above-ground life biomass and leaf area index in tropical rain forests", Biogeoscience, 7, 2531-2543, doi:10.5194/bg-7-2531-2010, 2010

[176] Koskinen J. T., Palliainen J. T., Hyyppa J. M., Engdahl M. E., Hallikainen M. T., "The seasonal behavior of interferometric coherence in boreal forest", IEEE Transactions on Geoscience and Remote Sensing, 05/2001

[177] Kraft G., "Beiträge zur Lehre von den Durchforstungen, Schlagstellung und Lichtungshieb", Hannover 1883

[178] Krieger G., Papathanassiou K. & Cloude S., "Spaceborne Polarimetric SAR Interferometry: Performance Analysis and Mission Concepts.", EURASIP Journal of Applied Signal Processing (20), pp. 3272-3292. Hindawi 2005

[179] Krieger G., Moreira A., Fiedler H., Hajnsek I., Werner M., Younis M., & Zink M., "TanDEM-X: A Satellite Formation for High-Resolution SAR Interferometry", IEEE Transactions on Geoscience and Remote Sensing, vol. 45, no. 11, pp. 3317-3341, 2007

[180] Krieger G., Gebert N. and Moreira A., "Multidimensional waveform encoding: A new digital beamforming technique for synthetic aperture radar remote sensing", IEEE Transactions on Geoscience and Remote Sensing, vol. 46, pp. 31–46, Jan. 2008.

[181] Krieger G., Hajnsek I., Papathanassiou K., Eineder M., Younis M., De Zan F., Prats P., Huber S., Werner M., Fiedler H., Freeman A., Rosen P., Hensley S., Johnson W., Veilleux L., Grafmüller B., Werninghaus R., Bamler R., Moreira A., "The Tandem-L Mission Proposal: Monitoring Earth's Dynamics with High Resolution

SAR Interferometry“, Proceedings of the IEEE Radar Conference (RadarCon), IEEE Radar Conference (RadarCon), 2009-05-04 - 2009-05-08, Pasadena, U.S.A, 2009

[182]Krieger G., Hajnsek I., Papathanassiou K., Eineder M., Younis M., DeZan F., Lopez-Dekker P., Huber S., Werner M., Prats P., Fiedler H., Werninghaus R., Freeman A., Rosen P., Hensley S., Grafmüller B., Bamler R., Moreira A., “Tandem-L: A Mission for Monitoring Earth System Dynamics with High Resolution SAR Interferometry.”, In: Proceedings of European Conference on Synthetic Aperture Radar (EUSAR), pp. 506-509, VDE Verlag GmbH. European Conference on Synthetic Aperture Radar (EUSAR), 2010-06-07 - 2010-06-10, Aachen, Germany. ISBN 978-3-8007-3272-2, 2010

[183]Krieger G., Hajnsek I., Papathanassiou K., Eineder M., Younis M., De Zan F., Huber S., Lopez-Dekker P., Prats P., Werner M., Shen Y., Freeman A., Rosen P., Hensley S., Johnson B., Villeux L., Grafmüller B., Werninghaus R., Bamler R., Moreira A., “Tandem-L: An Innovative Interferometric and Polarimetric SAR Mission to Monitor Earth System Dynamics with High Resolution.”, Proceedings of the IEEE Geoscience and Remote Sensing Symposium (IGARSS), pp. 1-4, IEEE. IGARSS 2010, 2010-07-26 - 2010-07-30, Honolulu, Hawaii, USA, 2010

[184]Krieger G., Hajnsek I., Papathanassiou P. K., Younis M., Moreira A., “Interferometric Synthetic Aperture (SAR) Missions Employing Formation Flying”, Proceedings of the IEEE, Volume 98, Issue: 5, 2010

[185]Krieger G., Zink M., Bachmann M., Bräutigam B., Schulze D., Martone M., Rizzoli P., Steinbrecher U., Antony J. W., De Zan F., Hajnsek I., Papathanassiou K., Kugler F., Rodriguez Cassola M., Younis M., Baumgartner S., López-Dekker P., Prats P., Moreira A., “TanDEM-X: A radar interferometer with two formation-flying satellites”, Acta Astronautica 89 83–98, 2013

[186]Krul L., “Principles of radar measurements”, Radar Calibration, Proceedings of EARSeL Workshop, Alpbach, Austria, 6. - 10. December, pp. 11 – 2-, 1982

[187]**Kugler F.**, Papathanassiou K., Hajnsek I., Hoekman D., “INDREX-II - Tropical Forest Height Estimation with L- and P-Band Polarimetric Interferometric SAR.”, European Conference on Synthetic Aperture Radar (EUSAR), 2006-05-16 - 2006-05-18, Dresden, Germany, 2006

[188]**Kugler F.**, Koudogbo F. N., Papathanassiou K. P. & K. Gutjahr , “Frequency Effects in Pol-InSAR Forest Height Estimation”, Proceedings of European Conference on Synthetic Aperture Radar EUSAR'06, Dresden, Germany, May 16-18, 2006

[189]**Kugler F.**, Papathanassiou K. P., Hajnsek I. & Hoekman D., “Forest Height Estimation in Tropical Rain Forest using Pol-InSAR Techniques”, Proceedings of the IEEE International Geoscience and Remote Sensing Symposium (IGARSS), 31 July -04 August, Denver, USA, 2006.

[190]**Kugler F.**, Coscia A., Papathanassiou K., Hajnsek I., “Potential of forest height estimation using X-band by means of two different inversion scenarios.“ Proceedings of the IEEE Geoscience and Remote Sensing Symposium (IGARSS), 2007-07-23 - 2007-07-27, Barcelona, Spain, 2007

[191]**Kugler F.**, Lee S. - K., Papathanassiou K. P., “Estimation of Forest Vertical Structure Parameter by means on Multi-baseline Pol-InSAR”, Proceedings Geoscience and Remote Sensing Symposium IGARSS (Cape Town), 2009

[192] **Kugler F.**, Sauer S., Lee S. - K., Papathanassiou K., Hajnsek I., "Potential of TanDEM-X for forest parameter estimation", 8th European Conference on Synthetic Aperture Radar (EUSAR) Aachen, 2010

[193] **Kugler F.**, & Hajnsek, I., Papathanassiou K., Krieger G. & Moreira A., "Global 3D Forest Structure Mapping with TANDEM-L: Monitoring the Earth's Dynamics.", ForestSat, 2010-09-07 - 2010-09-10, Lugo, Spain, 2010

[194] **Kugler F.**, I. Hajnsek, Papathanassiou K., "Forest Parameter Characterisation by means of TerraSAR-X and TanDEM-X (Polarimetric and) Interferometric data.", Proceedings of PolInSAR 2011, 24th -28th of January Frascati, Italy, 2011

[195] **Kugler F.**, & Hajnsek I., 2011, "Forest Characterisation by means of TerraSAR-X and TanDEM-X (Polarimetric and) Interferometric data." Proceedings of the IEEE International Geoscience and Remote Sensing Symposium (IGARSS), 2011-07-24 - 2011-07-29, Vancouver, Canada, 2011

[196] **Kugler F.**, Hajnsek I., Papathanassiou K., 2012 "Dual Pol-InSAR Forest Height Estimation By Means of TanDEM-X Data.", Proceedings of IEEE international Geoscience and Remote Sensing Symposium (IGARSS), 2012-07-22 - 2012-07-27, München, Deutschland , 2012

[197] **Kugler F.**, Papathanassiou K., Hajnsek I., Rosenqvist A., Cloude S., "ALOS-PalSAR & TanDEM-X Acquisitions for Forest Disturbance & Degradation Mapping", K&C Phase 3 Final report, 2014

[198] Kugler F., Schulze D., Hajnsek I., Pretzsch H., Papathanassiou K.P., „TanDEM-X Pol-InSAR Performance for Forest Height Estimation", IEEE Transactions on Geoscience and Remote Sensing, vol. 52 , Issue. 10, 2014, © [2014] IEEE

[199] Kugler F., Lee S.-K., Hajnsek I., Papathanassiou K., "Forest Height Estimation by means of Pol-InSAR: The role of the vertical wavenumber", IEEE Transactions on Geoscience and Remote Sensing, vol. 53, Issue. 10, 2015, © [2015] IEEE

[200] Kuntz S., "A multi-stage inventory scheme for REDD inventories in tropical countries.", International Society for Photogrammetry and Remote Sensing (ISPRS), 2012

[201] Kwak D.-A., Lee W.-K., Lee J.-H., Biging G. S., Gong P., "Detection of individual trees and estimation of tree height", Journal of Forest Research, Volume 12, Issue 6, pp. 425 – 434, December 2007

[202] van Laar A., Akca A., "Forest Mensuration (Managing Forest Ecosystems)", Published by Springer, ISBN-13 978-1-4020-5990-2, 2007

[203] Lamprecht H., "Waldbau in den Tropen Die tropischen Waldökosysteme und ihre Baumarten – Möglichkeiten und Methoden zu ihrer nachhaltigen Nutzung", Verlag Paul Parey Hamburg und Berlin ISBN 3-490-05216-1, 1986

[204] Lavalle M., Simard M., Hensely S., "A Temporal Decorrelation Model for Polarimetric Radar Interferometers", IEEE Transactions on Geoscience and Remote Sensing, vol. 50 Issue 7, July 2012

[205] Lavalle M., Khun K., "Three – Baseline InSAR Estimation of Forest Height", IEEE Geoscience and remote sensing letters, 2014

[206] Lee J. S., Grunes M. R., & Kwok R., "Classification of multi-look polarimetric SAR imagery based on complex Wishart distribution," Int. J. Remote Sens., vol. 15, no. 11, pp. 2299–2311, 1994

[207]Lee J. S., Hoppel K. W., Mango S. A., and Miller A. R., "Intensity and Phase Statistics of Multilook Polarimetric and Interferometric SAR Imagery", IEEE Transactions on Geoscience and Remote Sensing, vol. 32, no. 5, pp. 1017-1028, 1994

[208]Lee J. S., Pottier E., "POLARIMETRIC RADAR IMAGING FROM BASICS TO APPLICATIONS", CRC Press Taylor & Francis Group Boca Raton, ISBN 978-1-4200-5497-2 London New York, 2009

[209]Lee J. S., Grunes M. R., Ainsworth T., Papathanassiou K., Hajnsek I., Mette T., & Ferro-Famil L., "Forest classification based on multi-baseline interferometric and polarimetric E-SAR data", Proceedings of European Conference on Synthetic Aperture Radar, EUSAR'06, Dresden, Germany, 2006

[210]Lee S.-K., **Kugler, F**., Hajnsek I. & Papathanassiou K. P., "Quantifying Temporal Decorrelation over Boreal Forest at L-and P-band", Proceedings of European Conference on Synthetic Aperture Radar, EUSAR'08, Friedrichshafen, Germany, 2008

[211]Lee S. K., **Kugler F.**, Hajnsek I., Papathanassiou K. P., "The Impact of Temporal Decorrelation over Forest Terrain in Polarimetric SAR Interferometry", Proceedings of the 5th International Workshop POLinSAR 2009, 26.-30. January, Frascati, Italy 2009

[212]Lee S.-K., **Kugler F.**, Hajnsek I., Papathanassiou K. P., "Polarimetric SAR interferometry for forest applications at P-band: Potential and challenges", Proceedings of IEEE international Geoscience and Remote Sensing Symposium (IGARSS), 2009-07-12 - 2009-07-17, Cape Town, South Africa, 2009

[213]Lee S.-K., **Kugler F.**, Scheiber R., Hajnsek I., Papathanassiou K. P., "Potential and Challenges of Pol-InSAR Techniques for Forest Height Estimation in the context of the BIOMASS Mission" Proceedings of IEEE international Geoscience and Remote Sensing Symposium (IGARSS), 2011-07-24 - 2011-07-29, Vancouver, Canada, 2011

[214]Lee S.-K. **Kugler F.**, Hajnsek I., Papathanassiou K. P., "The Potential and Challenges of Polarimetric SAR Interferometry Techniques for Forest Parameter Estimation at P-band", Proceedings of European Conference on Synthetic Aperture Radar, EUSAR'10, Aachen, Germany, 2010

[215]Lee S.-K. **Kugler F.**, Hajnsek I., Papathanassiou K. P., "Multi-baseline Pol-InSAR Forest Height Estimation in the presence of temporal decorrelation", Proceedings of European Conference on Synthetic Aperture Radar, EUSAR'10, Aachen, Germany, 2010

[216]Lee S. K., **Kugler F.**, Papathanassiou K., Hajnsek I., "Multibaseline Polarimetric SAR interferometry Forest Height Inversion Approaches", POLinSAR ESA-ESRIN, Frascati, Italy, 2011

[217]Lee S-K., **Kugler F.**, Papathanassiou K., Hajnsek I., "Quantification and Compensation of Temporal Decorrelation Effects In Polarimetric SAR Interferometry", Proceeding of the International Geoscience and Remote Sensing Symposium IGARSS Munich, 2012

[218]Lee S.-K., Kugler F., Papathanassiou K. & Hajnsek I., "Quantification of Temporal Decorrelation Effects at L-band for Polarimetric SAR Interferometry Applications", IEEE Transactions on Geoscience and Remote Sensing, Selected Topics in Applied Earth Observations and Remote Sensing, IEEE Journal of, vol. 6, No. 3, June, , 2013

[219] Lee S.-K. **Kugler F.**, Papathanassiou K., Hajnsek I., "First Pol-InSAR Forest Height Inversion by means of L-band F-SAR Data." ESA POLinSAR 2013 Workshop, 2013-01-28 - 2013-02-01, Frascati, Italy, 2013

[220] Lee S.-K. "Forest Parameter Estimation Using Polarimetric SAR Interferometry Techniques at Low Frequencies", Dissertation, Forschungsbericht 2013-09, Deutsches Zentrum für Luft- und Raumfahrt e. V. in der Helmholtz-Gemeinschaft, ISSN 1434-8454, 2013

[221] Leech J.W., Correll R.L., "Sampling precision of plantation inventory in South Australia", Forest Ecology and Management, Volume 57, Issues 1–4, March, Pages 191-200, 1993

[222] Lefsky A. M., Cohen W. B., Parker G. C., & Harding D. J., "LIDAR Remote Sensing for Ecosystem Studies", Bioscience, 52, pp. 19 – 30, 2002

[223] Lefsky M. A., Harding D. J., Keller M., Cohen W. B., Carabajal C. C., Del B., Hunter M. O., de Oliveira R. jr., " Estimates of forest canopy height and aboveground biomass using ICESat.", Geophysical Research letters Vol. 32 L22S02, 2005

[224] Lefsky A. M., "A global forest canopy height map from the Moderate Resolution Imaging Spectroradiometer and the Geosciences Laser Altimeter", Geophysical research letters. Vol. 37, L15401, 2010

[225] Lehmann E. A., "Joint processing of Landsat and ALOS-PALSAR data for forest mapping and monitoring.", IEEE Transactions on Geoscience and Remote Sensing, Vol. 50, pp. 55-67. 2012

[226] Lillesand T. M., Kiefer R. W., "Remote Sensing and image interpretation", John Wiley & Sons (New York), 1999

[227] Lodhiyal N. Lohyial L. S., "Biomass and net primary productivity of Bhab Shisham forests in central Himalaya, India." Forest Ecology and Management 176 (1-3):217-235, 2003

[228] Loetsch F. & Haller K. E., „ Forest Inventory, Volume 1: Statistics of Forest Inventory and Information from Aerial Photographs.", BLV Verlagsgesellschaft München, Basel, Wien 1964

[229] Lopez-Sanchez J.M., Hajnsek I., Ballester-Berman J.D., "First Demonstration of Agriculture Height Retrieval With Pol-InSAR Airborne Data", Geoscience and Remote Sensing Letters, IEEE Volume: 9 , Issue: 2, 2012

[230] Lucas R. M., "Updating the Phase 1 habitat map of Wales, UK, using satellite sensor data", ISPRS Journal of Photogrammetry and Remote Sensing, Vol. 66, pp. 81-102, 2011

[231] Lüneburg E., "Principles of radar polarimetry", Proceedings of the IEICE Transactions on the Electronic Theory, E78-C, 1339-1345, 1995

[232] Lüneburg E., "Polarimetric target matrix decomposition and Karhunen-Loeve expansion", Proceedings of IGARSS'99, Hamburg, Germany, June 28 – July 2, 1999

[233] Magnusson S. & Boudewyn P., "Derivation of stand height from airborne laser scanner data with canopy-based quantile estimators", Canadian Journal of Forest Research. 28: 1016 – 1031, 1998

[234] Mallet C. & Bretar F., "Full waveform topographic LIDAR: state-of-the-art", ISPRS Journal of Photogrammetry and Remote Sensing, pp. 64: 1-16, 2009

[235] Markham, B.L., Knight, E.J., Canova, B., Donley, E., Kvaran, G., Lee, K., Barsi, J.A., Pedelty, J.A., Dabney, P.W., Irons, J.R., "The Landsat Data Continuity

Mission Operational Land Imager (OLI) sensor", Geoscience and Remote Sensing Symposium (IGARSS), 2012 IEEE International in Munich, 22-27 July, 2012

[236] Martin K., Ackermann J., Engels F., Hoffmann K., "Erfassung von Sturmschäden an Wäldern durch Radardaten", AFZ-Der Wald, pp 30 – 33, 6/2013

[237] Melaas E. K, Friedl M. A., Zhu Z., „Detecting inter-annual variation in deciduous broadleaf forest phenology using Landsat TM/ETM + data",Remote Sensing of Environment, Volume 132, 15 May 2013, Pages 176-185, 2013

[238] Mette T., Papathanassiou K., Hajnsek I., "Height-Biomass Allometry in Temperate Forests – Performance accuracy of height-biomass allometry." Proc. IGARSS, 21 – 25 Ju., Toulouse, 2003

[239] Mette T., Papathanassiou K. P., Hajnsek I., "Biomass estimation from polarimetric SAR interferometry over heterogeneous forest terrain", Proceeding of IEEE Geoscience and Remote Sensing Symposium (IGARSS 2004), 20. - 24. September, Anchorage, Alaska, 2004

[240] Mette T., Papathanassiou, K., Hajnsek, I., Pretzsch, H., Biber, P., "Applying a common allometric equation to convert forest height from Pol-InSAR data to forest biomass", Geoscience and Remote Sensing Symposium, 2004. IGARSS '04. Proceedings, 2004

[241] Mette T., **Kugler F.**, Papathanassiou K., Hajnsek I., "Forest and the Random Volume over Ground - Nature and Effect of 3 Possible Error Types." European Conference on Synthetic Aperture Radar (EUSAR), 2006-05-16 - 2006-05-18, Dresden, Germany, 2006

[242] Mette T. "Forest Biomass Estimation from polarimetric SAR interferometry", Dissertation, Forschungsbericht 2007-10, Deutsches Zentrum für Luft- und Raumfahrt e. V. in der Helmholtz-Gemeinschaft, ISSN 1434-8454, 2007

[243] Miller D. R., Quine C. P., Hadley W., "An investigation of the potential of digital photogrammetry to provide measurements of forest characteristics and abiotic damage", Forest Ecology and Management 135 (2000) 279-288, 2000

[244] Mitscherlich G., "Das Wachstum der Fichte in Baden.", Allgemeine Forst- und Jagdzeitung (AFJZ), 1957

[245] Mladenoff D. J., Baker W. L., "Spatial Modeling of Forest Landscape Change Approaches and Application", Cambridge University Press, ISBN 0-521-63122-X, 1999

[246] Montesano P. M., Nelson R. F., Dubayah R. O., Sun G., Cook B. D., Ranson K. J. R., Næsset E., Kharuk V., "The uncertainty of biomass estimates from LIDAR and SAR across a boreal forest structure gradient", Remote Sensing of Environment, Accepted 4 January, 2014

[247] Morel A. C., Saatchi S. S., Malhi Y., Berry N. J., Banin L., Burslem D., Nilus R., Ong R. C., "Estimating aboveground biomass in forest and oil palm plantation in Sabah, Malaysian Borneo using ALOS PALSAR data", Forest Ecology and Management, Volume 262, Issue 9, 1 November 2011, Pages 1786-1798, 2011

[248] Moreira A., "An improved Multi-Look technique to produce SAR imagery", IEEE Intern. Radar Confer., Arlington, USA, 7-10 May 1990, S. 75-63, 1990

[249] Moreira A., Schreiber R., "Coregistration of interferometric SAR images using spectral diversity.", IEEE Transactions on Geoscience an Remote Sensing, 38(5):2179-2191, 2000

[250] Moreira A., Hajnsek I. Krieger G., Papathanassiou K., Eineder M., De Zan F. Younis M., Werner M., "Tandem-L: Monitoring the Earth's Dynamics with InSAR

and Pol-InSAR.", In: Proceedings of PolInSAR 2009, ESA-SP, pp. 1-5, spacebooks online. International Workshop on Applications of Polarimetry and Polarimetric Interferometry (Pol-InSAR), 2009-01-26 - 2009-01-30, Frascati, Italy, ISBN 978-92-9221-232-2, 2009

[251] Moreira A., Krieger G., Younis M., Hajnsek I., Papathanassiou K., Eineder M., De Zan F., "Tandem-L: A Mission Proposal for Monitoring Dynamic Earth Processes." In: Proceedings of IEEE International Geoscience and Remote Sensing Symposium (IGARSS), pp. 1-4, IEEE. IGARSS 2011, 2011-07-25 - 2011-07-29, Vancouver, Canada, 2011

[252] Moreira-Neto J. R., "Bewegungsextraktionsverfahren für Radar mit synthetischer Apertur", Forschungsbericht am DLR (Deutsche Forschungsanstalt für Luft- und Raumfahrt) Institut für Hochfrequenztechnik Oberpfaffenhofen. DLR-FB 92-31 Dissertation, September, 1992

[253] Murnaghan F. D., "On the field of values of a square matrix", N. A., S. Mathematics, 246 – 248, 1932

[254] Naesset E., Oekland T., "Estimating tree height and tree crown properties using airborne scanning laser in a boreal nature reserve." Remote Sensing of Environment 79:105–115, 2002

[255] Naesset E., "Comparison of precision of biomass estimates in regional field sample surveys and airborne LIDAR-assisted surveys in Hedmark County, Norway.", Remote Sensing of Environment, Vol. 130, pp. 108-120, 2013

[256] Nannini M., "Advanced Synthetic Aperture Radar Tomography: Processing Algorithms and Constellation Design", Dissertation, Forschungsbericht 2010-06, Deutsches Zentrum für Luft- und Raumfahrt e. V. in der Helmholtz-Gemeinschaft, ISSN 1434-8454, 2010

[257] Neumann M., Ferro-Famil L., Reigber A., " Estimation of Forest Structure, Ground, and Canopy Layer Characteristics From Multibaseline Polarimetric Interferometric SAR Data", Geoscience and Remote Sensing, IEEE Transactions on Volume: 48 , Issue: 3 , Part: 1, 2010

[258] Nilsson M., " Estimation of tree height and stand volume using an airborne LIDAR system", Remote Sensing of Environment 92: 292-301, 1996

[259] Nilsson M., Holmgren J., "Prediction of Forest Variables Using LIDAR Measurements with Different Footprint Sizes and Measurement Densities.", Proceedings of the ScandLaser Scientific Workshop on Airborne Laser Scanning of Forests, Sweden, 3–4 September 2003; pp. 125-133, 2003

[260] Odenthal-Kahabka, J. „Handreichung Sturmschadensbewältigung." Hrsg. Landesforstverwaltung Baden-Württemberg und Landesforsten Rheinland-Pfalz. **http://waldwissen.net**, 21.07.2008 (überarbeitete Version), "Handbuch Sturm - eine Arbeitshilfe für die Sturmschadensbewältigung", 2005

[261] Okada Y., Nakamura S., Iribe K., Yokota Y., Tsuji M., Hariu K., Kankaku Y., Suzuki S., Osawa Y. & Shimada M. "System characteristics for wide swath L-band SAR onboard ALOS-2/PALSAR-2", Asia Pacific Conference on Synthetic Aperture Radar (APSAR), Tsukuba, Japan, 2013

[262] Oliver C. & Quegan S., "Understanding Synthetic Aperture Radar Images", Artech House, p. 479, 1998

[263] Ossig B., Rappl H., Schneider T. . Unterstützung terrestrischer Inventuren aus dem Weltall? Verknüpfung von terrestrischen Inventuren und Fernerkundung. Allg. Forst Z. Waldwirtsch. Umweltvorsorge 66 (19): 11-13, 2011

[264]Page R. M., “The Origin of Radar”, Anchor Books Inc., New York, NY, 1977

[265]Pan et al, A Large and Persistent Carbon Sink in the World’s Forests, Science19 August 2011, Vol. 333 no. 6045 pp. 988-993, 2011

[266]Pandey D., “National Forest Inventory in India.” Paris, France : s.n., COMIFAC Workshop on Monitoring of reduction of emissions from forest degradation, 2008

[267]Papathanassiou K. P., Reigber A., Cloude S. R., “Vegetation and ground parameter estimation using polarimetric interferometry – Part I: the role of polarization.” Proceedings CEOS SAR, Toulouse, 26 – 29. OCT, 1999

[268]Papathanassiou K. P., Reigber A., Cloude S. R., “Vegetation and ground parameter estimation using polarimetric interferometry – Part II: parameter inversion and optimal polarization.” Proceedings CEOS SAR, Toulouse, 26 – 29. OCT, 1999

[269]Papathanassiou K. .P., and Cloude S. R., ‘‘Single-baseline Polarimetric SAR Interferometry’’, IEEE Transactions on Geoscience and Remote Sensing, vol. 39, no. 11, pp. 2352-2363, 2001

[270]Papathanassiou K.P. & Cloude S.R., “The Effect of Temporal Decorrelation on the Inversion of Forest Parameters from Pol-InSAR Data”, Proceedings IGARSS'03 (CD-ROM), Toulouse, France, 2003

[271]Papathanassiou K. P., **Kugler F.**, Lee S.-K., Marotti L., Hajnsek I., “Recent advances in Polarimetric SAR Interferometry for forest parameter estimation”, IEEE Radar Conference, RADAR’08, 2008

[272]Pardini M., Torano Caicoya A., **Kugler F.**, Lee S.-K., Hajnsek I., Papathanassiou K., “On the estimation of forest vertical structure from multibaseline polarimetric SAR data“, Proceedings of the IEEE International Geoscience and Remote Sensing Symposium (IGARSS) in Munich, 2012

[273]Pardini M., Caicoya Torano A., **Kugler F.**, Papathanassiou K., “Estimating and understanding vertical structure of forests from multibaseline TanDEM-X Pol-InSAR data”, Proceedings of the IEEE International Geoscience and Remote Sensing Symposium (IGARSS) in Melbourne, 2013

[274]Pedrotti, Bausch, Schmidt, “Optik Eine Einführung”, Prentice Hall Verlag GmbH, ISBN 3-8272-9510-6, 1993

[275]PEFC, **https://pefc.de/**, 06.11.2013

[276]Pekkarinen A., Reithmaier L. & Strobl, P., “Pan-European forest/non-forest mapping with Landsat ETM+ and CORINE land cover 2000 data.”, ISPRS Journal of Photogrammetry and Remote Sensing, Vol. 64, pp. 171-183., 2009

[277]Perko R., Raggam H., Deutscher J., Gutjahr K., Schardt M., “Forest assessment using high resolution SAR data in x-band.” Remote Sensing of Environment, 3, 792–815, 2011

[278]Peterson B., Dubayah R., Hyde P., Hofton, M., Blair J. B., and Fites-Kaufman J., “Use of LIDAR for Forest Inventory and Forest Management Application”, Proceedings of the seventh Annual Forest Inventory and Analysis Symposium, 2005

[279]Potapov P., Turubanova S., & Hansen M. C., “Regional-scale boreal forest cover and change mapping using Landsat data composites for European Russia.”, Remote Sensing of Environment, Vol. 115, pp. 548-561, 2011

[280]Praks J. Hallikainen M., **Kugler F.**, Papathanassiou K., & Hajnsek I., “L-band Polarimetric Interferometry in Boreal Forest Parameter Estimation, a Case study.“, IEEE International Geoscience and Remote Sensing Symposium (IGARSS), 2006-07-31 - 2006-08-04, Denver, Colorado (USA), 2006

[281] Praks J., Kugler F., Papathanssiou K. P., Hajnsek I. & Hallikainen M., "Tree height estimation for boreal forest by means of L and X band POL-InSAR and HUTSCAT scatterometer", IEEE Transactions on Geoscience and Remote Sensing letters, vol. 37, Issue3, pp. 466 – 470, 2007, © [2007] IEEE

[282] Praks J., **Kugler F.**, Papathanassiou K., Hallikainen M., "Forest Height Estimates for Boreal Forest Using L and X Band Pol-InSAR and Hutscat Scatterometer." Proceedings of the International Workshop on Applications of Polarimetry and Polarimetric Interferometry (Pol-InSAR), 2007-01-22 - 2007-01-26, Frascati, Italy, 2007

[283] Praks J., **Kugler F.**, Papathanassiou K., Hallikainen M., "X-band Extinction in Boreal Forest: Estimation by Using E-SAR Pol-InSAR and HUTSCAT.", Proceedings of the IEEE Geoscience and Remote Sensing Symposium (IGARSS), 2007-07-23 - 2007-07-27, Barcelona, Spain, 2007

[284] Praks, J., Hallikainen M., **Kugler F.**, Papathanassiou K. P., "Coherence Tomography for Boreal Forest: Comparison with HUTSCAT Scatterometer Measurements." Proceedings of the European Conference on Synthetic Aperture Radar (EUSAR), 2008-06-02 - 2008-06-05, Friedrichshafen, Germany, 2008

[285] Praks J., **Kugler F.**, Hyypä J., Papathanassiou K., Hallikainen M., "SAR Coherence Tomography for Boreal Forest with Aid of Laser Measurements." Proceedings of the IEEE Geoscience and Remote Sensing Symposium (IGARSS), 2008-07-06 - 2008-07-11, Boston, Massachusetts, USA, 2008

[286] Praks J., Antropov O., Hallikainen M. T., "LIDAR-Aided SAR Interferometry Studies in Boreal Forest: Scattering Phase Center and Extinction Coefficient at X- and L-band", IEEE Transaction on Geoscience and Remote Sensing, vol. 50, Nr.10, pp. 3831 – 3843, October 2012

[287] Pretzsch, H., „Grundlagen der Waldwachstumsforschung", Parey Buchverlag, ISBN 2-8263-3223-7, 2002

[288] Pretzsch, H., Biber, P. and Dursky, J., "The single tree-based stand simulator SILVA: construction, application and evaluation." Forest Ecology and Management 162 3-21, 2002

[289] Pretzsch H., "Forest Dynamics, Growth and Yield: From Measurement to Model", Springer Verlag Berlin Heidelberg, ISBN 978-3-540-88306-7, 2009

[290] Prien S., „Prioritäten bei der Aufarbeitung von Sturmholz", AFZ-Der Wald 9/ pp 464-467, 2007

[291] Prodan M. „Holzmesslehre", translation: "Wood Mensuration" J. D. Sauerländer's Verlag Frankfurt a. Main, 1965

[292] Quegan S., Chave J., Dall J., Le Toan T., Papathanassiou K., Rocca F., Saatchi S., Scipal K., Shugart H., Ulander L., Williams M., "THE SCIENCE AND MEASUREMENT CONCEPTS UNDERLYING THE BIOMASS MISSION", IEEE Geoscience and Remote Sensing Symposium (IGARSS), Munich, 22-27 July 2012

[293] Raggam H., Gutjahr K., Perko, R., Schardt M., "Assessment of the Stereo-Radargrammetric Mapping Potential of TerraSAR-X Multibeam Spotlight data", IEEE Geoscience and Remote Sensing, Transactions on Volume: 48 , Issue: 2, 2010

[294] Ramongassie S., Valle P., Arpesi P. G. Heliere F., "P-band SAR instrument for BIOMASS", Proceedings of EUSAR 2014; 10th European Conference on Synthetic Aperture Radar, Berlin, 2014

[295]Redmann M., Ossit B. & Weinreich A., „Perspektiven für eine wertschöpfende mittelfristige Betriebsplanung“, AFZ-Der Wald, pp. 28-30, 21/2013

[296]Reese H., Nilsson M., Granqvist Pahlén T., Hagner O., Joyce S., Tingelöf U., Egberth M., and Olsson H., “Countrywide Estimates of Forest Variables Using Satellite Data and Field Data from the National Forest Inventory“, Bio One, Ambio Vol. 32 No. 8, Royal Swedish Academy of Sciences 2003

[297]Reigber A., Moreira A., “First demonstration of airborne SAR tomography using multibaseline L-band data”, IEEE Geoscience and Remote Sensing, Vol. 38 No. 5 Part 1 pp. 2142 – 2152, 2000

[298]Reigber A., “Airborne Polarimetric SAR Tomography“, Dissertation, Forschungsbericht 2002-02, Deutsches Zentrum für Luft- und Raumfahrt e. V. in der Helmholtz-Gemeinschaft, ISSN 1434-8454, 2002

[299]Rocca F., “Modeling interferogram stacks,” IEEE Transactions on Geoscience and Remote Sensing., vol. 30, no. 5, pp. 3289–3299, Oct. 2007

[300]Rogers M. N., “From points to products – business benefits from LIDAR using ArcGIS”, http://www.saforestrymag.co.za/articles/detail/from_points_to_products_business_benefits_from_lidar_using_arcgis, June 2013

[301]Rosen P. A., Hensley S., Joughin I. R., Li F. K., Madsen S. N., Rodriguez E., & Goldstein R., “Synthetic Aperture Radar Interferometry”, Proceedings IEEE, vol. 88, no. 3, pp. 333-382, 2000

[302]Rosenqvist A., Shimada M. & Watanabe M.,“ALOS PALSAR: Technical outline and mission concepts”, 4th International Symposium on Retrieval of Bio- and Geophysical Parameters from SAR Data for Land Applications Innsbruck, Austria, November 16-19, 2004

[303]Saatchi S. S., Halligan K., Despain D. G., & Crabtree R. L., “Estimation of forest fuel load from radar remote sensing.”, IEEE Transactions on Geoscience and Remote Sensing, 45(6), 1726–1740, 2007

[304]Sagl W., “Bewertung in Forstbetrieben“, Blackwell Wissenschafts-Verlag, Berlin, Wien 1995, ISBN 3-8263-3060-9, 1995

[305]Salisch H. v., “Forstästhetik”, neue Auflage von 2009, Verlag Kessel,, ISBN 978-3-941300-06-4, 1911

[306]Sandberg G., Ulander L. M. H., Fransson J. E. S., Holmgren J. & Le Toan T., “L-band versus P-band SAR for biomass retrieval in semi-boreal forest”, Remote Sensing of Environment, 2011

[307]Santoro M., Askne J., Smith G., Fransson J. E. S., “Stem volume retrieval in boreal forests from ERS 1/2 interferometry”, Remote Sensing of Environment, 81(1): 19 – 35, 2002

[308]Santoro, M, “Clear-cut detection in Swedish boreal forest using multi-temporal ALOS PALSAR backscatter data.”, IEEE Journal of Selected Topics in Applied Earth Observations and Remote Sensing, Vol. 3, pp. 618-631, 2010

[309]Santoro M., et al., “Retrieval of growing stock volume in boreal forest using hyper-temporal series of Envisat ASAR ScanSAR backscatter measurements”, Remote Sensing of Environment, vol. 114, pp. 490-507, 2011

[310]Santos J. R., Mura J. C., Kux H. J. H., Garcia C. E., Kuntz S., Brown I. F., Pantoja N. V., “Classification of TerraSAR-X imagery for the characterization of Amazon tropical forests.” Proceedings of the 30th EARSeL Symposium: Remote Sensing for Science, Education and Culture, 31 May - 3 June 2010, pp. 329-334, 2010

[311] Sauer S., “Interferometric SAR Remote Sensing of Urban Areas at L-Band Using Multibaseline and Polarimetric Spectral Analysis Techniques“, Dissertation, Forschungsbericht 2008-26, Deutsches Zentrum für Luft- und Raumfahrt e. V. in der Helmholtz-Gemeinschaft, ISSN 1434-8454, 2008

[312] Sauer S., Ferro-Famil L., Reigber A., Pottier E., “Polarimetric Dual-Baseline InSAR Building Height Estimation at L-Band”, IEEE Geoscience and Remote Sensing Letters Volume: 6, Issue: 3, 2009

[313] Sauer S., Ferro-Famil L., Reigber A., Pottier E., “3D Urban Remote Sensing using Dual-baseline POL-InSAR Images at L-Band”, Proceedings of the IEEE International Geoscience and Remote Sensing Symposium (IGARSS) 06.07.2008 – 11.07.2008, Boston, USA, 2008

[314] Sauer S., **Kugler F.**, Lee S.- K., Papathanassiou K., “Polarimetric Decomposition for forest Biomass Retrieval“, Proceedings of the IEEE Geoscience and Remote Sensing Symposium (IGARSS 2010), 2010-07-26 - 2010-07-30, Honolulu, Hawaii, USA, 2010

[315] Sauer S., Ferro-Famil L., Reigber A., Pottier E., “Three-Dimensional Imaging and Scattering Mechanism Estimation Over Urban Scenes Using Dual-Baseline Polarimetric InSAR Observations at L-Band”, Transactions on Geoscience and Remote Sensing, IEEE Volume: 49 , Issue: 11 , Part: 2, 2011

[316] Sauer S., **Kugler F.**, Lee, S.-K., Papathanassiou K., “Polarimetric Decomposition Applied to 3D SAR Images of Forested Terrain“, 8th European Conference on Synthetic Aperture Radar (EUSAR), 2010

[317] Sauer S., Jagdhuber T., **Kugler F.**, Lee F.-K., Papathanassiou K., “Orientation Angle Estimation Over Forested Terrain Using P-band POLSAR Data”, Proceedings of the IEEE International Geoscience and Remote Sensing Symposium (IGARSS) 22.07.2012 – 27.07.2012 in Munich, 2012

[318] Scheiber R., “Hochauflösende Interferometrie für Radar mit synthetischer Apertur”, Dissertation, Forschungsbericht 2004-12, Deutsches Zentrum für Luft- und Raumfahrt e. V. in der Helmholtz-Gemeinschaft, ISSN 1434-8454, 2004

[319] Schlund M., von Poncet F., Hoekman D., Kuntz S., Schmullius C., “Importance of bistatic SAR features from TanDEM-X for forest mapping and monitoring.”, Remote Sensing of Environment, 2013

[320] Schmullius C., Koch B., “ Literaturstudie Übersicht Satelliten-gestützter Fernerkundungsverfahren zur Unterstützung von UN-REDD Projektbericht“, Förderkennzeichen: 50EE108, Bundesministerium für Wirtschaft und Technologie, 2011

[321] Schwerdtfeger F., “Waldkrankheiten“, translation: “forest diseases“, Paul Parey Verlag, ISBN 3-490-08516-7, 1970

[322] Seizinger E., “Überarbeitung der nationalen Standards von FSC Deutschland”, AFZ- Der Wald 9/2014, pp. 35-36

[323] Sexton O. J., Bax T., Siqueira P., Swenson J. J., Hensley S., “A comparison of LIDAR, radar and field measurements of canopy height in pine and hardwood forests of southeastern North America”, Forest Ecology and Management, 257 (2009) 1136 – 1147, 2009

[324] Sharma, J.J., Hajnsek I., Papathanassiou K.P., Moreira A., “Estimation of Glacier Ice Extinction Using Long-Wavelength Airborne Pol-InSAR”, IEEE Transactions on Geoscience and Remote Sensing, Volume: 51 , Issue: 6 , Page(s): 3715 – 3732, 2013

[325]Shi L, Zhao S, Tang Z, Fang J “The Changes in China's Forests: An Analysis Using the Forest Identity.” PLoS ONE 6(6), 2011

[326]Shimada M., Itoh T., Motooka T., Watanabe M., Shiraishi T., Thapa R., Lucas R., “New global forest/non-forest maps from ALOS PALSAR data (2007–2010)”, Remote Sensing of Environment, early access, Mai 2014

[327]Simard M., Zhang K., Ross M.S., Rivera Monroy V.H., Castaeda Moya E., Twilley R., “Using Shuttle Radar Topography Mission Elevation Data to Map Mangrove Forest Height in the Caribbean”, IEEE International Conference on Geoscience and Remote Sensing IGARSS, 2006

[328]Simard M., et al., “Mapping forest canopy height globally with spaceborne LIDAR”, Journal of geophysical research, vol. 116, G04021, 2011.

[329]Simonett D.S., “The development and principles of remote Sensing“, MRS, ASP, 2nd Edition, pp. 1-30, 1983

[330]Sitte P., Ziegler H., Ehrendorfer F., Bresinsky A., ”Straßburger Lehrbuch der Botanik“, Spektrum Akademischer Verlag Gustav Fischer, 34. Neubearbeitete Auflage, ISBN 3-8274-0779-6, 1999

[331]Souza Jr. C., “Mapping and monitoring deforestation and forest degradation in the Brazilian Amazon.” Jena, Germany : s.n., GOFC-GOLD Symposium on Forest and Land Cover Observations.”, 2006

[332]Spruce J. P., “Assessment of MODIS NDVI time series data products for detecting forest defoliation by gypsy moth outbreaks.”, Remote Sensing of Environment, Vol. 115, pp. 427-437, 2011

[333]Solberg S., Astrup R., Gobakken T., Næsset E., & Weydahl D.J., “Estimating spruce and pine biomass with interferometric X-band SAR.” Remote Sensing of Environment 114: 2353-2360, 2010

[334]Solberg S., Astrup R., Breidenbach J., Nilsen, B. & Weydahl, D. J. “Monitoring spruce volume and biomass with InSAR data from TanDEM-X.” Remote Sensing of Environment 139: 60-67, 2013

[335]Song C., “Optical remote sensing of forest leaf area index and biomass”, Progress in Physical Geography 1-16, 2012

[336]Staupendahl K., Gadow K., “Eingriffsinventuren und dynamisches Betriebswerk – Instrumente der operativen Planung im Forstbetrieb“, Forstarchiv 79 Jhrg, pp. 16 – 27, 2008

[337]Stibig H.-J., Achard F. & Fritz S., “A new forest cover map of continental Southeast Asia derived from SPOT-VEGETATION satellite imagery.”, Applied Vegetation Science, Vol. 7, pp. 153-162. 63, 2004

[338]StMELF – Bayer Staatsministerium für Ernährung, Landwirtschaft und Forsten (1982). Richtlinien für die mittel- und Langfristige Forstbetriebsplanung in der Bayerischen Staatsforstverwaltung (Forsteinrichtungsrichtlinien) FER 1982, aktualisiert 1990 u. 1991

[339]Straubb C., Seitz R., “Schätzung von forstlichen Kenngrößen auf der Grundlage von Punktwolken aus digitaler Photogrammetrie und flugzeuggetragener Laserscannermessung“, DGPF Tagungsband 21/2012, S. 75 – 82, 2012

[340]Sun G., Ranson K. J., “Forest vertical structure from GLAS: An evaluation using LVIS and SRTM data”, Remote Sensing of Environment, 112, pp. 107 – 117, 2008

[341]Suzuki S., Kankaku Y., Shimada M., “ALOS-2 Acquisition Strategy”, IEEE Geoscience and Remote Sensing Symposium (IGARSS), Melbourne, Australia, 2013

[342] Tabb M. & Carande R., "Robust Inversion of Vegetation Structure Parameters from Low Frequency Polarimetric Interferometric SAR", Proceedings of the IEEE International Geoscience and Remote Sensing Symposium (IGARSS), 9-13 July, Sydney, Australia, 2001

[343] TanDEM-X Ground Segment, T. Fritz, S. Duque, B. Bräutigam, J. L. Bueso Bello, G. Krieger, M. Zink "TanDEM-X Experimental Product Description", Remote Sensing Technology Institute, https://tandemx-science.dlr.de/, 2012

[344] Tebaldini S., Rocca F., "Multibaseline Polarimetric SAR Tomography of a Boreal Forest at P- and L-Bands.", IEEE Transactions on Geoscience and Remote Sensing, 01/2012; 50:232-246., 2012

[345] Le Toan T., Beaudoin A., Riom J. & Guyon, D., "Relating forest biomass to SAR data." IEEE Transactions on Geoscience and Remote Sensing, 30, 403–411, 1992

[346] Le Toan T., Quegan S., Davidson M. W. J., Baltzer. H., Paillou P., Papathanassiou K., Plummer S., Rocca F., Saatchi S., Shugart H., Ulander L., "The BIOMASS mission: Mapping global forest biomass to better understand the terrestrial carbon cycle.", Remote Sensing of Environment, 115, pp. 2850-2860, 2011

[347] Tomiyasu K., "Tutorial Review of Synthetic Aperture Radar", Proceedings IGARSS 1978, vol. 66, no.5, pp. 563 – 583, 1978

[348] Tomppo E., Haakana M., Katila M., Peräsaari J., "Multi-Source National Forest Inventory", Springer Science + Business Media, ISBN 978-1-4020-8713-4, 2008

[349] Touzi R., Lopes A., "Statistics of the Stokes Parameters and of the Complex Coherence Parameters in One-Look and Multilook Speckle Fields", IEEE Transactions on Geoscience and Remote Sensing, vol. 34, no. 2, pp. 519-531, 1996

[350] Touzi R., Lopes A., Bruniquel J., Vachon P. W., "Coherence Estimation for SAR Imagery", ", IEEE Transactions on Geoscience and Remote Sensing, vol. 1, no. 37, pp. 135-149, 1999

[351] Trenberth K. E., Jones P.D., Ambenje P., Bojariu R., Easterling D., Klein Tank A., Parker D., Rahimzadeh F., Renwick J.A., Rusticucci M., Soden B. & Zhai P., "Observations: Surface and Atmospheric Climate Change. In: Climate Change 2007: The Physical Science Basis. Contribution of Working Group I to the Fourth Assessment Report of the Intergovernmental Panel on Climate Change [Solomon, S., D. Qin, M. Manning, Z. Chen, M. Marquis, K. B. Averyt, M. Tignor and H. L. Miller (eds.)]. Cambridge University Press, Cambridge, United Kingdom and New York, NY, USA, 2007

[352] Treuhaft R. N., Madsen S.N., Moghaddam M., & van Zyl J.J., "Vegetation Characteristics and Underlying Topography from Interferometric Data", Radio Science, vol. 31, pp. 1449-1495, 1996.

[353] Treuhaft R. and Cloude S.R., "The Structure of Oriented Vegetation from Polarimetric Interferometry", IEEE Transactions on Geoscience and Remote Sensing, vol. 37, no. 5, pp. 2620-2624, 1999

[354] Treuhaft R. N. & Siqueira P. R., "The Vertical Structure of Vegetated Land Surfaces from Interferometric and Polarimetric Radar", Radio Science, vol. 35, no. 1, pp. 141-177, 2000

[355] Treuhaft R. N., Chapman B. D., dos Santos J. R., Gonçalves F. G., Dutra L. V., Graça P. M. L. A. & Drake J. B., "Vegetation profiles in tropical forests from multibaseline interferometric synthetic aperture radar, field, and LIDAR measurements." Journal of Geophysical Research, 114:1-16, December 2009

[356] Treuhaft R. N., Gonçalves F. G., Drake J. B., Chapman B. D., dos Santos J. R., Dutra L. V., Graça P. M. L. A., & Purcell G. H., "Biomass estimation in a tropical wet forest using Fourier transforms of profiles from LIDAR or interferometric SAR", Geophysical Research Letters, Volume 37, Issue 23, December, 2010

[357] Treuhaft R., Gonçalves F., dos Santos J.R., Keller M., Palace M., Madsen S.N., Sullivan F., Graça P.M.L.A., " Tropical-Forest Biomass Estimation at X-Band From the Spaceborne TanDEM-X Interferometer", IEEE Geoscience and Remote Sensing letters, Volume: 12, Issue: 2, 2015

[358] Ulaby F. T., Moore R. K., Fung A. K., "Microwave remote sensing: active and passive. Vol.", Radar remote sensing and surface scattering and emission theory", Addision-Wesley, Reading, 1982

[359] Ulander L.M.H., Hellsten H. & Stenström G., "Synthetic aperture radar processing using fast factorized back projection", IEEE Trans. Aerosp. Electron. Syst., vol.39, no.3, pp. 760 – 776, July 2003

[360] UNFCC (United Nations Framework Convention on Climate Change), "The Marrakesh Accords & The Marrakesh Declaration", 2002.

[361] UNECE, United Nations Economic Commission for Europe, „State of Europe's Forests 2011", UNECE FAO Forestry Department, 2011

[362] US government, Forest and Rangeland Renewable Resources Planning Act of 1974

[363] US government, National Forest Management Act of 1976

[364] Vanclay J. K., "Assessing site productivity in tropical moist forests: a review", Forest Ecology and Management, Volume 54, Issues 1–4, November 1992, Pages 257-287, 1992

[365] Vastaranta M., Holopainen M., Karjalainen M., Kankare V., Hyyppä J., Kaasalainen S., "TerraSAR-X stereo radargrammetry and airborne scanning LIDAR height metrics in imputation of forest aboveground biomass and stem volume." IEEE Transactions on Geoscience and Remote Sensing, 2014

[366] Verhegghen A., "Mapping Congo Basin forest types from 300 m and 1 km multi-sensor time series for carbon stocks and forest areas estimation.", Biogeosciences Discuss, Vol. 9, pp. 7499-7553, 2012

[367] Vidal, C., Lanz, A., Tomppo, E., Schadauer, K., Gschwantner, T., di Cosmo, L. & Robert, N., „Establishing Forest Inventory Reference Definitions for Forest and Growing Stock: a Study towards Common Reporting", Silva Fennica 42(2) research articles, 2008

[368] Waite W.P., "Historical Development of Imaging Radar In: Geoscience Applications of Imaging Radar Systems", RSMES (Remote Sensing of the Electro Magnetic Spectrum). (A.J. Lewis, ed.) Association of American Geographers. 3(3):1-22, 1976

[369] Wagner W., "Large-scale mapping of boreal forest in SIBERIA using ERS tandem coherence and JERS backscatter data", Remote Sensing of Environment, vol. 85, pp. 125-144, 2003

[370] Walker W.S., Pierce L.E., Kellndorfer J.M., Dobson M.C., Hunsaker C.T., Fites J.A., "A comparison of forest canopy height estimates derived from SRTM and TOPSAR in the Sierra Nevada of California", IEEE International Geoscience and Remote Sensing Symposium, 2004. IGARSS '04. Proceedings. 2004

[371] Walker W. S., "Large-area classification and mapping of forest and land cover in the Brazilian Amazon: a comparative analysis of ALOS/PALSAR and Landsat data

sources.", IEEE Journal of Selected Topics in Applied Earth Observations and Remote Sensing, Vol. 3, pp. 594-604, 2010

[372] Wang G., Weng Q., "Remote Sensing of Natural Resources Taylor and Francis Series in Remote Sensing Applications" CRC Press Taylor and Francis group, ISBN 978-1-4665-5692-8, 2014.

[373] Way J., Evans D., Elachi C., "The SIR-C/X-SAR mission", IEEE Geoscience and Remote Sensing Symposium (IGARSS), Milan Italy 1993

[374] Weidenbach M., Wezyk P., Tompalski P., Hoffmann K., & Martens S., "Erfassung von Einzelbaumparametern mit Airborne-Laser-Scanning-Daten", AFZ-Der Wald, 21/2012, pp 12- 15, 2012

[375] Weise W., "Ertragstafel für die Kiefer", Berlin, 1880

[376] Wohlrab B., Ernstberger H., Meuser A., Sokollek V., "Landschaftswasserhaushalt", Verlag Paul Parey Hamburg und Berlin, ISBN 3-490-19116-1, 1992

[377] WRI, World Resource Institute, „World Resources 2000 – 2001: People and ecosystem: The fraying web of life", ISBN: 1-56973-443-7, 2005

[378] Wu S.-T., "Potential application of multipolarization SAR for pine- plantation biomass estimation", IEEE Transactions on Geoscience and Remote Sensing, vol.25, Issue: 3, 403 – 409, 1987

[379] Wulder M. A., Bater C.W., Coops N. C., Hilker T. & White J. C., "The role of LIDAR in sustainable forest management", The Forestry Chronicle Vol.84, N0. 6, 2008

[380] Yamakura T., Hagihara A., Sukardjo S., and Ogawa H., "Aboveground biomass of tropical rain forest stands in Indonesia Borneo", Vegetation 68: 71 – 82, 1986

[381] Yude P., Birdsey R. A., Fang J., Houghton R., Kauppi P. E., Kurz W. A., Phillips O. L., Shvidenko A., Lewis S. L., Canadell J. G., Ciais P., Jackson R. B., Pacala S. W., McGuire A. D., Piao S., Rautiainen A., Sitch S., Hayes D., "A Large and Persistent Carbon Sink in the World's Forests", Science, VOL 333, August 2011

[382] Zebker H.A., & Villasenor J., "Decorrelation in interferometric radar echoes", IEEE Trans. Geoscience and Remote Sensing, vol. 30, no. 5, pp.950-959, 1992

[383] Zhu Z., Woodcock C. E. & Olofsson P., "Continuous monitoring of forest disturbance using all available Landsat imagery.", Remote Sensing of Environment, Vol. 122, pp. 75-91, 2012

[384] Ziegeler M., Schneider E.-M., „Steuerung der forstbetrieblichen Vermögensentwicklung", AFZ-Der Wald, pp. 24 – 27, 21/2013

[385] De Zan F., Krieger G., López-Dekker P., "On Some Spectral Properties of TanDEM-X Interferograms Over Forested Areas", IEEE Geoscience and Remote Sensing Letters, vol. 10, No. 1, January 2013

[386] van Zyl J. J., Kim Yunjin M. A., "Requirements for Model-based Polarimetric Decompositions", International Geoscience and Remote Symposium (IGARSS 08), Proceedings, Pages: V - 417 - V – 420, Boston 7.-11. July 2008

[387] **http://www.fire.uni-freiburg.de** from 31.08.2013

[388] **http://bfw.ac.at/ort1/Vortraege_als_pdf/verklausung/Waldkatastrophenplan_OOE_Jasser.pdf**, information from 31.08.2013

[389] **http://inventaire-forestier.ign.fr/spip/IMG/pdf/120314-2p-newmetho.pdf**, information from 31.08.2013

[390] **http://inventaire-forestier.ign.fr/spip/spip.php?rubrique4, information** from 31.08.2013

[391] http://www.cbfp.org/Stateoftheforest.html, „Les Foréts du Bassin du Congo État des Foréts 2010“, information from 31.08.2013

[392] http://www.smul.sachsen.de/sbs/download/Vortrag_Polaczek.pdf, November 2013

[393] http://video.esri.com/watch/1573/improving-operational-planning-using-lidar-forest-inventories-and-gis, November 2013

[394] http://blomasa.com/news/bergvik-skog-forestry-using-lidar-for-better-decision-making.html, November 2013

Appendix I: Publication list

Journal publications:

1. Praks J., **Kugler F**., Papathanssiou K. P., Hajnsek I. & Hallikainen M., "Tree height estimation for boreal forest by means of L and X band POL-InSAR and HUTSCAT scatterometer", IEEE Transactions on Geoscience and Remote Sensing letters, vol. 37, issue 3, pp. 466 – 470, 2007
   DOI: 10.1109/LGRS.2007.898083
2. Hajnsek I., **Kugler F.**, Lee S.-K., Papathanassiou K., "Tropical Forest Parameter Estimation by means of Pol-InSAR: The INDREX II Campaign", IEEE Transactions on Geoscience and Remote Sensing, vol. 47, No. 2, 2009
   DOI: 10.1109/LGRS.2007.898083
3. Lee S.-K., **Kugler F.**, Papathanassiou K. & Hajnsek I., "Quantification of Temporal Decorrelation Effects at L-band for Polarimetric SAR Interferometry Applications", IEEE Transactions on Geoscience and Remote Sensing, IEEE Journal of Selected Topics in Applied Earth Observations and Remote Sensing, vol. 6, No. 3, June, 2013
   DOI: 10.1109/JSTARS.2013.2253448
4. Krieger G., Zink M., Bachmann M., Bräutigam B., Schulze D., Martone M., Rizzoli P., Steinbrecher U., Antony J. W., De Zan F., Hajnsek I., Papathanassiou K., **Kugler F.**, Rodriguez Cassola M., Younis M., Baumgartner S., López-Dekker P., Prats P., Moreira A., "TanDEM-X: A radar interferometer with two formation-flying satellites", Acta Astronautica 89 83–98, 2013
   DOI: 10.1016/j.actaastro.2013.03.008
5. **Kugler F.**, Schulze D., Hajnsek I., Pretzsch H., Papathanassiou K.P., „TanDEM-X Pol-InSAR Performance for Forest Height Estimation", IEEE Transactions on Geoscience and Remote Sensing, vol. 52 , Issue. 10, 2014
   DOI: 10.1109/TGRS.2013.2296533
6. **Kugler F.**, Lee S.-K., Hajnsek I., Papathanassiou K., "Forest Height Estimation by means of Pol-InSAR: The role of the vertical wavenumber", IEEE Transactions on Geoscience and Remote Sensing, vol. 53, Issue. 10, 2015
   DOI: 10.1109/TGRS.2015.2420996
7. Caicoya T. A., **Kugler F.**, Pretzsch H. and Papathanassiou K., "Forest vertical structure characterization for estimating forest aboveground biomass", Canadian Journal of Forest Research, 46(1), 2016
   DOI: 10.1139/cjfr-2015-0052
8. Caicoya T. A., **Kugler F.**, Hajnsek I., Papathanassiou K., "Large Scale Biomass Classification in Boreal Forests with TanDEM-X Data", IEEE Transactions on Geoscience and Remote Sensing, Volume: PP, Issue: 99, 2016
   DOI: 10.1109/TGRS.2016.2575542

9. Abdullahi S., **Kugler F.**, Pretzsch H., "Prediction of stem volume in complex temperate forest stands using TanDEM-X SAR data", Remote Sensing of Environment, Volume 174, Pages 197–211, 2016 DOI:10.1016/j.rse.2015.12.012

Selected Conference publications

1. Hajnsek I., Kugler F., Papathanassiou K., Horn R., Scheiber R., Moreira A., Hoekman D., Davidson M., "INDREX II – Indonesian airborne radar experiment campaign over tropical forest in L- and P-band: first results", Proceedings of the IEEE international Geoscience and Remote Sensing Symposium IGARSS 05, Seoul, Korea, Volume 6, P. 4335 – 4338, 2005
2. Hajnsek I., Kugler F., Papathanassiou K., Scheiber R., Horn R., Moreira A., Hoekman D., Davidson M., Attema E., "INDREX II Indonesian Airborne Radar Experiment campaign over tropical forest in L- and P-band, Proceedings of the 2nd International Workshop POLinSAR 2005 (CD), 17-21 January, Frascati, Italy, 2005
3. Kugler F., Papathanassiou K., Hajnsek I., Hoekman D., "INDREX-II - Tropical Forest Height Estimation with L- and P-Band Polarimetric Interferometric SAR.", European Conference on Synthetic Aperture Radar (EUSAR), 2006-05-16 - 2006-05-18, Dresden, Germany, 2006
4. Kugler F., Koudogbo F. N., Papathanassiou K. P. & K. Gutjahr , "Frequency Effects in Pol-InSAR Forest Height Estimation", Proceedings of European Conference on Synthetic Aperture Radar EUSAR'06, Dresden, Germany, May 16-18, 2006
5. Kugler F., Papathanassiou K. P., Hajnsek I. & Hoekman D., "Forest Height Estimation in Tropical Rain Forest using Pol-InSAR Techniques", Proceedings of the IEEE International Geoscience and Remote Sensing Symposium (IGARSS), 31 July -04 August, Denver, USA, 2006.
6. Mette T., Kugler F., Papathanassiou K., Hajnsek I., "Forest and the Random Volume over Ground - Nature and Effect of 3 Possible Error Types." European Conference on Synthetic Aperture Radar (EUSAR), 2006-05-16 - 2006-05-18, Dresden, Germany, 2006
7. Praks J. Hallikainen M., Kugler F., Papathanassiou K., & Hajnsek I., "L-band Polarimetric Interferometry in Boreal Forest Parameter Estimation, a Case study.", IEEE International Geoscience and Remote Sensing Symposium (IGARSS), 2006-07-31 - 2006-08-04, Denver, Colorado (USA), 2006
8. Ferro-Famil L., Kugler F., Pottier E., Lee J.-S., "Forest Mapping and Classification at L-band using Pol-InSAR Optimal Coherence Set statistics", Proceedings on the 6th European Conference on Synthetic Aperture Radar (EUSAR), 2006
9. Kugler F., Coscia A., Papathanassiou K., Hajnsek I., "Potential of forest height estimation using X band by means of two different inversion scenarios." Proceedings of the IEEE Geoscience and Remote Sensing Symposium (IGARSS), 2007-07-23 - 2007-07-27, Barcelona, Spain, 2007

10. Praks J., Kugler F., Papathanassiou K., Hallikainen M., “Forest Height Estimates for Boreal Forest Using L and X band Pol-InSAR and Hutscat Scatterometer.“ Proceedings of the International Workshop on Applications of Polarimetry and Polarimetric Interferometry (Pol-InSAR), 2007-01-22 - 2007-01-26, Frascati, Italy, 2007
11. Praks J., Kugler F., Papathanassiou K., Hallikainen M., “X-band Extinction in Boreal Forest: Estimation by Using E-SAR Pol-InSAR and HUTSCAT.”, Proceedings of the IEEE Geoscience and Remote Sensing Symposium (IGARSS), 2007-07-23 - 2007-07-27, Barcelona, Spain, 2007
12. Lee S.-K., Kugler, F., Hajnsek I. & Papathanassiou K. P., “Quantifying Temporal Decorrelation over Boreal Forest at L-and P-band”, Proceedings of European Conference on Synthetic Aperture Radar, EUSAR’08, Friedrichshafen, Germany, 2008
13. Praks, J., Hallikainen M., Kugler F., Papathanassiou K. P., “Coherence Tomography for Boreal Forest: Comparison with HUTSCAT Scatterometer Measurements.“ Proceedings of the European Conference on Synthetic Aperture Radar (EUSAR), 2008-06-02 - 2008-06-05, Friedrichshafen, Germany, 2008
14. Praks J., Kugler F., Hyypä J., Papathanassiou K., Hallikainen M., “SAR Coherence Tomography for Boreal Forest with Aid of Laser Measurements.“ Proceedings of the IEEE Geoscience and Remote Sensing Symposium (IGARSS), 2008-07-06 - 2008-07-11, Boston, Massachusetts, USA, 2008
15. Papathanassiou K. P., Kugler F., Lee S.-K., Marotti L., Hajnsek I., “Recent advances in Polarimetric SAR Interferometry for forest parameter estimation”, IEEE Radar Conference, RADAR’08, 2008
16. Kugler F., Lee S. - K., Papathanassiou K. P., “Estimation of Forest Vertical Structure Parameter by means on Multi-baseline Pol-InSAR”, Proceedings Geoscience and Remote Sensing Symposium IGARSS (Cape Town), 2009
17. Lee S. K., Kugler F., Hajnsek I., Papathanassiou K. P., “The Impact of Temporal Decorrelation over Forest Terrain in Polarimetric SAR Interferometry”, Proceedings of the 5th International Workshop POLinSAR 2009, 26.-30. January, Frascati, Italy 2009
18. Lee S.-K., Kugler F., Hajnsek I., Papathanassiou K. P., “Polarimetric SAR interferometry for forest applications at P-band: Potential and challenges”, Proceedings of IEEE international Geoscience and Remote Sensing Symposium (IGARSS), 2009-07-12 - 2009-07-17, Cape Town, South Africa, 2009
19. Kugler F., Sauer S., Lee S. - K., Papathanassiou K., Hajnsek I., “Potential of TanDEM-X for forest parameter estimation“, 8th European Conference on Synthetic Aperture Radar (EUSAR) Aachen, 2010
20. Caicoya A. T., Kugler F., Papathanassiou K., Biber P., Pretzsch H., ” Biomass estimation as a function of vertical forest structure and forest height - Potential and limitations for Radar Remote Sensing”, 8th European Conference on Synthetic Aperture Radar (EUSAR), 2010
21. Sauer S., Kugler F., Lee, S.-K., Papathanassiou K., “Polarimetric Decomposition Applied to 3D SAR Images of Forested Terrain“, 8th European Conference on Synthetic Aperture Radar (EUSAR), 2010

22. Kugler F., & Hajnsek, I., Papathanassiou K., Krieger G. & Moreira A., ”Global 3D Forest Structure Mapping with TANDEM-L: Monitoring the Earth's Dynamics.“, ForestSat, 2010-09-07 - 2010-09-10, Lugo, Spain, 2010
23. Lee S.-K. Kugler F., Hajnsek I., Papathanassiou K. P., “The Potential and Challenges of Polarimetric SAR Interferometry Techniques for Forest Parameter Estimation at P-band”, Proceedings of European Conference on Synthetic Aperture Radar, EUSAR’10, Aachen, Germany, 2010
24. Lee S.-K. Kugler F., Hajnsek I., Papathanassiou K. P., “Multi-baseline Pol-InSAR Forest Height Estimation in the presence of temporal decorrelation”, Proceedings of European Conference on Synthetic Aperture Radar, EUSAR’10, Aachen, Germany, 2010
25. Lee S. K., Kugler F., Papathanassiou K., Hajnsek I., “Multibaseline Polarimetric SAR interferometry Forest Height Inversion Approaches”, POLinSAR ESA-ESRIN, Frascati, Italy, 2011
26. Kugler F., I. Hajnsek, Papathanassiou K., “Forest Parameter Characterisation by means of TerraSAR-X and TanDEM-X (Polarimetric and) Interferometric data.”, Proceedings of PolInSAR 2011, 24th -28th of January Frascati, Italy, 2011
27. Kugler F., & Hajnsek I., 2011, “Forest Characterisation by means of TerraSAR-X and TanDEM-X (Polarimetric and) Interferometric data.“ Proceedings of the IEEE International Geoscience and Remote Sensing Symposium (IGARSS), 2011-07-24 - 2011-07-29, Vancouver, Canada, 2011
28. Lee S.-K., Kugler F., Scheiber R., Hajnsek I., Papathanassiou K. P., “Potential and Challenges of Pol-InSAR Techniques for Forest Height Estimation in the context of the BIOMASS Mission” Proceedings of IEEE international Geoscience and Remote Sensing Symposium (IGARSS), 2011-07-24 - 2011-07-29, Vancouver, Canada, 2011
29. Kugler F., Hajnsek I., Papathanassiou K., 2012 “Dual Pol-InSAR Forest Height Estimation By Means of TanDEM-X Data.”, Proceedings of IEEE international Geoscience and Remote Sensing Symposium (IGARSS), 2012-07-22 - 2012-07-27, München, Deutschland , 2012
30. Pardini M., Torano Caicoya A., Kugler F., Lee S.-K., Hajnsek I., Papathanassiou K., “On the estimation of forest vertical structure from multibaseline polarimetric SAR data“, Proceedings of the IEEE International Geoscience and Remote Sensing Symposium (IGARSS) in Munich, 2012
31. Sauer S., Jagdhuber T., Kugler F., Lee F.-K., Papathanassiou K., “Orientation Angle Estimation Over Forested Terrain Using P-band POLSAR Data”, Proceedings of the IEEE International Geoscience and Remote Sensing Symposium (IGARSS) 22.07.2012 – 27.07.2012 in Munich, 2012
32. Lee S-K., Kugler F., Papathanassiou K., Hajnsek I., “Quantification and Compensation of Temporal Decorrelation Effects In Polarimetric SAR Interferometry”, Proceeding of the International Geoscience and Remote Sensing Symposium IGARSS Munich, 2012
33. Caicoya A. T., Kugler F., Hajnsek I., Papathanassiou K., “Boreal Forest Biomass Classification with TanDEM-X”, Proceedings of the Geoscience and Remote Sensing Symposium (IGARSS), Munich July, 2012

34. Caicoya A. T., Kugler F., Hajnsek I, Papathanassiou, K., “Boreal Forest Biomass Classification with TANDEM-X”, Proceedings of POLinSAR, Workshop, 2013
35. Lee S.-K. Kugler F., Papathanassiou K., Hajnsek I., “First Pol-InSAR Forest Height Inversion by means of L-band F-SAR Data.“ ESA POLinSAR 2013 Workshop, 2013-01-28 - 2013-02-01, Frascati, Italy, 2013
36. Pardini M., Caicoya Torano A., Kugler F., Papathanassiou K., “Estimating and understanding vertical structure of forests from multibaseline TanDEM-X Pol-InSAR data”, Proceedings of the IEEE International Geoscience and Remote Sensing Symposium (IGARSS) in Melbourne, 2013
37. Kugler F., Papathanassiou K., Hajnsek I., Rosenqvist A., Cloude S., “ALOS-PalSAR & TanDEM-X Acquisitions for Forest Disturbance & Degradation Mapping”, K&C Phase 3 Final report, 2014
38. Caicoya A. T., Kugler F., Hajnsek I., Papathanassiou K., “Vertical forest structure characterization for the estimation of Above Ground Biomass. Potential and limitations for Radar Remote Sensing“, Proceedings of the 10th European Conference on Synthetic Aperture Radar (EUSAR), Berlin, 2014
39. Caicoya A., T., Kugler F., Pardini M., Hajnsek I., Papathanassiou K., “Vertical forest structure characterization for the estimation of Above Ground Biomass: first experimental results using SAR vertical reflectivity profiles.“, IEEE International Geoscience and Remote Sensing Symposium (IGARSS), 13-07-2014 - 18-07-2014, Quebec, Canada, 2014
40. Pardini M., Cantini, A., Kugler F., Papathanassiou K., Lombardini F., “Monitoring dynamics int tim of forest vertical structure with multibaseline PolInSAR data”, IEEE International Geoscience and Remote Sensing Symposium (IGARSS), 13-07-2014 - 18-07-2014, Quebec, Canada, 2014

Supervised Diploma- and Masterthesis:

1. Angelo Coscia, “Estimation of Extinction in L and X band using PolInSAR and the RVoG Model”, Seconda Università di Napoli, Italy, 2009
2. Astor Toraño Caicoya, “Forest biomass estimations derived from 3D forest structure in Remote Sensing (LIDAR, Radar)“, Technische Universität München, Germany, 2010
3. Ernesto Imbembo, “Effect of temporal decorrelation for forest height inversion using repeat pass TerraSAR-X data”, Università degli Studi di Napoli Federico II, Italy 2010
4. Giuseppe Parrella, “Analysis of LiDAR data for multi-parametric SAR derived forest height validation”, Università degli Studi di Napoli Federico II, Italy 2010

Appendix II: Articles

In this chapter all publications relevant for this thesis are printed in a logical order (not chronologically).

Copyright Note:

The IEEE does not require individuals working on a thesis to obtain a formal reuse license

[Kugler F., Lee S.-K., Hajnsek I., Papathanassiou K., "Forest Height Estimation by means of Pol-InSAR: The role of the vertical wavenumber", IEEE Transactions on Geoscience and Remote Sensing, vol. 53, Issue. 10, 2015]

DOI: 10.1109/TGRS.2015.2420996

[Praks J., Kugler F., Papathanssiou K. P., Hajnsek I. & Hallikainen M., "Tree height estimation for boreal forest by means of L and X band POL-InSAR and HUTSCAT scatterometer", IEEE Transactions on Geoscience and Remote Sensing letters, vol. 37, issue 3, pp. 466 – 470, 2007]

DOI: 10.1109/LGRS.2007.898083

[**Hajnsek I., Kugler F., Lee S.-K., Papathanassiou K., "Tropical Forest Parameter Estimation by means of Pol-InSAR: The INDREX II Campaign", IEEE Transactions on Geoscience and Remote Sensing, vol. 47, No. 2, 2009]**

DOI: 10.1109/LGRS.2007.898083

[Lee S.-K., Kugler F., Papathanassiou K. & Hajnsek I., "Quantification of Temporal Decorrelation Effects at L-band for Polarimetric SAR Interferometry Applications", IEEE Transactions on Geoscience and Remote Sensing, IEEE Journal of Selected Topics in Applied Earth Observations and Remote Sensing, vol. 6, No. 3, June, 2013]

DOI: 10.1109/JSTARS.2013.2253448

[Kugler F., Schulze D., Hajnsek I., Pretzsch H., Papathanassiou K.P., „TanDEM-X Pol-InSAR Performance for Forest Height Estimation", IEEE Transactions on Geoscience and Remote Sensing, vol. 52 , Issue. 10, 2014]

DOI: 10.1109/TGRS.2013.2296533

collective works for resale or redistribution, please go to http://www.ieee.org/publications_standards/publications/rights/rights_link.html to learn how to obtain a License from RightsLink.

An Elsevier journal author has various rights including: Inclusion of the article in a thesis or dissertation (provided that this is not to be published commercially) whether in part or in toto.

[Krieger G., Zink M., Bachmann M., Bräutigam B., Schulze D., Martone M., Rizzoli P., Steinbrecher U., Antony J. W., De Zan F., Hajnsek I., Papathanassiou K., Kugler F., Rodriguez Cassola M., Younis M., Baumgartner S., López-Dekker P., Prats P., Moreira A., "TanDEM-X: A radar interferometer with two formation-flying satellites", Acta Astronautica 89 83–98, 2013]

DOI: 10.1016/j.actaastro.2013.03.008

Forest Height Estimation by Means of Pol-InSAR Data Inversion: The Role of the Vertical Wavenumber

Florian Kugler, Seung-Kuk Lee, Irena Hajnsek, *Fellow, IEEE*, and Konstantinos P. Papathanassiou, *Fellow, IEEE*

***Abstract*—This paper examines the multifaceted effect of the effective spatial baseline, as expressed through the vertical (interferometric) wavenumber, on the inversion of forest height from polarimetric interferometric synthetic aperture radar (Pol-InSAR) data. First, the role of the vertical wavenumber in relating forest height to the interferometric (volume) coherence is introduced. Through the review of the forest height inversion from Pol-InSAR data, the effect of the vertical wavenumber on the inversion performance is evaluated. The selection of optimum with respect to forest height inversion performance, vertical wavenumbers is discussed. The impact of the acquisition geometry and terrain slopes on the vertical wavenumber and their consideration in the inversion methodology is addressed. The individual effects discussed are demonstrated by means of airborne repeat pass Pol-InSAR acquisitions in L- and P-band acquired over different forest conditions, including a boreal, a temperate, and a tropical forest test site. The achieved forest height inversion performance is validated against reference height data derived from airborne LIDAR acquisitions.**

***Index Terms*—Forest height, L-band, P-band, polarimetric synthetic aperture radar interferometry (Pol-InSAR), spatial baseline, terrain slope.**

I. Introduction

FOREST height is one of the most important parameters for stand characterization along with basal area, stock volume, and species composition. It provides information on stand condition, site index, and allows characterizing the successional state of the forest and thus can be used to describe forest dynamics. Forest height is an indicator for the site dependent timber production potential of a stand is closely related to forest biomass, and can be used to constrain model estimates of above-ground biomass and associated carbon flux components between the vegetation and the atmosphere. The distribution of forest heights within a stand may be used to assess the disturbance regime. High spatial and temporal resolution forest height maps can be used to detect logging activities [1]–[10].

When it comes to characterizing dynamic forest processes, knowledge of forest height change is even more important than forest height itself. Forest height changes can be directly used to characterize forest growth, mortality, and deforestation and to conclude about the associated carbon fluxes widely independent from the successional status of the forest [1], [2], [9], [11].

For most of the mentioned applications, an estimation accuracy on the order of 5%–10% appears sufficient [1], [11], [12]. Typical estimation accuracy of forest height at inventory measurements on stand level is on the order of 7%–10%, however increasing with forest height and density [1], [2], [13]. In terms of remote sensing techniques, air, and spaceborne LIDAR configurations have been established as reference (with regard to vertical and spatial resolution and measurement accuracy) for measuring forest height on a local and regional scale. The appropriate estimation methodologies have been developed and validated through a variety of experiments [14]–[25].

In the last years, a new approach based on polarimetric interferometric synthetic aperture radar (Pol-InSAR) measurements has been established for forest height mapping. Indeed, model-based forest height estimation from air and spaceborne Pol-InSAR data has been demonstrated and validated at different frequencies (from X-down to P-band) for a variety of temperate, boreal, and tropical sites, characterized by different stand and terrain conditions [26]–[37].

Pol-InSAR inversion performance has been first addressed in [49], with more detail in [43] and [82], regarding different components of the inversion process and in [38] by means of Cramer–Rao lower bound analysis. This paper discusses the critical effect of the spatial baseline, expressed through the vertical wavenumber, on the performance of forest height estimation by means of a model-based inversion of Pol-InSAR data in a comprehensive way. In Sections II and III, the inversion methodology is reviewed, whereas nonvolumetric decorrelation contributions are quantified and their compensation is discussed. In Section IV, the essential role that the selection of the spatial baseline plays on the inversion performance is analyzed. Section VI addresses the variation of the vertical wavenumber induced by the imaging geometry and the topographic variation within a scene and how this can be accounted for toward an accurate forest height estimation. In Section VII, the previously described effects are discussed by means of

Manuscript received May 31, 2014; revised November 2, 2014; accepted February 24, 2015. This work was supported in part by the HGF Helmholtz Alliance "Remote Sensing & Earth System Dynamics." Krycklan data were acquired in the frame of ESA's BioSAR II campaign under Contract 22052/08/NL/CT).

F. Kugler and K. P. Papathanassiou are with the Microwaves and Radar Institute, German Aerospace Center, Oberpfaffenhofen 82234, Germany (e-mail: florian.kugler@dlr.de; kostas.papathanassiou@dlr.de).

S.-K. Lee is with the NASA, Goddard Space Flight Center, Greenbelt, MD 20771 USA (e-mail: seungkuk.lee@nasa.gov).

I. Hajnsek is with the Institut für Umweltingenieurwissenschaften, ETH Zürich, Zürich 8093, Switzerland, and also with the Microwaves and Radar Institute, German Aerospace Center (DLR-HR), Oberpfaffenhofen 82234, Germany (e-mail: irena.hajnsek@dlr.de; hajnsek@ifu.baug.ethz.ch).

Color versions of one or more of the figures in this paper are available online at http://ieeexplore.ieee.org.

Digital Object Identifier 10.1109/TGRS.2015.2420996

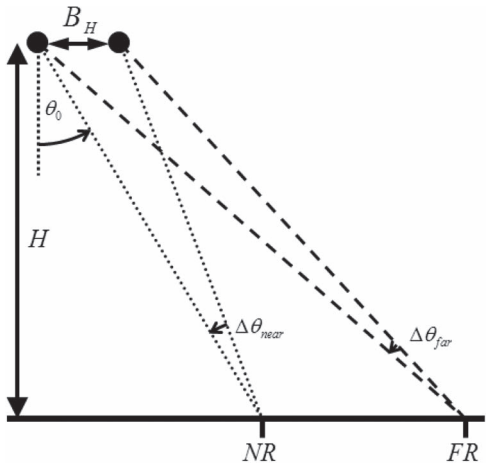

Fig. 1. Interferometric acquisition geometry, airborne scenario with strong change of incidence angle from near range (NR) to far range (FR). B_H is the horizontal baseline, H is the flight height, θ_0 the radar look angle, and $\Delta\theta$ the difference in the radar look angle induced by the baseline.

forest height inversion from airborne Pol-InSAR data at L- and P-band and validated against airborne LIDAR data. Finally, the conclusions are drawn in Section VIII.

II. Pol-InSAR Coherence and Forest Height

Let $s_1(\vec{w})$ and $s_2(\vec{w})$ be two images acquired with a given spatial and temporal baseline (see geometry in Fig. 1) at a given polarization indicated by the unit vector $\vec{w}$ and assuming the same polarization for both images $\vec{w}_1 = \vec{w}_2 = \vec{w}$ [38]–[40], the (complex) interferometric coherence $\widetilde{\gamma}_{\mathrm{Obs}}(\vec{w})$ is given by

$$\widetilde{\gamma}_{\mathrm{Obs}}(\vec{w}) := \frac{\langle s_1(\vec{w}) \cdot s_2^*(\vec{w}) \rangle}{\sqrt{\langle s_1(\vec{w}) \cdot s_1^*(\vec{w}) \rangle \langle s_2(\vec{w}) \cdot s_2^*(\vec{w}) \rangle}} \tag{1}$$

including both the interferometric coherence (or correlation coefficient) $|\widetilde{\gamma}_{\mathrm{Obs}}(\vec{w})|$ and the interferometric phase $\arg(\widetilde{\gamma}_{\mathrm{Obs}}(\vec{w}))$ where $\langle\ \rangle$ denotes the expected value. Using polar coordinates $\widetilde{\gamma}_{\mathrm{Obs}}(\vec{w})$ is represented by a point on the complex plane within the unit circle. Equation (1) indicates that the interferometric coherence depends on the polarization of the two images $s_1(\vec{w})$ and $s_2(\vec{w})$ used to form the interferogram. The set of interferometric coherences $\widetilde{\gamma}_{\mathrm{Obs}}(\vec{w})$ obtained for all the possible polarizations $\vec{w}$ plotted on the complex plane defines the so-called coherence region [41]–[43].

A. InSAR Coherence Interpretation

$\widetilde{\gamma}_{\mathrm{Obs}}(\vec{w})$ comprises several decorrelation processes [44], [45], [49], [50] and can therefore be rewritten as

$$\widetilde{\gamma}_{\mathrm{Obs}}(\vec{w}) = \widetilde{\gamma}_{Sys}(\vec{w})\widetilde{\gamma}_{Tmp}(\vec{w})\widetilde{\gamma}_{\mathrm{Scat}}(\vec{w}). \tag{2}$$

Starting from the right side of (2), $\widetilde{\gamma}_{\mathrm{Scat}}$ reflects the phase stability of the scatterer under the different incidence angles induced by the interferometric baseline. The fact that the two interferometric acquisitions are acquired with (slightly) different look angles make the projection of the 3-D complex reflectivity of the scene (described in the x, y, z coordinate system) into the 2-D SAR image (described in the range, azimuth coordinate system) to be different for the two images $s_1(\vec{w})$ and $s_2(\vec{w})$. As a result, this introduces a decorrelation when forming the interferogram [44], [45]. In (2), $\widetilde{\gamma}_{\mathrm{Scat}}$ can be further decomposed into

$$\widetilde{\gamma}_{\mathrm{Scat}(\vec{w})} = \gamma_{Az}\gamma_{Rg}\widetilde{\gamma}_{\mathrm{Vol}}(\vec{w}). \tag{3}$$

The range γ_{Rg} and azimuth γ_{Az} spectral decorrelation contributions are introduced by the slightly different projection of the horizontal component of the scatterer reflectivity into the slant-range and Doppler-zero (azimuth) direction, respectively [45].

The volume decorrelation contribution $\widetilde{\gamma}_{\mathrm{Vol}}(\vec{w})$ appears when different scattering processes occur at different heights within the resolution cell. In this case, the vertical component of the scatterer reflectivity projects differently into the two images and causes a loss of coherence when forming the interferogram [38], [43], [46]. Accordingly, $\widetilde{\gamma}_{\mathrm{Vol}}(\vec{w})$ is related to the vertical structure of the individual scatterers. This relation will be further explored in Section II-B.

The temporal decorrelation contribution $\widetilde{\gamma}_{Tmp}$ is introduced by geometric and/or dielectric changes of the scatterers within the scene in the time between the two acquisitions. It is the most critical decorrelation contribution when it comes to interferometric acquisitions with nonzero temporal baseline; a detailed discussion on effects, modeling, and compensation of temporal decorrelation can be found in [29], [34], [47] and [48]. Note that, in the most general case when different vertical scattering structures are "seen" by the two acquisitions, a simple factorization of $\widetilde{\gamma}_{Tmp}$ and $\widetilde{\gamma}_{\mathrm{Vol}}(\vec{w})$, as indicated in (2), is no longer possible.

Finally, $\widetilde{\gamma}_{Sys}(\vec{w})$ comprises a wide range of decorrelation effects induced by the nonideal SAR system and processing implementations including contributions induced by additive noise, range and azimuth ambiguities, quantization, and other effects.

B. Modeling of Volume Decorrelation

As already mentioned, the volume decorrelation contribution $\widetilde{\gamma}_{\mathrm{Vol}}(\vec{w})$ is directly related to the vertical distribution of (effective) scatterers $F(z)$ (where z is the vertical position) by a normalized Fourier transformation relationship [26], [38], [43], [81]

$$\widetilde{\gamma}_{\mathrm{Vol}}(\vec{w}, \kappa_z) = \frac{\int_{z_0}^{z_0+h_V} F(z)\exp(i\kappa_z z)dz}{\int_{z_0}^{z_0+h_V} F(z)dz} \tag{4}$$

where h_V is the total extent of $F(z)$, which corresponds in the case of a volume scatterer to the height of the volume. The reference height z_0 corresponds to the lower boundary of the volume. κ_z is the vertical (interferometric) wavenumber [50], [80]

$$\kappa_z = m\frac{2\pi}{\lambda}\frac{\Delta\theta}{\sin\theta_0} \approx m\frac{2\pi}{\lambda}\frac{B_\perp}{R\sin\theta_0} \tag{5}$$

where θ_0 is the nominal incidence angle, λ the wavelength, $\Delta\theta$ the change of the incidence angle induced by the spatial baseline, $B_\perp$ the perpendicular component of the spatial baseline, and R the slant range distance. The factor m accounts for the acquisition mode: $m = 2$ for monostatic acquisitions and

$m = 1$ for bistatic acquisitions. In conventional interferometric applications, κ_z expresses the sensitivity of the interferometric phase to (terrain) height variations [50]. In the context of (4), κ_z maps $F(z)$ to $\widetilde{\gamma}_{\mathrm{Vol}}(\vec{w})$ determining the sensitivity of the interferometer to a given $F(z)$ and particularly to a given h_V.

Equation (4) allows the estimation of $F(z)$ (and associated structure parameters) from measurements of $\gamma_{\mathrm{Vol}}(\vec{w}, \kappa_z)$. One way to do so is to parameterize $F(z)$ into a set of geometrical parameters and scattering parameters and to use then $\gamma_{\mathrm{Vol}}(\vec{w}, \kappa_z)$ measurements to estimate these parameters by inverting (4) [51], [52]. In general, for a robust inversion the number of parameters used to parameterize $F(z)$ has to be balanced by the number of available $\gamma_{\mathrm{Vol}}(\vec{w}, \kappa_z)$ measurements. For vegetation applications two-layer statistical models have been proven to be sufficient (in terms of robustness and performance) particularly at lower frequencies [26], [27], [38], [43]. Accordingly, $F(z)$ comprises vegetation and ground scattering contributions. For monostatic acquisitions direct surface, as well as dihedral (i.e., vegetation-surface or surface-vegetation), scattering contributions are both represented by a single isolated Dirac-like component $m_G(\vec{w})\delta(z - z_0)$ and do not need to be distinguished

$$F(z, \vec{w}) = f_V(z, \vec{w}) + m_G(\vec{w})\delta(z - z_0) \tag{6}$$

where m_G is the ground scattering amplitude. Substituting (6) into (4) leads to

$$\widetilde{\gamma}_{\mathrm{Vol}}(\vec{w}, \kappa_z) = e^{i\phi_0} \frac{\widetilde{\gamma}_{V0}(\kappa_z) + m(\vec{w})}{1 + m(\vec{w})} \tag{7}$$

where $\phi_0 = \kappa_z z_0$ is the phase related to the ground topography

$$\widetilde{\gamma}_{V0}(\kappa_z, \vec{w}) = \frac{\int_0^{h_V} f_V(z, \vec{w}) \exp(i\kappa_z z) dz}{\int_0^{h_V} f_V(z, \vec{w}) dz} \tag{8}$$

is the volume only coherence and $m(\vec{w}) = m_G(\vec{w}) / \int_o^{h_V} f_V(z, \vec{w}) dz$ is the effective ground-to-volume amplitude ratio.

Note that for bistatic acquisitions the dihedral scattering component cannot be longer represented by a single Dirac-like scattering contribution [59] and contributes to the interferometric coherence with a (spatial) baseline dependent component [78], [79]. In order to avoid any confusion, and without loss of generality, a monostatic acquisition geometry is assumed in the following.

For the (vertical) distribution of scatterers in the vegetation layer $f_V(z, \vec{w})$ different models have been proposed. A very successful and widely used model is an exponential distribution of scatterers [26], [38], [43], [46]

$$f_V(z) = \exp\left[2\sigma(\vec{w})z / \cos(\theta_0)\right] \tag{9}$$

where $\sigma(\vec{w})$ is a mean extinction value for the vegetation layer that defines the "attenuation rate" of the profile and is usually expressed in [dB/m]. According to (7), the location of the interferometric phase center depends in this case on $m(\vec{w})$ and $\sigma(\vec{w})$. The special case of $\sigma = 0$ dB/m represents a uniform distribution of the scatterer and leads to the characteristic sinc-decorrelation function

$$\widetilde{\gamma}_{V0}(\sigma = 0) = \exp(i\kappa_z z_0) \exp\left(i\frac{\kappa_z h_V}{2}\right) \mathrm{sinc}\left(\frac{\kappa_z h_V}{2}\right) \tag{10}$$

where $\mathrm{sinc}(x) := \sin(x)/x$. According to (10), the coherence, at a given baseline, depends only on the volume height h_V, whereas the phase center is located at the middle of the volume height.

Aside from the exponential profile that appears to fit better higher frequencies, Gaussian [53], [54], or even linear scattering distributions have been proposed and used particularly at lower frequencies [55].

The solution space of (7) for the exponential distribution of scatterers (9) $m(\vec{w}) = 0$ is represented on the unit circle is indicated by the red dots in Fig. 2(a) and (b). The light blue dots in Fig. 2(a) represent the loci obtained for a constant height $h_V = 10$ m with varying σ, the green dots the loci obtained for a constant height $h_V = 20$ m with varying σ and the orange dots the loci obtained for a constant height $h_V = 30$ m with varying σ. The light blue dots in Fig. 2(b) represent the loci obtained for a constant extinction $\sigma = 0.05$ dB/m with varying h_V, the green dots the loci obtained for a constant extinction $\sigma = 0.2$ dB/m with varying h_V.and the orange dots the loci obtained for a constant extinction $\sigma = 0.50$ dB/m with varying h_V.

Equally important as the shape of the vertical distribution of scatterers $F(z, \vec{w})$ is its polarimetric characterization.

While the ground scattering component is strongly polarized $m_G = m_G(\vec{w})$, the volume scattering component can be both: polarization dependent, i.e., $f_V(z) = f_V(z, \vec{w})$, or independent of polarization, $f_V(z)$. In the first case the volume is called oriented volume [56], [57]; in the second the volume is referred to as random volume (RV) [58], [59]. The analysis of a large number of experimental data indicates that across a wide range of frequencies (from X-down to P-band) the RV assumption is valid for several different forest conditions [26], [29].

Assuming a RV, (7) is known as the random volume over ground (RVoG) model. In this case, (7) can be rewritten as [27]

$$\widetilde{\gamma}_{\mathrm{Vol}}(\vec{w}) = e^{i\varphi_0} \left(\widetilde{\gamma}_{V0} + \frac{\widetilde{\gamma}_{V0} + m(\vec{w})}{1 + m(\vec{w})}(1 - \widetilde{\gamma}_{V0})\right). \tag{11}$$

Equation (11) indicates that as long as $\widetilde{\gamma}_{V0}$ is independent of polarization, the RVoG coherence region is a segment of a straight line [26]. This simple geometrical representation has been exploited for the validation and inversion of the RVoG model and will be further discussed in the following section.

C. Role of the Vertical Wavenumber

As already mentioned, the vertical wavenumber κ_z scales the interferometric phase and coherence to forest height h_V. For the RVoG case, this is given by using (9) in (8) and using (8) in (7). Fig. 3 shows in the left column the absolute value of the volume coherence $|\widetilde{\gamma}_{V0}|$ as a function of the vertical wavenumber κ_z for five different forest heights (10, 20, 30, 40, and 50 m) and

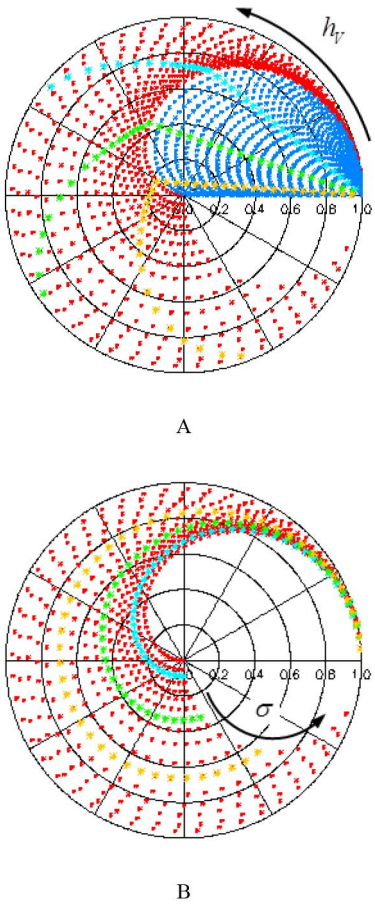

Fig. 2. RVoG solution space for different h_V (up to 50 m) and σ (0 dB/m to 2 dB/m) values for a κ_Z of 0.13 rad/m and $\theta = 30°$ as given by (7); red dots: $\widetilde{\gamma}_{V0}(h_V, \sigma|\kappa_Z, m = 0)$. (a) Dark blue dots indicate solution space for $\sigma = 0$ dB/m and a ground to volume ratio m ranging from 0 to 10: $\widetilde{\gamma}_{V0}(h_V, m|\kappa_Z, \sigma = 0$ dB/m), the light blue dots indicate a constant height of 10 m: $\widetilde{\gamma}_{V0}(\sigma|h_V = 10\,\text{m}, \kappa_Z, m = 0)$ and $\widetilde{\gamma}_{V0}(m|h_V = 10\,\text{m}, \kappa_Z, \sigma = 0)$, the green dots a constant height of 20 m: $\widetilde{\gamma}_{V0}(\sigma|h_V = 20\,\text{m}, \kappa_Z, m = 0)$ and $\widetilde{\gamma}_{V0}(m|h_V = 20\,\text{m}, \kappa_Z, \sigma = 0)$ and the orange dots a constant height of 30 m: $\widetilde{\gamma}_{V0}(\sigma|h_V = 30\,\text{m}, \kappa_Z, m = 0)$ and $\widetilde{\gamma}_{V0}(m|h_V = 30\,\text{m}, \kappa_Z, \sigma = 0)$, the black arrow indicates increment of h_V. (b) Light blue dots indicate a constant extinction of $\sigma = 0.05$ dB/m: $\widetilde{\gamma}_{V0}(h_V|\sigma = 0.05\,\text{dB/m}\kappa_Z, m = 0)$, the green dots a constant extinction of $\sigma = 0.20$ dB/m: $\widetilde{\gamma}_{V0}(h_V|\sigma = 0.20\,\text{dB/m}, \kappa_Z, m = 0)$ and the orange dots a constant extinction of $\sigma = 0.50$ dB/m: $\widetilde{\gamma}_{V0}(h_V|\sigma = 0.50\,\text{dB/m}, \kappa_Z, m = 0)$, the black arrow indicates increment of σ.

for three extinction values, 0 dB/m (top), 0.1 dB/m (middle), and 0.5 dB/m (bottom). For a constant forest height, the volume coherence decreases with increasing κ_z. Decreasing extinctions also lead for a constant height and a fixed κ_z to lower coherence levels.

On the right column of Fig. 3, the corresponding plots for the interferometric phase $\arg(\widetilde{\gamma}_{V0})$ are shown. The coherence-to-height sensitivity is larger at low σ levels and decreases with increasing σ, whereas the phase-to-height sensitivity is higher for higher extinction levels. Accordingly, forest height inversion performance relies on the choice of an appropriate vertical wavenumber κ_z. For (too) large κ_z values, the sensitivity of the coherence to forest height saturates at a given height so that larger heights become underestimated.

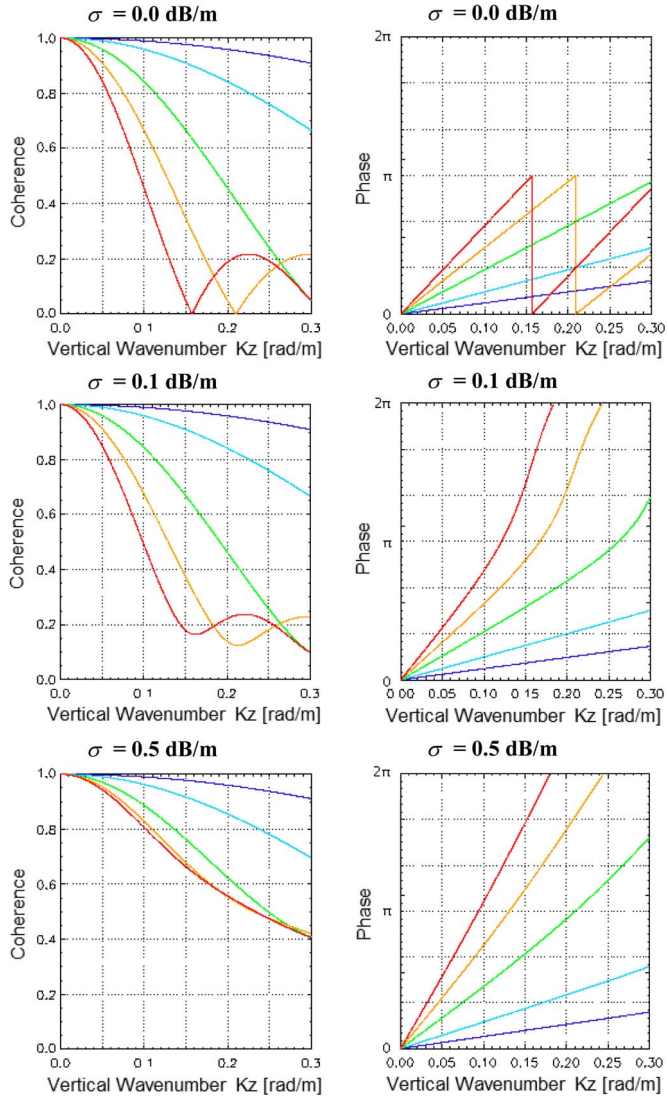

Fig. 3. Volume coherence $\widetilde{\gamma}_{V0}$, amplitude $|\widetilde{\gamma}_{V0}|$ on the left and phase on the right $\arg(\widetilde{\gamma}_{V0})$, as function of κ_z for five different forest heights: 10 m (dark blue), 20 m (light blue), 30 m (green), 40 m (orange), and 50 m (red) and for three different σ values: top 0.0 dB/m, middle: 0.1 dB/m and bottom: 0.5 dB/m.

On the other hand, for (too) small κ_z values, even small (residual) decorrelations introduce large height errors due to the unfavorable coherence to height scaling.

III. RVoG Inversion

Forest height inversion by means of the RVoG model of (7) using a single-baseline quad-polarimetric acquisition can be addressed either in terms of a multidimensional optimization problem [37], [60] or by using the geometrical representation of (7) on the unit circle [26], [27], [30]. While the first approach allows a simultaneous inversion of all parameters, the second approach allows a more intuitive and controlled inversion. The original idea for the geometrical inversion of (7) was proposed in [27]. In the following, a (slightly) modified approach is discussed.

1) Coherence Calibration: The RVoG model in (7) accounts only for volume decorrelation ignoring all other decorrelation

contributions in (2). As a consequence, any (even small) nonvolumetric decorrelation is interpreted as additional volume decorrelation (induced for example by a higher volume layer) and may lead therefore to significant height estimation errors [34], [47], [48], [60]. Therefore, it is essential to compensate for any nonvolumetric decorrelation contribution.

An exact estimation of all decorrelation sources is challenging so that the calibrated coherence $\widetilde{\gamma}_{\mathrm{Vol}}(\vec{w})$ may be either overcompensated (due to an overestimation of the noise level) or still affected by a residual decorrelation contribution. Additionally, in the case of nonzero temporal baselines, temporal decorrelation $\widetilde{\gamma}_{Tmp}$ may be always present. Note that in most cases the calibration of nonvolumetric decorrelation contributions compensates the coherence bias but not the increased variance, in phase and coherence amplitude, which is caused by the lower coherence level.

Spectral Decorrelation Calibration: In the spectral domain, the baseline-induced difference in the projection of the horizontal component of the scatterer reflectivity onto the two acquisitions make the scatterer reflectivity spectrum in the two images to be shifted with respect to each other. Assuming range/azimuth spectral separability the spectral shifts in the range Δf_{Rg} and azimuth Δf_{Az} spectrum, are given by [44], [45], [61]

$$\Delta f_{Rg} = f_0 \Delta\theta / \tan(\theta_0) \qquad \Delta f_{Az} = \Delta f_{\mathrm{DC}} \tag{12}$$

where f_0 is the central system frequency, and Δf_{DC} the Doppler-centroid difference between the two acquisitions. For distributed scatterers with a white reflectivity spectrum, the decorrelations induced by the spectral shift are [45], [61]

$$\gamma_{Rg} = 1 - \frac{|\Delta f_{Rg}|}{W_{Rg}} \qquad \gamma_{Az} = 1 - \frac{|\Delta f_{\mathrm{DC}}|}{W_{Az}} \tag{13}$$

in which W_{Rg} and W_{Az} are the (processed) range and azimuth bandwidths, respectively. These coherences decrease linearly with increasing (angular) baseline $\Delta\theta$ and/or with increasing Doppler-centroid difference. Note that (13) holds as long as the spectral shifts are small compared with the bandwidth, i.e., for $|\Delta f_{Rg}| \ll W_{Rg}$ and $|\Delta f_{\mathrm{DC}}| \ll W_{Az}$.

Both contributions can be compensated by bandpass filtering of the two images before forming the interferogram [45]. In this case, both the coherence bias and the increased phase variance introduced by γ_{Rg} and γ_{Az} are compensated at the price of a loss of spatial resolution. Alternatively, the coherence bias induced by γ_{Rg} and γ_{Az} can be compensated directly by means of (13) without any loss in spatial resolution. However, in this case, the increased phase variance induced by γ_{Rg} and γ_{Az} remains unaffected.

SNR Decorrelation Calibration: The most prominent contribution to the overall system induced decorrelation $\widetilde{\gamma}_{Sys}(\vec{w})$ is the additive noise decorrelation $\gamma_{\mathrm{SNR}}(\vec{w})$. Modeling the received signal to be composed by the scattering amplitude $a(\vec{w})$ and the noise amplitude $n(\vec{w})$, i.e., $s(\vec{w}) := a(\vec{w}) + n(\vec{w})$, $\gamma_{\mathrm{SNR}}(\vec{w})$ can be written as [44], [61]

$$\gamma_{\mathrm{SNR}}(\vec{w}) = \frac{1}{1+SNR(\vec{w})^{-1}} = \frac{A(\vec{w})}{A(\vec{w})+N(\vec{w})} = \frac{A(\vec{w})}{P(\vec{w})} \tag{14}$$

where $SNR(\vec{w}) = P(\vec{w})/N(\vec{w})$ is the signal-to-noise ratio, with $P(\vec{w}) = \langle s(\vec{w}) \cdot s^*(\vec{w}) \rangle$ the received power, $A(\vec{w}) = \langle a(\vec{w}) \cdot a^*(\vec{w}) \rangle$ the scattered power and $N(\vec{w}) = \langle n(\vec{w}) \cdot n^*(\vec{w}) \rangle$ the noise power.

The availability of fully polarimetric data allows an accurate estimation of $\gamma_{\mathrm{SNR}}(\vec{w})$ based on the polarimetric coherence between the two cross-polarized channels. Indeed, due to reciprocity, the two cross-polarized channels are identical up to the additive noise contributions. In this sense, the (polarimetric) coherence between the two cross-polarized channels corresponds to the cross-polarized SNR decorrelation [62]

$$\gamma_{\mathrm{SNR}}^{HV} = \frac{|\langle S_{HV} S_{VH}^* \rangle|}{\sqrt{\langle S_{HV} S_{HV}^* \rangle \langle S_{VH} S_{HV}^* \rangle}} = \frac{A_{HV}}{P_{HV}}. \tag{15}$$

The associated scattering and noise power are given by

$$A_{HV} = \gamma_{\mathrm{SNR}}^{HV} P_{HV} \quad N_{HV} = \left(1 - \gamma_{\mathrm{SNR}}^{HV}\right) P_{HV}. \tag{16}$$

Assuming the noise power to be the same in all polarimetric channels, i.e., $N(\vec{w}) = N_{HV}$, the SNR decorrelation in each channel can be estimated as

$$\gamma_{\mathrm{SNR}}(\vec{w}) = \frac{P(\vec{w}) - N(\vec{w})}{P(\vec{w})} = \frac{P(\vec{w}) - N_{HV}}{P(\vec{w})}. \tag{17}$$

2) Line Fit: The most critical step in the inversion procedure is probably the estimation of the straight line segment represented by the coherence region. In general, this step is performed by a line fit exploiting a set of coherence loci on the complex plane. The quality of the line fit is affected by three parameters: 1) the validity of the RV assumption; 2) the statistical variance of the coherence loci on the complex plane defined by the individual coherence levels and the number of looks used for their estimation [63], [64]; and 3) the length of the visible line segment that depends on the physical properties of the volume and of the underlying ground [26], [29]. For an optimum line fit, the boundary of the coherence region (indicated by the dotted ellipse in Fig. 4) is estimated first [41], [42], [65], [66]. The two coherence loci on this boundary that are furthest apart from each other are then assumed to be $\widetilde{\gamma}_{\mathrm{Obs}}(m_{\min})$ and $\widetilde{\gamma}_{\mathrm{Obs}}(m_{\max})$ given by the yellow points in Fig. 4. The line fit is then performed by connecting these two points in the unit circle (blue line in Fig. 4).

3) Estimation of the Underlying Ground: The two intersection points of the fitted line with the unit circle are the two possible solutions for the "ground only" point, i.e., the coherence that corresponds to the underlying ground

$$\widetilde{\gamma}_{\mathrm{Vol}}(m \to \infty) = e^{i\varphi_0} = e^{i\kappa_z z_0}. \tag{18}$$

In [27], the selection of the right "ground only" was proposed based on the fact that, according to (11), the movement along the "visible" line segment corresponds to a monotonic change of m. Assuming the smallest ground-to-volume ratio in the cross-polarized channel $m(HV)$, the right "ground only" is the one with the bigger distance from $\widetilde{\gamma}_{\mathrm{Obs}}(HV)$ than from other (for example, copolar), coherence loci. However, it turned out that this criterion is too weak for reliable ground estimation. In fact, $\widetilde{\gamma}_{\mathrm{Obs}}(HV)$ may be in some cases closer to the ground

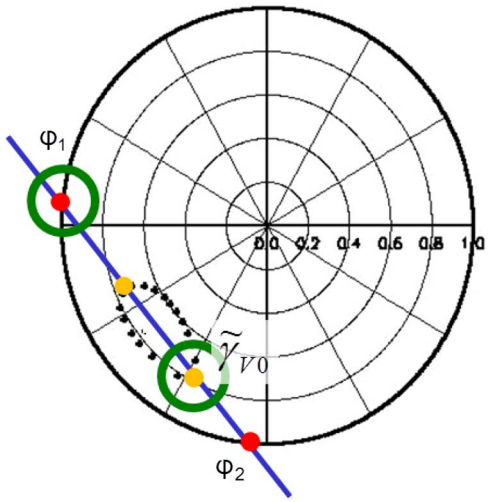

Fig. 4. Inversion scenario in the unit circle; black dots: coherence region; blue line: line fitted through coherence region; red dots: ground phase candidates φ_1 or φ_2; yellow dots: volume only coherence $\widetilde{\gamma}_{V0}$ candidates green circle: mark selected ground phase φ_1 and the selected volume only coherence $\widetilde{\gamma}_{V0}$.

than other polarizations distorting the estimation of the ground phase.

A more robust criterion can be derived from the monotonic lowering (i.e., movement toward the ground) of the phase center with increasing ground-to-volume ratio $m(\vec{w})$. Assuming tree heights less than π/κ_Z, and φ_1 and φ_2 to be the phases of the two intersection points, the following decision rules can be derived:

For $\kappa_Z > 0$:

$$\text{if } \arg\left(\exp(i\varphi_1)\exp(i\varphi_2)^*\right) > 0 \quad \text{then } \varphi_0 = \varphi_1 \tag{19a}$$
$$\text{if } \arg\left(\exp(i\varphi_1)\exp(i\varphi_2)^*\right) < 0 \quad \text{then } \varphi_0 = \varphi_2. \tag{19b}$$

For $\kappa_Z < 0$:

$$\text{if } \arg\left(\exp(i\varphi_1)\exp(i\varphi_2)^*\right) < 0 \quad \text{then } \varphi_0 = \varphi_1 \tag{20a}$$
$$\text{if } \arg\left(\exp(i\varphi_1)\exp(i\varphi_2)^*\right) > 0 \quad \text{then } \varphi_0 = \varphi_2. \tag{20b}$$

This approach holds for tree heights up to $1.3 * \pi/\kappa_Z$ as long as the extinction remains smaller than 0.3 dB/m. For tree heights higher than $1.3 * \pi/\kappa_Z$, the estimated coherence levels become very low (< 0.3, see Fig. 3 and Section IV), making the selection of the right "ground only" point problematic.

4) Height Inversion: Having estimated φ_0 and assuming $m_{\min} = 0$, i.e., no response from the ground in at least one polarization channel, $\widetilde{\gamma}_{\text{Obs}}(m_{\min})\exp(-i\varphi_0) = \widetilde{\gamma}_{V0}$ whereas $\widetilde{\gamma}_{\text{Obs}}(m_{\min})$ is corrected for nonvolumetric decorrelation processes. Height h_V and extinction σ can be estimated unambiguously by means of a 2-D nonlinear optimization problem

$$\min_{h_V,\sigma} \left\| [\widetilde{\gamma}_{\text{Obs}}(m_{\min})\exp(-i\varphi_0)] \, [\widetilde{\gamma}_{V0}(h_V,\sigma,\kappa_Z)] \right\| \tag{21}$$

that can be implemented in terms of a 2-D lookup table [see red dots in Fig. 2(a) and (b)].

The inversion complicates when $m_{\min} > 0$, i.e., when a (significant) ground scattering contribution is present in all polarizations. In this case, neglecting the ground scattering contribution and associating $\widetilde{\gamma}_{V0}(h_V,\sigma,\kappa_Z)$ to $\widetilde{\gamma}_{\text{Vol}}(h_V,\sigma,m_{\min}) = \widetilde{\gamma}_{\text{Obs}}(m_{\min})\exp(-i\varphi_0)$ may lead to coherences outside the solution space of (8) [the solution space of (8) is indicated by the red dots in Fig. 2(a) and (b)].

At the same time, accepting $\widetilde{\gamma}_{\text{Vol}}(h_V,\sigma,m_{\min}) = \widetilde{\gamma}_{\text{Obs}}(m_{\min})\exp(-i\phi_0)$ the three unknown parameters in (7) (i.e., $h_V,\sigma,m_{\min}$) cannot be estimated from a single $\widetilde{\gamma}_{\text{Obs}}(m_{\min})$ measurement only. One way to overcome this problem without introducing more measurements is to fix the extinction value as suggested in [35]. In many cases, a high ground scattering contribution is the result of a low extinction level, justifying to fix $\sigma := 0$ dB/m. In this case, the inversion of (21) becomes

$$\min_{h_V,m} \left\| [\widetilde{\gamma}_{\text{Obs}}(m_{\min})\exp(-i\varphi_0)] - [\widetilde{\gamma}_{\text{Vol}}(h_V,m,\kappa_Z,\sigma = 0\ \text{dB/m}] \right\|. \tag{22}$$

The solution space of (22) is indicated by the blue dots in Fig. 2(a).

IV. Role of κ_Z in Inversion Performance

The measured interferometric coherence may—even after coherence calibration—still be biased by a residual nonvolumetric decorrelation contribution $\gamma_{\text{Res}}(\vec{w})$. In order to quantify the height error introduced by such a residual nonvolumetric decorrelation contribution, a Monte Carlo simulation is performed in the following. For this, we assume the observed volume-only coherence $\widetilde{\gamma}_{\text{Obs}}(m_{\min})$ (with $m_{\min} = 0$) to be

$$\widetilde{\gamma}_{\text{Obs}}(m_{\min}) = \widetilde{\gamma}_{V0}(h_V,\sigma,\kappa_z)\gamma_{\text{Res}}. \tag{23}$$

The estimation accuracy of $\widetilde{\gamma}_{\text{Obs}}$ is given by the standard deviation of its magnitude $\sigma_\gamma(|\widetilde{\gamma}_{\text{Obs}}|,N)$ and its phase $\sigma_\varphi(|\widetilde{\gamma}_{\text{Obs}}|,N)$ both defined by the coherence level $|\widetilde{\gamma}_{\text{Obs}}|$ and the number of looks N used for the estimation of $\widetilde{\gamma}_{\text{Obs}}$ [50], [61], [63], [64]

$$\sigma_\gamma^2\left(|\widetilde{\gamma}_{\text{Obs}}|,N\right) = \left[\frac{\Gamma(N)\Gamma(2)}{\Gamma(N+1)} \cdot {}_3F_2 \cdot \left(2,N,N;N+1,1;|\widetilde{\gamma}_{\text{Obs}}|^2\right) \times \left(1-|\widetilde{\gamma}_{\text{Obs}}|^2\right)^N\right] - E\left\{|\widetilde{\gamma}_{\text{Obs}}|\right\}^2 \tag{24}$$

where $E\{|\widetilde{\gamma}_{\text{Obs}}|\}$ is the expectation value of $|\widetilde{\gamma}_{\text{Obs}}|$, $\Gamma(\ldots)$ the Gamma function and

$$\sigma_\varphi^2\left(|\widetilde{\gamma}_{\text{Obs}}|,N\right) = \int_{-\pi}^{\pi} \left[\varphi - E\{\varphi\}\right]^2 \, pdf(\varphi\|\widetilde{\gamma}_{\text{Obs}}|,N)\, d\varphi \tag{25}$$

where

$$pdf(\varphi\|\widetilde{\gamma}_{\text{Obs}}|,N) = \frac{\Gamma(L+0.5)(1-|\widetilde{\gamma}_{\text{Obs}}|^2)^2|\widetilde{\gamma}_E|\cos(\varphi-\varphi_0)}{2\sqrt{\pi}\Gamma(L)\left(1-|\widetilde{\gamma}_{\text{Obs}}|^2\cos^2(\varphi-\varphi_0)\right)^{N+0.5}} + \frac{(1-|\widetilde{\gamma}_{\text{Obs}}|^2)}{2\pi} {}_2F_1\left(N,1,0.5,|\widetilde{\gamma}_{\text{Obs}}|^2\cos^2(\varphi-\varphi_0)\right)$$

with $\varphi = \arg(\widetilde{\gamma}_{\text{Obs}})$ and $E\{\varphi\}$ is the expectation value of φ.

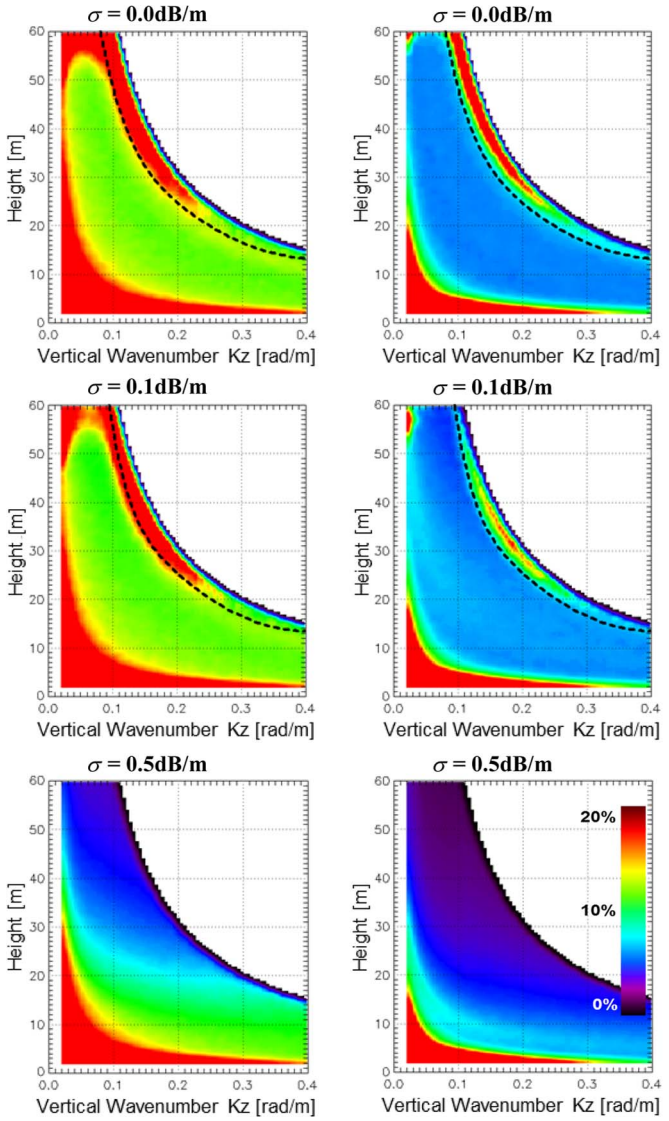

Fig. 5. Standard deviation $\sigma_{\Delta h}$ of the obtained forest height estimates h_{V_i} scaled from 0% to 20% (see legend in the lower right side-valid for all graphs) for three extinctions with a residual decorrelation coefficient $\gamma_{\mathrm{Res}} = 0.98$; left: number of looks $N = 16$; right: $N = 64$; black dashed line indicates a coherence level of 0.3.

For a given volume characterized by h_V, σ and a given κ_z, first, $\widetilde{\gamma}_{V0}(h_V, \sigma, \kappa_z)$ is estimated by using (9) and (8). Using a fixed γ_{Res} level, $\widetilde{\gamma}_{\mathrm{Obs}}(m_{\min}) = \widetilde{\gamma}_{V0}(h_V, \sigma, \kappa_z)\gamma_{\mathrm{Res}}$ is evaluated. Then, a set of (1000) $\widetilde{\gamma}_{\mathrm{Obs}_i}$ samples is created according to (24) and (26). For each of the generated $\widetilde{\gamma}_{\mathrm{Obs}_i}$ samples, forest height inversion was performed by means of (21) and (22) leading to a set of estimated forest heights h_{V_i}.

This procedure has been performed for $\gamma_{\mathrm{Res}} = 0.98$, a height range from 2 to 60 m (234 samples with 0.25-m steps) and a vertical wavenumber range from 0.02 to 0.4 rad/m (154 samples in 0.0025 rad/m steps), for three extinction levels (0.0, 0.1 and 0.5 dB/m) and two different number of looks ($N = 16$ and 64). Fig. 5 shows the standard deviation $\sigma_{\Delta h}$ of the obtained forest height estimates h_{V_i} plotted as a function of forest height h_V and vertical wavenumber κ_z for the three extinction levels (top: $\sigma = 0.0$ dB/m, middle: 0.1 dB/m and bottom: $\sigma = 0.5$ dB/m). On the left are the results obtained for $N = 16$ looks and on the right the ones for $N = 64$ looks.

The plots show that for a given vertical wavenumber κ_z, there is only a certain height range, where the inversion performance is optimum. For forest heights below this range, the variance increases as a result of the reduced sensitivity: even small(er) variances of the $\widetilde{\gamma}_{\mathrm{Obs}}(m_{\min})$ induce a large variance of height.

For forest heights above the optimum range, the height variance increases as a result of the higher variance of $\widetilde{\gamma}_{\mathrm{Obs}}(m_{\min})$ due to the low coherence level. Below a given coherence level of 0.3 $\sigma_{\Delta h}$ becomes in all scenarios larger than 10% (as indicated by the black dashed line in Fig. 5). In the case of a high extinction level (i.e., $\sigma = 0.5$ dB/m) $\widetilde{\gamma}_{\mathrm{Obs}_i}$ is always larger than 0.3. In this case the upper boundary is defined by the height of ambiguity $HoA = 2\pi/\kappa_z$.

For $N = 16$, $\sigma_{\Delta h}$ is for most κ_z and h_V values clearly worse than 10% and becomes marginal better than 10% only in the high extinction case (i.e., $\sigma = 0.5$ dB/m). For $N = 64$, $\sigma_{\Delta h}$ improves to (on average) 7% or better and reaches only at the edges (low and high heights for a certain κ_z) values larger than 10% height error.

For a given vertical wavenumber κ_z, the induced bias is larger at small heights and decreases with increasing forest height (see Fig. 6 left side).

On the right of Fig. 6, the bias of the height estimates $B_{\Delta h}$ is plotted as a function of forest height h_V and γ_{Res} (ranging from 0.6 to 1.0) for three different vertical wavenumbers (0.05 rad/m top, 0.10 rad/m middle and 0.20 rad/m bottom). A mean extinction of 0.1 dB/m and $N = 64$ is used. Small κ_z bear only small γ_{Res}, whereas larger κ_z can cope with higher γ_{Res}. Equivalently, low forest heights are more affected by γ_{Res} than tall forest heights. A vertical wavenumber of $\kappa_z = 0.1$ rad/m allows the estimation of heights greater than 30 m at a decorrelation level of 0.8 with an accuracy better than 10%.

Summarizing the aforementioned results, Fig. 7 shows the performance region where the total height error $B_{\Delta h} + \sigma_{\Delta h}$ is better than 10% for the three different extinction levels: 0 dB/m, 0.1 dB/m and 0.5 dB/m.

For a given vertical wavenumber κ_z, the height range fulfilling the 10% performance is limited toward higher heights by the loss in coherence (the corresponding boundary for a given number of looks is indicated by the red line), whereas toward lower heights primarily by the bias induced by the residual nonvolumetric decorrelation contribution (the corresponding boundary is indicated by the blue line).

The simulations indicate that in order to meet 10% accuracy for a height range from 5- to 60-m various baselines (vertical wavenumbers κ_z) are required.

The number of required baselines depends on the occurring extinctions.

Across all extinctions three baselines are sufficient to map heights from 5 to 60 m with an h_{VErr} better than 10% [see Fig. 7(a)–(c)]. For higher extinctions (> 0.5 dB/m) two baselines would be sufficient [see Fig. 7(c)], as here the higher coherence values reduce the statistical variance. In Fig. 7, the baselines (green arrows) are selected to cover a height range between 5 and 60 m with a minimum number of baselines. Note that the obtained results are in agreement with the results

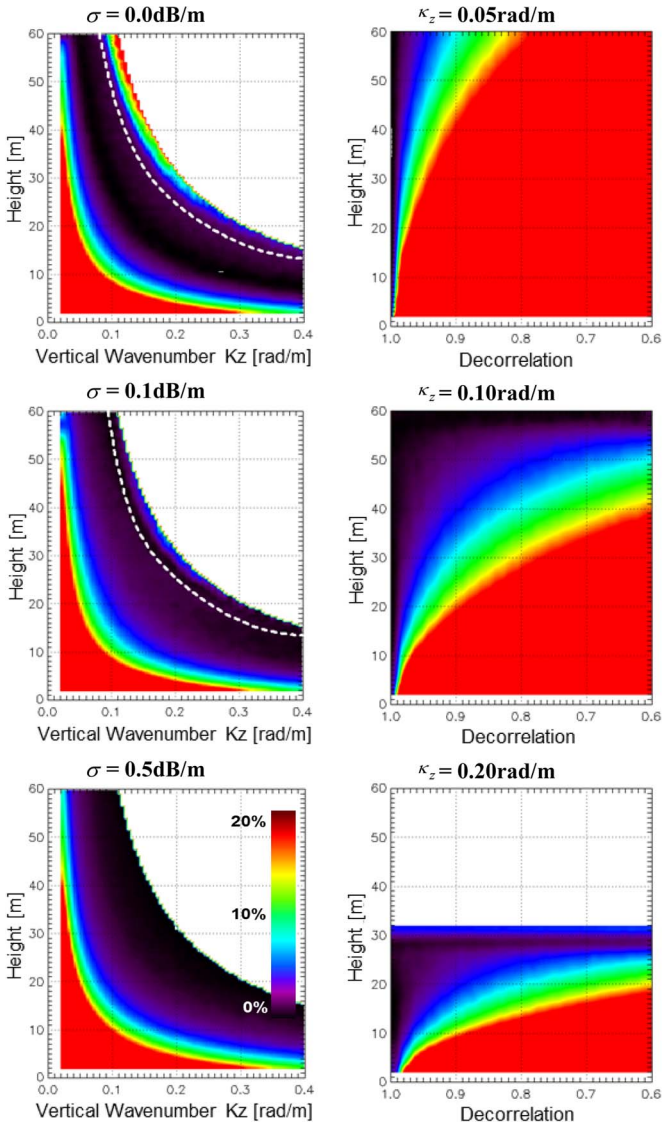

Fig. 6. Bias $B_{\Delta h}$ of the obtained forest height estimates h_{V_i} estimated scaled from 0% to 20% (see legend in the lower left side-valid for all graphs); left: $B_{\Delta h}$ for three extinctions and a residual decorrelation coefficient $\gamma_{\mathrm{Res}}(\vec{w}) = 0.98$, white dashed line indicates a coherence level of 0.3; right: $B_{\Delta h}$ as a function of decorrelation $\gamma_{\mathrm{Res}}(\vec{w})$ for three different vertical wavenumbers κ_z and a mean extinction of 0.1 dB/m.

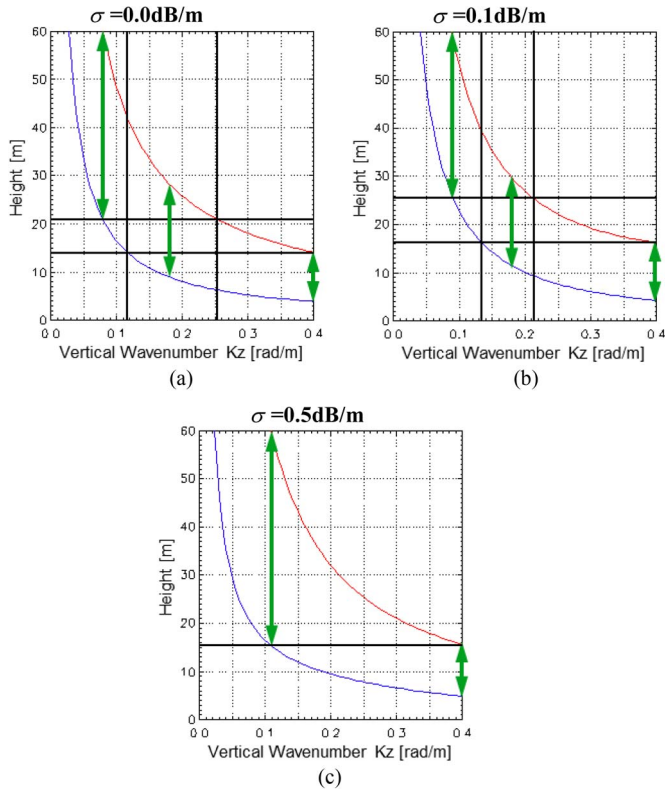

Fig. 7. Inversion performance as a function of forest height h_V and vertical wavenumber κ_z for three extinctions assuming a height error better than 10%, $N = 64$ with $\gamma_{\mathrm{Res}}(\vec{w}) = 0.98$; blue: lower boundary; red: upper boundary; green arrows: baselines to cover a height range from 5 to 60 m.

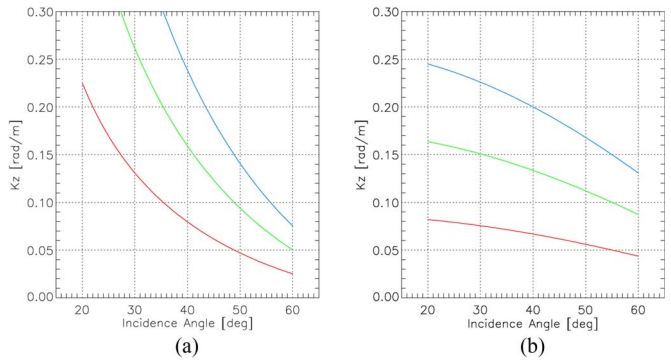

Fig. 8. Vertical wavenumber κ_z as a function of the Incidence angle (5) ($H = 3000$ m, L-band). (a) For three different horizontal baselines B_H, red $= 5$ m, green $= 10$ m, blue $= 15$ m. (b) For three different vertical baselines B_V, red $= 5$ m, green $= 10$ m, blue $= 15$ m.

obtained in [43], [82] even if different parameters/thresholds have been used to optimize the κ_z range.

V. Incidence Angle Variation

According to (5), a change of incidence angle θ goes along with a change of κ_z, even if the spatial baseline remains the same. This is why in airborne (repeat-pass) interferometric systems κ_z is 2-D: it varies along azimuth with the variation of the spatial baseline components induced by the nonideal platform motion and across range with the incidence angle. An example of such an airborne 2-D κ_z map is shown in Fig. 12(c). It is apparent that the for airborne SAR systems typical wide variation of the incidence angle in range causes a (significant) variation of κ_z. For a flight height of 3000 m above ground and a horizontal baseline $B_H = 10$ m in L-band, an incidence angle of $\theta_0 = 25°$ (NR) results in $\kappa_z = 0.35$ rad/m, whereas an incidence angle of $\theta_0 = 55°$ in FR results in $\kappa_z = 0.07$ rad/m with a variation of about a factor of five. As indicated in [68], the variation of κ_z across range is less when instead of a horizontal a vertical baseline B_V is applied. For the same flight configuration as before this time with $B_V = 10$ m, at near-range $(\theta_0 = 25°)$ $\kappa_z = 0.16$ rad/m, whereas at far-range $(\theta_0 = 55°)$ $\kappa_z = 0.10$ rad/m corresponding to a variation of a factor of 1.6.

In Fig. 8, κ_z is plotted as a function of the incidence angle according to (5) for three horizontal baselines B_H [in Fig. 8(a)]

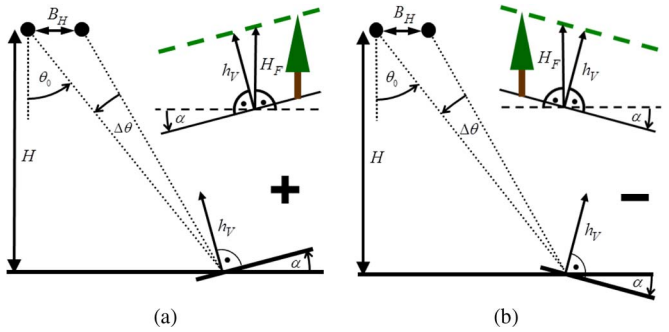

Fig. 9. Acquisition geometry with terrain slope. (a) Positive terrain slope. (b) Negative terrain slope.α = terrain slope, B_{Ho} is the horizontal baseline H is the flight height, θ_0 the radar look angle, $\Delta\theta$ the difference in the radar look angle induced by the baseline, h_V the height of the volume and H_F the height of the forest.

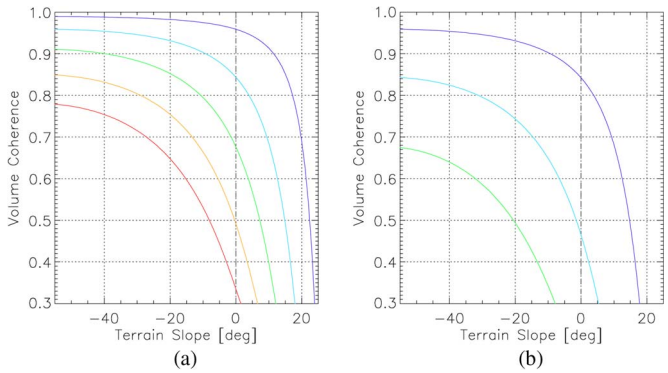

Fig. 10. Impact of terrain slope on volume coherence γ_{V0} as a function of terrain slope for a 10 m (dark blue), 20 m (light blue), 30 m (green), 40 m (orange), and 50 m (red) high forest with $\sigma = 0.1$ dB/m, $\theta_0 = 30°$. (a) Nominal (not terrain corrected) $\kappa_Z = 0.10$ rad/m. (b) Nominal $\kappa_Z = 0.20$ rad/m.

and three vertical baselines B_V [in Fig. 8(b)] for a flight height of 3000 m above ground at L-band. The red line in Fig. 8 indicates $B_H = B_V = 5$ m, the green $B_H = B_V = 10$ m and the blue $B_H = B_V = 15$ m. As shown in Section IV, in order to map a predefined range of forest heights with similar accuracy, multiple airborne interferometric acquisitions are necessary. Flight constellations using a vertical baseline require less acquisitions to cover the whole image (in NR, as well as in FR) with a combination of similar κ_z values.

An insufficient number of baselines or baselines with unfavorable κ_z values lead to a reduced inversion performance. Accordingly, too low and/or too high κ_z values have to be masked out during the inversion (in accordance with the expected forest height range).

Additionally, low coherences lead for a given number of looks N to large forest height error variances (see Section IV) making an accurate inversion at a reasonable spatial resolution impossible. In consequence, areas with low coherences have to be masked out as areas with expected sub-optimal performance. In this case, coherences $|\widetilde{\gamma}_{V0}|$ lower than 0.3 are excluded from inversion.

The impact of the incidence angle on acquisition geometry for spaceborne scenarios is discussed in detail in [25].

VI. Topographic Variation

A. Impact of Slope on Baseline (κ_Z)

The importance of terrain slopes in the inversion process has been already indicated by different studies [38], [69], [70]. While terrain slopes in azimuth have only a secondary effect on κ_z, terrain slopes in range direction (indicated by α in Fig. 9) modify the local incidence angle $\theta = \theta_0 + \alpha$ and as a consequence [see (5)] the vertical wavenumber κ_z results in

$$\kappa_z = m\frac{2\pi}{\lambda}\frac{\Delta\theta}{\sin(\theta_0+\alpha)}. \tag{26}$$

Accordingly, terrain slopes tilted toward the interferometer, in the following called positive slopes, decrease the local incidence angle θ [see Fig. 9(a)] and increase κ_z. Slopes tilted away from the interferometer—in the following called negative slopes—increase θ [see Fig. 9(b)] and decrease κ_z. The terrain-induced modulation of κ_z causes a terrain induced modulation of the coherence: volume coherence decreases on positive slopes and increases on negative slopes. This makes clear that for an unbiased inversion, the dependence of κ_z on range terrain slopes has to be accounted.

At the same time, terrain slopes in range modulate the (range) spectral shift Δf_{Rg} inducing, if not accounted for, an additional error source. On the other hand, terrain adaptive (range) spectral filtering can lead to a terrain dependent spatial resolution that may also impact inversion performance (particularly when referred to a certain spatial grid).

In Fig. 10, simulated volume coherences $\widetilde{\gamma}_{V0}$ are displayed as a function of terrain slope for two constant baselines [nominal κ_Z for flat terrain is in Fig. 10(a) 0.1 rad/m and in Fig. 10(b) 0.2 rad/m] for different volume heights (10 m = dark blue, 20 m = light blue, 30 m = green, 40 m = orange and 50 m = red). The simulations rely on (8) with $\sigma = 0.1$ dB/m and a nominal incidence angle $\theta_0 = 30°$. Ground scattering is not considered, i.e., $m = 0$.

For the same volume height, positive slopes decrease and negative slopes increase the interferometric coherence.

B. Correction of Terrain Slope

To compensate slope-induced effects in the Pol-InSAR inversion, a digital elevation model (DEM) is required. Several DEM's of different quality and coverage are available.

1) The shuttle radar topography mission (SRTM) DEM [71] has a spatial resolution of 90 m × 90 m with a relative height error better than 10 m and global coverage between −60° and 60° latitude.
2) The TanDEM-X DEM [72] has a spatial resolution of 12 m × 12 m with a relative height error better than 2 m and is globally available.
3) (Airborne) LIDAR DTM's [14], [73] have a system dependent spatial resolution, usually on the order of 1 m × 1 m, with a relative height error better than 1 m. LIDAR DTM's are available on local and regional scales.

4) Pol-InSAR DEM's derived from the Pol-InSAR data used to estimate forest height [50]. Their spatial resolution and height error depend strongly on the Pol-InSAR configuration used.

SRTM (C- and/or X-band) and TanDEM-X (X-band) DEM's are digital surface models (DSMs), i.e., they refer to the interferometric phase center height. Abrupt changes in forest height are interpreted as strong terrain slopes. Thus, a low-pass DEM filtering is recommended before slope estimation. Airborne LIDAR DEM's are highly accurate and reflect the terrain topography below vegetation, but they are by far not globally available.

Finally, using the DEM produced from the Pol-InSAR data itself has the advantage of referring to the same (phase center) height and having the same geometry and spatial spacing of the inversion data. Nevertheless, regions of low coherence (caused by high forest heights) affect the DEM accuracy due to the increased phase variance. However, the availability of a multi-baseline acquisition with a κ_Z range appropriate to invert a wide range of forest heights allows in general the generation of accurate DEM's. The comparison of the inversion performance by using the different DEM's for terrain compensation will be discussed in Section VII-C.

Compensation of terrain slope can be regarded as a two-step process in the height inversion.

First, the range component of the terrain slope α is used to correct the (nominal) incidence angle θ_0. For this, the used DEM is projected in the slant range geometry. Neglecting the rather small dependence on the azimuth slope, the local terrain slope α is given by

$$\alpha = \tan^{-1}\left(\frac{\Delta H}{\frac{PS_{rg}}{\sin(\theta)} + \frac{\Delta H}{\tan(\theta)}}\right) \tag{27}$$

where ΔH is the height difference between two consecutive range samples and PS_{rg} the corresponding slant range distance.

Second, the resulting volume heights h_V are transferred into a forest height H_F. The correction for terrain slope by correcting the local incidence angle θ tilts the reference ground level (line of tilted terrain in Fig. 9). The volume height h_V is then defined as the perpendicular height to the ground level. On the contrary forest height H_F is defined as the height perpendicular to the horizon. Then, for flat terrain it results in

$$H_F = h_V \tag{28}$$

whereas for sloped terrain

$$H_F = \frac{h_V}{\cos|\alpha|} \tag{29}$$

is valid. The amount of correction in (29) is for $|\alpha| \leq 30°$ still below 15% of the estimated volume height h_v. Without correction the estimated forest heights become slightly underestimated.

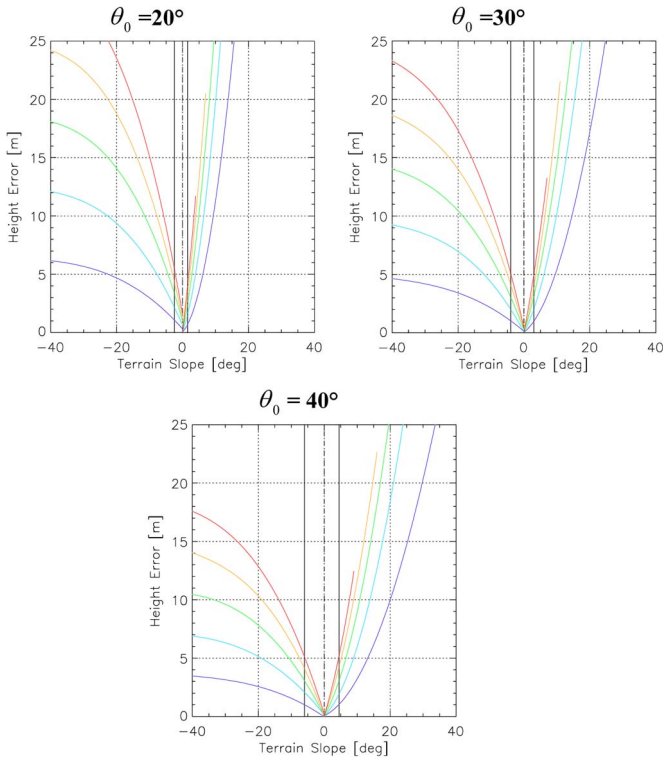

Fig. 11. Height error induced by uncompensated terrain slope as a function of terrain slope on a 10 m (dark blue), 20 m (light blue), 30 m (green), 40 m (yellow), and 50 m (red) high forest with $\sigma = 0.1$ dB/m and a nominal (not terrain corrected) κ_Z of 0.1 rad/m for three different radar look angles θ_0.

TABLE I
OVERVIEW DATA

Test site	Radar Acq.	LIDAR Acq.	Number of Tracks	Baselines B_{HOR} [m]	Mean κ_Z * [rad/m]
Kobernausser Wald	L- band 2004	2004	1	7	0.14
Krycklan (315°)	L- band 2008	2008	7	6, 12, 18, 24, 30, 36	0.12, 0.24, 0.36, 0.48, 0.60, 0.72
Krycklan (135°)	L- band 2008	2008	7	6, 12, 18, 24, 30, 36	0.12, 0.24, 0.36, 0.48, 0.60, 0.72
Sungai Wain	P- band 2004	2011	5	0, 15, 30, 60	0.00, 0.08, 0.17, 0.34

*for mid-range (~35° incidence angle)

C. Uncompensated Terrain Slopes

Accuracy of the slope correction depends strongly on the accuracy of the DEM at hand (exhaustively investigated in Section VII-C). Fig. 11 shows the height error caused by applying (21) without correcting κ_Z for terrain slopes as a function of terrain slope for different forest heights $H_F(\theta_{\text{real}})$ ranging from 10 m (dark blue) to 50 m (red) [by means of (27) and (7)] assuming an extinction of 0.1 and $m = 0$) and different incidence angles $\theta_0 = 20°$, $\theta_0 = 30°$ and $\theta_0 = 40°$. The 10% height error (bias) is indicated by the black lines in Fig. 11.

Accordingly, positive terrain slopes result in an overestimation of forest height and negative terrain slopes in an

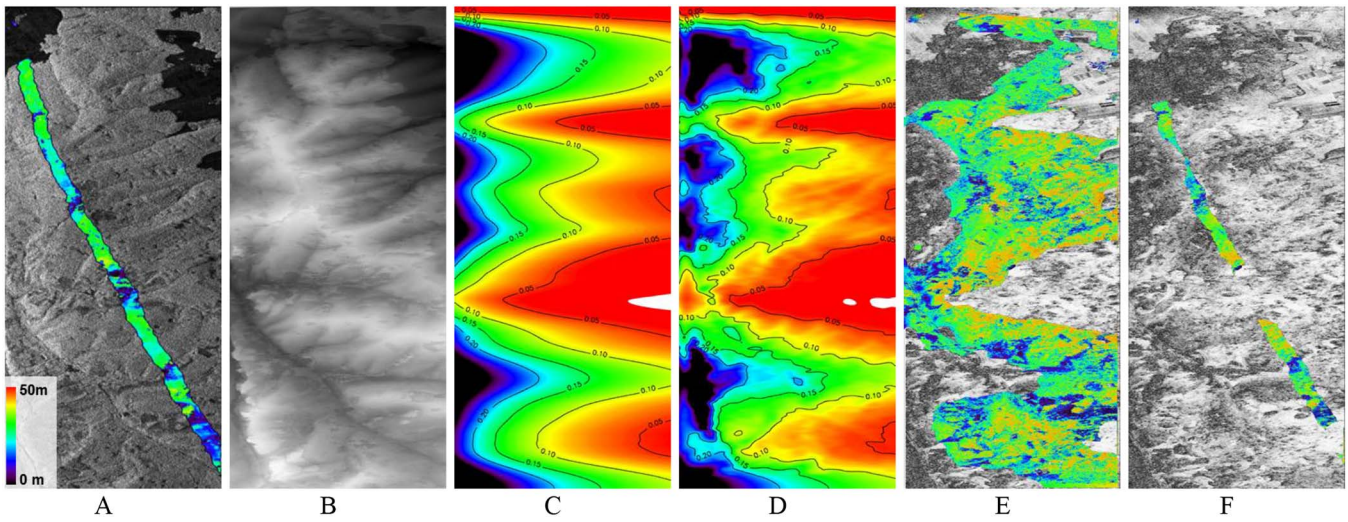

Fig. 12. Test site "Kobernausser Wald"; NR ($\theta = 25°$) on the left side, far-range ($\theta = 55°$) on the right side; image dimension: 3 km (range) × 10 km (azimuth). (a) Amplitude image HV polarization, superimposed by LIDAR H100 forest height strip scaled from 0 to 50 m (see legend). (b) DEM scaled from 580 m (black) to 820 m (white). (c) Vertical wavenumber κ_z 2-D (variations in azimuth) scaled in color from 0.02 rad/m (black) to 0.20 rad/m (white). (d) Vertical wavenumber κ_z 2-D terrain corrected scaled from 0.02 rad/m (black) to 0.20 rad/m (white). (e) Interferometric coherence HV polarization scaled from 0 (black) to 1 (white) superimposed by Pol-InSAR forest height map scaled from 0 to 50 m (see legend). (f) Interferometric coherence HV polarization scaled from 0 (black) to 1 (white) superimposed by Pol-InSAR forest heights masked with LIDAR reference height; Pol-InSAR forest heights are only shown for $0.05 < \kappa_z < 0.15$.

underestimation of forest height. Uncompensated positive terrain slopes introduce a much larger error than negative terrain slopes. The impact of terrain slope depends also on the nominal incidence angle θ_0. Steep nominal incidence angle require a more precise slope estimation than shallow θ_0.

VII. Results

In the following, Pol-InSAR forest height inversion is demonstrated by means of three different test sites. Data were acquired by DLR's E-SAR system [67] and are listed in Table I.

For a validation of the Pol-InSAR height, estimates in all test sites LIDAR reference measurements were used. Cross validation was carried out on stand level, by using homogeneous forest areas with a mean size of approximately 3 to 5 ha.

Both Pol-InSAR forest heights estimates and LIDAR measurements refer to the same reference height, i.e., the forest canopy top height H100 as described in [25]. LIDAR H100 was calculated by a maximum filtering of the LIDAR DSM. A detailed description about the calculation of LIDAR H100 is given in [25] and [74].

A. Kobernausser Wald

The Kobernausser forest site is located in upper Austria (48°04′ north, 13°14′ east) and represents typical temperate forest conditions. It is a managed forest with stands of different age and height. Forest stands are usually even aged and dominated by coniferous trees (spruce, pine, and fir). Measured forest heights range from 5 to 40 m. The topography of the site is gently sloped.

Airborne LIDAR data were acquired in 2004 (same year as Pol-InSAR measurements) on a diagonal strip across the SAR image. The strip is 150 m broad and 9 km long [see Fig. 12(a)]. 25 homogenous stands were chosen for cross validation.

For this test site, only a single Pol-InSAR repeat pass acquisition in L- band is available which covers an area of 3 km in range and 10 km in azimuth.

The test site is nearly completely covered by forest excluding some agricultural areas in the upper right part of the scene. Fig. 12(a) shows the amplitude image in HV polarization superimposed by the LIDAR reference heights scaled from 0 m to 50 m.

In Fig. 12(b), the used X-band DEM is shown scaled from 580 to 820 m above mean sea level (AMSL) with 6 m × 6 m spatial resolution. Fig. 12(c) shows the nominal vertical wavenumber κ_z scaled from 0.02 rad/m (black) to 0.20 rad/m (white) scaled in different colors and Fig. 12(d) κ_z corrected for terrain slope. The strong fluctuations of κ_z along azimuth indicate the motions of the aircraft during the acquisition (windy flight conditions).

The terrain corrected κ_z image indicates already that large parts of the image have too small or too large κ_z values for a successful height inversion. The coherence amplitude image in HV polarization is displayed in Fig. 12(e) and (f). Here, areas of low coherence (on the left in NR) correspond to areas of high κ_z (black regions) and indicate a saturation of the coherence-to-height sensitivity.

In order to cover a height range up to 40 m, Pol-InSAR forest height inversion was only carried out for κ_z values ranging from 0.05 rad/m to 0.15 rad/m, whereas areas with unfavorable κ_z values are excluded from inversion. The obtained Pol-InSAR forest height map scaled from 0 m to 50 m is superimposed on the coherence image in Fig. 12(e).

For a better visual comparison only Pol-InSAR heights covered by the LIDAR measurements are superimposed in the coherence image in Fig. 12(f).

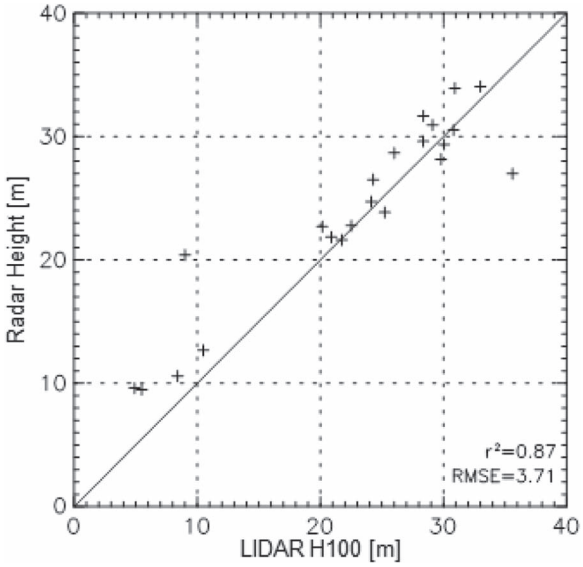

Fig. 13. Validation plot for single baseline inversion "Kobernausser Wald" test site; Pol-InSAR height estimates versus LIDAR H100; 25 stands were used for validation.

The validation plot for "Kobernausser Wald" against LIDAR H100 is shown in Fig. 13 indicating a correlation coefficient r^2 of 0.87 and an RMSE of 3.71 m, for a height range from 5 m to 35 m. As only a single baseline was available to cover the full height range, inversion performance is reduced for large parts of the inverted forest heights. Extinction ranges mainly between 0 dB/m and 0.2 dB/m and reaches rarely values greater than 0.5 dB/m. At 10% of the inverted pixels a ground contribution could be detected which does not exceed an m of 0.15.

For two stands, Pol-InSAR forest height estimates differ strongly from LIDAR measurements. Overestimation could be caused by wind induced temporal decorrelation [27], [29], [47] appearing in form of patches without affecting the entire image. One stand is underestimated, probably due to a limited κ_z-to-height sensitivity in this part of the scene. When the two stands are excluded, then r^2 raises to 0.97 with an RMSE of 2.22 m.

B. Krycklan Test Site

Krycklan forest is located in Middle Sweden (64°10′ north and 20°01′ east) and represents typical forest conditions for boreal forest systems of Scandinavia. It is a managed forest with a mean forest height of 18 m and a mean biomass level of 90 t/ha. The measured maximum forest height is 30 m. The forest is dominated by coniferous trees (Norway spruce and Scots pine) with fractions of birch. The site has a hilly topography characterized by moderate slopes and a height variation between 20 m and 400 m AMSL. Airborne LIDAR measurements were collected in late summer 2008 (same year as Pol-InSAR measurements) and are shown in Fig. 14(a). For cross validation, 252 homogeneous stands were chosen.

Pol-InSAR data over Krycklan site were acquired in L- band during the BIOSAR II campaign and are summarized in Table I. For this test site, two headings are available looking to the scene from the two opposite sites. Due to the large number of baselines for each heading, for each position in the image several baselines with κ_z values between 0.01 rad/m and 0.3 rad/m are available. In the case in which for one pixel there are several high-performance height estimates available, one height estimate is selected applying the method described in [33].

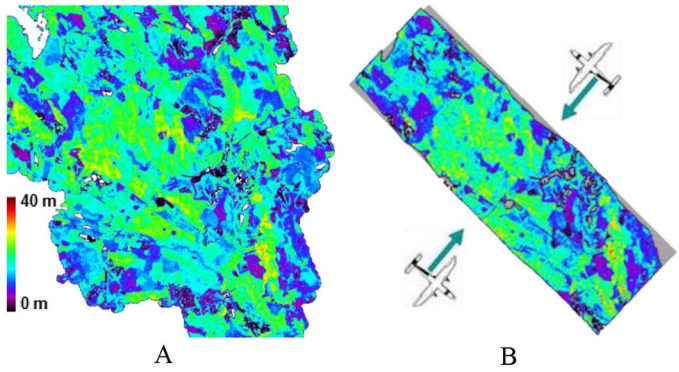

Fig. 14. L-band forest height maps for the Krycklan test site geocoded in UTM and scaled from 0 to 40 m (see legend on the left side). (a) LIDAR H100 image. (b) Pol-InSAR forest height combined from heading: 134° and heading: 314°.

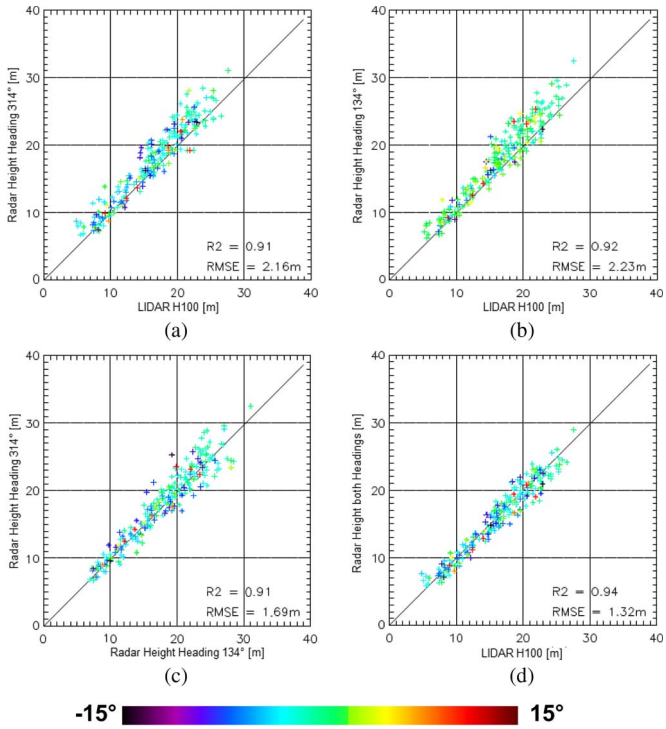

Fig. 15. Validation plots of multibaseline inversion "Krycklan" test site; Pol-InSAR height estimates versus LIDAR H100 reference height. (a) Heading: 314°. (b) Heading: 134°. (c) Heading: 314° versus heading: 134°. (d) Combined inversion results of both headings versus LIDAR H100 reference height; color of the stand dots represents terrain slope, scaled form $-15°$ to 15°; 228 stands were used for validation.

A Pol-InSAR forest height map obtained from both headings of Krycklan site is shown in Fig. 14(b) scaled from 0 to 40 m.

Cross-validation plots of the Pol-InSAR height estimates against the LIDAR H100 plots are displayed in Fig. 15. The color of each plotted point represents the mean slope of each stand, scaled between $-15°$ and 15°. Due to the opposite flight

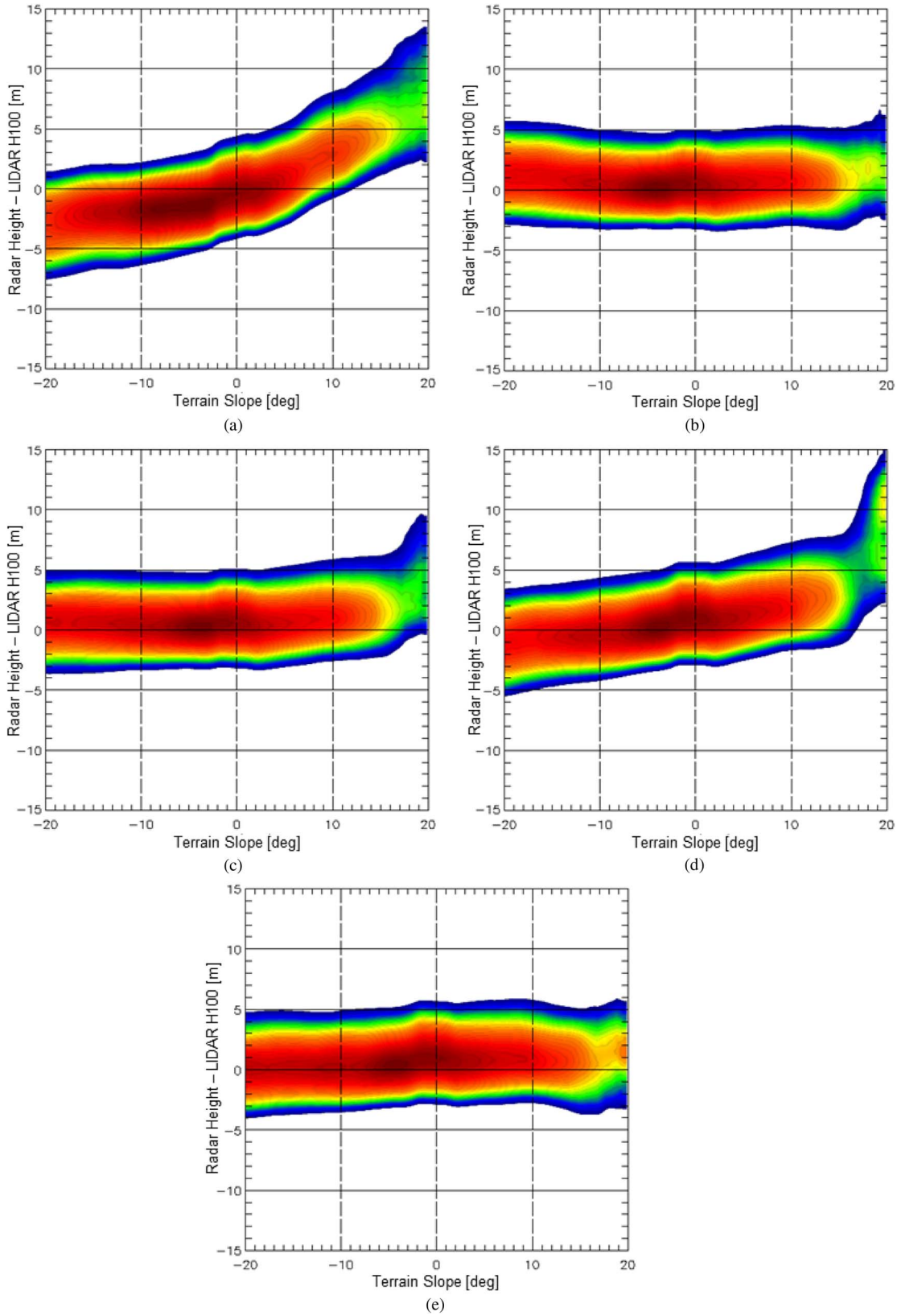

Fig. 16. 2-D Histograms of Pol-InSAR heights minus LIDAR H100 versus terrain slope α for different DEM's; scaling from blue (low occurance) to green to red (high occurance). (a) No DEM correction. (b) LIDAR DEM 1 m $\times$ 1 m. (c) L- band DEM. (d) SRTM DEM 90 m $\times$ 90 m. (e) TanDEM-X DEM 12 m $\times$ 12 m.

direction in the two headings, the positive slope in the first heading becomes negative in the second heading and vice versa. Inversion results from the 314° and 134° headings reach a correlation coefficient of 0.91/0.92 with an RMSE of 2.16/2.23 m for a height range from 5 m to 30 m. Extinction ranges mainly between 0 dB/m and 0.1 dB/m and reaches rarely values

greater than 0.2 dB/m. At 15% of the inverted pixels a ground contribution could be detected which does not exceed an m of 0.20.

Both headings seem to slightly overestimate forest heights. The consistency of the results obtained from the two headings is underlined by a direct comparison of the forest height estimates from the two heading with an r^2 of 0.91 and an RMSE of 1.69 m [see Fig. 15(c)]. For the combined scenario of the two different headings, the correlation coefficient improves slightly with an r^2 of 0.94, whereas the RMSE reduces to 1.32 m [see Fig. 15(d)]. The slight overestimation of forest height as observed in the single headings disappeared. The forest height estimates from the two headings proof that Pol-InSAR forest height inversion with topographic correction provides consistent forest height maps independent of topography and radar look direction.

C. Impact of the Used DEM on Inversion

In Section VI-B, it was outlined that the accuracy of Pol-InSAR height inversion depends strongly on the accuracy of the used DEM. The quality of the used DEM depends mainly on the spatial resolution, which should be compatible to the resolution of the Pol-InSAR data. In the following an SRTM DEM, a TanDEM-X DEM, an L- band DEM (calculated from a single interferogram with 12-m baseline) and a LIDAR DEM will be used to test their applicability for Pol-InSAR forest height inversion using the 135° heading data set from Krycklan site. As for the Krycklan site no SRTM measurements are available (64° latitude) SRTM was simulated reducing the resolution of the TDX measurements to 90 m × 90 m.

Fig. 16 show the 2-D histogram plots (color reflects the quantity, blue = low quantity, dark red = high quantity) of the difference between Pol-InSAR forest height and LIDAR H100 versus terrain slope for the DEM's used for slope correction, including one scenario without DEM correction. The best performance corresponds to the scenario with the lowest height difference along the whole range of terrain slopes. Without DEM correction [see Fig. 16(a)] negative slopes are strongly underestimated and positive slopes are strongly overestimated.

The LIDAR DEM, the L-band DEM, and the TanDEM-X DEM [see Fig. 16(b), (c), and (e)] perform similarly. In all three scenarios the terrain slope is sufficiently corrected and the obtained results reflect the results from the validation plot displayed in Fig. 15(b) (slight overestimation along all terrain slopes). Only terrain slopes larger than 15° seem to perform less well. For the SRTM DEM-corrected height estimates [see Fig. 16(d)] negative slopes are still underestimated and positive slopes are still overestimated. Resolution of the SRTM is not sufficient for a proper correction of terrain slope in these data .

D. Sungai Wain Test Site (Tropical Scenario)

Sungai Wain forest is a tropical lowland dipterocarp forest typical for Southeast Asia and is located in east Kalimantan on the island of Borneo (lat: −1.10° long: 116.82°). This test site was part of the Indrex-II campaign [75]. A detailed description

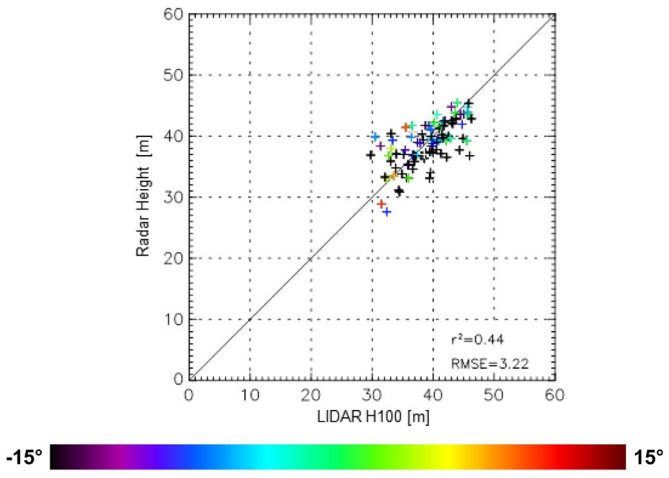

Fig. 17. Validation plots of multibaseline inversion "Sungai Wain" test site; Pol-InSAR height estimates versus LIDAR H100 reference height; the color of the stand dots represents terrain slope, scaled from −15° to 15°; 100 stands were used for validation.

of the test site and validated forest heights can be found in [29]. The maximum tree height is ∼60 m (mean tree height 40 m) with a biomass which is partly beyond 400 t/ha. The test site is placed in a hilly topography with partly steep slopes, as indicated by the X-band DEM in Fig. 18(b).

Pol-InSAR data were acquired in November 2004. A list of the used baselines is given in Table I and an amplitude image of the scene in HV polarization superimposed by the LIDAR measurements is shown in Fig. 18(a). For terrain correction the low-pass filtered X-band DEM was used.

Fig. 18(d) and (e) show two coherence images (with different baseline), acquired in HV polarization at P-band. The scene is nearly completely covered with forest. Forest height fluctuates nearly all over the image around 40 m (indicating similar scattering all over the image). Typical for the test site are the strong topographic variations (slopes up to 25°), as shown in the DEM [see Fig. 18(b)] and the slope image [see Fig. 18(c)]. Valleys are indicated by a blue line (deepest point) and hill tops by a red line (highest point) in Fig. 18(b)–(e). The coherence image in Fig. 18(d) was acquired with $B_{\mathrm{HOR}} = 30$ m and the coherence image in Fig. 18(e) with $B_{\mathrm{HOR}} = 15$ m. Coherence increases from the small to the large baseline indicating that volume decorrelation is the main decorrelation term and underlines the dependence of volume decorrelation on the vertical wavenumber κ_z.

In the coherence images in Fig. 18(d) and (e), it can be observed that in range direction, coherence is lower on positive slopes compared with the adjacent coherence estimates on the negative slopes. Furthermore, it can be observed that coherence changes mostly from low (dark) values to high (bright) values on the hill tops and the lowest valley points [red and blue lines in Fig. 18(d) and (e)].

Of course, a slope-induced change of the ground-to-volume ratio in the scattering could contribute to the observed changes in coherence as well. Nevertheless, in HV polarization, ground scattering can be assumed to play only a minor role.

Until now, inversion results could be validated with only one large ground measurement plot (540 m × 286 m) [29].

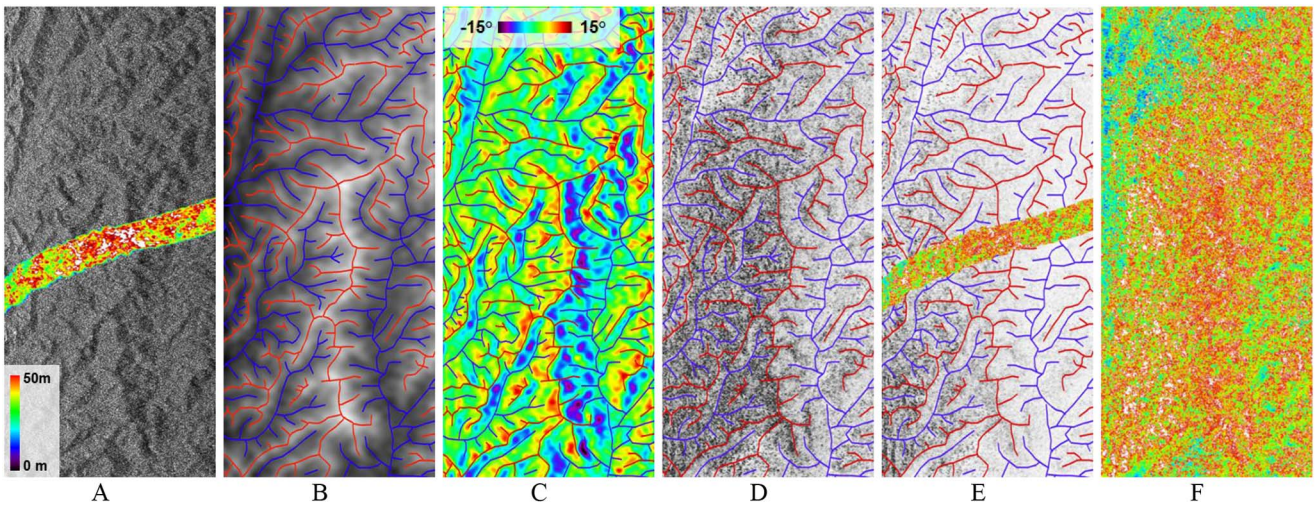

Fig. 18. Test site "Sungai Wain"; NR ($\theta = 25°$) on the left side, far-range ($\theta = 55°$) on the right side. (a) Amplitude image HV polarization, superimposed by LIDAR H100 forest height strip (scaled from 0 to 50 m). (b) low-pass filtered DEM of the test site obtained from airborne X-band interferometric data, scaled from 50 m (black) to 200 m (white). (c) Terrain slope map scaled from $-15°$ to $15°$ (see legend). (d): interferometric coherences in HV polarization scaled from 0 (black) to 1 (white) with $B_H = 30$ m. (e) interferometric coherences in HV polarization scaled from 0 (black) to 1 (white) with $B_H = 15$ m superimposed by Pol-InSAR forest heights masked with LIDAR reference height scaled from 0 to 50 m (see legend on the right side). (f) Pol-InSAR full area forest height map scaled from 0 m to 50 m: blue lines = valleys (deepest point), red lines = mountain ridges (highest point).

In August 2011, LIDAR measurements were performed over Sungai Wain site and allow now a more sophisticated validation of the estimated Pol-InSAR forest heights; therefore, cross validation is repeated in this paper for the P-band scenario.

LIDAR data cover only a small strip of the image with approximately 500 m width. The LIDAR strip crosses the image in the middle from near to FR [see Fig. 18(a)].

For cross-validation purposes, the LIDAR was cut into 100 segments of same size and the mean value of each segment was plotted against the mean value of the corresponding Pol-InSAR forest heights.

Despite the seven-year time difference between the LIDAR and the Pol-InSAR acquisitions, no severe changes of the forest are expected for this time span. The forest reached its climax stadium this means height growth is extremely slow and heavy changes occur exclusively by die back processes [77].

A complete Pol-InSAR forest height map of the whole scene is displayed in Fig. 18(f). In the case in which for one pixel there are several high-performance height estimates available, one height estimate is selected applying the method described in [33]. Forest height reaches several times values larger than 50 m. Lower forest parts on the top and the lower left arise from the severe forest fires during the El Nino events in 1982 and 1998. Here, the pristine forest was completely destroyed by the fire and the area is now covered with Macaranga secondary forest. Over large areas of the image the Dipterocarp forest is still untouched.

For the sake of comparison the Pol-InSAR height corresponding to the area covered by the LIDAR strip is superimposed to the coherence image in Fig. 18(e).

A validation plot is displayed in Fig. 17 each validation point is colored according to the mean terrain slope of the segment. The validated heights seem to be independent from terrain slope and have, even after seven years of time difference between LIDAR and radar acquisition, only an RMSE of 3.2 m. The correlation coefficient is rather low (0.44), but this can be explained by the lack of forest heights lower than 30 m in the cross-validation area. The forest heights of the single segments range only between 30 and 45 m (only 15 m span) and the small height span in combination with the RMSE of 3.2 m lowers the correlation coefficient dramatically. Extinction ranges mainly between 0 and 0.2 dB/m and reaches rarely values greater than 0.5 dB/m. At 8% of the inverted pixels a ground contribution could be detected which does not exceed an m of 0.20.

VIII. Discussion and Conclusion

Forest height estimation by means of model-based inversion of Pol-InSAR has the potential for accurate, i.e., within 10% or even better, forest height mapping across a wide range of forest and terrain conditions. However, the inversion performance depends strongly on the accurate compensation of nonvolumetric decorrelation contributions, the choice of the appropriate vertical wavenumber κ_z and the knowledge about its variation within the scene.

This paper focuses on the impact of the vertical interferometric wavenumber κ_z on the performance of forest height estimation. In a quantitative analysis it was demonstrated that a single κ_z allows accurate inversion only for a limited range of forest heights. For taller stands, the performance is limited by the variance induced by the low coherence levels. This can partially be compensated by increasing the number of looks at the expense of spatial resolution. With further increasing stand height the sensitivity of the interferometric coherence to forest height saturates leading to underestimated forest height estimates. For shorter stands, the performance is limited primarily by the bias induced by the residual nonvolumetric decorrelation contributions. In consequence, in order to obtain the optimum inversion performance over a wide range of forest heights,

multiple Pol-InSAR acquisitions with variable κ_z values are required. A concept for defining the optimum κ_z values for a given height range has been introduced in Section IV. Accordingly, a 10% height estimation accuracy, for a height range from 5 to 60 m requires—in general—three different κ_z values.

If only one baseline is available, then, the estimation performance depends strongly on the prevailing forest heights.

A good compromise in order to obtain reliable forest height estimates with sufficient accuracy for single baseline acquisitions is to mask $\kappa_z < 0.05$ rad/m and $\kappa_z > 0.15$ rad/m.

The vertical interferometric wavenumber κ_z is defined by the acquisition geometry and depends on the incidence angle and on the range component of the local terrain slope. Consequently, for a precise estimation of κ_z a DEM is required. In order to assess the required DEM quality, several available DEM products have been tested on their suitability for topographic correction in the Pol-InSAR inversion process. While the low-resolution SRTM DEM was not able to fully compensate terrain slope effects, the TanDEM-X DEM, as well as the LIDAR DEM and the (L-Band) DEM obtained from the Pol-InSAR measurements itself performed similar and were able to correct the topographic effects.

Finally, Pol-InSAR forest height estimation was successfully demonstrated in L- and P-band for forest heights up to 40 m in three different test sites representing three ecologically different forest types: boreal forest, temperate forest and tropical forest. A P-band acquisition over dense tropical lowland forest in Indonesia with tree heights up to 60 m could be successfully inverted and cross validated with LIDAR measurements.

ACKNOWLEDGMENT

The authors would like to thank K. Gutjahr from Joanneum Research Center for his support in evaluating the "Kobernausser Wald" data and for providing the LIDAR reference measurements. The authors also thank R. Scheiber for his effort in processing the acquired data sets. The authors also thank A. Marino for his support in Interactive Data Language programming.

REFERENCES

[1] A. van Laar and A. Akca, *Forest Mensuration (Managing Forest Ecosystems)*. Berlin, Germany: Springer-Verlag, 2007, pp. 118–121.

[2] H. Pretzsch, *Forest Dynamics, Growth and Yield: From Measurement to Model*. Berlin, Germany: Springer-Verlag, 2009.

[3] T. Mette, "Forest biomass estimation from polarimetric SAR interferometry, Ph.D. dissertation, Forschungsbericht 2007-10, Deutsches Zentrum für Luft-und Raumfahrt e. V. in der Helmholtz-Gemeinschaft, Tech. Univ. München, 2007.

[4] T. Mette, K. Papathanassiou, I. Hajnsek, H. Pretzsch, and P. Biber, "Applying a common allometric equation to convert forest height from Pol-InSAR data to forest biomass," in *Proc. IEEE IGARSS*, Anchorage, AK, USA, Sep. 20–24, 2004, pp. 269–272.

[5] P. Köhler and A. Huth, "Towards ground-truthing of spaceborne estimates of above-ground life biomass and leaf area index in tropical rain forests," *Biogeosciences*, vol. 7, no. 8, pp. 2531–2543, Aug. 2010.

[6] P. M. Montesano *et al.*, "The uncertainty of biomass estimates from LiDAR and SAR across a boreal forest structure gradient," *Remote Sens. Environ.*, vol. 154, pp. 398–407, Nov. 2014.

[7] J. Chave *et al.*, "Tree allometry and improved estimation of carbon stocks and balance in tropical forests," *Oecologia*, vol. 145, no. 1, pp. 87–99, Aug. 2005.

[8] H.-D. V. Böhm, V. Liesenberg, and S. H. Limin, "Multi-temporal airborne LiDAR-survey and field measurements of tropical peat swamp forest," *IEEE J. Sel. Topics Appl. Earth Observ. Remote Sens.*, vol. 6, no. 5, pp. 1524–1530, Jun. 2013.

[9] F. G. Hall *et al.*, "Characterizing 3D vegetation structure from space: Mission requirements," *Remote Sens. Environ.*, vol. 115, no. 11, pp. 2753–2775, Nov. 2011.

[10] Y. Pan *et al.*, "A large and persistent carbon sink in the world's forests," *Science*, vol. 333, no. 6045, pp. 988–993, Aug. 2011.

[11] A. Kangas and M. Maltamo, *Forest Inventory: Methodology and Application*. Berlin, Germany: Springer-Verlag, 2006.

[12] Global Forest Observation Initiative (GFOI)–Review of Priority Research and Development Topics, GEO Geneva, Switzerland, 2013.

[13] M. Prodan, *Holzmesslehre*. Frankfurt am Main, Germany: J. D. Sauerländer's Verlag, 1965.

[14] M. A. Wulder, C. W. Bater, N. C. Coops, T. Hilker, and J. C. White, "The role of LiDAR in sustainable forest management," *Forestry Chronicle*, vol. 84, no. 6, pp. 807–826, 2008.

[15] E. Naesset and T. Oekland, "Estimating tree height and tree crown properties using airborne scanning laser in a boreal nature reserve," *Remote Sens. Environ.*, vol. 79, no. 1, pp. 105–115, Jan. 2002.

[16] C. Mallet and C. Bretar, "Full waveform topographic lidar: State-of-the-art," *ISPRS J. Photogramm. Remote Sens.*, vol. 64, no. 1, pp. 1–16, Jan. 2009.

[17] R. O. Dubayah *et al.*, "Estimation of tropical forest height and biomass dynamics using lidar remote sensing at La Selva, Costa Rica," *J. Geophys. Res. Biogeosci.*, vol. 115, no. G2, Jun. 2010, Art. ID. G00E09.

[18] M. A. Lefsky *et al.*, "Estimates of forest canopy height and aboveground biomass using ICESat," *Geophys. Res. Lett.*, vol. 32, no. L22, Nov. 2005, Art. ID. L22S02.

[19] M. Simard, N. Pinto, J. B. Fisher, and A. Baccini, "Mapping forest canopy height globally with spaceborne LIDAR," *J. Geophys. Res.*, vol. 116, no. G04, Dec. 2011, Art. ID. G04021.

[20] A. M. Lefsky *et al.*, "LIDAR remote sensing of forest canopy structure and biophysical properties of Douglas-Fir Western Hemlock forests," *Remote Sens. Environ.*, vol. 70, no. 3, pp. 339–361, Dec. 1999.

[21] A. M. Lefsky, W. B. Cohen, G. C. Parker, and D. J. Harding "LIDAR remote sensing for ecosystem studies," *Bioscience*, vol. 52, no. 1, pp. 19–30, Jan. 2002.

[22] G. Sun, K. J. Ranson, D. S. Kimes, J. B. Blair, and K. Kovacs, "Forest vertical structure from GLAS: An evaluation using LVIS and SRTM data," *Remote Sens. Environ.*, vol. 112, no. 1 pp. 107–117, Jan. 2008.

[23] D. J. Harding and C. C. Carabajal, "ICESat waveform measurements of within-footprint topographic relief and vegetation vertical structure," *Geophys. Res. Lett.*, vol. 32, no. 21, Nov. 2005, Art. ID. L21S10.

[24] D. J. Harding, A. M. Lefsky, G. Parker, and J. Blair, "Laser altimeter canopy height profiles. Methods and validation for closed canopy broadleaved forest," *Remote Sens. Environ.*, vol. 96, no. 3, pp. 283–297, Jun. 2001.

[25] F. Kugler, D. Schulze, I. Hajnsek, H. Pretzsch, and K. P. Papathanassiou, "TanDEM-X Pol-InSAR performance for forest height estimation," *IEEE Trans. Geosci. Remote Sens.*, vol. 52, no. 10, pp. 6404–6422, Oct. 2014.

[26] K. P. Papathanassiou and S. R. Cloude, "Single-baseline polarimetric SAR interferometry," *IEEE Trans. Geosci. Remote Sens.*, vol. 39, no. 11, pp. 2352–2363, Nov. 2001.

[27] S. R. Cloude and K. P. Papathanassiou, "Three-stage inversion process for polarimetric SAR interferometry," *Proc. Inst. Elect. Eng.—Radar Sonar Navig.*, vol. 150, no. 3, pp. 125–134, Jun. 2003.

[28] J. Praks, F. Kugler, K. P. Papathanassiou, I. Hajnsek, and M. Hallikainen, "Height estimation of Boreal Forest: interferometric model-based inversion at L- and X-band versus HUTSCAT profiling scatterometer," *IEEE Geosci. Remote Sens. Lett.*, vol. 4, no. 3, pp. 466–470, Jul. 2007.

[29] I. Hajnsek, F. Kugler, S. Lee, and K. Papathanassiou, "Tropical forest parameter estimation by means of Pol-InSAR: The INDREX II campaign," *IEEE Trans. Geosci. Remote Sens.*, vol. 47, no. 2, pp. 481–493, Feb. 2009.

[30] F. Kugler, F. N. Koudogbo, K. P. Papathanassiou, and K. Gutjahr, "Frequency effects in Pol-InSAR forest height estimation," in *Proc. EUSAR Conf.*, Dresden, Germany, 2006, pp. 1–4.

[31] M. Neumann, L. Ferro-Famil, and A. Reigber, "Estimation of forest structure, ground an canopy layer characteristics from multibaseline polarimetric interferometric SAR data," *IEEE Trans. Geosci. Remote Sens.*, vol. 48, no. 3, Part 1, pp. 1086–1104, Mar. 2009.

[32] F. Garestier, P. C. Dubois-Fernandez, and K. P. Papathanassiou, "Pine forest height inversion using single-pass X- band PolInSAR data," *IEEE Trans. Geosci. Remote Sens.*, vol. 46, no. 1, pp. 59–68, Jan. 2008.

[33] S.-K. Lee, F. Kugler, I. Hajnsek, and K. Papathanassiou, "Multibaseline polarimetric SAR interferometry forest height inversion approaches," presented at the 5th Int. Workshop Sci. Appl. POLINSAR, Frascati, Italy, Jan. 24–28, 2011, pp. 1–7.

[34] S.-K. Lee, F. Kugler, K. P. Papathanassiou, and I. Hajnsek, "Quantification of temporal decorrelation effects at L- band for polarimetric SAR interferometry applications," *IEEE J. Sel. Topics Appl. Earth Observ. Remote Sens.*, vol. 6, no. 3, pp. 1351–1367, Jun. 2013.

[35] F. Garestier, P. C. Dubois-Fernandez, and I. Champion, "Forest height inversion using high-resolution P- band Pol-InSAR data," *IEEE Trans. Geosci. Remote Sens.*, vol. 46, no. 11, Part 1, pp. 3544–3559, Nov. 2008.

[36] J. Praks, O. Antropov, and M. T. Hallikainen, "LIDAR-aided SAR interferometry studies in Boreal forest: Scattering phase center and extinction coefficient at X- and L- band," *IEEE Trans. Geosci. Remote Sens.*, vol. 50, no. 10, pp. 3831–3843, Oct. 2012.

[37] M. Lavalle and K. Khun, "Three-baseline InSAR estimation of forest height," *IEEE Geosci. Remote Sens. Lett.*, vol. 11, no. 10, pp. 1737–1741, Oct. 2014.

[38] A. Roueff, A. Arnaubec, P. Dubois-Fernandez, and P. Réfrégier, "Cramer–Rao lower bound analysis of vegetation height estimation with random volume over ground model and polarimetric SAR interferometry," *IEEE Geosci. Remote Sens. Lett.*, vol. 8, no. 6, pp. 1115–1119, Nov. 2011.

[39] R. N. Treuhaft, S. N. Madsen, M. Moghaddam, and J. J. van Zyl, "Vegetation characteristics and underlying topography from interferometric data," *Radio Sci.*, vol. 31, no. 6, pp. 1449–1495, Nov./Dec. 1996.

[40] S. R. Cloude and K. P. Papathanassiou, "Polarimetric SAR interferometry," *IEEE Trans. Geosci. Remote Sens.*, vol. 36, no. 5, pp. 1551–1565, Sep. 1998.

[41] T. Flynn, M. Tabb, and R. Carande, "Coherence region shape extraction for vegetation parameter estimation in polarimetric SAR interferometry," in *Proc. IEEE IGARSS*, Toronto, ON Canada, Jun. 24–28, 2002, pp. 2596–2598.

[42] M. Tabb and R. Carande, "Robust inversion of vegetation structure parameters from low frequency polarimetric interferometric SAR," in *Proc. IEEE IGARSS*, Sydney, N.S.W., Australia, Jul. 9–13, 2001, pp. 3188–3190.

[43] S. R. Cloude, *Polarisation*. London, U.K.: Oxford Univ. Press, 2010

[44] H. A. Zebker and J. Villasenor, "Decorrelation in interferometric radar echoes," *IEEE Trans. Geosci. Remote Sens.*, vol. 30, no. 5, pp. 950–959, Sep. 1992.

[45] F. Gatelli *et al.*, "The wavenumber shift in SAR interferometry," *IEEE Trans. Geosci. Remote Sens.*, vol. 32, no. 4, pp. 855–865, Jul. 1994.

[46] J. O. Hagberg, L. M. Ulander, and J. Askne, "Repeat-pass SAR interferometry over forested terrain," *IEEE Trans. Geosci. Remote Sens.*, vol. 33, no. 2, pp. 331–340, Mar. 1995.

[47] K. P. Papathanassiou and S. R. Cloude, "The effect of temporal decorrelation on the inversion of forest parameters from Pol-InSAR data," in *Proc. IEEE IGARSS*, Toulouse, France, Jul. 21–25, 2003, pp. 1429–1431.

[48] S. K. Lee, F. Kugler, I. Hajnsek, and K. P. Papathanassiou, "The impact of temporal decorrelation over forest terrain in polarimetric SAR interferometry," presented at the 4th Int. Workshop Sci. Appl. POLinSAR, Frascati, Italy, Jan. 26–30, 2009, pp. 1–6.

[49] G. Krieger, K. Papathanassiou, and S. Cloude, "Spaceborne polarimetric SAR interferometry: Performance analysis and mission concepts," *EURASIP J. Appl. Signal Process.*, vol. 2005, no. 20, pp. 3272–3292, Dec. 2005.

[50] R. Bamler and P. Hartl, "Synthetic aperture radar interferometry," *Inv. Probl.*, vol. 14, no. 4, pp. R1–R54, Aug. 1998.

[51] S. R. Cloude, "Polarisation coherence tomography," *Radio Sci.*, vol. 41, no. 4, Aug. 2006, Art. ID. RS4017.

[52] S. R. Cloude, "Dual baseline coherence tomography, "*IEEE Geosci. Remote Sens. Lett.*, vol. 4, no. 1, pp. 127–131, Jan. 2007.

[53] F. Garestier and T. Le Toan, "Forest modelling for height inversion using single-baseline InSAR/Pol-InSAR data," *IEEE Trans. Geosci. Remote Sens.*, vol. 48, no. 3, pp. 1528–1539, Mar. 2010.

[54] F. Garestier and T. Le Toan, "Estimation of the backscatter vertical profile of a pine forest using single baseline P- band (Pol-)InSAR data," *IEEE Trans. Geosci. Remote Sens.*, vol. 48, no. 9, pp. 3340–3348, Sep. 2010.

[55] F. Kugler, S.-K. Lee, and K. Papathanassiou, "Estimation of forest vertical structure parameters by means of multi-baseline Pol-InSAR," in *Proc. IEEE IGARSS*, Cape Town, South Africa, Jul. 12–17, 2009, pp. IV-721–IV-724.

[56] R. Treuhaft and S. R. Cloude, "The structure of oriented vegetation from polarimetric interferometry," *IEEE Trans. Geosci. Remote Sens.*, vol. 37, no. 5, pp. 2620–2624, Sep. 1999.

[57] I. Hajnsek and S. R. Cloude, "Differential extinction estimation over agricultural vegetation from POL-InSAR," presented at the 2nd Int. Workshop Sci. Appl. POLinSAR, Frascati, Italy, Jan. 17–21, 2005.

[58] E. P. W. Attema and F. T. Ulaby, "Vegetation modeled as a water cloud," *Radio Sci.*, vol. 13, no. 2, pp. 357–364, Mar./Apr. 1978.

[59] R. N. Treuhaft and P. R. Siqueira, "The vertical structure of vegetated land surfaces from interferometric and polarimetric radar," *Radio Sci.*, vol. 35, no. 1, pp. 141–177, Jan./Feb. 2000.

[60] M. Lavalle, M. Simard, and S. Hensley, "A temporal decorrelation model for polarimetric radar interferometers," *IEEE Trans. Geosci. Remote Sens.*, vol. 50, no. 7, Part 2, pp. 2880–2888, Jul. 2012

[61] D. Just and R. Bamler, "Phase statistics of interferograms with applications to synthetic aperture radar," *Appl. Opt.*, vol. 33, no. 20, pp. 4361–4368, Jul. 1994.

[62] I. Hajnsek, K. P. Hajnsek, K. P. Papthanssiou, and S. R. Cloude, "Removal of additive noise in polarimetric eigenvalue processing," in *Proc. IEEE IGARSS*, Sydney, N.S.W., Australia, Jul. 9–13, 2001, pp. 2778–2780.

[63] R. Touzi, A. Lopes, J. Bruniquel, and P. W. Vachon, "Coherence estimation for SAR imagery," *IEEE Trans. Geosci. Remote Sens.*, vol. 37, no. 1, pp. 135–149, Jan. 1999.

[64] R. Touzi and A. Lopes, "Statistics of the stokes parameters and of the complex coherence parameters in one-look and multilook speckle fields," *IEEE Trans. Geosci. Remote Sens.*, vol. 34, no. 2, pp. 519–531, Mar. 1996.

[65] R. T. Fomena and S. R. Cloude, "On the role of coherence optimization in polarimetric SAR interferometry," presented at the CEOS SAR Cal/Val Workshop, Adelaide, SA, Australia, Sep. 28–30, 2005, pp. 1–6.

[66] L. Ferro-Famil, M. Neumann, and Y. Huang, "Multi-baseline Pol-InSAR statistical techniques for the characterization of distributed media," in *Proc. IEEE IGARSS*, Cape Town, South Africa, Jul. 24–29, 2009, pp. III-971–III-974.

[67] R. Horn, "The DLR airborne SAR project E-SAR," in *Proc. IEEE IGARSS*, Lincoln, NE, USA, May 27–31, 1996, pp. 1624–1628.

[68] P. Dubois-Fernandez *et al.*, "TropiSAR, A SAR data acquisition campaign in French Guiana," presented at the 8th EUSAR Conf., Aachen, Germany, Jun. 7–10, 2010, pp. 1–4.

[69] L. Hongxi, S. Hziyong, G. Rui, and G. Rui, "S-RVoG model for forest parameters inversion over underlying topography," *Electron. Lett.*, vol. 49, no. 9, pp. 618–620, Apr. 2013.

[70] M. Lavalle, D. Solimini, E. Pottier, and Y.-L. Desnos, "Forest parameters inversion using polarimetric and interferometric SAR data," in *Proc. IEEE IGARSS*, Cape Town, South Africa, Jul. 24–29, 2009.

[71] T. G. Farr *et al.*, "The shuttle radar topography mission," *Rev. Geophys.*, vol. 45, no. 2, Jun. 2007, Art. ID. RG2004.

[72] G. Krieger *et al.*, "TanDEM-X: A satellite formation for high-resolution SAR interferometry," *IEEE Trans. Geosci. Remote Sens.*, vol. 45, no. 11, pp. 3317–3341, Nov. 2007

[73] T. M. Lillesand, R. W. Kiefer, and J. W. Chipman, *Remote Sensing and Image Interpretation*. Hoboken, NJ, USA: Wiley, 2004, p. XIV+763.

[74] T. Aulinger *et al.*, "Validation of heights from Interferometric SAR and LIDAR over the temperate Forest Site Nationalpark Bayerischer Wald," presented at the 2nd Int. Workshop Sci. Appl. POLinSAR, Frascati, Italy, Jan. 17–21, 2005, pp. 1–6.

[75] I. Hajnsek *et al.*, "INDREX II-Indonesian airborne radar experiment campaign overt tropical forest in L- and P-band," presented at the 2nd Int. Workshop Sci. Appl. PolinSAR, Frascati, Italy, Jan. 17–21, 2005.

[76] P. A. Rosen *et al.*, "Synthetic aperture radar interferometry," *Proc. IEEE*, vol. 88, no. 3, pp. 333–382, Mar. 2000

[77] F. Montagini and C. F. Jordan, *Tropical Forest Ecology the Basis for Conservation and Management*. Berlin, Germany: Springer-Verlag, 2005

[78] J. D. Ballester-Berman and J. M. Lopez-Sanchez, "Coherence Loci for a homogeneous volume over a double-bounce ground return," *IEEE Geosci. Remote Sens. Lett.*, vol. 4, no. 2, pp. 317–321, Apr. 2007.

[79] J. D. Ballester-Berman and J. M. Lopez-Sanchez, "Combination of direct and double-bounce ground responses in the homogeneous oriented volume over ground model," *IEEE Geosci. Remote Sens. Lett.*, vol. 8, no. 1, pp. 54–58, Jan. 2011.

[80] H. A. Zebker and R. Goldstein, "Topographic mapping from interferometric synthetic aperture radar," *J. Geophys. Res.*, vol. 91, no. B5, pp. 4993–4999, Apr. 1986.

[81] E. Rodriguez and J. Martin, "Theory and design of interferometric synthetic aperture radars," *Proc. Inst. Elect. Eng. F—Radar Signal Process.*, vol. 139, no. 2, pp. 147–159, Apr. 1992.

[82] S. Cloude, D. Corr, and M. Williams, "Target detection beneath foliage using polarimetric synthetic aperture radar interferometry," *Waves Random Media*, vol. 14, no. 2, pp. 393–414, Apr. 2004.

Florian Kugler was born in Bavaria, Germany, in 1974. He received the Diploma degree (Dipl. Ing. silv.) in forestry science from the Technische Universität München, Freising, Germany, in 2004. He has been currently working toward the Ph.D. degree since 2004.

Since October 2008, he has been a Research Scientist with the German Aerospace Center (DLR), Oberpfaffenfoffen, Germany. His research focuses on remote sensing on forests by using polarimetric synthetic aperture radar interferometry.

Seung-Kuk Lee received the B.S. and M.S. degrees from Yonsei University, Seoul, Korea, in 2000 and 2005, respectively, and the Ph.D. degree from Eidgenoessische Technische Hochschule, Zurich, Switzerland, in 2013.

From 2006 to 2013, he was with the Microwaves and Radar Institute (HR), German Aerospace Center (DLR), Oberpfaffenfoffen, Germany. Since 2013, he has been with NASA Goddard Space Flight Center (GSFC), Greenbelt, MD, USA. He is currently a NASA Postdoctoral Fellow with NASA/GSFC. His main interests are 3-D forest parameter estimation using polarimetric interferometric synthetic aperture radar (SAR) techniques and analysis SAR images for terrestrial ecosystem applications.

Irena Hajnsek (AM'01–M'06–SM'09–F'14) received the Dipl. degree (Honors) from the Free University of Berlin, Berlin, Germany, in 1996 and the Dr. degree (Honors) from Friedrich Schiller University of Jena, Jena, Germany, in 2001.

From 1996 to 1999, she was with the Microwaves and Radar Institute (DLR-HF), German Aerospace Center (DLR), Oberpfaffenhofen, Germany. From 1999 to 2000, she has been 10 months with the Institut d'Electronique et de Télécommunications de Rennes, University of Rennes 1, France and 4 months with Applied Electromagnetics (AEL) in St. Andrews, Scotland, in the frame of the EC-TMR Radar Polarimetry Network. In 2005, she was for 6 weeks, Guest Scientist with the University of Adelaide, Adelaide, S.A., Australia. She is the Science Coordinator of the German satellite mission TanDEM-X. Since November 2009, he has been a Professor of Earth observation with the Swiss Federal Institute of Technology (ETH) Zürich Institute of Environmental Engineering and, at the same time, Head of the polarimetric synthetic aperture radar (SAR) Interferometry Research Group, German Aerospace Center Microwaves and Radar Institute. Her main research interests are in electromagnetic propagation and scattering theory, radar polarimetry, SAR and interferometric SAR data processing techniques, environmental parameter modeling, and estimation.

Dr. Hajnsek was a member of the ESA Mission Advisory Group (MAG) of the 7th Explorer Mission CoReH2O from 2009–2013. She was Technical Program Cochair of the IEEE IGARSS 2012 Symposium in Munich. Since 2013, she has been a member of the IEEE GRSS AdCom.

Konstantinos P. Papathanassiou (AM'01–M'06–SM'09–F'13) received the Dipl. Ing degree (Honors) from Technical University of Graz, Graz, Austria and the Dr. degree (Honors) in 1994 and 1999, respectively.

From 1992 to 1994, he was with the Institute for Digital Image Processing (DIBAG) of Joanneum Research, Graz. Between 1995 and 1999, he was with the Microwaves and Radar Institute (HR, German Aerospace Center (DLR), Oberpfaffenhofen, Germany. From 1999 to 2000, he was an EU Postdoctoral Fellow with Applied Electromagnetics (AEL) in St. Andrews, Scotland. Since October 2000, he is again with the Microwaves and Radar Institute (HR) of the German Aerospace Center (DLR). He is a Senior Scientist leading the Information Retrieval research group with DLR-HR. His main research interests are in polarimetric and interferometric processing and calibration techniques, polarimetric SAR interferometry, and the quantitative parameter estimation from SAR data, as well as in SAR mission design and SAR mission performance analysis. He has more than 100 publications in international journals, conferences, and workshops.

Dr. Papathanassiou was the recipient of the IEEE GRSS IGARSS Symposium Prize Paper Award in 1998, the Best Paper Award of the European SAR Conference (EUSAR) in 2002, and the DLR science award in 2002. In 2011, he was awarded with DLR's Senior Scientist Award.

Height Estimation of Boreal Forest: Interferometric Model-Based Inversion at L- and X-Band Versus HUTSCAT Profiling Scatterometer

Jaan Praks, *Member, IEEE*, Florian Kugler, Konstantinos P. Papathanassiou, *Senior Member, IEEE*, Irena Hajnsek, *Member, IEEE*, and Martti Hallikainen, *Fellow, IEEE*

***Abstract*—In this letter, we present results from the FinSAR project, where the E-SAR and Helsinki University of Technology Scatterometer (HUTSCAT) instruments were operated together in order to validate tree-height retrieval algorithms for boreal forest. The campaign was carried out in Finland in fall 2003. The main instruments of the campaign were the E-SAR airborne radar (operating at L- and X-band) and the HUTSCAT helicopter-borne profiling scatterometer (operating at X- and C-band). We compare and discuss forest height obtained from the inversion quad-pol polarimetric interferometric synthetic aperture radar (SAR) data sets at L-band and forest height obtained from the inversion of single-pol X-band in SAR data with forest height estimates from HUTSCAT scatterometer data. Our results show that the forest height values, which are estimated by means of two different radar instruments, are in good agreement. The correlation between HUTSCAT and E-SAR height estimates ($R = 0.77$ at L-band and $R = 0.75$ at X-band) underlines the good agreement between the results obtained by the two approaches.**

***Index Terms*—Boreal forest, polarimetric interferometry, scatterometer, synthetic aperture radar (SAR), tree height.**

I. Introduction

As a result of the launch of the new spaceborne synthetic aperture radar (SAR) sensor generation in 2006–2007, great interest has been taken in coherent image processing techniques. One of the promising new technologies proposed for forest mapping and monitoring is forest height estimation by model-based inversion of polarimetric interferometric SAR (POLInSAR) data [1], [2]. The estimation performance has been validated for a large variety of forests and terrain conditions, including tropical rainforest [3] and tempered broad-leaved forests [4]. Looking now on boreal forests, while conventional InSAR techniques have been used to investigate vertical profile [5] and biomass [6]–[8], no validation of POLInSAR methodology has been performed up to now. To this end, we have conducted a case study where we evaluate for the first time how the POLInSAR approach performs for mixed boreal forests. The measurement campaign was conducted in southern Finland, at the end of September and the beginning of October 2003. The POLInSAR data were collected by the German Aerospace Center's (DLR) E-SAR airborne radar [9] at L- and X-band over an area of 3 × 15 km. Additionally, C- and X-band backscattering profiles of the test site forest were measured with the helicopter-mounted Helsinki University of Technology Scatterometer (HUTSCAT) profiling scatterometer [10], [11]. Ground measurements were performed during the campaign, and a large database of supporting material was established. This letter is structured as follows. First, we describe the test site, the measurement campaign, and the collected datasets. Then, we address the forest height inversion from the different measurements and the cross validation of the obtained estimates. Finally, we discuss the results and draw the conclusions.

Manuscript received November 1, 2006; revised March 3, 2007.

J. Praks and M. Hallikainen are with the Laboratory of Space Technology, Helsinki University of Technology, 02015 Espoo, Finland.

F. Kugler, K. P. Papathanassiou, and I. Hajnsek are with the Microwaves and Radar Institute, German Aerospace Center, Deutsches Zentrum für Luft- und Raumfahrt, 82234 Wessling, Germany.

Digital Object Identifier 10.1109/LGRS.2007.898083

II. Measurement Campaign

A. Test Site

The test site is located in southern Finland (N 60° 11′, E 24° 29′), near Helsinki. The area represents typical land use for southern Finland, where agricultural fields alternate with forest patches and lakes. The forest in the test area is heterogeneous and consists of rather small stands. The test area incorporates young and old coniferous stands and mixed (coniferous/deciduous) stands, clear cuts, and mires. The dominant tree species are Scotch pine, Norwegian spruce, birch, and alder. According to a forest inventory conducted in 2001, which is covering part of the study site, the median stand size in the area is approximately 1 ha, median age is 46 years, median stand mean height is 6.3 m, highest stand mean height is 22 m, and median stem volume of a stand is 160 m^3/ha. Elevation varies from 15 to 80 m above mean sea level. The terrain is relatively rough and rocky, particularly in the forest. Rapid elevation changes, and rough surface makes the site challenging for POLInSAR methods. During the campaign, the deciduous forest was still in full leaf, but discoloration had already begun for the broad-leaved species.

B. E-SAR Flight

The E-SAR flight took place on September 29, 2003, between eight and nine o'clock in the morning. The instrument flew in about 3-km altitude along five parallel tracks, each separated by a spatial baseline of 5 m, and collected repeat pass quad-pol images at L-band (1.3 GHz) and along a single track in a single-pass single-pol vertical-vertical (VV) polarization, radar transmitting and receiving antenna polarizations

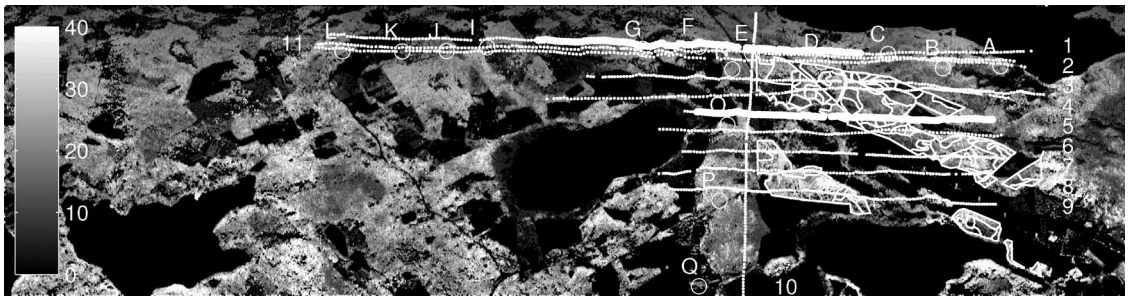

Fig. 1. Forest height map generated by model inversion using L-band POLInSAR combined with ancillary data. Slant range geometry. (Top) Near range, (bottom) far range. Dotted lines are the HUTSCAT measurement tracks identified by numbers. Part of tracks 1 and 5 are highlighted and presented in detail in Fig. 2. Solid lines show available forest stand map. Circles marked with letters denote ground sample plots. Forest height (meters) scales on the left. The black regions correspond to nonforested areas such as lakes and fields.

interferometric mode at X-band (9.6 GHz). The temporal baseline between subsequent tracks was approximately 12–14 min. Both frequencies have been acquired using a 100-MHz bandwidth and processed to a 2 × 2 m (range and azimuth) resolution grid. The weather during the image acquisition was, according to our weather station located in the area, mostly calm with an average wind from WSW from 0 to 1.8 m/s. The wind was measured at 2-m height from the ground. Air temperature in the forest was around 10 °C.

C. HUTSCAT Flight

Reference tree-height data were collected by the helicopter-borne HUTSCAT scatterometer [10], which is able to collect a vertical backscattering profile along the flight track at C-band (5.4 GHz) and X-band (9.8 GHz). The HUTSCAT measurement was carried out two days later, due to thick fog, under similar weather conditions. The incidence angle was vertical, and the helicopter location was measured by differential GPS (the attitude was not acquired). HUTSCAT measured 11 transects, altogether 36 km. Most of the HUTSCAT measurements are concentrated on a 2 × 2 km area (see Fig. 1), covering the E-SAR near and midrange. Accuracy of the HUTSCAT tree-height measurement capability has been determined to be 1.6 m [12]. The HUTSCAT range resolution is 0.65 m, and antenna beam width is 3.8° resulting 6.6-m footprint on the ground from 100 m altitude. However, the system sampling frequency is 20 Hz which corresponds to along-track sampling distance which is 1.25 m when helicopter moves with ideal speed of 25 m/s.

D. Ground Measurements and Supplementary Material

Ground measurements were made both during the E-SAR and during the HUTSCAT flight day. The test plots were located along the HUTSCAT flight lines. Soil moisture, temperature, and leaf area index (with LAI2000) were measured, and digital photographs were taken. Weather information was collected by two portable weather stations. Forest inventory data were made available by the local forest authority for 76 stands, covering a 136-ha area. The forest stand information was gathered in April 2001, and unfortunately, it may not be sufficiently up to date for some rapidly growing stands. Aerial image mosaic and maps are available for the whole test site.

III. Methods

A. E-SAR

The estimation of forest height from interferometric coherence measurements is based on the inversion of the random volume over ground (RVoG) scattering model by using in principle the three-stage inversion process described in [2]. The model describes the vegetation layer (canopy + branches + trunks) as a homogeneous layer of given height (corresponding to a mean for forest height h_{V}) located over an impenetrable ground that accounts for any scattering contribution with an isolated phase center located on the ground. For a given nonzero spatial baseline, the model gives the modeled interferometric coherence $\tilde{\gamma}_{\mathrm{m}}$ as a function of polarization $\vec{w}$ as follows:

$$\tilde{\gamma}_{\mathrm{m}}(\vec{w}) = \exp(i\phi_0)\frac{\tilde{\gamma}_{\mathrm{V}} + m(\vec{w})}{1 + m(\vec{w})} \tag{1}$$

where $\phi_0 = \kappa_z z_0$ is the phase related to the ground topography z_0, and κ_z is the effective vertical interferometric wavenumber after range spectral filtering that depends on the imaging geometry and the radar wavelength. $\tilde{\gamma}_{\mathrm{V}}$ is the volume-only coherence (i.e., the volume decorrelation caused in the absence of the ground layer), and m is the effective ground-to-volume amplitude ratio accounting for the attenuation through the volume

$$m(\vec{w}) = \frac{m_{\mathrm{G}}(\vec{w})}{m_{\mathrm{V}}(\vec{w})}\exp\left(-\frac{2\sigma h_{\mathrm{V}}}{\cos\theta_0}\right) \tag{2}$$

where m_{G} and m_{V} are the ground and volume scattering amplitudes, σ is the mean extinction coefficient of the volume layer, h_{V} is the thickness of the volume layer, and θ_0 is the mean incidence angle [1], [2]. Volume decorrelation for the vegetation layer alone is given by

$$\tilde{\gamma}_{\mathrm{V}} = \frac{\int_0^{h_{\mathrm{V}}} \exp\left(\frac{2\sigma z'}{\cos\theta_0}\right)\exp\left(i\kappa_z z'\right)dz'}{\int_0^{h_{\mathrm{V}}} \exp\left(\frac{2\sigma z'}{\cos\theta_0}\right)dz'}. \tag{3}$$

Assuming that all decorrelation is caused by volume decorrelation and neglecting other decorrelation sources [as temporal, signal-to-noise ratio (SNR), and/or processing induced decorrelation contributions], the inversion problem of (1) can be

written in terms of a minimization problem between measured coherence $\tilde{\gamma}$ and modeled coherence $\tilde{\gamma}_{\mathrm{m}}$

$$\min_{h_{\mathrm{V}},\sigma,m(\vec{w}),\phi_0} \left\| \tilde{\gamma}(\vec{w}) - \tilde{\gamma}_{\mathrm{m}}\left(h_{\mathrm{V}},\sigma,m(\vec{w}),\phi_0\right) \right\|. \tag{4}$$

Note that the terms inside the brackets indicate the four unknowns. The problem can be solved uniquely in terms of a quad-pol single baseline acquisition [1] that provides three independent polarizations

$$\min_{h_{\mathrm{V}},\sigma,m_n,\phi_0} \Big\| \left[\tilde{\gamma}(\vec{w}_1)\tilde{\gamma}(\vec{w}_2)\tilde{\gamma}(\vec{w}_3)\right]^{\mathrm{T}} - \left[\tilde{\gamma}_{\mathrm{m}}(h_{\mathrm{V}},\sigma,m_1|_{\phi_0})\right. \\ \left. \tilde{\gamma}_{\mathrm{m}}(h_{\mathrm{V}},\sigma,m_2|_{\phi_0})\tilde{\gamma}_{\mathrm{m}}(h_{\mathrm{V}},\sigma,\phi_0|_{m_s=0})\right]^{\mathrm{T}} \Big\| \tag{5}$$

as described in [2]. In this letter, a quad-pol L-band 10-m nominal spatial baseline (corresponding to a nominal $\kappa_z = 0.11$) acquisition is chosen for the inversion of (1) because it provides best inversion performance in terms of vertical wavenumber. For the coherence estimation, a 7×7 estimation window has been used.

In addition, the single-pass single-pol X-band acquisition is used for height inversion, as proposed in [13]. The inversion problem of (1) is underdetermined for a single-baseline single-pol observation space, where only two observables are available to recover four unknowns. Nevertheless, a determined problem can be enforced by neglecting the ground scattering component and fixing the extinction coefficient. The reasoning behind this is as follows. Compared to L-band, X-band extinction in forest canopy is higher, attenuating strongly the ground scattering. In this case, with increasing extinction, the interferometric coherence increases as the effective phase center moves toward the top of the trees. Fixing also the extinction coefficient σ value ($\sigma_0 = 0.1$ dB/m in this letter) and assuming $m = 0$ for all polarizations, the inversion problem for polarization $\vec{w}$ (VV in our case) takes the form

$$\min_{h_{\mathrm{V}},\phi_0} \left\| \tilde{\gamma}(\vec{w}_{\mathrm{VV}}) - \tilde{\gamma}_{\mathrm{m}}(h_{\mathrm{V}},\phi_0|\sigma=\sigma_0) \right\| \tag{6}$$

that can be further reduced to a single-parameter (real) problem by ignoring the ground phase ϕ_0

$$\min_{h_{\mathrm{V}}} \left\| \, |\tilde{\gamma}(\vec{w}_{\mathrm{VV}})| - |\tilde{\gamma}_{\mathrm{m}}(h_{\mathrm{V}},\phi_0|\sigma=\sigma_0)| \, \right\|. \tag{7}$$

After discarding the ground phase and fixing extinction, X-band height inversion is based on coherence amplitude. As a part of tree-height estimation, a forest mask was generated by using SNR decorrelation [14] for L-band to differentiate forested and nonforested areas.

B. HUTSCAT

The HUTSCAT-measured vertical backscattering profile data were linked to the GPS measurements by using the HUTSCAT time stamp. The tree height was determined from the scattering profiles as the difference between ground and tree-top reflections. HUTSCAT's resolution in range direction is 0.65 m. For detecting the ground and the tree tops form the profile, an automatic algorithm was developed. The algorithm was applied for both X- and C-band-profiles. Derived tree-height profiles were slightly different for X- and C-band because C-band penetration depth is slightly greater. C-band measurement has also more noise because of instrument properties. The HUTSCAT system does not have an ability to measure attitude, and therefore, the helicopter's X and Y coordinates were used as an approximation for the antenna beam location on the ground. This can cause a localization error, depending on the measurement system tilt angle. The beam localization error is assumed in most cases to be less than 15 m; this was checked by using orthophotos. HUTSCAT data collection provided approximately 32 000 measurements along 11 transects, comprising approximately 24 000 height estimates calculated separately for X- and C-band.

C. Comparison of Tree-Height Measurements

In order to validate forest height estimates from model inversion, we compared them to HUTSCAT measurements and forest inventory data. For this, ancillary data were converted to the slant range geometry of L-band. Fig. 1 shows POLInSAR-generated forest height map in slant range geometry combined with HUTSCAT measurement tracks and stand-inventory vector map. The comparison with the stand inventory data was done for stand averages, where stand borders were taken from inventory stand map. In order to compare the SAR and HUTSCAT tree-height estimates, the HUTSCAT estimates were converted to SAR slant-range coordinates to make the comparison on pixel basis. The pixel-based comparison approach was found difficult: problems were caused particularly due to the localization errors in the HUTSCAT data. The tree height in mixed forest can have rapid fluctuations, and therefore, localization uncertainties may cause large height errors which are difficult to identify on pixel-by-pixel scatterplots. Therefore, POLInSAR estimates were converted also to the HUTSCAT range profile coordinates to compare the estimates right on the HUTSCAT measured scattering profiles. This approach allows better identification of various error sources and gives better overview of inversion performance and possible problems.

IV. Results and Discussion

Fig. 1 shows a forest height map retrieved from L-band inversion. As it can be seen, locally (mainly in far range) large height errors appear due to uncompensated decorrelation contributions, like temporal, etc. The impact of uncorrelated decorrelation contribution accelerates from near to far range. However, stands with different height can be clearly identified.

Fig. 2 shows part of the HUTSCAT measurement profile at X-band with the POLInSAR tree-height measurements on top of it. The x-axis is HUTSCAT sample number, corresponding to helicopter forward velocity, and the y-axis is HUTSCAT vertical range. Lighter areas correspond to backscattering (decibel) from trees and ground. The black line corresponds to

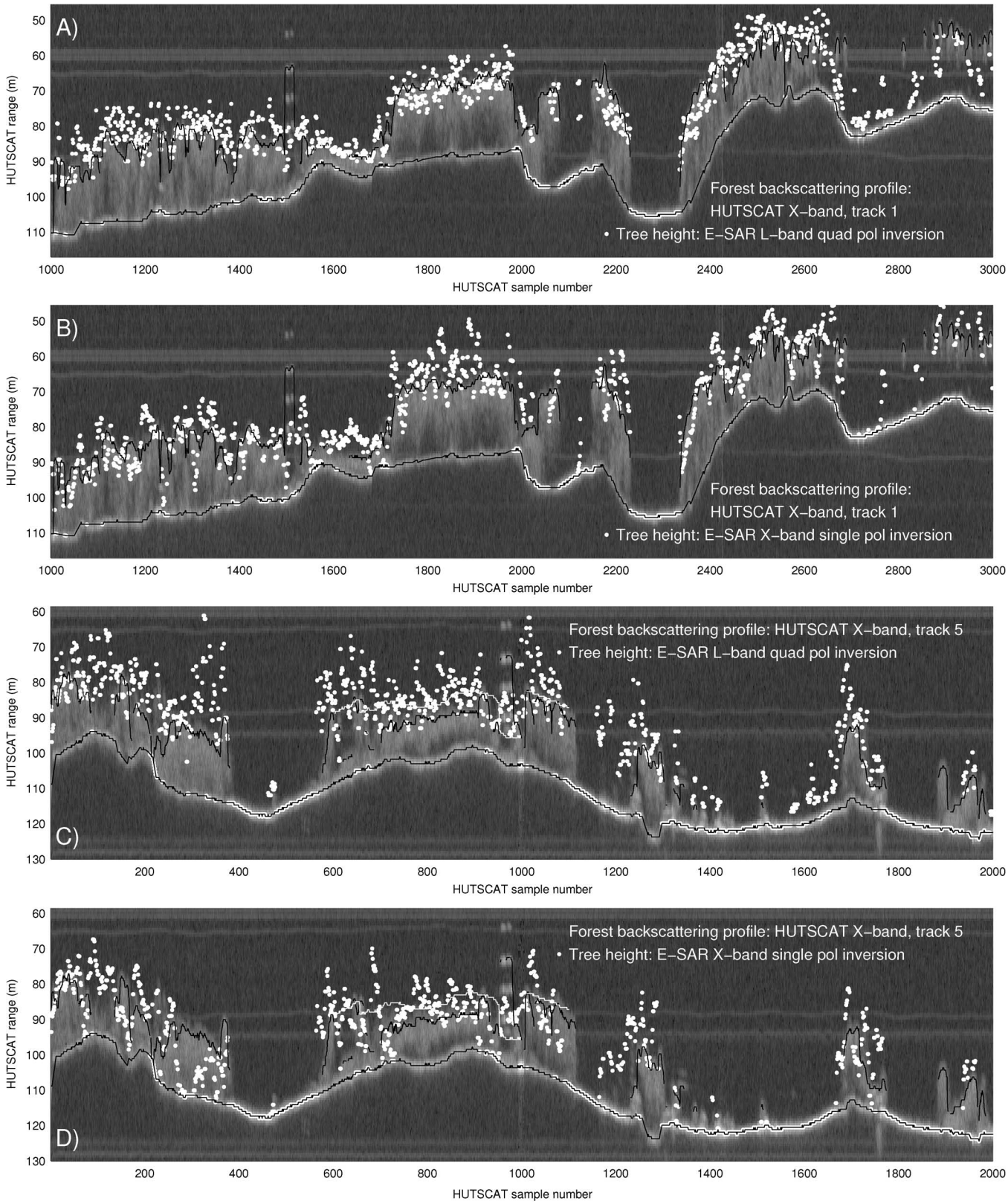

Fig. 2. POLInSAR L- and X-band forest height estimates on top of HUTSCAT X-band vertical forest backscattering profile. (A) and (B) HUTSCAT track 1 (E-SAR near range). (C) and (D) HUTSCAT track 5 (E-SAR midrange). White dots represent the POLInSAR forest-height estimates for (A) and (C) L-band 10-m baseline and (B) and (D) X-band 0.8-m baseline. The x-axis is HUTSCAT sample number, corresponding to helicopter movement. One sample corresponds approximately to 1.25 m. The y-axis is HUTSCAT vertical range and tree height in meters. Lighter areas correspond to backscattering (decibel) from trees and ground. The black line corresponds to the automatically detected ground and tree top level for HUTSCAT profile. The white line shows the stand mean height from forest inventory, where available. The length of track in the image is approximately 2.5 km. Flight direction in reference to Fig. 1 is from right to left.

the automatically detected ground level. White dots correspond to POLInSAR tree-height estimates relative to HUTSCAT detected ground line; therefore, zero tree-height (open areas) dots appear on the HUTSCAT ground line. The white line indicates the mean tree-height line from inventory data, where available. The results in Fig. 2(a) indicate that the estimates derived from L-band POLInSAR model inversion are in a good agreement with HUTSCAT measurements in the SAR near-range area. Single measurements are somewhat noisy, but the general trend follows tree top level rather closely. For the higher forest stands, the variability in height estimates is higher while for smaller forest stands, the variability is smaller, due to the variance of the volumetric coherence. It seems that some of the POLInSAR-derived tree heights are slightly underestimated (i.e., lower than the highest tree tops), but this is in average compensated. For very sparse (open canopy) forest on the right-hand side of the image, the POLInSAR estimates at L-band underestimate the tree heights. When moving to midrange [Fig. 2(c)], L-band estimates tend to overestimate isolated areas. In general, the detected tree top level is somewhat higher than that detected by HUTSCAT, and in noisy areas, it tends to have unrealistically high values. The reason for this are primarily uncompensated nonvolumetric decorrelation effects that are more unfavorable at the smaller baseline region at mid and far range, than at the larger baselines at near range. The experimental X-band derived tree-height estimates are shown in Fig. 2(b) and (d). As discussed in Section III-A and mentioned in [13], the inversion is underdetermined and possible only under rather strong assumptions. However, as shown in Fig. 2(b), the obtained X-band estimates perform surprisingly well. Despite some overestimation and noise effects, the X-band seems even to follow better the actual tree crown structure and to detect better the gaps between the trees than at L-band. In the sparse forested areas, it tracks better the tree height than at L-band. Because of the HUTSCAT localization uncertainty and some noise in inversion results, we use averaging in comparison of HUTSCAT and E-SAR results. When using 60 sample average blocks along HUTSCAT track (approximately 75 m), the correlation between HUTSCAT height estimates (for track 1, partly presented in Fig. 2) and E-SAR L-band heights is $R = 0.77$; the corresponding value for X-band is $R = 0.75$. Tree-height estimates were also compared to a standwise inventory by calculating an average height estimate for 76 inventoried stands. The correlation between X-band height and stand mean height from inventory is $R = 0.68$, and for L-band, $R = 0.64$. It is interesting to note that POLInSAR-derived stand height has a better correlation with the inventory mean height than HUTSCAT-derived mean height estimates (correlation $R = 0.55$). This can be explained by the fact that HUTSCAT had a significantly smaller sampling area per stand, and HUTSCAT measurement covered only 43 of inventoried stands. We should also keep in mind that the HUTSCAT and E-SAR inversion estimate the top height, where inventory estimates the mean height [4]. Compared to E-SAR L-band results, the simplified inversion of X-band performs surprisingly well. Partly because the L-band inversion performance is limited by repeat pass, acquisition introduced temporal and system decorrelation effects, which do not appear in the X-band single pass acquisition scenario.

V. Conclusion

In this letter, we have shown that tree-height estimation by means of L-band interferometric polarimetry and inversion of the RVoG model works well for boreal forests. POLInSAR-derived height agrees well with independent tree-height measurements made with the HUTSCAT profiling scatterometer. We also conclude that X-band inversion for tree height has a potential at least at low-density forest ecosystems (e.g., boreal region). This is important for future InSAR systems at X-band, such as the Tandem-X configuration. A profiling scatterometer instrument like HUTSCAT can give valuable information to support validation of POLInSAR methods and can help to better understand backscattering processes in vertically distributed media like forests. The material collected for the letter is extensive and gives many possibilities for further studies.

Acknowledgment

The authors would like to thank the DLR E-SAR team, leaded by R. Horn, for data acquisition, R. Scheiber for E-SAR data processing, the TKK crew for HUTSCAT operation leaded by E. Rinne, and the ground team for data collection.

References

[1] K. P. Papathanassiou and S. R. Cloude, "Single baseline polarimetric SAR interferometry," *IEEE Trans. Geosci. Remote Sens.*, vol. 39, no. 11, pp. 2352–2363, Nov. 2001.

[2] S. R. Cloude and K. P. Papathanassiou, "Three-stage inversion process for polarimetric SAR interferometry," *Proc. Inst. Electr. Eng.—Radar Sonar Navig.*, vol. 150, no. 3, pp. 125–134, Jun. 2003.

[3] M. Brandfass, C. Hofmann, J. C. Mura, and K. P. Papathanassiou, "Polarimetric SAR interferometry as applied to fully polarimetric rain forest data," in *Proc. IGARSS*, Jul. 9–13, 2001, vol. 6, pp. 2575–2577.

[4] T. Mette, K. P. Papathanassiou, and I. Hajnsek, "Biomass estimation from polarimetric SAR interferometry over heterogeneous forest terrain," in *Proc. IGARSS*, Sep. 20–24, 2004, vol. 1, pp. 511–514.

[5] R. N. Treuhaft, G. P. Asner, B. E. Law, and S. Van Zyl, "Forest leaf area density profiles from the quantitative fusion of radar and hyperspectral data," *J. Geophys. Res.*, vol. 107, no. D21, pp. 4568–4580, 2002.

[6] R. N. Treuhaft, G. P. Asner, and B. E. Law, "Structure-based forest biomass from fusion of radar and hyperspectral observations," *Geophys. Res. Lett.*, vol. 30, no. 9, pp. 1472–1475, 2003.

[7] M. Santoro, J. Askne, G. Smith, and J. E. S. Fransson, "Stem volume retrieval in boreal forests from ERS-1/2 interferometry," *Remote Sens. Environ.*, vol. 81, no. 1, pp. 19–35, Jul. 2002.

[8] J. Askne, M. Santoro, G. Smith, and J. E. S. Fransson, "Multitemporal repeat-pass SAR interferometry of boreal forests," *IEEE Trans. Geosci. Remote Sens.*, vol. 41, pt. 1, no. 7, pp. 1540–1550, Jul. 2003.

[9] A. Moreira, R. Spielbauer, and W. Pötzsch, "Conceptual design, performance analysis and results of the high resolution real-time processor of the DLR airborne SAR system," in *Proc. IGARSS*, Pasadena, CA, 1994, vol. 2, pp. 912–914.

[10] M. Hallikainen, J. Hyyppä, J. Haapanen, T. Tares, P. Ahola, J. Pulliainen, and M. Toikka, "A helicopter-borne eight-channel ranging scatterometer for remote sensing—Part I: System description," *IEEE Trans. Geosci. Remote Sens.*, vol. 31, no. 1, pp. 161–169, Jan. 1993.

[11] J. Hyyppä and M. Hallikainen, "A helicopter-borne eight-channel ranging scatterometer for remote sensing—Part II: Forest inventory," *IEEE Trans. Geosci. Remote Sens.*, vol. 31, no. 1, pp. 170–179, Jan. 1993.

[12] J. Hyyppä and M. Hallikainen, "Applicability of airborne profiling radar to forest inventory," *Remote Sens. Environ.*, vol. 57, no. 1, pp. 39–57, Jul. 1996.

[13] F. Kugler, F. N. Koudogbo, K. Gutjahr, and K. P. Papathanassiou, "Frequency effects in Pol-InSAR forest height estimation," in *Proc. 6th EUSAR*, Dresden, Germany, May 16–18, 2006. CD-ROM.

[14] I. Hajnsek, K. P. Papathanassiou, and S. R. Cloude, "Removal of additive noise in polarimetric eigenvalue processing," in *Proc. IGARSS*, Sydney, Australia, 2001, vol. 6, pp. 2778–2780.

Tropical-Forest-Parameter Estimation by Means of Pol-InSAR: The INDREX-II Campaign

Irena Hajnsek, *Member, IEEE*, Florian Kugler, Seung-Kuk Lee, and Konstantinos Panagiotis Papathanassiou, *Senior Member, IEEE*

***Abstract*—This paper addresses the potential and limitations of polarimetric synthetic aperture radar (SAR) interferometry (Pol-InSAR) inversion techniques for quantitative forest-parameter estimation in tropical forests by making use of the unique data set acquired in the frame of the second Indonesian Airborne Radar Experiment (INDREX-II) campaign—including Pol-InSAR, light detection and ranging (LIDAR), and ground measurements—over typical Southeast Asia forest formations. The performance of Pol-InSAR inversion is not only assessed primarily at L- and P-band but also at higher frequencies, namely, X-band. Critical performance parameters such as the "visibility of the ground" at L- and P-band as well as temporal decorrelation in short–time repeat-pass interferometry are discussed and quantitatively assessed. Inversion performance is validated against LIDAR and ground measurements over different test sites.**

***Index Terms*—Forest height, polarimetric SAR interferometry (Pol-InSAR), synthetic aperture radar (SAR), temporal decorrelation, tropical forest.**

I. Introduction

TROPICAL RAIN forest ecosystems are highly complex and heterogeneous in terms of species composition and structure and are often difficult to access. Today, radar remote sensing is, for many tropical regions, the only regular available information source. Indeed, Japan Aerospace Exploration Agency's (JAXA) L-band spaceborne synthetic aperture radar (SAR) sensors onboard Japan Earth Resources Satellite-1 (JERS-1) [1] and Advanced Land Observing Satellite (ALOS) [2] demonstrated, in an impressive way, the potential of low-frequency SAR imaging for mapping and monitoring tropical forest ecosystems.

Toward a continuous quantitative forest monitoring, information about horizontal and vertical structures and/or integrative forest parameters such as forest biomass is essential. In contrast to qualitative applications, quantitative approaches by means of SAR are less developed particularly in tropical environments due to the limited data availability and the complexity of such environments. Most of the quantitative approaches are developed on temperate and/or boreal test sites where reference and validation data are easier to collect. The very different structure of tropical forests makes an offhand generalization not possible and requires dedicated experiments for development and validation. Pioneering work based on early airborne SAR experiments addressed tropical forest biomass classification and estimation, hence demonstrating the potential of low-frequency polarimetric SAR (PolSAR) measurements [3], [4]. However, the complexity of radar scattering in forest environments makes the interpretation and inversion of individual SAR and PolSAR observables on the basis of empirical, semiempirical, or theoretical models difficult. The establishment of interferometric SAR (InSAR) techniques for forest monitoring in the late 1990s triggered the first InSAR experiments in the tropics that indicated the potential of interferometric observables at low frequencies for the estimation of vertical structure parameters [5]–[9].

In the last years, the coherent combination of both interferometric and polarimetric observations by means of PolSAR interferometry (Pol-InSAR) was the key for an essential breakthrough in quantitative forest-parameter estimation [10], [11]. Indeed, the quantitative-model-based estimation of forest parameters—based on a single-frequency fully polarimetric single-baseline configuration—has been successfully demonstrated at L- and P-band and, more recently, even at X-band. Several experiments demonstrated the potential of Pol-InSAR techniques to estimate with high accuracy key forest parameters like forest height and above-ground forest biomass over a variety of natural and commercial temperate and boreal test sites characterized by different stand and terrain conditions. Validated results for boreal forests at X- and L-band are shown by [12]. Validated results for temperate forests at X-, L-, and P-band were presented in [11], [13]–[15]. However, the performance in tropical forest conditions could not be validated due to the lack of suitable data.

This lack of actual tropical and subtropical forest Pol-InSAR data sets including both adequate SAR and ground measurements, and the importance of these forest ecosystems with respect to a global forest mapping and monitoring was one of the main drivers for the second Indonesian Airborne Radar Experiment (INDREX-II) that took place in 2004. The analysis, inversion, and validation using this unique data set are presented in this paper. In Section II, the INDREX-II campaign objectives, test sites, and collected data sets are introduced. Section III reviews the physical background and the implementation of Pol-InSAR forest-parameter inversion. In Section IV,

Manuscript received March 9, 2008; revised July 29, 2008. Current version published January 28, 2009. This work was supported in part by the European Space Agency under Contract 3-11536/06/I-EC.

The authors are with the Polarimetric SAR Interferometry Research Group, Radar Concepts Department, Microwaves and Radar Institute, German Aerospace Center, 82234 Wessling, Germany (e-mail: irena.hajnsek@dlr.de; florian.kugler@dlr.de; seungkuk.lee@dlr.de; kostas.papathanassiou@dlr.de).

Digital Object Identifier 10.1109/TGRS.2008.2009437

the key issue of the "visibility" of the ground at L- and P-band in dense tropical forest conditions is addressed and evaluated. The accuracy of the obtained forest-height estimates at L- and P-band is assessed against light detection and ranging (LIDAR) and ground measurements in Section V. In addition, a constrained modification of the conventional Pol-InSAR inversion scheme adapted to single channel X-band interferometry is introduced and validated against the LIDAR measurements. In Section VI, short-time temporal decorrelation effects are quantified. Finally, the obtained results are reviewed and discussed in Section VII.

II. INDREX-II Campaign

A. Campaign Objectives

The main objective of the INDREX-II mission was to build up a unique database of tropical and subtropical test sites with adequate SAR and ground measurements to support the development and validation of bio-/geophysical forest-parameter inversion techniques from multiparameter SAR data. It was expected that the data collected in the frame of the campaign would answer key scientific questions and validate inversion techniques not only at higher (X- and C-bands) but also mainly at lower SAR frequencies (L- and P-band).

Regarding Pol-InSAR inversion techniques, the interest was focused on two main points.

1) The polarimetric diversity of the interferometric coherence and, thus, the information content of the Pol-InSAR observation space depends—in forest environments—on the visibility of the ground under the vegetation layer. This makes the question about the capability of P- or even L-band to penetrate through dense tropical vegetation layer of fundamental importance with respect to the performance of Pol-InSAR techniques in tropical forest environments.
2) The demonstration and quantitative evaluation of the Pol-InSAR inversion performance in different tropical and subtropical forest conditions.

Both points will be addressed, discussed, and analyzed in the following sections.

B. Test Sites and Ground Measurements

Two main test areas both located on the island of Borneo, Kalimantan, Indonesia, have been selected for INDREX-II. The first test site is the Mawas conservation area (latitude: -2.15°, longitude: 114.45°) located in Central Kalimantan in the vicinity of its capital city Palangkaraya. The second area is located in East Kalimantan in the vicinity of the city of Balikpapan (latitude: -1.10°, longitude: 116.82°). The two areas comprise the main broad forest types in Indonesia: lowland dipterocarp, peat swamp, and mangrove forest, as well as a variety of the common plantation types such as oil palm and rubber tree. Eight test sites have been defined, two located in the Mawas area and six in the Balikpapan area. Our investigations concentrate on two of the eight test sites that represent typical forest formations of Southeast Asia like lowland dipterocarp and peat-swamp forests with disturbed and undisturbed stands at very different terrain conditions.

1) The *Sungai Wain* test site is a hilly area with steep slopes located close to the city of Balikpapan in East Kalimantan. It is covered by typical lowland dipterocarp forests with biomass levels up to 400 t/ha and tree heights up to 60 m. On a large scale, this forest type can be seen as rather homogeneous, while on a small scale, patches of different succession stages go along with changes in height. Large areas were burnt during the El Niño events of 1982 and 1998. They are now covered with Macaranga, a secondary forest type.

   A 15.4-ha large forest plot was established in the Sungai Wain dipterocarp forest, with a 540-m length and 286-m width. Within this plot, 26 blocks of 26×32 m (in total, 2.1 ha) have been registered. The catalogue includes diameter at breast height (DbH) and tree height measurements for each canopy tree with DbH ≥ 10 cm.
2) The *Mawas* test site is located in central Kalimantan. It is, in general, flat including several large (ombrogenous) peat domes and is covered by tropical peat-swamp forest types. Forest height varies gradually from relatively tall (30 m) and dense forests at the edges toward small (15 m or lower) and open forests at the center of a dome with biomass levels from 20 to 350 t/ha. Mixed swamp (some topogenous) and floodplain forests are located along the river flow. The southern and eastern parts are disturbed by excessive drainage (through canals) and peat forest fires.

In August 2007, LIDAR measurements were performed with a swath width of about 300 m along a 22-km-long strip located in the middle of the SAR swath. The spatial resolution is of 3–4 m, dependent on the amount of returning samples; the pixel density decreases from the center (nadir) to the corners of the image. From the LIDAR raw data, forest-height and ground terrain digital elevation models (DEM) have been processed [16], [17]. During the three years between the LIDAR and the radar campaign, changes in the forest caused by tree growth (on the order of 1–2 m), tree dieback, and human impact may be an additional error source when comparing LIDAR and radar measurements to each other.

C. SAR Data

The SAR data acquisitions have been performed with the German Aerospace Center (DLR)'s experimental airborne SAR system (E-SAR) in November and December 2004. For each test site, the following modes have been acquired:

1) one X-band single-pass InSAR acquisition at a single channel (VV polarization) for DEM generation;
2) two C-band dual-polarization acquisitions (one in the VH–HH and the other in the HV–VV mode);
3) three L-band quad-polarization acquisitions flown in a repeat-pass InSAR mode;
4) four P-band quad-polarization acquisitions flown in a repeat-pass InSAR mode.

The spatial (repeat-pass) baselines at L- and P-bands have been chosen to cover the same height sensitivity and to allow an

TABLE I
INDREX-II DATA SETS

Test Site	*Frequency*	*Baseline [m] / kz range*	*Acquisition InSAR/PolSAR*
Sungai Wain	*L-band*	10 / 0.04 – 0.21	*Repeat / Quad*
Sungai Wain	*P-band*	30 / 0.04 – 0.17	*Repeat / Quad*
Mawas River	*X-band*	0.8 / 0.07 – 0.13	*Single / VV*
Mawas River	*L-band*	05 / 0.03 – 0.16	*Repeat / Quad*
Mawas River	*L-band*	10 / 0.08 – 0.34	*Repeat / Quad*
Mawas River	*L-band*	15 / 0.11 – 0.51	*Repeat / Quad*
Mawas River	*P-band*	15 / 0.03 – 0.13	*Repeat / Quad*
Mawas River	*P-band*	30 / 0.06 – 0.26	*Repeat / Quad*
Mawas River	*P-band*	30 / 0.07 – 0-27	*Repeat / Quad*
Mawas River	*P-band*	40 / 0.08 – 0.40	*Repeat / Quad*
Mawas Dome	*X-band*	0.8 / 0.07 – 0.13	*Single / VV*
Mawas Dome	*L-band*	05 / 0.04 – 0.17	*Repeat / Quad*
Mawas Dome	*L-band*	05 / 0.02 – 0.15	*Repeat / Quad*
Mawas Dome	*P-band*	15 / 0.03 – 0.13	*Repeat / Quad*

optimum inversion performance with respect to the expected forest conditions.

As INDREX-II was performed at the beginning of the rainy season, some of the data acquisition flights had to be flown under windy conditions. Consequently, some of the repeat-pass acquisitions (i.e., at L- or P-band) particularly in the Mawas Dome test site have been affected by wind-induced temporal decorrelation. For this reason, the acquisitions have been repeated, providing the possibility to analyze temporal decorrelation effects. Table I provides a summary of the SAR data sets used in this work. Note that the Mawas Dome data sets are strongly affected by temporal decorrelation.

III. Pol-InSAR Parameter Inversion

The key observable used in Pol-InSAR applications is the complex interferometric coherence $\tilde{\gamma}$ (including both the interferometric correlation coefficient and interferometric phase) measured/estimated at different polarizations (indicated by the unitary vector $\vec{w}$ [10], [11]). $\tilde{\gamma}$ is given by the normalized cross correlation of the two SAR images obtained from the interferometric acquisition s_1 and s_2

$$\tilde{\gamma}(\vec{w}) := \frac{\langle s_1(\vec{w}) s_2^*(\vec{w}) \rangle}{\sqrt{\langle s_1(\vec{w}) s_1^*(\vec{w}) \rangle \langle s_2(\vec{w}) s_2^*(\vec{w}) \rangle}}. \tag{1}$$

The coherence depends on instrument and acquisition parameters as well as on dielectric and structural parameters of the scatterer. A detailed discussion of system-induced coherence errors can be found in [18]. After the calibration of system-induced decorrelation contributions and compensation of spectral decorrelation in azimuth and range, the estimated interferometric coherence can be decomposed into three main decorrelation processes [19]

$$\tilde{\gamma} := \tilde{\gamma}_{\mathrm{Temp}} \quad \gamma_{\mathrm{SNR}} \quad \tilde{\gamma}_{\mathrm{Vol}}. \tag{2}$$

1) Temporal decorrelation $\tilde{\gamma}_{\mathrm{Temp}}$ can be real (i.e., effecting the absolute value of $\tilde{\gamma}$ only) or complex (i.e., biasing the phase of $\tilde{\gamma}$). It depends on the structure and the temporal stability of the scatterer, the temporal baseline of the interferometric acquisition, and the dynamic environmental processes occurring in the time between the acquisitions.
2) Noise decorrelation γ_{SNR} is introduced by the additive white noise contribution on the received signal [20], [21]. It affects primarily the scatterers with low (back-) scattering and is, in general, of secondary importance when looking at a forest at conventional frequencies.
3) Volume decorrelation $\tilde{\gamma}_{\mathrm{Vol}}$ is the decorrelation caused by the different projection of the vertical component of the scatterer into the two images $s_1(\vec{w})$ and $s_2(\vec{w})$. $\tilde{\gamma}_{\mathrm{Vol}}$ is directly linked to the vertical distribution of scatterers $F(z)$ through a (normalized) Fourier transformation relationship

$$\tilde{\gamma}_{\mathrm{Vol}} = \exp(i\kappa_z z_0) \frac{\int_0^{h_V} F(z') \exp(i\kappa_z z') dz'}{\int_0^{h_V} F(z') dz'} \tag{3}$$

where h_V is the height of the volume and κ_z is the effective vertical (interferometric) wavenumber that depends on the imaging geometry and the radar wavelength λ

$$\kappa_z = \frac{\kappa \Delta\theta}{\sin(\theta_0)} \qquad \kappa = n\frac{2\pi}{\lambda} \tag{4}$$

and $\Delta\theta$ is the incidence angle difference between the two interferometric images induced by the baseline. z_0 is a reference height, and $\varphi_0 = \kappa_z z_0$ is the corresponding interferometric phase. For monostatic acquisitions, as flown in INDREX-II, $n := 2$, while for bistatic acquisitions, $n := 1$. Accordingly, $\tilde{\gamma}_{\mathrm{Vol}}$ contains the information about the vertical structure of the scatterer and is therefore the key observable for quantitative forest-parameter estimation [10], [11].

The estimation of vertical forest structure parameters from interferometric measurements can be addressed as a two-step process: In the first step (modeling), $F(z)$ is parameterized in terms of a limited set of physical forest parameters that are related through (3) to the interferometric coherence. In the second step (*inversion*), the volume contribution of the measured interferometric coherence is then used to estimate $F(z)$ and to derive the corresponding parameters. A widely and successfully used model for $F(z)$ is the so-called random volume over ground (RVoG), a two-layer model consisting of a volume and a ground layer [22], which can be described as

$$F(z) = \tilde{m}_V \, e^{\left(\frac{2\sigma}{\cos(\theta_0)} z\right)} + m_G \, e^{\left(\frac{2\sigma}{\cos(\theta_0)} h_V\right)} \delta(z - z_0) \tag{5}$$

where m_V and m_G are the ground and volume scattering amplitudes and σ is a mean extinction coefficient. Equation (5) leads to

$$\tilde{\gamma}_{\mathrm{Vol}} = \exp(i\kappa_z z_0) \frac{\tilde{\gamma}_{V0} + m}{1 + m}. \tag{6}$$

The phase $\varphi_0 = \kappa_z z_0$ is related to the ground topography z_0, and m is the effective ground-to-volume amplitude ratio accounting for the attenuation through the volume

$m = m_G/(m_V I_0)$. $\tilde{\gamma}_{V0}$ is the volume decorrelation caused by the vegetation layer only, given by

$$\tilde{\gamma}_{V0} = \exp(i\kappa_z z_0)\frac{\int_0^{h_V} \exp(i\kappa_z z')\exp\left(\frac{2\sigma z'}{\cos\theta_0}\right)dz'}{\int_0^{h_V} \exp\left(\frac{2\sigma z'}{\cos\theta_0}\right)dz'}. \quad (7)$$

Neglecting temporal decorrelation and assuming a sufficient calibration/compensation of system- (e.g., SNR) and geometry-(range/azimuth spectral shift) induced decorrelation contributions, (6) can be inverted in terms of a quad-polarization single-baseline acquisition [11], [13], [23], [24]. Assuming no response from the ground in one polarization channel (i.e., $m_3 = 0$), the inversion problem has a unique solution and is balanced with five real unknowns $(h_V, \sigma, m_{1-2}, \varphi_0)$ and three measured complex coherences $[\tilde{\gamma}(\vec{w}_1) \quad \tilde{\gamma}(\vec{w}_2) \quad \tilde{\gamma}(\vec{w}_3)]$ each for any independent polarization channel [23]

$$\min_{h_V,\sigma,m_i,\phi_0} \left\| \begin{bmatrix} \rho & \rho & \rho \\ \tilde{\gamma}(w_1) & \tilde{\gamma}(w_2) & \tilde{\gamma}(w_3) \end{bmatrix}^{\mathrm{T}} - [\,\tilde{\gamma}_{\mathrm{Vol}}(h_V,\sigma,m_1) \quad \tilde{\gamma}_{\mathrm{Vol}}(h_V,\sigma,m_2) \quad \tilde{\gamma}_{V0}\exp(i\phi_0)\,]^{\mathrm{T}} \right\|. \quad (8)$$

Equation (8) is used to invert INDREX-II data sets at L- and P-band. The same regularization $(m_3 = 0)$ has been used at L-band as well as at P-band. Because of the dense vegetation layer, a modified regularization at P-band is not required. Note that the assumption for no ground response is not necessarily linked to the HV channel.

IV. Effect of the Ground

Starting with the first scientific question expected to be answered from INDREX-II, the visibility of the ground is investigated. The investigation is focused on the densest vegetated test site, the Sungai Wain test site covered by dense lowland dipterocarp forests with individual tree heights up to 60 m and a mean biomass level up to 400 t/ha. A secondary low-vegetation layer located on the ground additionally increases the attenuation of any ground-scattering component. However, the hilly terrain of the site can be used to evaluate the terrain dependence of the individual parameters and conclude on the visibility of the ground.

The strong polarized behavior of ground scattering (including direct ground and/or dihedral scattering) combined with the directivity of the dihedral scattering component make the type and amount of ground scattering strongly dependent on the terrain slope in range direction. This supports the idea of "seeing" the ground through the modulation of the polarimetric signature by the terrain slope in the Sungai Wain data set.

Fig. 1 shows the 2-D histogram of the polarimetric alpha angle [25] that characterizes the nature of the polarimetric scattering process as a function of the terrain range slope at L- (top) and P-band (bottom). Positive slopes indicate an inclination toward the radar, while negative slopes indicate inclinations away from the radar. In both cases, the alpha angles are around

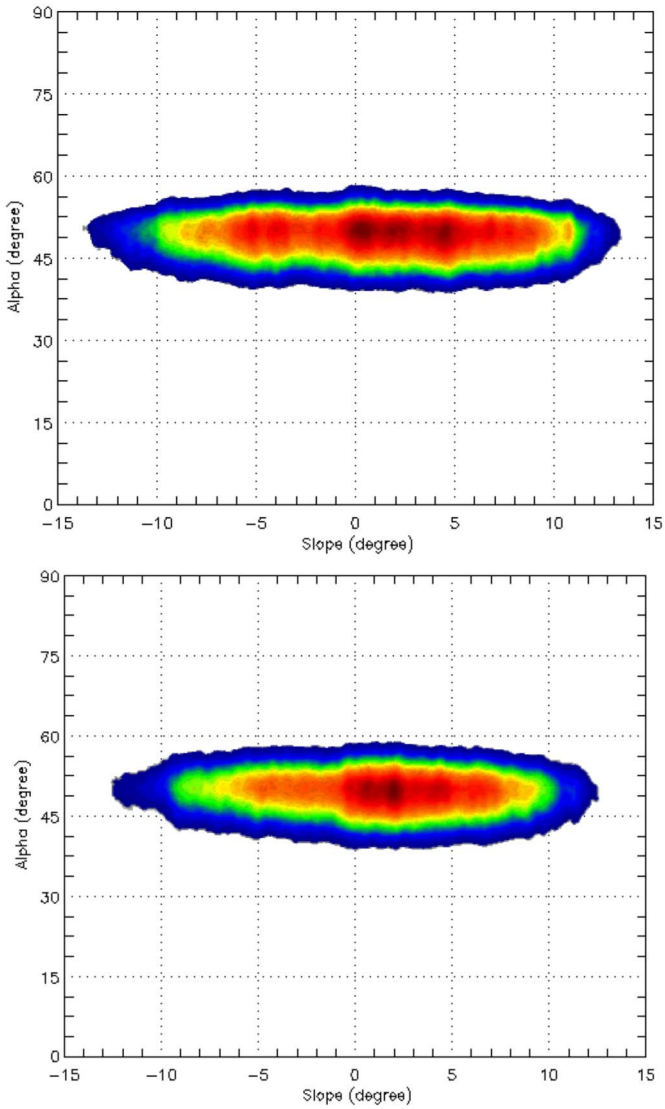

Fig. 1. Polarimetric alpha-angle histogram as a function of range terrain slopes at (top) L- and (bottom) P-band.

50° that, combined with the high polarimetric entropy levels obtained, indicates a dominant volume scattering component. The absence of any slope dependence at L-band as well as at P-band can be seen as an indicator for the absence of a ground-scattering component signature.

A far more sensitive indicator for the visibility of the ground is the location of the scattering phase center estimated in the interferogram. According to (6), the location of the interferometric phase center within the vegetation layer depends on the ground-scattering amplitude. Larger ground-to-volume amplitude ratio m values correspond to stronger ground-scattering amplitudes and move the phase center toward the ground and *vice versa.* The polarization dependence of m relates the variance of the interferometric phase center as a function of polarization directly to the variance of the amplitude of the ground-scattering component. In order to illustrate this, Fig. 2 shows the coherence region of the interferometric coherence [28]–[30] as a gray cloud of coherence loci plotted on the unit circle for a stand within the Sungai Wain site at L- (top) and P-band (bottom). The coherence region is defined as the

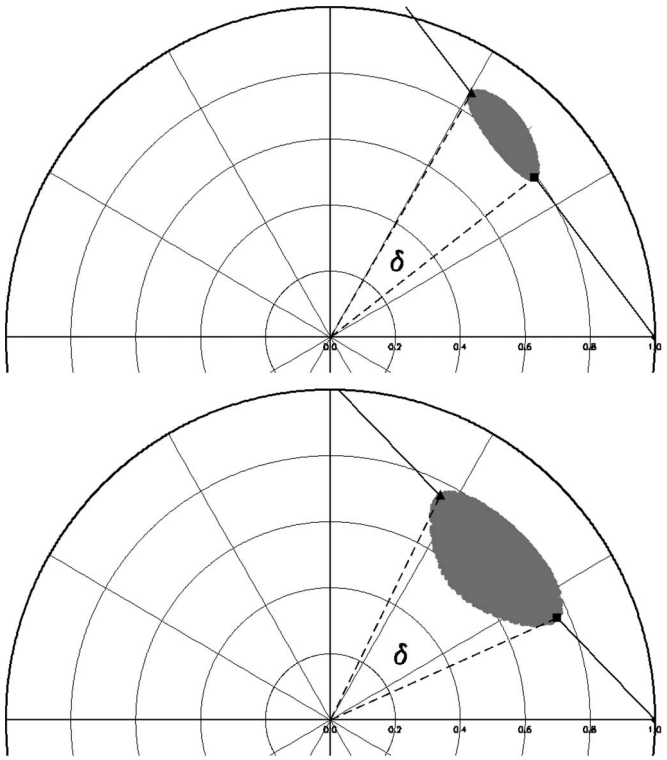

Fig. 2. Coherence region at (top) L- and (bottom) P-band for the same forest stand (Sungai Wein test site).

region that includes the loci of the (complex) interferometric coherences obtained for all polarizations [31]. Consequently, the angle δ that corresponds to the maximum variation of the phase center with polarization is a sensitive indicator for the amount of ground scattering visible. In the case of an increased attenuation of the ground-scattering component, the coherence region shrinks and becomes a point in the limit. In this case, $\delta = 0$. Of course, one has to account for the variance of the amplitude and, primarily, the phase of $\tilde{\gamma}(\vec{w}_i)$ induced by the nonunity coherence using a sufficient large number of looks when estimating $\tilde{\gamma}(\vec{w}_i)$. In the case of Fig. 2, 81 independent looks have been used. In order to make a direct comparison possible, the stand is located on flat terrain and has a similar wavenumber at both frequencies. The variation of the interferometric phase at L-band in Fig. 2 shows the visibility of a polarized ground-scattering component under the vegetation layer. The phase difference is on the order of 22° corresponding to 9.5 m. At P-band, the height difference between the phase centers is larger, about 43° corresponding to 13.5 m, indicating a stronger ground-scattering component at P-band than at L-band. Note that a polarization-dependent propagation through the volume layer caused by orientation effects in the vegetation structure and expressed by a polarization-dependent extinction coefficient in (7) can also introduce a variance of the phase center with polarization. However, this is rather unusual for dense forest vegetation at L-band but also at P-band.

Fig. 3 shows the 2-D histogram of the δ angle (scaled by using the vertical wavenumber in meters) as a function of terrain range slope obtained at L- (top) and P-band (bottom). The height difference decreases monotonically at both frequencies as the range slope decreases, indicating the expected stronger

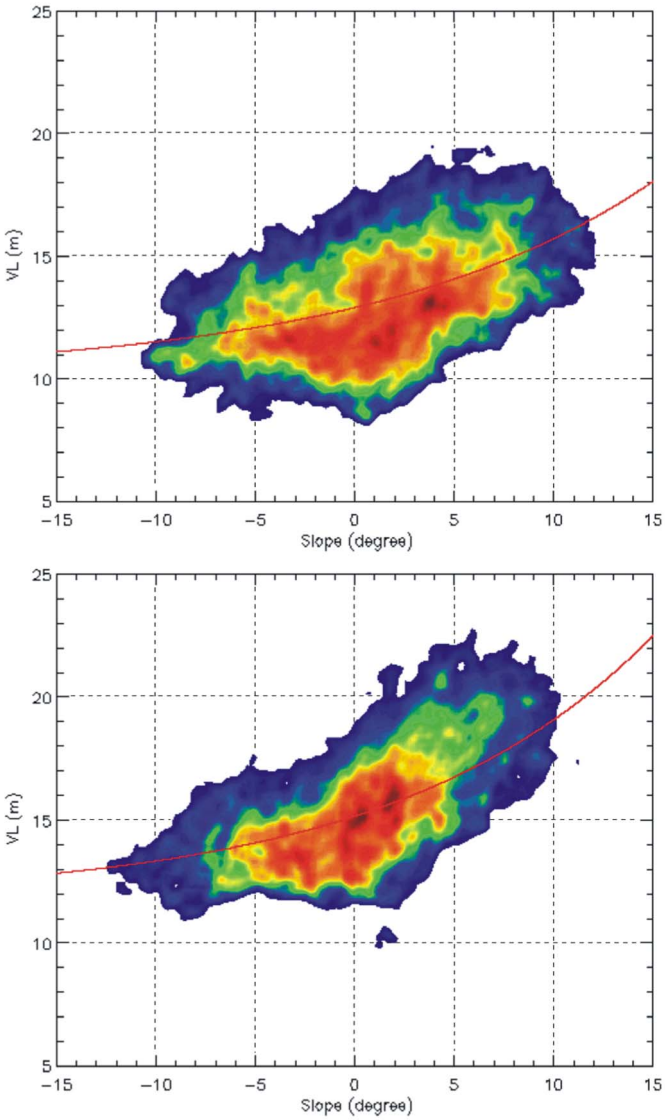

Fig. 3. Phase center height difference (maximum) histogram as a function of range terrain slopes at (top) L- and (bottom) P-band.

ground response at higher (i.e., positive) slopes and, thus, the visibility of the ground at L- and P-bands across the whole site. Positive slopes are tilted toward the radar while negative slopes are tilted away from the radar. The height difference is, as expected, larger at P-band than at L-band through the whole range of slopes, indicating the visibility of a stronger ground component in P-band compared to L-band. Because there is no reason that orientation effects in vegetation are correlated to terrain slope, Fig. 3 is a direct proof for the visibility of the ground at both frequencies in dense tropical forest environments.

V. Inversion Results

Forest height was estimated and validated against the ground measurements for both test sites: the Mawas peat-swamp forest (i.e., Mawas River test site) and the Sungai Wain lowland dipterocarp forest. As the reference height for validation, the so-called "H100" from forest measurements [32] was used, which

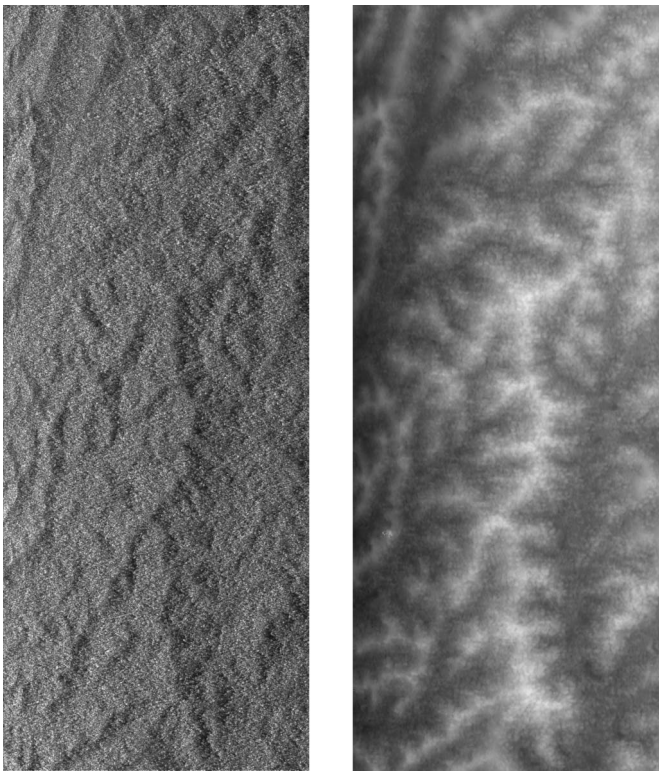

Fig. 4. Sungai Wain test site. (Left) L-band HH amplitude image (grayscale) near range left side. (Right) DEM calculated from X-band data (black = 50 m, white = 180 m AMSL) 3.5 × 6.5 km.

is defined as the mean height of the 100 highest trees per hectare [33]. H100 is a forestry standard canopy top height measure and corresponds quite well to radar forest-height estimates, as it is calculated out of the trees forming the canopy, i.e., the height of the volume.

For the Sungai Wain test site, the ground measurements where converted to H100 values for each block individually. In the Mawas test site, the H100 has been obtained from the LIDAR data by taking the maximum value of a 10 × 10 m window (corresponding to 1/100 of a hectare) [33], [34].

A. Sungai Wain Test Site

Fig. 4, on the left, shows an L-band HH amplitude image of the Sungai Wain scene while, on the right, the X-band DEM is shown. The scene is completely covered with forest situated in hilly terrain with steep slopes (up to 30°). Variations in the amplitude are only due to changes in topography. For accurate inversion, the estimation of incidence angle and interferometric baseline needs to account for the topographic variation. In addition, terrain adaptive range spectral filtering using the low-pass filtered X-band InSAR DEM has been applied, on the price of a variable spatial range resolution across the image.

The measured forest heights (H100) are ranging from 20 up to 40 m, whereas most of the plots have heights between 24 and 28 m as shown by the blue histogram in Figs. 5 and 6.

The normalized histograms of the heights obtained at L- and P-bands over the whole plot of 200 × 500 m are shown in red in Figs. 5 and 6, respectively. The L-band height estimates range

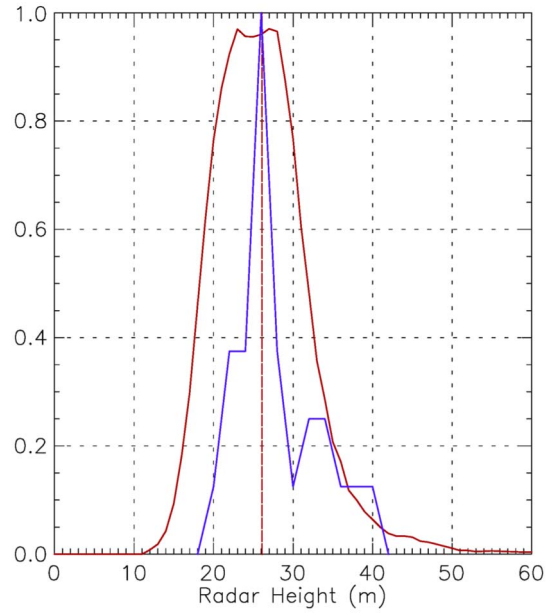

Fig. 5. Forest-height histograms. (Blue) Ground measured heights. (Red) Pol-InSAR height estimates at L-band (Sungai Wain test site).

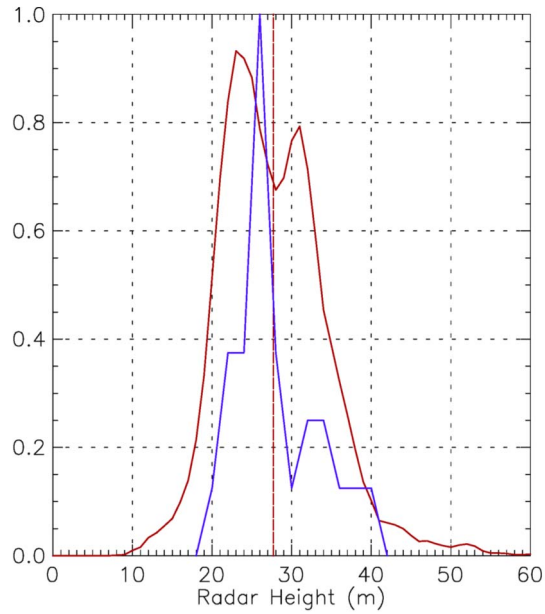

Fig. 6. Forest-height histograms. (Blue) Ground measured heights. (Red) Pol-InSAR height estimates at P-band (Sungai Wain test site).

from 15 to 45 m with a mean forest height of about 28 m. At P-band, the obtained results range from 13 to 43 m with a similar mean of about 26 m. Overestimation (i.e., estimated heights above 45 m) appears as a consequence of temporal or other uncompensated decorrelation contributions. This can be due to remaining SNR and processing decorrelation contributions. In particular, accurate image coregistration becomes challenging in sloped terrain and low coherence levels. At both frequencies, the radar estimates cover the same range of heights and have a similar height distribution and a mean value better than 10% of the mean given by the ground measurements (i.e., 27 m, see blue histogram in Figs. 5 and 6). The maxima and minima diverge on the order of 5 m, probably due to an

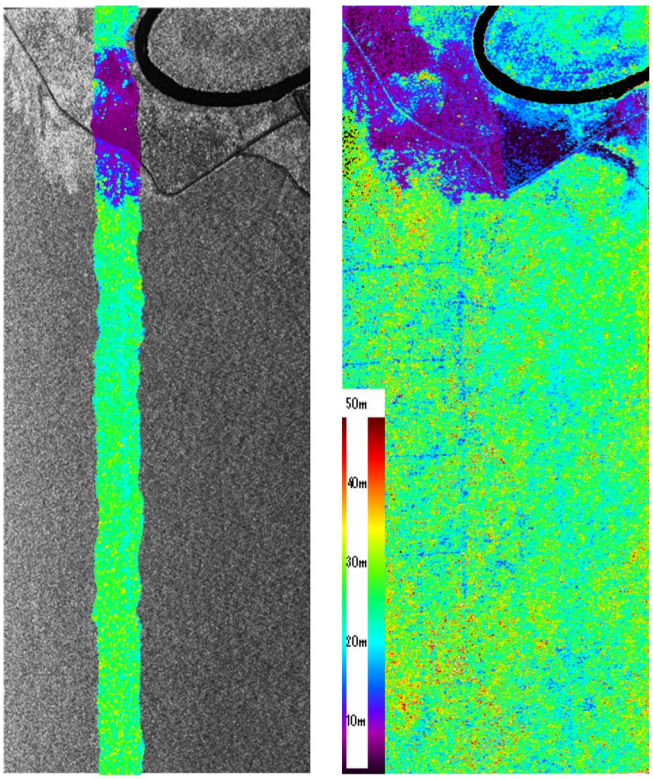

Fig. 7. Mawas River test site. (Left) (grayscale; near range: Left) P-band amplitude image with (color) LIDAR H100 measurements. (Right) P-band forest-height map, combination of four baselines, scaled from 0 to 50 m (region larger than 50 m are white). 3.5 × 6.5 km.

insufficient number of ground measurement samples. It appears that P-band is able to resolve the bimodal height distribution (see Fig. 6) as measured on the ground while L-band is able to resolve only the envelope distribution (see Fig. 5). As the spatial resolution and the vertical wavenumber are almost the same for both frequencies, and furthermore, the interferometric coherence levels are comparable, the reason can be a higher sensitivity of L-band to temporal decorrelation effects that lead to a reduced estimation accuracy.

B. Mawas River Test Site

The amplitude image of the P-band HH channel for the Mawas River test site is shown in Fig. 7 (left). The amplitude image already indicates the terrain flatness. The transition from the burned area located on the top of the image to the forested area covering 2/3 of the image is characterized partly by low (up to 2 m) secondary shrublike vegetation and, particularly at the edge of the forest, by patches of heavily disturbed forest. The river crosses the upper part of the image embedded in a secondary riverine forest. The LIDAR strip is superimposed on the amplitude image. Forest height along the LIDAR strip is constant within ±5 m around 27 m with lower heights in the parts close to the river and the disturbed forest areas. The terrain rises from the middle to the right part of the image toward the peat dome (covered by the relevant forest part) from 20 to 25 m above mean sea level (AMSL) in height while the area around the river has a constant height of 17.5 m AMSL.

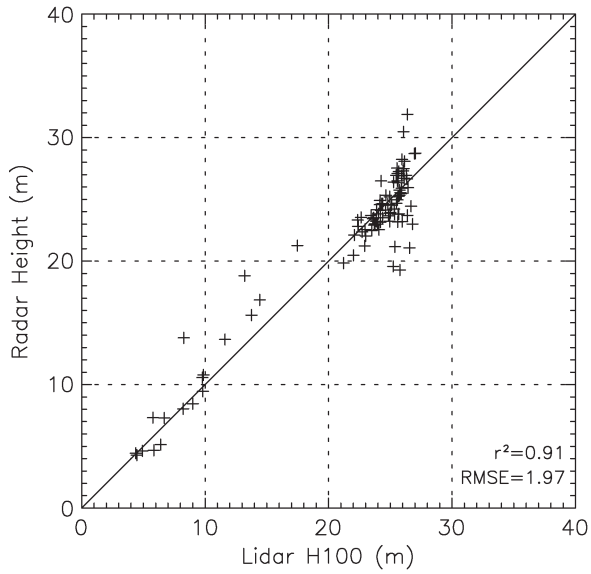

Fig. 8. Pol-InSAR height estimates at L-band versus LIDAR H100 validation plot for the Mawas River test site (100 samples).

Forest heights were estimated at L- and P-bands using a multiple-baseline inversion approach. The reason for this is in the E-SAR acquisition geometry at L- and P-bands where the radar look angle changes from near to far range from 25° to 55° [35]. This variation of the look angle goes along with a change of baseline (up to a factor of four), implying an inversion performance that varies along range. An optimum inversion performance across the whole range can then be achieved by combining the optimum range of multiple baselines. Accordingly, regions with low inversion performance caused by too high or too low volume sensitivity characterized by a vertical wavenumber larger than 0.20 or smaller than 0.05 are masked out for each individual baseline. Also, areas with a coherence lower than 0.3 are masked. The valid areas of each baseline are then combined together toward a single height image. In the case of two valid height estimates, a weighted height is used, reducing, in these areas, errors caused by nonsystematic uncompensated decorrelation contributions [23], [24].

Results were validated against the H100 derived from the LIDAR data. For this, the LIDAR H100 strip was divided into 100 subplots, and for each plot, the mean H100 is validated against the corresponding mean forest height as obtained from the Pol-InSAR inversion.

An L-band Pol-InSAR height map was obtained by combining height estimates from three baselines (5, 10, and 15 m). The comparison against the LIDAR H100 is shown in Fig. 8: with an r^2 of 0.91 and an RMSE of 1.97 m, for a height range from 5 to 28 m, indicating an estimation accuracy better than 10% which lies within the estimation accuracy of the LIDAR H100 set.

The P-band Pol-InSAR height map has been obtained by combining height estimates from four baselines (15, 30, 30, and 40 m) and is shown on the right of Fig. 7. The black dots in the near range are masked according to the wavenumber and coherence criteria discussed previously. In the forested part, the logging trails caused by logging activities 10–15 years ago appear clearly. For validation, two independent 30-m baselines formed by four different tracks (first baseline using track 1402

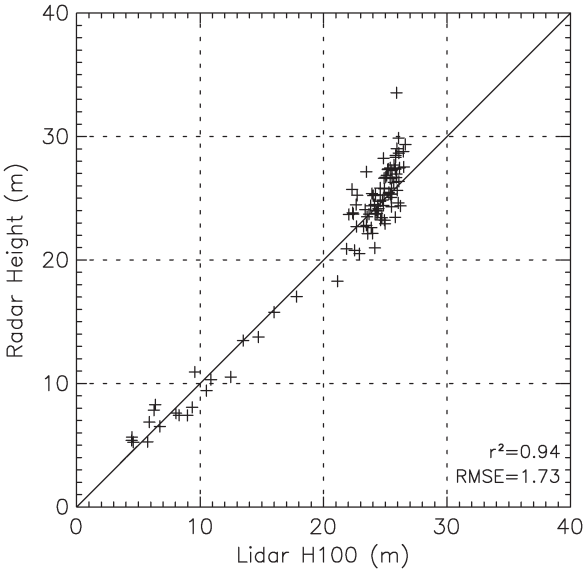

Fig. 9. Pol-InSAR height estimates at P-band versus LIDAR H100 validation plot for the Mawas River test site (100 samples, tracks 1402 and 1408).

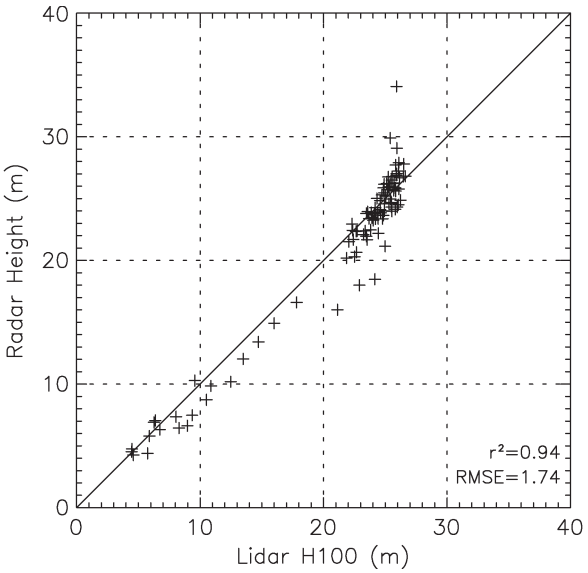

Fig. 10. Pol-InSAR height estimates at P-band versus LIDAR H100 validation plot for the Mawas River test site (100 samples, tracks 1405 and 1411).

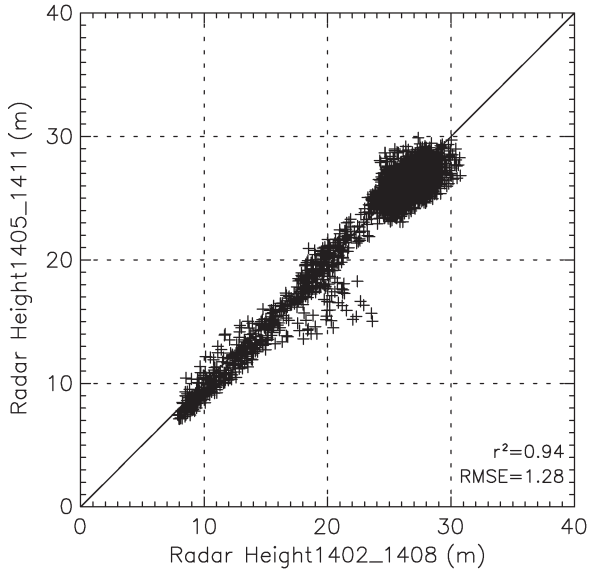

Fig. 11. Pol-InSAR height estimates at P-band (tracks 1405 and 1411) versus Pol-InSAR height estimates at P-band (tracks 1402 and 1408) for the Mawas River test site (3000 samples).

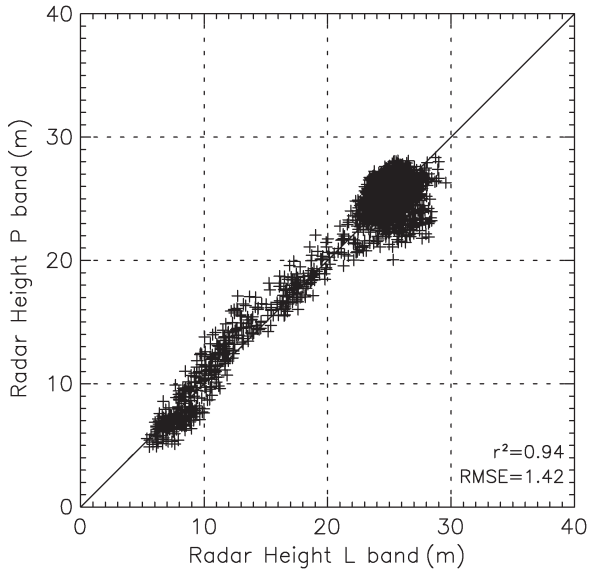

Fig. 12. Pol-InSAR height estimates at P-band (all tracks) versus Pol-InSAR height estimates at L-band (all scenes) for the Mawas River test site (3000 samples).

and 1408, second baseline using track 1405 and 1411) were used. In this case, a single baseline is sufficient as the optimum performance region for both baselines covers the whole LIDAR strip. Figs. 9 and 10 show the corresponding validation plots: The correlation coefficient with an r^2 of 0.94 for both baselines is quite high, and the RMSE is 1.73 m for the first and 1.74 m for the second baseline clearly below 2 m, hence showing an estimation accuracy better than 10% of the mean forest height. Clearly, the estimation performance is within the LIDAR estimation performance used as reference. Individual single points located particularly in the higher forest region tend to be overestimated probably due to uncompensated decorrelation effects. The comparison of the heights obtained from the two 30-m baselines is shown in Fig. 11 and is characterized by an r^2 of 0.94 and an RMSE of 1.28 m for a height range from 5 to 28 m, indicating the high consistency in the obtained results. The differences may be caused by the different amount of temporal decorrelation in the individual interferograms. The comparison was performed over 3000 samples distributed over the whole optimum performance region.

Compared to P-band, the L-band estimates (see Fig. 8) appear slightly noisier. This is because L-band is more affected by temporal decorrelation (see Section VI). The comparison of the L-band against the P-band estimates shown in Fig. 12 is based on the forest-height maps obtained by combining all available baselines (i.e., the 15-, 30-, 30-, and 40-m baselines at P-band and the 5-, 10-, and 15-m baselines at L-band) in order to obtain a performance comparison over 3000 samples distributed over the whole image: The obtained r^2 of 0.94 and

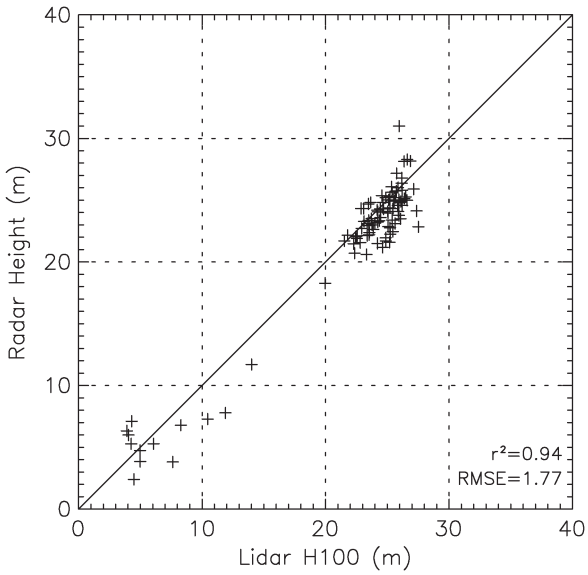

Fig. 13. InSAR height estimates (9) at X-band versus LIDAR H100 validation plot for the Mawas River test site (100 samples).

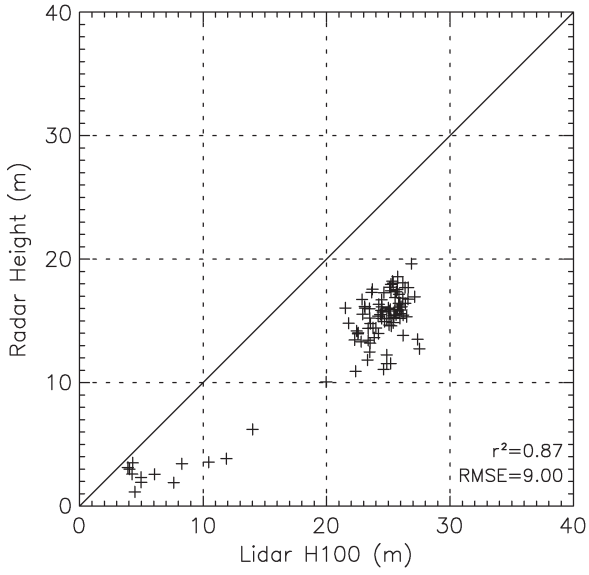

Fig. 14. InSAR phase center height at X-band versus LIDAR H100 validation plot for the Mawas River test site (100 samples).

an RMSE of 1.42 m manifest the consistency of the obtained estimates, indicating the validity of the physical structure underlying the Pol-InSAR inversion process. Divergences on the order of 2–3 m can be due to the variance introduced by temporal decorrelation and/or geolocation inaccuracy when transforming the P-band results to the L-band geometry.

In contrast to L- and P-band, X-band interferometry was performed in a single-pass mode. Consequently, the X-band interferometric coherence estimates are unaffected by temporal decorrelation. However, the availability of a single X-band channel (VV polarization) only makes the inversion of (6) by means of (8) not possible. A solution can be enforced by simplifying $F(z)$ and/or making use of *a priori* information. At higher frequencies, the vegetation extinction increases, attenuating more and more the strongly polarized ground-scattering contribution. One obvious approximation toward a simplified single-channel inversion scenario is to discard the ground-scattering component [assuming that $m = 0$ in (6)]. In this case, the single-channel interferometric inversion problem has three unknowns (i.e., height, extinction, and topographic phase) and only one (complex) observable. Using the ground phase obtained from the LIDAR ground DEM, it is then possible to obtain a balanced inversion problem

$$\min_{h_V,\sigma_0} \|\tilde{\gamma}(\vec{w}) - \tilde{\gamma}_V(h_V,\sigma|\phi_0 = \phi_{\mathrm{DEM}})\|\,. \tag{9}$$

Equation (9) can be inverted by a single interferometric channel providing forest-height estimates.

Similar to the L- and P-band validation, the LIDAR H100 strip was divided into 100 subplots. For each of the subplots, the mean H100 is used to validate the corresponding mean forest height as obtained from the X-band inversion. The validation plot is shown in Fig. 13. An r^2 of 0.94 and an RMSE of 1.77 m for a height range of 5–29 m prove a surprisingly good estimation performance at X-band. The estimated extinction values range from 0.1 up to 0.9 dB/m with a mean value on the order of 0.3 dB/m.

One has to keep in mind that (6) assumes a homogeneous vegetation layer. Volume inhomogeneities that introduce an additional variation of the phase center, for example, in the case of sparse forests with high single tree extinction (i.e., at higher frequencies), can bias the estimated volume coherence by an additional decorrelation term that corresponds to the "forest topography" variation within the estimation window. However, the fact that the obtained inversion results are not biased indicates that, at least for the Mawas case, the introduced bias is of secondary importance.

In Fig. 14, the height of the scattering center at X-band is plotted against the LIDAR H100 height: The comparison of the estimated phase centers with the ground makes it obvious that the scattering center of X-band is located clearly below the forest canopy. The RMSE of 9 m corresponds to the mean penetration depth into vegetation at X-band, indicating a higher estimation variance compared to forest top height (H100).

The r^2 of 0.87 is lower than the corresponding r^2 of 0.94 obtained from the height estimates of (9). This is a significant result indicating the systematic error that underlies height-estimation approaches based on the assumption that the X-band phase center is located on the top of the canopy [5], [26], [27]. On the other hand, it indicates the potential of Pol-InSAR inversion schemes.

In the absence of an external ground DEM, an alternative way to enforce a balanced inversion problem is to fix the extinction value. Ignoring the ground phase, by considering the absolute values only, a single parameter inversion problem is obtained

$$\min_{h_V} \| \,|\tilde{\gamma}(\vec{w})| - |\tilde{\gamma}_V(h_V,\phi_0|\sigma = \sigma_0)|\, \|\,. \tag{10}$$

Inversion has been performed using different extinction values; the best performance has been obtained for extinction around 0.3 dB/m that corresponds to the mean extinction value obtained from (9). Fig. 15 shows the validation plot for the forest-height estimates obtained by applying (10) and assuming an

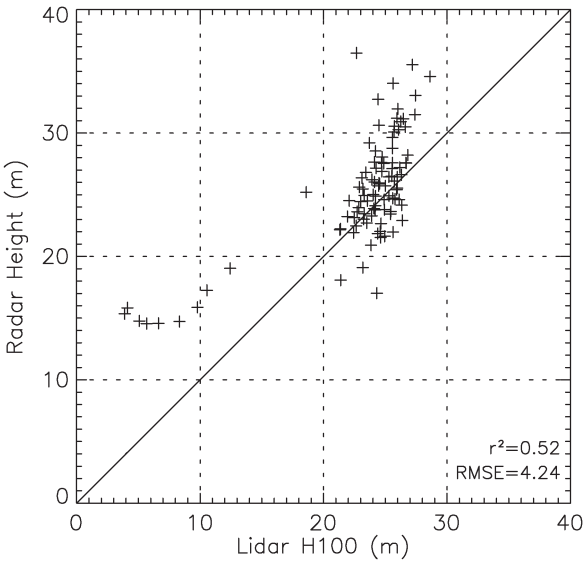

Fig. 15. InSAR height estimates (10) at X-band versus LIDAR H100 validation plot for the Mawas River test site (100 samples).

extinction of 0.3 dB/m. The r^2 of 0.52 and an RMSE of 4.24 m indicate a clearly inferior performance when compared to the inversion results obtained by means of (9). This is a direct consequence of the strong variation of the extinction value across the forest: An underestimation of the real extinction leads to overestimated forest heights and vice versa. Looking at Fig. 15, one sees that, particularly in the middle and lower forest parts, the height is overestimated due to the underestimation of extinction. Finally, under the assumption that both ground topography or extinction level are known, a height inversion independent of the ground-to-volume ratio becomes theoretically possible. However, also in this case, the variation of the extinction value across the forest will limit the performance.

VI. Temporal Decorrelation

The quantification of temporal decorrelation in repeat-pass interferograms is discussed next based on the data sets acquired over the Mawas Dome test site that, in contrast to the Mawas River data sets discussed in the previous section, are significantly affected by temporal decorrelation. The most common temporal decorrelation effect over a forested terrain is the wind-induced movement of scatterers within the canopy layer, for example, leaves, branches, etc. In terms of the RVoG model, this corresponds to a change in the position of the scattering particles within the volume. However, in this case, the scattering amplitudes as well as the propagation properties of the volume remain the same. Assuming further that the scattering properties of the ground do not change, the RVoG model with temporal decorrelation in the volume component becomes [23], [36]

$$\tilde{\gamma}_{\mathrm{Vol}}(\vec{w}) = \exp(i\kappa_z z_0)\frac{\gamma_{\mathrm{Temp}}\tilde{\gamma}_{V0} + m(\vec{w})}{1 + m(\vec{w})} \tag{11}$$

where γ_{Temp} denotes the correlation coefficient describing the temporal decorrelation of the volume scatterer. Inversion of forest height by means of (11) without accounting or compensating for γ_{Temp} leads to overestimated results [10]. In the special case of a zero spatial baseline interferogram (i.e., $\kappa_z = 0$ and $\tilde{\gamma}_{V0} = 1$), γ_{Temp} and $\tilde{\gamma}_{V0}$ can be separated from each other

$$\tilde{\gamma}_{\mathrm{Vol}}(\vec{w}) = \frac{\gamma_{\mathrm{Temp}} + m(\vec{w})}{1 + m(\vec{w})}. \tag{12}$$

However, in a general case of nonzero spatial baselines, the two contributions are superimposed and cannot be separated from each other on a single-baseline basis and/or without *a priori* information.

One way to obtain sensible estimates for γ_{Temp} at L- or P-band is to make use of the forest heights obtained by the X-band inversion h_V^X as derived by means of (10). The X-band forest-height estimates can be used to approximate the volume decorrelation contributions $|\tilde{\gamma}^L_{\mathrm{Vol}}(HV)|$ at L- or P-band. However, this is not offhand possible and requires additional assumptions. Constraining the analysis to the HV channels, one can assume zero ground scattering $(m(HV) = 0)$. Assuming further a zero extinction (i.e., $\sigma_L = 0$), (7) becomes

$$\left|\tilde{\gamma}^L_{\mathrm{Vol}}(HV)\right| = \left|\tilde{\gamma}^L_{V0}(HV)\right| = \mathrm{sinc}\quad\frac{\kappa_z^L h_V}{2}\quad. \tag{13}$$

Having an estimate of the (absolute) volume decorrelation contribution at HV permits now to estimate the temporal decorrelation contribution at L- or P- band

$$\gamma_{\mathrm{Temp}} = |\tilde{\gamma}(HV)| \,/\, \left|\tilde{\gamma}^L_{V0}(HV)\right|. \tag{14}$$

Equation (14) has been finally used to estimate the temporal decorrelation in two L-band and one P-band wind-affected repeat-pass interferograms. The temporal baseline for all three interferograms is on the order of 40 min. A relative homogeneous area of about 1000 $\times$ 1000 m has been selected in order to reduce the impact of forest inhomogeneity. An X-band amplitude image of the selected area is shown in the top figure of Fig. 16, demonstrating the homogeneity of the forest. The estimated γ_{Temp} maps are shown below in Fig. 16. The decorrelation patterns do not correlate with the forest structure and change from interferogram to interferogram; the wisplike decorrelation patterns are typical for wind-induced decorrelation. The corresponding histograms are shown in Fig. 17. At L-band, γ_{Temp} is about 0.89 for the first interferogram and 0.85 for the second, while at P-band, γ_{Temp} is, as expected, higher and about 0.93.

Note that a potential underestimation of the forest height by using (14) (caused, for example, by saturation) will bias the volume decorrelation estimation and lead to an underestimation of the temporal decorrelation. On the contrary, an overestimation of the forest height (due to an underestimated extinction) will lead to an overestimation of the temporal decorrelation or even to ratios larger than one. The localized high decorrelation "points" visible at L-band and even more at P-band are due to single large trees that are underestimated when inverting the X-band coherence, leading therefore to high temporal decorrelation regions.

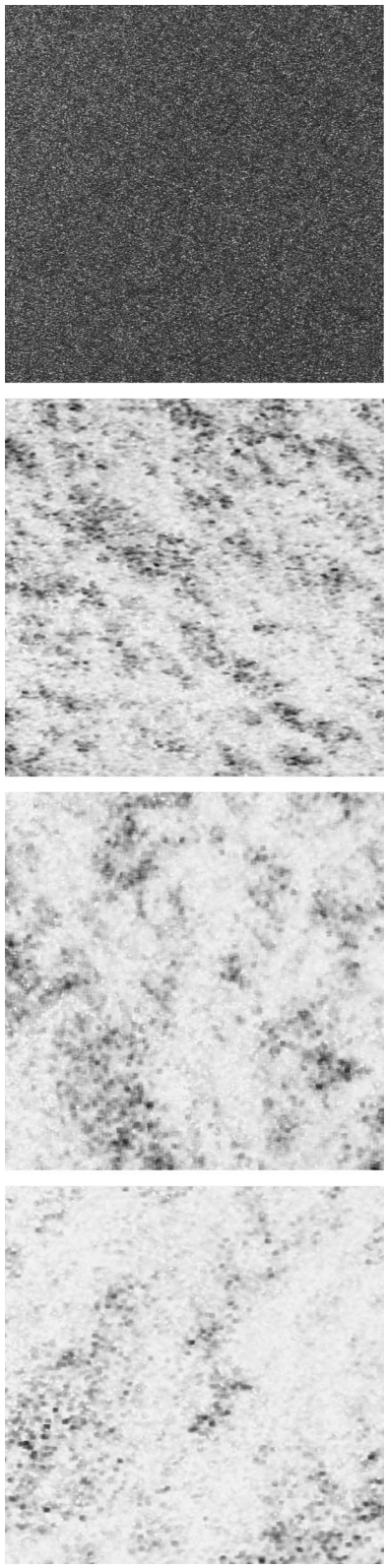

Fig. 16. (Top; grayscale) Amplitude and (middle two) estimated temporal decorrelation images at L- and (bottom) P-band for the Mawas Dome test site scaled from black: $\gamma_{\mathrm{Temp}} = 0$ to white: $\gamma_{\mathrm{Temp}} = 1.\,1000 \times 1000$ m.

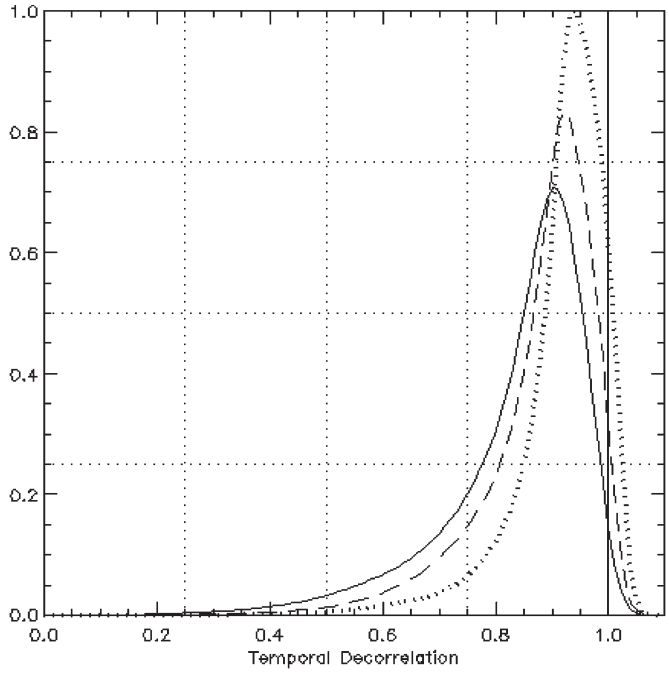

Fig. 17. Histograms of estimated temporal decorrealtion, (Solid and dashed lines with a mean of 0.89 and 0.85 respectively) at L-band and (dotted line with a mean of 0.93) at P-band for temporal baselines on the order of 40 min at Mawas Dome test site.

VII. Discussion and Conclusion

In this paper, the analysis, inversion, and validation of Pol-InSAR data collected in the frame of the INDREX-II campaign have been addressed and discussed. From the six INDREX-II test sites, the two most important in terms of available ground measurements and forest conditions have been selected for the investigations presented. The selected test sites include typical (disturbed and undisturbed) forest formations of Southeast Asia like dense lowland dipterocarp and peat-swamp forests which are the most important regional forest types.

First, the question about the visibility of the ground was faced. The polarimetric and interferometric analysis of the Sungai Wain data in Section IV demonstrated clearly the capability of both frequencies, L- and P-band, to penetrate until the ground through dense dipterocarp forests, with individual tree heights up to 60 m and local biomass levels even beyond 600 t/ha. This is a significant result toward the implementation of a low-frequency spaceborne SAR observation system.

The forest-height inversion performance has been assessed in Section V. In the case of the Sungai Wain test site, the Pol-InSAR estimates have been validated against H100 values estimated from the ground measurements. For forest heights ranging from 15 up to 45 m, the L- and P-band estimates where within 10% accuracy, even in hilly terrain. For the Mawas River test site, the validation was done against the LIDAR-derived H100. For forest heights ranging from 5 to 27 m, L-band estimates where characterized by an r^2 of 0.91 with an RMSE of 1.97 m, while the best P-band estimates show an r^2 of 0.94 with an RMSE of 1.74 m. The overall estimation accuracy for both test sites was better than 10% for both frequencies. The key limiting factor in estimation accuracy appears to be the uncompensated nonvolumetric decorrelation effects, particularly temporal decorrelation.

A key element in the quantitative assessment of temporal decorrelation was the single-pass single-channel (VV) X-band

data set. In a first step, a modification of the conventional Pol-InSAR forest-height inversion scheme has been proposed, adapted to the single-channel X-band interferometric observation space. The neglect of the ground-scattering component and the use of an external (LIDAR-derived) ground DEM allowed us to obtain sensitive height estimates and to validate them against the LIDAR measurements for the Mawas River test site. In the less-dense peat-swamp forest, X-band is able to penetrate until the ground, providing estimates characterized by surprisingly high r^2 values on the order of 0.94 with an RMSE of 1.77 m. This is a strong indication for the potential Pol-InSAR performance expected in the absence of temporal decorrelation. The generalization of the X-band performance is however critical as the visibility of the ground required for unbiased inversion gets lost when going to denser forest conditions. Nevertheless, keeping in mind the high-resolution single-pass X-band Pol-InSAR spaceborne configuration of TanDEM-X [37] scheduled for launch in 2009, the results become significant, particularly with respect to the wall-to-wall mapping of less-dense forest ecosystems as the boreal ones.

In a second step, in Section VI, the X-band height estimates have been used to assess the amount of temporal decorrelation at L- and P-band. Looking at temporal baselines of about 40 min, the obtained results indicate, as expected, a higher temporal stability at P-band (with temporal decorrelation on the order of 0.93) than at L-band (with temporal decorrelation on the order of 0.85–0.89). However, the decorrelation levels are, at both frequencies, sufficient to cause—if not compensated—an overestimation on the order of 30%–40% depending on the actual forest-height level.

In closing, it is important to make clear that the results achieved up to now and the conclusions drawn from the evaluation of this unique data, set point out the scientific importance of challenging and successful campaigns such as INDREX-II.

ACKNOWLEDGMENT

The INDREX II campaign was funded by the European Space Agency (ESA) under Contract 18602/04/NLCB. The authors would like to thank M. Quinones and D. Hoekman for their invaluable work in providing the ground measurements for the Sungai Wain test site, the Indonesian Ministry of Forestry, Borneo Orangutan Survival Foundation, and SAR Vision Indonesia for their help throughout the INDREX II campaign, Y. L. Desnos and M. Davidson from ESA for their essential support in the realization and execution of the campaign, DLR's E-SAR operation and SAR processing team for its priceless motivation and effort during the whole campaign and after, Dr. H.-D. Viktor Boehm from Kalteng Consultants for providing the LIDAR data, and last but not least, P. Prats for his valuable comments and discussions contributed to this paper.

REFERENCES

[1] A. Rosenqvist, M. Shimada, B. Chapman, A. Freeman, G. de Grandi, S. Saatchi, and Y. Rauste, "The global rain forest mapping project—A review," *Int. J. Remote Sens.*, vol. 21, no. 6/7, pp. 1375–1387, 2000.

[2] A. Rosenqvist, T. Ogawa, M. Shimada, and T. Igarashi, "Initiating the ALOS Kyoto & carbon initiative," in *Proc. IEEE IGARSS*, Toulouse, France, July 2003, pp. 21.–25.

[3] M. J. Quinones and D. Hoekman, "Exploration of factors limiting biomass estimation by polarimetric radar in tropical forests," *IEEE Trans. Geosci. Remote Sens.*, vol. 42, no. 1, pp. 86–104, Jan. 2004.

[4] D. Hoekman and M. J. Quinones, "Biophysical forest type characterization in the Colombian Amazon by airborne polarimetric SAR," *IEEE Trans. Geosci. Remote Sens.*, vol. 40, no. 6, pp. 1288–1300, Jun. 2002.

[5] J. C. Mura, L. Sant'Anna Bins, F. F. Gama, C. Da Costa Freitas, J. R. dos Santos, and L. V. Dutra, "Identification of the tropical forest in Brasilian Amazon based on the DEM difference from P- and X-band interferometric data," in *Proc. IEEE IGARSS*, Sydney, Australia, Jul. 9–13, 2001, vol. 2, pp. 789–791.

[6] T. Neef, G. S. Biging, L. V. Dutra, C. C. Freitas, and J. R. dos Santos, "Markov point processes for modeling of spatial forest patterns in Amazonia derived from interferometric height," *Remote Sens. Environ.*, vol. 97, no. 4, pp. 484–494, Sep. 2005.

[7] T. Neef, L. V. Dutra, J. R. dos Santos, C. C. Freitas, and L. V. Dutra, "Tropical forest measurement by interferometric height modeling and P-band radar backscatter," *For. Sci.*, vol. 51, no. 6, pp. 585–594, Dec. 2005.

[8] D. H. Hoekman and C. Varekamp, "Observation of tropical rain forest trees by airborne high-resolution interferometric radar," *IEEE Trans. Geosci. Remote Sens.*, vol. 39, no. 3, pp. 584–594, Mar. 2001.

[9] C. Varekamp and D. Hoekman, "High-resolution InSAR image simulation for forest canopies," *IEEE Trans. Geosci. Remote Sens.*, vol. 40, no. 7, pp. 1648–1655, Jul. 2002.

[10] S. R. Cloude and K. P. Papathanassiou, "Polarimetric SAR interferometry," *IEEE Trans. Geosci. Remote Sens.*, vol. 36, no. 5, pp. 1551–1565, Sep. 1998.

[11] K. P. Papathanassiou and S. R. Cloude, "Single-baseline polarimetric SAR interferometry," *IEEE Trans. Geosci. Remote Sens.*, vol. 39, no. 11, pp. 2352–2363, Nov. 2001.

[12] J. Praks, F. Kugler, K. P. Papathanassiou, I. Hajnsek, and M. Hallikainen, "Height estimation of boreal forest: Interferometric model-based inversion at L- and X-band versus HUTSCAT profiling scatterometer," *IEEE Geosci. Remote Sens. Lett.*, vol. 4, no. 3, pp. 466–470, Jul. 2007.

[13] F. Kugler, F. N. Koudogbo, K. P. Papathanassiou, and K. Gutjahr, "Frequency effects in POL-InSAR forest height estimation," in *Proc. EUSAR*, Dresden, Germany, May 16–18, 2006.

[14] T. Mette, K. P. Papathanassiou, and I. Hajnsek, "Estimating forest biomass from polarimetric interferometric SAR data in combination with forest allometry—Results from temperate spruce forest test site traunstein," in *Proc. Retrieval Bio Geophys. Parameters SAR Data Land Appl.*, Innsbruck, Austria, Nov. 16–19, 2004.

[15] F. Garestier, P. C. Dubois-Fernandez, and K. P. Papathanassiou, "Pine forest height inversion using single-pass X-band PolInSAR data," *IEEE Trans. Geosci. Remote Sens.*, vol. 46, no. 1, pp. 59–68, Jan. 2008.

[16] S. Magnussen, P. Eggermont, and V. N. La Ricca, "Recovering tree heights from airborne laser scanner data," *For. Sci.*, vol. 45, no. 3, pp. 402–422, Aug. 1999.

[17] J. Hyyppä, H. Hyyppä, M. Inkinen, and M. Engdahl, "Verification of the potential of various remote sensing datasources for forest inventory," in *Proc. IEEE Int. Geosci. Remote Sens. Soc.*, Pasadena, CA, 1998, pp. 1812–1814.

[18] G. Krieger, K. P. Papathanassiou, and S. R. Cloude, "Spaceborne polarimetric SAR interferometry: Performance analysis and mission concepts," *EURASIP J. Appl. Signal Process.*, vol. 2005, no. 1, pp. 3272–3292, Jan. 2005.

[19] R. Bamler and P. Hartl, "Synthetic aperture radar interferometry," *Inverse Probl.*, vol. 14, no. 4, pp. R1–R54, Aug. 1998.

[20] I. Hajnsek, K. P. Papthanssiou, and S. R. Cloude, "Removal of additive noise in polarimetric eigenvalue processing," in *Proc. IEEE IGARSS*, Sydney, Australia, 2001, pp. 2778–2780.

[21] H. A. Zebker and J. Villasenor, "Decorrelation in interferometric radar echoes," *IEEE Trans. Geosci. Remote Sens.*, vol. 30, no. 9, pp. 950–959, Jan. 1992.

[22] R. N. Treuhaft, S. N. Madsen, M. Moghaddam, and J. J. van Zyl, "Vegetation characteristics and underlying topography from interferometric radar," *Radio Sci.*, vol. 31, no. 6, pp. 1449–1495, 1996.

[23] S. R. Cloude and K. P. Papathanassiou, "Three-stage inversion process for polarimetric SAR interferometry," *Proc. Inst. Elect. Eng.—Radar Sonar Navig.*, vol. 150, no. 3, pp. 125–134, Jun. 2003.

[24] F. Kugler, K. P. Papathanassiou, S. K. Lee, I. Hajnsek, H. Pretzsch, "Forest height estimation by means of airborne repeat-pass polarimetric SAR interferometry," to be published.

[25] S. R. Cloude and E. Pottier, "A review of target decomposition theorems in radar polarimetry," *IEEE Trans. Geosci. Remote Sens.*, vol. 34, no. 2, pp. 498–518, Mar. 1996.

[26] Izzawati, E. D. Wallington, and I. H. Woodhouse, "Forest height retrieval from commercial X-band SAR products," *IEEE Trans. Geosci. Remote Sens.*, vol. 44, no. 4, pp. 863–870, Apr. 2006.
[27] H. Balzter, C. Rowland, R. Milne, O. Stebler, G. Patenaude, T. Dawson, and P. Sachi, "Potential of polarimetric SAR interferometry for forest carbon accounting," in *Proc. IEEE IGARSS*, Toulouse, France, 2003, pp. 1945–1947.
[28] M. Tabb, J. Orrey, T. Flynn, and R. Carande, "Phase diversity: A decomposition for vegetation parameter estimation using polarimetric SAR interferometry," in *Proc. EUSAR*, 2002, pp. 721–724.
[29] T. Flynn, M. Tabb, and R. Carande, "Coherence region shape extraction for vegetation parameter estimation in polarimetric SAR interferometry," in *Proc. IEEE IGARSS*, Toronto, ON, Canada, Jun. 2002, vol. 5, pp. 2596–2598.
[30] E. Colin, C. Tintin-Schnaider, and W. Tabbarra, "An interferometric coherence optimization method in radar polarimetry for high-resolution imagery," *IEEE Trans. Geosci. Remote Sens.*, vol. 44, no. 1, pp. 167–175, Jan. 2006.
[31] R. T. Fomena and S. R. Cloude, "On the role of coherence optimization in polarimetric SAR interferometry," in *Proc. CEOS SAR CAL/VAL Workshop*, Adelaide, Australia, Sep. 28–30, 2005.
[32] T. Mette, K. P. Papathanassiou, and I. Hajnsek, "Biomass estimation from polarimetric SAR interferometry over heterogeneous forest terrain," in *Proc. IEEE IGARSS*, Anchorage, AK, Sep. 20–24, 2004, pp. 511–514.
[33] H. Kramer and A. Akca, *Leitfaden zur Waldmesslehre*. Frankfurt, Germany: Sauerländer, 1995, p. 145.
[34] T. Aulinger, T. Mette, K. P. Papathanssiou, I. Hajnsek, M. Heurich, and P. Krzystek, "Validation of heights from interferometric SAR and LIDAR over the temperate forest site 'national park bayerischer wald'," in *Proc. 2nd Int. Workshop POLinSAR*, Frascati, Italy, Jan. 17–21, 2005. CD.
[35] R. Horn, "The DLR airborne SAR project E-SAR," in *Proc. IEEE Geosci. Remote Sens. Symp.*, Lincoln, NE, May 1996, vol. 3, pp. 1624–1628.
[36] K. P. Papathanassiou and S. R. Cloude, "The effect of temporal decorrelation on the inversion of forest parameters from Pol-InSAR data," in *Proc. IEEE IGARSS*, Toulouse, France, 2003, pp. 1429–1431. CD-ROM.
[37] G. Krieger, A. Moreira, H. Fiedler, I. Hajnsek, M. Werner, M. Younis, and M. Zink, "TanDEM-X: A satellite formation for high-resolution SAR interferometry," *IEEE Trans. Geosci. Remote Sens.*, vol. 45, no. 11, pp. 3317–3341, Nov. 2007.

Irena Hajnsek (A'01–M'01) received the Dipl. degree (with honors) from the Free University of Berlin, Berlin, Germany, in 1996 and the Ph.D. degree (with honors) from the Friedrich Schiller University of Jena, Jena, Germany, in 2001.

From 1996 to 1999, she was a Project Scientist with the Microwaves and Radar Institute, German Aerospace Center (DLR), Wessling, Germany. From 1999 to 2000, she was an European Union Fellow with the Institut d'Electronique et de Telecommunications de Rennes, University of Rennes I, Rennes, France, for ten months, and with Applied Electromagnetics, St. Andrews, U.K., for four months. In 2000, she rejoined the Radar Concepts Department, Microwaves and Radar Institute, DLR, where she has been leading the Polarimetric SAR Interferometry Research Group since 2002. In 2005, she was a Visiting Scientist at The University of Adelaide, Adelaide, Australia. She is responsible for the polarimetric science exploration of TerraSAR-X and is the Coordinator of the TanDEM-X science team. Her current research interests include electromagnetic propagation and scattering theory, radar polarimetry, synthetic aperture radar (SAR) and interferometric SAR data processing techniques, and environmental parameter modeling and estimation.

Dr. Hajnsek is the recipient of the DLR Science Award in 2002.

Florian Kugler was born in Bavaria, Germany, in 1974. He received the Dipl. Ing. Silv. degree in forestry science from the Technische Universität München, Freising, Germany, in 2004. He is currently working toward the Ph.D. degree in the Microwaves and Radar Institute, German Aerospace Center, Wessling, Germany.

His research interests include remote sensing on forests using polarimetric synthetic aperture radar interferometry.

Seung-Kuk Lee received the B.S. and M.S. degrees in earth system sciences from Yonsei University, Seoul, Korea, in 2000 and 2005, respectively. He is currently working toward the Ph.D. degree in the Microwaves and Radar Institute, German Aerospace Center (DLR), Wessling, Germany.

Since 2007, he has been with Microwaves and Radar Institute, DLR, as a Guest Scientist, through a scholarship from the Korea Research Foundation. His research interests include polarimetric synthetic aperture radar interferometry.

Konstantinos Panagiotis Papathanassiou (M'02–SM'03) received the Dipl.Ing. degree (with honors) and the Ph.D. degree (with honors) from the Technical University of Graz, Graz, Austria, in 1994 and 1999, respectively.

From 1992 to 1994, he was with the Institute for Digital Image Processing, Joanneum Research, Graz. From 1995 to 1999, he was with the Microwaves and Radar Institute, German Aerospace Center (DLR), Wessling, Germany. From 1999 to 2000, he was a European Union Postdoctoral Fellow with Applied Electromagnetics, St. Andrews, U.K. In October 2000, he rejoined the Radar Concepts Department, Microwaves and Radar Institute, DLR, where he is currently a Senior Scientist within the Polarimetric SAR Interferometry (Pol-InSAR) Research Group, working on Pol-InSAR and the development of inversion algorithms for physical parameters from synthetic aperture radar (SAR) data. He is the author of more than 100 publications in international journals and conference and workshop proceedings. His research interests include polarimetric and interferometric processing and calibration techniques, polarimetric SAR interferometry, quantitative parameter estimation from SAR data, and SAR mission design and performance analysis.

Dr. Papathanassiou was the recipient of the IEEE Geoscience and Remote Sensing Society International Geoscience and Remote Sensing Symposium Prize Paper Award in 1998, the Best Paper Award of the European SAR Conference in 2001, and the DLR Science Award in 2002.

Quantification of Temporal Decorrelation Effects at L-Band for Polarimetric SAR Interferometry Applications

Seung-Kuk Lee, Florian Kugler, Konstantinos P. Papathanassiou, *Senior Member, IEEE*, and Irena Hajnsek, *Member, IEEE*

***Abstract*—Temporal decorrelation is the most critical issue for the successful inversion of polarimetric SAR interferometry (Pol-InSAR) data acquired in an interferometric repeat-pass mode, typical for satellite or lower frequency airborne SAR systems. This paper provides a quantitative estimation of temporal decorrelation effects at L-band for a wide range of temporal baselines based on a unique set of multibaseline Pol-InSAR data. A new methodology that allows to quantify individual temporal decorrelation components has been developed and applied. Temporal decorrelation coefficients are estimated for temporal baselines ranging from 10 min to 54 days and converted to height inversion errors caused by them. The temporal decorrelations of γ_{TV} (volume temporal decorrelation) and γ_{TG} (ground temporal decorrelation) depend not only on the wind-induced movement but also strongly on the rain-induced dielectric changes in volume and on the ground at temporal baseline on the order of day or longer. At temporal baselines on the order of minutes, the wind speed is a critical parameter and the speed of 2 m/s already hampers the application of Pol-InSAR forest parameter inversion. The approach is supported and validated by using L-band E-SAR repeat-pass data acquired in the frame of three dedicated campaigns, BioSAR 2007, TempoSAR 2008, and TempoSAR 2009.**

***Index Terms*—Height inversion, polarimetric synthetic aperture radar interferometry (Pol-InSAR), temporal baseline, temporal decorrelation.**

I. Introduction

POLARIMETRIC synthetic aperture radar interferometry (Pol-InSAR) has been developed to a powerful technique for quantitative forest applications. The Pol-InSAR technique is based on the combination of two important SAR measurements: interferometry and polarimetry. Interferometric SAR (InSAR) is sensitive to the vertical structure of volume scatterers as forest and allows to estimate accurately the vertical position of the scattering center. Polarimetric SAR (PolSAR) is able to identify shape, orientation and dielectric properties of scatters allowing the understanding of scattering mechanisms. In [1], the coherent combination of the two techniques was first introduced to provide the separation and the identification of different scattering contributions within the resolution cell. In the last decade, a variety of quantitative models for the estimation of forest parameters from Pol-InSAR data, as the Random Volume over Ground (RVoG) model, have been developed and successfully validated over a variety of forest test sites [2]–[5].

The key observable used in Pol-InSAR application is the complex interferometric coherence estimated at different polarizations. The interferometric coherence depends on instrument and acquisition parameters as well as on dielectric and structural parameters of the scatterer. The total interferometric coherence can be decomposed into several decorrelation processes [6], [7]: System induced noise decorrelation, temporal decorrelation, volume decorrelation and so on. To invert forest parameters by means of Pol-InSAR technique, volume decorrelation $\tilde{\gamma}_V$ must be separated from other decorrelation contributions because the RVoG model only considers the volume decorrelation contribution of the interferometric coherence ignoring other decorrelation contributions. Uncompensated nonvolumetric decorrelation contributions lower the interferometric coherence, and increase the variation of the interferometric phase leading to a biased and less accurate parameter estimation performance. In repeat-pass air- or spaceborne InSAR configurations, the most critical nonvolumetric decorrelation contribution is the temporal decorrelation caused by the change of the geometric and/or dielectric properties of the scatterers within the scene occurring in the time between the two acquisitions.

In previous studies, temporal decorrelation was modeled assuming only changes in the position of the scatterers. If the motion of the scatterers is characterized by a Gaussian-statistic an exponential temporal decorrelation model is derived [7]. This model was first validated using L-band SEASAT data. The exponential model was extended by a Brownian motion [8]. The Brownian motion implies an exponential decay of the temporal decorrelation with time. However, the temporal decorrelation in forest at small temporal baselines (i.e., shorter than an hour) is mainly caused by wind-induced motion making the Brownian motion inadequate to model temporal decorrelation at these temporal baseline scales [16]. More recently, a physical model of temporal decorrelation was proposed assuming a variable Gaussian motion along the vertical direction of forests [15]. This model was validated at L-band using zero spatial baseline and 40-min temporal baseline data acquired by the JPL's UAVSAR system.

However, all temporal decorrelation models proposed the assumption that the dielectric properties of the scatterers remain

Manuscript received October 07, 2012; revised December 07, 2012; accepted February 07, 2013. Date of publication April 26, 2013; date of current version June 17, 2013.

S.-K. Lee and I. Hajnsek are with the Institute of Environmental Engineering, ETH Zurich, CH-8093 Zurich, Switzerland and with Microwaves and Radar Institute, German Aerospace Center, 82234 Wessling, Germany (e-mail: leeseu@ethz.ch; seungkuk.lee@dlr.de; ihajnsek@ethz.ch; irena.hajnsek@dlr.de).

F. Kugler and K. P. Papathanassiou are with Microwaves and Radar Institute, German Aerospace Center, 82234 Wessling, Germany (e-mail: florian.kugler@dlr.de; kostas.papathanassiou@dlr.de).

Color versions of one or more of the figures in this paper are available online at http://ieeexplore.ieee.org.

Digital Object Identifier 10.1109/JSTARS.2013.2253448

unchanged between the two acquisitions. At long temporal baselines (i.e., longer than a day), temporal decorrelation may be also caused by the change of dielectric properties due to environmental and weather effects.

There are different approaches to assess the impact of temporal decorrelation on the Pol-InSAR forest height inversion. The RVoG with Volume Temporal Decorrelation (RVoG + VTD) model was introduced in [9], [4] incorporating a temporal decorrelation component into the two-layer (volume/ground) scattering model. The inversion results in the presence of temporal decorrelation (2 day) demonstrated that forest height inversion without accounting or compensating for temporal decorrelation leads to significantly overestimated heights [9]. In [5], the quantification of temporal decorrelation in L- and P-band repeat-pass interferograms was discussed in the context of the INDREX-II data sets acquired with about 40-min temporal baseline assuming that the scattering properties of the ground do not change in that time. For the special case of a zero (spatial) baseline interferogram, temporal decorrelations at L- and P-band are separated from volume decorrelation. The obtained results in homogenous forest area indicated, as expected, a lower temporal stability for higher frequencies, and that patterns of wind-induced temporal decorrelation do not correlate with forest structure and may change from interferogram to interferogram even if they are acquired with the same temporal baseline (i.e., 40 min). While this method can provide an estimation of temporal decorrelation, the impact of temporal decorrelation on Pol-InSAR forest height inversion cannot be directly addressed due to the absence of volume decorrelation $\tilde{\gamma}_V$.

This paper focuses on a quantitative analysis of temporal decorrelation on Pol-InSAR inversion performance at L-band as a function of temporal baseline based on multitemporal and multispatial airborne experimental data acquired in the frame of three dedicated airborne SAR experiments. Different temporal decorrelation coefficients for volume and the ground scattering are incorporated into RVoG model. Both deteriorate the interferometric coherence on different time scales. By using the experimental data, the decorrelation contributions are separated from each other even for nonzero spatial baselines. The behavior of both temporal decorrelations and their impact on forest height inversion performance is analyzed and discussed as a function of time.

To investigate the analysis of temporal decorrelation in time, three dedicated airborne SAR campaigns (BioSAR 2007, TempoSAR 2008 and TempoSAR 2009) carried out over boreal and temperate forest sites by DLR's airborne Experimental SAR system, E-SAR [11] are investigated. During the campaigns, DLR's E-SAR system collected fully polarimetric and repeat-pass interferometric SAR data on a variety of temporal and spatial baselines. Section II of this paper will introduce the RVoG model with two temporal decorrelation parameters and show simulation results of their impact on forest height inversion performance. The airborne campaigns are described including test sites and Pol-InSAR data sets in Section III. In Section IV, the impact of temporal decorrelation on Pol-InSAR inversion performance is discussed and validated by real airborne experimental data at temporal baselines on the order of 10 min to 54 d. Finally, the obtained results are reviewed and discussed in Section VI.

II. Temporal Decorrelation in Pol-InSAR

Quantitative estimation of forest parameters has been successfully performed by using a two-layer model, the so-called Random Volume over Ground (RVoG) model [3]–[5]. The RVoG model consists of a volume layer containing randomly oriented scatterers and an impenetrable ground layer. The interferometric coherence is directly linked to the vertical distribution of scatterers through a (normalized) Fourier transformation relationship [1]–[3]. Accordingly, the ground layer is modeled by the Dirac delta function located at interface between the two media. After range filtering [6] and compensation of system induced noise decorrelation [10], the interferometric coherence at the ground layer becomes unity and the phase center in the vertical direction (z) is located on the ground ϕ_0:

$$\tilde{\gamma} = e^{i\kappa_z z_0} \frac{\int_0^{h_v} \delta(z') e^{i\kappa_z z'} dz'}{\int_0^{h_v} \delta(z') dz'} = e^{i\phi_0} \tag{1}$$

κ_z is the effective vertical (interferometric) wavenumber and the phase $\phi_0 = \kappa_z z_0$ is related to the ground topography. Differently than the surface scattering, the volume layer is characterized by an extended distribution of scatterers. In the simplest case, the vertical distribution of scatterers in volume is assumed to be an exponential function defined by a mean extinction coefficient expressing both scattering and absorption losses. Accordingly the interferometric coherence for the volume is given as [3]–[5]

$$\tilde{\gamma}_V = \frac{\int_0^{h_v} F(z') e^{i\kappa_z z'} \, dz'}{\int_0^{h_v} F(z') \, dz'} = \frac{\int_0^{h_v} e^{\frac{2\sigma z'}{\cos\theta_0}} e^{i\kappa_z z'} \, dz'}{\int_0^{h_v} e^{\frac{2\sigma z'}{\cos\theta_0}} \, dz'}. \tag{2}$$

Combining surface and volume scatterings, the coherence for the RVoG model is obtained as [4], [5]

$$\begin{aligned} \tilde{\gamma}(\vec{w}) &= e^{i\phi_0} \frac{\tilde{\gamma}_V + m(\vec{w})}{1 + m(\vec{w})} \\ &= e^{i\phi_0} \left(\tilde{\gamma}_V + \frac{m(\vec{w})}{1 + m(\vec{w})} (1 - \tilde{\gamma}_V) \right) \end{aligned} \tag{3}$$

where m is the effective surface-to-volume scattering amplitude ratio accounting for the attenuation through the volume. The coherences $\tilde{\gamma}(\vec{w})$ at different polarizations $\vec{w}$ vary only due to the variation of the ground-to-volume amplitude ratio with polarization. In Fig. 1, they are plotted on the complex plane. These loci lie on a straight line. Neglecting temporal decorrelation and assuming a sufficient calibration/compensation of system- and geometry-induced decorrelation contributions, (3) can be inverted using a quad-polarization single-baseline acquisition. In the conventional monostatic case, three interferometric coherences formed by using the three independent polarizations are available to estimate five unknown parameters $(h_v, \sigma, \phi_0, m_1, m_2)$ assuming that one polarization has no ground response $(m_3 = 0)$ [2], [4], [5].

However, in repeat-pass airborne/satellite InSAR (or Pol-InSAR) system, temporal decorrelation introduced by dynamic changes within the scene cannot be neglected. Temporal decorrelation affects in general both the volume component that represents the vegetation layer and the underlying ground layer, but the decorrelation processes occur differently in the two layers. Temporal decorrelation on the ground layer can arise from surface changes between the two acquisitions. The

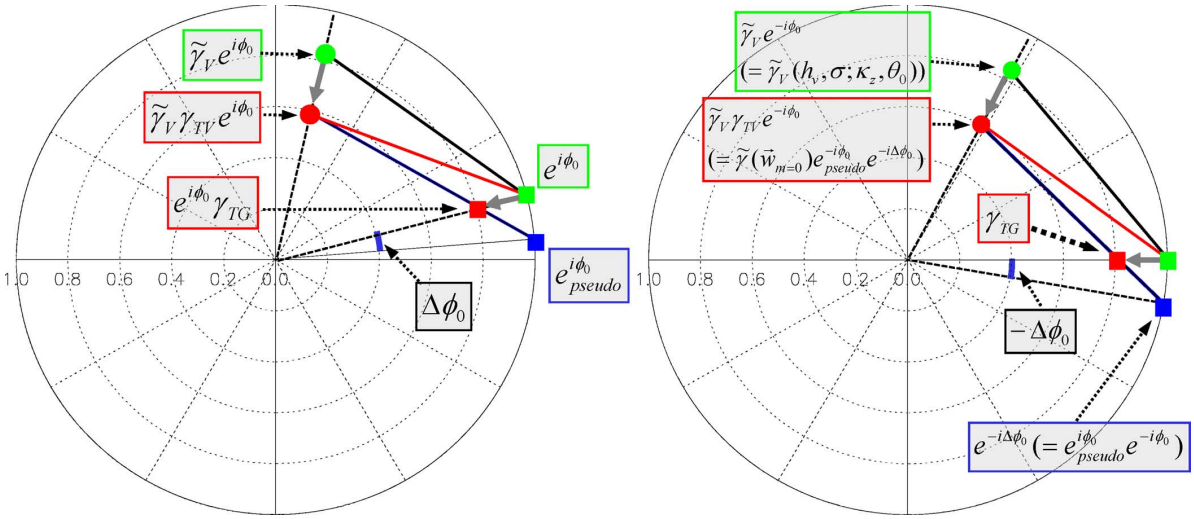

(a) (b)

Fig. 1. (a) Coherence loci for the RVoG model with temporal decorrelations of γ_{TV} and γ_{TG}. (b) Coherence loci rotated by ground phase $e^{-i\phi_0}(=e^{-i\phi_0}_{pseudo}e^{-i\Delta\phi_0})$; Temporal decorrelation on the ground layer γ_{TG} is located on x-axis.

ground point that represents the interferometric coherence on the ground can be modified as

$$\tilde{\gamma}(\vec{w}_{m=\infty}) = \gamma_{\mathrm{TG}} e^{i\kappa_z z_0} \frac{\int_0^{h_v} \delta(z') e^{i\kappa_z z'}\, dz'}{\int_0^{h_v} \delta(z')\, dz'} = \gamma_{\mathrm{TG}} e^{i\phi_0} \quad (4)$$

where $\delta(\,\cdot\,)$ is a Dirac delta function and γ_{TG} represents the *scalar* correlation coefficient describing temporal decorrelation of the underlying surface scatterers [9]. In a unit circle, γ_{TG} results in a shift of the ground point $e^{i\phi_0}$ radially towards the origin as shown in Fig. 1, but the phase center remains unchanged. On the other hand, temporal decorrelation in volume is more complex and critical due to its susceptibility to wind which is nonstationary neither temporally nor spatially even on very short time- and small spatial-scales. Assuming that temporal decorrelation varies along the vertical structure function, volume decorrelation in (2) can be modified by a temporal decorrelation structure function $F_t(z)$ given as [15]

$$\tilde{\gamma}(\vec{w}_{m=0}) = \frac{\int_0^{h_v} F_t(z') F(z') e^{i\kappa_z z'}\, dz'}{\int_0^{h_v} F(z')\, dz'} = \tilde{\gamma}_{\mathrm{TV}} \tilde{\gamma}_V. \quad (5)$$

$\tilde{\gamma}_{\mathrm{TV}}$ denotes the *complex* correlation coefficient describing the temporal decorrelation of the volume layer. In this case, temporal decorrelation reduces the amplitude of volume decorrelation and changes the effective phase center depending on the temporal structure function. In case of a constant temporal decorrelation function, temporal decorrelation in volume becomes a *scalar* value γ_{TV} (i.e., no bias of phase).

Both temporal decorrelation effects can be incorporated in the two-layer scattering model. The equation of RVoG model [see (3)] with two temporal decorrelations can be described as [9], [15]

$$\tilde{\gamma}(\vec{w}) = e^{i\phi_0} \frac{\tilde{\gamma}_{\mathrm{TV}} \tilde{\gamma}_V + \gamma_{\mathrm{TG}} m(\vec{w})}{1 + m(\vec{w})}. \quad (6)$$

Both $\tilde{\gamma}_{\mathrm{TV}}$ and γ_{TG} are functions of the temporal baseline; however the decorrelation processes in the volume layer occur at different—in general much smaller—time scales than the decorrelation of the surface layer. Moreover, both temporal decorrelation coefficients may be polarization dependent: For example, changes in the dielectric properties of the canopy layer (due to changes in moisture content) or even more changes in its structural characteristics (caused by the annual phenological cycle or fire events) lead to different changes at different polarizations in the volume scatterers. Furthermore, a change in the dielectric properties of the ground—as for example due to a change in soil moisture—effects the scattering at each polarization differently and leads to a polarization dependent temporal decorrelation of the ground.

Using a quad-polarization single baseline acquisition (three complex coherences), (6) cannot be inverted even in a multibaseline configuration due to the two additional unknown parameters $(\tilde{\gamma}_{\mathrm{TV}}, \gamma_{\mathrm{TG}})$ introduced by any (temporal) baseline. However, even if the general temporal decorrelation scenario of (6) is underdetermined, special temporal decorrelation scenarios allowing simple assumptions may be accounted for in the context of multibaseline Pol-InSAR acquisitions, as it will be discussed in the next section.

A. Wind Induced Temporal Decorrelation

When the temporal baseline is sufficiently short (i.e., smaller than 1 h), it is realistic to assume that the ground remains stable (i.e., $\gamma_{\mathrm{TG}} = 1$), and that the dielectric and statistical properties of the volume do not change. Thus, the most common temporal decorrelation in forest is due to wind-induced movement of the scatterers within the volume layer. In this case, the RVoG model with temporal decorrelation contributions mentioned in (6) can be simplified as [4], [5], [9]

$$\begin{aligned}\tilde{\gamma}(\vec{w}) &= e^{i\phi_0} \frac{\gamma_{\mathrm{TV}} \tilde{\gamma}_V + m(\vec{w})}{1 + m(\vec{w})} \\ &= e^{i\phi_0} \left(\gamma_{\mathrm{TV}} \tilde{\gamma}_V + \frac{m(\vec{w})}{1 + m(\vec{w})} (1 - \gamma_{\mathrm{TV}} \tilde{\gamma}_V) \right). \quad (7)\end{aligned}$$

The Pol-InSAR coherence loci contaminated by γ_{TV} still lie on a straight line segment in the complex plane. The ground

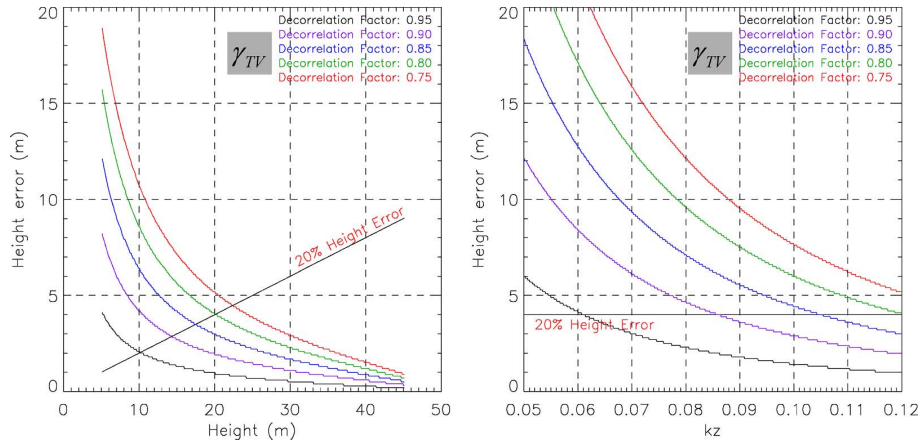

Fig. 2. (a) Height bias (overestimation) induced by different levels of temporal decorrelation as a function of forest heights assuming a constant vertical wavenumber of $\kappa_z = 0.12$ rad/m. (b) Height bias induced by different levels of temporal decorrelation as a function of vertical wavenumber κ_z, assuming a constant forest height of 20 m.

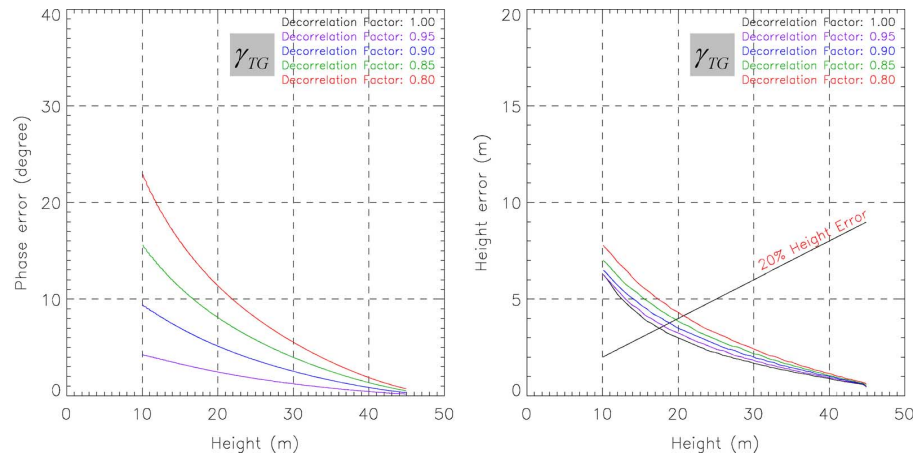

Fig. 3. Biases caused by γ_{TG}. Ground phase bias $\Delta\phi_0$ (a) and height bias Δh (b) induced by different levels of temporal decorrelation γ_{TG} as a function of forest height assuming a vertical wavenumber of $\kappa_z = 0.12$ rad/m and temporal decorrelation of $\gamma_{\mathrm{TV}} = 0.85$.

TABLE I
BIOSAR 2007 CAMPAIGN DATA SET: (X2) DENOTES THAT TWO BASELINES ARE AVAILABLE THROUGH DIFFERENT COMBINATIONS OF THE MASTER AND SLAVE TRACKS

Campaign	Scene_ID	Acquisition Date	Nr. of Tracks	Temporal Baseline (day)	Spatial Baseline (m)
BioSAR 2007	07_01xx	2007/03/09	6	32, 54	0(x2), 8(x3)
	07_02xx	2007/03/31	5		0, 8, 16, 24
	07_04xx	2007/05/02	5		0, 8, 16, 24

point [green rectangular point in Fig. 1(a)] remains unchanged, while the volume coherence $\tilde{\gamma}_V$ is shifted towards the origin byγ_{TV}.

The inversion of Pol-InSAR data contaminated by temporal decorrelation γ_{TV} leads to biased forest height estimates: The lower coherences (due to the temporal decorrelation γ_{TV}) are interpreted by the model as to be caused by higher forest heights. In other words, height estimates obtained by inverting (7) instead of (3), are overestimated depending on the level of temporal decorrelation γ_{TV}. Fig. 2(a) shows the height bias obtained by inverting (7) for different levels of temporal decorrelation ($\gamma_{\mathrm{TV}} = 0.95$ to 0.75) as a function of forest height assuming an effective vertical (interferometric) wavenumber of $\kappa_z = 0.12$ rad/m. One can clearly see that the estimation biases are significantly higher for low heights than for high heights and that the height biases increase with increasing temporal decorrelation. Note that even for low temporal decorrelation levels (on the order of 0.9) the height bias becomes critical for low forest heights.

Fig. 2(a) makes clear that for achieving acceptable height estimates temporal decorrelation has to be compensated. Unfortunately, wind-induced temporal decorrelation occurs especially in a stochastic manner within the scene [5] and can be accounted only for on the basis of detailed information about the environ-

TABLE II
TEMPOSAR 2008 AND 2009 CAMPAIGNS DATA SET: (X2) DENOTES THAT TWO BASELINES ARE AVAILABLE THROUGH DIFFERENT COMBINATIONS OF THE MASTER AND SLAVE TRACKS

Campaign	Scene_ID	Acquisition Date	Nr. of Tracks	Temporal Baseline (day)	Spatial Baseline (m)
TempoSAR 2008	08_01xx	2008/06/07	6	1, 2, 3, 5, 7, 8, 9, 10, 12, 13	-15, -5, 0, 5,10
	08_03xx	2008/06/10	6		-15, -5, 0, 5,10
	08_04xx	2008/06/12	6		-15, -5, 0, 5,10
	08_05xx	2008/06/19	6		-15, -5, 0, 5,10
	08_06xx	2008/06/20	6		-15, -5, 0, 5,10
TempoSAR 2009	09_01xx	2009/04/27	8	1(x2), 6, 7(x2), 8, 13, 14(x2), 15	-15, -10, -5, 0, 5, 10, 15
	09_02xx	2009/04/28	8		-15, -10, -5, 0, 5, 10, 15
	09_03xx	2009/05/05	6		-15, -5, 0, 5, 15
	09_04xx	2009/05/11	8		-15, -10, -5, 0, 5, 10, 15
	09_05xx	2009/05/12	8		-15, -10, -5, 0, 5, 10, 15
	09_08xx	2009/10/27	4	1, 8, 9	0, 5, 10
	09_09xx	2009/10/28	5		0, 5, 10, 15
	09_11xx	2009/11/05	1		-

TABLE III
METEOROLOGICAL INFORMATION: WIND SPEED AND PRECIPITATION. (-) DENOTES NO PRECIPITATION

TempoSAR Scene_ID	Acquisition Time		Schönharting					Nilling				
	yy:mm:dd	hh	Precipitation (mm)				Wind (m/s)	Precipitation (mm)				Wind (m/s)
			12h	24h	36h	48h		12h	24h	36h	48h	
08_01xx	2008/06/07	11	0.1	0.7	4.9	4.9	1.3-1.6	0.0	3.4	10.2	10.2	2.2
08_03xx	2008/06/10	8	-	-	-	-	0.8-1.3	-	-	0.1	4.2	0.7-0.9
08_04xx	2008/06/12	8	-	29.7	31.7	31.7	0.8-0.7	0.1	14.7	15.2	15.2	0.5-0.7
08_05xx	2008/06/19	8	-	-	-	6.5	0.8-1.0	0.1	1.9	1.9	5.5	0.6-0.7
08_06xx	2008/06/20	7	-	-	-	-	2.3-3.2	-	-	0.1	1.9	1.9-1.5
09_01xx	2009/04/27	8	-	-	-	-	1.1-0.7	-	-	-	-	1.0
09_02xx	2009/04/28	8	-	-	-	-	1.6	-	-	-	-	1.7-1.2
09_03xx	2009/05/05	8	-	1.9	10.4	10.4	1.6-1.8	0.1	1.2	7.5	7.5	0.6-1.4
09_04xx	2009/05/11	8	-	-	-	-	1.2-1.0	-	-	-	-	0.8
09_05xx	2009/05/12	8	4.1	5.1	5.1	5.1	2.0	2.1	3.3	3.3	3.3	1.5-1.6
09_08xx	2009/10/27	14	-	-	1.8	2.3	1.0-1.7	-	-	2.3	2.3	1.0-1.1
09_09xx	2009/10/28	12	0.1	0.1	0.1	0.1	0.7-0.6	0.2	0.2	0.2	0.2	0.6
09_11xx	2009/11/05	11	-	-	6.0	6.4	1.2	-	-	7.6	7.9	1.0

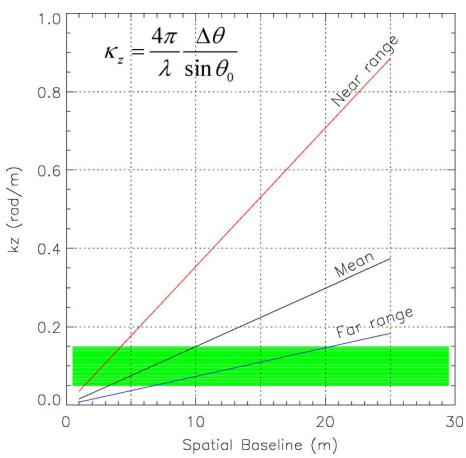

Fig. 4. Vertical wavenumber κ_z as a function of nominal baseline for L-band E-SAR system. The altitude of E-SAR is 3000 m. The incidence angle changes from 25° to 55°. Red: κ_z in near range, Blue: κ_z in far range, Black: mean κ_z from near to far range, Green: The range of κ_z between 0.05 and 0.15 rad/m.

mental conditions over the time during the two acquisitions. A valuable option to reduce the impact of nonvolumetric decorrelation contributions on the forest height estimation is to increase the volume decorrelation contribution with respect to the nonvolumetric decorrelation by increasing the spatial baseline. This is shown on the right side of Fig. 2 where the height bias obtained by inverting (7) for different levels of temporal decorrelation ($\gamma_{\mathrm{TV}} = 0.95$ to 0.75) is plotted as a function of the vertical wavenumber κ_z, assuming a constant forest height of 20 m. Even for low temporal decorrelation levels (on the order of 0.9), the height bias is critical at small baselines (12 m (i.e., 60%) for $\kappa_z = 0.05$ rad/m), but decreases with increasing baseline: for the same level of temporal decorrelation the height bias decreases to 2 m (i.e., 10%) when using a vertical wavenumber of $\kappa_z = 0.12$ rad/m. This makes clear that larger spatial baselines are of advantage in the presence of weak to moderate temporal decorrelation as they minimize the bias introduced by the temporal baseline. The price to be paid is an overall lower coherence level—due to the increased volume decorrelation contribution—that increases the phase variance of the interferometric coherence.

B. Temporal Decorrelation of the Ground Layer

For temporal baselines on the order of days and larger, temporal decorrelation contributions induced by changes in the scattering properties of the ground layer cannot be neglected

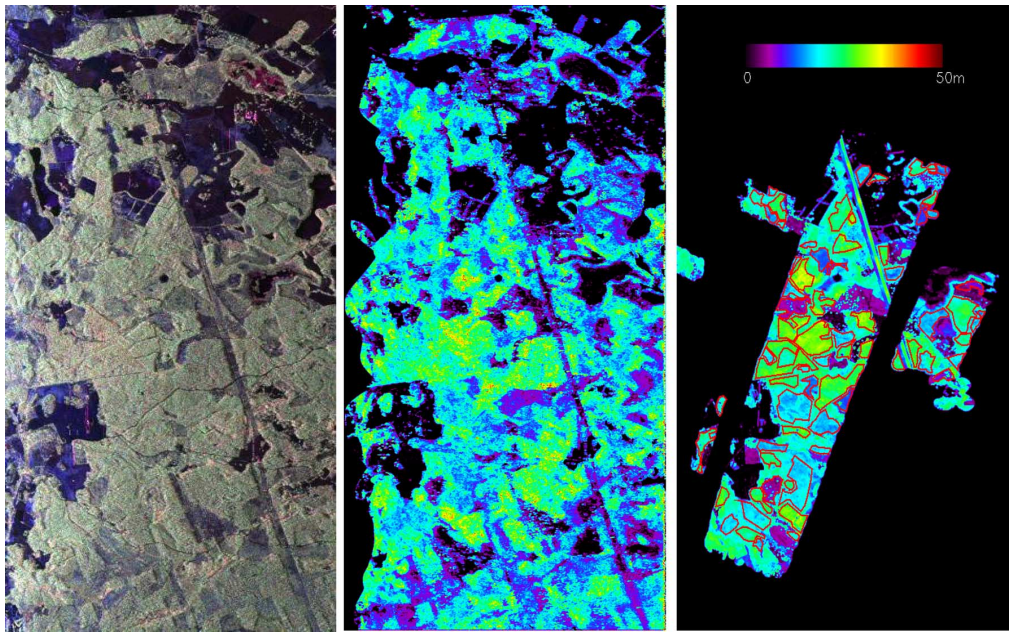

(a) (b) (c)

Fig. 5. Remningstorp test site. (a) Radar image of the Pauli components, Red: HH-VV, Green: HV, Blue: HH+VV. (b) Pol-InSAR forest height map in Remningstorp forest; scaled from 0 m to 50 m, (c) Polygons superimposed on LIDAR derived H100.

(i.e., $\gamma_{\mathrm{TG}} < 1$). The two real decorrelation contributions of γ_{TV} and γ_{TG} result in a shift of the volume decorrelation $\tilde{\gamma}_V$ and the ground point $e^{i\phi_0}$ radially towards the origin as shown in the left of Fig. 1. Note that the presence of γ_{TV} and γ_{TG} move the line-circle intersection point to $e^{i\phi_0}_{\mathrm{pseudo}}$ (blue rectangular point) and induce a ground phase error $\Delta\phi_0$. As a consequence of $\Delta\phi_0$, the phase center of volume decorrelation $\tilde{\gamma}_V$ is overestimated and leads to a height error in the Pol-InSAR inversion.

Fig. 3 shows the ground phase bias and the height bias induced by different levels of temporal decorrelation on the ground layer ($\gamma_{\mathrm{TG}} = 1.0$ to 0.8) as a function of forest height assuming a vertical wavenumber of $\kappa_z = 0.12$ rad/m and the temporal decorrelation in volume of $\gamma_{\mathrm{TV}} = 0.85$. While no ground phase bias appears for $\gamma_{\mathrm{TG}} = 1.0$, the ground phase bias $\Delta\phi_0$ increases as γ_{TG} decreases. Fig. 3(b) shows the height biases corresponding to phase biases shown on the left of Fig. 3. Compared to the impact of temporal volume decorrelation γ_{TV}, a phase bias caused by γ_{TG} introduces a smaller bias in the Pol-InSAR inversion. For example, at a forest height of 20 m, the temporal decorrelation of $\gamma_{\mathrm{TV}} = 0.85$ causes a 3 m (i.e., 15%) height bias, while the temporal decorrelation of $\gamma_{\mathrm{TG}} = 0.85$ bias to the phase error of 8° and the overestimation of about 1 m (i.e., 5%).

In Section V, the quantification of both temporal decorrelations and their impact on forest height inversion for different repeat-pass intervals will be estimated and discussed using airborne SAR data sets.

III. Temporal Decorrelation Campaigns

In order to assess the impact of temporal decorrelation, three important airborne experiments were conducted: BioSAR 2007, TempoSAR 2008, and TempoSAR 2009 campaigns. An overview of forest campaigns including the test sites and the experimental Pol-InSAR data acquired by DLR's E-SAR system [11], as well as ground measurement data is described in the following.

A. BioSAR 2007 Campaign

The BioSAR 2007 campaign was performed over the Remningstorp test site [see Fig. 5(a)] located in southern Sweden [58°28′ north, 13°38′ east). DLR's E-SAR system acquired data over the Remningstorp forest at three different dates: March 9, March 31, and May 2, 2007. During the three acquisitions, L-band Quad-polarimetric data have been acquired in a repeat-pass interferometric mode. The configurations flown and the available Pol-InSAR data sets are summarized in Table I. The experiment allows us to investigate long-term temporal baselines on the order of 32 and 54 days.

The Remningstorp forest is a part of the southern ridge of the boreal forest zone in transition to the temperate forest zone. Topography is fairly flat with some small hills and ranges between 120 m and 145 m amsl. It is a managed forest, divided into several stands with similar forest structure. Prevailing tree species are Norway spruce (*Picea abies*), Scots pine (*Pinus sylvestris*), and birch (*Betula spp.*). Forest height ranges from 5 to 35 m, with biomass levels from 50 to 300 t/ha. For the test site LIDAR data set is available for validation. 78 homogeneous stands have been delineated on the basis of LIDAR measured heights. The H100 [see Fig. 5(c)] was obtained from LIDAR height measurements by taking the maximum value of a 10 m × 10 m window corresponding to 1/100 of a hectare [17], [5]. A mean area of a stand is about 5.9 ha.

B. TempoSAR 2008 and 2009 Campaigns

The repeat-pass E-SAR system acquired fully polarimetric and interferometric SAR data over the Traunstein test site. A total of 13 radar campaigns was carried out over three different periods: five times (June 7– June 20, 2008); five times (April

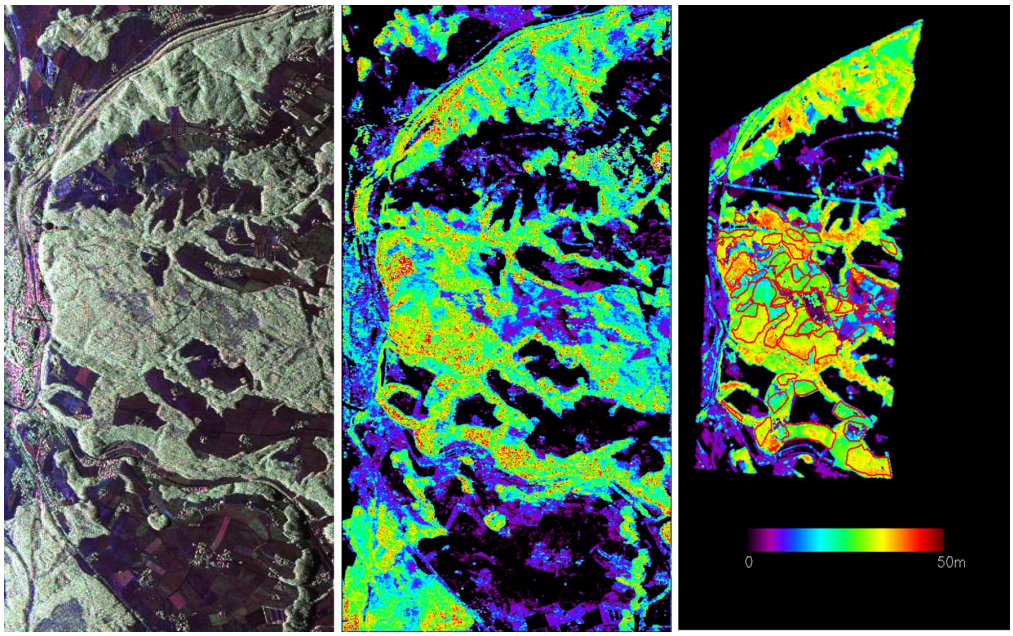

(a) (b) (c)

Fig. 6. Traunstein test site. (a) Radar image of the Pauli components, Red: HH-VV, Green: HV, Blue: HH+VV. (b) Pol-InSAR forest height map Traunstein forest; scaled from 0 m to 50 m. (c) LIDAR derived H100 overlaid with stands.

27–May 12, 2009); and three times (October 28–November 5, 2009). Fig. 6(a) shows the Pauli component images for TempoSAR 2008. From a series of Pol-InSAR acquisitions, it is possible to generate various temporal baselines up to 15 days. Thus, the TempoSAR data form a unique data set to investigate the impact of temporal decorrelation in time on Pol-InSAR inversion performance. The data sets have a sufficient number of tracks in order to perform a multibaseline approach for successful height inversion. The spatial baselines for the TempoSAR campaigns vary basically from -15 m to 15 m, with a spacing of 5 m. The available tracks and temporal/spatial baselines are summarized in Table II.

The Traunstein test site is situated in the southeast of Germany ($47°52'$ north, $12°39'$ east), about 100 km east from DLR Oberpfaffenhofen. Due to the short distance to DLR, it is easy for the E-SAR system to acquire Pol-InSAR data from Oberpfaffenhofen airport. Geologically, the test site is placed in the prealpine-moraine landscape of southern Germany. Topography varies from 600 m to 800 m amsl, with only few steep slopes. The forests are dominated by Norway spruce (*Picea abies*), beech (*Fagus sylvatica*) and fir (*Abies alba*). On a global scale this forest type is part of the temperate forest zone. It is a managed forest composed of even-aged stands which cover forest heights from 10 to 40 m. The mean biomass level is on the order of 210 t/ha while some old forest stands can reach biomass levels up to 500 t/ha. Compared to other managed forests in this ecological zone (mean biomass of 121 t/ha) the biomass values at the Traunstein test site are significantly higher. Validation of TempoSAR campaign results was based on LIDAR measurement data which was acquired on September 28, 2008. LIDAR derived H100 was shown on the right side of Fig. 6.

Meteorological data for the Traunstein test site were obtained by two local weather stations [13]. The Schönharting and Nilling stations are about 24 km northeast and northwest from the Traunstein test site. Meteorological measurements were collected at an hourly rate including air temperature (at a height of 20 and 200 cm), soil temperature (in a depth of 5 and 20 cm), relative humidity, wind velocity and precipitation during the TempoSAR campaigns. For this study, the weather data of wind speed and precipitation were used in order to check temporal changes of forest. Wind speeds from beginning to end (approximately 1 h) of each SAR acquisition are summarized in Table III. There was a relatively strong wind velocity on June 7 and June 20, 2008, with maximum wind speed of 3.2 m/s. While the wind speeds represent the values recorded at exact acquisition time, the total precipitation over the period of 12, 24, 36, and 48 h prior to the beginning of the SAR acquisition were estimated in Table III. The forest conditions on June 12, 2008 and May 12, 2009 could be wet due to significant precipitation before airborne SAR experiment.

IV. Multi-Baseline Pol-InSAR Inversion Results

Forest heights for Remningstorp and Traunstein test sites were estimated by applying an incoherent multibaseline Pol-InSAR inversion approach [12] in order to optimize the performance with respect to the actual κ_z level. For the E-SAR acquisition geometry, the radar incidence angle θ_0 varies form 25° to 55° [11], [5] implying a variation of the vertical wavenumber from near to far range, up to a factor of five. Fig. 4 shows the vertical wavenumbers κ_z of the L-band E-SAR acquisition as a function of nominal spatial baseline, assuming the altitude of E-SAR of 3000 m. The vertical wavenumber range for each spatial baseline for the BioSAR 2007 and TempoSAR campaigns is obtained by using the nominal spatial baseline values given in Tables I and II. An optimum inversion performance across whole range can be achieved by combining the optimum range of the multiple available baselines. Accordingly, regions with low inversion performance caused

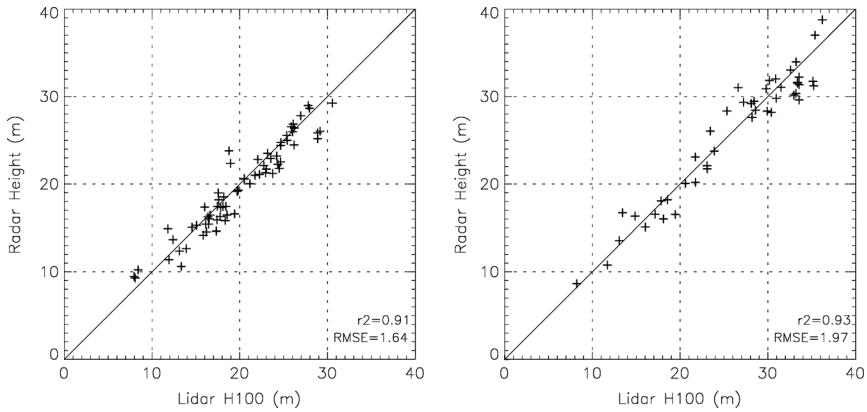

Fig. 7. Validation plots: LIDAR reference height vs. multibaseline Pol-InSAR forest height estimates for Remningstorp (a) and Traunstein (b) test sites.

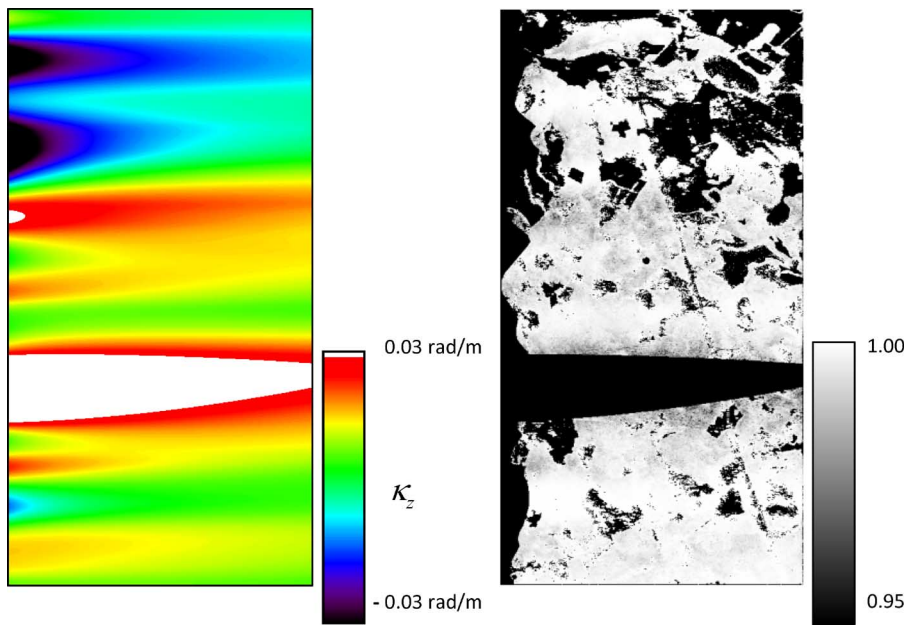

Fig. 8. Left: The vertical wavenumber at zero nominal spatial baseline, scaled from -0.03 to 0.03 rad/m. White and black indicate the vertical wavenumber characterized by larger than 0.03 and smaller than -0.03. Right: The volume decorrelation obtained by the forest height in Fig. 5 and the vertical wavenumber from left image assuming the mean extinction of $\sigma = 0$ dB/m, scaled from 0.95 to 1.00. Areas with the absolute vertical wavenumber larger than 0.03 and nonforest part are masked out (black).

by too high and too low volume sensitivity characterized by a vertical wavenumber larger than 0.15 and smaller than 0.05 are masked out for each individual baseline [5]. Also areas with a coherence level lower than 0.3 are masked out where accurate inversion cannot be expected for a reasonable number of looks. Height estimation accuracy is finally used to select the best estimate from multibaseline inversion results by using a criterion (i.e., the minimum value) defined by the conventional interferometry height accuracy, the amplitude of coherence and the vertical wavenumber [12].

For the Remningstorp test site the multibaseline Pol-InSAR inversion was done on the data set acquired on March 31, 2007 and validated against H100. Fig. 5 in the middle shows the obtained forest height map, scaled from 0 m to 50 m. The validation plot is shown on the left side of Fig. 7 where a correlation coefficient r^2 of 0.91 with a root mean square error (RMSE) of 1.64 m is reached. The correlation between LIDAR and radar height measurements is highly significant within 10%.

For the Traunstein test site forest heights have been estimated for two data sets acquired in 2008 and 2009. Height estimates for the TempoSAR 2008 data set (acquired on June 12, 2008) are validated against LIDAR measurements (i.e., H100) acquired in two months after the SAR campaign. The Pol-InSAR forest height map is shown in the middle of Fig. 6 and on the right the LIDAR measurement used for validation. Both height maps are also scaled from 0 m to 50 m. A comparison of Pol-InSAR forest heights against LIDAR measurements is shown in Fig. 7 (on the right) whereas the correlation coefficient r^2 reaches 0.93 with a RMSE of 1.97 m, covering a height range from 10 to 35 m. At the same time, mean extinction coefficients have been estimated

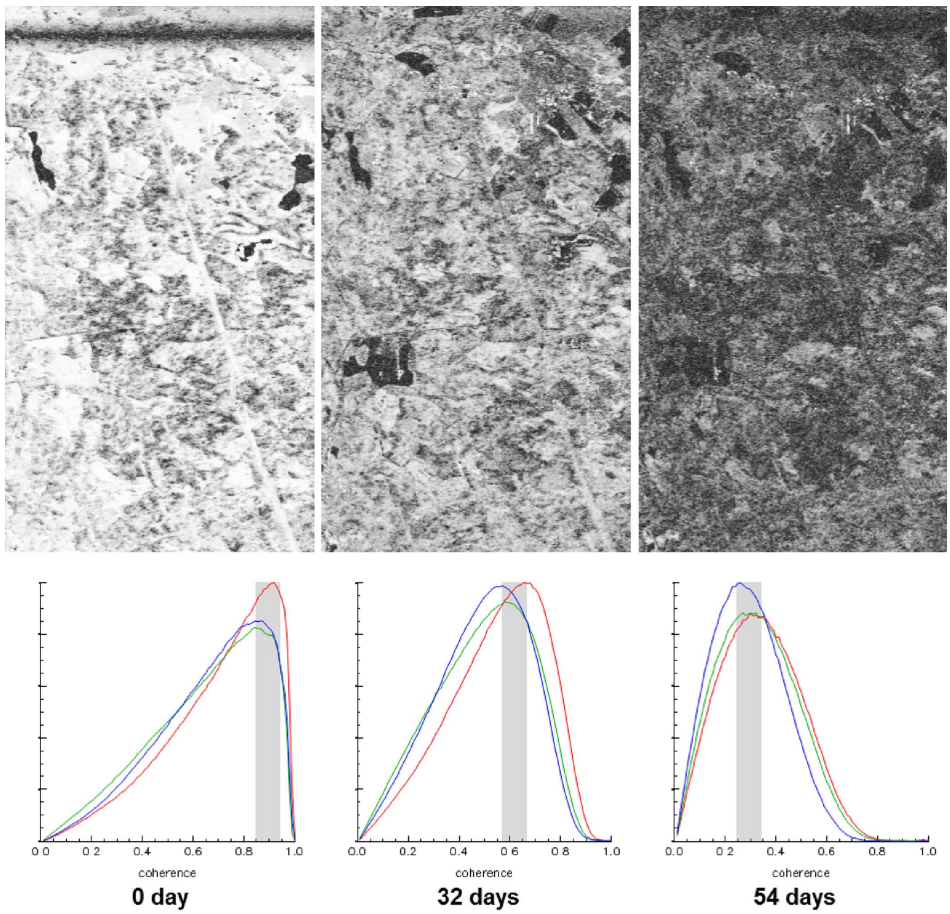

Fig. 9. (Top) HH Coherence maps. Bottom: Coherence histograms (of forested area) for a 0-, 32-, and 54-day temporal baselines in Remningstorp test site in different polarizations; HH (red), HV (green), and VV (blue). Grey columns are of the highest frequency at different polarizations in coherence histograms.

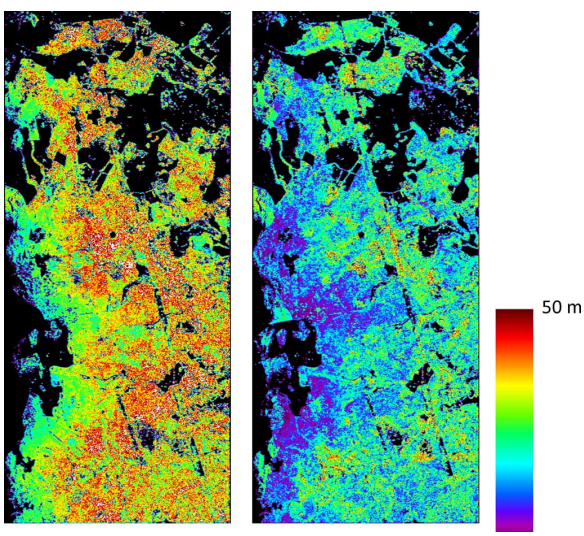

Fig. 10. Forest height map and height bias for Remningstorp forest, scaled 0 m to 50 m. Left: Inversion height map with one month temporal baseline, Right: Different height map between left image and the middle image of Fig. 5.

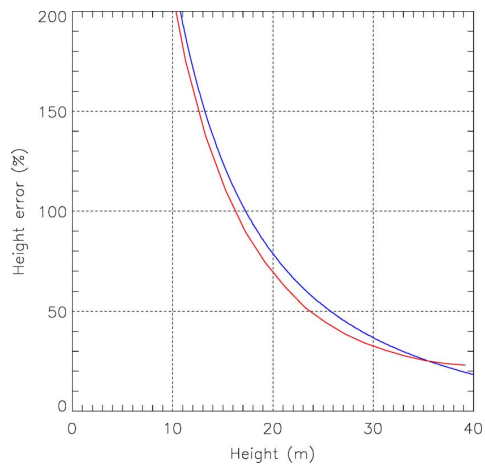

Fig. 11. Height error (%) versus forest height for Remningstorp test site. Red: Estimated height error on 32-day temporal baseline (temporal decorrelation $\approx$ 0.65). Blue: Simulated height bias with temporal decorrelation on the order of 0.65 as Fig. 2(a).

for the Traunstein test site. The extinctions vary mainly from 0 to 0.5 dB/m with a median value of 0.14 dB/m.

The results of both test sites demonstrate that multibaseline Pol-InSAR forest height inversion provides consistent forest height maps for different type of forests in the case of small temporal baselines (on the order of minutes). In the next section, the impact of temporal decorrelation is evaluated from the multibaseline inversion results.

V. Assessment of Temporal Decorrelation

In this section the impact of temporal decorrelation on Pol-InSAR inversion performance is quantitatively estimated and

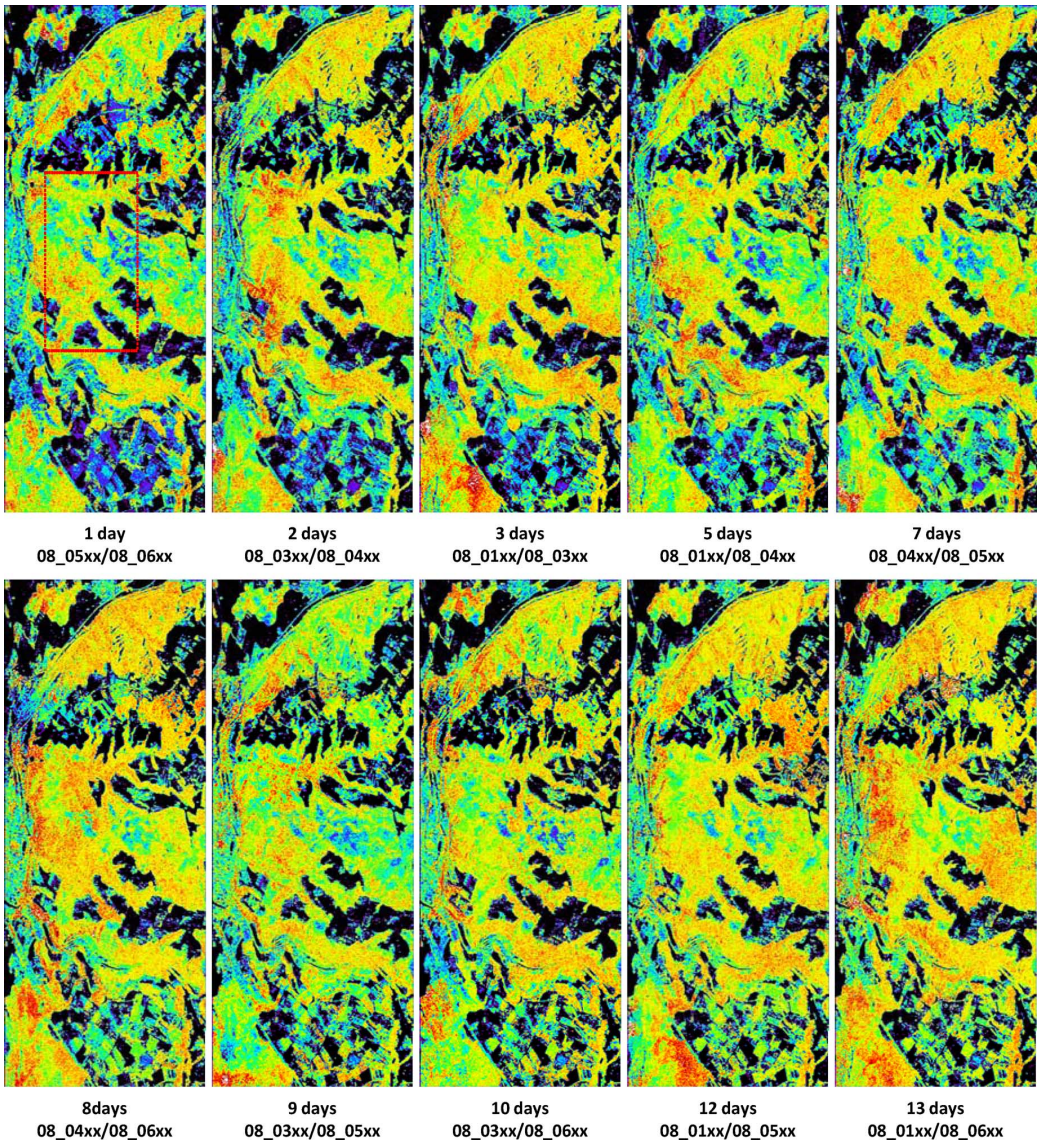

Fig. 12. Forest height maps for TempoSAR 2008 campaign with temporal baselines from 1 to 13 d; scaled 0 m to 50 m; color table in Fig. 5. Forest heights with temporal decorrelation on the order of days are overestimated compared to the multibaseline Pol-InSAR inversion result shown in Fig. 6.

analyzed. Two different approaches are proposed to quantify the temporal decorrelation and its impact on forest parameter inversion. The simplest way to quantify temporal decorrelation at a given temporal baseline is to avoid any (spatial) baseline induced decorrelation contribution (e.g., volume decorrelation) by using a "zero spatial baseline" configuration and compensating for system induced decorrelation effects (e.g., SNR decorrelation). In this special case of a zero spatial baseline interferogram (i.e., $\kappa_z = 0$ and $\tilde{\gamma}_V = 1$), temporal decorrelation can be directly estimated from (7) [5], [9], [15]. The second approach is based on the estimation of the height error induced by temporal decorrelation at nonzero multispatial baselines (i.e., $\kappa_z \neq 0$ and $\tilde{\gamma}_V < 1$). It has the advantage of establishing a direct relationship between temporal decorrelation level and the height error. And, it also allows at the same time the estimation of the individual temporal decorrelation levels of γ_{TV} and γ_{TG}. For this, it is necessary to have information on forest height and mean extinction. In this case, both parameters are obtained by means of multibaseline Pol-InSAR inversion [12] using only small temporal baselines assumed free of temporal decorrelation as shown in Section IV. The results are then used to assess the height error induced by the individual temporal baselines and to estimate temporal decorrelation levels of γ_{TV} and γ_{TG} as a function of temporal baseline.

As summarized in Tables I and II, the BioSAR 2007 and TempoSAR campaigns have a variety of temporal baselines varying from minutes, days, and weeks, up to 54 days. In this study, temporal baselines are categorized into three time scale classes; long-term (weeks to months), mid-term (day to weeks) and short-term (minutes to hours) temporal baselines. The results about temporal decorrelation at different time scales are discussed in the next sections.

A. Long-Term Temporal Baseline: Weeks to Months

To investigate the temporal decorrelation at long-term temporal baselines, the data sets of the BioSAR 2007 campaign were selected where three different acquisitions provide long-term temporal baselines on the order of about one and two months.

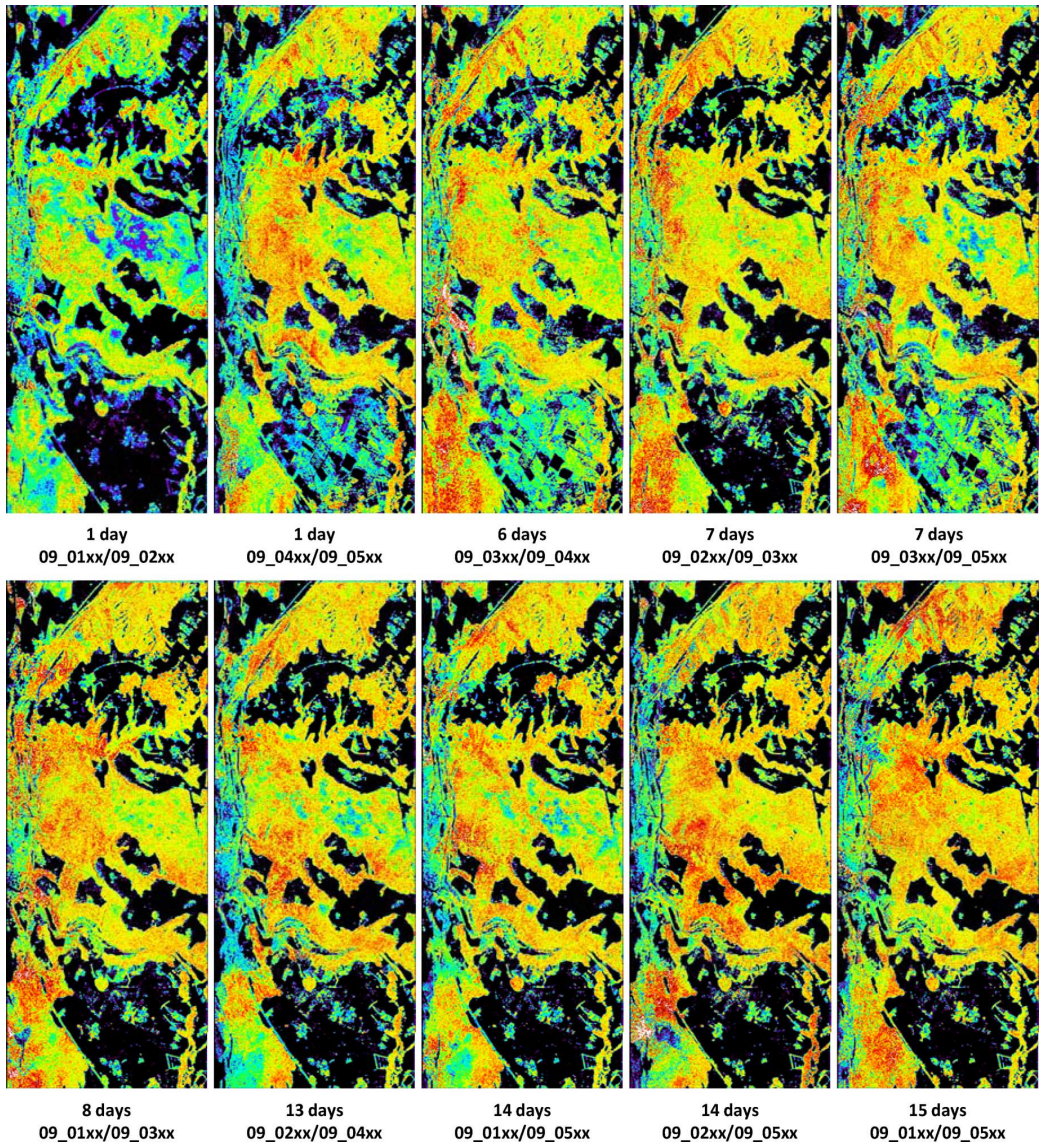

Fig. 13. Forest height maps for TempoSAR 2009 campaign with temporal baselines from 1 to 15 d; scaled 0 to 50 m; color table in Fig. 5. Forest heights are with temporal decorrelation on the order of days are overestimated compared to the multibaseline Pol-InSAR inversion result shown in Fig. 6.

As mentioned, the straightforward way to quantify temporal decorrelation is to use a zero spatial baseline configuration. Acquisitions at zero spatial baseline were used by selecting the forested areas within the scene where the spatial baseline is if not zero at least sufficiently small (i.e., $|\kappa_z| < 0.03$). Fig. 8(a) shows an image of κ_z at zero nominal spatial baseline, scaled from -0.03 to 0.03 rad/m. Regions with a vertical wavenumber larger than 0.03 and smaller than -0.03 are not considered and masked out. The volume decorrelation of the remaining areas is simulated by the forest height information available [see Fig. 5(b)] assuming a mean extinction $\sigma = 0$ dB/m. Fig. 8(b) shows the volume decorrelation of the relevant areas (i.e., $|\kappa_z| < 0.03$), scaled from 0.95 to 1.00. The volume decorrelations are nearly unity with an average level of 0.999. Accordingly, the approach eliminates all baseline induced decorrelation sources so that the loss in coherence is only due to temporal decorrelation.

Temporal decorrelation maps (HH polarization) for a zero spatial baseline are shown in Fig. 9. At the bottom of Fig. 9, the coherence histograms for HH (red), HV (green), and VV (blue) polarizations over the forested areas in the scene are shown for three different temporal baselines. As expected, the impact of temporal decorrelation increases with increasing temporal baseline in all polarizations. Even for the 0-day case acquired with a temporal baseline shorter than 1 h, the loss in coherence indicates the presence of temporal decorrelation: The temporal decorrelation levels are on the order of 0.65 for 32 days and 0.30 for the 54 days. The coherence level for 54 days was already so low that almost the entire image is covered by the nonvalid coherence mask.

Pol-InSAR inversion with a temporal baseline of 32 days was performed using the nonzero spatial baselines. The inversion result and height bias (overestimation) are shown in Fig. 10. In this case, the obtained forest heights are fairly overestimated all over the image [compared to Fig. 5(a)] due to the temporal decorrelation. The height error introduced by temporal decorrelation can be estimated by

$$\text{Height error}(\%) = \frac{\Delta h_v}{h_v} \times 100 \tag{8}$$

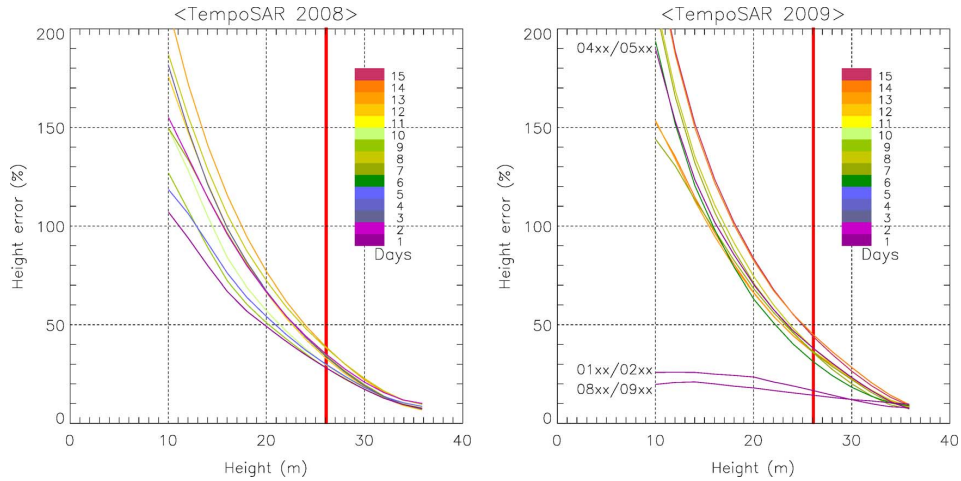

Fig. 14. Height error (%) versus forest height for temporal baselines from 1 to 15 d; Color-coding represents the temporal baselines. (a) Height error for TempoSAR 2008. (b) Height error for TempoSAR 2009. Red line represents the mean forest height of 26 m in the rectangle in Fig. 12.

where h_v is the forest height from multibaseline inversion [see Fig. 5(b)] and Δh_v the height bias (overestimation) introduced by the uncompensated temporal decorrelation [see Fig. 10(right)]. The estimated height error for the 32-day temporal baseline is plotted in Fig. 11. The red line represents the estimated height error for a 32-day temporal baseline while the blue line shows the simulated height bias (as shown in Fig. 2(a) in Section II-A) obtained by inverting (7) for $\gamma_{\mathrm{TV}} = 0.65$ corresponding to the mean temporal decorrelation as obtained from the histograms for the 32-day temporal baseline in Fig. 9. There is a clear tendency of increasing height error with decreasing forest height in accordance with the simulation shown in Fig. 2. Lower forest stands are much more affected by uncompensated volumetric decorrelation contributions than higher forest stands. The level of temporal decorrelation with one month repeat-pass time interval still allows applying Pol-InSAR height inversion, but it introduces a large height bias, especially in low forest stands.

B. Mid-Term Temporal Baseline: Day to Weeks

Temporal decorrelation at mid-term temporal baselines (on the order of days up to weeks) is now investigated and quantified. During the TempoSAR 2008 and 2009 campaigns, Pol-InSAR data were acquired 13 times distributed over a period of 15 days. This allows to form interferograms with temporal baselines ranging from 1 up to 15 days (see Table II).

Forest height maps have been estimated by using multibaseline Pol-InSAR inversion [12]; the inversion results are shown in Figs. 12 and 13. As expected, forest heights were clearly overestimated when compared to the forest height shown in the middle of Fig. 6. In general, overestimation increases with increasing temporal baseline. The height errors for TempoSAR 2008 and 2009 are estimated using (8) and are shown in Fig. 14. The color-coding indicates the temporal baselines ranging from 1 to 15 days. The inversion error increases with decreasing forest height and increasing temporal baseline, similar to the results obtained in the previous section. Note that the height errors obtained from the different 1-day temporal baselines can be fairly different as shown in Fig. 14(b). The acquisition pairs (09_01xx/09_02xx and 09_08xx/09_09xx) for TempoSAR 2009 [see Fig. 14(b)] lead to 10–25% height error depending on forest heights, while the pair (09_04xx/09_05xx) acquired also with 1-day temporal decorrelation leads to much larger height errors of 20–200%, due to the rather unstable weather conditions (e.g., wind and/or precipitation) during the acquisitions. In the following, both temporal decorrelations of γ_{TV} and γ_{TG} will be estimated by using nonzero multibaseline Pol-InSAR data and be discussed with meteorological information.

1) Temporal Decorrelation on the Ground Layer γ_{TG}: As discussed in Section II-B, the temporal decorrelation on the ground γ_{TG} biases the estimate of the ground phase and leads to an overestimation of forest height. It is hard to estimate the impact of γ_{TG} by means of a "zero spatial baseline" because of no phase difference of interferograms at different polarizations. Using the reference forest height h_v and a mean extinction σ (obtained in Section IV) from multibaseline Pol-InSAR inversion, the volume decorrelation $\tilde{\gamma}_V(h_v, \sigma, \kappa_z, \theta_0)$ is calculated from (2) (by setting $\phi_0 = 0$) and plotted [corresponding to the green circle in Fig. 1(b)]. For any Pol-InSAR acquisition, the associated volume-only coherence $\tilde{\gamma}(\vec{w}_{m=0})$ and the biased ground point $e^{i\phi_0}_{\mathrm{pseudo}}$ are obtained. The ground phase error $\Delta\phi_0$ is estimated by the phase difference between $\tilde{\gamma}_V(h_v, \sigma, \kappa_z, \theta_0)$ and $\tilde{\gamma}(\vec{w}_{m=0})e^{-i\phi_0}_{\mathrm{pseudo}}$. Temporal decorrelation on the ground layer γ_{TG} is obtained by the x-intercept of the line defined by $\tilde{\gamma}(\vec{w}_{m=0})e^{-i\phi_0}_{\mathrm{pseudo}}e^{-i\Delta\phi_0}$ and $e^{-i\Delta\phi_0}$ [red circle and blue rectangular points in Fig. 1(b)]

$$\gamma_{\mathrm{TG}} = \mathrm{Re}\left(\tilde{\gamma}(\vec{w}_{m=0})e^{-i\phi_0}_{\mathrm{pseudo}}e^{-i\Delta\phi_0}\right) - \mathrm{Im}\left(\tilde{\gamma}(\vec{w}_{m=0})e^{-i\phi_0}_{\mathrm{pseudo}}e^{-i\Delta\phi_0}\right) \Big/ \tan\theta_{\mathrm{gr}} \quad (9)$$

where $\tan\theta_{\mathrm{gr}}$ represents the gradient of the line.

The quantitative estimation of γ_{TG} for the Traunstein test site (corresponding to the red rectangle in Fig. 12) is performed using Pol-InSAR data sets acquired during the TempoSAR 2008 and 2009 with temporal baselines up to 15 days. Fig. 17 shows the mean estimated temporal decorrelation γ_{TG} plotted against all possible TempoSAR 2008 and 2009 temporal

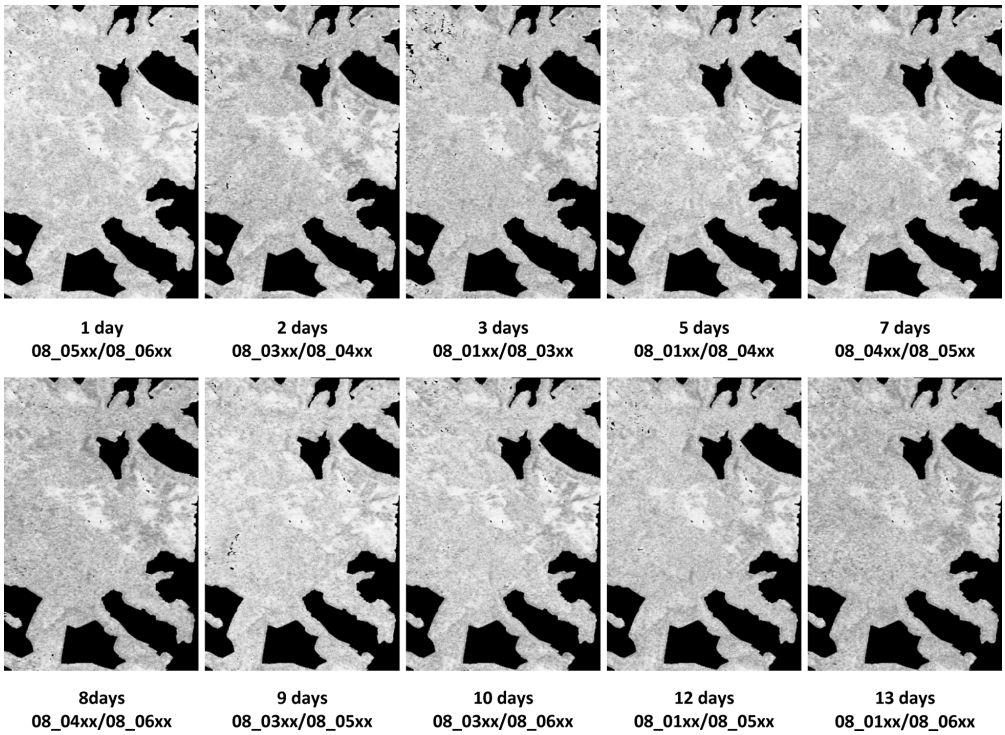

Fig. 15. Temporal decorrelation on the ground layer γ_{TG} for TempoSAR 2008 campaign from 1- to 13-day temporal baseline, scaled from 0 (black) to 1 (white); Section of Traunstein test site—red dotted rectangle in Fig. 12.

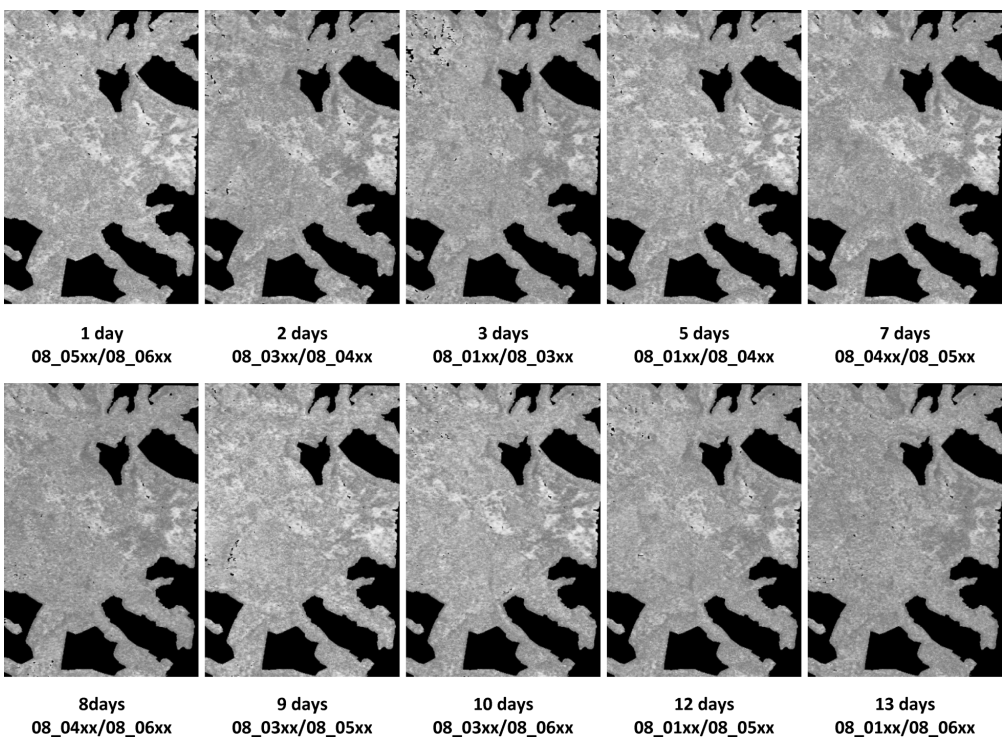

Fig. 16. Temporal decorrelation in volume γ_{TV} for TempoSAR 2008 campaign from 1- to 13-day temporal baseline, scaled from 0 (black) to 1 (white); Section of Traunstein test site—red dotted rectangle in Fig. 12.

baselines. The asterisks represent the averaged temporal decorrelations γ_{TG} for TempoSAR 2008 and the rectangles the ones for TempoSAR 2009. Temporal decorrelation γ_{TG} decreases from 0.91 to 0.68 with increasing temporal baseline. However, comparing on the three 1-day baseline results of TempoSAR 2009 (Sence_ID: 09_01xx/09_02xx, 09_04xx/09_05xx, and 09_08xx/09_09xx), the level of γ_{TG} for the 09_04xx and 09_05xx pair is much lower ($\gamma_{\mathrm{TG}} = 0.76$). This can be due to a change in the dielectric properties of the ground induced, for example, by precipitation. Indeed, during the TempoSAR

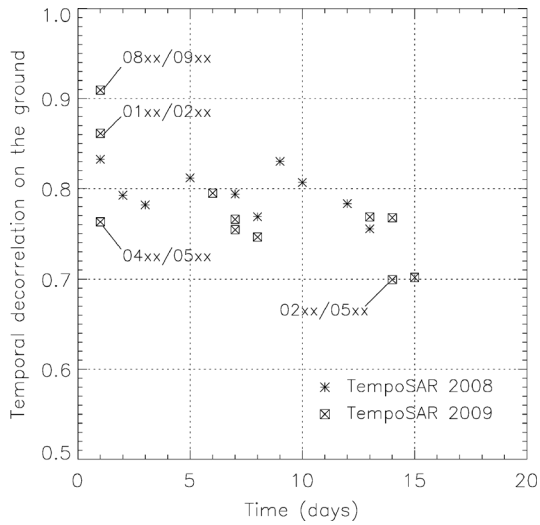

Fig. 17. Mean temporal decorrelations γ_{TG} on the ground layer against temporal baseline up to 15 days for TempoSAR 2008 and 2009; Section of Traunstein test site—red dotted rectangle in Fig. 12. Asterisk point: TempoSAR 2008 and rectangular point: TempoSAR 2009.

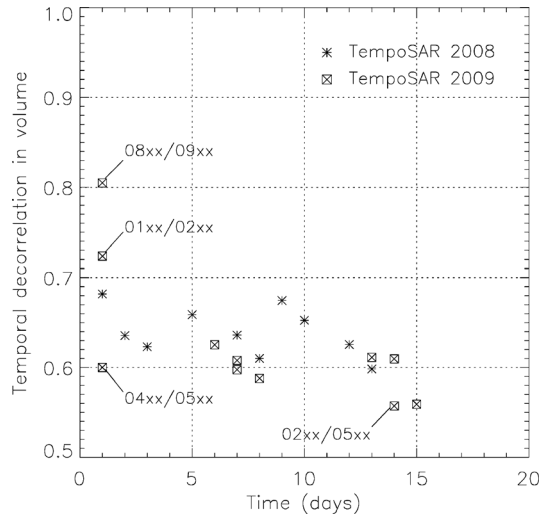

Fig. 18. Mean temporal decorrelations γ_{TV} in volume against temporal baseline up to 15 days for TempoSAR 2008 and 2009; Section of Traunstein test site—red dotted rectangle in Fig. 12. Asterisk point: TempoSAR 2008 and rectangular point: TempoSAR 2009.

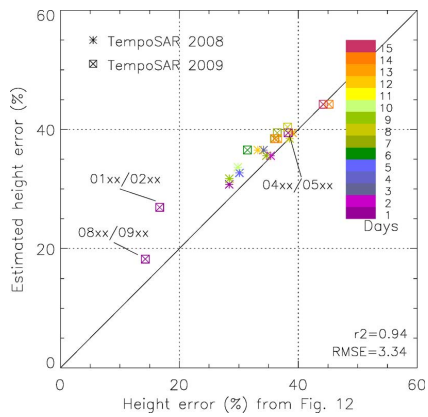

Fig. 19. Validation of the estimated height error. X-axis: Height error on a mean forest height of 26 m from Fig. 14. Y-axis: Height error estimated by inverting (6) with temporal decorrelation γ_{TG} on the ground layer from Fig. 17 and temporal decorrelation γ_{TV} in volume from Fig. 18. Color-coding represents the temporal baselines. Asterisk point: TempoSAR 2008 and rectangular point: TempoSAR 2009.

2009 campaign, there was a 4.1 mm rain event just before the 09_05xx acquisition on May 12, 2009 (see Table III) changing probably the dielectric properties of the ground layer. Therefore, γ_{TG} values estimated by the interferometric pairs including track 09_05xx (i.e., 09_04xx/09_05xx, and 09_02xx/09_05xx) at temporal baselines of 1 and 14 days show much lower coherence levels than those without the 09_05xx acquisition at same temporal baselines (i.e., 09_01xx/09_02xx, 09_08xx/09_09xx, and 09_01xx/09_04xx) as shown in Fig. 17. This is a significant result indicating that precipitation is critical affecting the temporal stability of the ground.

2) Temporal Decorrelation in Volume Layer γ_{TV}: Temporal decorrelation γ_{TV} for temporal baselines on the order of days depends on short term changes of the dielectric properties of the volume (and the ground) and on the rather stochastic (wind-induced) motion. As mentioned in Section II-A, temporal decorrelation of the volume γ_{TV} reduces the amplitude of the volume decorrelation $\tilde{\gamma}_V$ in (6). Accordingly, γ_{TV} can be estimated from the amplitude ratio of $\tilde{\gamma}_V(h_v, \sigma, \kappa_z, \theta_0)$ and $\tilde{\gamma}(\vec{w}_{m=0}) e^{-i\phi_0}_{\mathrm{pseudo}} e^{-i\Delta\phi_0}$ [corresponding to the green and red circle points in Fig. 1(b)].

The estimated temporal decorrelation coefficients γ_{TV} for all temporal baselines in TempoSAR 2008 are shown in Fig. 16 making two main points obvious: The first one is that temporal decorrelation γ_{TV} tends to decrease with increasing temporal baseline, but faster than γ_{TG} as shown in Fig. 15. The second point is that the decrease of γ_{TV} is not necessarily monotonic in time and space. It depends not only on the random behavior of wind-induced motion but also on different levels of water content (e.g., dielectric constant) in the volume due to precipitation and vaporization. Fig. 18 shows the averaged temporal decorrelation γ_{TV} for all temporal baselines up to 15 days. Temporal decorrelation γ_{TV} tends to decrease with increasing temporal baseline similar to temporal decorrelation γ_{TG}. For temporal baselines of a few days a rapid drop of coherence level going along with a large variation of coherence levels can be observed. The lower values of γ_{TV} at temporal baselines of 1 day (09_04xx/09_05xx) and 14 days (09_02xx/09_05xx) result from the changes of dielectric properties of the scatterers in the volume layer due to the precipitation event on May 12, 2009 (see Table III).

For the validation of the obtained results, a simulated height error for the estimated γ_{TG} and γ_{TV} obtained from each temporal baseline for a κ_z of 0.1 rad/m and a forest height of 26 m (mean forest height value within red rectangle in Fig. 12) is calculated and plotted against the real height error on height of 26 m in Fig. 14. Fig. 14 shows this plot: on the x-axis is the real height error while on the y-axis the simulated height error obtained by using the estimated temporal decorrelations (γ_{TV} and γ_{TG}) from Figs. 17 and 18 are given. Asterisks and rectangles indicate the height errors (%) for TempoSAR 2008 and 2009 and the color-coding indicates the temporal baseline, from 1 to 15 days. For example, a height error of 18% is estimated corresponding to $\gamma_{\mathrm{TV}} = 0.80$ and $\gamma_{\mathrm{TG}} = 0.91$ at a temporal baseline on the order of 1 day (09_08xx/09_09xx),

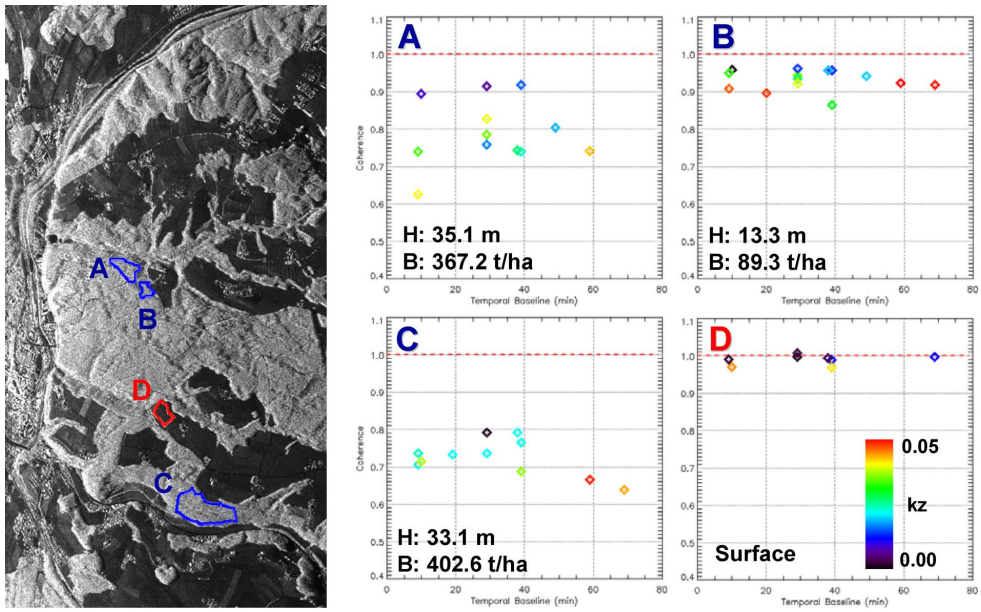

Fig. 20. (Left) Amplitude image of the Traunstein test site in HH polarization with positions of the investigated forest stands. (A), (C) High forest (blue). (B): Low forest (blue). (D) Field (red). (Right) Coherence versus temporal baseline (in minutes) plots for each of the selected areas A, B, C, and D; Color of point represents vertical wavenumber κ_z (see legend bottom right).

while a 14% height error is obtained for a height of 26 m in Fig. 14(b). However, temporal decorrelations on the order of $\gamma_{\mathrm{TV}} = 0.60$ and $\gamma_{\mathrm{TG}} = 0.76$ at another 1-day temporal baseline (09_04xx/09_05xx) result in stronger height errors of 39% due to the precipitation between two acquisitions. In this case, the value in Fig. 14 is quite similar indicating a height error of 38%. The comparison of temporal decorrelations and height errors shows a surprisingly high r^2 of 0.94 with an RMSE of 3.34%. This means that the modeling of γ_{TV} and γ_{TG} is in accordance with the experimental results achieved.

C. Short-Term Temporal Baseline: Minutes to Hours

Pol-InSAR acquisitions with DLR's E-SAR system operating in a repeat-pass mode can be realized with minimum temporal baselines on the order of 10–15 min depending on the dimension of the scene acquired. In the frame of the TempoSAR 2008 campaign, temporal baselines vary usually from 10 min up to 1 h with a maximum of 74 min. In this case, temporal baselines are short enough to ignore the temporal decorrelation on the ground layer (i.e., $\gamma_{\mathrm{TG}} = 1$).

In the following the behavior of temporal decorrelation in the volume γ_{TV} for short-term temporal baselines is investigated by using (7). In order to reduce volume decorrelation ($\tilde{\gamma}_V \cong 1$) and isolate temporal decorrelation effects, only interferometric pairs with small vertical wavenumber values ($\kappa_z < 0.05$) have been selected.

To investigate the behavior of coherence for short-term temporal baselines and very small spatial baselines, three forested stands and one bare field were selected. The forest stands were selected using the ground measurements in order to get uniform stands in terms of forest height and biomass [14]. Fig. 20(left) shows the HH amplitude image of the Traunstein test site indicating the four selected areas. Stand A and C are characterized by higher forest height and biomass (A: 35.1 m, 367.2 t/ha, and C: 33.1 m, 402.6 t/ha), while the height of stand B is rather low (B: 13.3 m, 89.3 t/ha). The bare field D is used as a reference.

The plots in Fig. 20 on the right show the variation of coherence over the selected areas as a function of vertical wavenumber (color) and temporal baseline. The color-coding indicates the average vertical wavenumber κ_z per stand and the x-axis shows the temporal baseline. Plot D for the bare field shows a high coherence level for all spatial and temporal baselines indicating a high temporal stability at least for the observed period of 74 min. In contrast, volume scatterers decorrelate at short-term temporal baseline (see Fig. 20 plots A, B, and C), where decorrelation is caused by wind-induced motion. Especially the changes in coherence at the taller forests stands (plot A and C) are significant. To exclude any impact of remaining volume decorrelation on the interpretation of the results, only the behavior of acquisitions with very similar vertical wavenumber is discussed. Due to the variation of κ_z within each interferogram not all available interferograms can be used for all stands. In plot A, a strong variation of coherence, independent of temporal baseline, can be observed. Coherences in plot B (low forest case) have less variation than those in plot A. Similar vertical wavenumbers κ_z (red points) maintain the coherence level up to 60 min. Plot C shows coherences with similar spatial baseline (sky blue points) with a maximum coherence after 40-min temporal baseline. Comparing the observations from plot A, B and C, wind-induced temporal decorrelation effects over forested regions seem to be of random nature.

Fig. 21 shows the impact of wind-induced temporal decorrelation on forest height estimates. Multibaseline Pol-InSAR inversion results from five acquisition dates in 2008 (see Tables II and III) are connected to wind speed measurements. Wind speed measurements were taken from two meteorological stations (Nilling and Schönharting) close to the Traunstein test site and are shown in Fig. 21(bottom) and Table III. Height

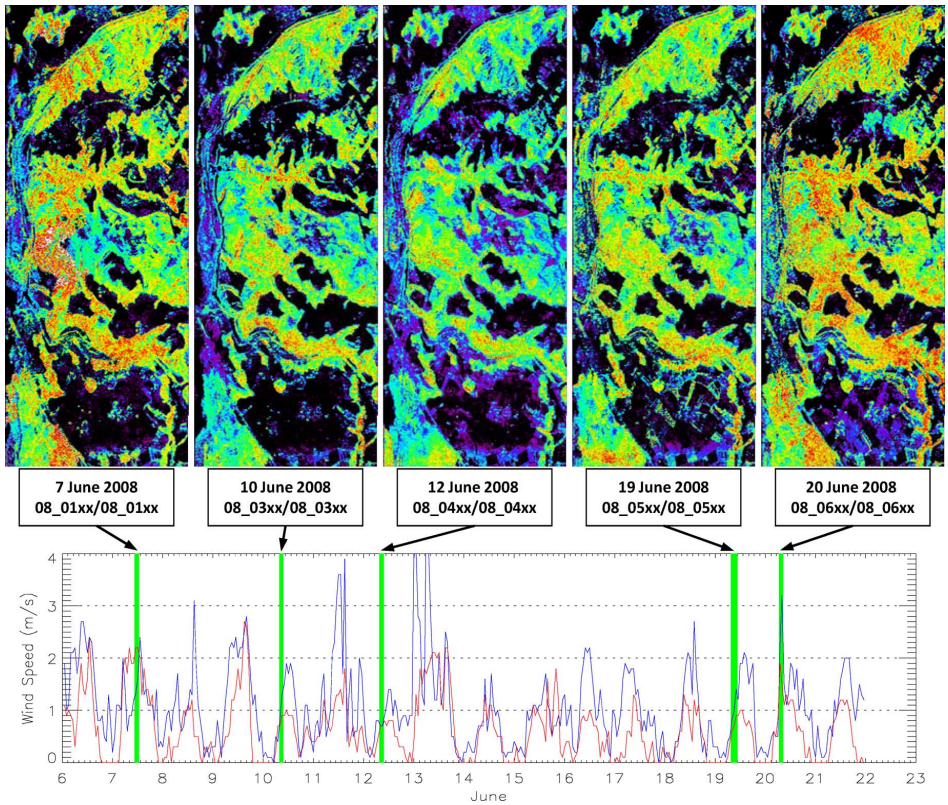

Fig. 21. Impact of wind-induce temporal decorrelation on forest height estimates. The stronger wind causes the more bias in Pol-InSAR inversion. (Top) Forest height maps from five different acquisition dates in TempoSAR 2008, scaled 0 to 50 m. (First row) Acquisition date. (Second row) Scene_ID in Table III. (Bottom) Wind speed during TempoSAR 2008 campaign. Red: Schönharting station, Blue: Nilling station, and Green: Acquisition time.

estimates from acquisitions with wind speeds of up to 2 m/s are significantly higher (08_01xx and 08_06xx in Fig. 21) than height estimates where wind speed was below 1 m/s (08_03xx, 08_04xx, and 08_05xx in Fig. 21). Fig. 21 shows the impact of weather (wind) condition on forest height estimates by means of repeat-pass SAR systems. Reliable heights were obtained only for acquisitions on June 10 and 12, 2008, with less wind (mean wind speed less than 1 m/s).

VI. Discussion and Conclusion

In order to successfully perform Pol-InSAR forest structure parameter estimation, the characterization of temporal decorrelation over forest is essential for the design of airborne SAR campaigns and much more for the implementation of future spaceborne missions operating in a repeat-pass mode. In this paper, the impact of temporal decorrelation on Pol-InSAR forest height inversion performance has been addressed and temporal decorrelation as a function of temporal baseline has been investigated for a wide range of temporal baselines. Different temporal decorrelations for the volume and the ground layer have been incorporated into the two-layer (volume/ground) RVoG scattering model, in order to account for the different decorrelation behaviors. Both decorrelations bias the Pol-InSAR inversion results, but in a different way: While volume temporal decorrelation γ_{TV} reduces the amplitude of the volume decorrelation contribution, temporal decorrelation γ_{TG} on the ground layer introduces a ground phase error. Both effects lead to an overestimation of forest heights. This phase error is the key idea for estimating the temporal decorrelation γ_{TG} of the ground layer.

The Pol-InSAR data sets acquired in BioSAR 2007 and TempoSAR 2008 and 2009 campaigns were used for the quantitative assessment of temporal decorrelation for temporal baselines ranging from 10 min up to 54 days. The impact of temporal decorrelation has been separately assessed on three different levels of temporal baseline: long-term (months—weeks), mid-term (weeks–day) and short-term (hour–minutes) temporal baselines.

The level of temporal decorrelation (0.3) with 54-day repeat-pass time of BioSAR 2007 data makes Pol-InSAR applications not possible due to by the nonvalid coherence mask. In the case of 32-day temporal baseline, the level of coherences in forest was higher than 0.3 so that Pol-InSAR inversion was still able to be applied but forest height was quite overestimated due to the uncompensated temporal decorrelation. The decorrelation level is sufficient to cause height error on the order of 20–200% depending on forest heights and spatial baseline setup.

Using multibaseline Pol-InSAR data sets acquired during the TempoSAR campaigns with temporal baselines on the order of 1 day, up to 2 weeks (15 days), it is possible to estimate the different temporal decorrelation contribution γ_{TV} and γ_{TG}. Both γ_{TV} and γ_{TG} tend to decrease with increasing temporal baseline. However, the decorrelation processes within volume layer occur much faster than on the ground. The reason for this is that the scatterers in the canopy are less stable than ones on the ground. On the other hand, the temporal decorrelations of γ_{TV} and γ_{TG} are not only dependent on the wind-induced movement but also rely strongly on the rain-induced dielectric changes in volume and on the ground at temporal baselines on the order of days or

longer. Finally, the estimated temporal decorrelations γ_{TV} and γ_{TG} were converted to height errors and validated against the directly estimated height error from Pol-InSAR inversion. The obtained results are highly correlated on the order of 0.94 with an RMSE of 3.34%. This is a strong indication for the validity of the model used as well as for a successful estimation of γ_{TV} and γ_{TG} at temporal baselines on the order of days.

The behavior of temporal decorrelation on the order of minutes was strongly related to wind-induced movement and showed a rather random nature in forest due to the variability of wind pattern in space and time. For this time scale, changes in the electric properties of the canopy and the ground layer can be ignored. The wind speed of 2 m/s already reduces the performance of Pol-InSAR inversion dramatically by biasing the volume decorrelation over the test site. Therefore, the wind speed during the acquisition is the most critical parameter for the amount of temporal decorrelation for short repeat-pass time.

REFERENCES

[1] S. R. Cloude and K. P. Papathanassiou, "Polarimetric SAR interferometry," *IEEE Trans. Geosci. Remote Sens.*, vol. 36, no. 5, pp. 1551–1565, Sep. 1998.

[2] K. P. Papathanassiou and S. R. Cloude, "Single baseline polarimetric SAR interferometry," *IEEE Trans. Geosci. Remote Sens.*, vol. 39, no. 11, pp. 2352–2363, Nov. 2001.

[3] R. N. Treuhaft, S. N. Madsen, M. Moghaddam, and J. J. van Zyl, "Vegetation characteristics and underlying topography from interferometric radar," *Radio Sci.*, vol. 31, no. 6, pp. 1449–1495, 1996.

[4] S. R. Cloude and K. P. Papathanassiou, "Three-stage inversion process for polarimetric SAR interferometry," in *IEE Proc.—Radar Sonar Nav.*, Jun. 2003, vol. 150, no. 3, pp. 125–134.

[5] I. Hajnsek, F. Kugler, S.-K. Lee, and K. P. Papathanassiou, "Tropical-forest-parameter estimation by means of Pol-InSAR: The INDREX II campaign," *IEEE Trans. Geosci. Remote Sens.*, vol. 47, no. 2, pp. 481–493, Feb. 2009.

[6] R. Bamler and P. Hartl, "Synthetic aperture radar interferometry," *Inversion Probl.*, vol. 14, no. 4, pp. R1–R54, Aug. 1998.

[7] H. Zebker and J. Villasenor, "Decorrelation in interferometric radar echoes," *IEEE Trans. Geosci. Remote Sens.*, vol. 45, no. 10, pp. 950–959, Sep. 1992.

[8] F. Rocca, "Modeling interferogram stacks," *IEEE Trans. Geosci. Remote Sens.*, vol. 30, no. 5, pp. 3289–3299, Oct. 2007.

[9] K. P. Papathanassiou and S. R. Cloude, "The effect of temporal decorrelation on the inversion of forest parameters from Pol-InSAR data," presented at the IEEE IGARSS, Toulouse, France, 2003.

[10] I. Hajnsek, K. P. Papathanassiou, and S. R. Cloude, "Removal of additive noise in polarimetric eigenvalue processing," presented at the IEEE IGARSS, Sydney, Australia, 2001.

[11] R. Horn, "The DLR airborne SAR project E-SAR," presented at the IEEE IGRASS, Lincoln, NE, USA, May 1996.

[12] S. K. Lee, F. Kugler, K. P. Papathanassiou, and I. Hajnsek, "Multi-baseline polarimetric SAR interferometry forest height inversion approaches," presented at the POLinSAR, ESA-ESRIN, Frascati, Italy, Jan. 2011.

[13] Agrarmeteorologische Stationen [Online]. Available: http://www.lfl.bayern.de/agm/start.php

[14] T. Mette, "Forest biomass estimation from polarimetric and interferometry," Ph.D. dissertation, Technischen Universtät München, München, Germany, 2007.

[15] M. Lavalle, M. Simard, and S. Hensly, "A temporal decorrelation model for polarimetric radar interferometers," *IEEE Trans. Geosci. Remote Sens.*, vol. 50, no. 7, pp. 2880–2888, Jul. 2012.

[16] M. Neumann, L. Ferro-Famil, and A. Reigber, "Estimation of forest structure, ground, and canopy layer characteristics from multibaseline polarimetric interferometric SAR data," *IEEE Trans. Geosci. Remote Sens.*, vol. 48, no. 3, pp. 1086–1104, Mar. 2010.

[17] H. Kramer and A. Akca, *Leitfaden zur Waldmesslehre*. Frankfurt: Sauerländer, 1995, p. 145.

Seung-Kuk Lee received the B.S. and M.S. degrees from the Yonsei University, Yonsei, Korea, in 2000 and 2005, respectively, and the Dr. degree from ETH Zurich, Zurich, Switzerland, in 2012.

In 2007, he started working at German Aerospace Center (DLR), Wessling, Germany, as a Ph.D. student. He is currently working as a Research Scientist in Polarimetric SAR Interferometry research group at DLR. His main interests are 3-D forest parameter estimation using Pol-InSAR techniques, and quantification of temporal decorrelation effects for Pol-InSAR forest applications.

Florian Kugler was born in Bavaria, Germany, in 1974. He received a Diploma degree (Dipl.Ing.silv.) in forestry science from the Technische Universität München, Freising, Germany, in 2004. Since October 2004, he has been working toward the Ph.D. degree at the German Aerospace Center (DLR).

Since October 2008, he has been a Research Scientist at DLR. His research focuses on remote sensing on forests using polarimetric SAR interferometry.

Konstantinos Panagiotis Papathanassiou (M'02–SM'03) received the Dipl.Ing. degree (Hons.) and the Ph.D. degree (Hons.) from the Technical University of Graz, Austria, in 1994 and 1999, respectively.

From 1992 to 1994, he was with the Institute for Digital Image Processing (DIBAG) of Joanneum Research, Graz, Austria. Between 1995 and 1999, he worked at the Microwaves and Radar Institute (HR) of the German Aerospace Center (DLR), Oberpfaffenhofen, Germany. From 1999 to 2000, he was an EU Postdoctoral Fellow with Applied Electromagnetics (AEL) in St. Andrews, Scotland. Since October 2000, he has been with the Microwaves and Radar Institute (HR) of the German Aerospace Center (DLR), where he is a Senior Scientist leading the Information Retrieval research group. He has more than 100 publications in international journals, conferences and workshops. His main research interests are in polarimetric and interferometric processing and calibration techniques, polarimetric SAR interferometry, and the quantitative parameter estimation from SAR data, as well as in SAR mission design and SAR mission performance analysis.

Dr. Papthanassion was the recipient of the IEEE GRSS IGARSS Symposium Prize Paper Award in 1998, the Best Paper Award of the European SAR Conference (EUSAR) in 2002, and the DLR Science Award in 2002. In 2011, he was awarded with the DLR's Senior Scientist Award.

Irena Hajnsek (A'01–M'06–SM'09) received the Dipl. degree (Hons.) from the Free University of Berlin, Berlin, Germany, in 1996, and the Ph.D. degree (Hons.) from the Friedrich Schiller University of Jena, Jena, Germany, in 2001.

From 1996 to 1999, she was with the Microwaves and Radar Institute (DLR-HF) of the German Aerospace Center (DLR), in Oberpfaffenhofen, Germany. From 1999 to 2000 she was with the Institut d'Electronique et de Télécommunications de Rennes at the University of Rennes 1, France for 10 months, and with the Applied Electromagnetics (AEL) in St. Andrews, Scotland, four months in the frame of the EC-TMR Radar Polarimetry Network. In 2005, she was a guest Scientist at the University of Adelaide, Adelaide, South Australia, for six weeks. She is the Science Coordinator of the German satellite mission TanDEM-X. Her main research interests are in electromagnetic propagation and scattering theory, radar polarimetry, SAR and interferometric SAR data processing techniques, environmental parameter modelling and estimation.

TanDEM-X Pol-InSAR Performance for Forest Height Estimation

Florian Kugler, Daniel Schulze, Irena Hajnsek, *Fellow, IEEE*, Hans Pretzsch, and Konstantinos P. Papathanassiou, *Fellow, IEEE*

***Abstract*—TanDEM-X and TerraSAR-X platforms form together the first spaceborne single-pass polarimetric interferometer in space. This allows, for the first time, the acquisition of spaceborne polarimetric synthetic aperture radar interferometry (Pol-InSAR) data without the disturbing effect of temporal decorrelation. This paper aims to assess the potential of such data for forest applications. For this, single- and dual-pol data acquired over a boreal, a temperate, and a tropical site were investigated to characterize X-band penetration and polarization diversity of the interferometric coherence measurements. Pol-InSAR forest height inversion schemes have been proposed and implemented for the single- and dual-pol cases and cross validated against LIDAR reference measurements for all sites. The single-pol inversion relies on an external ground digital terrain model (DTM) and performed well for all sites with correlation coefficients r^2 between 0.80 and 0.98. The dual-pol inversion does not require an external DTM but depends on the visibility of the whole forest layer. Accordingly, its performance varied with forest structure and season: The best performance was achieved for the summer acquisition of the boreal test site ($r^2 = 0.86$) and for the winter acquisition of the temperate test site ($r^2 = 0.77$). For the tropical test site, only a weak correlation ($r^2 = \sim 0.50$) could be established.**

***Index Terms*—Forest, forest height, forest parameter, interferometry, polarimetric synthetic aperture radar interferometry (Pol-InSAR), synthetic aperture radar (SAR), TanDEM-X, TerraSAR-X, X-band.**

I. Introduction

POLARIMETRIC synthetic aperture radar interferometry (Pol-InSAR) has been demonstrated to be a powerful radar remote sensing technique for the quantitative estimation of forest structure parameters [1]. The interferometric coherence is directly related to the vertical distribution of scatterers. In consequence, the coherent combination of single- or multibaseline interferograms at different polarizations allows the characterization of the vertical scattering structure of a volume scatterer [1], [3], [4]. Indeed, forest height and structure parameter estimation from polarimetric single- and multibaseline data acquired at lower frequencies (L- and P-bands) have been successfully demonstrated in a series of airborne experiments in natural, as well as commercial, boreal, temperate, and tropical test sites for different stand and terrain conditions [3], [5]–[8].

However, when it comes to spaceborne repeat pass implementations, the inherent presence of temporal decorrelation biases the interferometric coherence estimates, thus degrading the sensitivity to vertical scattering structure and limiting the performance of Pol-InSAR inversion techniques [5], [9]–[11]. Short-term decorrelation effects (for example, wind-induced temporal decorrelation) affect Pol-InSAR acquisitions even at short temporal baselines on the order of a few hours up to a few days [5], [10]. This is the main reason why polarimetric spaceborne missions such as Canadian Space Agency's RadarSAT-2 (C-band) or the Japanese Aerospace Exploration Agency's ALOS-PalSAR (L-band) could not essentially contribute neither to a large-scale demonstration of Pol-InSAR techniques nor to the development of new Pol-InSAR applications [10], [11].

The TanDEM-X (TDX, launched in June 2010) and TerraSAR-X (TSX, launched in June 2007) platforms together form the first single-pass polarimetric interferometer in space and allow, for the first time, the acquisition of single-, dual-, and quad-polarimetric Pol-InSAR data without the disturbing effect of temporal decorrelation. Unfortunately, the fact that vegetation extinction increases with frequency, reducing the penetration into (and through) vegetation layers, makes X-band a rather suboptimal choice for forest structure mapping, at least in a global sense.

However, a number of InSAR experiments have indicated that, in several cases—primarily in boreal and less dense forest environments—a rather surprising penetration into forest and vegetation scatterers occurs [5]–[7], [12], [13]. This has been supported by interferometric and radargrametric analyses of spaceborne repeat pass data from TSX and COSMO-SkyMed [14].

Pol-InSAR forest height inversion at X-band was first demonstrated in the boreal zone on the basis of a single-polarization interferometric acquisition and by fixing the extinction [7]. In [8], forest height inversion was performed using dual-pol (HH and HV) interferometric acquisitions over a number of pine stands in France. More recent experiments have demonstrated the sensitivity of X-band interferometric measurements on forest vertical structure attributes in temperate

Manuscript received June 9, 2013; revised November 2, 2013; accepted November 11, 2013.

F. Kugler, D. Schulze, and K. P. Papathanassiou are with the Microwaves and Radar Institute, German Aerospace Center (DLR-HR), 82234 Oberpfaffenhofen, Germany (e-mail: florian.kugler@dlr.de; daniel.schulze@dlr.de; kostas.papathanassiou@dlr.de).

I. Hajnsek is with the Institut für Umweltingenieurwissenschaften, Swiss Federal Institute of Technology (ETH) Zürich, 8093 Zürich, Switzerland and also with the Microwaves and Radar Institute, German Aerospace Center (DLR-HR), 82234 Oberpfaffenhofen, Germany (e-mail: hajnsek@ifu.baug.ethz.ch; irena.hajnsek@dlr.de).

H. Pretzsch is with the Chair for Forest Growth and Yield Science, Department for Ecosystem and Landscape Management, Center of Life and Food Sciences, Technische Universität München, 85354 Freising, Germany (e-mail: hans.pretzsch@lrz.tum.de).

Color versions of one or more of the figures in this paper are available online at http://ieeexplore.ieee.org.

Digital Object Identifier 10.1109/TGRS.2013.2296533

forests [12], [16], [17]. In tropical forests, one of the first interferometric scattering models describing penetration and backscattering at X-band was developed in [18] and [19] and was used to interpret the observed coherence loss on emergent trees in tropical rain forests. Finally, in [5], forest height estimation over a tropical peat swamp forest was demonstrated using a single-polarization interferometric acquisition and a LIDAR-derived ground digital terrain model (DTM). These results have triggered the interest to explore the potential and the limitations of Pol-InSAR applications at X-band. TDX provides the unique opportunity to systematically investigate Pol-InSAR data over a wide range of forest sites under different seasonal and environmental conditions in order to improve the understanding of vegetation scattering processes at X-band and to assess the potential of Pol-InSAR techniques at this frequency band.

For this investigation, a number of single- and dual-pol data acquired by TDX at different operation modes (briefly described in Section II) and geometries over a number of forests in different ecosystems have been evaluated. Three different forest types representative for different forest ecosystems at different seasons were investigated: a boreal forest (Krycklan, $64°10'$ north and $20°01'$ east), a temperate forest (Traunstein, $47°52'$ north, $12°39'$ east), and a tropical forest (Mawas, $-2°09'$ south and $114°27'$ east). The test sites, the data sets, and the calculation of the reference height, i.e., forest top height H100, from LIDAR data are described in Section III. In order to draw conclusions about the potential of TanDEM-X to derive forest height by means of Pol-InSAR techniques, three important questions need to be answered: The first one is the question about the penetration of X-band into different forest types and forest conditions. The second one is the question about the role of polarimetry, i.e., about the degree of polarimetric diversity of the interferometric measurements. Finally, the third one is the question about how accurate (and how robust) forest height can be estimated exploring the information content of the polarimetric interferometric measurements. In Section IV, the penetration of X-band into the forest volume and the polarimetric diversity of the interferometric coherence measurements are investigated. To accomplish this, the height of the scattering center and the maximized polarimetric phase difference were cross validated against forest top height H100 (estimated from LIDAR data). In addition, here, seasonal differences in the scattering behavior are discussed. In Section V, a single- and a dual-pol Pol-InSAR inversion scheme are introduced. Forest height inversion results for each test site and both inversion scenarios are cross validated against LIDAR-derived reference measurements in Section VI. Finally, the achieved results are summarized and discussed in Section VII.

II. TanDEM-X Interferometric Parameters

A. Interferometric Modes

TDX can operate in different interferometric configurations, of which the most common are [20], [21] the following.

1) The pursuit monostatic mode, where the two satellites (TDX and TSX) are independently operated and separated by an along-track distance that induces a temporal baseline. This configuration was used in the monostatic commissioning phase of TDX with an along-track separation on the order of 20 km that translated to a temporal baseline of approximately 3 s.
2) The bistatic mode, where one of the two satellites (either TDX or TSX) acts as a transmitter and both satellites receive the scattered signal simultaneously, reducing the temporal baseline to practically zero.
3) The alternating bistatic mode, where, similar to the conventional bistatic mode, one satellite is transmitting and both satellites simultaneously receive. However, in this mode, the transmitter role is alternated between the two satellites on a pulse-by-pulse basis. Accordingly, the images acquired in the alternating bistatic mode allow the formation of one interferogram corresponding to the monostatic, i.e., to the "both antennas transmit–both antennas receive" configuration, and one corresponding to the bistatic, i.e., the "one antenna transmits–both antennas receive" configuration, at the same time. The second interferogram has half effective baseline of the first [20].

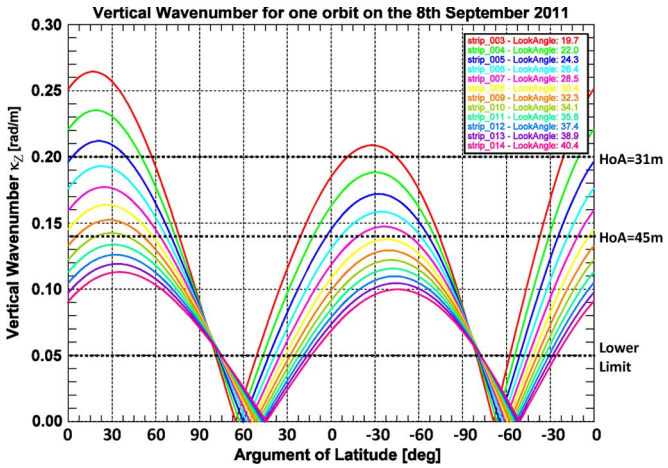

Fig. 1. Vertical wavenumber κ_Z as a function of orbit position (latitude) for one orbit cycle (360°) starting from the equator (0°) in ascending orbit pass for the 12 full-performance TDX beams in stripmap mode (beam "strip_003" to beam "strip_014"). Each beam is associated with a certain look angle.

All three interferometric modes can be realized in stripmap, ScanSAR, spotlight, and sliding spotlight imaging modes operated in a single- or a dual-polarimetric mode with look angles ranging between 15° and 55° (20° and 41° for the 12 dedicated full-performance stripmap beams) [22].

B. Effective Spatial Baseline

The performance of quantitative polarimetric interferometric techniques critically depends on the effective spatial baseline used for the interferometric acquisition(s). The parameter commonly used to express the effective spatial baseline is the vertical wavenumber κ_Z approximated by

$$\kappa_Z = m\frac{2\pi\Delta\theta}{\lambda\sin(\theta)} \approx m\frac{2\pi B_\perp}{\lambda\sin(\theta)R} \tag{1}$$

where $\Delta\theta$ is the angular separation of the two acquisitions in the direction of the resolution cell, $B_\perp$ is the effective

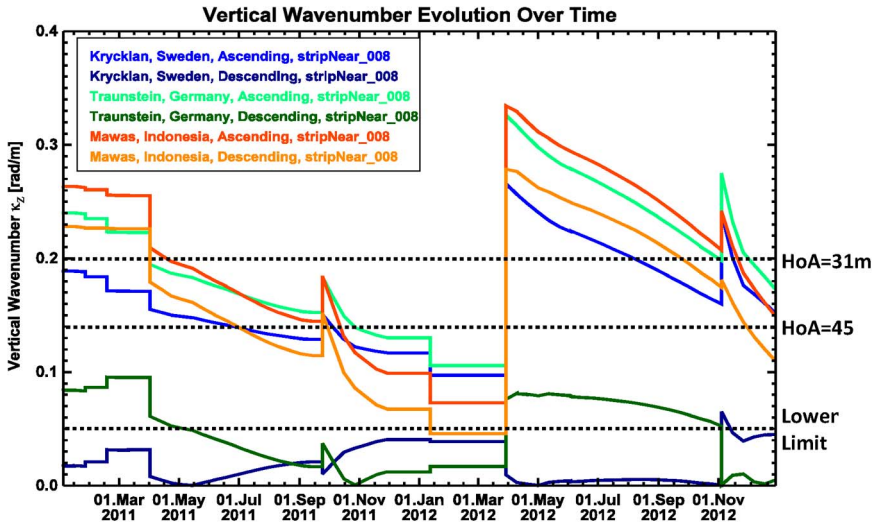

Fig. 2. Development of the vertical wavenumber κ_Z as a function of mission time for beam strip_008 (look angle $= \sim 30.4°$) for the three test sites Krycklan (latitude: $64°10'$), Traunstein (latitude: $47°52'$), and Mawas (latitude: $-2°19'$) in ascending and descending orbit pass.

(perpendicular) baseline, θ is the local incidence angle, λ is the used wavelength, R is the slant range distance, and m accounts for the acquisition mode. For monostatic acquisitions, $m = 2$, whereas for bistatic acquisitions, $m = 1$. The vertical wavenumber κ_Z scales the interferometric phase to height. In the case of TanDEM-X, the parameter used to express the effective spatial baseline is the height of ambiguity HoA $= 2\pi/\kappa_Z$, i.e., the height that corresponds to an interferometric phase change of 2π.

The TanDEM-X mission scenario and orbit parameters are designed to fulfill the specification of the digital elevation model (DEM) product. To accomplish this, the Earth's total landmass will be mapped at least twice, in two acquisition periods, with heights of ambiguity ranging from 35 to 60 m. Global DEM data acquisition with varying baselines will continue until 2014 [23].

During the mission time, the two satellites (TSX and TDX) are flying in a close helix formation (for a detailed description, see [20], [21], and [24]). The helix formation is characterized by a steadily changing baseline over one orbit cycle. Fig. 1 shows the development of the vertical wavenumber κ_Z for one orbit cycle $(360°)$ for the 12 full-performance TDX beams (each associated to a different look angle) in the first acquisition period (from September 8, 2011). The simulation of the orbit cycle starts from the equator (0° latitude) in an ascending orbit pass, goes across the North Pole (90° latitude), changes to a descending orbit pass, crosses the equator in a descending orbit pass (0° latitude), passes the South pole ($-90°$ latitude), changes again to an ascending orbit pass, and crosses the equator again in an ascending orbit pass (0° latitude). During one orbit cycle, κ_Z goes twice down to zero (no height sensitivity). This happens, depending on the used beam, in the northern hemisphere between 35° and 75° latitudes for the descending orbit pass and in the southern hemisphere between $-40°$ and $-80°$ latitudes for the ascending orbit pass. Meaningful (sensitive) acquisitions, as required for a successful height inversion, start from $\kappa_Z > 0.05$ rad/m [10]. This means that, for the baseline configuration as displayed in Fig. 1, areas between 35° and 75° latitudes can be only covered with a sensitive κ_Z in the ascending orbit pass, whereas the areas between $-40°$ and $-80°$ latitudes can be only covered with a sensitive κ_Z in the descending orbit pass. For all other areas, too, high or too low κ_Z values can be avoided by a proper selection of the beam (look angle). Decreasing the look angle increases κ_Z and vice versa.

Fig. 2 shows a plot of the development of κ_Z as a function of mission time for the years 2011 and 2012 (roughly covering the two acquisition periods) for the three test sites Krycklan, Traunstein, and Mawas (representing different arguments of latitude) in ascending and descending orbit pass. The plot was done for beam "strip_008," which corresponds to a look angle of $\sim 30.4°$.

The first acquisition period started in the beginning of February 2011. The abrupt increase in κ_Z at the beginning of April 2012 indicates the change between the first and second acquisition periods of the TDX mission. All other small peaks result from orbit adjustments due to acquisition needs.

For the Mawas site, which is located close to the equator, the difference in κ_Z between the ascending and descending orbit passes is small (red and orange lines in Fig. 2). However, for the Krycklan site (light blue and dark blue lines in Fig. 2) and the Traunstein site (light green and dark green lines in Fig. 2), the difference between the ascending and descending κ_Z is large. In the descending orbit pass, κ_Z was mostly lower than 0.05 rad/m for both sites. Only the Traunstein site could be covered with vertical wavenumbers larger than 0.05 rad/m from April 2012 until November 2012 in the descending orbit pass.

During the first acquisition period, almost all tests sites could be acquired, in ascending mode, with baselines appropriate for forest structure investigation (i.e., HoA $>$ maximum forest height). Only for the Traunstein site was κ_Z too large to cover the prevailing forest heights on the ground, but this problem could be overcome by choosing an acquisition at a larger incidence angle. In the second acquisition period, all test sites could be acquired, in ascending mode, with effective baselines that are in general too large ($\kappa_Z > 0.2$ rad/m, corresponding to HoAs < 31 m) to provide the sensitivity required for forest structure

estimation (coherence mostly insensitive). More appropriate baselines (with κ_Z values below 0.2 rad/m) appeared only after November 2012. In addition, here, acquisitions at larger incidence angles would decrease κ_Z.

The plot in Fig. 2 is limited to a single beam, and there was still potential to optimize κ_Z by a proper selection of the look angle. However, it shows also that a careful planning of an acquisition is necessary if a certain κ_Z is required.

III. Test Sites and Data Sets

In this paper, data from three forest sites representative of three key forest ecosystems (i.e., boreal, temperate, and tropical) characterized by very different forest and terrain conditions were used. All sites have been used in the past as test sites for airborne Pol-InSAR experiments. Actual airborne LIDAR measurements were available.

Cross validation was done on stand level homogeneous forest areas with a mean size of ∼3–5 ha. Every stand is represented by its mean value. This is necessary to compensate for the residual spatial misregistration between SAR and LIDAR reference data, occurring when georeferencing both data sets. Of course, this averaging also reduces the variation of the obtained estimates.

From the LIDAR data, the forest canopy top height H100 was calculated and used as a reference. H100 is a standard parameter in forest mensuration and is defined as the mean height of the largest 100 trees per hectare [25]. H100 is considered to represent the upper height of the tree crowns in a forest.

Airborne LIDAR penetrates into the forest and therefore underestimates the top vegetation height [14], [15], [25]. An estimate of the forest top height H100 was obtained by taking the maximum LIDAR vegetation height within a 10 m × 10 m window. This allows compensating for the underestimation of the LIDAR forest height estimates [5], [27]. This method has been successfully used for small footprint (∼15-cm diameter) airborne LIDAR systems with ∼1 to ∼4 hits per square meter.

Even if the LIDAR and radar measurements were up to three years/growth periods apart, a proper cross validation was still possible as maximum possible forest height growth for this time period was, for most forest stands, on the order of ∼1 m or even below (see test site descriptions in Section III-A and B). Therefore, forest height changes due to growth were neglected in the cross validation. Large areas of wood harvest or naturally destroyed forest areas (caused by wind throw or forest fires) clearly appear as outliers in the validation plots.

The TDX data sets available and used for each site are summarized in Table I. The test sites are described in the following sections.

TABLE I
Summary of Used TDX and E-SAR Data

Test site	Date	Look angle [°]	κ_Z [rad/m]	HoA [m]	Polarization	Mode
Krycklan	2010/07/28	32°	0.17	38	HH VV	ascending, Stripmap, pursuit monostatic
Krycklan	2010/12/17	19°	0.09	69	HH	descending, Stripmap, bistatic
Krycklan	2011/06/11	19°	0.05	125	HH	descending, Stripmap, bistatic
Traunstein	2012/01/09	43°	0.09	69	HH VV	ascending, Stripmap, bistatic
Traunstein	2009/06/09	25° -55°	0.14 -0.27	23 -46	VV	airborne (E-SAR), Stripmap, monostatic
Mawas	2011/08/25	31°	0.12	52	HH VV	descending, Stripmap, bistatic
Mawas	2011/12/13	31°	0.07	89	HH VV	descending, Stripmap, Bistatic
Mawas	2011/12/24	31°	0.07	89	HH VV	descending, Stripmap, bistatic
Mawas	2012/01/04	31°	0.08	79	HH VV	descending, Stripmap, bistatic

A. Krycklan Test Site

The Krycklan forest is located in central Sweden ($64°10'$ north and $20°01'$ east) and represents typical forest conditions for Scandinavian boreal forest systems. It is a managed forest with a mean forest height of 18 m and a mean biomass level of 90 t/ha. Maximum forest height measured is 30 m with a biomass of 220 t/ha. The forest is dominated by coniferous tree species (Norway spruce and Scots pine) with fractions of birch. The site has a hilly topography characterized by moderate slopes and a height variation between 20 and 400 m above mean sea level (AMSL).

Airborne LIDAR measurements were collected in late summer 2008. For cross validation, 252 homogeneous stands with a mean stand size of 3 ha were chosen. In terms of TDX data sets, three acquisitions were analyzed. One dual-pol (HH and VV) pursuit monostatic acquisition from July 2010 acquired with a 32° look angel from an ascending orbit (see Fig. 3), and two bistatic single-pol (HH) acquisitions acquired with a 19° look angle from a descending orbit in December 2010 and June 2011, respectively. All data were acquired in the stripmap mode.

The time between the LIDAR data acquisition and the last TDX data acquisition comprised three growth periods. The maximum height growth for this time period is ∼1.2 m (0.4 m per year), but only for trees with an age between 20 and 40 years (∼13 m high) [28]. For all other trees (age classes), forest growth is below 1 m. Forest growth of approximately 1 m is below the sensitivity of the used methods and can therefore be neglected for cross validation at this site. For the cross validation of model-based forest height estimates (see Section V), only two growth periods need to be considered.

Fig. 3(a) shows the VV amplitude image of the July 2010 acquisition. The image dimension is approximately 18 km × 50 km. In Fig. 3(b), the interferometric coherence image is shown scaled from 0 (black) to 1 (white), and in Fig. 3(c) on the right, the associated TDX DEM is shown. The area covered by the LIDAR measurements is indicated by the black rectangle.

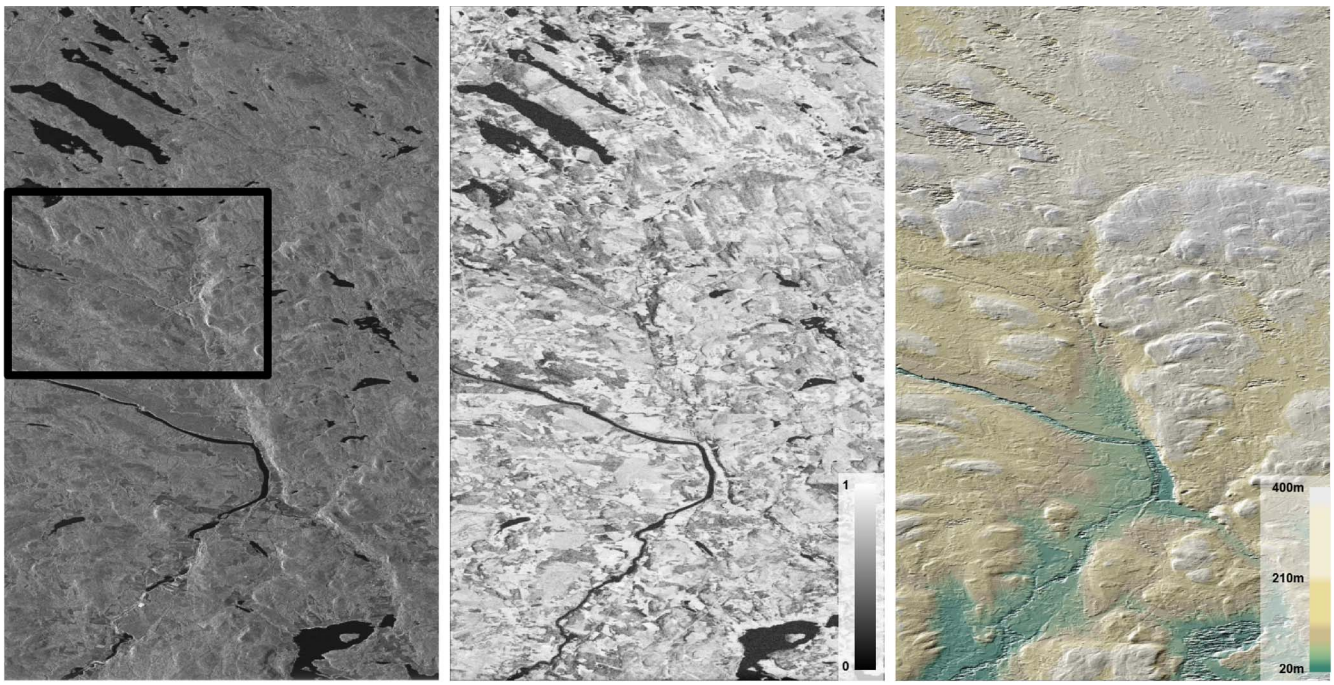

(a) (b) (c)

Fig. 3. Krycklan test site (July 28, 2010 acquisition). (a) VV amplitude image; the area covered by the LIDAR measurements is indicated by the black rectangle. (b) VV interferometric coherence scaled from 0 (black) to 1 (white). (c) TDX DEM scaled from 20 m (dark green) to 400 m (white). Image dimension: $\sim$18 km (range) $\times$ $\sim$50 km (azimuth).

B. Traunstein Test Site

The Traunstein site is located in the southeast of Germany ($47°52'$ north, $12°39'$ east), east of the town Traunstein, in the prealpine moraine landscape of southern Germany.

The climatic conditions favor temperate mixed mountainous forest stands, dominated by Norway spruce, beech, and fir. It is a managed forest composed of even-aged stands (mainly older forest parts) and mixed uneven-aged stands (mainly younger forest parts) with forest heights from 10 up to 40 m and higher. Mean biomass level is on the order of 210 t/ha; individual old forest stands can reach biomass levels up to 600 t/ha (above average compared with other temperate forests). The topography of the site varies from 530 to 650 m AMSL, with only a few steep slopes.

Airborne LIDAR height measurements were performed in the summer of 2008. For cross validation, 22 homogeneous stands with a mean stand size of $\sim$3 ha were chosen. In terms of TDX, only one stripmap bistatic dual-pol (HH and VV) acquisition acquired with a 42° look angle from an ascending orbit in January 2012 was investigated. During the acquisition, the scene was covered with an $\sim$0.3-m-thick snow layer. Additionally, an airborne summer acquisition from June 2009 acquired at X-band in a single-pass interferometric mode in VV polarization by the E-SAR system of DLR [29], [30] was analyzed to evaluate differences in backscattering between summer and winter conditions. Here, as in the Krycklan test site, the time difference between the LIDAR data acquisition and the TDX data acquisition comprised three growth periods.

Under the growth conditions in Traunstein, the maximum height growth within three years is $\sim$1.9 m (0.63 m per year) for trees in the age between 20 and 40 years ($\sim$17 m high), reduces to $\sim$0.9 m for trees in the age of 60 years ($\sim$30 m high), and reduces even more for trees older than 80 years [28]. As most of the validation stands were larger than 20 m and forest growth of $\sim$1 m is below the sensitivity of the used methods, forest growth was neglected for cross validation at this site.

Fig. 4(a) shows the VV amplitude image of the TDX data. The image dimension is approximately 18 km $\times$ 15 km. In Fig. 4(b), the interferometric coherence image is shown scaled from 0 (black) to 1 (white), and in Fig. 4(c) the associated TDX DEM is shown. The area covered by the LIDAR measurements is indicated by a black rectangle.

C. Mawas Test Site

The Mawas site is an Indonesian forest conservation area located in Central Kalimantan ($-2°09'$ south and $114°27'$ east). It is covered with a tropical peat swamp forest that is still marked by strong logging activities carried out in the early 90s of the last century. Logging tracks are still visible today—on the ground and on the LIDAR and SAR data. Two forest types can be distinguished in the test site, namely, riverine forest in the proximity of the river and peat swamp forest covering the rest of the scene (see Fig. 5).

Typical for the Mawas site is the distinct change between dry and wet seasons: At the end of the wet season, the forest is widely flooded, whereas at the peak of the dry season, the trees partly drop off their leaves to endure the lack of water [5]. Forest height reaches up to 30 m; the mean biomass is around 200 t/ha with maximum values up to 300 t/ha. The terrain topography is rather flat and slowly varies from 5 to 50 m AMSL across the whole scene. A detailed description of the Mawas test site is given in [5] and [31].

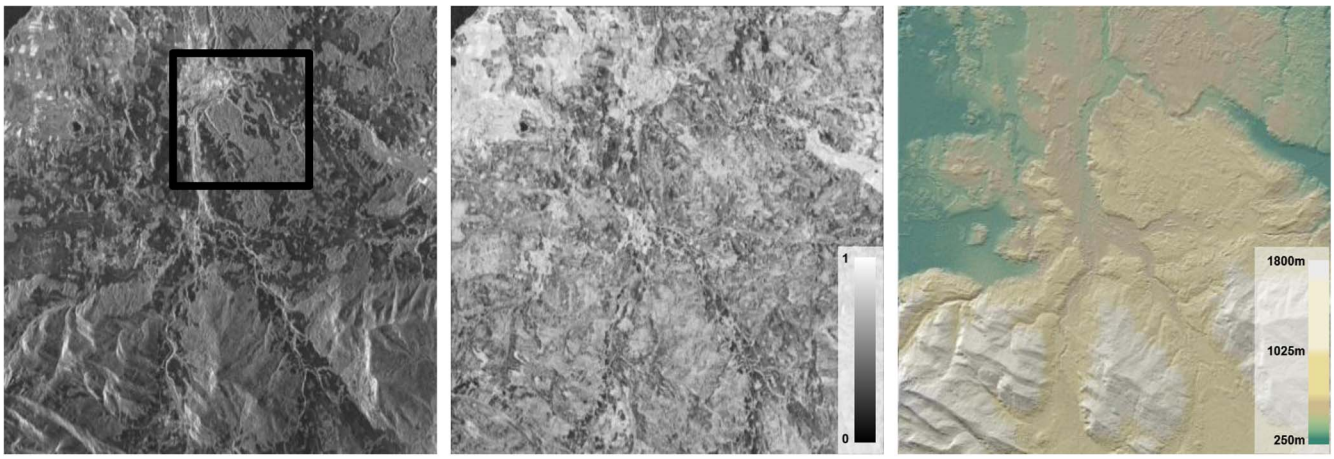

Fig. 4. Traunstein test site (August 25, 2011 acquisition). (a) VV amplitude image; the area covered by the LIDAR measurements is indicated by the black rectangle. (b) VV interferometric coherence scaled from 0 (black) to 1 (white). (c) TDX DEM scaled from 250 m (dark green) to 1800 m (white). Image dimension: $\sim$18 km (range) $\times$ $\sim$15 km (azimuth).

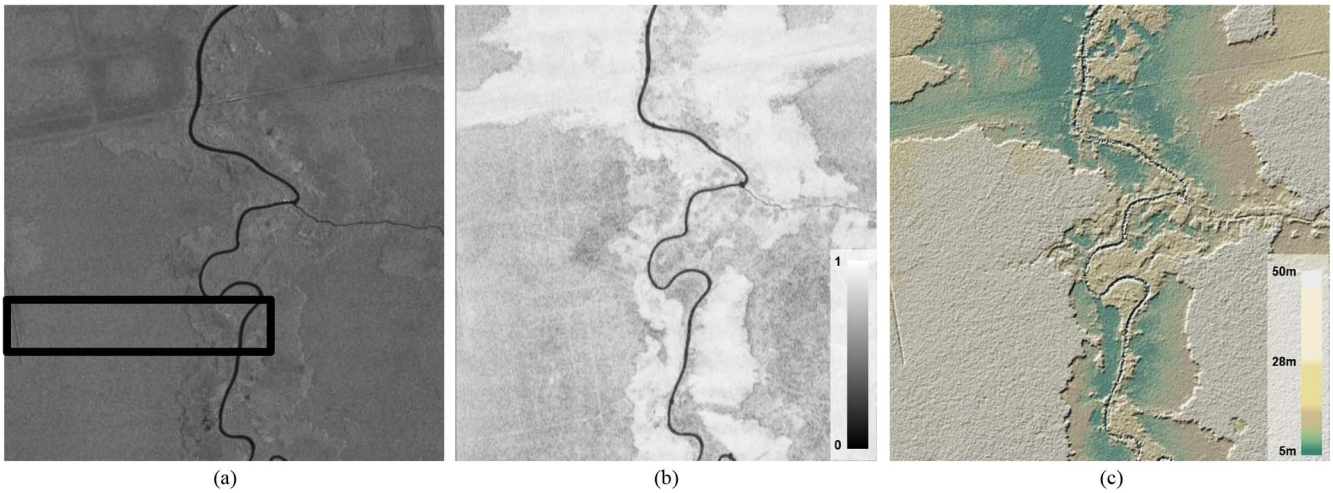

Fig. 5. Mawas test site (August 25, 2011 acquisition). (a) VV amplitude image; the area covered by the LIDAR measurements is indicated by the black rectangle. (b) VV interferometric coherence scaled from 0 (black) to 1 (white). (c) TDX DEM scaled from 5 m (dark green) to 50 m (white). Image dimension: $\sim$20 km (range) $\times$ $\sim$20 km (azimuth).

In August 2011, airborne LIDAR measurements were performed with a swath width of about 500 m crossing the TDX images. The LIDAR strip was divided for cross validation into 100 parts of equal size with an area of $\sim$4.5 ha, and each part is assigned one H100 value. For this site, a time series of four stripmap bistatic dual-pol (HH and VV) acquisitions acquired with a 31° look angle from a descending orbit in summer and late autumn/winter 2012 has been investigated.

The first acquisition is from August 25, 2011 (peak of dry season), followed by three acquisitions separated by 11 days on December 13 (start of the rainy season), December 24, and January 4, 2012. LIDAR measurements and TDX acquisitions took place in the same year so that no significant forest changes between the LIDAR and TDX acquisitions are expected.

Fig. 5(a) shows the VV amplitude image from the August 2011 acquisition. The image dimension is approximately 20 km $\times$ 20 km. In Fig. 5(b), the interferometric coherence image is shown scaled from 0 (black) to 1 (white), and Fig. 5(c) shows the associated TDX DEM. In the DEM, the flatness of the area becomes obvious; the largest height changes are induced by changes in vegetation height. The area covered by the LIDAR measurements is indicated by the black rectangle.

IV. X-Band Forest Height Estimation Performance

Feasibility and performance of forest Pol-InSAR applications at X-band critically depend on two effects.

1) The capability of X-band to penetrate into and through the forest: The penetration is required in order to "see" enough from the forest volume: The maximum vegetation height that can be resolved is given by the penetration depth. With further increasing height, the interferometer does not see anymore the whole volume, and the height estimation "saturates." The penetration capability depends in general on the density and dielectric properties of the forest/canopy layer. Both parameters vary spatially and in time for many forest types in a seasonal cycle.

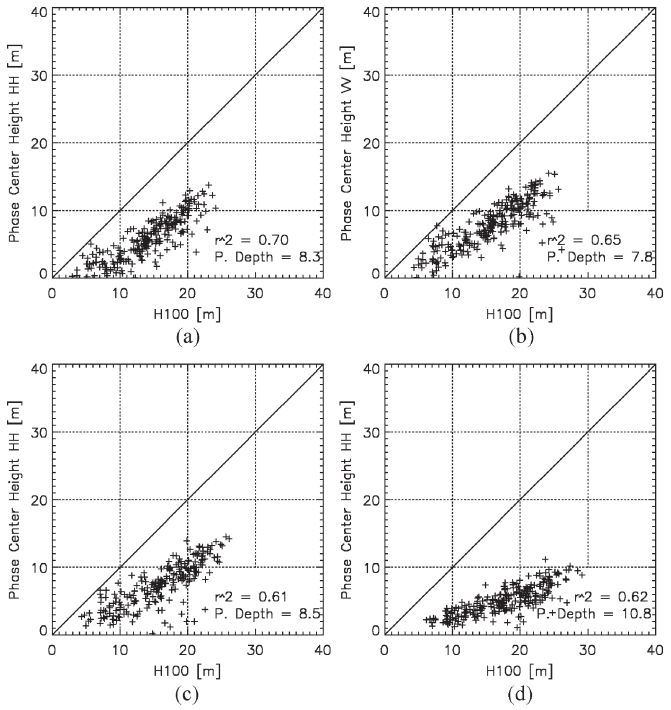

Fig. 6. Krycklan test site validation plots: phase center height versus LIDAR forest height for different polarizations, look angles, and seasons. (a) HH polarization acquired in July 2010 with look angle $= 32°$. (b) VV polarization acquired in July 2010 with look angle $= 32°$. (c) HH polarization acquired in June 2011 with look angle $= 19°$. (d) HH polarization acquired in December 2010 with look angle $= 19°$.

2) The dependence of the interferometric coherence (in amplitude and phase) on the polarization(s) of the images is used to form the interferogram. This again depends on the polarimetric properties of the individual scatterers and their distribution in height. Reduced polarization dependence indicates a limit in the information content of the Pol-InSAR observation space, reducing the value of the polarimetric diversity in interferometric measurements.

Both effects are investigated in the following sections.

A. Penetration Depth

In order to establish the penetration depth in the forest volume, the height difference between the available LIDAR DTM and the X-band DEM (corresponding to the interferometric phase center height) was estimated for each TDX data set for all stands available in the three test sites and plotted against the individual LIDAR H100 forest height. For each plot, the correlation coefficient, i.e., r^2, and the mean penetration depth were calculated.

1) Krycklan Test Site: The plots for the Krycklan site are shown in Fig. 6. Fig. 6(a) corresponds to the HH polarization of the (monostatic) summer (July 2011) acquisition with a 32° look angle, and Fig. 6(b) corresponds to the VV polarization of the same acquisition. For both polarizations, the phase center height is close to half the forest height, indicating a low extinction level for this test site. The comparison of the plots makes it clear that the HH phase centers, characterized by a penetration depth of 8.3 m, are, on average, located 0.5 m "deeper" than the corresponding VV phase centers, characterized by a penetration depth of 7.8 m.

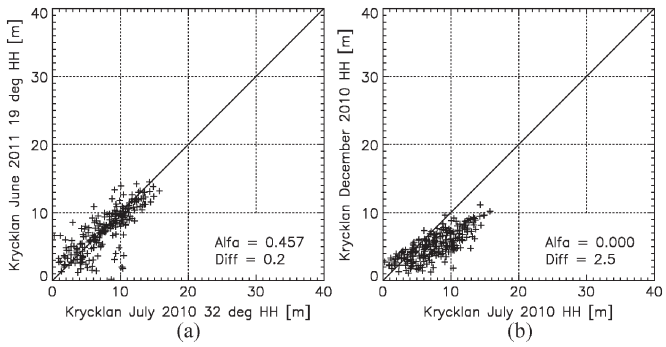

Fig. 7. Krycklan test site phase center heights comparison. (a) HH polarization acquired in July 2010 with look angle $= 32°$ versus HH polarization acquired in June 2011 with look angle $= 19°$. (b) HH polarization acquired in July 2010 with look angle $= 32°$ versus HH polarization acquired in December 2010 with look angle $= 32°$; Alfa is the significance, a value between 0 and 1. A small value (up to 0.01) indicates significantly different means. Diff is the mean difference in meters between the two phase center heights.

This difference can be interpreted by a (slightly) higher ground contribution in the HH polarization than in the VV polarization.

Fig. 6(c) corresponds to the HH polarization of the second (bistatic) summer (June 2011) acquisition acquired at a steeper look angle of 19°. The phase centers are located at comparable heights as in the July acquisition [see Fig. 6(a)] acquired with a shallower 32° look angle at comparable penetration depth levels (8.5 m at 19° look angle in June versus 8.3 m at 32° look angle in July). The small difference in penetration between the two look angles implies that this look angle difference of 13° has a rather minor effect on the location of the scattering centers.

Fig. 6(d) corresponds to the HH polarization of the December 2010 acquisition acquired with the same mode and geometry (i.e., 19° look angle) as the June 2011 acquisition [see Fig. 6(c)]. The comparison of the winter and summer plots [see Fig. 6(c) and (d)] shows a significant lower phase center location, indicating a larger penetration in the winter (10.8 m) than in the summer (8.3 m). A possible interpretation is an increased ground scattering contribution as a consequence of the frozen vegetation conditions (decreased vegetation dielectric constant) combined with the loss of leaves. Both effects decrease volume attenuation.

Fig. 7(a) shows a plot of phase center heights in HH polarization acquired in July 2010 with a 32° look angle versus the phase center heights in HH polarization acquired in June 2011 with a 19° look angle, and Fig. 7(b) shows a plot of phase center heights in HH polarization acquired in July 2010 with a 32° look angle versus the phase center heights in HH polarization acquired in December 2010 with a 32° look angle. The significance of the difference in phase center height was tested with the t-test (Student's t distribution). The difference of the phase center heights between 19° and 32° look angles appears not to be significant, but the difference of the phase center heights between the July and December acquisitions is highly significant.

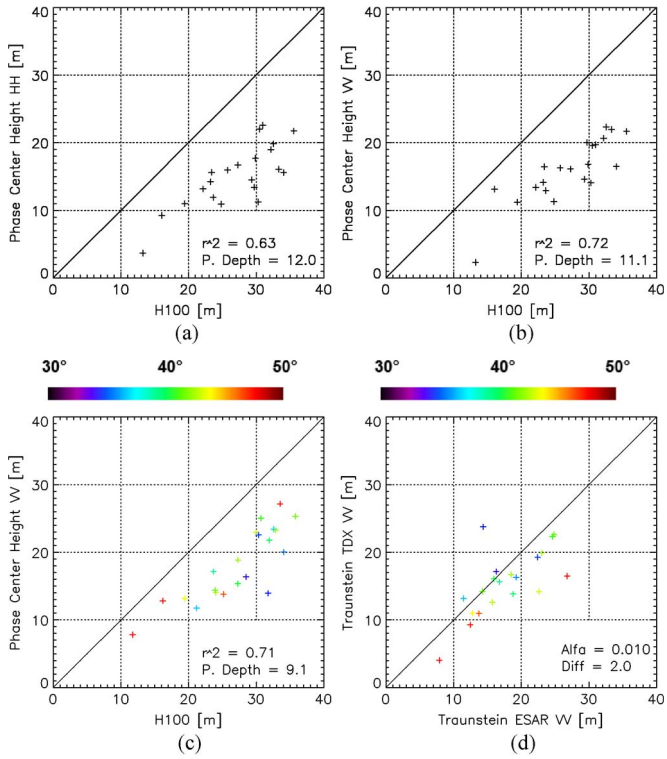

Fig. 8. Traunstein test site validation plot: phase center height versus LIDAR forest height. (a) TDX data in HH polarization acquired in January 2012 with a 45° incidence angle. (b) TDX data in VV polarization acquired in January 2012 with a 45° incidence angle. (c) E-SAR airborne data in VV polarization acquired in June 2009 (plot is color-coded according to the mean incidence angle of the stands). (d) Phase center heights comparison: E-SAR VV polarization acquired in June 2009 versus TDX VV polarization acquired in January 2012 with a 45° incidence angle (plot was color-coded according to the mean incidence angle of the stands in the E-SAR acquisition). Alfa is the significance, a value between 0 and 1. A small value (up to 0.01) indicates significantly different means. Diff is the mean difference in meters between the two phase center heights.

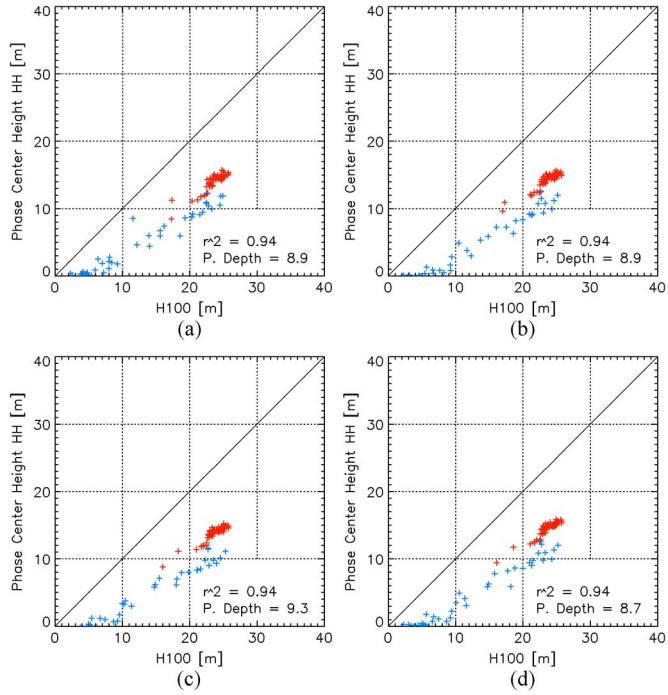

Fig. 9. Mawas test site validation plot: phase center height versus LIDAR forest height in HH polarization. (a) August 25, 2011. (b) December 13, 2011. (c) December 24, 2012. (d) January 4, 2012. (Blue dots) Riverine forest. (Red dots) Peat swamp forest.

2) Traunstein Test Site: The phase center height plots for the single acquisition over the Traunstein site acquired in January 2012 are shown in Fig. 8. Fig. 8(a) shows the HH and Fig. 8(b) the VV phase center heights plotted against the forest height for each available validation stand. Similar to the observations in Krycklan, in Traunstein, the HH polarization phase centers characterized by a 12-m mean penetration depth are located, on average, 0.9 m closer to the ground than the VV phase centers (characterized by an 11.1-m penetration depth). In the absence of a suitable TanDEM-X summer acquisition, a data set acquired by the airborne E-SAR system of DLR in June 2009 was used to evaluate the seasonal behavior of the site. The corresponding phase center height plot is shown in Fig. 8(c) (the plot is color-coded according to the mean incidence angle of the stands) and indicates about 2 m higher located phase centers (characterized by a 9.1-m penetration depth). This underlines again the different penetration depths in summer and winter. However, compared with the Krycklan site, the phase center height is located in Traunstein—even in winter—clearly above the half forest height reflecting the denser forest conditions of this test site.

A direct comparison between the phase center heights of the TDX acquisition from January 2012 and the phase center heights of the E-SAR acquisition from June 2009 is shown in Fig. 8(d) (the plot is color-coded according to the mean incidence angle of the stands in the E-SAR acquisition; incidence angle in the TDX acquisition was considered constant). The t-test indicates that the difference in phase center height is highly significant. Only stands with a steeper incidence angle in the E-SAR acquisition than in the TDX acquisition have a higher phase center height in the winter than in the summer (35° in case of E-SAR versus 45° in case of TDX). In this constellation, the incidence angle seems to affect the position of the phase center height. A steeper incidence angle seems to lower the phase center height, i.e., allowing a deeper penetration. However, here, the results need to be carefully interpreted as incidence angle effects and seasonal effects mix up.

3) Mawas Test Site: The phase center height plots for the four available bistatic acquisitions (see Table I), i.e., one acquired in summer 2011 (dry season) and three in winter 2011–2012 (at the beginning of the wet season), are shown in Fig. 9 for the HH polarization and in Fig. 10 for the VV polarization.

The penetration depth changed only marginally from acquisition to acquisition and between polarizations. However, there seems to be a decrease in penetration depth between wet and dry seasons. In addition, for the Mawas site, the height of the phase center was with penetration depths ranging from 8.5 m (VV polarization from January 4, 2012) to 9.4 m (VV polarization from August 25, 2011) clearly below the forest canopy.

In the phase center height plots (see Figs. 9 and 10), the two forest types (riverine forest and peat swamp forest) of the scene can be clearly identified.

The riverine forest is displayed with blue dots in Figs. 9 and 10, and the peat swamp forest is displayed with red dots.

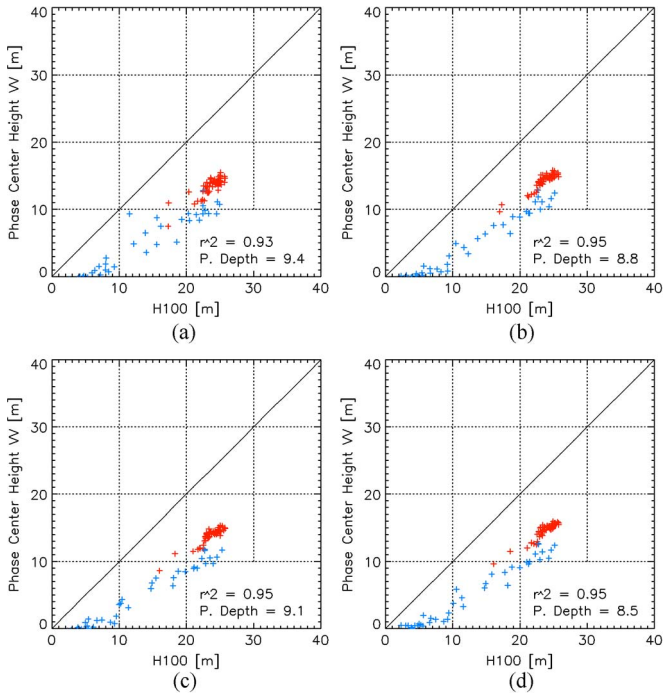

Fig. 10. Mawas test site validation plot: phase center height versus LIDAR forest height in VV polarization. (a) August 25, 2011. (b) December 13, 2011. (c) December 24, 2012. (d) January 4, 2012. (Blue dots) Riverine forest. (Red dots) Peat swamp forest.

B. Polarimetric Diversity

The polarimetric diversity of the interferometric coherence is established by the coherence region concept [1]. In the case of a dual-pol InSAR configuration operating in HH and VV, a 2-D scattering vector $\vec{k}_1 = [S^1_{\mathrm{HH}}\ S^1_{\mathrm{VV}}]^T$ and $\vec{k}_2 = [S^2_{\mathrm{HH}}\ S^2_{\mathrm{VV}}]^T$ is acquired at each end of the (spatial) baseline, where S^i_{JJ} are the copolarized (complex) scattering amplitudes of the corresponding scattering matrix. The scattering amplitude $S(\vec{w})$ of any polarization state $\vec{w}$ in the 2-D subspace defined by S_{HH} and S_{VV} can be defined by the projection of the scattering vector $\vec{k}$ on the unitary complex vector $\vec{w}$ as [1]

$$S_1(\vec{w}) := \vec{w}^{+} \cdot \vec{k}_1 \quad S_2(\vec{w}) := \vec{w}^{+} \cdot \vec{k}_2. \tag{2}$$

The interferometric coherence is then given by

$$\tilde{\gamma}(\kappa_z, \vec{w}) = \frac{\vec{w}^{+}\left[\Omega_{12}(\kappa_z)\right]\vec{w}}{\sqrt{\left(\vec{w}^{+}[T_{11}]\vec{w}\right)\left(\vec{w}^{+}[T_{22}]\vec{w}\right)}} \tag{3}$$

where

$$[\Omega_{12}(\kappa_z)] := \left\langle \vec{k}_1 \cdot \vec{k}_2^{T} \right\rangle \quad [T_{11}] := \left\langle \vec{k}_1 \cdot \vec{k}_1^{T} \right\rangle$$
$$[T_{22}] := \left\langle \vec{k}_2 \cdot \vec{k}_2^{T} \right\rangle.$$

Using its polar form, the interferometric coherence $\tilde{\gamma}(\kappa_Z, \vec{w})$ can be represented on the unit circle (see Fig. 11) by a point with radius $0 \leq |\tilde{\gamma}(\kappa_Z, \vec{w})| \leq 1$ and phase $\varphi = \arg\{\tilde{\gamma}(\kappa_Z, \vec{w})\}$ [4].

The region on the unit circle defined by the loci of the interferometric coherences $\tilde{\gamma}(\kappa_Z, \vec{w}_i)$ for all possible $\vec{w}_i$ is called the coherence region (red ellipse in Fig. 11) and is used to interpret the polarimetric interferometric signature of the underlying scatterer. The radial extent of the coherence region indicates the variation of the absolute value of the interferometric coherence as a function of polarization. The angular extent of the coherence region indicates the variance of the interferometric phase (center) as a function of polarization. The maximum phase difference $\Delta\varphi$ established by the coherence region indicates the maximum variation of the interferometric phase (center) obtained by changing the polarization of the images used to form the interferogram, and it can be converted to a (baseline independent) height difference Δh by scaling with the vertical wavenumber, i.e., $\Delta h = \Delta\varphi/\kappa_z$. Large $\Delta\varphi$ values indicate the presence of (polarized) scattering contributions at different heights within the scattering volume. However, a note of caution is required when interpreting the interferometric coherence on the unit circle: the estimation of both the absolute value and the argument of the interferometric coherence is affected by an inherent variance defined by the (absolute) coherence value and the number of looks used for its estimation [33].

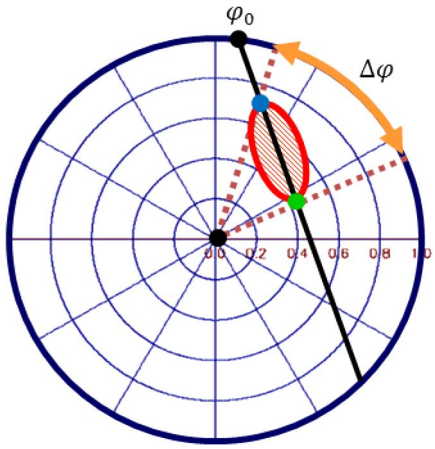

Fig. 11. (Red ellipse) Unit circle with coherence region. (Blue dot) $\tilde{\gamma}_{\mathrm{Vol}}(\vec{w}_{\max})$. (Green dot) $\tilde{\gamma}_{\mathrm{Vol}}(\vec{w}_{\min})$. (Black dot) ground phase φ_0. (Double-headed arrow) Maximum phase difference $\Delta\varphi$.

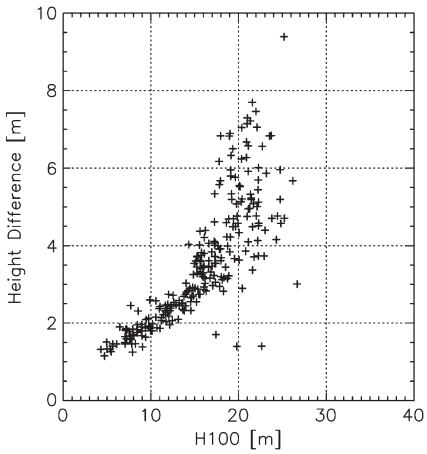

Fig. 12. Krycklan test site validation plot: polarimetric phase height Δh difference versus LIDAR forest height for the TDX dual-pol acquisition from July 2010.

1) Krycklan Test Site: In Fig. 12, the maximum phase difference $\Delta\varphi$ (scaled to a maximum height difference Δh) estimated from the dual-pol July 2010 acquisition (see Table I)

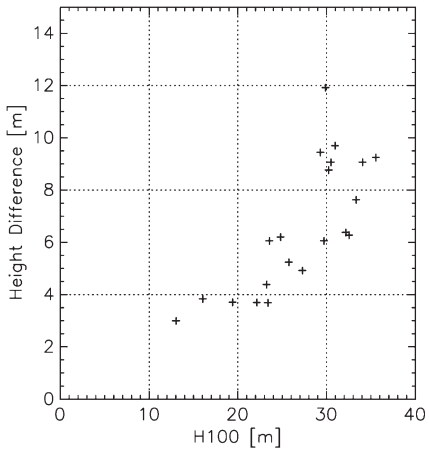

Fig. 13. Traunstein test site validation plot: polarimetric phase height difference Δh versus LIDAR forest height for the dual-pol acquisition from January 2012.

is plotted against the LIDAR-derived H100 (i.e., top forest height) for each of the validation stands in Krycklan. The height difference Δh increases with increasing forest height (2–3 m in 10-m-tall stands to 6–8 m in 25-m-tall stands), which points, as expected, to a larger height difference between the interferometric phase centers in higher stands than in lower. At the same time, with increasing forest height, the variance of the polarimetric distance increases due to the variation in density.

2) Traunstein Test Site: The corresponding plot for the Traunstein site, i.e., the maximum height difference Δh estimated from the dual-pol acquisition of January 2012 (see Table I), for each validation stand plotted against the corresponding LIDAR derived H100, is shown in Fig. 13. Also in this case Δh (and its variance) increases with increasing forest height: 2 m to 4 m for forest stands with heights between 10 m to 20 m up to 8 m to 10 m for stands of about 35 m.

3) Mawas Test Site: Finally, the maximum height difference Δh estimated for each validation stand plotted against the corresponding LIDAR-derived H100 for the Mawas site for all four available dual-pol acquisitions (see Table I) is shown in Fig. 14. Fig. 14(a) corresponds to the August acquisition in the dry season, Fig. 14(b) and (c) corresponds to the acquisition from December 13 and 24, 2011, and Fig. 14(d) corresponds to the acquisition from January 4, 2012, of the wet season.

Compared with the European test sites, the dependence of Δh on forest height was less pronounced in the Mawas case. The two forest classes (riverine forest = blue dots in Fig. 14 and peat swamp forest = red dots in Fig. 14) separated in the phase center height plots can be also separated in the Δh plots.

In the dry period (August acquisition), Δh is about 2 m for the lower forest parts ($<$ 10 m) and 3–4 m for the higher forest parts ($>$ 20 m). In the rainy season (December and January acquisitions), Δh increases for all forest heights by approximately 1 m: Δh is now about 3 m for the lower forest parts and 4–5 m for the higher forest parts. Δh is stable for all three acquisitions in the rainy season (i.e., the two in December and the one in January). Compared with the European test sites (Krycklan and Traunstein), Mawas is characterized by smaller Δh levels, particularly for the taller forest fractions.

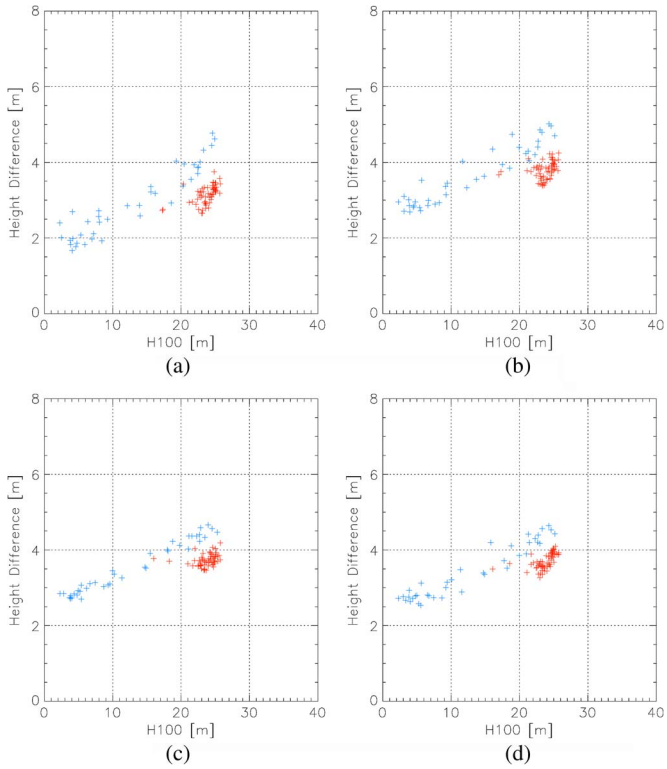

Fig. 14. Mawas test site validation plots: polarimetric phase height difference Δh versus LIDAR forest height. (a) August 25, 2011. (b) December 13, 2011. (c) December 24, 2012. (d) January 4, 2012. (Blue dots) Riverine forest (Red dots) Peat swamp forest.

V. Data Inversion

Having established the two main preconditions, i.e., sufficient penetration into the forest volume and the polarimetric diversity of the interferometric coherence measurements over all test sites, the inversion of Pol-InSAR TDX data is discussed here. In forest Pol-InSAR applications, the volume decorrelation contribution of the interferometric coherence $\tilde{\gamma}_{\mathrm{Vol}}(\kappa_Z \vec{w})$ measured at a given spatial baseline κ_Z and at a given polarization $\vec{w}$ can be modeled in terms of a two-layer model, the so-called random volume over ground (RVoG) model. Accordingly, the RVoG model consists of a polarization-independent vertical distribution of scatterers $f_V(z)$ that accounts for the forest canopy (scattering and propagation) contribution and a Dirac-like component $m_G(\vec{w})\delta(z - z_0)$ that accounts for the direct and dihedral (scattering) contribution(s) of the underlying ground [1]–[3], [34]. For monostatic configurations

$$\tilde{\gamma}_{\mathrm{Vol}}(\kappa_Z, \vec{w}) = \exp(i\varphi_0)\frac{\tilde{\gamma}_V(\kappa_Z) + m(\vec{w})}{1 + m(\vec{w})} \tag{4}$$

with

$$\tilde{\gamma}_V(\kappa_Z) = \frac{\int_0^{h_v} f_V(z)\exp(i\kappa_Z z')dz'}{\int_0^{h_v} f_V(z)dz'}$$

where h_V is the top height of the forest volume corresponding to the forest top height H100, $\varphi_0 = \kappa_Z z_0$ is the phase related to the ground topography z_0, and $m(\vec{w}) = m_G(\vec{w})/\int_0^{h_v} f_V(z)dz'$ is the effective ground-to-volume amplitude ratio. In the case of bistatic configurations, the direct and dihedral

contributions of the underlying ground are no longer equivalent [1], [35]: While the direct ground contribution remains deterministic (i.e., associated to a coherence that, after range spectral filtering, is equal to 1), the dihedral contribution becomes distributed in height and thus affected by volume decorrelation

$$\tilde{\gamma}_{\mathrm{Vol}}(\kappa_Z,\vec{w}) = \exp(i\varphi_0)\frac{\tilde{\gamma}_V(\kappa_Z)+m_S(\vec{w})+m_D(\vec{w})\frac{\sin(\kappa_Z h_v)}{(\kappa_Z h_v)}}{1+m_S(\vec{w})+m_D(\vec{w})} \tag{5}$$

where m_S is the direct ground (surface) contribution, and m_D is the dihedral scattering contribution. However, the small bistatic angle of TanDEM-X combined with the rather low dihedral scattering contributions at X-band (when compared with lower frequencies) legitimatizes the use of (4) instead of (5).

Different parameterizations of the vertical distribution of scatterers in the vegetation layer $f_V(z)$ have been proposed and used in literature. A widely and very successfully used approach—particularly at higher frequencies—is to assume an exponential distribution of scatterers [4], [6], [7], [12], i.e.,

$$f_V(z) = \exp\left(2\sigma z/\cos(\theta_0)\right) \tag{6}$$

where σ describes the shape of the vertical distribution of scatterers, but it can be also interpreted as a mean extinction value that defines the attenuation rate of the vegetation layer. The high attenuation regime at X-band allows both interpretations, making the validation of σ ambiguous, particularly at the rather high spatial resolution scale of the TanDEM-X data.

The challenge now is the estimation of forest height h_V or other associated structure parameters used to parameterize $f_V(z)$ from $\tilde{\gamma}_{\mathrm{Vol}}(\kappa_Z,\vec{w})$ measurements at different polarizations and (spatial) baselines by means of (4). The achieved performance critically depends on two steps. The first step is the estimation of the volume decorrelation contribution $\tilde{\gamma}_{\mathrm{Vol}}(\kappa_Z,\vec{w})$ from the overall measured interferometric coherence by compensating for all other (nonvolumetric) decorrelation contributions. The second step is to establish a balanced and well-conditioned inversion problem based on the available observation space, introducing—if required—additional assumptions and/or external information. Both steps for the TDX case will be discussed in the next sections.

A. Coherence Calibration

A detailed overview of the relevant decorrelation contributions occurring in the case of TDX is provided in [20]. In the bistatic TDX mode, after range spectral filtering [36], the main nonvolumetric decorrelation contribution that has to be compensated is the additive noise decorrelation γ_{SNR}. The standard TDX data products [22] contain the noise equivalent sigma zero (NESZ) patterns for each channel in the form of a set of polynomial coefficients for one range line. Every $\sim$1.5- to $\sim$2-s azimuth time (acquisition dependent), a new set of polynomial coefficients is provided. They depend on the beam used for the acquisitions, the polarization, and the satellite. Fig. 15 shows an example of the NESZ pattern for the beam strip_008 at HH and VV polarizations for TDX and TSX (from the Krycklan monostatic acquisition on July 28, 2010). TDX has, in near and far ranges [~ -22 dB; see Fig. 15(a) and (b)], about 1 dB lower noise level than TSX [~ -21 dB; see Fig. 15(c) and (d)]. The difference in midrange is below $\sim$0.5 dB. The noise level of TDX in HH polarization is nearly identical with the noise level in VV polarization [see Fig. 15(a) and (b)]. In case of TSX, the noise level in midrange is about 0.3 dB lower in the HH channel [$\sim$24.5 dB; see Fig. 15(c)] than in the VV channel [-24.2 dB; see Fig. 15(d)].

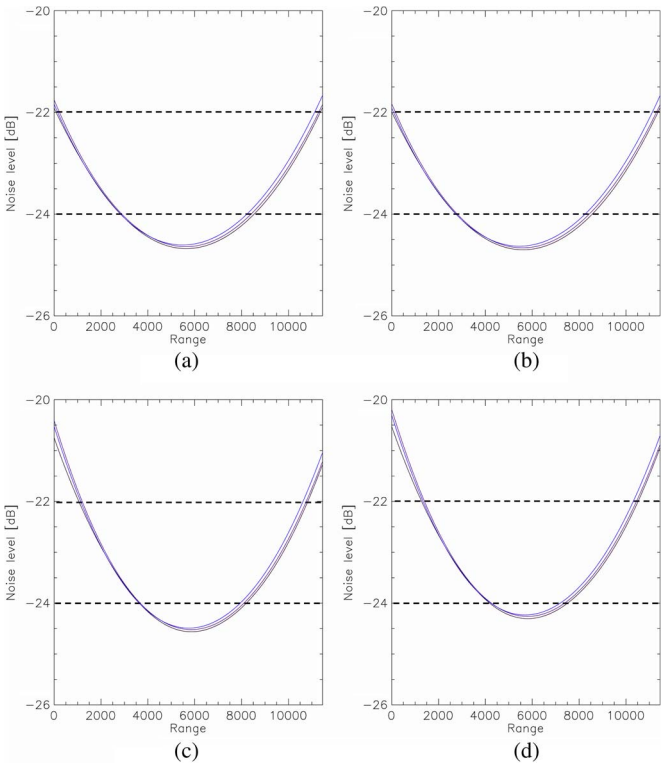

Fig. 15. Noise pattern for both polarizations of both satellites: five measurements along azimuth per channel (example monostatic acquisition over Krycklan on July 28, 2010, beam strip_008). (a) TDX HH polarization. (b) TDX VV polarization. (c) TSX HH polarization. (d) TSX VV polarization.

For each channel, the signal-to-noise ratio (SNR) can be calculated by using the corresponding NESZ pattern and estimating the backscattering coefficient sigma nought σ_0, i.e.,

$$\mathrm{SNR}^{\mathrm{Pol\ Sat}} = \frac{\sigma_0^{\mathrm{Pol\ Sat}} - \mathrm{NESZ}^{\mathrm{Pol\ Sat}}}{\mathrm{NESZ}^{\mathrm{Pol\ Sat}}} \tag{7}$$

where Pol indicates the polarization channel, and Sat is TDX or TSX. The SNR-induced decorrelation in the corresponding TDX interferogram is then obtained as [33]

$$\gamma_{\mathrm{SNR}}^{\mathrm{Pol}} = \frac{1}{\sqrt{\left(1+\frac{1}{\mathrm{SNR}^{\mathrm{Pol\ TSX}}}\right)\left(1+\frac{1}{\mathrm{SNR}^{\mathrm{Pol\ TDX}}}\right)}} \tag{8}$$

and is used to calibrate the interferometric coherence: $\tilde{\gamma}_{\mathrm{Vol}}(\kappa_Z, \mathrm{Pol}) = \tilde{\gamma}(\kappa_Z, \mathrm{Pol})/\gamma_{\mathrm{SNR}}^{\mathrm{Pol}}$. Fig. 16(a) and (c) shows the histograms of the obtained $\gamma_{\mathrm{SNR}}^{\mathrm{Pol}}$ for the HH and VV polarizations, and Fig. 16(b) and (d) shows the histograms of the interferometric coherence before (red) and after (blue) correcting for $\gamma_{\mathrm{SNR}}^{\mathrm{Pol}}$ for the Krycklan monostatic acquisition (July 28, 2010).

The mean noise decorrelation is about 0.95 for the HH channel and 0.93 for the VV channel and needs to be corrected

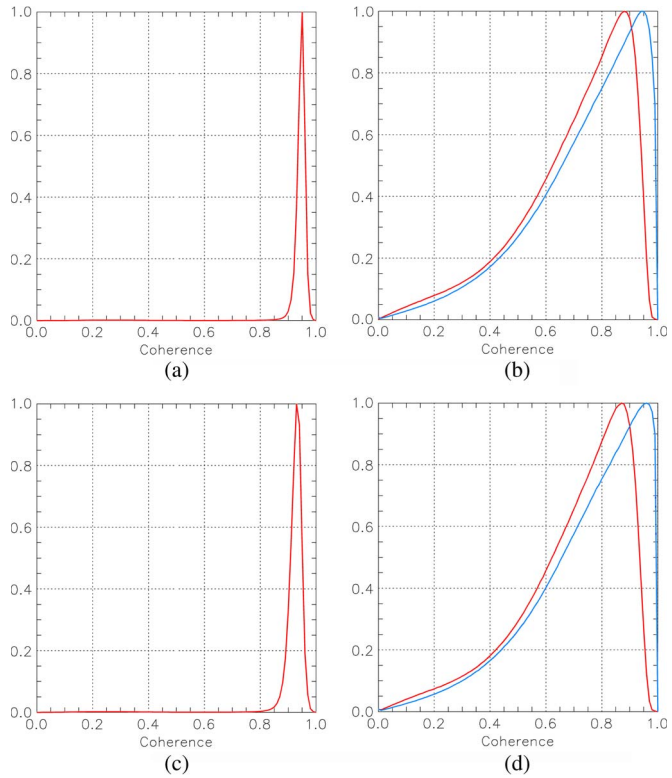

Fig. 16. Noise decorrelation (example monostatic acquisition over Krycklan on July 28, 2010). (a) Histograms of noise decorrelation $\boldsymbol{\gamma}_{\boldsymbol{SNR}}^{\mathrm{HH}}$. (b) Histograms of the interferometric coherence before (red) and after (blue) $\boldsymbol{\gamma}_{\boldsymbol{SNR}}^{\mathrm{HH}}$ correction in HH polarization. (c) Histograms of noise decorrelation $\boldsymbol{\gamma}_{\boldsymbol{SNR}}^{\mathrm{VV}}$. (d) Histograms of the interferometric coherence before (red) and after (blue) $\boldsymbol{\gamma}_{\boldsymbol{SNR}}^{\mathrm{VV}}$ correction in VV polarization.

for a successful Pol-InSAR height inversion [10]. After $\gamma_{\mathrm{SNR}}^{\mathrm{Pol}}$ compensation, the interferometric coherences are ready to be used for inversion.

B. Dual-Pol Inversion

In the case of a dual-polarimetric TDX acquisition, the parameterization of the two interferometric coherences in terms of (4) requires five parameters: the forest height h_V, the extinction σ, the ground topography phase φ_0, and the two ground-to-volume amplitude ratios $m(\vec{w})$, one for each polarization. A balanced inversion problem can be achieved by assuming a zero ground-to-volume amplitude ratio for at least one polarization [3], [4]. In order to estimate the interferometric coherence with the minimum ground contribution $\tilde{\gamma}(\kappa_Z, \vec{w}_{\min})$, the assumption that the coherence region of the RVoG model is a straight line along the ground-to-volume amplitude ratio $m(\vec{w})$ is used. The 2-D coherence region is calculated, and the two extreme interferometric coherences $\tilde{\gamma}(\kappa_Z, \vec{w}_{\max})$ and $\tilde{\gamma}(\kappa_Z, \vec{w}_{\min})$ are estimated—associated to the polarization states $\vec{w}_{\max}$ and $\vec{w}_{\min}$ characterized by the maximum and minimum ground contributions—and are then used for inversion assuming $m(\vec{w}_{\min}) = 0$, i.e.,

$$\min_{h_v,\sigma,m,\varphi_0} \left\| \begin{bmatrix} \tilde{\gamma}(\kappa_Z, \vec{w}_{\max}) e^{-i\varphi_0} \\ \tilde{\gamma}(\kappa_Z, \vec{w}_{\min}) e^{-i\varphi_0} \end{bmatrix} - \begin{bmatrix} \tilde{\gamma}_V(\kappa_Z, h_V, \sigma, m) \\ \tilde{\gamma}_V(\kappa_Z, h_V, \sigma, m=0) \end{bmatrix} \right\|. \quad (9)$$

The phase $\exp(i\varphi_0)$ corresponding to the ground topography is obtained by the intersection of the line defined by $\tilde{\gamma}(\kappa_Z, \vec{w}_{\min})$ and $\tilde{\gamma}(\kappa_Z, \vec{w}_{\max})$ and the unit circle moving from $\tilde{\gamma}(\kappa_Z, \vec{w}_{\min})$ to $\tilde{\gamma}(\kappa_Z, \vec{w}_{\max})$ [1], [4], i.e.,

$$\varphi_0 = \arg\left\{\tilde{\gamma}(\kappa_Z, \vec{w}_{\max}) - \tilde{\gamma}(\kappa_Z, \vec{w}_{\min})(1-F)\right\} \quad (10)$$

with $F = (-B - \sqrt{B^2 - 4AC})/(2A)$, coefficient $A = |\tilde{\gamma}(\kappa_Z, \vec{w}_{\min})|^2 - 1$, coefficient $B = 2\mathrm{Re}\{[\tilde{\gamma}(\kappa_Z, \vec{w}_{\max}) - \tilde{\gamma}(\kappa_Z, \vec{w}_{\min})] \tilde{\gamma}^*(\kappa_Z, \vec{w}_{\min})\}$, and coefficient $C = |\tilde{\gamma}(\kappa_Z, \vec{w}_{\max}) - \tilde{\gamma}(\kappa_Z, \vec{w}_{\min})|^2$.

C. Single-Pol Inversion

The standard DEM mode of TDX is, however, a single-pol mode operated in HH (or VV) polarization. In the case of a single-polarimetric acquisition, the parameterization of the measured interferometric coherence in terms of (4) requires four parameters: the forest height h_V, the extinction σ, the ground topography phase φ_0, and the ground-to-volume amplitude ratio $m(\vec{w})$. The assumption of no ground contribution, i.e., of zero ground-to-volume amplitude ratio, is not sufficient for getting a balanced inversion problem. In this case, inversion relies on additional assumptions or the availability of external information. Fixing the extinction σ has been proved to compromise the inversion performance as it restricts the ability of the RVoG model to interpret the spatial variability of forest structure.

The best—with respect to inversion performance—scenario is to use an external DTM to estimate the ground topographic phase $\exp(i\varphi_0)$. For this, the DTM is converted to phase: $\exp(i\varphi_{\mathrm{DTM}}) = \exp(i\, h_{\mathrm{DTM}}\, \kappa_Z)$. Then, the phase offset between $\exp(i\varphi_{\mathrm{DTM}})$ and $\gamma(\kappa_Z, \vec{w}_i)$ is calibrated by means of a corner reflector or a bare area with sufficient high coherence $|\tilde{\gamma}(\kappa_Z, \vec{w}_i)| > 0.98$. $\tilde{\gamma}(\kappa_Z, \vec{w}_i)$ can then be inverted for forest height h_V and extinction σ by

$$\min_{h_v,\sigma} \left\| \tilde{\gamma}(\kappa_Z, \vec{w}_i) \exp(-i\varphi_0) - \tilde{\gamma}_V(\kappa_Z, h_V, \sigma) \right\|. \quad (11)$$

For all test sites, a DTM calculated from LIDAR data was used to estimate $\exp(i\varphi_0)$.

VI. Inversion Results

The two inversion scenarios were implemented and applied on all three sites. The obtained forest height maps for both cases and the reference LIDAR-derived H100 maps are shown in Fig. 18 for the Krycklan site, in Fig. 20 for the Traunstein site, and in Figs. 24 and 25 for the Mawas site.

In the single-pol case, for all test sites, in approximately 10%–15% of the samples, the inversion failed to provide a solution, probably due to a too large ground scattering contribution. Furthermore, noninvertible samples turned up in areas of low backscattering and high γ_{SNR}, where coherence estimates become imprecise. This mainly appeared in areas with "shadow" effects, i.e., on forest edges and on the transition from low forest to high forest areas.

In addition to the inversion problems found in the single-pol case, in the dual-pol case, the inversion performance critically depends on the difference between the phase center locations

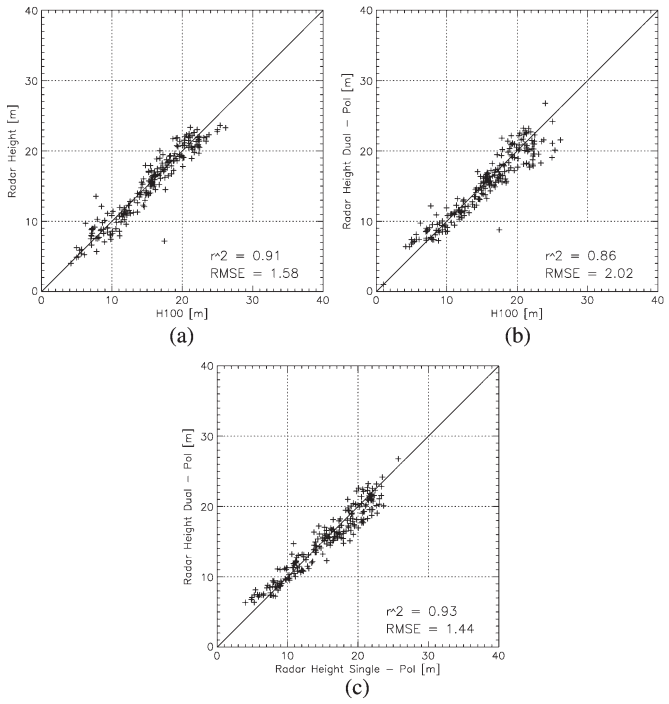

Fig. 17. Krycklan test site validation plots. (a) Single-pol inversion forest height versus LIDAR forest height. (b) Dual-pol inversion forest height versus LIDAR forest height. (c) Comparison of single-pol inversion forest height versus dual-pol inversion forest height.

in the two polarizations. In all three sites, about 20% of the samples (pixels) could not be inverted—probably because of an insufficient strong or an insufficient different ground contribution across the polarizations—making a solution of the inversion problem impossible.

Noninvertible samples were masked out and have not been considered in the cross validation.

A. Krycklan Test Site

1) Single-Pol Inversion: The low phase center height locations and the large polarimetric distances (see Figs. 6 and 12) predicted a good forest height inversion performance for the Krycklan site.

As the ground contribution in the VV channel appeared to be less than in the HH channel (see discussion in Section IV-A1), the VV channel was used for the single-baseline inversion. The validation plot for the single-pol inversion shown in Fig. 17(a) is characterized by a correlation coefficient $r^2 = 0.91$ with a root-mean-square error RMSE $= 1.58$ m. One single stand was clearly underestimated (LIDAR H100 $= 18$ m, single-pol inversion height $= 7$ m)—probably affected by harvesting activities in the two years occurring between the LIDAR measurements and the TDX acquisitions. Excluding this outlier, the correlation coefficient increases to 0.93.

2) Dual-Pol Inversion: The validation plot for the dual-pol inversion is shown in Fig. 17(b).

Compared with the single-pol inversion, the validation for dual-pol inversion was noisier, particularly for the taller forest stands, but the overall correlation coefficient $r^2 = 0.86$ and an RMSE of 2.02 m are convincing.

The same single stand that strongly deviated in the single-pol inversion validation also deviated here (LIDAR H100 $= 18$ m, dual-pol inversion height $= 8$ m). Again excluding this outlier, the correlation coefficient becomes 0.90.

In Fig. 17(c), the single-pol inversion forest heights were plotted against the dual-pol inversion forest heights. A correlation coefficient $r^2 = 0.93$ in combination with an RMSE of 1.44 m underlines the consistency of the results obtained by the two approaches. In the direct comparison, the outlier stand disappeared as expected. The performance starts to degrade (in the form of an increased variance) in the region of taller forest heights in part as a consequence of the low coherence levels induced by the large vertical wavenumber ($\kappa_Z = 0.17$).

The topographic variation within the scene has limited the final inversion performance due to the slope-induced modulation of the vertical wavenumber: κ_Z reached the maximum and minimum values for strong positive and negative slopes for which a meaningful inversion was not possible. As the forest height reaches 30 m ($\kappa_Z = \sim 0.2$ rad/m for an HoA of 30 m), κ_Z values larger than 0.2 rad/m were excluded from the inversion to guarantee an unambiguous inversion. A minimum threshold for κ_Z was not necessary as all κ_Z values in the scene are larger than 0.09 rad/m (full inversion performance is granted [10]). (The Krycklan site forest height maps are presented in Fig. 18.)

B. Traunstein Test Site

1) Single-Pol Inversion: For the Traunstein site, the single-pol inversion was applied using the HH and VV polarizations. The corresponding validation plots are shown in Fig. 19(a) for the HH polarization case and in Fig. 19(b) for the VV polarization case.

Forest heights up to 30 m have, in both cases, been accurately estimated; beyond 30 m, the performance degraded mainly because of the low coherence level. For the HH polarization, a correlation coefficient of 0.80 with an RMSE of 3.3 m has been achieved. For the VV channel, a correlation coefficient of 0.80 with an RMSE of 3.7 m has been reached. In the absence of a second appropriate TDX acquisition and in order to assess the seasonal effect on the inversion performance as the available data set was acquired in the winter in snow-covered conditions, an airborne acquisition was utilized (see Table I).

The airborne inversion performance for the VV channel is shown on the bottom left in Fig. 19(c), which is characterized by a similar performance as achieved with the TDX data (winter) set: a correlation coefficient of 0.89 with an RMSE of 2.3 m. Large stands are underestimated because the vertical wavenumber κ_Z is too large in some parts of the image to cover the whole height range of the prevailing forest heights (typical for airborne scenarios).

2) Dual-Pol Inversion: The dual-pol inversion results for Traunstein are shown in the plot in Fig. 19(d). The correlation of the LIDAR with the dual-pol inversion results is noisier ($r^2 = 0.77$). The RMSE is 2.8 m, clearly lower than for the single-pol inversion. Similar to the single-pol case, the inversion performance degrades for stands larger than 30 m. (The Traunstein test site forest height maps are presented in Fig. 20.)

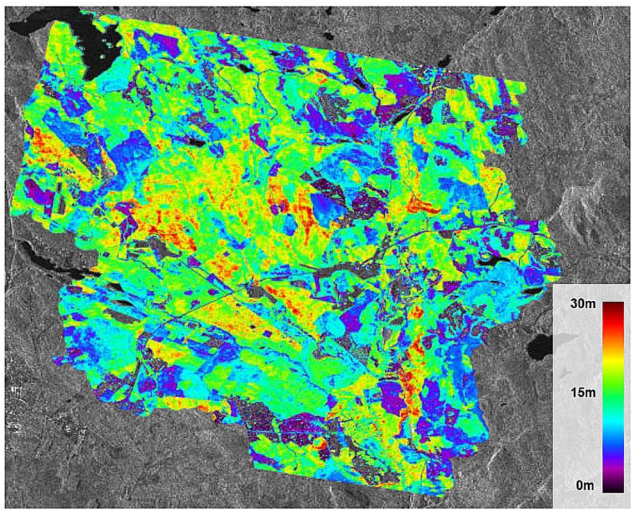

(a)

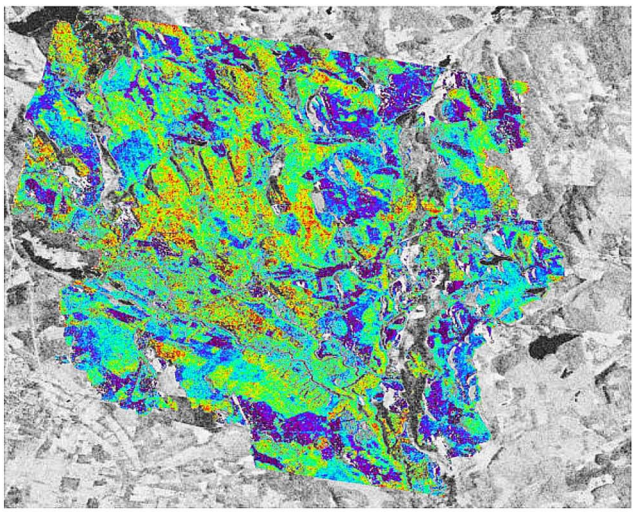

(b)

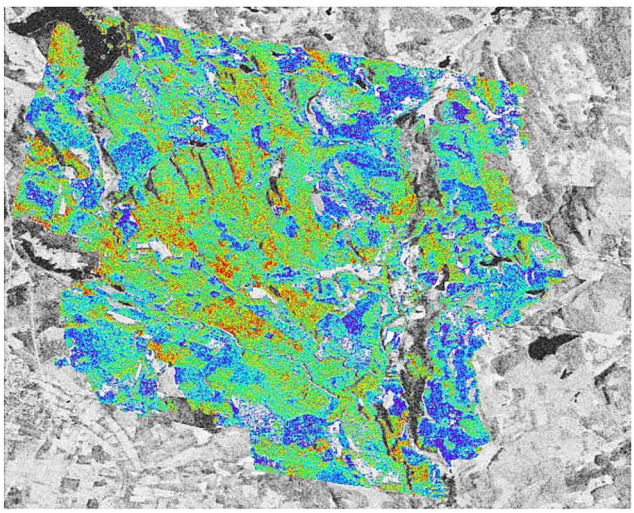

(c)

Fig. 18. Krycklan test site forest height maps. (a) LIDAR H100 superimposed on radar amplitude image. (b) Single-pol inversion forest heights (VV) superimposed on interferometric coherence scaled from 0 (black) to 1 (white). (c) Dual-pol inversion forest heights superimposed on interferometric coherence scaled from 0 (black) to 1 (white).

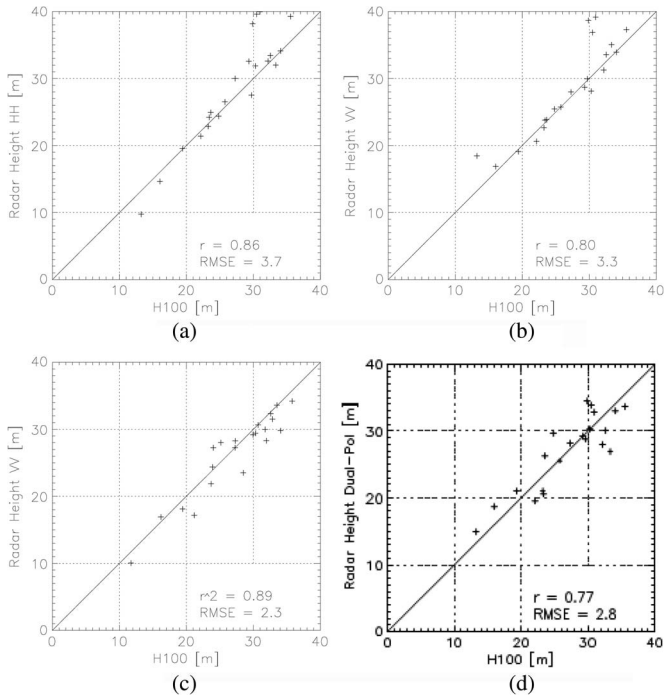

Fig. 19. Traunstein test site validation plots. (a) TDX single-pol inversion forest height HH polarization versus LIDAR forest height. (b) TDX single-pol inversion VV polarization versus LIDAR forest height. (c) E-SAR airborne single-pol inversion forest height VV polarization versus LIDAR forest height. (d) TDX dual-pol inversion forest height versus LIDAR forest height.

C. Mawas Test Site

1) Single-Pol Inversion: The single-pol inversion was applied on all four available Mawas acquisitions using the HH and VV polarizations. The corresponding validation plots are shown in Figs. 21 and 22 (riverine forest = blue dots, peat swamp forest = red dots). As already indicated by the phase center height plots, no significant differences between the HH and VV polarization were expected.

The acquisition in the dry season (August 25) clearly underestimated the forest height with an RMSE of 3.3 m. This was probably caused by the insufficiency of the inversion model to fit the actual situation. At the end of the dry season, tree tops are dried out, and the leaves have sometimes fallen off. The open canopy consisting of single trees with dried out tree tops and partially bare branches at the end of the dry season could have caused scattering from the tree crowns to be less pronounced and could have violated the assumption of an exponential backscatter function as used in the inversion model; in addition, the presence of a ground scattering contribution in all polarizations available cannot be excluded, particularly in the dry season.

With the beginning of the rainy season, forest height estimates are clearly improved and reach RMSE levels down to 2.2 m for the HH channel and 1.9 m for the VV channel. The correlation coefficients are, for all acquisitions, very high, with values between 0.97 and 0.98.

2) Dual-Pol Inversion: The validation plots for all four acquisition dates are shown in Fig. 23.

The two forest types, i.e., the riverine forest (blue dots in Fig. 23) and the peat swamp forest (red dots in Fig. 23), has

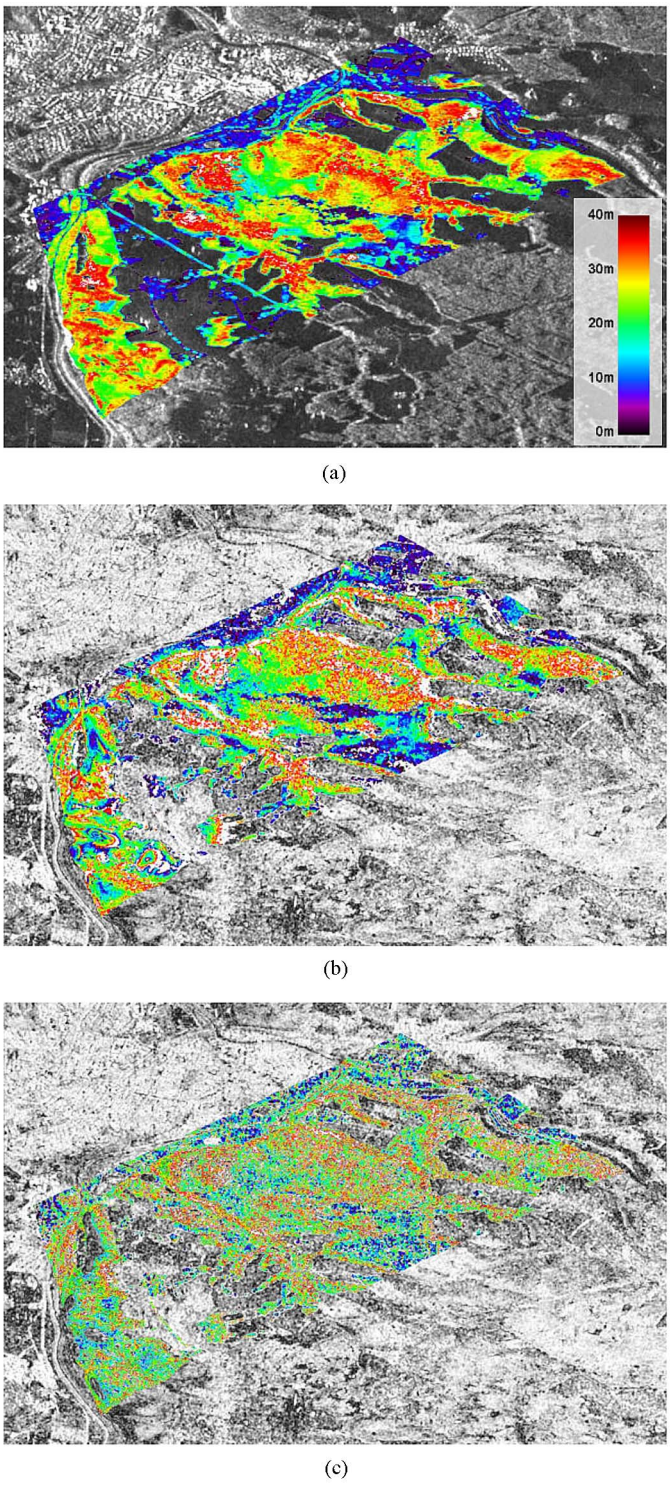

Fig. 20. Traunstein test site forest height maps. (a) LIDAR H100 superimposed on radar amplitude image. (b) Single-pol inversion forest heights (VV) superimposed on interferometric coherence scaled from 0 (black) to 1 (white). (c) Dual-pol inversion forest heights superimposed on interferometric coherence scaled from 0 (black) to 1 (white).

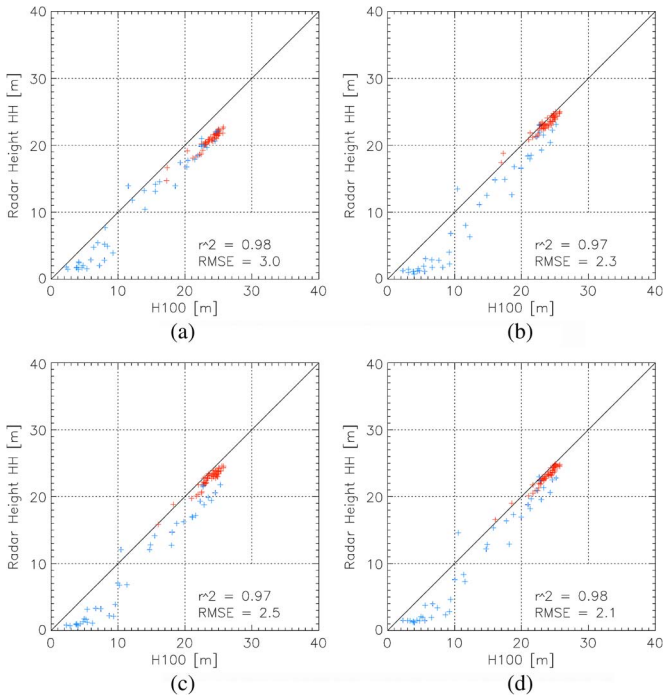

Fig. 21. Mawas test site validation plots: single-pol inversion forest height versus LIDAR forest height in HH polarization. (a) August 25, 2011. (b) December 13, 2011. (c) December 24, 2011. (d) January 4, 2012. (Blue dots) Riverine forest. (Red dots) Peat swamp forest.

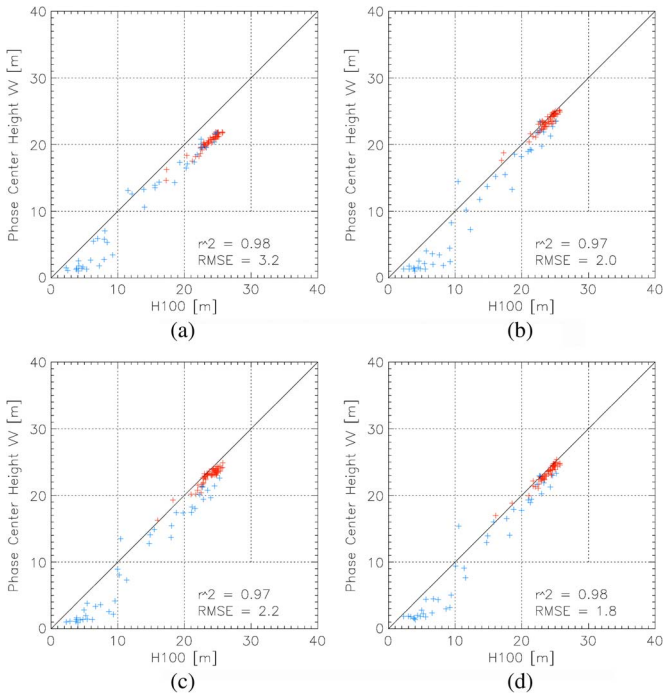

Fig. 22. Mawas test site validation plots: single-pol inversion forest height versus LIDAR forest height in VV polarization. (a) August 25, 2011. (b) December 13, 2011. (c) December 24, 2011. (d) January 4, 2012. (Blue dots) Riverine forest. (Red dots) Peat swamp forest.

each shown different behaviors: The estimates of the riverine forest are approximately 5 m higher than the estimates of the peat swamp forest.

The dual-pol inversion performed worse compared with the single-pol inversion for the Mawas site. Even in the dry season acquisition (August 25, 2011), low forests heights were overestimated, but tall forests stands (the peat swamp forest) were underestimated. With the beginning of the rainy season, all estimates increase by 4 m–5 m. Now, all riverine forest stands

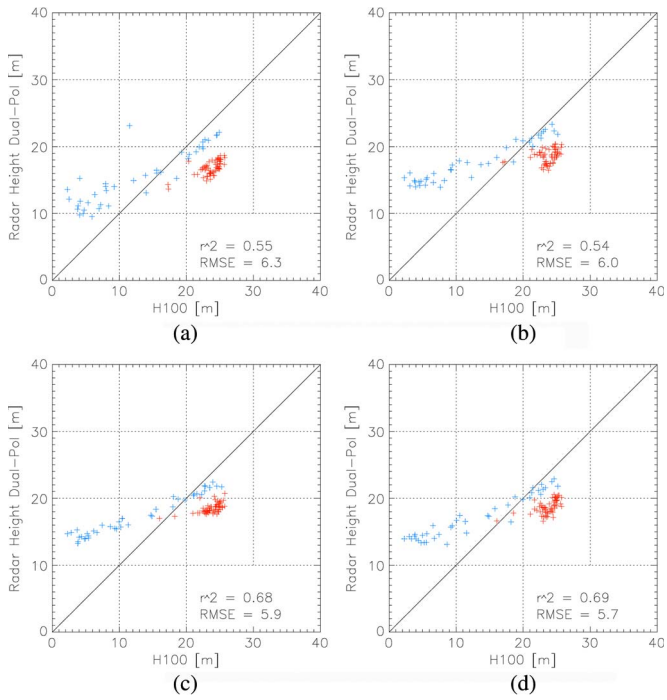

Fig. 23. Mawas test site validation plots: dual-pol inversion. (a) August 25, 2011. (b) December 13, 2011. (c) December 24, 2011. (d) January 4, 2012. (Blue dots) Riverine forest. (Red dots) Peat swamp forest.

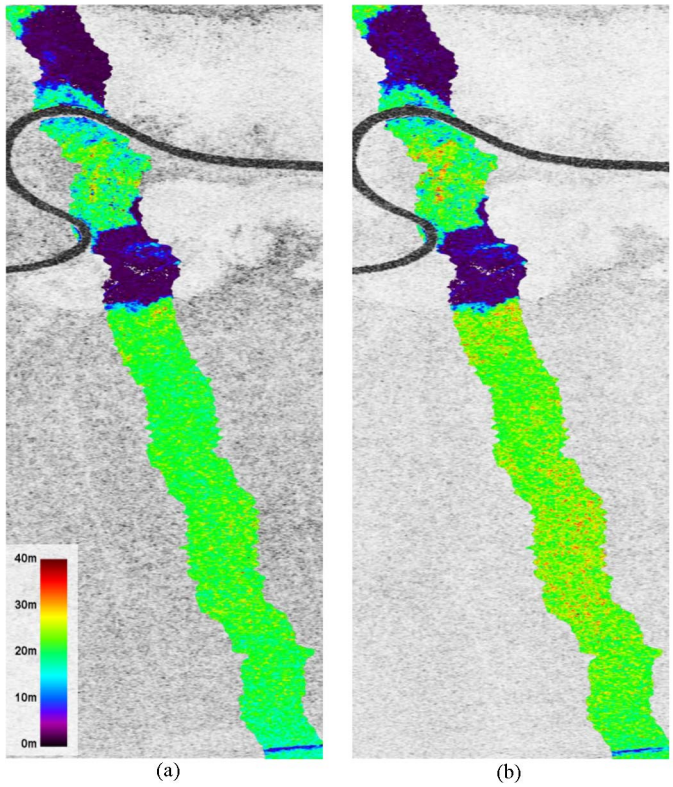

Fig. 24. Mawas test site forest heights maps (bottom: near range, top: far range). (a) Interferometric coherence scaled from 0 (black) to 1 (white) superimposed by single-pol inversion forest heights in HH polarization from the acquisition of August 25, 2011. (b) Interferometric coherence scaled from (black) 0 to (white) 1 superimposed by single-pol inversion forest heights in VV polarization from the acquisition of January 4, 2012.

were overestimated, and the peat swamp forest stands were still underestimated.

There were no significant improvements of the result for the last two acquisitions of the rainy season. The poor performance is caused by two reasons: The overestimation of the lower height ranges of the riverine forest is primarily induced by the small vertical wavenumber that is insufficient to compensate the impact of residual nonvolumetric decorrelation contributions [10]. With increasing forest height, the impact of the residual nonvolumetric decorrelation contributions becomes smaller, and the estimates of the taller riverine forest stands are unbiased. This error source may be compensated by using larger spatial baselines (i.e., larger vertical wavenumbers). Indeed, the overestimation is stronger in the rainy season acquisitions acquired with a vertical wavenumber of 0.07 rad/m and weaker for the dry season acquisition acquired with a slightly larger vertical wavenumber of 0.12 rad/m. In the Krycklan site, the large(r) vertical wavenumber of 0.17 rad/m allows the unbiased estimation of low forest heights, as shown in Fig. 17.

The underestimation of the peat-swamp forest is more difficult to interpret. It was probably induced by the used inversion model, which failed to reflect the right vertical scattering distribution.

The single emergent tree over a less dense canopy with extensive undergrowth violates the assumption of an exponential backscatter function with zero ground and leads to an underestimation of height [37]. Note that both errors were, by far, less important in the single-pol inversion (comparison with Figs. 21 and 22). The ground location information implied by the use of the external DEM allowed for the compensation of a wide range of estimation biases. (The Mawas site forest height maps are presented in Figs. 24 and 25.)

VII. Conclusion

In this paper, the potential of TDX Pol-InSAR data for quantitative forest parameter estimation has been investigated. For this, a large number of single- and dual-pol TDX data sets acquired over three different forest sites—a boreal, a temperate, and a tropical site—at different acquisition modes have been analyzed.

The suitability of TDX for Pol-InSAR forest applications depends on the penetration capability of X-band into forest vegetation and on the polarimetric diversity of the interferometric coherence. Both effects were evaluated over all three sites for different acquisition geometries (i.e., on the incidence angle and spatial baseline) and for different environmental and seasonal conditions.

For all sites, a strong correlation between the (height of the) phase center location and forest (top) height could be established. The corresponding correlation coefficients reached values of 0.9 and higher. The correlation varies with seasonal and environmental changes. Clear seasonal dependence could be observed between summer and winter acquisitions at the European test sites. For the tropical site, the difference between wet and dry seasons was weaker.

For the Krycklan site, acquisitions at different look angles (19° and 32°) were analyzed, indicating only a weak effect of the incidence angle on the penetration. For the Traunstein site, impact of incidence (look) angle appeared stronger than at the Krycklan site. However, here, differences in phase center

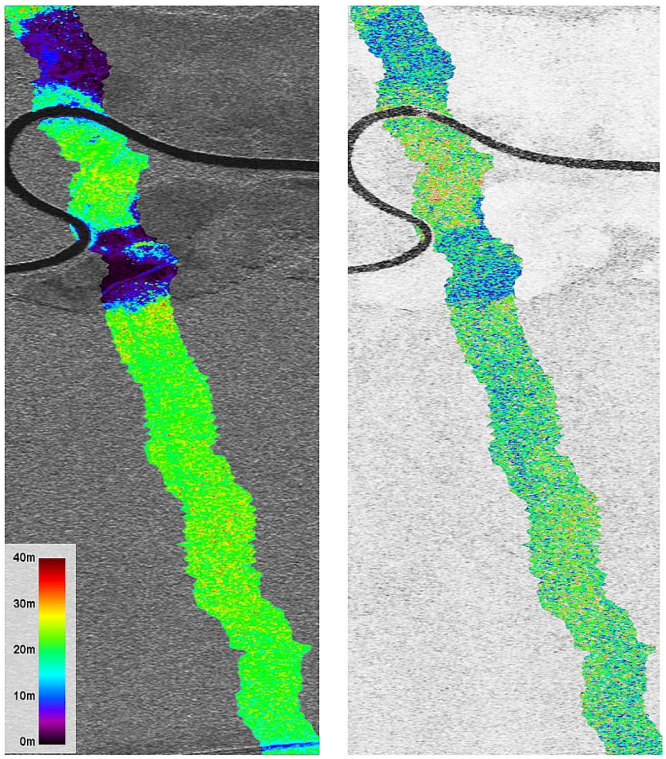

Fig. 25. Mawas test site forest heights maps (bottom: near range, top: far range). (a) Radar amplitude image in HH polarization superimposed by LIDAR H100. (b) Interferometric coherence scaled from 0 (black) to 1 (white) superimposed by dual-pol forest heights from the acquisition of January 4, 2012.

height due to different incidence (look) angles are mixed up with seasonal effects.

The synthesis of the results suggests an unexpected high penetration at X-band but leaves open the question of whether the penetration is induced by the propagation through the vegetation volume or partially through gaps in the vegetation layer that become relevant at the spatial resolution of the TDX data [38].

The polarimetric dependence of the interferometric coherence (expressed by means of the length of the dual-pol coherence region) was strongly correlated to forest height in all sites. At the same time, the effect of seasonal and environmental variability was clearly visible: For the boreal site, the penetration during the winter can be interpreted only with a sufficient large ground scattering contribution that makes an inversion based on the assumption of a "zero ground component" suboptimal.

The summer acquisitions were characterized by a smaller ground contribution supporting "zero ground component" inversion schemes. For the temperate site, the winter acquisitions seemed to be better suited for inversion than the summer acquisitions as penetration was higher and the whole volume is "seen" by the radar (due to the lower attenuation in winter). In the tropical case, the impact of seasonal effects on the polarimetric diversity was rather small. This allows concluding that seasonal adapted acquisitions could improve the inversion performance and probably increase the number of forest types that can be investigated by means of Pol-InSAR techniques at X-band.

Based on these observations, two forest height estimation approaches—one for the single-pol case based on the availability of an external DTM and one for the dual-pol case that does not require any *a priori* knowledge—have been proposed, implemented, and applied on the available data sets. The obtained height estimates have been cross validated against LIDAR reference measurements.

In forest conditions that allow a sufficient penetration at X-band, the performance of the two approaches was comparable and surprisingly high, with a correlation of $r^2 = 0.86$ in the boreal site and $r^2 = 0.77$ in the temperate site for the dual-pol case. At denser conditions, the variance of the dual-pol estimates increased ($r^2 = \sim 0.50$ in the tropical site) and finally saturated with increasing height due to the insufficient penetration. Note that the single-pol inversion was not affected by saturation as it does not require a penetration until the ground.

The choice of spatial baseline (expressed in terms of the vertical wavenumber) has a critical impact on the inversion performance. Too small spatial baselines limit the sensitivity to forest height variation and/or increase the errors induced by uncompensated nonvolumetric decorrelation contributions [10]. Too large baselines lead to (too) low coherence levels and limit the range of heights that can be mapped. The fact that TDX (as discussed in Section II-B) follows predefined vertical wavenumber cycles that are optimized with respect to the DEM acquisition strategy restricts the availability of optimum vertical wavenumber regimes for forest parameter estimation. However, the selection of a more appropriate beam (i.e., look angle) provides one degree of freedom to partially optimize the given spatial baseline configuration.

Regarding now the choice of polarization, the TDX and TSX instruments allow the acquisition not only of conventional cross-polarized dual-pol data (i.e., HH and VH or VV and HV) but also copolarized dual-pol data (i.e., HH and VV). The relative small ground scattering contributions at X-band compared with the high additive noise level at the cross-polarized channels (with a noise equivalent sigma zero NESZ on the order of 20–24 dB; see Fig. 15) make the copolarized dual-pol mode better suited (in terms of performance) for Pol-InSAR applications [34], [39].

The availability of quad-pol acquisitions—acquired in a later dedicated quad-pol operation phase—can improve the performance in terms of variance and reduce the number of samples with nonvalid solutions. However, the constraints imposed by the penetration depth and the low NESZ will remain. Finally, the inversion of multiple acquisitions acquired with different spatial baselines may be an alternative way to improve inversion performance. In this case, in addition to the inherent limitation of penetration into dense(r) forest conditions, the variability of the forest structure in the time between the acquisitions has to be accounted. An exception is the alternating bistatic mode, but this mode is limited to two baselines in a single polarization.

Finally, the achieved performance clearly indicates the advantage of a spaceborne single-pass interferometric implementation for forest applications. The absence of temporal decorrelation allows the achievement of a new quality in measurement accuracy that may allow the development of new applications and make systematic monitoring of forest structure parameters—preferably at a lower frequency band—possible.

ACKNOWLEDGMENT

The authors would like to thank the TDX team for the fast access to the data and C. Wecklich for his valuable comments to improve the quality of this paper. They would also like to thank P. Prats for his support in data processing issues and V. Böhm from KALTENG Consultants for providing the LIDAR data over Mawas.

REFERENCES

[1] S. R. Cloude, *Polarisation Applications in Remote Sensing*. London, U.K.: Oxford Univ. Press, 2010.

[2] S. R. Cloude and K. P. Papathanassiou, "Polarimetric SAR interferometry," *IEEE Trans. Geosci. Remote Sens.*, vol. 36, no. 5, pp. 1551–1565, Sep. 1998.

[3] K. P. Papathanassiou and S. R. Cloude, "Single-baseline polarimetric SAR interferometry," *IEEE Trans. Geosci. Remote Sens.*, vol. 39, no. 11, pp. 2352–2363, Nov. 2001.

[4] R. N. Treuhaft, S. N. Madsen, M. Moghaddam, and J. J. van Zyl, "Vegetation characteristics and underlying topography from interferometric data," *Radio Sci.*, vol. 31, no. 6, pp. 1449–1495, Nov./Dec. 1996.

[5] I. Hajnsek, F. Kugler, S. Lee, and K. Papathanassiou, "Tropical forest parameter estimation by means of Pol-InSAR: The INDREX II campaign," *IEEE Trans. Geosci. Remote Sens.*, vol. 47, no. 2, pp. 481–493, Feb. 2009.

[6] J. Praks, F. Kugler, K. P. Papathanssiou, I. Hajnsek, and M. Hallikainen, "Tree height estimation for boreal forest by means of L and X band PolInSAR and HUTSCAT scatterometer," *IEEE Trans. Geosci. Remote Sens. Lett.*, vol. 4, no. 3, pp. 466–470, Jul. 2007.

[7] F. Garestier, P. C. Dubois-Fernandez, and K. P. Papathanassiou, "Pine forest height inversion using single-pass X-band PolInSAR data," *IEEE Trans. Geosci. Remote Sens.*, vol. 46, no. 1, pp. 56–68, Jan. 2008.

[8] J. Praks, O. Antropov, and M. T. Hallikainen, "LIDAR-aided SAR interferometry studies in boreal forest: Scattering phase center and extinction coefficient at X- and L-band," *IEEE Trans. Geosci. Remote Sens.*, vol. 50, no. 10, pp. 3831–3843, Oct. 2012.

[9] K. P. Papathanassiou and S. R. Cloude, "The effect of temporal decorrelation on the inversion of forest parameters from Pol-InSAR data," in *Proc. IGARSS*, Toulouse, France, 2003, pp. 1429–1431, [CD-ROM].

[10] S.-K. Lee, F. Kugler, K. Papathanassiou, and I. Hajnsek, "Quantification of temporal decorrelation effects at L-band for polarimetric SAR interferometry applications," *IEEE J. Sel. Top. Appl. Earth Obs. Remote Sens.*, vol. 6, no. 3, pp. 1351–1367, Jun. 2013.

[11] M. Lavalle, M. Simard, and S. Hensely, "A temporal decorrelation model for polarimetric radar interferometers," *IEEE Trans. Geosci. Remote Sens.*, vol. 50, no. 7, pp. 2880–2888, Jul. 2012.

[12] F. Kugler, S. Sauer, S.-K. Lee, K. Papathanassiou, and I. Hajnsek, "Potential of TanDEM-X for forest parameter estimation," in *Proc. EUSAR*, Aachen, Germany, 2010, pp. 1–4.

[13] S. Solberg, R. Astrup, T. Gobakken, E. Nsset, and D. J. Weydahl, "Estimating spruce and pine biomass with interferometric X-band SAR," *Remote Sens. Environ.*, vol. 114, no. 10, pp. 2353–2360, Oct. 15, 2010.

[14] R. Perko, H. Raggam, J. Deutscher, K. Gutjahr, and M. Schardt, "Forest assessment using high resolution SAR data in x-band," *Remote Sens.*, vol. 3, no. 4, pp. 792–815, Apr. 2011.

[15] M. Nilsson and J. Holmgren, "Prediction of forest variables using LiDAR measurements with different footprint sizes and measurement densities," in *Proc. ScandLaser Sci. Workshop Airborne Laser Scanning Forests*, Umeå, Sweden, Sep. 3–4, 2003, pp. 125–133.

[16] Izzawati, E. D. Wallington, and I. H. Woodhouse, "Forest height retrieval from commercial X-band SAR products," *IEEE Trans. Geosci. Remote Sens.*, vol. 44, no. 4, pp. 863–870, Apr. 2006.

[17] I. H. Woodhouse and E. D. Izzawati, "Edge effects on tree height retrieval using X-band interferometry," *IEEE Geosci. Remote Sens. Lett.*, vol. 3, no. 3, pp. 344–348, Jul. 2006.

[18] D. H. Hoekman and C. Varekamp, "Observation of tropical rain forest trees by airborne high-resolution radar," *IEEE Trans. Geosci. Remote Sens.*, vol. 39, no. 3, pp. 584–594, Mar. 2001.

[19] C. Varekamp and D. H. Hoekman, "High-resolution InSAR image simulation for forest canopies," *IEEE Trans. Geosci. Remote Sens.*, vol. 40, no. 7, pp. 1648–1655, Jul. 2002.

[20] G. Krieger, A. Moreira, H. Fiedler, I. Hajnsek, M. Werner, M. Younis, and M. Zink, "TanDEM-X: A satellite formation for high-resolution SAR interferometry," *IEEE Trans. Geosci. Remote Sens.*, vol. 45, no. 11, pp. 3317–3341, Nov. 2007.

[21] G. Krieger, M. Zink, M. Bachmann, B. Bräutigam, D. Schulze, M. Martone, P. Rizzoli, U. Steinbrecher, J. W. Antony, F. De Zan, I. Hajnsek, K. Papathanassiou, F. Kugler, M. Rodriguez Cassola, M. Younis, S. Baumgartner, P. López-Dekker, P. Prats, and A. Moreira, "TanDEM-X: A radar interferometer with two formation-flying satellites," *Acta Astron.*, vol. 89, pp. 83–98, Aug./Sep. 2013.

[22] "TerraSAR-X ground segment basic product specification document," DLR, Oberpfaffenhofen, Germany, TX-GS-DD-3302, Issue: 1.6, Mar. 18, 2009. [Online]. Available: https://tandemx-science.dlr.de/TX-GS-DD-3302_Basic-Products-Specification-Document_V1.6.pdf

[23] M. Bachmann, D. Schulze, C. Ortega-Miguez, D. Polimeni, J. Böer, J. Hueso Gonzalez, J. Walter Antony, G. Krieger, B. Bräutigam, M. Schwerdt, and M. Zink, "Acquisition status and calibration of the interferometric system," in *Proc. IGARSS*, Munich, Germany, Jul. 2012, pp. 1900–1903.

[24] H. Fiedler and G. Krieger, "Close formation of passive receiving microsatellites," in *Proc. 18th Int. Symp. Space Flight Dyn.*, Munich, Germany, 2004, pp. 47–52.

[25] A. van Laar and A. Akca, *Forest Mensuration (Managing Forest Ecosystems)*. Dordrecht, The Netherlands: Springer-Verlag, 2007, pp. 118–121.

[26] M. Heurich, T. Schneider, and E. Kennel, "Laser scanning for identification of forest structures in the Bavarian Forest National Park," in *Proc. ScandLaser Sci. Workshop Airborne Laser Scanning Forests*, Umeå, Sep. 3–4, 2003, pp. 125–133.

[27] T. Aulinger, T. Mette, K. P. Papathanssiou, I. Hajnsek, M. Heurich, and P. Krzystek, "Validation of heights from interferometric SAR and LIDAR over the temperate Forest Site National Park Bayerischer Wald," in *Proc. 2nd Int. Workshop POLinSAR*, Frascati, Italy, Jan. 17–21, 2005, pp. 1–6, [CD-ROM].

[28] E. Assmann and F. Franz, *Vorläufige Fichten-Ertragstafel für Bayern*. München, Germany: Institut für Ertragskunde der Forstl. Forschungsanst, 1963, 104 S.

[29] R. Horn, "The DLR airborne SAR project E-SAR," in *Proc. IEEE Trans. Geosci. Remote Sens. Symp.*, Lincoln, NE, USA, May 1996, vol. 3, pp. 1624–1628.

[30] A. Reigber, R. Horn, A. Nottensteiner, P. Prats, R. Scheiber, K. H. Bethke, and S. Baumgartner, "Current status of DLR's new F-SAR sensor," in *Proc. EUSAR*, Aachen, Germany, Jun. 7–10, 2010, pp. 1078–1081, VDE Verlag GmbH.

[31] H.-D. V. Böhm, V. Liesenberg, and S. H. Limin, "Multi-temporal airborne LiDAR-survey and field measurements of tropical peat swamp forest to monitor changes," *IEEE J. Sel. Top. Appl. Earth Obs. Eemote Sens.*, vol. 6, no. 3, pp. 1524–1530, Jun. 2013.

[32] S. R. Cloude and K. P. Papathanassiou, "Three-stage inversion process for polarimetric SAR interferometry," *Proc. Inst. Elect. Eng.—Radar Sonar Navigat.*, vol. 150, no. 3, pp. 125–134, Jun. 2003.

[33] D. Just and R. Bamler, "Phase statistics of interferograms with applications to synthetic aperture radar," *Appl. Opt.*, vol. 33, no. 20, pp. 4361–4368, Jul. 1994.

[34] S. Cloude, "An assessment of the PolInSAR performance of TanDEM-X for forestry applications," in *Proc. PolInSAR*, Frascati, Italy, Jan. 24–28, 2011, pp. 1–9.

[35] R. N. Treuhaft and P. Siquiera, "Vertical structure of vegetated land surfaces from interferometric and polarimetric radar," *Radio Sci.*, vol. 36, no. 1, pp. 141–177, Jan./Feb. 2000.

[36] F. Gatelli, A. Monti Guamieri, F. Parizzi, P. Pasquali, C. Prati, and F. Rocca, "The wavenumber shift in SAR interferometry," *IEEE Trans. Geosci. Remote Sens.*, vol. 32, no. 4, pp. 855–865, Jul. 1994.

[37] F. Kugler, S.-K. Lee, and K. Papathanassiou, "Estimation of forest vertical structure parameter by means of multi baseline Pol-InSAR," in *Proc. IGARSS*, Cape Town, South Africa, Jul. 2009, pp. IV-721–IV-724.

[38] F. De Zan, G. Krieger, and P. López-Dekker, "On some spectral properties of TanDEM-X interferograms over forested areas," *IEEE Geosci. Remote Sens. Lett.*, vol. 10, no. 1, pp. 71–75, Jan. 2013.

[39] F. Kugler, I. Hajnsek, and K. Papathanassiou, "Forest parameter characterisation by means of TerraSAR-X and TanDEM-X (polarimetric and) interferometric data," in *Proc. PolInSAR*, Vancouver, BC, USA, Jan. 24–29, 2011, pp. 2578–2581.

Florian Kugler was born in Bavaria, Germany, in 1974. He received the Dipl.Ing. degree in forestry science from Technische Universität München, Freising, Germany, in 2004. He is currrently working toward the Ph.D. degree at the German Aerospace Center (DLR), Oberpfaffenhofen, Germany.

Since October 2008, he has been also a Research Scientist with DLR. His research focuses on remote sensing on forests, by using polarimetric synthetic aperture radar interferometry.

Daniel Schulze was born in Germany in 1975. He received the Diploma degree in aerospace technology from the Technical University of Berlin, Berlin, Germany, in 2002.

Since 2004, he has been with the Satellite SAR System Department, Microwaves and Radar Institute, German Aerospace Center (DLR), Oberpfaffenhofen, Germany. He worked for the TerraSAR-X synthetic aperture radar (SAR) satellite project within the System Engineering and Calibration (SEC) Segment of Ground Segment. In the years 2004 and 2005, he implemented the Instrument Command Generator and supervised the Long Term Database implementation for Instrument Operations and Calibration Segment, which are the operational systems of SEC. From 2005 to 2008, he was a System Engineer for the SEC Segment. The SEC is in charge of all SAR relevant system engineering aspects and the SAR instrument operation and calibration. It is the interfaces between all SAR relevant parts of the space segment and the ground segment and thus includes the review of the space segment design and performance measurements. During his work as a System Engineer, the foundation for the successful TerraSAR-X commissioning and operational phase was laid. Since 2007, he has been working for the follow-on mission TanDEM-X. He became the Project Manager of the joined TerraSAR-X and TanDEM-X SEC Segment in 2008. Both SAR satellite missions exceeded their expectations regarding image performance and reliability. Apart from the work in the TerraSAR-X/TanDEM-X context, he was a Consultant for SAR-related topics of the DLR's Satellite SAR System Department involvement in the Spanish SAR satellite mission PAZ.

Irena Hajnsek (AM'01–M'06–SM'09–F'13) received the Dipl. degree (with honors) from the Free University of Berlin, Berlin, Germany, in 1996 and the Dr. degree (with honors) from the Friedrich Schiller University of Jena, Jena, Germany, in 2001.

From 1996 to 1999, she was with the Microwaves and Radar Institute, German Aerospace Center (DLR-HR), Oberpfaffenhofen, Germany. From 1999 to 2000, she was with the Institut d'Electronique et de Télécommunications de Rennes, University of Rennes 1, Rennes, France, for ten months and with Applied Electromagnetics, St. Andrews, Scotland, for four months, in the frame of the European Training and Mobility for Young Researches Program Radar Polarimetry Network. In 2005, she was a Guest Scientists with the University of Adelaide, Adelaide, Australia, for six weeks. She was the science Coordinator of the German satellite mission TanDEM-X. From 2009 to 2013, she was a member of the ESA Mission Advisory Group of the 7th Explorer Mission CoReH2O. Since November 2009, she has been a Professor of earth observation with the Institute of Environmental Engineering, Swiss Federal Institute of Technology (ETH) Zürich, Zurich, Switzerland, and the Head of the Polarimetric SAR Interferometry Research Group with DLR-HR. Her main research interests are in electromagnetic propagation and scattering theory, radar polarimetry, SAR and interferometric SAR data processing techniques, and environmental parameter modeling and estimation.

Dr. Hajnsek has been a member of the IEEE Geoscience and Remote Sensing Society AdCom since 2013 and was a Technical Program Cochair of the IEEE International Geoscience and Remote Sensing Symposium 2012 in Munich.

Hans Pretzsch was born in Düsseldorf, Germany, in 1957. He received the Ph.D. degree in forest growth and yield science and biometrics from Ludwig-Maximilians-Universität München, München, Germany, in 1985, the Prof. h.c. degree from the Czech University of Life Sciences in Prague, Prague, Czech Republic, in 2001, and the Dr. h.c. degree from the Czech University of Agriculture of Prague, Prague, in 2008.

Since 1994, he has been a Professor of forest growth and yield science with Technische Universität München, München, where he is responsible for the network of long-term experimental plots in Bavaria, which date back to 1860, and for the management of the municipal forest enterprise Traunstein/Bavaria. He currently teaches forestry and sustainable resource management to undergraduate and graduate students, as well as professional foresters. He has authored/coauthored over 100 publications in international journals, conferences, and workshops. For the past 20 years, he has focused his research on general rules of tree and stand growth, forest modeling, mixed stand analysis, structural allometry under competitive stress, diagnosis of forest growth disturbances, and applications of terrestrial LiDAR and computer tomography for analysis of structures on tree and stand level.

Dr. Pretzsch is an Editor of the *European Journal of Forest Research*. He was a recipient of the Biometric Research Award from the Biometrical Society, the Danzer Research Award from the Danzer Group, and the W. L. Pfeil Award from Toepfer Stiftung F.V.S.

Konstantinos P. Papathanassiou (AM'01–M'06–SM'09–F'13) received the Dipl.Ing degree (with honors) and the Dr. degree (with honors) from the Technical University of Graz, Graz, Austria, in 1994 and 1999, respectively.

From 1992 to 1994, he was with the Institute for Digital Image Processing (DIBAG), Joanneum Research, Graz. Between 1995 and 1999, he was with the Microwaves and Radar Institute, German Aerospace Center (DLR-HR), Oberpfaffenhofen, Germany. From 1999 to 2000, he was a European Union Postdoctoral Fellow with Applied Electromagnetics, St. Andrews, Scotland. Since October 2000, he has been a Senior Scientist with DLR-HR, leading the Information Retrieval Research Group. He has authored/coauthored over 100 publications in international journals, conferences, and workshops. His main research interests are in polarimetric and interferometric processing and calibration techniques, polarimetric SAR interferometry, and the quantitative parameter estimation from SAR data, as well as in SAR mission design and SAR mission performance analysis.

Dr. Papathanassiou was the recipient of the IEEE GRSS IGARSS Symposium Prize Paper Award in 1998, the Best Paper Award of the European SAR Conference in 2002, the DLR Science Award in 2002, and the DLR Senior Scientist Award in 2011.

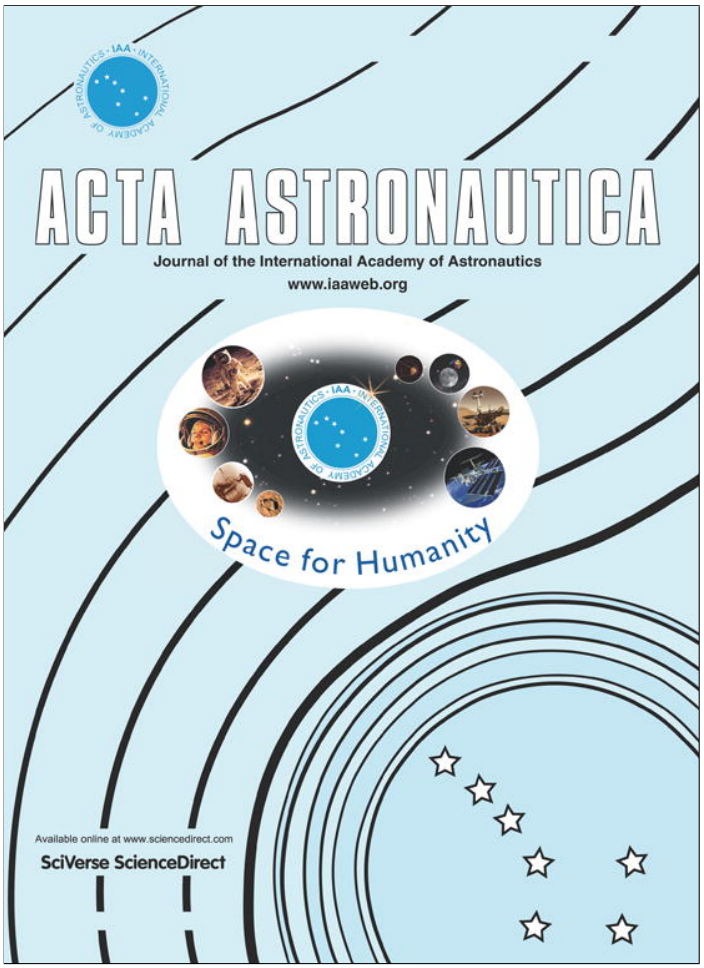

Acta Astronautica 89 (2013) 83–98

Contents lists available at SciVerse ScienceDirect

Acta Astronautica

journal homepage: www.elsevier.com/locate/actaastro

TanDEM-X: A radar interferometer with two formation-flying satellites ☆

Gerhard Krieger *, Manfred Zink, Markus Bachmann, Benjamin Bräutigam, Daniel Schulze, Michele Martone, Paola Rizzoli, Ulrich Steinbrecher, John Walter Antony, Francesco De Zan, Irena Hajnsek, Kostas Papathanassiou, Florian Kugler, Marc Rodriguez Cassola, Marwan Younis, Stefan Baumgartner, Paco López-Dekker, Pau Prats, Alberto Moreira

German Aerospace Center (DLR), Microwaves and Radar Institute, Münchner Strasse 20, 82234 Wessling, Oberpfaffenhofen, Germany

ARTICLE INFO

Article history:
Received 4 March 2013
Accepted 6 March 2013
Available online 6 April 2013

Keywords:
Remote sensing
Formation flying
Synthetic aperture radar (SAR)
Interferometry
Digital elevation model
Earth observation

ABSTRACT

TanDEM-X (*T*erraSAR-X *a*dd-o*n* for *D*igital *E*levation *M*easurements) is an innovative formation-flying radar mission that opens a new era in spaceborne radar remote sensing. The primary objective is the acquisition of a global digital elevation model (DEM) with unprecedented accuracy (12 m horizontal resolution and 2 m relative height accuracy). This goal is achieved by extending the TerraSAR-X synthetic aperture radar (SAR) mission by a second, TerraSAR-X like satellite (TDX) flying in close formation with TerraSAR-X (TSX). Both satellites form together a large single-pass SAR interferometer with the opportunity for flexible baseline selection. This enables the acquisition of highly accurate cross-track interferograms without the inherent accuracy limitations imposed by repeat-pass interferometry due to temporal decorrelation and atmospheric disturbances. Besides the primary goal of the mission, several secondary mission objectives based on along-track interferometry as well as new bistatic and multistatic SAR techniques have been defined, representing an important and innovative asset of the TanDEM-X mission. TanDEM-X is implemented in the framework of a public–private partnership between the German Aerospace Center (DLR) and EADS Astrium GmbH. The TanDEM-X satellite was successfully launched in June 2010 and the mission started its operational data acquisition in December 2010. This paper provides an overview of the TanDEM-X mission and summarizes its actual status and performance. Furthermore, results from several scientific radar experiments are presented that show the great potential of future formation-flying interferometric SAR missions to serve novel remote sensing applications.

1. Introduction

The primary objective of the TanDEM-X mission is the generation of a world-wide, consistent, timely, and high-precision digital elevation model (DEM) as the basis for a wide range of scientific research, as well as for commercial DEM production ([1], cf. Fig. 1). This goal is achieved by enhancing the TerraSAR-X synthetic aperture radar (SAR) mission [2] by a second radar satellite flying in close formation with TerraSAR-X [3]. Both satellites act together as a large single-pass SAR interferometer with the opportunity for flexible baseline selection. This enables the acquisition of highly accurate cross-track and along-track interferograms without the inherent accuracy limitations

☆ This paper was presented during the 63rd IAC in Naples.

* Corresponding author. Tel.: +49 8153 28 3054.
E-mail address: gerhard.krieger@dlr.de (G. Krieger).

0094-5765/$ - see front matter © 2013 IAA Published by Elsevier Ltd. All rights reserved.
http://dx.doi.org/10.1016/j.actaastro.2013.03.008

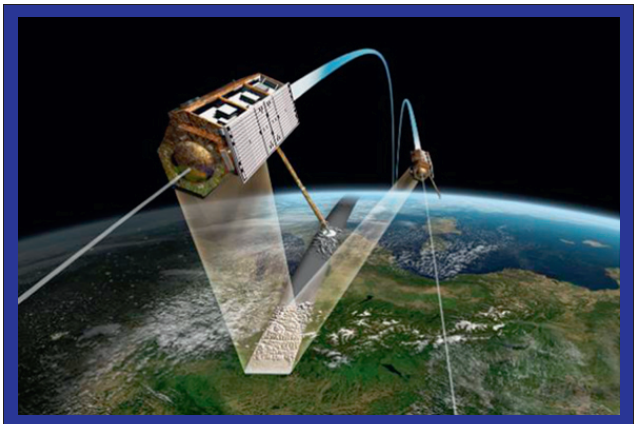

Acquisition of Global Digital Elevation Model		
Parameter	**Specification**	**Requirement**
Relative Vertical Accuracy	90% linear point-to-point error in 1° cell	2 m (slope < 20%) 4 m (slope > 20%)
Absolute Vertical Accuracy	90% linear error	10 m
Spatial Resolution	independent pixels	12 m (0.4 arc sec)

Fig. 1. Primary objective of the twin-satellite mission TanDEM-X is the acquisition of a global digital elevation model (DEM) with unprecedented accuracy.

imposed by repeat-pass interferometry due to temporal decorrelation and atmospheric disturbances. Thanks to its unique capabilities, TanDEM-X is not only acquiring a global DEM with unprecedented accuracy, but it is also well suited to demonstrate novel bistatic and multistatic SAR techniques and Earth observation applications that form the basis for future formation-flying SAR missions. TanDEM-X has been implemented in the framework of a public–private partnership between the German Aerospace Center (DLR) and EADS Astrium GmbH, as for TerraSAR-X.

2. Mission concept

The TanDEM-X mission is an extension of the TerraSAR-X radar mission, co-flying a second satellite of nearly identical capability in a close formation. The TerraSAR-X satellite (TSX), as basis for TanDEM-X, was successfully launched into a sun-synchronous dusk-dawn orbit with 97.44° inclination on June 15, 2007. The nominal orbit height is 514.8 km and the orbit repeat cycle is 11 days. TSX is not only a high performance SAR system, but it has already built in all necessary features required for the implementation of the TanDEM-X mission. Examples are additional X-band horn antennas for inter-satellite phase synchronization, the availability of a dual-frequency GPS receiver for precise orbit determination, excellent RF phase stability of the SAR instrument, and PRF synchronization based on GPS as a common time reference. The second satellite (TDX) is as much as possible a rebuild of TSX with only minor modifications like an additional cold gas propulsion system for the formation fine tuning, double-sized on-board solid-state memory for increased data recording capacity and an additional S-band receiver to enable the reception of telemetry and GPS position information broadcast by TSX. This similarity guaranteed a low development risk and offers the possibility for a flexible share of operational functions among the two satellites.

The instruments on both satellites are advanced high-resolution X-band synthetic aperture radars based on active phased array technology, which can be operated in Spotlight, Stripmap, and ScanSAR mode with full polarization capability [4]. The center frequency of the radar instruments is 9.65 GHz with a selectable chirp bandwidth of up to 300 MHz. The active phased array antenna, which has an overall aperture size of 4.8 m × 0.7 m, is fixed mounted to the spacecraft body and incorporates 12 panels with 32 dual-pol waveguide sub-arrays each. This enables agile beam pointing and flexible beam shaping as required for the acquisition of a wide range of image products with varying resolutions and scene sizes.

2.1. Orbit configuration and formation flying

The TanDEM-X operational scenario requires the coordinated operation of two satellites flying in close formation. The adjustment parameters for the formation are the orbits ascending nodes, the angle between the perigees, the orbit eccentricities and the phasing between the satellites. With these parameters, several options have been investigated during the phase A study, and the Helix satellite formation shown in Fig. 2 has finally been selected for operational DEM generation. This formation combines an out-of-plane (horizontal) orbital displacement by different ascending nodes with a radial (vertical) separation by different eccentricity vectors resulting in a helix like relative movement of the satellites along the orbit as illustrated in the lower plot of Fig. 2. Since there exists no crossing of the satellite orbits, arbitrary shifts and drifts of the satellites along their orbits are allowed. This enables a safe spacecraft operation without the necessity for autonomous control. It is furthermore possible to optimize the along-track displacement at predefined latitudes for different applications: cross-track interferometry aims at along-track baselines which are as short as possible to ensure an optimum overlap of the Doppler spectra and to avoid temporal decorrelation in vegetated areas, while other applications like along-track interferometry or super resolution require selectable along-track baselines in the range from hundred meters up to several kilometres. A fine tuning of the satellite formation is performed via the aforementioned cold gas propulsion system on TDX.

The Helix formation enables a complete mapping of the Earth with a stable height of ambiguity by using a small number of formation settings [3]. Southern and northern latitudes can be mapped with the same formation by using ascending orbits for one and descending orbits for the other hemisphere, as illustrated in Fig. 2 on the bottom. A fine tuning of the cross-track baselines can moreover be achieved by taking advantage of the natural rotation of the eccentricity vectors due to secular disturbances, also called motion of libration. The phases of this libration can be kept in a fixed relative position with small maneuvers using the cold gas thrusters on a daily basis, while major formation changes as well as a duplication of the orbit keeping

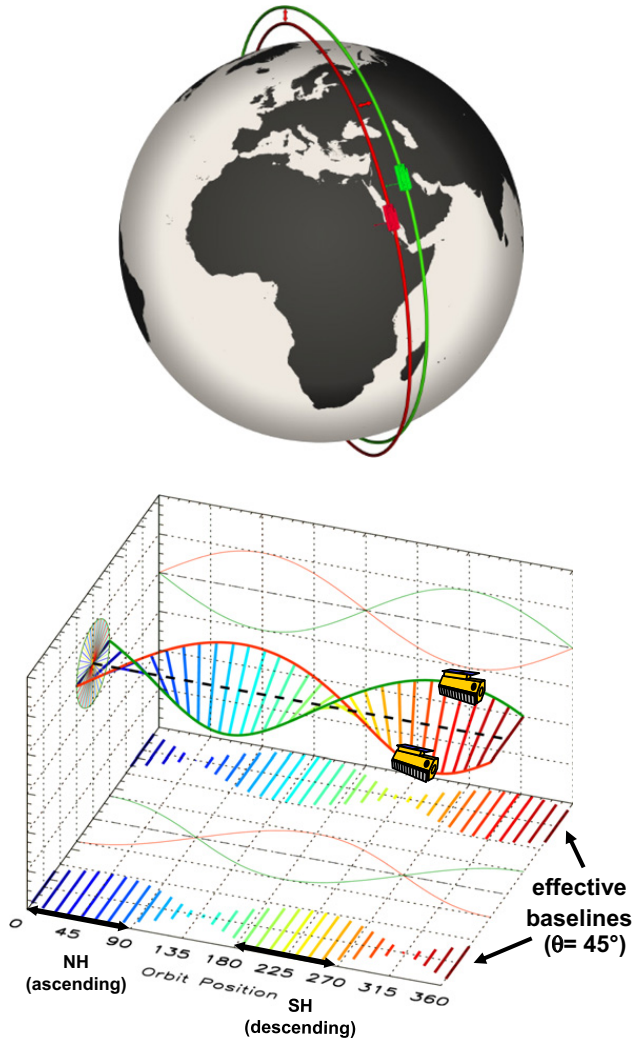

Fig. 2. Helix satellite formation for TanDEM-X. Top: illustration of orbits. Bottom: cross-track and radial baselines as a function of the argument of latitude. The latitude positions in the lower plot correspond to one complete orbit and the black arrows indicate those areas that can be mapped with a sufficient baseline length assuming a right-looking radar system with a look angle of θ=45°. NH, northern hemisphere; SH, southern hemisphere.

manoeuvres required by TSX will be performed by the hot gas thruster system.

2.2. Interferometric configurations and acquisition modes

TanDEM-X can acquire interferometric data in different configurations: Examples are the bistatic, monostatic, and alternating bistatic modes as illustrated in Fig. 3. The different interferometric configurations can be further combined with different TSX and TDX SAR imaging modes like Stripmap, ScanSAR, Spotlight, and Sliding Spotlight.

Operational DEM generation is planned to be performed using the bistatic Stripmap mode shown in Fig. 3 in the middle. This mode uses either TSX or TDX as a transmitter to illuminate a common radar footprint on the Earth's surface. The scattered signal is then recorded by both satellites simultaneously. This simultaneous data acquisition makes dual use of the available transmit power and is mandatory to avoid possible errors from temporal decorrelation (cf. Fig. 4) and atmospheric disturbances.

Another interferometric configuration is the pursuit monostatic mode which is illustrated in Fig. 3 on the left. The two satellites are operated independently from each other in this mode, thereby avoiding the need for time and phase synchronization. The along-track distance between the satellites should be 20 km or more to avoid mutual RF interference between the two radar signals. This configuration has been used in the “monostatic commissioning phase” of TanDEM-X where several unique experiments have been conducted. One such example is shown in Fig. 4, which clearly demonstrates the potential deteriorations due to temporal decorrelation in vegetated areas even for very short temporal baselines. Further examples will be shown in Section 4.

A third interferometric configuration is the alternating bistatic mode which is illustrated in Fig. 3 on the right. The alternating bistatic mode is similar to the bistatic mode with the exception that the transmitter is switched from one satellite to the other on a pulse-to-pulse basis. This enables the simultaneous acquisition of multiple interferograms with two different effective baselines. Several experiments exploit this mode to get additional information, e.g., in vegetated areas.

2.3. Exclusion zones

For DEM generation, TanDEM-X combines one monostatic and one bistatic radar image in a joint SAR interferogram. To ensure a sufficient overlap of the Doppler spectra, this requires a short along-track distance of typically less than 1 km between the two satellites, while the radial and cross-track baselines depend on the argument of latitude and vary between zero and a few hundred meters. As a result, there is the danger that one satellite illuminates its partner by its radar antenna, which could cause interference, or, in the worst case, damage of sensitive electronic equipment. This is illustrated in Fig. 5 which shows the predicted electric field strength as a function of the satellite distance in case of direct illumination. For the minimum allowed satellite distance of 150 m, the predicted value is 330 V/m, which exceeds by far the maximum allowed field strength of 50 V/m.

To avoid the risk of mutual illumination, the transmission of radar signals has to be suppressed for one satellite at specific arguments of latitude, which are known as exclusion zones (cf. Fig. 6). TanDEM-X ensures exclusion zone compliance by a double fail save approach including both a check on ground before command uploading and an additional real-time check on the satellite which suppresses signal transmission within predefined latitude windows.

2.4. System synchronization

A peculiarity of the bistatic data acquisition is the use of independent oscillators for the modulation and demodulation of the radar pulses. Any deviation between the two oscillators will hence cause a residual modulation of the recorded azimuth signal. The impact of oscillator phase

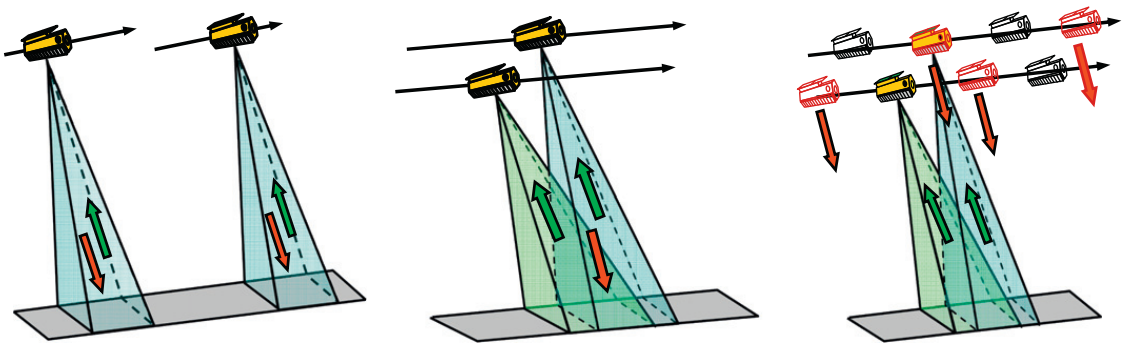

Fig. 3. Data acquisition configurations: pursuit monostatic (left), bistatic (middle), and alternating bistatic (right).

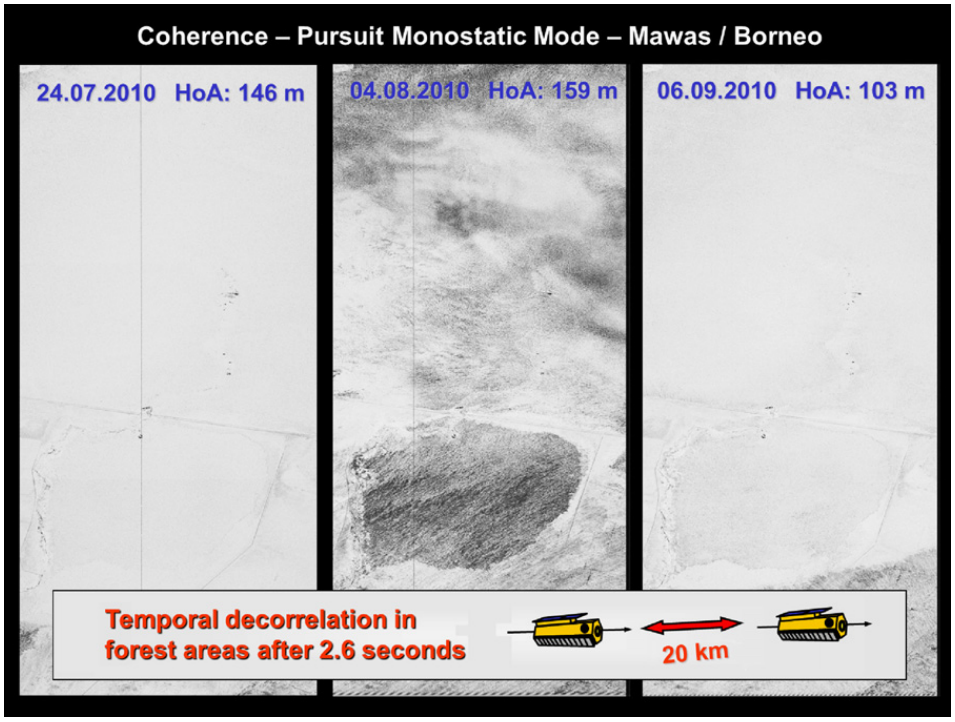

Fig. 4. Illustration of temporal decorrelation effects in pursuit monostatic mode where the satellites had an along-track distance of 20 km, corresponding to a temporal baseline of 2.6 s. The three images show the coherence (black: 0.0, white: 1.0) obtained for three different interferometric acquisitions over one and the same rain forest test site in Mawas/Borneo. All acquisitions had rather small interferometric baselines as indicated by their height of ambiguity (HoA). The loss of coherence due to temporal decorrelation in the middle acquisition is evident. The temporal decorrelation is even more striking if one takes into account that the middle scene was acquired with the shortest baseline (largest height of ambiguity) which should minimize the amount of volume decorrelation.

noise in bistatic SAR has been analyzed in [5] where it is shown that oscillator noise may cause significant errors in both the interferometric phase and SAR focusing. The stringent requirements for interferometric phase stability in the bistatic mode will hence require an appropriate relative phase referencing between the two SAR instruments or an operation in the alternating bistatic mode. For TanDEM-X, a dedicated inter-satellite X-band synchronization link has been established via mutual exchange of radar pulses between the two satellites. For this, the nominal bistatic SAR data acquisition is shortly interrupted, and a radar pulse is redirected from the main SAR antenna to one of six dedicated synchronization horn antennas mounted on each spacecraft. The pulse is then recorded by the other satellite which in turn transmits a short synchronization pulse (cf. Fig. 7, top). By this, a bidirectional link between the two radar instruments is established, which allows for mutual phase referencing without exact knowledge of the actual distance between the satellites. On ground, a correction signal can be derived from the recorded synchronization pulses. This compensates the oscillator induced phase errors in the bistatic SAR signal. The performance of such a synchronization link has been investigated in [6]. The bottom diagram in Fig. 7 shows the predicted standard deviation of the residual phase errors after synchronization as a function of the update frequency of the synchronization signals for different signal-to-noise ratios (SNR) of the bidirectional link. The actual SNR varies with the distance between the satellites as well as their relative attitude. For the typical DEM data acquisition mode with baselines below 1 km, the SNR will be in the order of 30–40 dB, and it becomes clear that a phase error below 1° can be achieved for synchronization frequencies above 5 Hz.

The performance of the synchronization link has been validated during the bistatic TanDEM-X commissioning phase [7]. An example of such a verification is shown in Fig. 8. The images show for one and the same scene the height differences between two DEMs that have been acquired in subsequent satellite formation passes. The top image shows the result obtained with an early version of the TanDEM-X processor. Due to a slight error in the synchronization signal processing, small undulations in the order of ± 1 m can be seen. After refining the interpolation between the synchronization pulses, the undulations are hardly visible and the large scale height errors are now below ± 0.1 m. Since the height of ambiguity was 38 m for both acquisitions, this corresponds to a relative synchronization phase error of less than $\pm 1^\circ$.

Note that in the previous analyses, a constant height offset between the two DEM acquisitions has been subtracted. A systematic evaluation of the height offsets of a large number of TanDEM-X DEMs distributed over the whole latitude spectrum revealed systematic height offsets that varied with the along-track distance between the satellites [12]. The reason for these variations turned out to

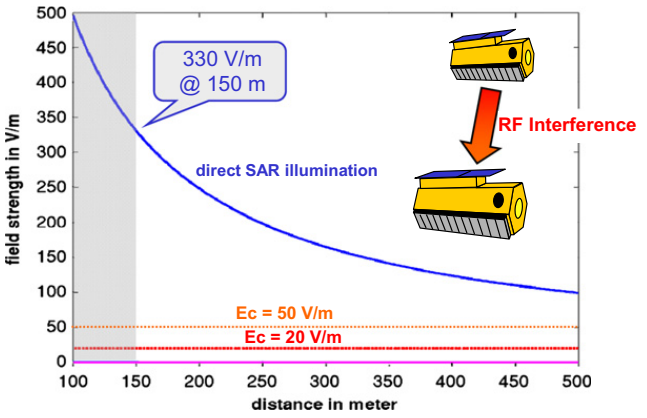

Fig. 5. Predicted electric field strength in case of direct illumination of one satellite by the radar antenna of the other satellite. For typical spacecraft, the maximum allowed field strength is 20 V/m. This value has been raised for TanDEM-X to 50 V/m, which is still below the field strength that may occur in case of direct illumination for the minimum allowed satellite distance of 150 m.

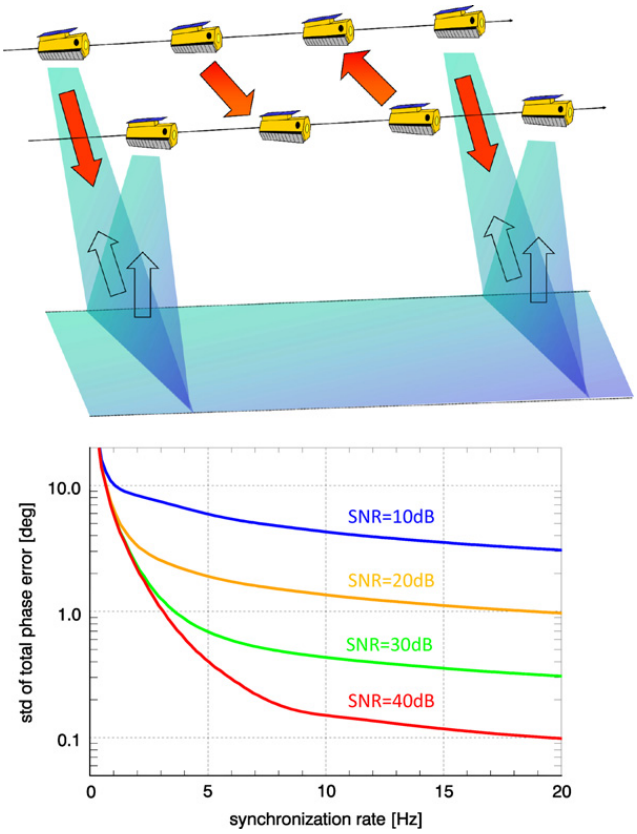

Fig. 7. Synchronization of the TanDEM-X satellites by mutual exchange of radar pulses (top) and predicted performance (bottom). The performance is shown in terms of the standard deviation of the total synchronization link phase error as a function of the synchronization frequency with signal-to-noise ratio as a parameter. Based on these performance analyses, a synchronization frequency of 5 Hz has been selected for operational DEM acquisition. For typical Helix formations used in the nominal DEM acquisition phase, this results in an expected phase error standard deviation of $\sim 1^\circ$.

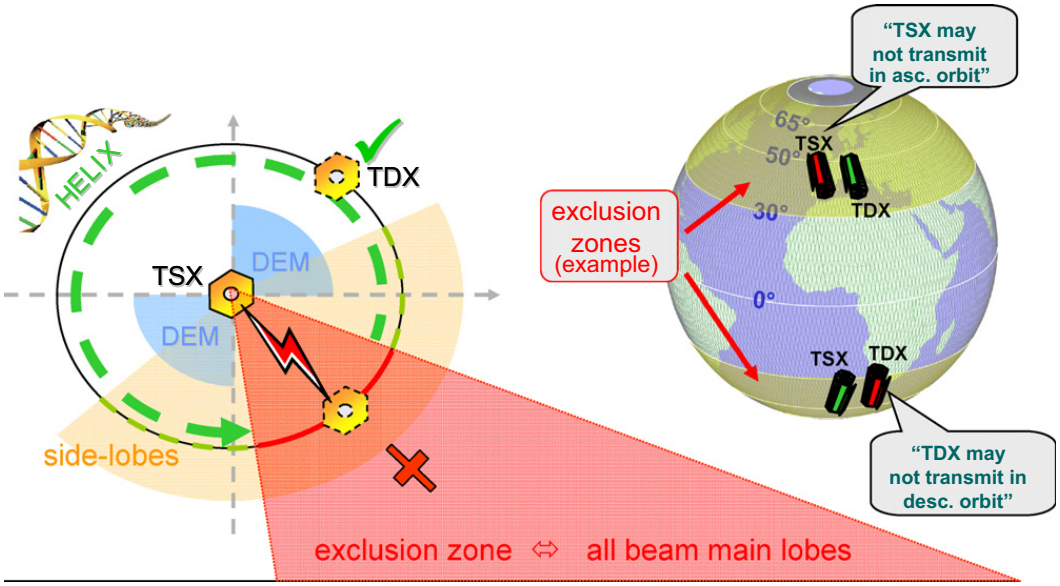

Fig. 6. TanDEM-X exclusion zones.

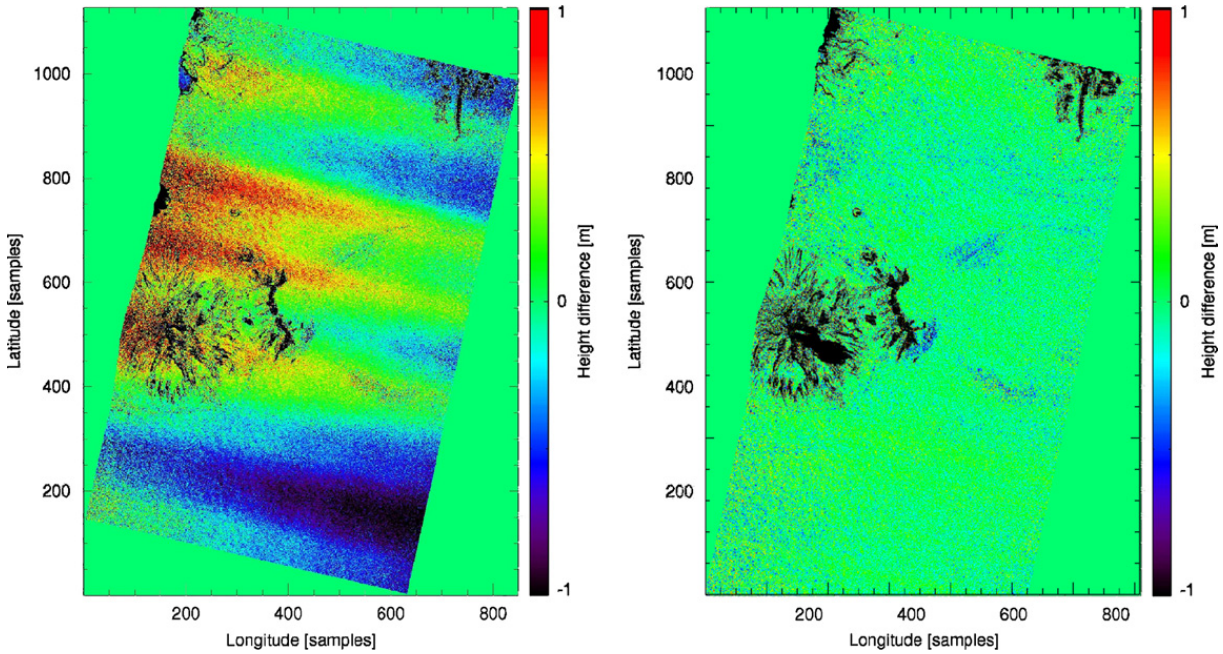

Fig. 8. Verification of the TanDEM-X synchronization link. The images show the height difference between two DEMs that have been acquired in subsequent formation passes. The height of ambiguity was 38 m for both acquisitions. Top: difference with early version of the TanDEM-X processor (uncalibrated synchronization link). Height error undulations in the order of ± 1 m are clearly visible which correspond to phase errors of $\pm 10^{\circ}$. Bottom: difference after refining the interpolation procedure for the synchronization signal. Systematic height undulations are now hardly visible and the residual height error is below ± 0.1 m, corresponding to a phase error of less than $\pm 1^{\circ}$.

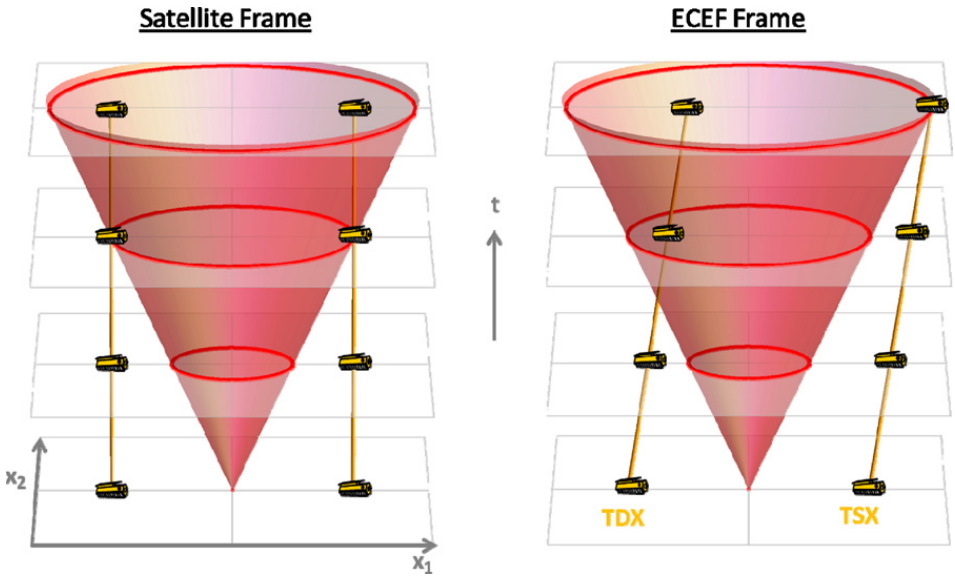

Fig. 9. Illustration of the non-simultaneity of events as observed from different reference frames. Left: observation within satellite frame. The spherical wavefront of a pulse emitted from a virtual transmitter in the middle of the two satellites arrives at both satellites at the same time. Right: observation from an Earth centered Earth fixed (ECEF) reference frame. The satellites move relative to the ECEF frame and the wavefront arrives first at TDX and later at TSX. It becomes clear that, events which are simultaneous in the satellite frame are no longer simultaneous in the ECEF frame.

be relativistic effects. For this, one should note that the correct application of the synchronization-link signal during bistatic SAR processing has to take into account that bistatic SAR processing and bistatic radar synchronization are performed in different reference frames moving relative to each other. This introduces a non-simultaneity of the transmit and receive events in the different frames which depends on the along-track distance between the two satellites ([8], cf. illustration in Fig. 9). The effect can be approximated based on Einstein's theory of special relativity by comparing the corresponding space–time intervals

$$s^2 = (c\cdot t_m)^2 - \left|\vec{B}_{Tx-Rx}\right|^2 = \left(c\cdot\frac{r_{bi}}{c}\right)^2 - \left|\vec{B}_{Tx-Rx} + \vec{v}_{Rx}\frac{r_{bi}}{c}\right|^2$$

$$\rightarrow r_{bi} \approx \vec{B}_{Tx-Rx}\frac{\vec{v}_{Rx}}{c} + c\cdot t_m \qquad (1)$$

where s denotes the space–time interval, c the velocity of light, t_m the radar pulse traveling time measured in the

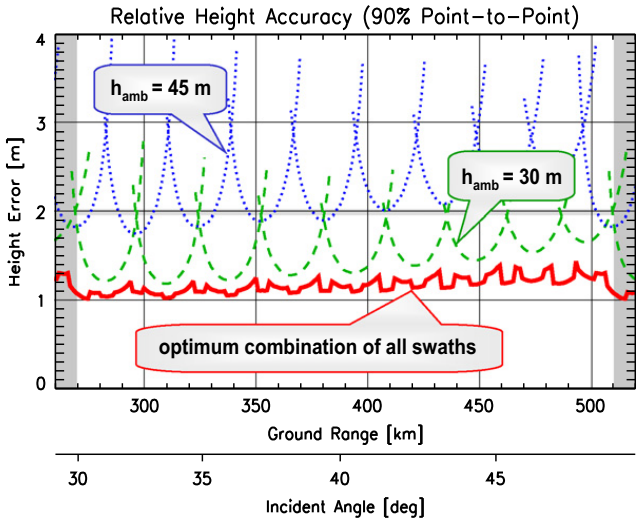

Fig. 10. Predicted relative height accuracy for a height of ambiguity of 45 m (dotted) and 30 m (dashed). The lower solid curve shows the error resulting from the combination of multiple swaths. All errors are point-to-point height errors for a 90% confidence interval.

satellite reference frame, $\vec{B}_{Tx-Rx}$ the baseline vector connecting the master and slave satellites (length contraction can be neglected), r_{bi} the bistatic range, and $\vec{v}_{Rx}$ the velocity of the receiving satellite. For TanDEM-X, the typical values for the bistatic range correction r_{bi} vary between ± 2 cm, which would, if not compensated, correspond to phase errors of $\pm 220^{\circ}$ and height offsets of more than ± 30 m for a height of ambiguity of 50 m. The actual results with TanDEM-X show that this approximation provides a sufficiently accurate correction, even though it neglects the effect of Earth rotation which introduces an accelerated reference frame that requires in the strict sense a more rigorous treatment.

2.5. *Interferometric performance and global data acquisition plan*

Radar interferometry is based on the evaluation of the phase difference between two coherent radar signals acquired from slightly different spatial and/or temporal

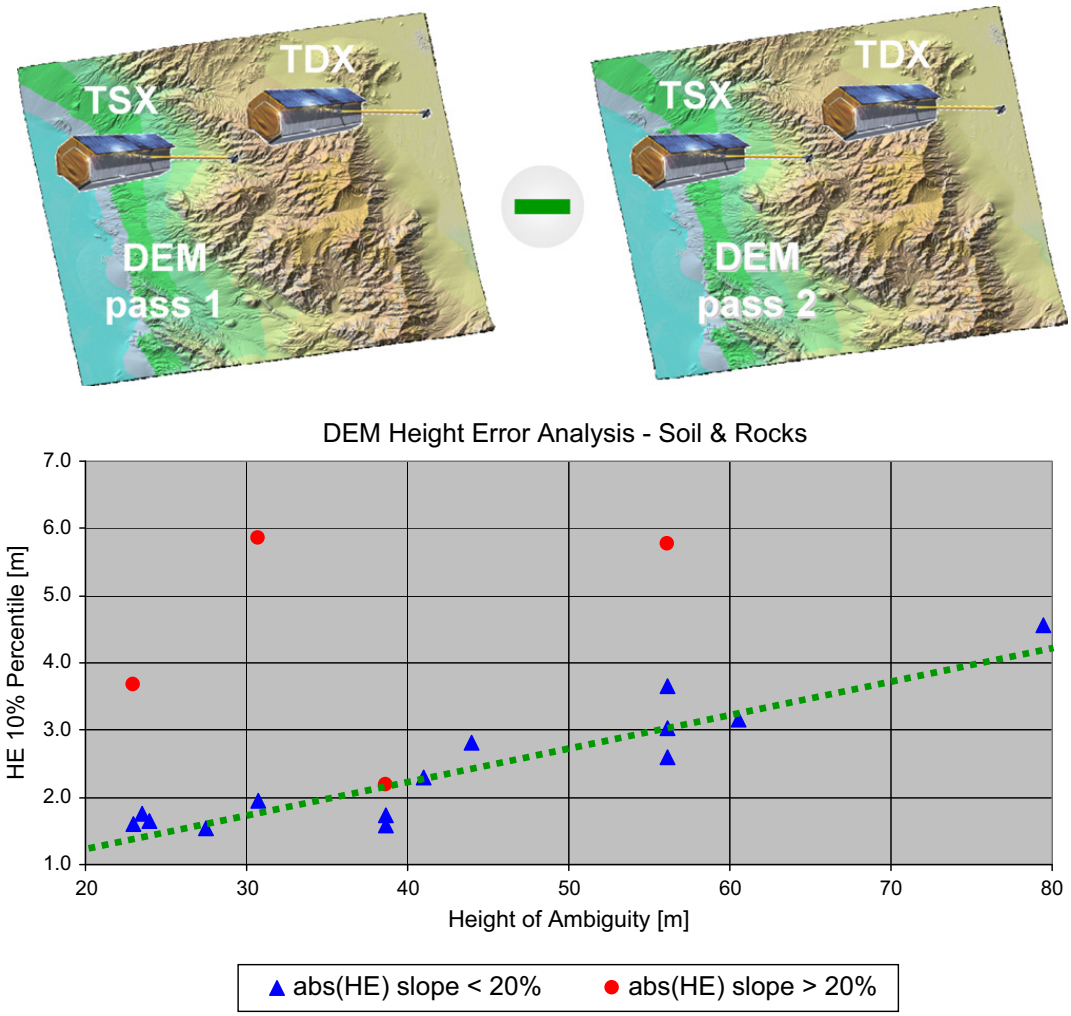

Fig. 11. Relative point-to-point height accuracies estimated from the comparison of two TanDEM-X DEM acquisitions for different soil and rock test sites. The blue triangles show the estimated point-to-point relative height error (HE) for terrain with predominant slopes below 20%, while the red dots show the corresponding height errors for terrain with predominant slopes above 20%. The estimates for the low slope areas show a good agreement with the predictions from the performance model in Fig. 10. See [9] for more details. (For interpretation of the references to color in this figure caption, the reader is referred to the web version of this article.)

positions. By this, TanDEM-X is able to measure the range difference between the two satellites and a given scatterer on the ground with millimetric accuracy. The height of the scatterer is inferred from this range difference by geometric triangulation. The sensitivity of the phase-to-height scaling depends on the distance between the two satellites, where a larger baseline increases the sensitivity of the radar interferometer to small height variations. However, the conversion from phase to range and hence the conversion of phase differences to height is not unique, since the range difference measurement via phases is ambiguous with the wavelength. Radar interferometry expresses this ambiguity by the so-called height of ambiguity

$$h_{amb} = \frac{\lambda r_0 \sin(\theta_i)}{B_\perp} \tag{2}$$

where λ is the wavelength, r_0 the slant range from the satellites to the scatterer under consideration, θ_i the local incident angle of the electromagnetic wave, and $B_\perp$ is the perpendicular baseline component. A good approximation for the scalar value $B_\perp$ is obtained by projecting the vector connecting both satellites onto a plane normal to the satellite orbit and then again onto a plane perpendicular to the line of sight.

Fig. 10 shows the predicted height accuracy as a function of ground range position and the height of ambiguity (cf. [3] for details). Systematic height accuracy evaluations of repeatedly acquired TanDEM-X DEMs show a good agreement with the performance model. This is illustrated in Fig. 11 which shows an example of the estimated relative height errors for several soil and rock test sites. The error estimates were obtained by comparing the point-to-point relative height deviations between two subsequent TanDEM-X acquisitions as explained in detail in [9].

From the performance prediction in Fig. 10 it becomes clear that a lower height of ambiguity (i.e. larger baseline $B_\perp$) improves the height accuracy. However, a lower height of ambiguity also increases the difficulties in selecting the correct ambiguity interval during DEM generation (phase unwrapping). To minimize such problems and to ensure a homogeneous performance, TanDEM-X combines acquisitions with different heights of ambiguity. This requires in turn frequent adjustments of the Helix formation parameters which are selected according to an optimized global data acquisition plan. Important constraints in this challenging optimization procedure are besides the interferometric performance the available amount of fuel and thruster cycles, limitations in the onboard storage and downlink capacity in combination with the finite time for global DEM acquisition, as well as power and thermal constraints. Further challenges arise from the interleaved usage of both satellites to continue the TerraSAR-X mission.

2.6. Baseline estimation and DEM calibration

Up to now, we have neglected errors due to the finite accuracy of relative baseline estimation. Such errors will mainly cause a low frequency modulation of the DEM, thereby contributing simultaneously to relative and absolute height errors. Most critical for TanDEM-X are baseline errors in the line of sight ($\Delta B_{||}$) which cause a rotation of the reconstructed DEM about the (master) satellite position. As a result, the DEM will be vertically displaced by

$$\Delta h = r_0 \cdot \sin(\theta_i) \cdot \frac{\Delta B_{||}}{B_\perp} = \frac{h_{amb}}{\lambda} \cdot \Delta B_{||} \tag{3}$$

This vertical displacement is $\Delta h = \pm 1.1$ m for $\Delta B_{||} = \pm 1$ mm and $h_{amb} = 35$ m. A parallel baseline error will furthermore cause a tilt of the DEM which is given by

$$\varphi_{tilt} = \frac{\Delta h}{\Delta s} = \frac{\Delta B_{||}}{B_\perp} \tag{4}$$

where Δs is the ground range distance from the selected reference point. The resulting tilt will be 3.8 mm/km and 2.3 mm/km for incident angles of $\theta_i = 30^\circ$ and $\theta_i = 45^\circ$, respectively ($\Delta B_{||} = 1$ mm and $h_{amb} = 35$ m, i.e., $B_\perp = 260$ m and $B_\perp = 440$ m for $\theta_i = 30^\circ$ and $\theta_i = 45^\circ$, respectively).

Fig. 12 illustrates the effect of baseline errors on the individual DEM data takes. Since the satellites in the close Helix formation are exposed to similar orbital disturbances, their relative motion can be predicted with high accuracy. In consequence, each interferometric data take is characterized by a nearly constant baseline offset (denoted as "bias" in Fig. 12) that causes a constant vertical shift and a small tilt in the corresponding DEM swath.

Precise baseline determination is performed by a double differential evaluation of GPS carrier phase measurements.

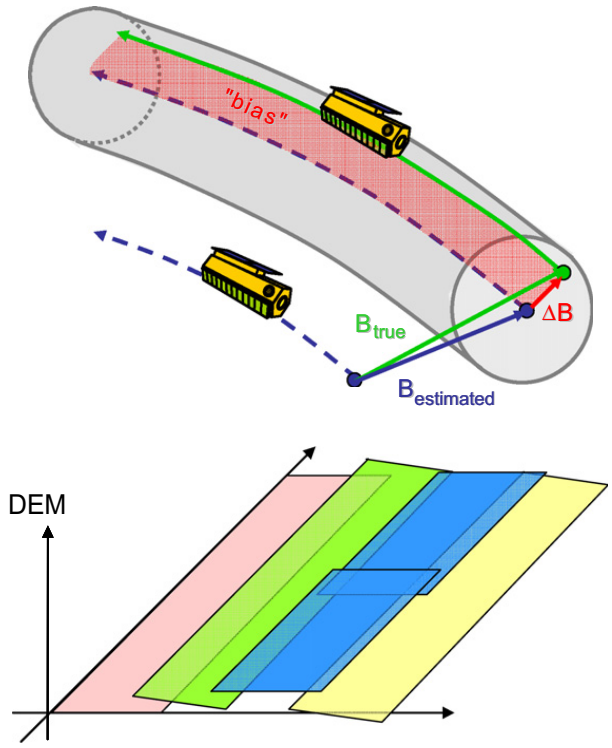

Fig. 12. Illustration of the impact of baseline estimation errors. Top: unknown baseline offset during each data take. The baseline measurement accuracy of 1–2 mm is indicated by the gray tube. Bottom: vertical displacement and tilt of adjacent swaths as a result of different baseline offsets during the data takes. (For interpretation of the references to color in this figure caption, the reader is referred to the web version of this article.)

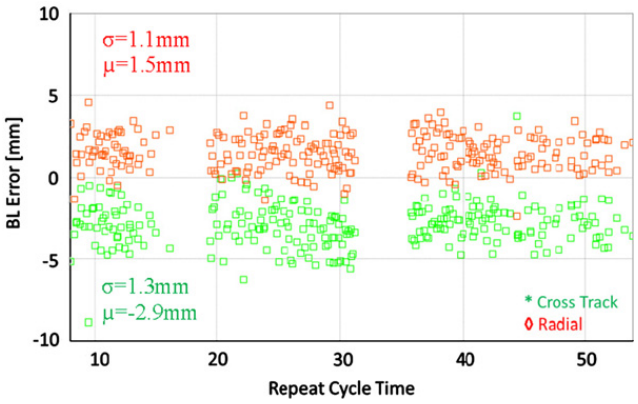

Fig. 13. Radial and cross-track component of the baseline bias estimated from repeated interferometric measurements over reference sites as a function of the 11-day repeat cycle. The standard deviation of $\sigma=1.1$ mm in radial direction and $\sigma=1.3$ mm in horizontal cross-track direction fits well with the theoretic predictions. The estimated bias is $\mu=1.5$ mm and $\mu=-2.9$ mm in radial and cross-track direction, respectively.

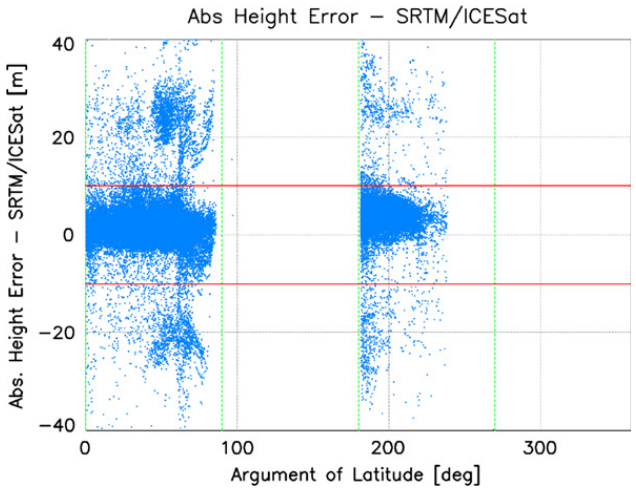

Fig. 14. Absolute height error of single DEM acquisitions derived from the comparison with SRTM [15] (within $\pm 60^\circ$ latitude) and with ICESat [16] data (outside $\pm 60^\circ$ latitude).

The results from the TanDEM-X mission show that the relative satellite positions can be estimated with accuracies in the order of 1–2 mm (cf. Fig. 13). These results are also in good agreement with theoretical predictions based on the prior experience with the GRACE mission [10]. However, primarily due to uncompensated offsets from the SAR antenna phase centers, the relative satellite positions derived from GPS measurements are biased. Interferometric acquisitions over well-known areas allow estimating the bias from the difference to the reference height. Fig. 13 shows stable estimates for the relevant radial and cross-track component of the baseline offsets. Mean values of −2.9/1.5 mm (cross-track/radial) are being applied in the generation of the final baseline products (cf. [11]).

Additional systematic height error sources include uncompensated internal delays in the SAR instruments, the use of different synchronization horn antennas for different orbit positions, the formation of the bistatic replica for both synchronization and bistatic imaging, as well as residual errors in the bistatic SAR processing, e.g. due to relativistic effects and Earth rotation (see also Section 2.4). A calibration for all these systematic phase offsets has been performed by evaluating the DEM height offset statistics over large data sets distributed all over the world [11]. By this, the typical height offsets of single DEM acquisitions are already well below the 10 m requirement from Fig. 1 [12]. This is illustrated in Fig. 14, which shows the TanDEM-X height offsets for a large number of DEM acquisitions distributed over a wide range of latitudes. Most of the height offsets are already, i.e. without any calibration and mosaicking, within the required ± 10 m band. The apparent clustering of height errors at ± 20 m is caused by so-called π-ambiguities that are caused by the bidirectional synchronization procedure (cf. Section 2.4). This ambiguity is resolved by reprocessing the interferometric data takes with the correct ambiguity band.

In assessing the variability, one should moreover take into account that the reference DEMs are by themselves inaccurate. The final calibration of the global DEM will be based on a bundle block adjustment using all overlapping TanDEM-X DEM data takes in combination with an appropriately selected subset of high quality height references which are primarily obtained from the ICESat mission [13,14]. From this, it may be expected that the absolute height accuracy of the globally mosaicked DEM will be significantly better than the required 10 m.

3. Status summary

TanDEM-X was successfully launched into orbit on June 21, 2010. The initial separation between TDX and TSX was 15,700 km and after 1 month of drifting a formation in pursuit monostatic configuration with an along-track distance of 20 km was reached [17]. This formation was maintained for 3 months to calibrate the TanDEM-X radar instruments and to perform first bistatic and interferometric experiments employing large baselines (cf. Section 4). On October 14, both satellites were maneuvered into a close formation to start the bistatic commissioning phase. During this phase, the radial and cross-track baselines were kept constant at 360 and 400 m, respectively, and the mean along-track distance was set to 0 m. The results from both the mono- and bistatic commissioning phase already demonstrated the unique interferometric performance of TanDEM-X [7]. Fig. 15 shows as an example two TanDEM-X DEMs that have been acquired during the commissioning phase.

Operational DEM acquisition started on December 12, 2010, less than 6 months after satellite launch. Since then, the total landmass of the Earth (except the Antarctic region) has been mapped once with a height of ambiguity ranging from 40 to 60 m. Fig. 16 shows as an example the color-coded relative height error derived from the coherence of this first global acquisition. Global DEM data acquisition with varying baselines will continue until 2014, mapping difficult terrain like mountains, valleys, tall vegetation, etc., with at least two heights of ambiguity as well as from multiple incidence/aspect angles. The latter will be achieved by swapping the Helix formation. This allows for a shift of the DEM acquisition quadrants from ascending to descending orbits in the northern hemisphere and vice versa in the southern hemisphere. First parts of the global TanDEM-X DEM will become available in 2014.

Ongoing work includes continuous performance monitoring and verification [18–21], the acquisition for the remaining DEM data takes with optimized imaging geometries [22], multibaseline interferometric processing [23,24], the final implementation, test and validation of the mosaicking and calibration processor [25], as well as the planning and conduction of bistatic and multistatic radar experiments within the science service segment [26].

4. TanDEM-X experiments

TanDEM-X provides the remote sensing scientific community not only with a global DEM of unprecedented accuracy, but also with a unique reconfigurable SAR system to demonstrate novel bistatic and multistatic radar techniques for enhanced bio- and geophysical parameter retrieval. The following subsections summarize some of the advanced capabilities of TanDEM-X which can be operated in a multitude of modes and configurations [3]. Most of the provided results were already obtained during the TanDEM-X commissioning phase. The main intention of this section is to give the reader an impression of the manifold capabilities of future formation-flying SAR missions to serve novel remote sensing applications. A complete description of the experiments and a detailed discussion of their results can be found in the provided references.

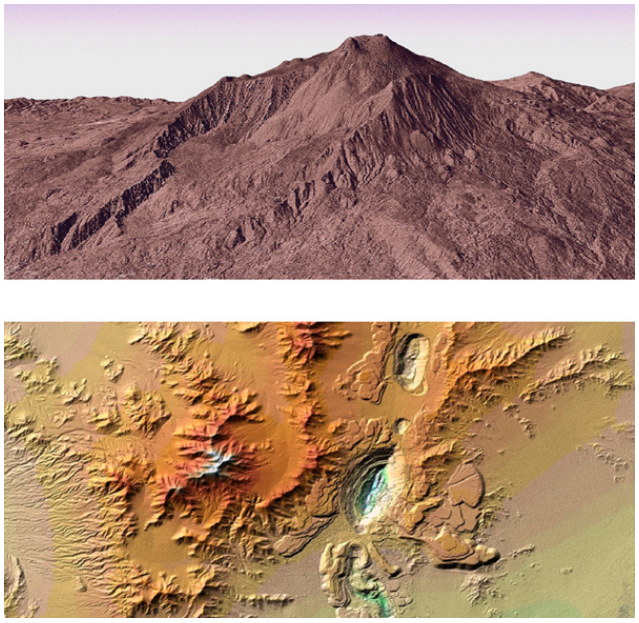

Fig. 15. Examples of digital elevation models (DEMs) acquired by TanDEM-X. Top: Italian volcano Etna, located on the east coast of Sicily. Bottom: Chuquicamata, the biggest copper mine in the world, located in the north of Chile.

4.1. Velocity measurements from space

TanDEM-X has the capability to provide highly accurate velocity measurements of moving objects within a large coverage area. This can be achieved by comparing the amplitude and phase of two SAR images acquired at slightly different times (Fig. 17). By adjusting the along-track displacement between the TDX and TSX satellites from almost zero to several tens of kilometres, TanDEM-X can adapt its sensitivity to a broad spectrum of velocities ranging from less than a millimetre per second to more than hundred kilometres per hour. The Helix satellite formation employed by TanDEM-X enables even a minimization of the effective across-track baseline for a given latitude and incident angle, thereby reducing the complexity in the velocity estimation process. Along-track interferometry can furthermore be enhanced by the so-called dual-receive antenna mode in each of the two tandem satellites, which provides additional phase centers separated by a short along-track baseline of 2.4 m. The combination of short and long baseline SAR data acquisitions improves both the detection and localization of moving objects and resolves phase ambiguities in case of fast

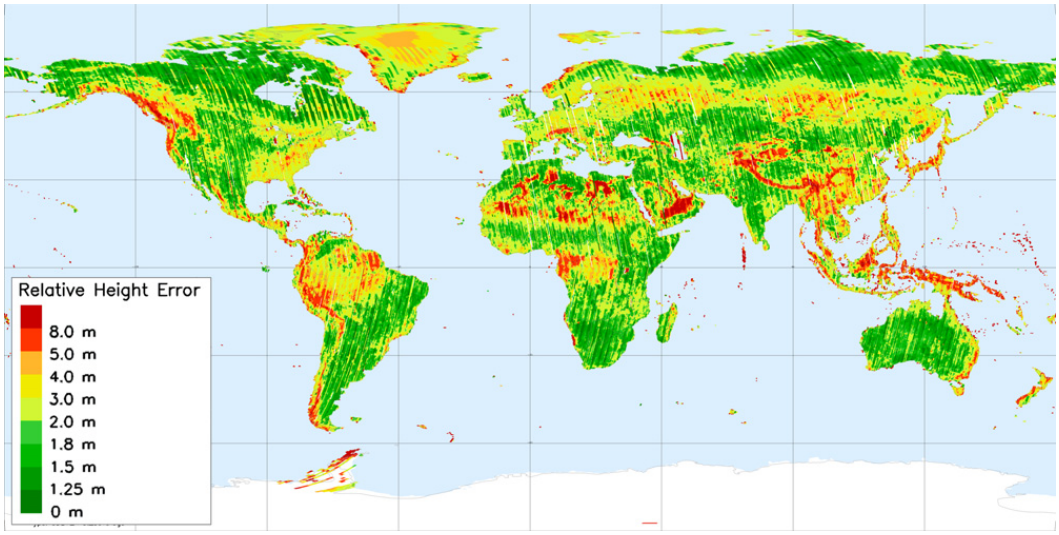

Fig. 16. Relative height error for the first global acquisition. Green colors indicate areas where the height error is already within the 2 m requirement, yellow parts will improve with the second coverage, difficult terrain appears in red and will require additional acquisitions in the opposite viewing geometry.

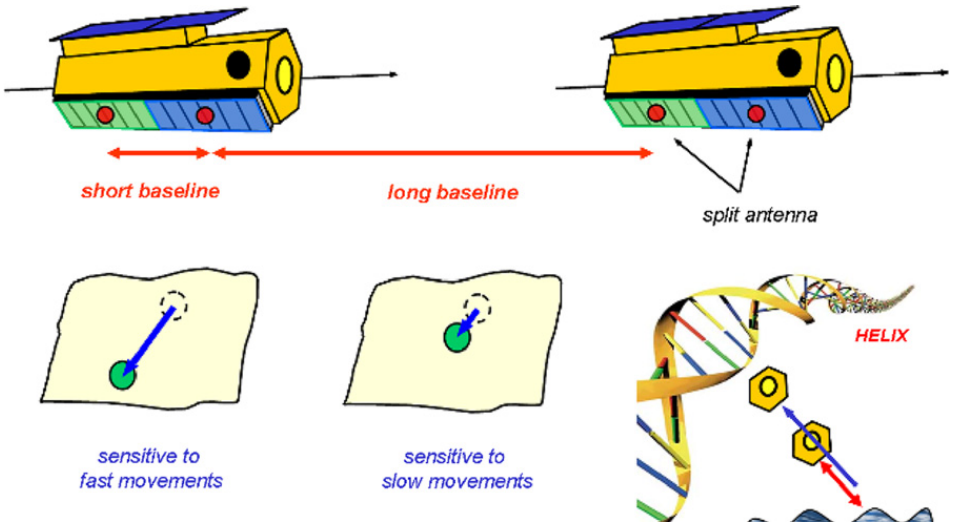

Fig. 17. Velocity measurements with TanDEM-X. The Helix satellite formation allows a flexible adjustment of the desired along-track separation between the satellites. In addition, a short along-track baseline is provided by each satellite.

scatterers. TanDEM-X provides hence a unique SAR system with four phase centers separated in the along-track direction. Potential applications are ground moving target indication (GMTI), the measurement of ocean surface currents, as well as the monitoring of sea ice drift and rotation.

Fig. 18 shows as a first example the observation of ship movements in the Strait of Gibraltar [27]. The data were acquired during the monostatic commissioning phase where the satellites had an along-track separation of 20 km. This separation corresponds to a time lag of 2.6 s. The 2-D velocity vector could be measured with an accuracy of 1 km/h by comparing the ship positions in the TSX and TDX SAR images (cf. [27] for details). The velocity measurements have been validated with independent data obtained from the automatic identification system (AIS).

4.2. Large baseline cross-track interferometry

Large baseline interferometry takes advantage of the high RF bandwidth of the TSX and TDX satellites, allowing for coherent data acquisitions with cross-track baselines of 5 km and more. Note that less than 5% of the maximum possible (critical) baseline length is used during nominal DEM data acquisition. Large baseline interferograms can hence significantly improve the height accuracy beyond the standard TanDEM-X DEM quality, but the associated low height of ambiguity requires typically a combination of multiple interferograms with different baseline lengths to resolve phase ambiguities, especially in hilly and mountainous terrain. Further opportunities arise from a comparison of multiple large baseline TanDEM-X interferograms acquired during different passes of the satellite formation (Fig. 19). This provides a sensitive measure for vertical scene and structure changes. Potential applications are a detection of the grounding line which separates the shelf from the inland ice in polar regions, monitoring of vegetation growth, mapping of atmospheric water vapor with high spatial resolution, measurement of snow accumulation or the detection of anthropogenic changes of the environment, e.g. due to deforestation. Note that most of these combinations rely on a comparison of two or more single-pass (large baseline) cross-track interferograms and hence do not require coherence between the different passes. Further information can be gained from an evaluation of coherence changes, potentially augmented by polarimetric information. This is, for instance, well suited to reveal even slight changes in the soil and vegetation structure reflecting vegetation growth and loss, freezing and thawing, fire destruction, human activities, and so on. The combination of repeated TanDEM-X single-pass interferograms enables therefore the entry into a new era of interferometric and tomographic 3-D and 4-D SAR imaging as it was the case with ERS-1/2 for the development of classical repeat-pass SAR interferometry.

Fig. 20 shows as a first example a large baseline DEM acquired by TanDEM-X on July 16, 2010, in the Russian Arctic (October Revolution Island) [28]. The DEM was part of a longer data take that used a sophisticated commanding to obtain a large baseline interferogram while TDX was still drifting towards TSX from its initial along-track separation of 15,700 km. At the time of data acquisition, the two satellites were 380 km apart from each other, resulting in a temporal separation of 50 s. Earth rotation caused a cross-track baseline of 2 km which corresponds to a height of ambiguity of only 3.8 m. A squinted operation was necessary to provide a sufficient overlap of the Doppler spectra. The lower part of Fig. 12 shows the predicted (blue curve) and estimated (green curve) standard deviation of the point-to-point relative height error for a linear slice through the DEM. The predicted error was calculated from the coherence measurements and the estimated error was obtained by high-pass filtering the DEM slice as explained in [28]. Both results show that the height accuracy is in the order of 20 cm. This demonstrates the great potential of formation-flying SAR missions to obtain repeated high-resolution elevation

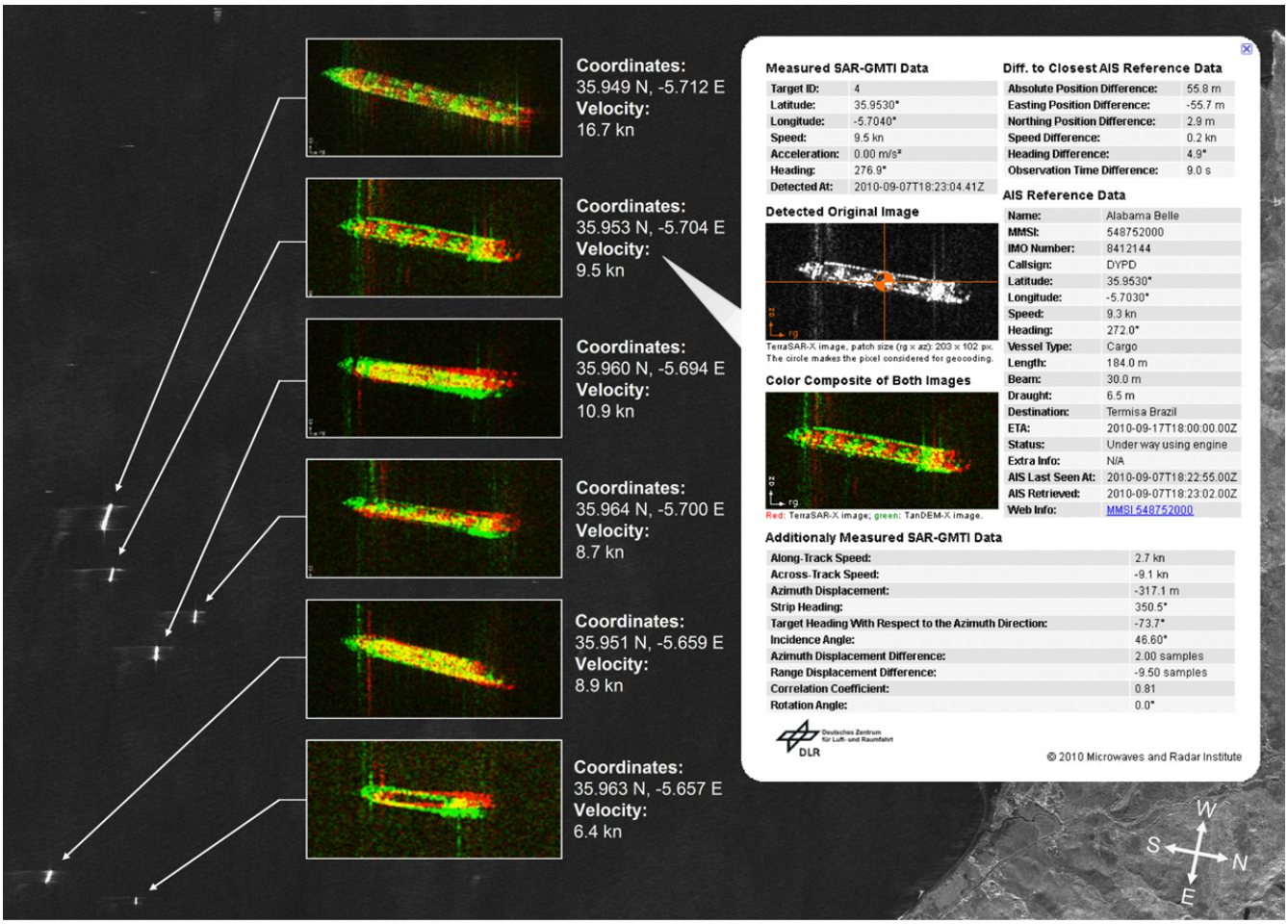

Fig. 18. Ship movements observed with TanDEM-X during the monostatic commissioning phase. The ship displacements can be seen from the insets showing TSX (red) and TDX (green) image patches overlaid in different colors. The estimated velocities are in excellent agreement with AIS reference data (right inset, cf. [27] for more details).

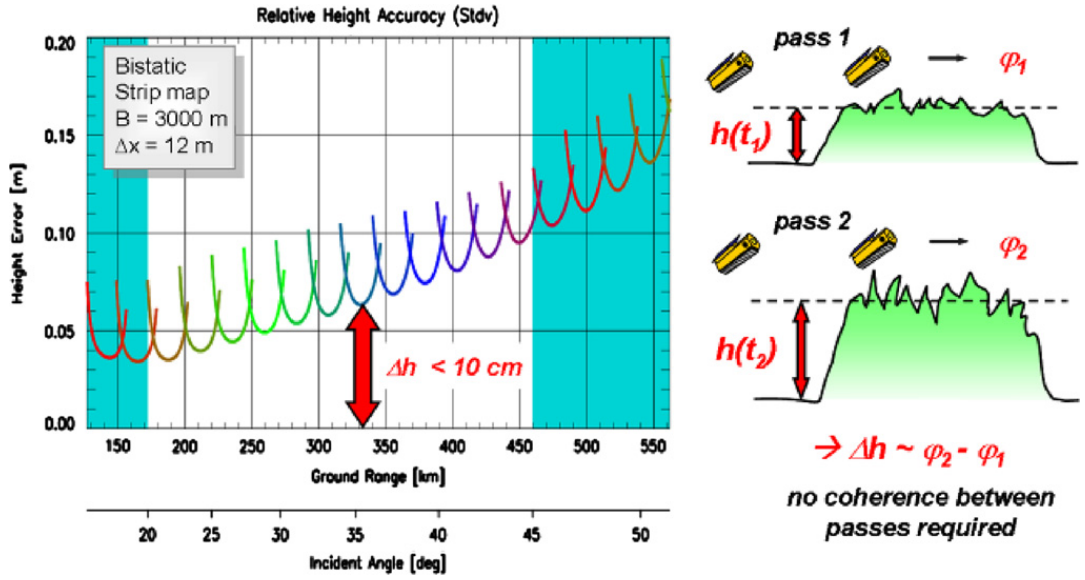

Fig. 19. Performance estimation for large baseline DEM acquisitions with TanDEM-X (cross-track baseline = 3000 m, posting = 12 m). A relative height accuracy (single point standard deviation) better than 10 cm is predicted.

information with decimetre accuracy, thereby enabling new remote sensing applications. A possible application is the systematic monitoring of height changes over glaciers, ice caps and ice sheets to quantify their ice mass balance. A dedicated SAR mission has already been proposed for this purpose [29].

4.3. Polarimetric SAR interferometry

Polarimetric SAR interferometry (Pol-InSAR) combines coherently single- or multi-baseline interferograms acquired at different polarizations to gain 3-D structure information from semi-transparent volume scatterers [30]. A prominent example is the measurement of vegetation structure parameters as forest height and layering. TanDEM-X is the first single-pass polarimetric radar interferometer in space that allows the acquisition and analysis of dual- and quad-pol InSAR data without the disturbing effect of temporal decorrelation. X-band has – when compared to lower frequencies – a reduced penetration capability into or through vegetation layers. TanDEM-X experiments nevertheless demonstrated sufficient penetration under sparse forest conditions [31,32]. This penetration is associated with a sensitivity of X-band interferometric measurements to forest vertical structure attributes as well as to their seasonal variation and allows the use of TanDEM-X data for forest monitoring applications in the boreal ecosystem.

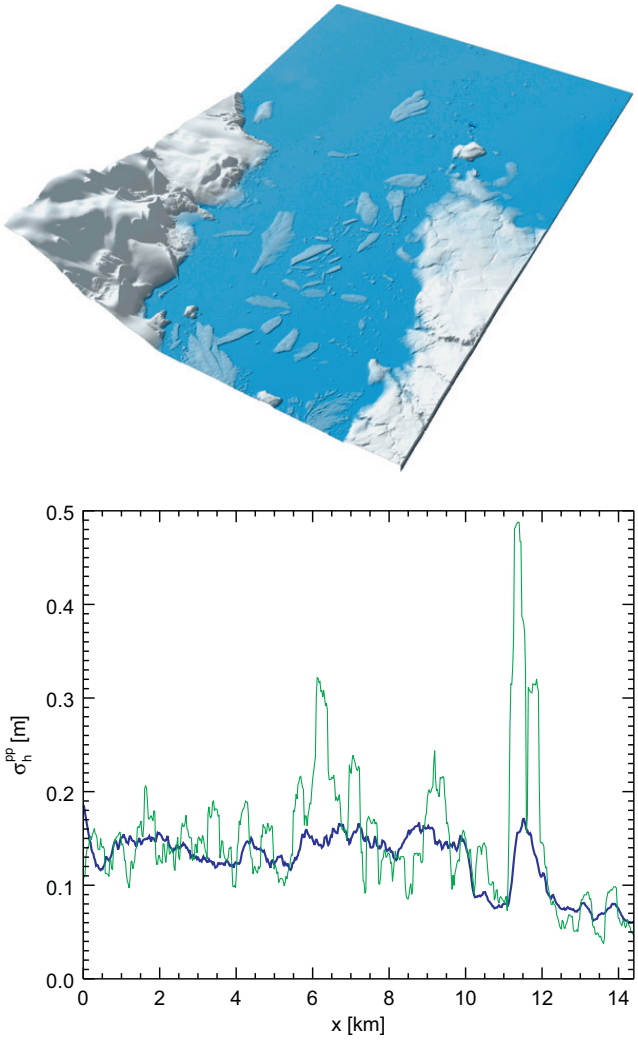

Fig. 20. Large baseline TanDEM-X DEM from the border of October Revolution island (top) and predicted (blue) vs. estimated (green) point-to-point height accuracy along a DEM slice (cf. [28] for details). (For interpretation of the references to color in this figure caption, the reader is referred to the web version of this article.)

Fig. 21 shows on the right a forest height map derived from TanDEM-X Pol-InSAR data and compares it with the one obtained from airborne lidar measurements (shown on the left). The correlation between the two forest height maps is about 90% and the standard deviation on the order of 1.5 m. The ability to estimate forest height in terms of TanDEM-X Pol-InSAR techniques is of course limited by the penetration depth at X-band that decreases with increasing attenuation, i.e. with increasing (electromagnetic) density of the forest. Accordingly, in denser forest conditions the penetration depth decreases so that the interferometer is no longer able to "see" the whole volume and the height estimation "saturates". In this sense, a future formation-flying SAR mission dedicated to global forest monitoring has to be operated in a lower frequency band [33].

When it comes to agriculture vegetation, higher frequencies like X-band are favored as they provide more balanced volume and ground scattering contributions and allow therefore a better volume characterization. Fig. 22 shows as a first example the height differences obtained for a dual-polarized TanDEM-X spotlight acquisition of an agricultural field in Russia. The data were acquired during the monostatic commissioning phase with a perpendicular baseline of 275 m, demonstrating the potential of Pol-InSAR for crop height estimation. Current and future experiments will also combine multiple interferometric data takes acquired in dual and fully polarimetric modes [31,32].

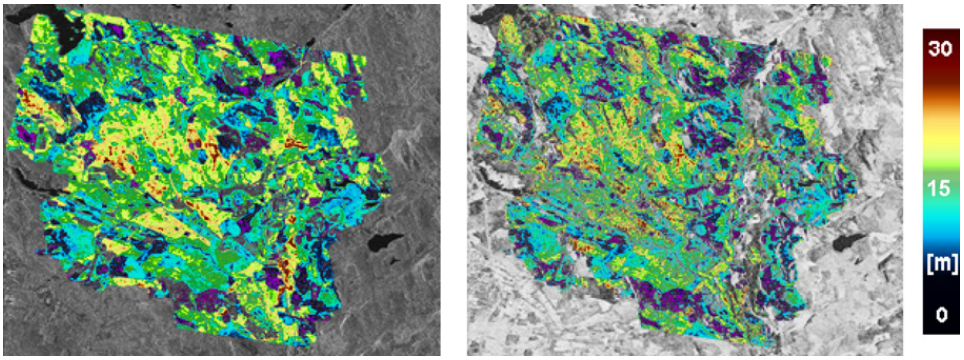

Fig. 21. Forest height maps, Kryclan test site, Sweden. Left: Lidar forest height map superimposed on X-band radar amplitude image. Right: Pol-InSAR derived forest height superimposed on interferometric coherence image scaled from 0 (black) to 1 (white).

4.4. Bistatic SAR imaging

Bistatic SAR imaging provides additional observables for the extraction of important scene and target parameters. TanDEM-X allows for the simultaneous acquisition of bistatic and monostatic images in a single data take to obtain a highly informative set of multi-angle observations. A quantitative evaluation of the bistatic radar cross-section (RCS) and a comparison with its monostatic equivalent facilitate the detection and recognition of targets. The segmentation and classification in radar images are expected to be improved by comparing the spatial statistics of mono- and bistatic scattering coefficients. This is supported by airborne bistatic radar experiments performed by DLR and ONERA, which revealed significant changes of the scattering behavior for both artificial and natural targets even in case of rather small bistatic angles [34]. A joint evaluation of mono- and bistatic SAR images could also be used to isolate different scattering mechanisms. An example is the distinction between highly directive dihedral returns from more isotropic volume scattering. Bistatic SAR has moreover potential for the retrieval of sea state parameters, the estimation of surface roughness and terrain slope, as well as stereogrammetric, meteorological and atmospheric applications [35,36]. The bistatic data acquired with TanDEM-X will hence provide a unique data source to improve our understanding of bistatic SAR imaging and its exploitation for future remote sensing applications. A first bistatic data take has been acquired over Brasilia, Brazil, during the monostatic

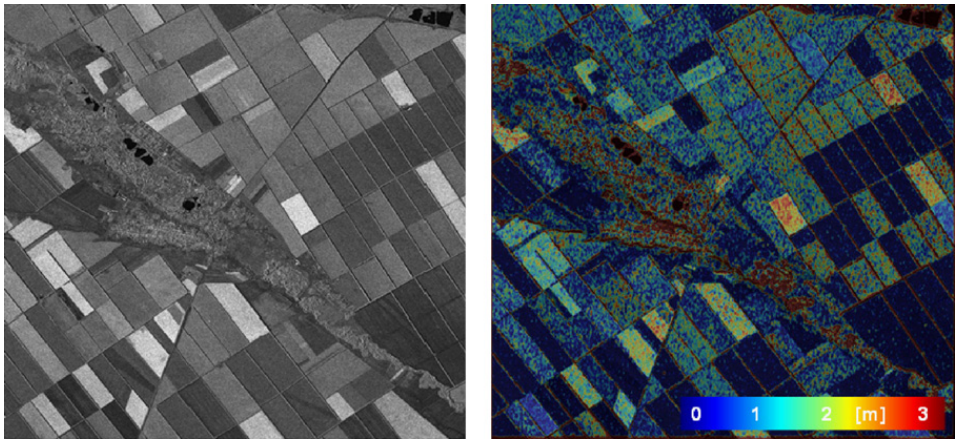

Fig. 22. Polarimetric SAR interferometry with TanDEM-X. Left: amplitude of SAR image. Right: interferometric height difference between HH and VV channels.

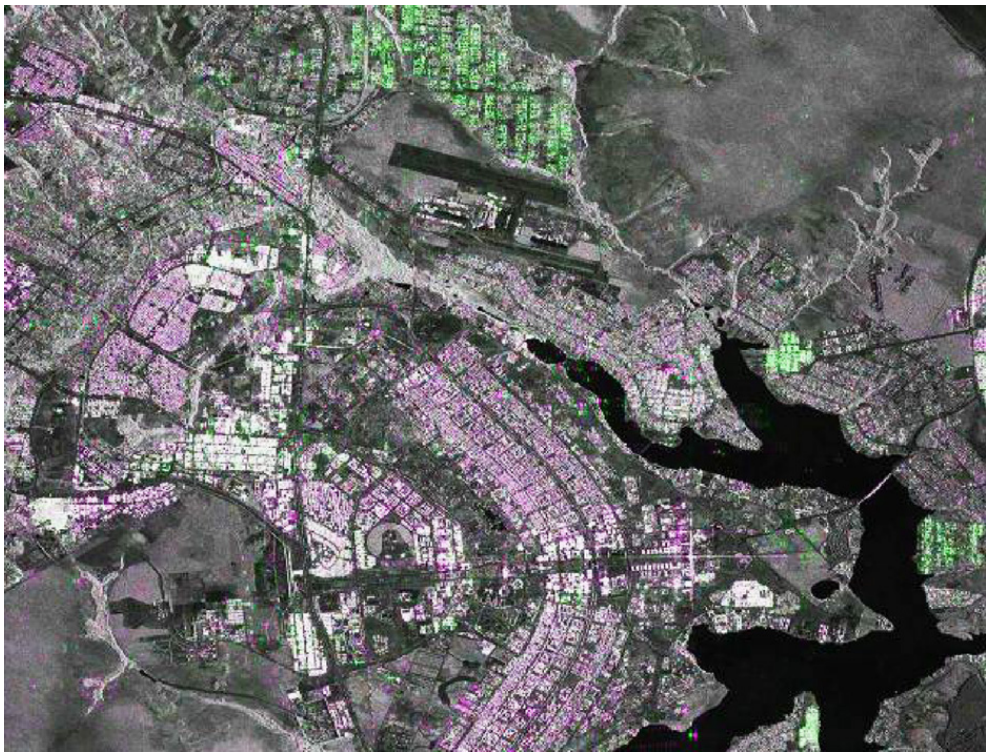

Fig. 23. Overlay of monostatic (magenta) and bistatic (green) SAR image. The images show Brasilia, Brazil.

commissioning phase where the satellites were separated by 20 km. Fig. 23 shows an overlay of the bistatic SAR image with its monostatic counterpart demonstrating significant scattering differences already for very small bistatic angles [37].

5. Conclusions

The TanDEM-X mission opens a new era in spaceborne radar remote sensing. A large single-pass SAR interferometer with adjustable baselines has been formed by adding a second, almost identical radar satellite to TerraSAR-X and flying both satellites in a closely controlled formation. This enables not only the acquisition of a global DEM with unprecedented accuracy, but also the demonstration of highly innovative bistatic and multistatic SAR techniques and applications. These experiments form the basis for future formation-flying SAR missions [38,39].

Key technologies like close formation flying, bistatic SAR operation and synchronization, precise baseline estimation and calibration as well as sophisticated bistatic and interferometric processing chains have been implemented. Appropriate safety mechanisms enable safe operation at satellite distances as close as 150 m. The complete mission is fully operational since December 2010 and both satellites as well as the ground system perform remarkably well. The global DEM with a relative height accuracy of 2 m will be available by the end of 2014. It is expected that this global DEM will become a new reference for commercial (http://www.astrium-geo.com/en/168-tandem-x-global-dem) and scientific applications (www.dlr.de/HR/tandem-x) since it is at least 30 times more accurate than the presently available global scale DEM data set. Current fuel consumption and battery degradation on the TerraSAR-X satellite are well below specification and will probably permit lifetime extensions of at least 2 years, i.e. close formation flying until 2015 seems feasible. The prolonged mission time can be used for additional DEM acquisitions with improved accuracy and resolution as well as for the conduction of advanced bistatic and multistatic SAR experiments in unique configurations, modes and geometries.

Acknowledgment

We highly acknowledge the great effort and enthusiasm of all our colleagues at DLR and EADS Astrium who made this ambitious mission a reality. TanDEM-X is partly funded by the German Federal Ministry for Economics and Technology (50 EE 1035) and realized in a public–private partnership between German Aerospace Center (DLR) and Astrium GmbH.

References

[1] A. Moreira, G. Krieger, I. Hajnsek, M. Werner, D. Hounam, S. Riegger, E. Settelmeyer, TanDEM-X: a TerraSAR-X add-on satellite for single-pass SAR interferometry, in: International Geoscience and Remote Sensing Symposium (IGARSS), Anchorage, USA, 2004.
[2] R. Werninghaus, S. Buckreuss, The TerraSAR-X mission and system design, IEEE Trans. Geosci. Remote Sens. 48 (No. 2) (2010) 606–614.
[3] G. Krieger, A. Moreira, H. Fiedler, I. Hajnsek, M. Werner, M. Younis, M. Zink, TanDEM-X: a satellite formation for high resolution SAR interferometry, IEEE Trans. Geosci. Remote Sens. 45 (No. 11) (2007) 3317–3341.
[4] W. Pitz, D. Miller, The TerraSAR-X satellite, IEEE Trans. Geosci. Remote Sens. 48 (No. 2) (2010) 615–622.
[5] G. Krieger, M. Younis, Impact of oscillator noise in bistatic and multistatic SAR, IEEE Geosci. Remote Sens. Lett. 3 (2006) 424–428.
[6] M. Younis, R. Metzig, G. Krieger, Performance prediction of a phase synchronization link for bistatic SAR, IEEE Geosci. Remote Sens. Lett. 3 (2006) 429–433.
[7] P. Rizzoli et al., Interferometric performance, Presentation at TanDEM-X Science Meeting, Oberpfaffenhofen, Germany, February 17, 2011, available online at http://www.dlr.de/Portaldata/32/Resources/dokumente/tdmx/sciencemeeting3/08-Interferometric_Performance_Handout_small.pdf.
[8] G. Krieger, F. de Zan, Relativistic effects in bistatic SAR processing and system synchronization, in: European Conference on Synthetic Aperture Radar (EUSAR), Nuremberg, Germany, 2012.
[9] P. Rizzoli, B. Bräutigam, T. Kraus, M. Martone, G. Krieger, Relative height error analysis of TanDEM-X elevation data, ISPRS J. Photogrammet. Remote Sens. 73 (2012) 30–38.
[10] M. Wermuth, O. Montenbruck, A. Wendleder, Relative navigation for the TanDEM-X mission and evaluation with DEM calibration results, in: 22nd International Symposium on Spaceflight Dynamics, Sao Jose dos Campos, Brazil, 2011.
[11] J. Hueso González, J. Walter Antony, M. Bachmann, G. Krieger, M. Zink, D. Schrank, M. Schwerdt, Bistatic system and baseline calibration in TanDEM-X to ensure the global digital elevation model quality, ISPRS J. Photogrammet. Remote Sens. 38 (2012) 3–11.
[12] M. Bachmann, J. Hueso Gonzalez, G. Krieger, M. Schwerdt, J. Walter Antony, F. De Zan, Calibration of the bistatic TanDEM-X interferometer, in: European Conference on Synthetic Aperture Radar (EUSAR), Nuremberg, Germany, 2012.
[13] J. Hueso Gonzalez, M. Bachmann, G. Krieger, H. Fiedler, Development of the TanDEM-X calibration concept: analysis of systematic errors, IEEE Trans. Geosci. Remote Sens. 48 (No. 2) (2010) 716–726.
[14] A. Gruber, B. Wessel, M. Huber, A. Roth, Operational TanDEM-X DEM calibration and first validation results, ISPRS J. Photogrammet. Remote Sens. 38 (2012) 39–49.
[15] T.G. Farr, P. Rosen, E. Caro, R. Crippen, R. Duren, S. Hensley, M. Kobrick, M. Paller, E. Rodriguez, L. Roth, D. Seal, S. Shaffer, J. Shimada, J. Umland, M. Werner, M. Oskin, D. Burbank, D. Alsdorf, The shuttle radar topography mission, Rev. Geophys. 45 (2007).
[16] B. Schutz, H. Zwally, C. Shuman, D. Hancock, J. DiMarzio, Overview of the ICESat mission, Geophys. Res. Lett. 32 (No. 21) (2005).
[17] R. Kahle, B. Schlepp, F. Meissner, M. Kirschner, R. Kiehling, TerraSAR-X/ TanDEM-X formation acquisition—analysis and flight results, in: 21st AAS/AIAA Space Flight Mechanics Meeting, New Orleans, LA, 2011.
[18] M. Martone, B. Bräutigam, P. Rizzoli, C. Gonzalez, M. Bachmann, G. Krieger, Coherence evaluation of TanDEM-X interferometric data, ISPRS J. Photogrammet. Remote Sens. 38 (2012) 21–29.
[19] B. Bräutigam, P. Rizzoli, M. Martone, M. Bachmann, T. Kraus, G. Krieger, InSAR and DEM quality monitoring of TanDEM-X, in: International Geoscience and Remote Sensing Symposium (IGARSS), Munich, Germany, 2012.
[20] M. Villano, G. Krieger, Impact of azimuth ambiguities on interferometric performance, IEEE Geosci. Remote Sens. Lett. 9 (No. 5) (2012) 896–900.
[21] F. De Zan, G. Krieger, P. Lopez Dekker, On some spectral properties of TanDEM-X interferograms over forested areas, IEEE Geosci. Remote Sens. Lett. 10 (No. 1) (2013) 71–75.
[22] M. Bachmann, D. Schulze, C. Ortega Miguez, D. Polimeni, J. Böer, J. Hueso Gonzalez, J. Walter Antony, G. Krieger, B. Bräutigam, M. Schwerdt, M. Zink, TanDEM-X acquisition status and calibration of the interferometric system, in: International Geoscience and Remote Sensing Symposium (IGARSS), Munich, Germany, 2012.
[23] T. Fritz, H. Breit, C. Rossi, U. Balss, M. Lachaise, S. Duque, Interferometric processing and products of the TanDEM-X mission, in: International Geoscience and Remote Sensing Symposium (IGARSS), Munich, Germany, 2012.
[24] M. Lachaise, U. Balss, T. Fritz, H. Breit, The dual-baseline interferometric processing chain for the TanDEM-X mission, in: International Geoscience and Remote Sensing Symposium (IGARSS), Munich, Germany, 2012.
[25] A. Gruber, B. Wessel, M. Huber, M. Breunig, S. Wagenbrenner, A. Roth, Quality assessment of first larger TanDEM-X DEM blocks, in: International Geoscience and Remote Sensing Symposium (IGARSS), Munich, Germany, 2012.

[26] I. Hajnsek, T. Busche, TanDEM-X: science activities, in: International Geoscience and Remote Sensing Symposium (IGARSS), Munich, Germany, 2012.
[27] S. Baumgartner, G. Krieger, Large along-track baseline SAR-GMTI: first results with the TerraSAR-X/TanDEM-X satellite constellation, in: International Geoscience and Remote Sensing Symposium (IGARSS), Vancouver, Canada, 2011.
[28] P. Lopez-Dekker, P. Prats, F. De Zan, D. Schulze, G. Krieger, A. Moreira, TanDEM-X first DEM acquisition: a crossing orbit experiment, IEEE Geosci. Remote Sens. Lett. 8 (No. 5) (2011) 943–947.
[29] T. Börner, F. De Zan, P. López-Dekker, G. Krieger, I. Hajnsek, K. Papathanassiou, M. Villano, M. Younis, A. Danklmayer, W. Dierking, T. Nagler, H. Rott, S. Lehner, T. Fügen, A. Moreira, SIGNAL: SAR for ice, glacier and global dynamics, in: International Geoscience and Remote Sensing Symposium (IGARSS), Honolulu, Hawaii, 2010.
[30] S. Cloude, K. Papathanassiou, Polarimetric SAR interferometry, IEEE Trans. Geosci. Remote Sens. 36 (1998) 1551–1565.
[31] F. Kugler, I. Hajnsek, K. Papathanassiou, Dual Pol-InSAR forest height estimation by means of TanDEM-X data, in: International Geoscience and Remote Sensing Symposium (IGARSS), Munich, Germany, 2012.
[32] K. Papathanassiou, F. Kugler, I. Hajnsek, Exploring the potential of Pol-InSAR techniques at X-band: results and experiments from TanDEM-X, in: International Geoscience and Remote Sensing Symposium (IGARSS), Munich, Germany, 2012.
[33] A. Moreira, I. Hajnsek, G. Krieger, K. Papathanassiou, M. Eineder, F. De Zan, M. Younis, M. Werner, Tandem-L: monitoring the Earth's dynamics with InSAR and Pol-InSAR, in: International Workshop on Applications of Polarimetry and Polarimetric Interferometry (Pol-InSAR), Frascati, Italy, 2009.
[34] P. Dubois-Fernandez, H. Cantalloube, B. Vaizan, G. Krieger, R. Horn, M. Wendler, V. Giroux, ONERA-DLR bistatic SAR campaign: planning, data acquisition, and first analysis of bistatic scattering behavior of natural and urban targets, IEE Proceedings: Radar, Sonar Navigation 153 (2006) 214–223.
[35] A. Moccia, N. Chiacchio, A. Capone, Spaceborne bistatic synthetic aperture radar for remote sensing applications, Int. J. Remote Sens. 21 (2000) 3395–3414.
[36] G. Krieger, A. Moreira, Spaceborne bi- and multistatic SAR: potential and challenges, IEE Proceedings: Radar, Sonar and Navigation 153 (2006) 184–198.
[37] M. Rodriguez-Cassola, P. Prats, D. Schulze, N. Tous-Ramon, U. Steinbrecher, L. Marotti, M. Nannini, M. Younis, P. Lopez-Dekker, M. Zink, A. Reigber, G. Krieger, A. Moreira, First bistatic spaceborne SAR experiments with TanDEM-X, IEEE Geosci. Remote Sens. Lett. 9 (No. 1) (2012) 33–37.
[38] M. D'Errico, Distributed Space Missions for Earth System Monitoring, Springer, New York, 2013.
[39] G. Krieger, I. Hajnsek, K. Papathanassiou, M. Younis, A. Moreira, Interferometric synthetic aperture radar (SAR) missions employing formation flying, Proceedings of the IEEE 58 (No. 5) (2010) 816–843.